

Transactions of the ASME®

Editor
LEE S. LANGSTON (2006)
Assistant to the Editor
LIZ LANGSTON
Associate Editors
Advanced Energy Systems
G. REISTAD (2005)
Fuels and Combustion Technologies
S. GOLLAHALLI (2004)
Internal Combustion Engines
D. ASSANIS (2005)
Nuclear
R. DUFFY (2004)
International Gas Turbine Institute
IGTI Review Chair
R. NATOLE (2001)
E. BENVENUTI (2002)
H. R. SIMMONS (2003)
Combustion and Fuels
P. MALTE (2003)
Structures and Dynamics
N. ARAKERE (2004)
M. MIGNOLET (2005)

BOARD ON COMMUNICATIONS
Chair and Vice-President
OZDEN OCHOA

OFFICERS OF THE ASME
President, **S. H. SKEMP**
Executive Director, **V. R. CARTER**
Treasurer, **R. E. NICKELL**

PUBLISHING STAFF
Managing Director, Engineering
THOMAS G. LOUGHLIN
Director, Technical Publishing
PHILIP DI VIETRO
Managing Editor, Technical Publishing
CYNTHIA B. CLARK
Manager, Journals
JOAN MERANZE
Production Coordinator
JUDITH SIERANT
Production Assistant
MARISOL ANDINO

Transactions of the ASME, Journal of Engineering for Gas Turbines and Power (ISSN 0742-4795) is published quarterly (Jan., April, July, Oct.) by The American Society of Mechanical Engineers, Three Park Avenue, New York, NY 10016. Periodicals postage paid at New York, NY and additional mailing offices. POSTMASTER: Send address changes to Transactions of the ASME, Journal of Engineering for Gas Turbines and Power, c/o THE AMERICAN SOCIETY OF MECHANICAL ENGINEERS, 22 Law Drive, Box 2300, Fairfield, NJ 07007-2300.

CHANGES OF ADDRESS must be received at Society headquarters seven weeks before they are to be effective. Please send old label and new address.

STATEMENT from By-Laws. The Society shall not be responsible for statements or opinions advanced in papers or ... printed in its publications (B7.1, par. 3).

COPYRIGHT © 2003 by the American Society of Mechanical Engineers. For authorization to photocopy material for internal or personal use under circumstances not falling within the fair use provisions of the Copyright Act, contact the Copyright Clearance Center (CCC), 222 Rosewood Drive, Danvers, MA 01923, Tel: 978-750-8400, www.copyright.com.

INDEXED by Applied Mechanics Reviews and Engineering Information, Inc. Canadian Goods & Services Tax Registration #126148048

Journal of Engineering for Gas Turbines and Power

Published Quarterly by The American Society of Mechanical Engineers

VOLUME 125 • NUMBER 2 • APRIL 2003

SPECIAL ISSUE ON INTERNAL COMBUSTION ENGINES

401 Preface

TECHNICAL PAPERS

Injection and Fuel Air Mixture Preparation

402 The Formation of a Combustible Mixture During the First Cycle of Cranking and Startup in a Port-Fuel-Injected Spark-Ignition Engine
J. S. Cowart

412 Parametric Characterization of High-Pressure Diesel Fuel Injection Systems
T.-C. Wang, J.-S. Han, X.-B. Xie, M.-C. Lai, N. A. Henein, E. Schwarz, and W. Bryzik

427 Development of Micro-Diesel Injector Nozzles via Microelectromechanical Systems Technology and Effects on Spray Characteristics
S. Baik, J. P. Blanchard, and M. L. Corradini

435 Effect of Subgrid Modeling on the In-Cylinder Unsteady Mixing Process in a Direct Injection Engine
K. Sone and S. Menon

444 Influence of the Injection Parameters on the Efficiency and Power Output of a Hydrogen Fueled Engine
R. Sierens and S. Verhelst

Auto-ignition and Homogeneous Charge Compression Ignition Engines

450 A Predictive Ignition Delay Correlation Under Steady-State and Transient Operation of a Direct Injection Diesel Engine
D. N. Assanis, Z. S. Filipi, S. B. Fiveland, and M. Syrimis

458 Experimental and Analytical Examination of the Development of Inhomogeneities and Autoignition During Rapid Compression of Hydrogen-Oxygen-Argon Mixtures
K. Chen, G. A. Karim, and H. C. Watson

466 Homogeneous Charge Compression Ignition Engine: A Simulation Study on the Effects of Inhomogeneities
P. Maigaard, F. Mauss, and M. Kraft

472 Characteristics of Homogeneous Charge Compression Ignition (HCCI) Engine Operation for Variations in Compression Ratio, Speed, and Intake Temperature While Using n-Butane as a Fuel
M. Iida, M. Hayashi, D. E. Foster, and J. K. Martin

Spark Ignition Engine Combustion

479 Modeling the Initial Growth of the Plasma and Flame Kernel in SI Engines
H. Willems and R. Sierens

485 An Investigation of Flame Expansion Speed With a Strong Swirl Motion Using High-Speed Visualization
S. H. Joo, K. M. Chun, Y. Shin, and K. C. Lee

494 Knocking Cylinder Pressure Data Characteristics in a Spark-Ignition Engine
M. Syrimis and D. N. Assanis

(Contents continued on inside back cover)

This journal is printed on acid-free paper, which exceeds the ANSI Z39.48-1992 specification for permanence of paper and library materials. ♻️™
♻️ 85% recycled content, including 10% post-consumer fibers.

- 500 Knock Rating of Gaseous Fuels
A. A. Attar and G. A. Karim

Emissions

- 505 Development of the Low-Emission GE-7FDL High-Power Medium-Speed Locomotive Diesel Engine
G. Chen, P. L. Flynn, S. M. Gallagher, and E. R. Dillen
- 513 Exhaust Particulate Matter Emission Factors and Deterioration Rate for In-Use Motor Vehicles
B. Ubanwa, A. Burnette, S. Kishan, and S. G. Fritz
- 524 Reduction of NO_x and Particulate Emissions by Using Oxygen-Enriched Combustion Air in a Locomotive Diesel Engine
R. B. Poola and R. Sekar
- 534 A Nonequilibrium Turbulence Dissipation Correction and Its Influence on Pollution Predictions for DI Diesel Engines
F. X. Tanner, G.-S. Zhu, and R. D. Reitz
- 541 Response Surface Method Optimization of a High-Speed Direct-Injection Diesel Engine Equipped With a Common Rail Injection System
T. Lee and R. D. Reitz
- 547 Dynamic Response of Automotive Catalytic Converters to Variations in Air-Fuel Ratio
T. Shamim and V. C. Medisetty

Manifold Gas Dynamics and Turbocharging

- 555 Numerical Analysis of Unsteady Exhaust Gas Flow and Its Application for Lambda Control Improvement
K. Yoshizawa, K. Mori, K. Arai, and A. Iiyama
- 563 Manifold Gas Dynamics Modeling and Its Coupling With Single-Cylinder Engine Models Using Simulink
G. Q. Zhang and D. N. Assanis
- 572 The Use of Neural Nets for Matching Fixed or Variable Geometry Compressors With Diesel Engines
S. A. Nelson II, Z. S. Filipi, and D. N. Assanis
- 580 Investigation of A Large High-Speed Diesel Engine Transient Behavior Including Compressor Surging and Emergency Shutdown
G. Theotokatos and N. P. Kyratos
- 590 Improvement of the Dynamic Characteristic of an Automotive Engine by a Turbocharger Assisted by an Electric Motor
T. Katrašnik, S. Rodman, F. Trenc, A. Hribernik, and V. Medica

Tribology and Wear

- 596 Analysis of Oil Film Thickness on a Piston Ring of Diesel Engine: Effect of Oil Film Temperature
Y. Harigaya, M. Suzuki, and M. Takiguchi
- 604 Effect of Biodiesel Utilization of Wear of Vital Parts in Compression Ignition Engine
A. K. Agarwal, J. Bijwe, and L. M. Das

ERRATA

- 612 "Schlieren Observation of Spark-Ignited Premixed Charge Combustion Phenomena Using a Transparent Collimating Cylinder Engine"
K. Kozuka, T. Ozasa, T. Fujikawa, and A. Saito

The ASME Journal of Engineering for Gas Turbines and Power is abstracted and indexed in the following:

AESIS (Australia's Geoscience, Minerals, & Petroleum Database), Applied Science & Technology Index, AMR Abstracts Database, Aquatic Sciences and Fisheries Abstracts, Civil Engineering Abstracts, Compendex (The electronic equivalent of Engineering Index), Computer & Information Systems Abstracts, Corrosion Abstracts, Current Contents, Engineered Materials Abstracts, Engineering Index, Enviroline (The electronic equivalent of Environment Abstracts), Environment Abstracts, Environmental Science and Pollution Management, Fluidex, INSPEC, Mechanical & Transportation Engineering Abstracts, Mechanical Engineering Abstracts, METADEX (The electronic equivalent of Metals Abstracts and Alloys Index), Pollution Abstracts, Referativnyi Zhurnal, Science Citation Index, SciSearch (The electronic equivalent of Science Citation Index), Shock and Vibration Digest

Special ICE Issue

Almost one and a half centuries since it became a practical reality, the Internal Combustion Engine (ICE) remains today the vastly dominant fuel energy converter in our society. The reasons for the ICE dominance in on and off-road vehicles, railroad, marine, home use, stationary power generation and some aircraft applications are its low specific cost, high power density, robustness, versatility, and fuel flexibility. Indeed, the internal combustion engine has met all performance, fuel economy and emissions requirements to date, and is well matched to available fuels.

Nevertheless, with ever increasing socio-economic pressures for developing yet cleaner and more efficient means for converting the chemical fuel energy into useful work, the ICE is facing emerging competition from hybrid power systems and fuel cells. In response to these new challenges, opportunities lie ahead to enhance dramatically the execution of the fundamental processes in the engine cylinder and to optimize design and system integration to meet new targets. The intensifying global research activities have resulted in a large number of technical papers, presented at the Fall and Spring Technical Conferences organized by the ICE Division of the ASME, which have dealt with both the basic thermo-fluid processes and various aspects of engine design.

This special issue of the *ASME Journal of Engineering for Gas*

Turbines and Power is devoted to a selection of the highest quality papers presented at ASME-ICE meetings, and other papers of long-term reference value, which were submitted directly to the Journal. The papers have been arranged in the following topical areas: Injection and Fuel-Air Mixture Preparation, Auto-ignition and Homogeneous Charge Compression Ignition Engines, Spark Ignition Engine Combustion, Emissions, Manifold Gas Dynamics and Turbocharging, Tribology and Wear. The papers make significant contributions to enhance our understanding of the fundamentals and apply them to design of advanced systems using sophisticated modeling and experimental techniques. The contributions of the authors, the anonymous referees, and the ICE Engine Division Associates, Conference and Session Organizers are gratefully acknowledged.

I want to end this preface with a special word of appreciation and thanks to Lee Langston, our Journal Editor for his encouragement to pursue this worthwhile project, and to Judy Sierant and her ASME staff for working diligently to make this special issue happen.

Dennis N. Assanis

Associate Editor

Internal Combustion Engines

The Formation of a Combustible Mixture During the First Cycle of Cranking and Startup in a Port-Fuel-Injected Spark-Ignition Engine

J. S. Cowart

Department of Mechanical Engineering,
University of Connecticut,
Storrs, CT 06269-3139

As automotive engine emission standards continue to become more stringent, excellent cranking, and startup fuel control will become imperative in order to achieve minimum engine-out emissions. Optimized engine starting requires the generation of a strong first firing cycle. Fortunately, an engine's first cycle event is physically less complex than future engine cycles, providing the opportunity for accurate modeling. A physically based crank mixture preparation model coupled with a multicomponent fuel model was developed to provide insights into the fuel vapor generation process during the first cycle of engine starting. Excellent agreement with experimental data is obtained over a range of operating conditions. Model results show that for increased engine temperatures, fuel distillation becomes of comparable importance to the convective mass transfer fuel vapor formation mechanism. Additionally, the modeling work suggests that fuel pooling near the intake valve is occurring at rich fueling levels. The important effect of engine speed during intake is correctly predicted by the model. [DOI: 10.1115/1.1563237]

Introduction

In order to achieve the lowest possible automotive engine emissions, engine cranking and startup behavior will need to be optimized in the future. Currently, engine starting performance is additionally receiving increased attention due to some hybrid vehicles using engine shutdown during idle periods. With such systems, numerous engine starts will be necessary each vehicle trip. Thus, obtaining a strong and optimized "first-fire" will be imperative to meet future customer demands and reduced engine emissions. Towards this end, a first cycle of crank mixture preparation model was developed that seeks to both improve the physical description of the mechanisms leading to in-cylinder fuel vapor generation, and to lay the groundwork for a practical engine calibration tool.

Mixture preparation in a port-fuel-injected (PFI) spark-ignition (SI) engine is an extremely complex process with widely varying two-phase physical behaviors as a function of engine geometry and operating conditions. Mixture preparation research has been very active during the past decade, with experimental (both engine and bench-top based) work providing the most abundant results. Some representative studies are contained in Refs. [1–17]. Models of PFI mixture preparation have also attempted to capture some of the fuel's physical behavior in the formation of a combustible mixture, as well as the liquid flows from the intake port into the engine's cylinder (see Refs. [18–25]). One excellent model that seeks to predict the multifaceted detailed behavior of mixture preparation during normal engine operation (including transients) is that of Curtis et al. [26]. A number of the modeling elements used by Curtis are employed in this study. Unfortunately, limited information exists on the mixture preparation process during engine startup transients. While a few cranking experimental studies have been pursued, to the author's knowledge no pub-

lished modeling work on the cranking cycles exists. The framework for this model (described below) is based upon the physical picture provided by many of the above-cited references.

Experimental Background

This modeling effort was preceded by an experimental study, [27], that produced some interesting results that could not be thoroughly explained by the experimental data alone. Thus, a secondary motivation for this study was to use the physical model to aid in interpreting these experimental results.

Experimental characterization of engine starting behavior was performed on a Ford Zetec 2.0L four-cylinder four-valve/cylinder engine. References [27–30] describe this engine, test cell and diagnostic equipment in detail. The geometry of the engine is characteristic of many 4 valve/cylinder engines that are in production today.

A brief summary of the startup behavior of this engine is outlined below. Data were collected using engine cylinder number four due to its ease of access for pressure and gas sampling. The primary diagnostic used in determining in-cylinder fuel vapor levels was a fast flame ionization detector (FFID), [31].

Engine Stopping/Starting Positions. For a four-cylinder four-stroke engine, the engine tends to stop with one of the pistons at mid stroke (~90 deg. from BDC) of compression. This is the point at which the positive to negative transition of the sum of the individual cylinder gas load powers is equal to zero:

$$P_g = \sum_{\text{all cylinders}} p \dot{V} = 0. \quad (1)$$

For a detailed analysis of this behavior, see Ref. [27]. For this study, cylinder #4 piston starting positions denoted by A, B, C, and E in Fig. 1 were used to replicate the typical configurations. In addition, position D was added to examine the engine behavior with the piston starting from TDC of the intake stroke.

Representative Ambient Engine Start. Characteristic ambient (20°C engine coolant temperature—ECT) start behavior is

Contributed by the Internal Combustion Engine Division of THE AMERICAN SOCIETY OF MECHANICAL ENGINEERS for publication in the ASME JOURNAL OF ENGINEERING FOR GAS TURBINES AND POWER. Manuscript received by the ICE Division, March 2002; final revision received by the ASME Headquarters, July 2002. Associate Technical Editor: D. Assanis.

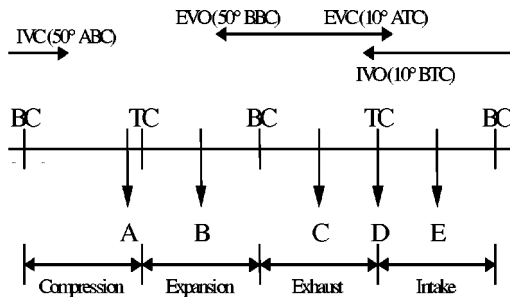


Fig. 1 Engine starting positions for cylinder #4

shown in Fig. 2. Prior to the start, the engine had come to rest at the midstroke of compression of cylinder #1. The firing order is 1-3-4-2. Cranking begins immediately after time zero on the abscissa. All the injectors were fired simultaneously at ~ 0.1 second after crank start. A substantial amount of fuel (~ 210 mg, $\lambda_{inj} \sim 0.15$ where λ is the relative air-fuel ratio) was injected to cylinder #4. The dips in the manifold absolute pressure (MAP) correspond to the air induction event of the individual cylinders. Cylinder #3 was the first cylinder to experience air intake (its starting position was at mid stroke intake). Cylinder #4 was the first to fire. The engine speed was cranked to ~ 200 rpm (the three dips in the rpm before engine firing were due to the compression gas loads of cylinders 1,3, and 4); then it accelerated with the power output of the firing cylinder. As the engine speeded up, the MAP decreased to ~ 0.45 bar at 1 second after cranking.

One of the distinct features of the first cycle of combustion is that it takes place at substantially lower rpm (~ 200) than normal engine operation. Furthermore, the crank accelerates substantially during the heat release period. As such, the airflow velocities, the heat transfer characteristics, and the combustion phasing for maximum brake torque (MBT) are substantially different than normal practice. These effects and an associated heat release analysis are described in detail in Ref. [27].

Effect of Starting Position on Startup Speed—rpm. The instantaneous rpm for the first combustion cycle of cylinder #4 also depends very much on the starting position. With starting position A, the crankshaft has been accelerated by two firing

cycles (from cylinders #1 and #3), and thus the speed reaches ~ 680 rpm. With positions B, the crankshaft has been accelerated by one firing cycle (from cylinder #3); the speed reaches ~ 500 rpm. For positions C, D, and E, there are no previous firing cycles; the speed is determined by the starter motor, and it is ~ 200 rpm.

The averaged intake valve open engine speeds were also measured. These speeds are important from the mixture preparation perspective, as they will be the force behind convective mass transfer and strip atomization processes. The data show average engine speed during the first engine cycle running at ~ 450 rpm for the early starting position (A) to ~ 100 rpm for later initial starting position (E).

Model Framework

Assumptions. Engine starting generally begins with a “dry” intake port. Visual intake port studies have shown this to be the case at various starting temperatures, [1,2]. Additionally, engine shutdown experiments indicate that residual port fuel is almost fully purged from the intake port during the decelerating engine cycles, [30]. The implications of such behavior requires that additional fuel needs to be injected on the first engine cycle to account for significant intake port wall wetting. The second and following cycles will then already contain residual intake port fuel. Thus, it is assumed that the intake port is dry upon commencement of engine crank.

This engine’s fuel injector has relatively large fuel droplets ($\sim 350 \mu\text{m}$ SMD), [10]. It is believed that all of the injected fuel impacts the surfaces (“walls”) of the intake port and valve first, and immediately becomes part of the puddle. This behavior is assumed true even for open valve injection (OVI). See Ref. [30] for a detailed discussion of this effect.

Due to the high MAP (close to atmospheric) on the first engine cycle, backflow effects, often seen at intake valve opening due to subatmospheric intake conditions, will be neglected. As a result, it is believed that the intake port puddle on the first engine cycle will not experience the fuel redistribution (often to the upstream port region) that has been observed during steady-state operation. Thus, the puddle formed by the injector remains intact until the intake valve opens and forward intake flow acts upon it.

Knowledge of the intake system surface temperature (“wall”) on which the intake port puddle is formed is necessary for evalu-

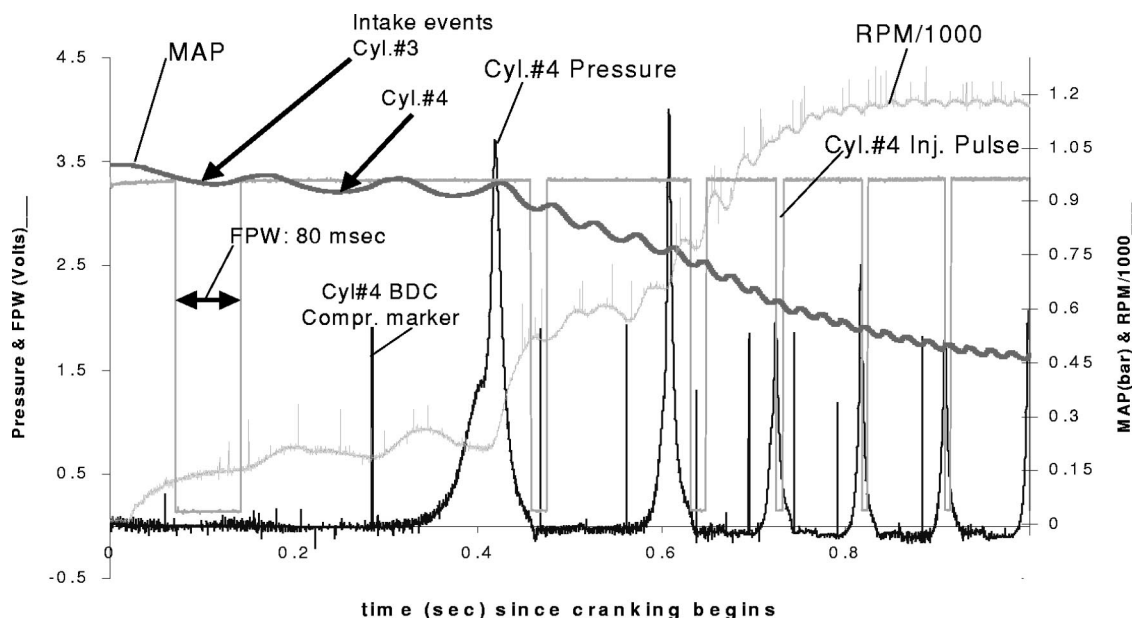


Fig. 2 Characteristic ambient engine start from initial position C

California Phase II Reformulated Fuel Volatility (RVP=6.9psi)

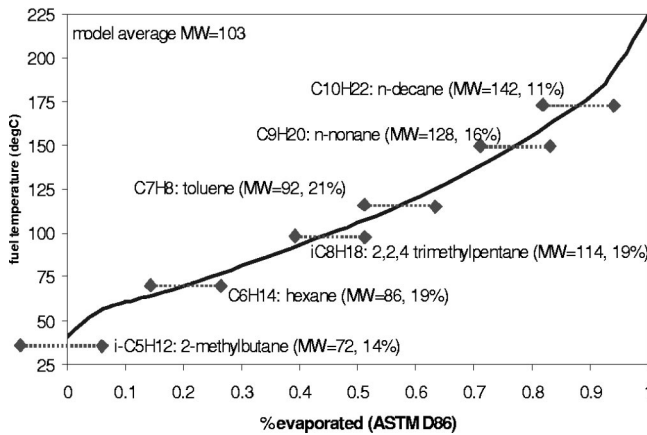


Fig. 3 Reformulated gasoline distillation curve with six specie multicomponent fuel model shown

ation of boiled-distilled fuel levels. It is known that the intake valve and intake port are at an equal temperature for all starting conditions, although both valve and port temperatures vary accordingly with overall engine starting temperature. In the case of ambient and cold engine starts, the entire engine has been allowed to cool to the starting temperature. Intake port and valve temperature measurements confirmed, [28], equality of temperature at the ambient state.

This temperature equality between the intake port and valve allows for the conceptualization of a single liquid fuel puddle mass, even though it may be distributed on both the lower intake port and valve. It has been shown that these thin fuel films quickly (fraction of an engine cycle time) achieve the surface temperature to which they've been applied, [18]. Knowledge of this wall and liquid film temperature will allow accurate estimates of puddle boiling/distillation as a function of intake wall temperature. Thus, this model is alternatively called the "one puddle model."

During crank, as with stabilized engine operation, it is the light fuel components that preferentially vaporize to provide a significant fraction of the vaporous fuel to start the engine. One study sampled combustion chamber gases before spark in order to determine the contribution of various fuel components to the mixture preparation, [32]. The study was able to quantify the expected strong role of light fuel components during the cranking process.

Thus, in order to obtain reasonably accurate puddle boiling/distillation estimates, a multicomponent fuel model was used. In this case, the experimental fuel (California Phase II Reformulated Gasoline) was represented by six fuel components. Figure 3 shows the actual experimental distillation curve for the gasoline used, along with the six fuel components chosen for the modeling effort. The modeled fractions of the six fuel components are similar to that developed by Curtis [26]. Curtis developed the reduced multicomponent fuel model specie fractions in order to simulate the evaporative characteristics of the real gasoline fuel. He then experimentally validated this reduced multicomponent fuel mixture to ensure similar evaporative behavior to that of the actual gasoline, [33].

Modeled Physical Processes. Once the puddle is formed by the injected fuel and defined to immediately reach the wall temperature, boiling/distillation of the lighter fuel components is allowed to immediately occur. The fuel vapor that forms from boiling/distillation is assumed to stay as vapor (no reverse processes allowed) and is all attributed to the in-cylinder fuel vapor mass once the intake valve opens.

Then, once the intake valve opens, the intake system air flow contributes to two more physical processes at work on the puddle.

After the forward fresh airflow displaces the distilled vapor into the engine, there is further evaporative mass transfer from the liquid pool to the incoming fresh air. This transfer will be referred to as the convective mass transfer.

The second process during the intake event is that of shear-driven (Couette-type) flow in the fuel film. This film is then assumed to break up into droplets as it is being blown off the edge of the valve and valve seat. Estimates of their size will be made to determine if they contribute to the fuel vapor formation process.

Finally, these three contributions to the engine's in-cylinder fuel vapor, boiled/distilled fuel vapor, convected fuel vapor and liquid film small droplets ($< 10 \mu\text{m}$) are added together to produce a modeled in-cylinder fuel vapor mass.

Model Details

Mass Conservation Equations. At every crank angle degree after the start of engine rotation, Eq. (2) is evaluated for each fuel specie, i , in the puddle. Fuel injection is defined to occur over the same crank angle duration as the experimental data. However, for the model, injection occurs in a discrete amount each crank angle degree. Boiling/distillation is assumed to reach equilibrium each crank angle degree after additional injection mass is added to the puddle. Convection and liquid transport occur only during the intake event period.

$$\Delta m_{\text{puddle},i} = m_{\text{fuelinj},i} - (m_{\text{distill},i} + m_{\text{convection},i} + m_{\text{liquid},i}) \quad (2)$$

Puddle Aspect. While the conservation of mass equations only track fuel mass, many of the physical processes modeled require knowledge of the puddle area and height (e.g., aspect ratio) in order to estimate their specific behaviors. Thus, a simplified fluid mechanics solution was pursued to understand the relation between puddle volume and its corresponding area and height, [30]. A numerical solution gives the puddle height as the following:

$$h_{\text{max}} = c^* \sqrt{\text{Volume}} \quad (3)$$

This solution agrees well with unpublished observations of puddle formation on a flat plate. For the complex geometry in the intake port, it is assumed that the volume^{0.5} dependence still holds approximately. The constant c in Eq. (3) was set from correlation to experimental results in which the puddle representative of one high load injection fuel mass ($\sim 30 \text{ mg}$) possessed a height of $\sim 15 \mu\text{m}$.

Distillation. Estimates of individual component boiling/distillation are made using Raoult's rule of the ideal solution. Ideal solution behavior is defined either for a dilute solution or for a mixture consisting of constituents of similar structure. It is the latter that is assumed valid in the current context. In this case, the solution assumes that each molecule of a given component experiences the same interactions whether its nearest neighbors are of the same or of another constituent. For each specie, Raoult's rule states that the vapor pressure of each individual fuel specie is independent of the other species and only a function of temperature. The following equation applies to each fuel specie:

$$x_{i,g}^* P_{\text{TOT}} = x_{i,f}^* P_{\text{SAT},i}(T) \quad (4)$$

where the index i refers to an individual fuel component. x is the mole fraction of a given fuel specie in both g -vapor form, and f -liquid form. P_{TOT} is the total intake port pressure, and $P_{\text{SAT},i}$ is the saturated vapor pressure of specie i at temperature T . These six equations along with the associated conservation (mass and moles) equations in the liquid and vapor phases provide a solution for the vapor mass of each fuel specie at the given T and P each crank angle degree.

Convection. Convective vapor mass transport estimates from the puddle are made using the Reynolds analogy for heat and mass transfer. Detailed studies of heat transfer in rough wall tubes

are included in most heat transfer texts (e.g., Refs. [34], and [35]). The Gnielinski equation (heat transfer relation) was converted to a mass transfer correlation by Reynolds analogy.

$$\text{Sh} = \frac{h_m^* D_{\text{port}}}{D_{f_i, \text{air}}} = \frac{(f/8)^* (\text{Re} - 1000)^* \text{Sc}}{1 + 12.7^* \sqrt{f/8^*} (\text{Sc}^{0.67} - 1)} \quad (5)$$

Sc is the Schmidt number. The other parameters are described below. This Sherwood (Sh) number was then used in a rate of vapor mass transfer correlation as established by Spalding [36]. The friction factor, f , in Eq. (5) is used as the calibration for the model. It has a physical meaning, and can be connected to a pipe roughness with the use of a Moody chart. Thus, the final convective fuel vapor mass transfer rate equation is as follows:

$$m_{\text{convection}, i} = \int_{\text{IVO}}^{\text{IVC}} (1 + \text{Sh})^* \left[\frac{A_{l_s}}{D_{\text{port}}} \rho_{g_m} D_{f_i, \text{air}} \times \ln \left(1 + \frac{\Delta \text{MFF}, i}{1 - \text{MMFs}, i} \right) \right] \cdot dt \quad (6)$$

MMFs, i is the mass fraction of fuel vapor at the surface of the puddle. $\Delta \text{MFF}, i$ is the difference between the fuel vapor mass fraction at the surface and the centerline free stream fuel vapor level (set to zero). A_{l_s} is the area of the liquid surface, from the puddle aspect ratio submodel. The density of the gas-vapor mixture at the puddle surface is ρ_{g_m} . D_{port} is the port diameter, and $D_{f_i, \text{air}}$ is the fuel-air diffusivity of fuel specie i .

Liquid (Couette) Flow and Breakup. Numerous authors have modeled shear driven intake port puddle film flow. Servati assumed that the liquid flow was of the Couette type, with a linear velocity profile, [18]. Curtis believed that a laminar boundary layer flow was in effect, and assumed the corresponding parabolic velocity profile, [26]. By equating the shear stress at the top of the liquid puddle film with the shear stress generated at the puddle surface by the forward airflow into the cylinder, the liquid fuel film transport into the engine's cylinder can be estimated (Eq. (10)). The scalar $m=1$ is for Couette flow, and $m=1/2$ for a laminar boundary layer type flow. The estimated difference in mass flow between the two types of liquid flow is more than a factor of two, with boundary layer flow being greater. In this study, Couette type flow is assumed.

$$m_{\text{liquid}, i} = y_{,i} \cdot m_{\text{liquid}} = \int_{\text{IVO}}^{\text{IVC}} y_{,i} \cdot P_w \cdot \rho_f \cdot \left(\frac{c_f \cdot V_o^2 \cdot h^2}{2 \cdot \mu_l} \right) \cdot dt \quad (7)$$

The liquid puddle mass fraction term, $y_{,i}$, is used to account for the predominately heavier fuel species that comprise the puddle. P_w is the wetted perimeter of the puddle. The liquid puddle density, viscosity, and height are ρ_f , μ_l , and h . The port centerline velocity is V_o , and the coefficient of friction between the air-flow and the liquid surface is c_f ($c_f = f/4$, f : friction factor from above).

Once the liquid flow mass is established, a wave breakup model is applied, [37], to determine the SMD of the droplets formed from the liquid film flow sheet breakup. A droplet distribution, [38], is then applied to determine the fraction of droplets that are below 10 μm . Droplets that are below this diameter are then assumed to remain suspended as vapor and contribute to the in-cylinder vapor mass. See Ref. [26] for an application of these two models to the engine environment.

Base Model Results

Base Model Inputs and Calibration. This "one puddle" first cycle of crank model (base model) was run at simulated hot starts (ECT=90°C) with the appropriate engine cycle phasing (starting positions: A, B, C, D, and E) and averaged first cycle engine speed as seen in the experimental data at the different engine positions. Thus position A started fuel injection at 180 deg (top center

compression—TCC, 0 deg=BCC), and had an average engine speed during intake of 450 rpm. Position D started injection at 568 deg, and had an average speed during intake of 200 rpm.

The average engine speed was scaled to a mean piston speed, and then instantaneous piston speed as a function of engine crank angle position. Next, instantaneous intake port air speed (averaged across the port cross section) was determined by scaling instantaneous piston speed by the ratio of piston area to port cross-sectional area.

The base model required that the friction factor be set to 0.06 for agreement between the model and the hot start experimental data for in-cylinder fueling near stoichiometric. A friction factor of 0.06 corresponds to a normalized port wall roughness of 3% ($\varepsilon = 0.03 = \text{roughness height/diameter}$). While the exact roughness of the Zetec port is not known, this value of ε is certainly reasonable due to the fairly coarse intake port surface caused by sand castings.

A comparison of model predictions with experimental data is shown in Fig. 4. In each group of bars are shown injected fuel mass, experimental in-cylinder fuel mass and model predicted in-cylinder fuel mass. Injected fueling of 27 mg generally provides for slightly lean of stoichiometric in-cylinder fueling. Injected fueling of 40 mg generally provides for slightly richer than stoichiometric in-cylinder fueling.

The model predicts in-cylinder fuel vapor levels well. The model predictions are within ten percent of the experimental data for positions A and D with fueling near stoichiometric levels. Additionally, the model reproduces the differences between positions A and D. Position A delivers an in-cylinder relative air-fuel ratio (λ) that is generally 0.1 λ richer than position D for the same injected fuel mass. This effect is a result of the higher engine speeds during the intake stroke experienced with position A, connectively drawing in more fuel vapor. Thus, higher engine speeds enhance the convective mass transport of fuel from the puddle to the combustion chamber.

Unfortunately, model agreement with the data at Position E is not good. Position E, late intake event fuel injection timing delivers an in-cylinder mixture that is inhomogeneous. Still, the model under predicts in-cylinder fuel vapor levels by almost a factor of two. The low in-cylinder fuel mass levels predicted by the model at E are a result both of the assumption that all injected fuel must first impact the port walls, and the shortened times of intake valve open period. These effects coupled with the reducing piston/port velocities during the later half of the intake stroke result in low model predictions. In reality, it is likely that direct fuel flow from the injector into the combustion chamber results. Estimates based on geometry show that approximately 1/4–1/3 of the injected fuel directly enters the combustion chamber from the fuel injector. With the large droplet size containing significant momentum, it is believed that this direct injector contribution to the cylinder will likely hit the bore wall. Evaporation of the light fuel ends will result. Convective mass transfer during compression will additionally vaporize more cylinder wall/piston liquid fuel.

While this OVI behavior could be modeled, it is extremely difficult to experimentally verify the different in-cylinder vaporization mechanism at work. Fortunately, position E is a poor engine position to develop a first fire, both due to its inhomogeneity and high engine out HCs. Thus, efforts to model its behavior are not essential. In practice, it would be advisable to skip fueling to the second cycle if the engine starting position is at E.

Next, the simulated ECT and intake system wall temperature is reduced to ambient condition (20°C). No other modification is made to the model.

The results for positions A and D are shown also in Fig. 4. In this case, 135 mg of injected fuel is necessary to deliver a near stoichiometric fuel vapor mass to the engine's cylinder. Above, for the hot starts, only ~40 mg of fuel was necessary. From the modeling results it is clear that the model is able to naturally adjust to the changing simulated temperature conditions. Much less fuel is predicted to boil/distill at the ambient conditions. This leads to a

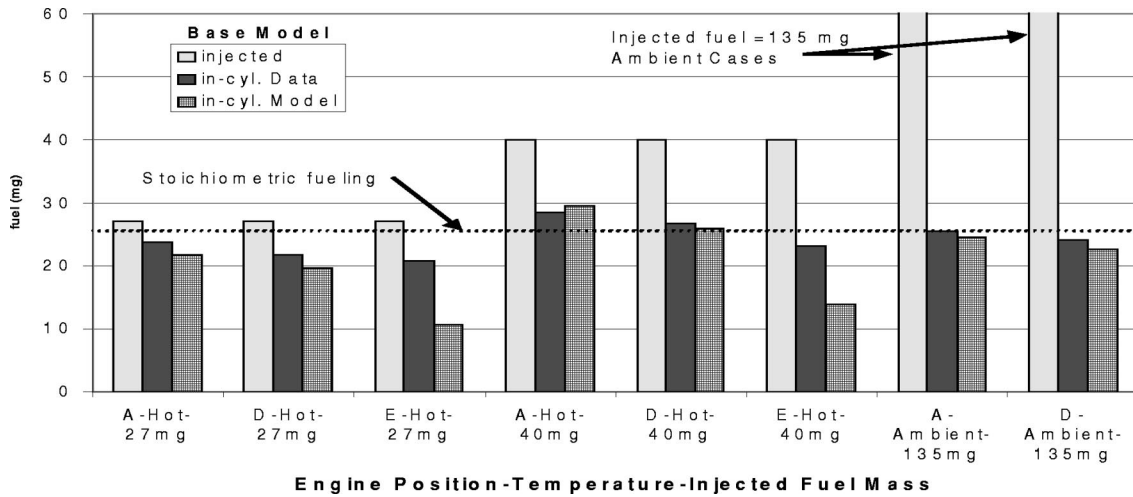


Fig. 4 Base model comparison with experimental data at various starting positions. Both hot and ambient start results are shown.

larger puddle with a broad surface area. Thus, convective mass transfer is greatly enhanced and becomes the dominant fuel vapor generation mechanism (this effect will be discussed in detail in the next section). As was the case for the hot starts, position A shows slightly higher in-cylinder fuel vapor levels due to the higher engine speed during the intake event. The agreement between the model and data at the varied starting positions, temperatures and injected fuelling is excellent, differences of less than ten % exist.

Physical Processes. In this section detailed results from the model reveal the physical mechanisms at work during the first cycle of crank. As described in the model description sections above, physical mechanisms that can generate in-cylinder vapor include boiling/distillation, convective mass transport, and liquid film flow breakup into small droplets. The relative importance of these mechanisms is now discussed.

Figure 5 shows a first cycle of crank model simulation for a hot start at initial engine position A with stoichiometric in-cylinder

fueling. All six fuel species are shown as a function of engine crank angle during the first engine cycle. The ordinate displays the fraction of injected fuel that remains in the puddle during the first crank cycle. Fuel injection occurs from 120 to 150 crank angle degrees. Next the quiescent period until the intake valve opens lasts until 530 crank angle degrees. Finally, the intake valve open period lasts until 50 deg after bottom center (ABC).

During the fuel injection period most of the *i*-pentane boils. Pentane is the lightest fuel specie modeled in the multicomponent fuel model. A few percent of the injected pentane is seen retained in the puddle at the start of injection, but quickly all of the pentane boils and remains in the port as vapor until drawn into the combustion chamber at IVO.

The next modeled specie heavier than pentane is hexane. As seen in Fig. 5, approximately 55% of the injected hexane remains in the puddle after injection is complete, with the remainder boiled/distilled off as vapor in the intake port.

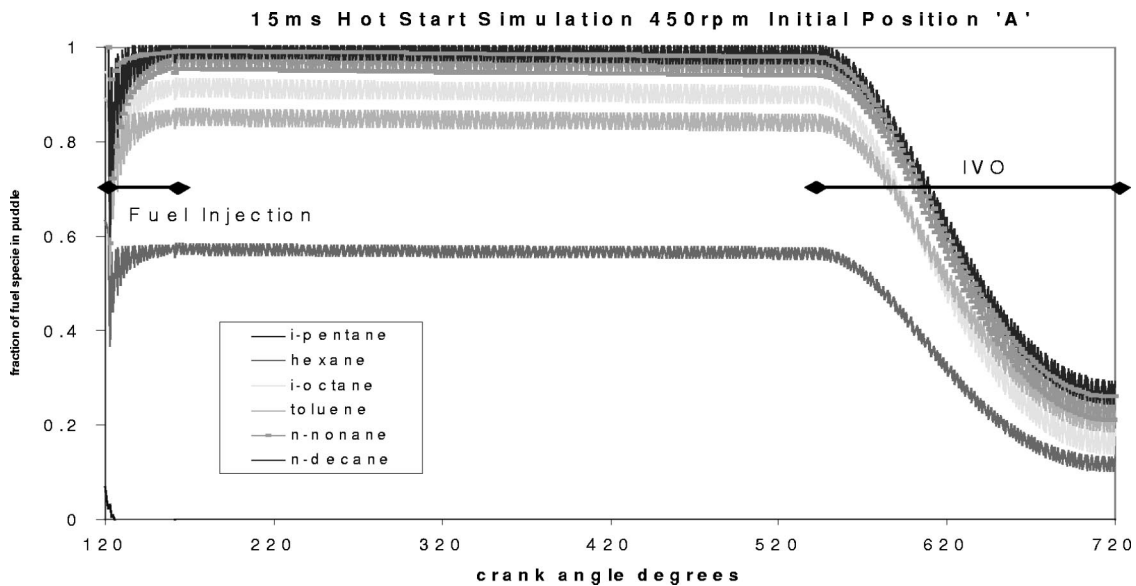


Fig. 5 A simulated hot start at position A. The fraction of each fuel specie that remains in the puddle during the first engine cycle is shown.

As the fuel species' molecular weight (MW) increases, so does the fraction of injected fuel that remains in the puddle as liquid after injection. At the upper end of the distillation curve due to its heavy nature, n-decane is seen to leave almost all of its injected mass in the puddle as liquid.

For these hot starts it is seen that a significant fraction of the injected fuel (especially lighter fuel components) immediately vaporizes in the port, creating fuel vapor that will enter the combustion chamber upon IVO.

During the intake event period, Fig. 5 shows all fuel species being drawn out of the puddle. This convective mass transfer phase is very strong, but how much of the puddle reduction is due to liquid fuel transport and how much is due to convective vapor mass transfer?

The model predicted distribution of the injected fuel on the first cycle of crank for a hot start with near stoichiometric fueling shows the following. Approximately 1/4 to 1/3 of the injected fuel becomes fuel vapor due to boiling/distillation. Next, ~1/2 of the injected fuel becomes fuel vapor due to intake event convection. Injected fuel that remains in the puddle past the first engine cycle comprises slightly less than 1/4 of the injected fuel. Liquid fuel transport into the cylinder comprises only a few percent.

Of the approximately 2% of injected fuel that is drawn into the cylinder as a liquid film, the wave breakup and distribution models predicts less than ten percent of it will be of a small enough diameter ($<10 \mu\text{m}$) to be entrained in the combustion chamber gases as fuel vapor. Thus, the vapor contribution from the liquid film flow-breakup is very small. Most of the liquid film drawn into the combustion chamber is likely residing on both the cylinder wall and piston surfaces as a liquid film.

When the starting temperature is then dropped to ambient conditions (20°C), most of the injected fuel remains in the port (80%). Convective mass transfer is the dominant vapor formation mechanism. Distillation and liquid flow breakup are negligible at this condition.

Thus, common to both hot and ambient starting (with in-cylinder fuel vapor levels near stoichiometric), both the diffusional and liquid film flow breakup mechanisms can be neglected with regards to their contribution towards generating in-cylinder fuel vapor. The model predicts that both effects are second order and not significant in the mixture preparation process. Convection and distillation are the dominant mixture preparation mechanisms that need to be considered.

The relative roles of convection and distillation are shown across the starting temperature range from ambient to hot in Fig. 6. These simulations show injected fuel levels necessary to achieve a stoichiometric in-cylinder fuel mass level across the temperature range. For ambient starting, convective mass trans-

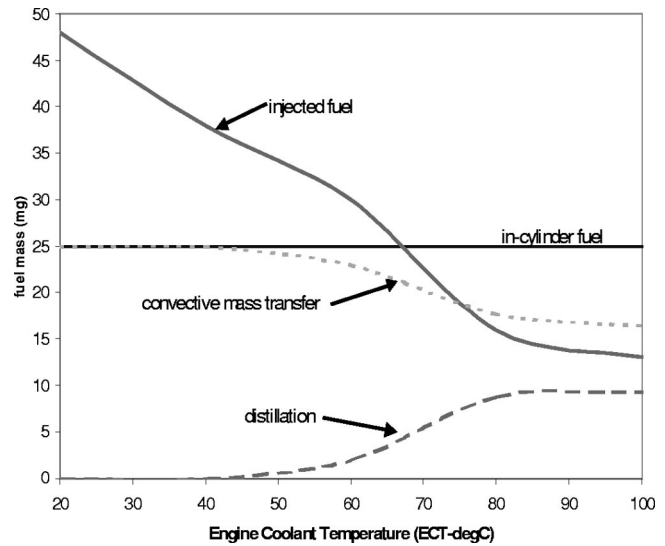


Fig. 6 Model predicted injection mass necessary for stoichiometric in-cylinder fueling from 20–100°C starting temperature

port is the only mechanism to deliver fuel vapor to the combustion chamber. The temperatures are too low for vapor generation. As the engine starting temperature warms from 50 to 80°C the relative importance of distillation vapor generation becomes important. Likewise, as fuel vapor is generated from boiling/distillation, the puddle size during intake valve open is reduced leading to the lessening importance of convective mass transfer at higher engine temperatures. At hot engine starting, convection and distillation are of comparable importance.

Comparison to Vehicle Data and Zetec Data. “One puddle” first cycle of crank simulations across a range of temperatures and fuel injections were performed to estimate appropriate first cycle of crank required fueling. Figure 7 shows the modeling results compared to three production vehicle calibrations and the Zetec data.

The series of dashed lines represent the model predictions for various in-cylinder air-fuel ratios. The lowest dashed line shows the injected fuel mass necessary in order to achieve a 10% lean of stoichiometric in-cylinder mixture. In the experimental works, [27,30], this 10% lean limit was seen across the range of starting temperatures in order to achieve a positive IMEP first cycle. The

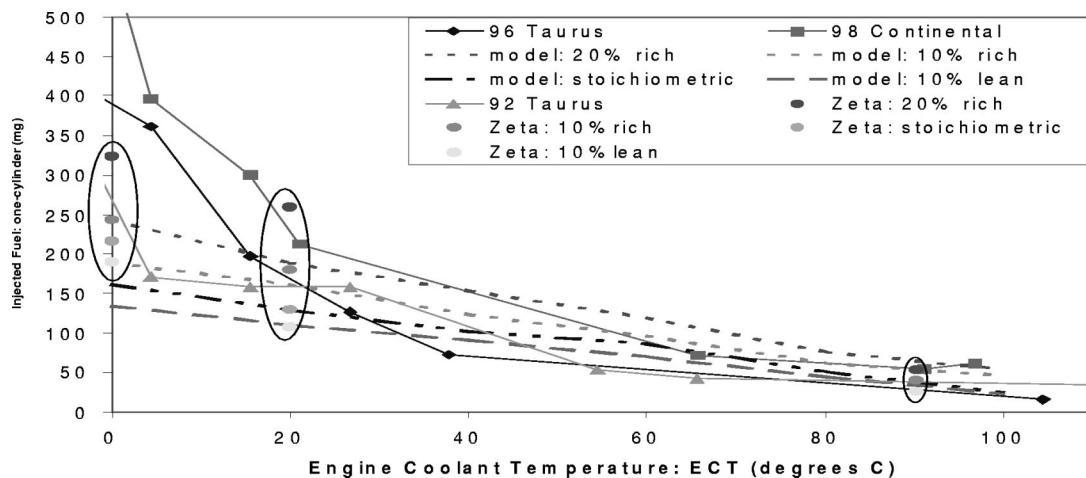


Fig. 7 Comparison of model results to production engine calibrations and Zetec experimental data

next three dashed lines (moving upwards in the figure) show the model predictions of injected fuel for stoichiometric, 10% rich and 20% rich in-cylinder fueling.

The diamond, triangle, and square symbols show the required fueling in three production Ford vehicles as a function of ECT. The agreement between the model and production fueling levels is very good from ambient to hot start conditions. For cooler than ambient starts ($ECT < 20^\circ C$), it is expected that strong liquid fuel effects become important, requiring high levels of actual fueling in order to achieve a combustible mixture.

Finally, the Zetec data is shown in the ovals at 0° , 20° and $90^\circ C$. Agreement between the model and data is excellent around stoichiometric fueling at both ambient and hot starting. However, for ambient rich fueling and cold starting the model under predicts the required first cycle fueling necessary. This behavior will be discussed in the next section.

Base+Fuel Crevice Model (Rich Fueling) Results

Model Improvements and Results. While the base model predicts well the required injected fuel behavior near stoichiometric fueling, it does not work well for rich to very rich in-cylinder fuelling. Figure 8 shows the first cycle in-cylinder relative air-fuel ratio (λ) as a function of first cycle injected fuel for hot starting at position A. For this case, and at all temperatures and starting positions, the experimental data shows that despite high fuel injection levels, the in-cylinder λ reaches a constant level despite even higher fuel injection amounts. Unfortunately, the base model results do not predict this behavior. As seen in Fig. 8, the base model shows continued enrichment with increasing first cycle fuel injection mass.

In looking at the detailed model results at high first-cycle fuel injections, it is evident that the associated high levels of predicted in-cylinder fuel mass are a result of the strong convective mass transfer action across a wide puddle area. In fact, this predicted puddle area is very wide, more than ten times the associated footprint area of the injection spray. This modeled spreading of the initial injection spray is likely too broad.

Both the intake port and valve are angled towards each other creating a crevice that is likely containing a pool of liquid fuel. The port centerline is angled approximately 30 deg off the horizontal. Likewise, the intake valve head is angled approximately 20 deg off the horizontal towards the intake port. The hypothesized location of the crevice pool is at the intersection of these two angled components.

By assuming that fuel is collecting in the form of a crevice pool, the modeled puddle area then is greatly reduced. This also

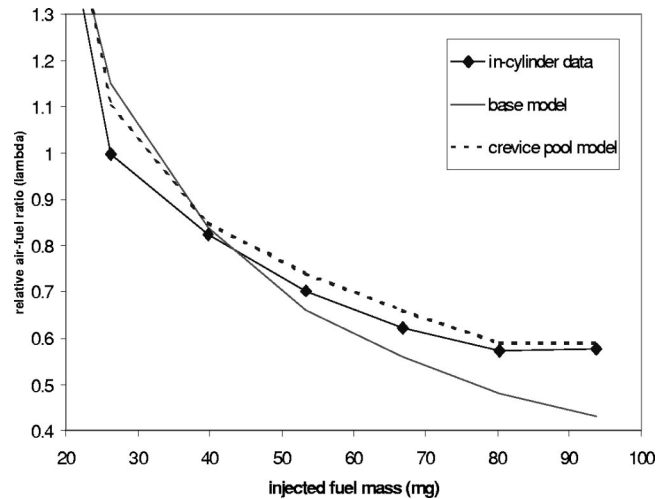


Fig. 8 Position A hot start experimental data and modeling results

reduces the convected in-cylinder fuel vapor mass since the convected mass is proportional to puddle area. But how much fuel is pooling in the crevice? Or alternatively, what is the overall thin film puddle area/mass?

One approach to determine the thin film puddle area/mass is to assume that the base thin film puddle can only contain as much fuel as exists in the intake port during normal engine operation at high load and low engine speed. In Ref. [30] experimental estimates of the residual intake port fuel levels were made using injector cutoff/disablement. For stabilized engine operation ($90^\circ C$ ECT), at 0.9 bar 1500 rpm the residual port fuel was seen to be ~ 30 mg of fuel. Stabilized ambient engine experiments were also performed showing ~ 200 mg of residual intake port fuel at $20^\circ C$ ECT.

Thus, these values will be used to define the maximum liquid fuel mass that is contained in the thin film puddle. When the modeled thin film puddle is predicted to exceed 30 mg (hot starting) the remainder of the fuel is assumed to pool in the crevice. It is additionally assumed that the crevice pool is not so thick as to restrict the conductive wall heat transfer to the crevice pool, such that the crevice pool is assumed to also reside at the wall temperature.

With this crevice pool model modification, the modeling pre-

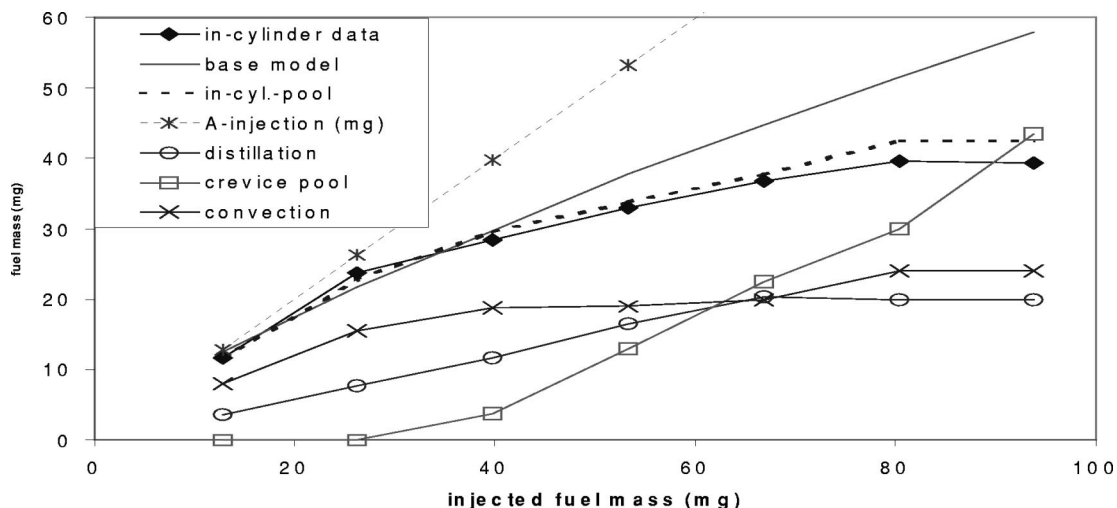


Fig. 9 Position A hot start modeling details with crevice pooling occurring at mid-high fuel injection levels

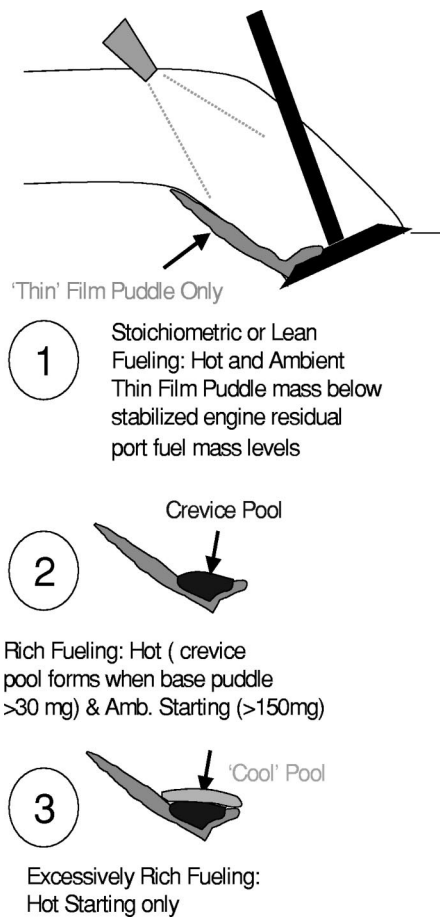


Fig. 10 A schematic representation of the intake port during (1) stoichiometric and lean fueling, (2) rich fueling with crevice, and (3) excessively rich fueling during hot starting

dictions are then shown in both Figs. 8 and 9. From 40 to 80 mg of injected fuel, the improved model follows the experimental trends well for in-cylinder fuel vapor. Figure 9 also shows both the convective mass transfer levels and boiling/distillation contributions to the in-cylinder fuel vapor. It is seen that by assuming

the occurrence of liquid crevice pooling, convective mass transfer is relatively constant with increased first-cycle injected fuel mass.

While this crevice pool model works well for high fuel injection levels, at very high fuel injection levels one further model modification needs to be made. Since the data shows in-cylinder fuel mass remaining constant at very high injection levels, it is likely that the crevice pool becomes so thick that insufficient time exists to conduct wall heat through the crevice pool (this assumption will be validated in the next section). Thus, the model shows that for hot starting, once the puddle plus crevice mass exceeds 45 mg, a cool upper pool is assumed to exist that doesn't reach the wall temperature, and thus does not distill/boil as with the thin film puddle and lower crevice pool. With this final model modification agreement across the entire range of injection levels is attained. The conceptual picture of crevice pooling and the deep "cool" pool are shown in Fig. 10.

This base plus crevice pool model was next applied to hot starting at engine positions D and E. The modeling and experimental results are shown in Fig. 11. The model predicts the reduced in-cylinder fueling differences as engine starting position is changed from A to D to E. This effect being a result of faster engine speeds at more advanced starting engine positions. Additionally, the crevice pooling plus deep cool pool assumptions work well for positions D and E, predicting a constant in-cylinder fuel vapor level with increasingly high fuel injection levels.

Next, the model is applied to increasing fuel injection levels at ambient starting. Similar behavior is observed as with hot starting. At high-rich fuel injection levels, the in-cylinder fuel mass becomes constant. Using 200 mg as the stable ambient thin film puddle level, the results are shown in Fig. 12. While the trends are correct, the 200 mg level needs to be reduced to 150 mg for agreement with the data.

Deep Crevice Liquid Pooling. If the above described deep cool crevice explanation is to be plausible, then a heat transfer analysis should confirm that when a deep crevice pool is formed, insufficient time exists to conduct wall heat through the deep crevice pool to the upper liquid surface.

Figure 13 shows conduction penetration thickness into a hypothetical liquid fuel film (initially at 20°C) versus time for conduction from a wall at 90°C. Curves for 10%, 50%, and 90% temperature changes are shown. These percentages at a given time and thickness reflect the temperature of the outer surface of the liquid film as a percentage of the hot wall temperature. These percentages correspond to an outer surface liquid film temperature

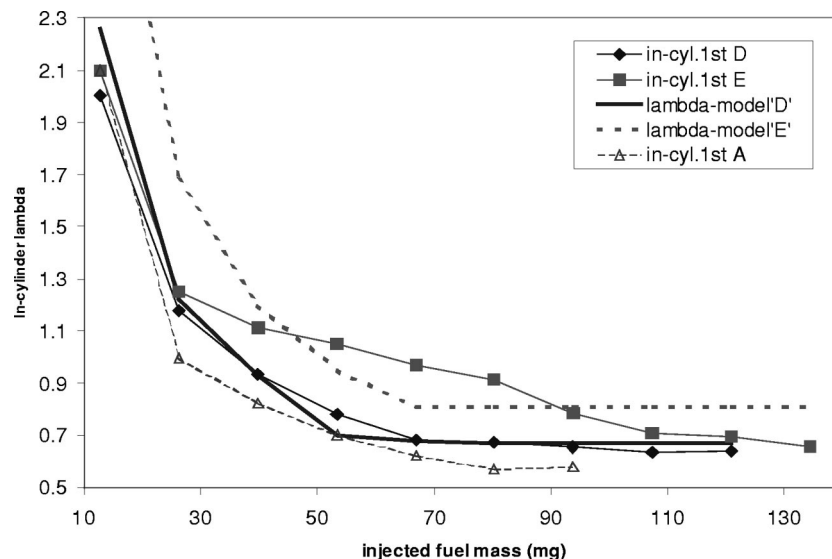


Fig. 11 Hot start model comparison to data at positions D and E

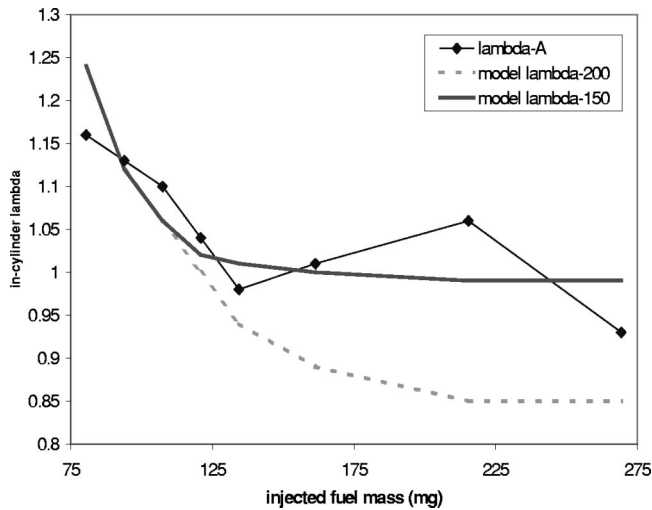


Fig. 12 Ambient starting model comparison to experimental data at position A

of 27°C, 55°C, and 83°C. The calculation of these curves was based on the transient plane slab assumption of a liquid fuel film with the lower outer surface of the liquid film at the temperature of the hot engine wall (90°C). Additionally, the upper liquid surface is assumed adiabatic. While the analysis is only approximate, it nonetheless gives an indication of the physical problem.

If fuel injection occurs very early in the engine cycle (e.g., initial position "A") the maximum time for conduction of wall heat through the liquid film exists until the intake valve opens. This "soak" time is the time on the abscissa. Some corresponding engine speeds for this maximum soak time are shown below the abscissa labeling. Thus, position A engine starting corresponds to an approximate 200 msec soak time due to its ~450 rpm average speed during the intake period. Since the abscissa reflects the maximum possible soak time (from ~IVC to IVO) this time scale is not appropriate for the later engine starting positions C, D, and E since only a fraction of an engine cycle exists for puddle/pool

soak despite their lower engine speeds. Thus, the late initial engine positions actually have soak times less than A despite their lower speeds.

As seen in Fig. 13, the 45 mg thin puddle plus crevice pool line (minimum residual intake port fuel mass for hot starting at which the deep cool pool is believed to be occurring) provides for a maximum pool height of ~350 μm. This height is based on the assumption that the crevice pool is triangular in cross section around 1/2 the valve circumference. At this point (450 rpm–200 msec), the puddle outer surface temperature is approaching a level 90% of the wall temperature. So distillation/boiling should still be occurring. However, as the injected fuel and thus crevice pool grows, as represented by the 80 mg thin puddle plus crevice pool line, the 90% (83°C) temperature penetration is ~400 μm short of the approximate deep crevice pool height. This suggests that boiling/distillation is not occurring in the upper part of the deep cool crevice pool. Engine speeds would need to be reduced by 2 1/2 times for the full deep crevice pool to fully reach the wall temperature. Thus it is very likely that the deep crevice cool pooling assumption is valid based upon heat transfer arguments.

Conclusions

- The relatively simple "one puddle" first cycle of crank model works remarkably well for predicting in-cylinder fuel vapor mass for near stoichiometric fueling across a broad range of temperatures (ambient to hot starting). A single calibration for the convective mass transfer relation performed at hot engine conditions and then applied to all operating conditions is the only requirement for in-cylinder fueling levels near stoichiometric or fuel lean. The model is capable of predicting the differences in in-cylinder fuel vapor that occur at different engine starting positions. This effect is a result of the increases in convective mass transfer from the puddle as initial engine position is advanced (and thus higher first-cycle engine speeds).
- Across the temperature range, for rich in-cylinder fueling, "crevice pooling" is believed to be occurring. Additional model calibration is necessary based on steady-state residual intake port fuel levels (as a function of ECT). The crevice pool is still thin enough to achieve the port wall temperature

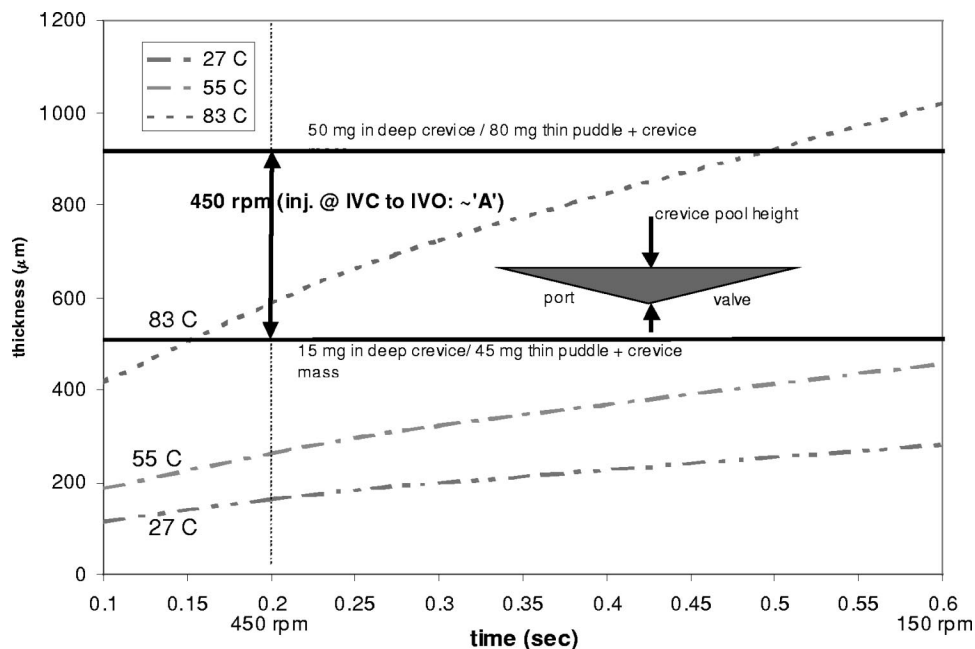


Fig. 13 Conduction length into a liquid fuel film initially at 20°C from a wall at 90°C versus time. Estimated deep crevice depths are also shown.

before the intake valve opens. The crevice pool likely “dumps” into the combustion chamber as large droplets and liquid film flows at IVO, and is not believed to be a factor in vapor generation on the first cycle.

- With very high first-cycle fuel injection levels during hot starting, the crevice pool is believed to be quite deep/thick, such that distillation/boiling is not occurring in the upper portion of the deep crevice pool.
- For hot starting, the mixture preparation mechanisms of distillation/boiling and convective mass transfer are of comparable importance. Distillation produces fuel vapor that consists of primarily light-end fuel components, while convection draws in more of the heavy-end fuel components from the puddle. Liquid film flow from the thin puddle is of secondary importance and can be neglected.
- For ambient and cold starting, convective mass transfer is the dominant fuel vapor generation mechanism. Once the crevice pool “dumps” into the combustion chamber, thin film liquid flow is then only a few percent of the remaining puddle mass.

Acknowledgments

The author performed much of this work while at MIT’s Sloan Automotive Laboratory. The author would like to thank Profs. W. K. Cheng, J. B. Heywood, J. C. Keck, B. Mikic and Drs. E. C. Curtis and T. Kenney for useful discussions regarding this work. This work was funded by Ford Motor Company and the MIT Engine and Fuels Research Consortium.

References

- [1] Saito, K., Sekiguti, K., Imatake, N., Takeda, K., Yaegashi, T., 1995, “A New Method to Analyze Fuel Behavior in an SI Engine,” SAE Paper No. 950044.
- [2] Shin, Y., Min, K. D., and Cheng, W. K., 1995, “Visualization of Mixture Preparation in a Port Fuel Injected Engine during Engine Warm-up,” SAE Paper No. 952481.
- [3] Imatake, N., Saito, K., Morishima, S., Kudo, S., and Ohhata, A., 1997, “Quantitative Analysis of Fuel Behavior in Port-Injection Gasoline Engines,” SAE Paper No. 971639.
- [4] Stanglmaier, R. H., Hall, M. J., and Matthews, R. D., 1997, “In-Cylinder Fuel Transport During the First Cranking Cycles in a Port Injected 4-Valve Engine,” SAE Paper No. 970043.
- [5] Koenig, M. H., Stanglmaier, R. H., Hall, M. J., and Matthews, R. D., 1997, “Mixture Preparation During Cranking in a Port-Injected 4-Valve SI Engine,” SAE Paper No. 972982.
- [6] Shayler, P. J., Issacs, R. M., and Ma, T. H., 1992, “The Variation of In-Cylinder Ratio During Engine Cranking at Low Ambient Temperatures,” Proc. Inst. Mech. Eng., **206**, pp. 55–62.
- [7] Shin, Y., Cheng, W. K., and Heywood, J. B., 1994, “Liquid Gasoline Behavior in the Engine Cylinder of a SI Engine,” SAE Paper No. 941872.
- [8] Shin, Y., Min, K. D., and Cheng, W. K., 1995, “Visualization of Mixture Preparation in a Port Fuel Injection Engine During Engine Warm-up,” SAE Paper No. 952481.
- [9] Fox, J. W., Min, K. D., Cheng, W. K., and Heywood, J. B., 1992, “Mixture Preparation in a SI Engine With Port Fuel Injection During Starting and Warm-up,” SAE Paper No. 922170.
- [10] Whelan, D. E., Kelly-Zion, P. L., Lee, C. F., Peters, J. E., and White, R. A., 1997, “Back-Flow Atomization in the Intake Port of Spark Ignition Engines,” SAE Paper No. 972988.
- [11] Nagaishi, H., Miwa, H., Kawamura, Y., and Saitoh, M., 1989, “An Analysis of Wall Flow and Behavior of Fuel in Induction Systems of Gasoline Engines,” SAE Paper No. 890837.
- [12] Almkvist, G., Denbratt, I., Josefsson, G., and Magnusson, I., 1995, “Measurements of Fuel Film Thickness in the Inlet Port of a SI Engine by Laser Induced Fluorescence,” SAE Paper No. 952483.
- [13] Koenig, M. H., and Hall, M. J., 1998, “Cycle-Resolved Measurements of Pre-Combustion Fuel Concentration Near the Spark Plug in a Gasoline SI Engine,” SAE Paper No. 981053.
- [14] Meyer, R., and Heywood, J. B., 1999, “Effect of Engine and Fuel Variables on Liquid Fuel Transport Into the Cylinder in Port-Injected SI Engines,” SAE Congress.
- [15] Senda, J., Ohnishi, M., Takahashi, T., Fujimoto, H., Utsunomiya, A., and Wakatabe, M., 1999, “Measurement and Modeling on Wall Wetted Fuel Film Profile and Mixture Preparation in Intake Port of SI Engine,” SAE Paper No. 99010789.
- [16] Witze, P. O., 1999, “Diagnostics for the Study of Cold Start Mixture Preparation in a Port Fuel Injected Engine,” SAE Paper No. 99011108.
- [17] Koederitz, K. R., and Drallmeier, J. A., 1999, “Film Atomization From Valve Surfaces during Cold Start,” SAE Paper No. 1999010566.
- [18] Servati, H. B., and Herman, E. W., 1989, “Spray/Wall Interactions Simulation,” SAE Paper No. 890566.
- [19] Chen, G., Vincent, M. T., and Guterth, T. R., 1994, “The Behavior of Multiphase Fuel-Flow in the Intake Port,” SAE Paper No. 940445.
- [20] O’Rourke, P. J., and Amsden, A. A., 1996, “A Particle Numerical Model for Wall Film Dynamics in Port-Injected Engines,” SAE Paper No. 961961.
- [21] Maroteaux, F., and LeMoine, L., 1995, “Modeling of Fuel Droplets Deposition Rate in Port Injected SI Engines,” SAE Paper No. 952484.
- [22] Schurov, S. M., and Collings, N., 1994, “A Numerical Simulation of Intake Port Phenomena in a SI Engine Under Cold Starting Conditions,” SAE Paper No. 941874.
- [23] Naber, J. D., and Reitz, R. D., 1988, “Modeling Engine Spray/Wall Impingement,” SAE Paper No. 880107.
- [24] Miyagawa, H., Nagaoka, M., Akihama, K., and Fujikawa, T., 1999, “Numerical Analysis on Multi-component Fuel Behaviors in a Port-Injected Gasoline Engine,” SAE Paper No. 99013642.
- [25] Nagaoka, M., Ohsawa, K., Crary, B., Yamada, T., Sugiura, S., and Imatake, N., 1997, “Numerical Analysis of Fuel Behavior in a Port-Injection Gasoline Engine,” SAE Paper No. 970878.
- [26] Curtis, E. W., Aquino, C. F., Trumpy, D. K., and Davis, G. C., 1996, “A New Port and Cylinder Wall Wetting Model to Predict Transient A/F Excursions in a PFI Engine,” SAE Paper No. 961186.
- [27] Castaing, B. M. P., Cowart, J. S., and Cheng, W. K., 2000, “Fuel Metering Effects on HC Emissions and Engine Stability During Cranking and Startup in a PFI SI Engine,” SAE Paper No. 00FL-0693, SAE Fall Fuels and Lubricants Meeting, Baltimore, MD.
- [28] Cowart, J. S., and Cheng, W. K., 1999, “Intake Valve Thermal Behavior During Steady-State and Transient Operation,” SAE Paper No. 99013643.
- [29] Cowart, J. S., and Cheng, W. K., 2000, “Throttle Movement Rate Effects on Transient Fuel Compensation in a Port Fuel Injected SI Engine,” SAE Paper No. 2000-01-1937.
- [30] Cowart, J. S., 2000, “Mixture Preparation Behavior in Port Fuel Injected Spark Ignition Engines During Transient Operation,” Ph.D. thesis, M.I.T., Cambridge, MA.
- [31] Cheng, W. K., Summers, T., and Collings, N., 1998, “The Fast Response Flame Ionization Detector,” Prog. Energy Combust. Sci., **24**, pp. 89–124.
- [32] Shayler, P. J., Issacs, R. M., and Ma, T. H., 1992, “The Variation of In-Cylinder Ratio During Engine Cranking at Low Ambient Temperatures,” Proc. Inst. Mech. Eng., **206**, pp. 55–62.
- [33] Curtis, E., 1999, personal communication.
- [34] Incropera, F. P., and DeWitt, D. P., *Fundamentals of Heat and Mass Transfer*, John Wiley and Sons, New York.
- [35] Mills, A. F., 1996, *Heat and Mass Transfer*, Prentice-Hall, Englewood Cliffs, NJ.
- [36] Spalding, D. B., 1979, *Combustion and Mass Transfer*, Pergamon Press, Tarrytown, NY.
- [37] Rosin, P., and Rammler, E., 1993, J. Inst. Fuel, **7**, p. 29.
- [38] Fraser, R. P., Dombrowski, N., and Routley, J. H., 1963, “The Atomization of a Liquid Sheet by an Impinging Air Stream,” *Chemical Engineering Science*, Pergamon Press Oxford, UK, **18**, pp. 339–353.

Parametric Characterization of High-Pressure Diesel Fuel Injection Systems

T.-C. Wang

J.-S. Han

X.-B. Xie

M.-C. Lai¹

N. A. Henein

Mechanical Engineering Department
Wayne State University
5050 Anthony Wayne Drive, #2123
Detroit, MI 48202

E. Schwarz

W. Bryzik

US TARDEC,
Detroit, MI

The focus of the study described herein is the characterization of the high-pressure hydraulic electronic unit injector (HEUI) and of the electronic unit injector (EUI) diesel injection systems. The characterization items include injection pressure, injection rate, injector response time, needle lift, start up injection transient, and dynamic discharge coefficient of the nozzles. Macroscopic and microscopic spray visualizations were also performed. The effects of injection conditions and nozzle configurations on injection characteristics were reviewed. Nozzle sac pressure was measured to correlate with the upstream injection pressure. A LabVIEW data acquisition and controls system was implemented to operate the injection systems and to acquire and analyze data. For an HEUI system, based on the results of the study, it can be concluded that common-rail pressure and length of the injection rate-shaping pipe determine the injection pressure, while the pressure rising rate and injection duration determine the peak injection pressure; it was also found that the nozzle flow area, common-rail pressure, and the length of the rate-shaping pipe are the dominating parameters that control the injection rate, and the rate shape is affected mainly by common-rail pressure, especially the pressure rising rate and length of the rate-shaping pipe. Both injection pressure and ambient pressure affected the spray tip penetration significantly. The penetration increased corresponding to the increase of injection pressure or decrease of ambient pressure. The variation of spray penetration depends on the type of injection system, nozzle configuration, and ambient pressure. The large penetration variation observed on the HEUI sprays could be caused by eccentricity of the VCO (valve-covered-orifices) nozzle. The variation of the mini-sac nozzle was 50% less than that of the VCO nozzle. The near-field spray behavior was shown to be highly transient and strongly depended on injector design, nozzle configuration, needle lift and oscillation, and injection pressure. [DOI: 10.1115/1.1498268]

Introduction

High-pressure electronic-controlled fuel injection systems, such as the electronic unit injector (EUI), the hydraulic electronic unit injector (HEUI), and the common-rail (CR; e.g., [1–3]), are the heart of advanced diesel engines. These systems could provide features required by an advanced engine such as a more precise injection quantity, a more flexible injection timing, and a higher injection pressure, compared to the conventional mechanical injection systems. A high injection pressure combined with a small hole diameter nozzle can provide (1) better spray formation, due to the finer initial drops exiting the nozzle, with a higher velocity; (2) better air entrainment and air-fuel mixing; (3) a more homogeneous mixture, with a lower local equivalence ratio and fewer over-rich regions. Achievement of these factors have been reported as the keys to generation of a low smoke combustion process as well as reduction of particulate emissions (Pierpont and Reitz [4] and Kato et al. [5]). This paper describes a study of the injection and spray characteristics of the high-pressure HEUI and EUI injection systems.

The HEUI system used in the study was an Indiana Research Institute (IRI) prototype high-pressure injection system for advanced diesel engine combustion research. The system consists of a low pressure fuel supply pump, a high pressure oil pump, a common-rail equipped with a pulse width modulation (PWM) pressure regulator, and an electronic-controlled intensified injector.

The high-pressure oil pump is the source of the system working pressure. It pressurizes and delivers the oil, the working fluid of the system, to the common rail that serves as the pressure accumulator. The pressure regulator then maintains the pressure of the accumulator at a setpoint that can be in the range of 20.7 to 38 MPa (207 to 380 bar). The pressurized oil is fed to the inlet of injector via the common-rail. Once the injector is energized, a spool valve in the injector is opened to allow the pressurized oil to flow through it. The oil then acts on an intensified plunger that subsequently pressurizes the fuel as the fuel is delivered through the injection nozzle. The low-pressure fuel supply pump continuously delivers fuel to the injector with the fuel pressure maintained at approximately 0.7 MPa (7 bar). More details about HEUI can be found in Refs. [6,7].

The EUI system used in the study consists of a low-pressure fuel supply pump, a cam-driven rocker arm, and an electronic-controlled mechanical driven injector. In the injector, a plunger is continuously actuated by the rocker arm when the engine is running, steadily pumping fuel into the plunger chamber. Once the solenoid of the injector is energized, the solenoid-driven poppet control valve closes the channel that connects the plunger chamber to the low pressure returning fuel gallery. Subsequently the pressure of the plunger chamber starts to increase. When the chamber pressure is greater than nozzle opening pressure, fuel injection starts and continues until the solenoid is de-energized and the chamber pressure drops below the opening pressure, which is 3.45 MPa (34.5 bar) for the nozzle used in the study. A strain gage is installed on the surface of the rocker arm for measuring the injection pressure indirectly.

The parameters of injection characterization investigated in this study include injection pressure, injection rate, injector response time, and needle lift. Based on these measured characteristics,

¹Corresponding author.

Contributed by the Internal Combustion Engine Division of THE AMERICAN SOCIETY OF MECHANICAL ENGINEERS for publication in the ASME JOURNAL OF ENGINEERING FOR GAS TURBINES AND POWER. Manuscript received by the ICE Division, Jun. 2000; final revision received by the ASME Headquarters, Mar. 2002. Editor: D. N. Assanis.

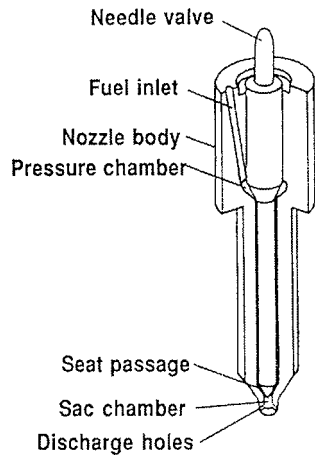


Fig. 1 Schematic of orifice-type nozzle

other useful information was derived, specifically the dynamic discharge coefficients of the nozzles. The parameters of spray characterization investigated in this study include penetration, overall structure, hole-to-hole variation, initial spray breakup, spray at end of injection, spray at peak-pressure injection, and near-nozzle-exit spray cone angle. Both macroscopic and microscopic visualization methods were applied to characterize the HEUI and EUI sprays.

The stability and asymmetry of the fuel sprays from high-pressure nozzles, especially the VCO-type nozzle, has a significant influence on the combustion and emission performance of diesel engines, mainly due to the decreased air utilization for the greater degrees of asymmetry. The variation in spray penetration and spray cone angle from hole to hole must be quantified both before and after the injector tip is utilized on the engine if emissions and combustion variations are to be understood and correlated. In this study, the spray characterization was carried out by injecting fuel into ambient air, and by injecting fuel into a room-temperature nitrogen-filled pressurized chamber. The chamber pressure was adjusted to simulate the air density at the end of the compression stroke of a compression ignition engine. In a real engine, the fuel is injected into the combustion chamber close to the end of the compression stroke. Hence, it is reasonable to assume that fuel sprays injected into a pressurized chamber encounters a similar drag force as that experienced by a fuel spray injected into a real engine. Since the chamber was filled with room temperature nitrogen gas, the fuel sprays mostly were in the form of liquid droplets and could be treated as nonevaporative sprays. Although under the same ambient density condition both the penetration and dispersion of an evaporative spray could be much less than those of a nonevaporative one, the characteristics obtained from a nonevaporative test condition still provides a good indication of the fuel injection performance.

The characterization parameters of macroscopic visualization carried out in this study were the spray penetration, the overall spray structure, and hole-to-hole variation. High-speed photography was used to complete this task by recording the time dependent structure and characteristics of the sprays. By studying the images recorded, the performance of the nozzle tips and the injection units were evaluated.

The characterization parameters of microscopic visualization of this study were the initial spray breakup, the spray at end of injection, spray at peak-pressure injection, and near-nozzle-exit spray cone angle. Although some research had been carried out to characterize the near exit spray behavior, the most current work had limitations. Most previous work used a single-hole nozzle which could not produce a turbulent flow field similar to that produced by multihole nozzles. Some works used scale-up models which could not exactly match the force-ratios and time scales in

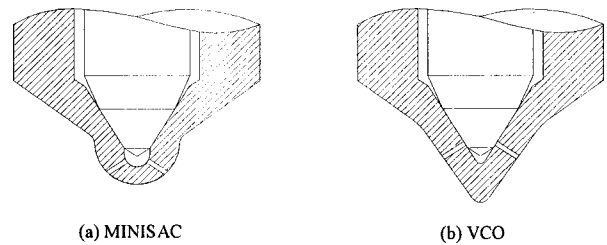


Fig. 2 Nozzle configurations

practical diesel sprays. These studies also used a single-image-per-injection photography technique, either using CCD or a traditional still camera. To overcome the limitations of the previous work, standard multihole nozzles and both a still camera and high-speed drum camera were used in this study.

Experimental Setup

Figures 1 and 2 show the details of the nozzle geometries. In this experiment, two types of multiple-orifice nozzles were used; valve cover orifice (VCO) nozzles and minisac nozzles. The experimental setup for the characterization of the HEUI injection system was as shown in Fig. 3. A Kistler 4067A2000 piezo-resistive pressure transducer was mounted at approximately 6.5 cm upstream of the inlet of the injection nozzle holder. A Bosch type injection rate meter, [8], recorded the injection rate by measuring the pressure wave produced by the injector when it issued an injection into a length of the compressible fluid-diesel fuel. A linear variable differential transformer (LVDT) displacement sensor was mounted on the pressure pin of the injection nozzle holder to detect the needle lift.

A nozzle tip was instrumented with a pressure transducer, as shown in Fig. 4, for the measurement of sac pressure, representative of the downstream injection pressure. By comparing the upstream and downstream injection pressures, the pressure drop and the fuel transportation time across the nozzle holder assembly was determined. A LabVIEW Data acquisition and controls system was implemented to operate the HEUI system during testing. The parameters controlled were the injection pressure, the injection duration, the number of injections, and the synchronization between injection and data acquisition. The LabVIEW system was also used to record and to analyze the test data. The nozzle tip specifications are summarized in Table 1. The flow number, for example, 610 of the VCO nozzle, represents steady state volume flow rate in cubic centimeter within 30 seconds test period with 100 bar injection pressure. And nozzle manufacturer provides the flow number. The experimental setup for the macroscopic spray visualization consisted of a copper-vapor laser system (Oxford CU15), a 35-mm still camera or a high-speed drum camera, a pressurized chamber and its peripheral, and the LabVIEW data acquisition and control system. The copper-vapor laser was expanded into a thin light sheet using a cylindrical lens, functioning as an optical shutter with a 12.5-kHz pulsing frequency and with a minimum exposure time of 10 ns. The drum camera was operated at 250 revolutions per second with a 1/15-second shutter speed. The LabVIEW Data Acquisition and Control System controlled the fuel injection pressure, timing and quantity. At the same time, the LabVIEW system also executed data acquisition and system synchronization among the laser, photography, and fuel injection systems. The injection pressure was recorded with the injection and laser command signals; concurrently images were taken by the photography system. The experimental setup for spray visualization was as shown in Fig. 5. Two levels of chamber pressure, 1.72 and 2.76 MPa (17.2 and 27.6 bar), were used to evaluate the effect of ambient density conditions on penetration and dispersion. For the HEUI spray investigation, a 620 minisac and a 610 VCO were used to analyze the effect of nozzle

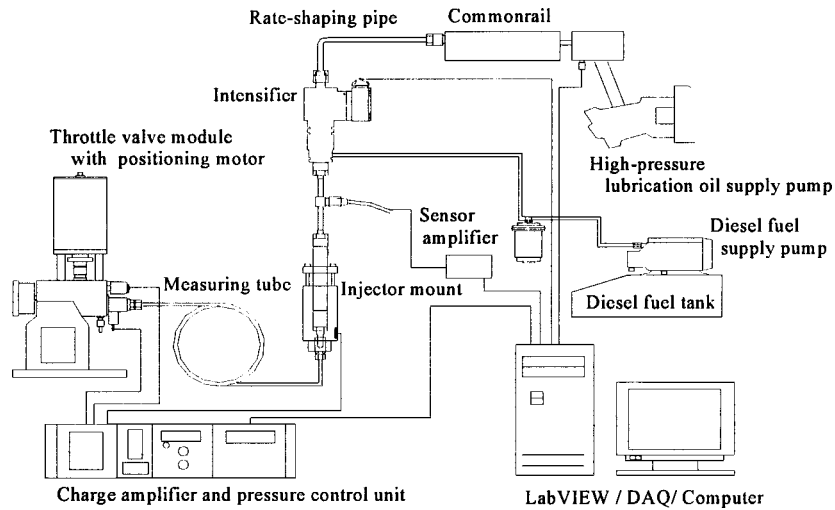


Fig. 3 Schematic diagram of the experimental setup and fuel system

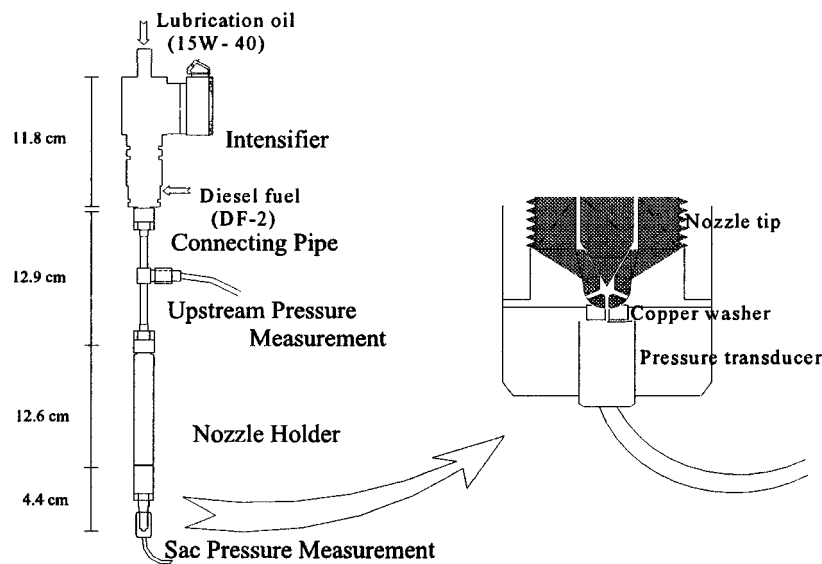


Fig. 4 Injection pressure measurement for both upstream and sac pressure

configuration on spray symmetry. These two different types of nozzles had a similar flow number. Diesel fuel no. # 2 was used in this study.

The optical system setup for microscopic visualization consisted of a long-distance microscope, a copper-vapor laser (Oxford CU15), and a still or high-speed-drum camera. To obtain better image resolution of the initial spray breakup, the peak-pressure injection, and the end of injection, still camera photography was used. The still camera photography methodology utilized 35

×24-mm photographic film, a long-distance microscope, and single-shot produced by laser as the light source. To obtain more insight of the near nozzle exit spray dynamics, the high-speed drum camera was used. The drum camera photography methodology utilized 10×24-mm photographic film, long-distance microscope, and 25-kHz pulsed copper laser. The copper laser was expanded into a thin sheet with a thickness less than 0.09 mm by using cylindrical lens. It was used as the optical shutter for both the one shot and the 25-kHz shots, with a minimum exposure time of 10 ns. The drum camera was operated at 250 revolutions per second with a 0.16-second shutter speed. The long-distance microscope, similar to the ones used by other researchers (Sjoberg et al. [9], Fath et al. [10], and Lai et al. [11]), was used to magnify the diesel spray structure very close to the nozzle exit. With the long distance microscope lens located 8.75 inches away from the observed object, the amplification factor was 17.4, resulting in a diffraction-limit resolution as small as 1–2 micron. The optical setup provided excellent resolution in both time and space, as shown in Fig. 6.

Table 1 Nozzle specifications

Nozzle Tip	No. of Holes	Hole diameter (mm)	Total Hole Flow area (m ²)	C_d (Steady-state flow)
610 (VCO)	6	0.218	2.24 E-7	0.58
620 Mini-sac	7	0.190	1.98 E-7	0.68
730 VCO	7	0.210	2.42 E-7	0.64

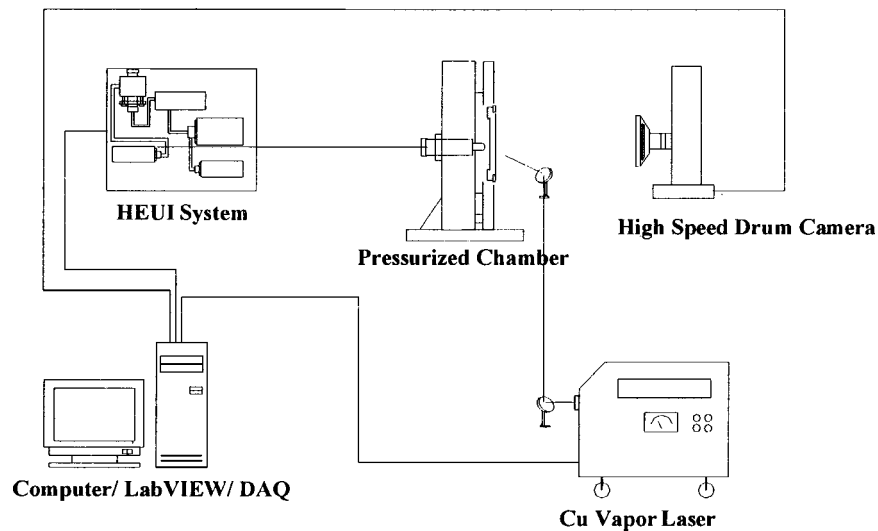


Fig. 5 Schematic of the experimental setup of nonevaporative spray visualization

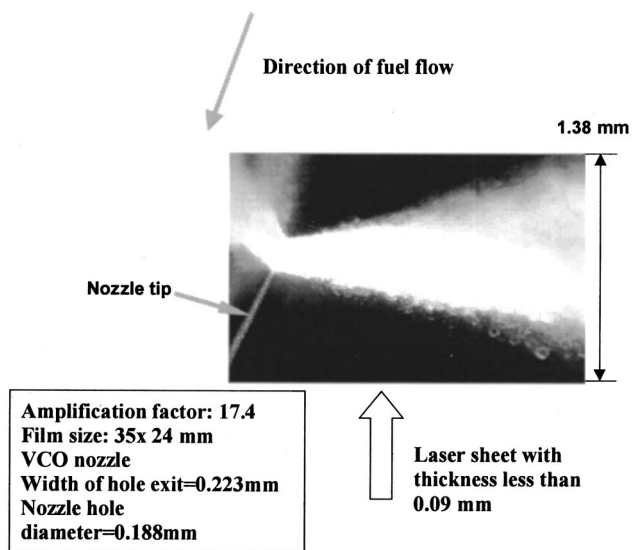


Fig. 6 Schematic of microscopic visualization of VCO nozzle of EUI system

Results And Discussion

1 Characterization of the Hydraulic Electronic Unit Injector (HEUI) system

Injection Pressure. The injection pressure of an HEUI system mainly depended on the common-rail pressure and injection duration. As shown in Fig. 7, with an injection duration of 2.25 ms, the injection pressures increased as common-rail pressures increased. At a 2.25-ms injection duration and 38 MPa (380 bar) common-rail pressure, the system was able to deliver the fuel at injection pressures up to 130 MPa. The intensified ratio, the ratio of injection pressure to common-rail pressure, of the injector for three common-rail pressure settings, 20.7, 27.6, and 38 MPa (207, 276, and 380 bar), were 3.71, 3.80, and 3.44, respectively. Figure 8 showed the effect of injection duration on injection pressure. A 1-ms increase of injection duration contributed to a 29 MPa increase in peak injection pressure. The thickness of the pressure adjusting shim inside nozzle holder also affected the injection pressure. As the shim thickness increased from 1.95 to 3.24 mm, the peak injection pressure increased from 4 to 6%.

Injector Response Time. The injector response time, the time between injection command and start-of-injection (SOI), was in the range of 1.4 to 1.8 ms. The injector was driven by a peak-and-hold type driver powered by 70-volt power supply. The injector response time consisted of two time increments. The first time

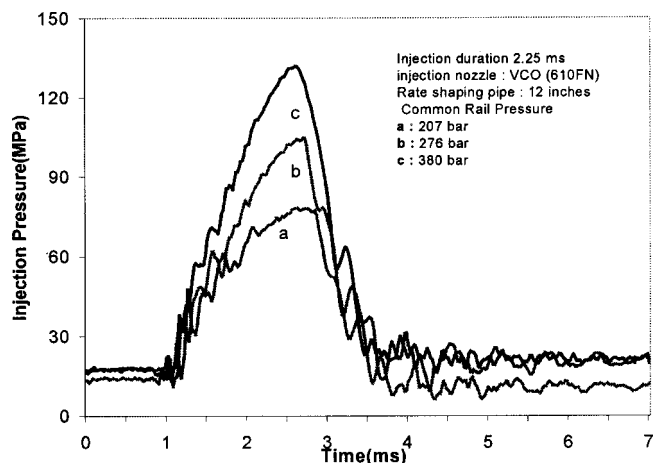


Fig. 7 The effect of common-rail pressure on injection pressure

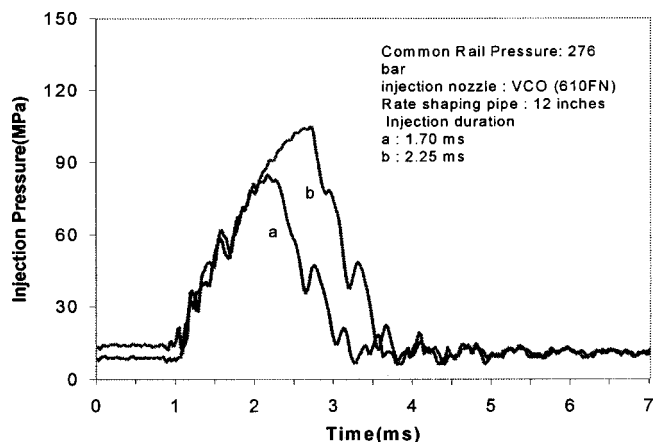


Fig. 8 The effect of injection duration on injection pressure

Table 2 The effect of common-rail pressure (C.R.P.) and length of rate-shaping pipe on response

Common-rail Pressure	Response time (ms)	
	24 Inches shaping pipe	12 Inches shaping pipe
207 bar (20.7 MPa)	2.0	1.8
276 bar (27.6 MPa)	1.7	1.6
380 bar (38 MPa)	1.5	1.4

Table 3 The effect of common-rail pressure and shim thickness on response

Common-rail Pressure	Response Time (ms)	
	3.24 mm Shim Thickness	2.16 mm Shim Thickness
207 bar (20.7 MPa)	1.6	1.8
276 bar (27.6 MPa)	1.5	1.6
380 bar (38 MPa)	1.4	1.4

increment is that required to energize the solenoid that drives the spool valve. The second time increment is that required for the spool valve to move to the open position and the line pressure to build up. The former depends on the power supply voltage applied to the driver; the latter depends mainly on common-rail pressure and the length of the rate-shaping pipe. The results summarized in Tables 2 and 3 that a long rate-shaping pipe, a low common-rail pressure, and a reduced pressure adjusting shim thickness increase the injector response time.

Injection Rate and Needle Lift. The injection rate mainly depended on the common-rail pressure, the needle lift, the nozzle hole area, and the length of the rate-shaping pipe. As shown in Fig. 9, a higher common-rail pressure provides a higher rising rate of injection pressure, and consequently a higher injection rate. When using a 24 inch rate-shaping pipe, the pressure rising rate decreased and the needle lifted more slowly, both of which resulted in lower injection rate (Fig. 10). Figure 11 shows the effect of nozzle hole area on injection rate. As the nozzle flow area increased, the injection rate increased but there was no significant effect on the shape of the injection rate. The injection duration, the type of nozzle tip (VCO or mini-sac), and the thickness of the pressure-adjusting shim had little effect on injection rate. The maximum needle lift of the nozzles used in the tests was 0.31 mm, as measured from the needle seat to the fully open position. The

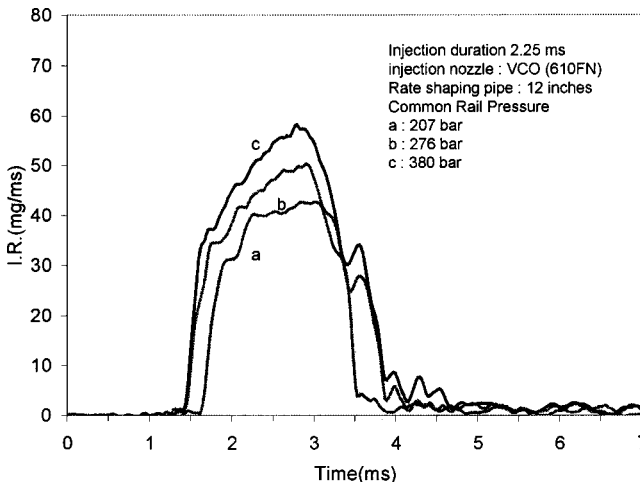


Fig. 9 The effect of C.R.P on the injection rate

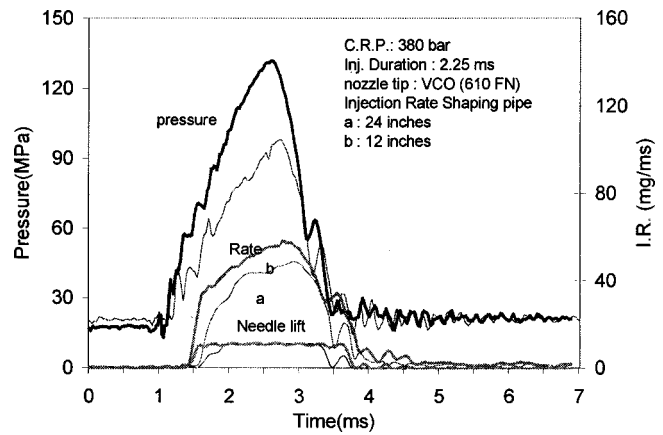


Fig. 10 The effect of length of rate-shaping pipe on the injection rate

pressure in the nozzle pressure chamber and the pressure applied to the top of the needle determine the needle lift behavior. In the case of HEUI nozzles, the pressure applied to the top of needle was equivalent to atmospheric pressure therefore the pressure in the nozzle pressure chamber dominated the needle lift pattern. As shown in Fig. 10, when a 12-inch rate-shaping pipe with a common-rail pressure of 380 bar (38 MPa) was used, it took 0.2 ms for the needle to reach the fully open position. However, with a longer injection rate-shaping pipe (24 inches) and a lower common-rail pressure (276 bar), the needle lift time increased to 0.6 ms. The test result also showed that an increase in the pressure adjusting shim thickness reduced needle bounce.

Nozzle Discharge Coefficient. The steady-state discharge coefficients (C_d) of the nozzles, tabulated in Table 1, were calculated from the nozzle data based on the following formula:

$$C_d = \frac{Q}{A \times \sqrt{\frac{2 \times P}{\rho}}}$$

where,

Q = volume flow rate, m^3/s

A = nozzle flow area, m^2

P = injection pressure, MPa

ρ = fuel density, Kg/m^3

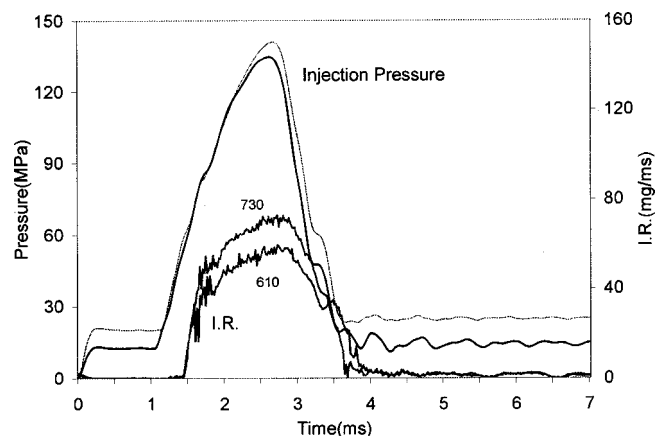


Fig. 11 The effect of nozzle flow area on the injection rate

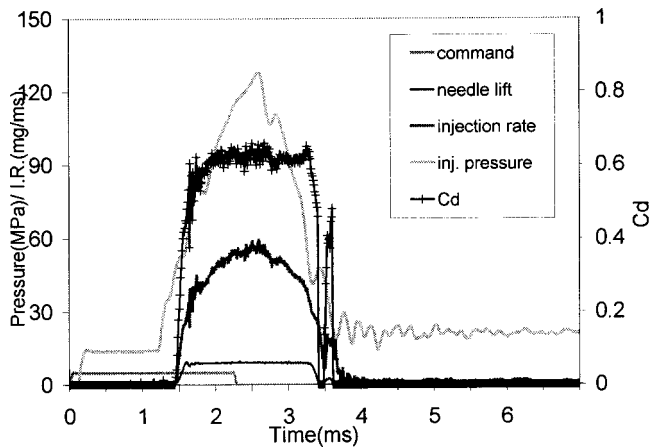


Fig. 12 Dynamic discharge coefficient—620 minisac nozzle

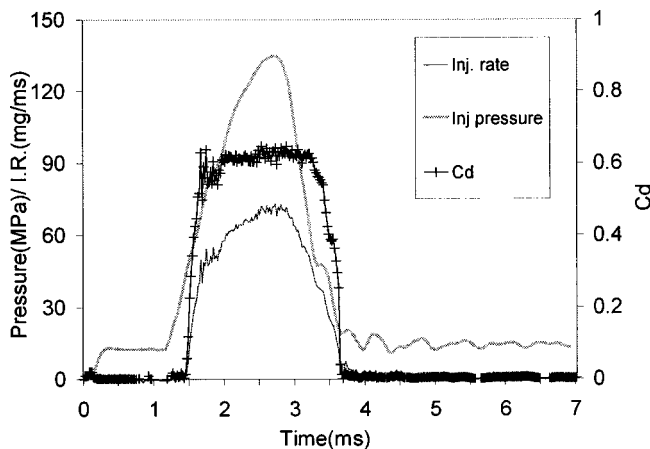


Fig. 13 Dynamic discharge coefficient—730 VCO nozzle

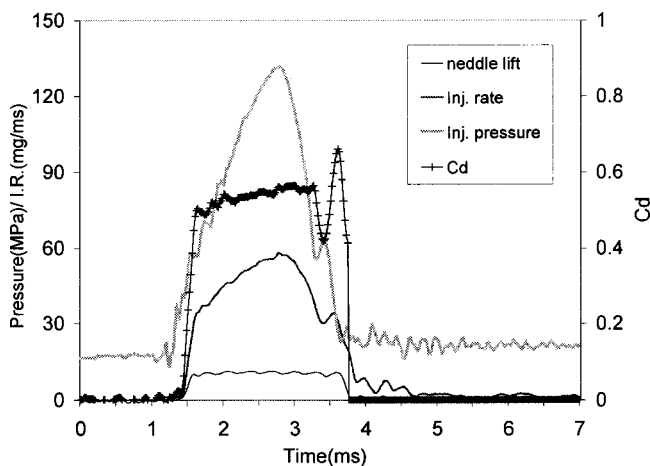


Fig. 14 Dynamic discharge coefficient—610 VCO nozzle

The dynamic discharge coefficients of the nozzle are calculated from the same formula; however, the measured upstream pressure and injection rate are used instead of the injection pressure and the volume flow rate. Shown in Figs. 12, 13, and 14 are typical traces of the dynamic C_d , the injection pressure, the injection rate, and needle lift for 620 minisac, 730 VCO and 610 VCO nozzle, respectively. Each of the C_d traces shown in the figures can be divided into three segments, corresponding to three phases of needle opening, full lift, and closing. For example, in Fig. 12,

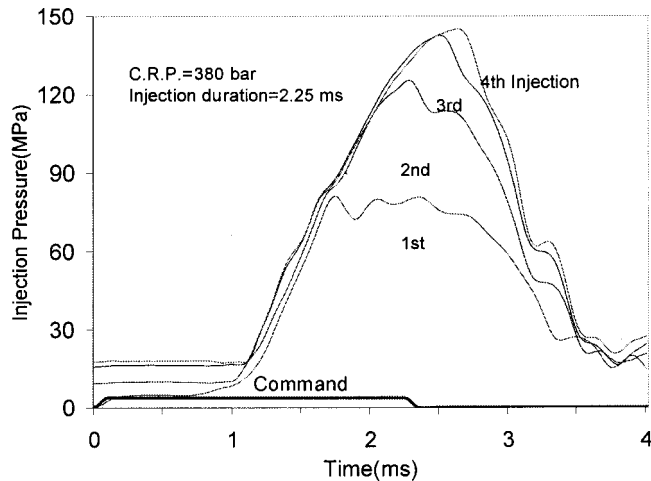


Fig. 15 Injection pressure transient at system startup

while the needle was opening the C_d increased from 0 to about 0.57. Once the needle reached the full lift position the C_d gradually approached 0.62 and maintained the same value until the needle started to close. While the needle was closing, the C_d decreased from 0.62 to 0. Needle bouncing was observed in this case. The calculated dynamic discharge coefficient, 0.62, at needle full-lift conditions, is about 6% lower than the steady-state discharge coefficient, 0.66. (see Figs. 13 and 14.)

Injection System Startup Behavior. Figures 15 and 16 show the transient injection pressure and the injection rate during system startup. When the common-rail pressure was maintained steadily at 380 bar (38 MPa), the injection system took three to four injections to build up pressure in both the intensifier and high-pressure line before a nominal injection was issued. The injection pressure, injection rate, and injection quantity became stable and repeatable after the third injection was issued. The test results are summarized in Table 4. For the first injection, the pressure reached 56% of the nominal (140 MPa) and the quantity reached 71% of the nominal (101 mg).

Pilot Injection. The system was capable of delivering pilot injection, however, the operating range of pilot injection in terms of its duration and dwell time was quite limited. The lower limit of injection duration for pilot injection was 0.6 ms for the current system. The injector could not perform pilot injection with a duration shorter than this. The dwell time, the time between issue of pilot and main injection, could not be shorter than 0.6 ms. Figure 17 typical measurement of the injection rate and needle lift for injection with the pilot and main. Figures 18 and 19 show the effect of dwell time on main injection in terms of injection rates and needle lift. With a shorter dwell time the peak pressure and quantity of the main injection on injection were lower than those of an injection with a longer dwell time. This could be due to the slow pressure recovery in the common-rail after a pilot was de-

Table 4 Transient of hydraulic electronic unit injector (HFUI) injection during system starting period

Injection Since Engine Startup	Injector Response Time (ms)	Peak Injection Pressure (MPa)	Injection Quantity (mg)
1st	1.5	80	72
2nd	1.44	127	90
3rd	1.38	143	99
4th	1.4	145	101
5th	1.38	140	101

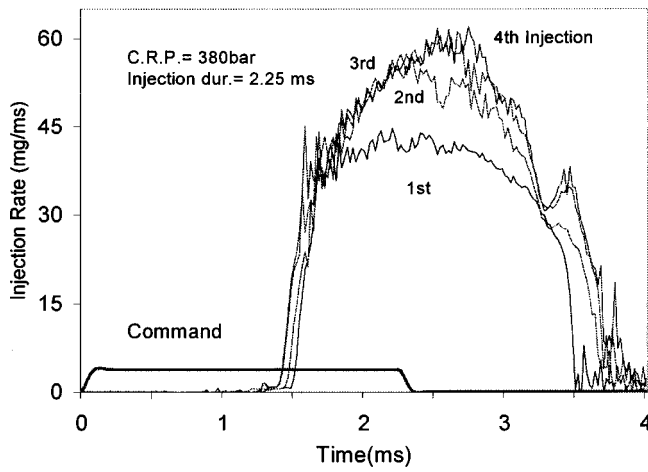


Fig. 16 Injection-rate transient at system startup

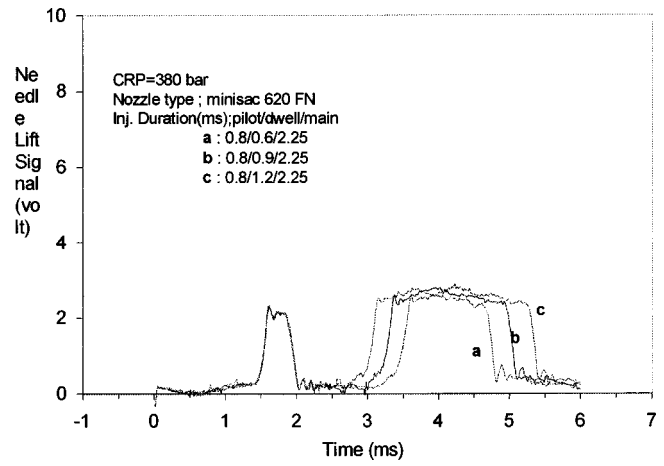


Fig. 19 The effect of dwell time on needle lift of the main injection

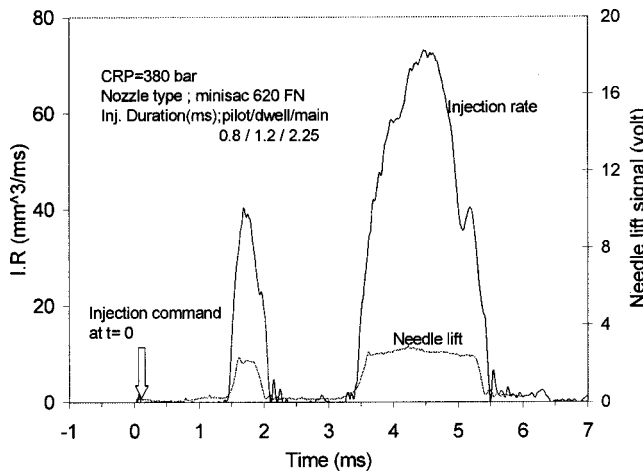


Fig. 17 Injection-rate and needle lift measurement for pilot/main

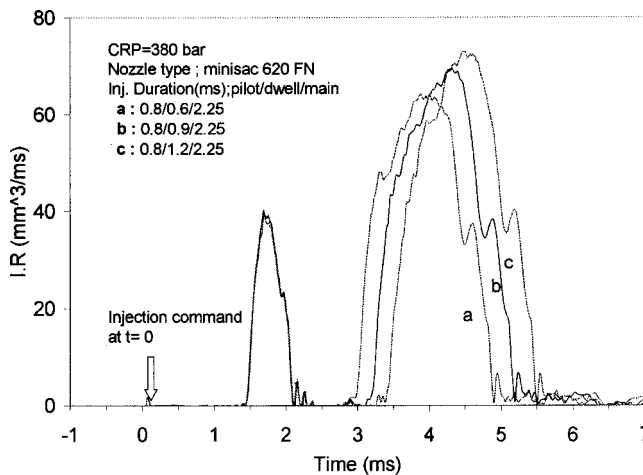


Fig. 18 The effect of dwell time on injection rate of the main injection

livered. Figure 20 shows the effect of dwell time on injection quantity. As dwell time decreased the injection quantity of the main injection decreased.

Figure 21 shows that the peak pressure of the main injection decreases as the peak pressure of the pilot injection increases.

Because the system could not make a pilot injection with 0.5-ms duration, condition “a” did not lead to a pilot injection. This resulted in a higher main peak injection pressure, as trace “a” in Fig. 21 shows. If the pressure of pilot injection increased due to a longer duration, a decrease of peak pressure of the main injection could be observed, as trace “b” and “c” in Fig. 21 shows.

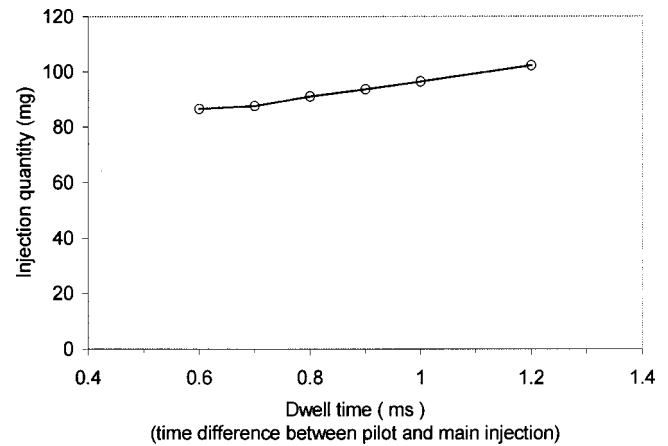


Fig. 20 The effect of dwell time on quantity of the main injection

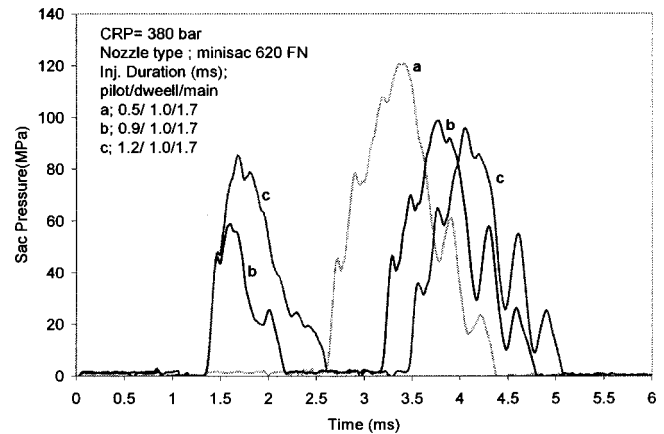


Fig. 21 The effect of pilot injection pressure to main injection pressure

Table 5 Summary of sac pressure measurement

Common Rail Pressure (MPa)	Injection Duration (ms)	Peak Upstream	Peak Sac Pressure (MPa)	Pressure Drop (MPa)	Time Lag (ms)
380	2.25	158	149	9	0.12
380	1.70	126	121	5	0.14
276	2.25	114	108	6	0.14
276	1.70	101	91	10	0.1

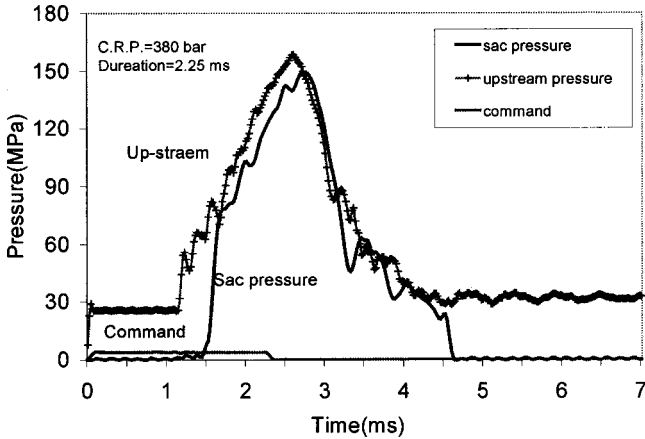


Fig. 22 Sac pressure and up-stream pressure with 380 bar C.R.P and 2.25 ms duration

Sac Pressure and Upstream Pressure. For the injection characterization study, the injection pressure was measured at 6.5 cm upstream of the fuel inlet of the injection nozzle holder (as shown in Fig. 4). To correlate the upstream pressure and the sac pressure (the pressure in the sac chamber of the nozzle tip), a special instrumented nozzle tip and adapter were made such that the pressure transducer could directly access the sac chamber of the nozzle tip. The upstream and sac pressures were measured at the same time. The test cases and results are summarized in Table 5. Figures 22 and 23 show the pressure traces for two of the test cases. The pressure drops between the upstream location and the sac chamber were in the range of 5 to 10 MPa. It is believed that the pressure drop occurred mainly at the needle seat region when high-pressure and high-velocity fuel flowed through it. The pressure transportation lags were in the range of 0.1 to 0.14 ms. The

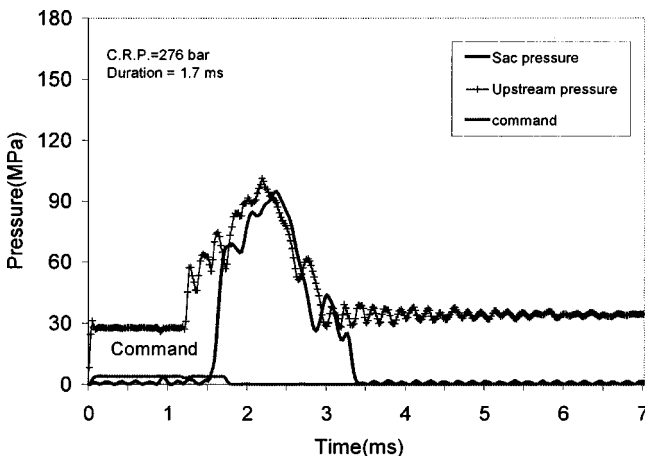


Fig. 23 Sac pressure and upstream pressure with 276 C.R.P and 1.7 ms duration

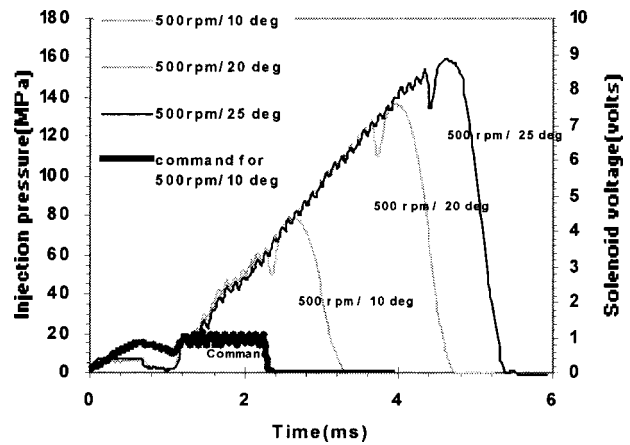


Fig. 24 Injection pressure of EUI system, with various injection duration and 500 rpm camshaft speed

correlation between the injection condition (common-rail pressure and injection duration), and transportation lag was not found.

Characterization of the Electronic Unit Injection (EUI) system. The necessary injection pressure of the EUI system was determined mainly by the engine camshaft speed, the cam profile and the injection duration. As shown in Fig. 24, with a 500-rpm camshaft speed, the pressure rising rate was 50 MPa per millisecond; with 25 crank angle injection duration, the peak injection pressure reached 160 MPa. The injection pressure decreased as the speed of the camshaft decreased, as shown in Fig. 25. The injector response time increased from 1.6 ms to 2.1 ms, corresponding to the decrease of camshaft speed from 600 to 300 rpm.

Macroscopic Spray Visualization

Spray Penetration and Correlation With Empirical Model. Figures 26 to 30 demonstrate how the tip penetration of the HEUI and EUI sprays change with various ambient pressures. On the average, an increase of the ambient pressure from 1.72 to 2.76 MPa (17.2 to 27.6 bar) reduces the penetration by 24% for the HEUI sprays (Figs. 26, 27) and by 10% for the EUI sprays (Figs. 29, 30).

Figure 31 shows the correlation between the measured and calculated penetration of the HEUI sprays under various ambient conditions. (Table 6.) The calculated penetration was based on the following empirical model proposed by Hiroyasu et al. [12]

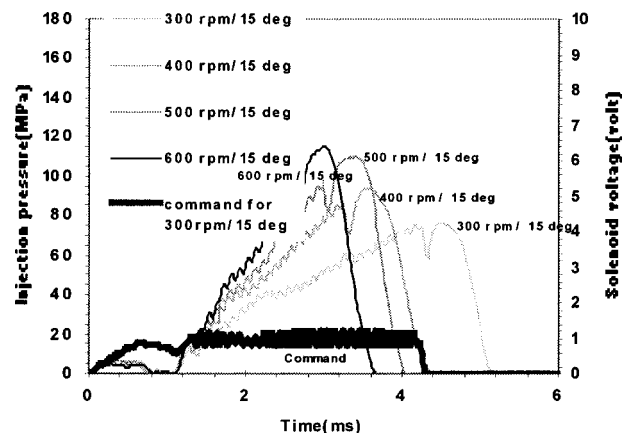


Fig. 25 Injection pressure of EUI system, with various camshaft speeds and 15-deg injection duration

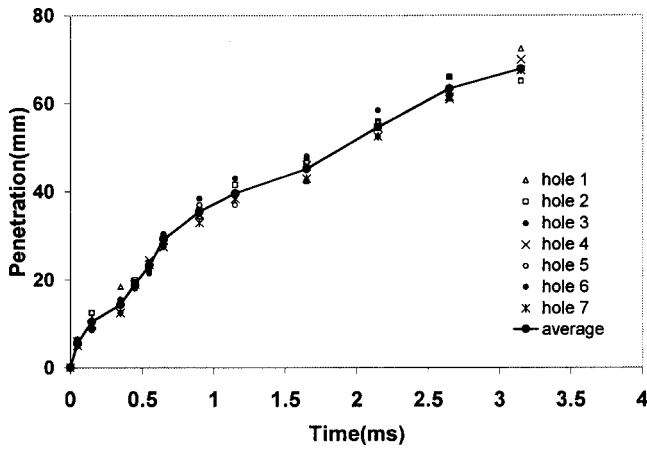


Fig. 26 Hole-to-hole penetration variation of the HEUI sprays, with 620 mini-sac nozzle, pressure of 77 MPa, duration of 2.85 ms, and ambient pressure of 2.76 MPa (27.6 bar)

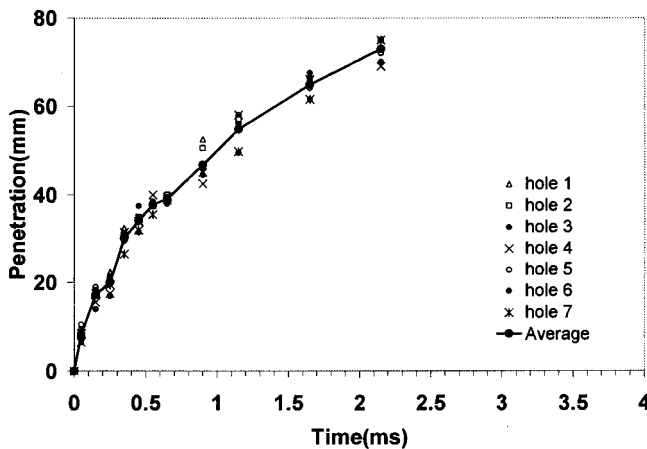


Fig. 27 Hole-to-hole penetration variation of the HEUI sprays, with 620 mini-sac nozzle, pressure of 77 MPa, duration of 2.85 ms, and ambient pressure of 1.72 MPa (17.2 bar)

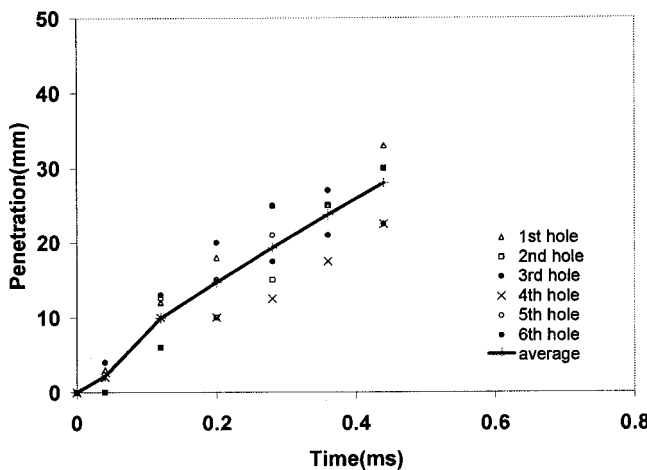


Fig. 28 Hole-to-hole penetration variation of the HEUI sprays, with 610 VCO nozzle, pressure of 126 MPa, duration of 2.25 ms, and ambient pressure of 2.76 MPa (27.6 bar)

$$S = C_V \sqrt{\frac{2\Delta P_t}{\rho_1}}, \quad 0 < t < t_b \quad (1)$$

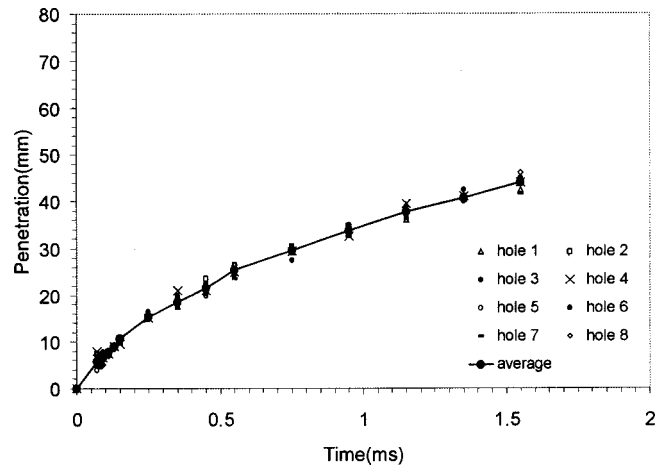


Fig. 29 Hole-to-hole penetration variation of the EUI sprays, with 0.188-mm VCO nozzle, pressure of 80 MPa, duration of 2.3 ms, and ambient pressure of 2.76 MPa (27.6 bar)

$$S = 2.95 \left(\frac{\Delta P}{\rho_a} \right)^{1/4} \sqrt{d_0 t}, \quad t \geq t_b \quad (2)$$

where $C_V = 0.55$,

Coefficient of effective injection velocity

$$t_b = 28.65 \frac{\rho_f d_0}{\sqrt{\rho_a \Delta P}}$$

S = penetration

ΔP = injection pressure

ρ_f = density of fuel

ρ_a = density of ambient gas

d_0 = diameter of nozzle hole

The input data for the above calculation includes nozzle specifications, injection quantity, injection rate, density of ambient gas, and density of fuel. A value of 0.8 was used as the coefficient of spray contraction for the calculation of the average injection velocity (Kuo [13]). To best fit with the measured data, 0.55 had been chosen as the value of coefficient of effective injection velocity for the calculation of penetration of HEUI sprays. In general, the model correlates fairly well with the measured data. However, the model tends to overpredict the early phase of the penetration and underpredict that of the later phase.

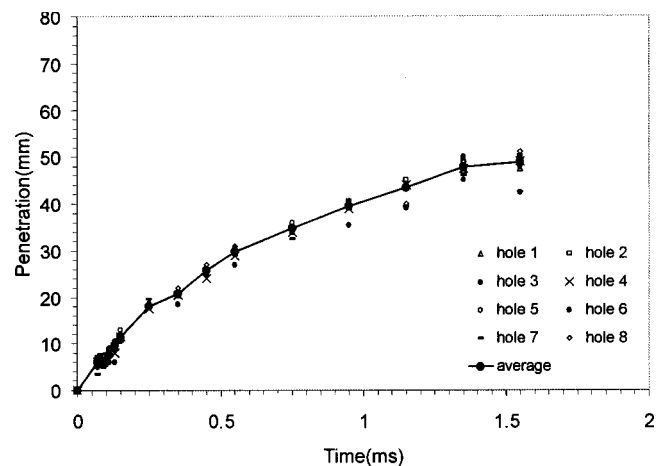


Fig. 30 Hole-to-hole penetration variation of the EUI sprays, with 0.188-mm VCO nozzle, pressure of 80 MPa, duration of 2.3 ms, and ambient pressure of 1.72 MPa (17.2 bar)

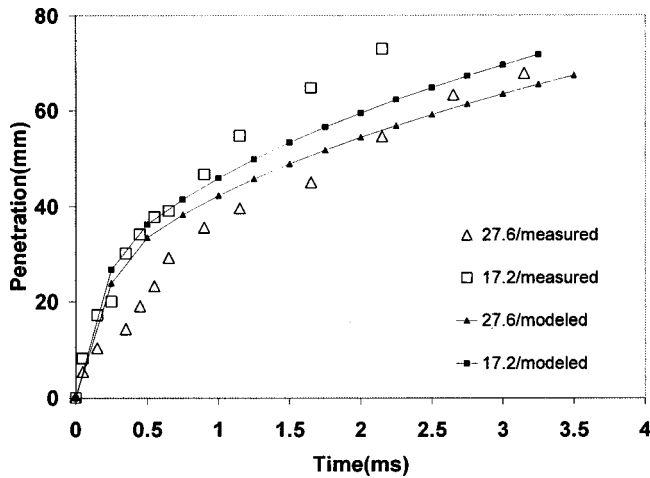


Fig. 31 Correlation between measured and modeled penetration of the HEUI system, with pressure of 77 MPa, duration of 2.25 ms, 620 mini-sac nozzle, and ambient pressures of 1.72 and 2.76 MPa (17.2 and 27.6 bar).

Figure 32 shows the HEUI system pilot injection maximum penetration under various peak injection pressures. With peak pressure of 25 MPa and ambient pressure of 2.7 MPa (27 bar), the maximum penetration of the pilot injection was 22 mm. The maximum penetration increased with increasing peak injection pressure. As the peak pressure increased to 50 MPa, the maximum penetration reached 50 mm.

Hole-To-Hole Spray Variation and Spray Structure. Figure 33 illustrates the early spray development of injections at a common-rail pressure of 38 MPa (380 bar). These time-sequence photographs were taken using a drum camera with a copper-vapor laser pulsing at 12.5 kHz. At atmospheric ambient pressure, sprays of the minisac nozzle showed an extremely asymmetric pattern (Fig. 33, L1 to L4). As the ambient pressure increased to 2.7 MPa (27 bar), the spray pattern became more symmetric and, at the same time, a substantial decrease of the penetration was observed (Fig. 33, M1 to M4). As compared to the minisac nozzle, the VCO nozzle shows significant hole-to-hole variation (Fig. 33, R1 to R4). The mini-sac nozzle demonstrated a more uniform spray penetration and structure. Asymmetry and a puffy structure were observed in the VCO nozzle sprays. Significant hole-to-hole variation in cone angle in the VCO nozzle sprays was also observed, especially at the early stage of spray development. The fastest spray of the VCO nozzle appeared in the 11 o'clock direction, while the slowest one was right on the opposite side, in the 5 o'clock direction. In addition, a puffy structure along the edges of the sprays was also observed for the 1, 3, 5, and 7 o'clock sprays. It is reasonable to conclude that the needle-to-seat eccentricity was most severe upon the 5 o'clock nozzle hole, which conse-



Fig. 32 Maximum penetration length of pilot injection with various injection pressure; 25 MPa (left), 30 MPa (middle), and 50 MPa (right)

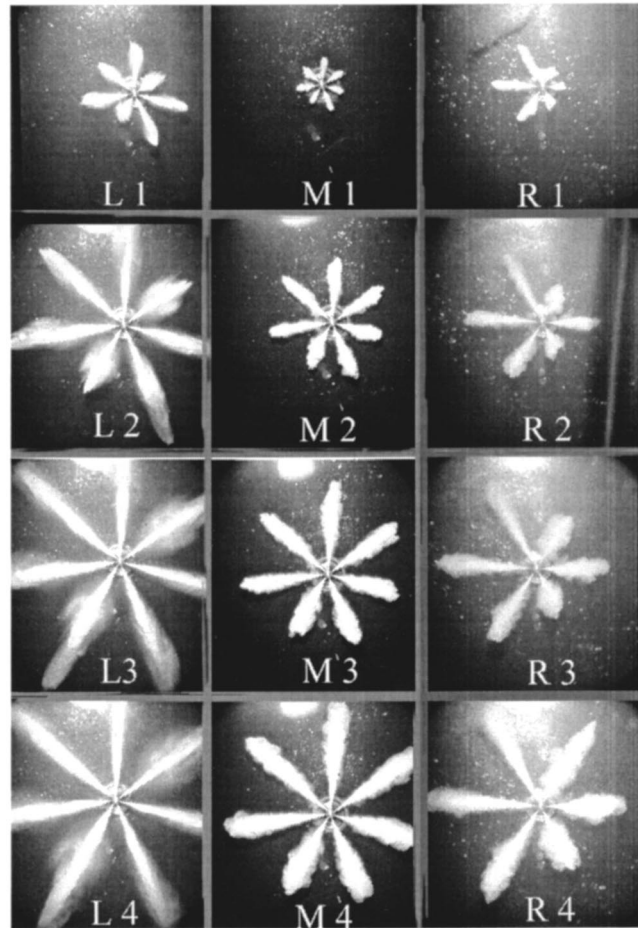


Fig. 33 Early spray developments

quently reduced the flow area of the corresponding hole at the early stage of spray development. The puffy structure at the early development of these sprays may be categorized as hollow cone spray with characteristics of wide angle, as previously identified by Soteriou et al. [14]. These early-developed sprays with puffy structure were surpassed and penetrated by the later coming solid cone sprays after 0.24 to 0.32 ms from start of injection.

Figures 26 to 30 show the variations in spray penetration of HEUI and EUI systems under two ambient pressures. Figure 33 shows penetration variations corresponding to Fig. 28. As summarized in Table 7, the variation of spray penetration depends upon the type of injection system, the nozzle configuration, and the ambient pressure. In general, the EUI system equipped with a VCO nozzle had the best performance in terms of penetration variation. The EUI system used in the test is designed for a heavy-duty engine; it has a sturdy injector construction with a larger nozzle, which generally results in a more symmetric spray. As that for the HEUI system, the variation of the mini-sac nozzle is about 47% less than that of the VCO nozzle. The testing also showed that an increase of ambient pressure slightly reduced the magnitude of variation for all cases.

Table 6 Description of macroscopic visualization of Fig. 33

	Nozzle type	C.R.P.	Ambient P	Inj. Duration	Injection P
Left	minisac 620 FN	380 bar	Atmosphere	2.25 ms	130 Mpa
Middle	minisac 620 FN	380 bar	27 bar	2.25 ms	133 Mpa
Right	VCO 610 FN	380 bar	27 bar	2.25 ms	126 Mpa

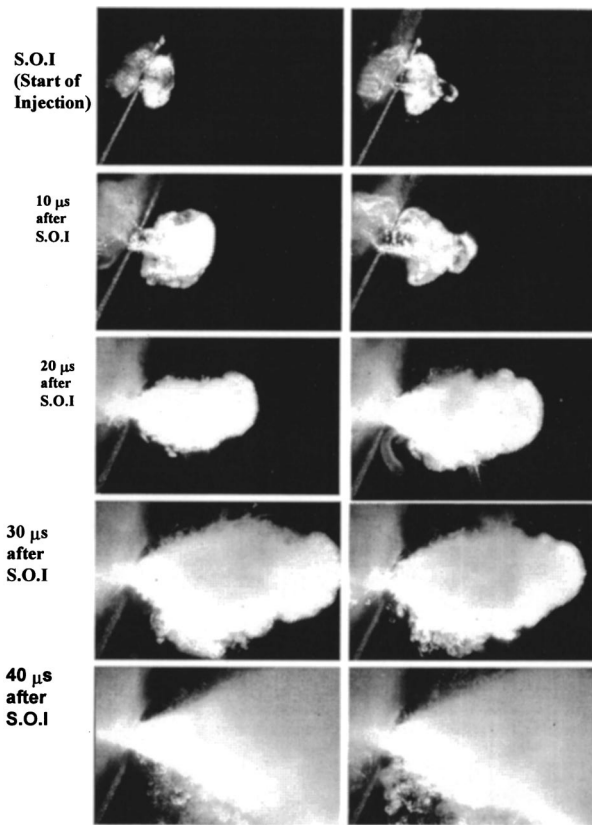


Fig. 34 Still photographs of early development of EUI sprays, with 0.188-mm VCO nozzle, 1500 rpm engine speed, and duration of 10 deg

4. Microscopic Spray Visualization

Initial Spray Breakup. The method of single-shot microscopic visualization using a 35-mm still camera was used to investigate the primary breakup mechanisms, in order to take higher resolution pictures and to avoid the vibration effects that could be introduced by the high-speed rotating drum camera. Figure 34 show a collection of the microscopic photographs of the EUI spray for initial spray development right after SOI. The still-photography captured the overall spray boundary and provided excellent contrast on black-and-white film. These closeups were taken to catch the onset of spray formation, where the spray just exited the nozzle orifice. The photographs show a very dynamic primary breakup process very close to the injector. For the EUI injection system, the injection pressure and its rising rate are directly proportional to engine speed. Figure 34 shows the primary breakup process of EUI spray with 1500-rpm engine speed and 10-deg injection duration. At the earliest instant that the camera was able to capture the spray exiting the nozzle, the liquid column appeared to have a translucent potential core wrapped by a separating boundary layer

Table 7 Comparison of hole-to-hole penetration variation of the injection systems

Injection System	Nozzle tip/hole diameter	Ambient pressure (bar)	Variation of penetration (mm)
EUI	VCO/0.188 mm	17.2	1.3
		27.6	1.0
HEUI	mini-sac/0.190 mm	17.2	2.2
		27.6	1.8
HEUI	VCO/0.210 mm	17.2	3.8
		27.6	3.7

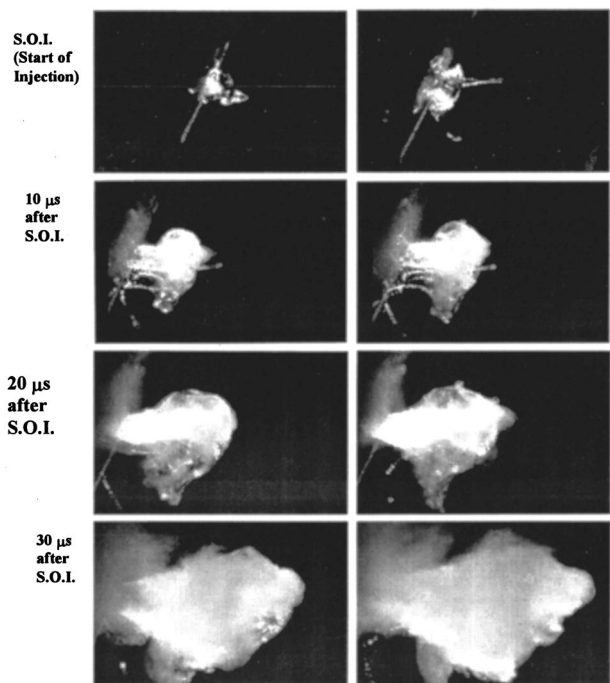


Fig. 35 Still photographs of early spray development of EUI sprays, with 0.188-mm VCO nozzle, 750 rpm engine speed, and injection duration of 10 deg

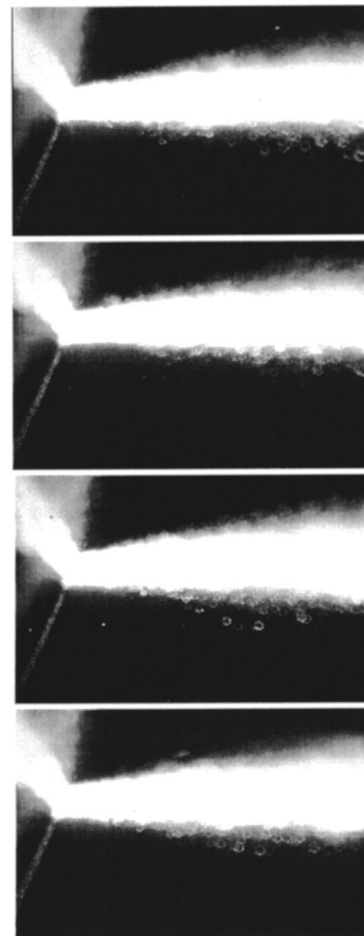
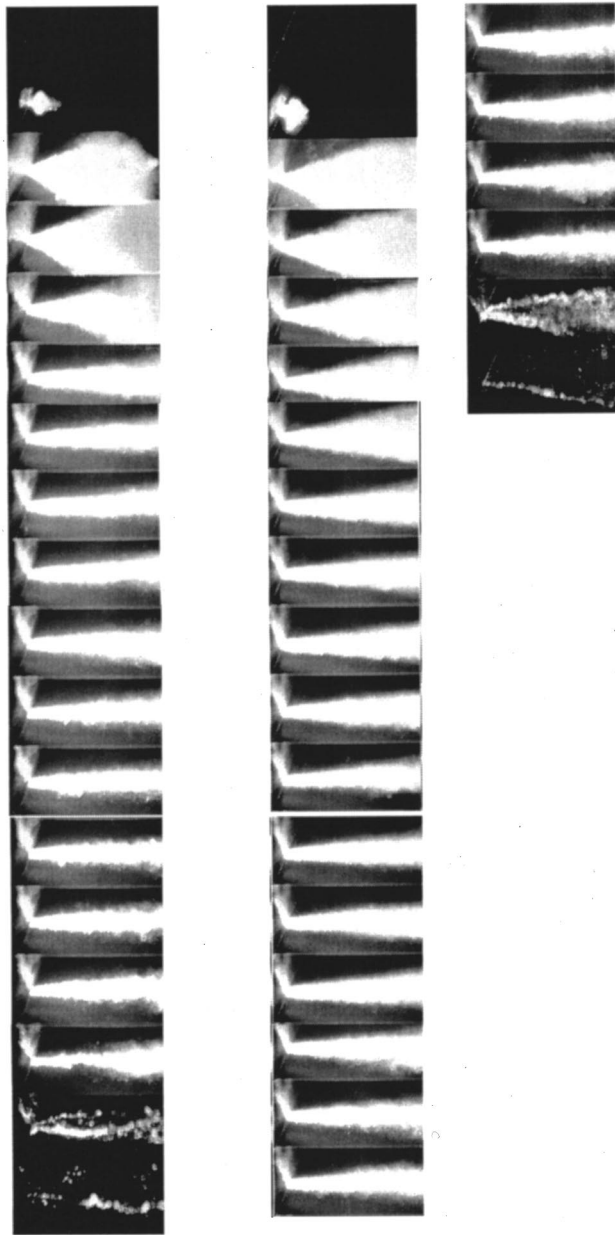


Fig. 36 Still photographs of EUI spray at peak injection of 200 MPa, with 1500 rpm engine speed and injection duration of 25 deg



375-rpm camshaft speed & 7 degree duration 750-rpm camshaft speed & 10 degree duration

Fig. 37 Microscopic visualization of EUI spray

that tended to mushroom and roll up, as shown on the 10- μ s image of Fig. 34. The asymmetry of the spray structure was obvious in the early spray development. Further into the spray development, at 40 μ s after start of injection, the spray evolved to have a very large cone-angle. A cluster of fuel particles with sizes as large as 55 μ m can be observed at the left bottom corner of the images. Figure 35 shows a similar test case, but with a lower pressure rising rate due to reducing the engine speed to 750 rpm. Because the pressure rising rate was reduced by a half, the early spray development process also slowed down. The shape of the sprays in the early spray development was more irregular as compared to the case of 1500 rpm. For these early spray developments, the spray penetration velocity was about 40 m/s, while the injection pressure was close to or slightly higher than the needle opening pressures of 34.5 MPa.

Microscopic photographs of the EUI spray at peak-pressure in-

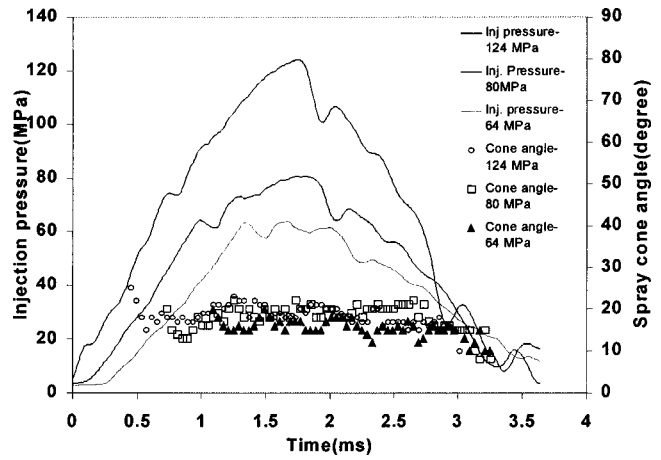


Fig. 38 Spray cone angle and injection pressures of HEUI spray, with fixed duration of 2.25 ms and 610 VCO nozzle

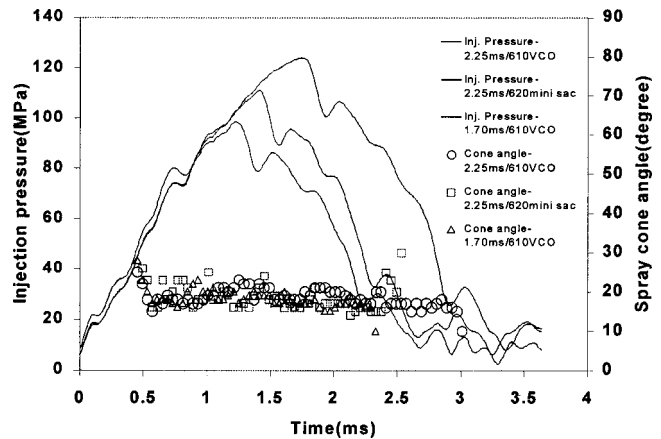


Fig. 39 Spray cone angle and injection pressure of HEUI spray, with fixed common-rail pressure of 37.9 MPa (379 bar)

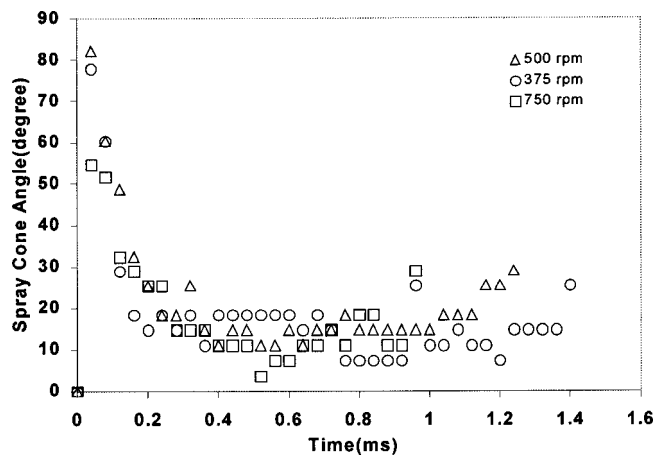


Fig. 40 Spray cone angle of EUI spray with various camshaft speeds

jection are shown in Fig. 36, which were taken at the maximum injection pressure of 200 MPa from four individual injections. The engine speed was 1500-rpm and the injection duration was 25 deg. The sprays showed a much smaller cone angle. The onset of spray breakup was immediately at the injector exit, indicating the presence of a turbulent primary breakup (Dan et al. [15] and Lai

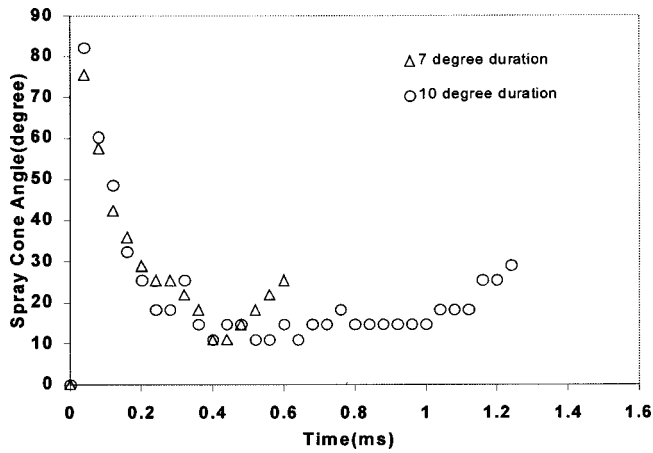


Fig. 41 Spray cone angle of EUI spray with fixed camshaft speed of 500 rpm and injection duration of 7 and 10 crank-angle degree

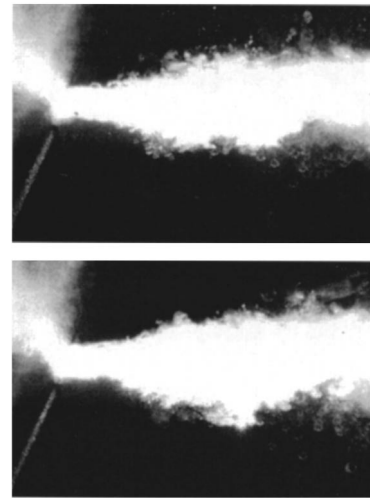


Fig. 43 Still photographs of end of injection of EUI system, with 1500-rpm engine speed and 10-degree duration

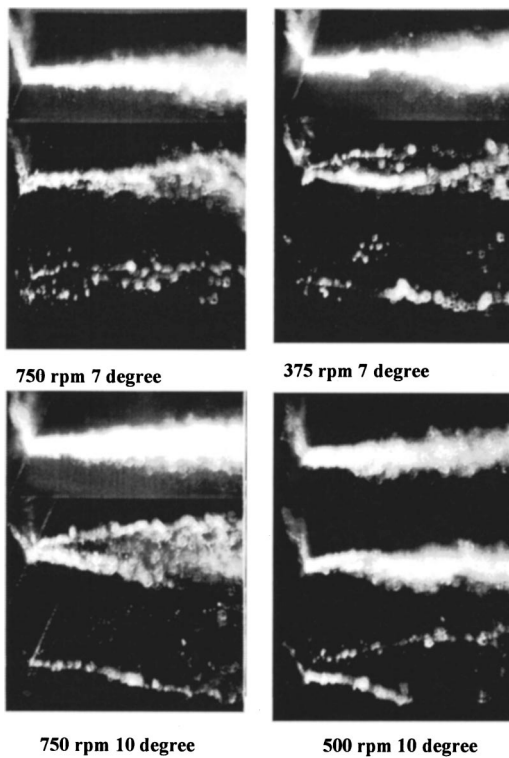
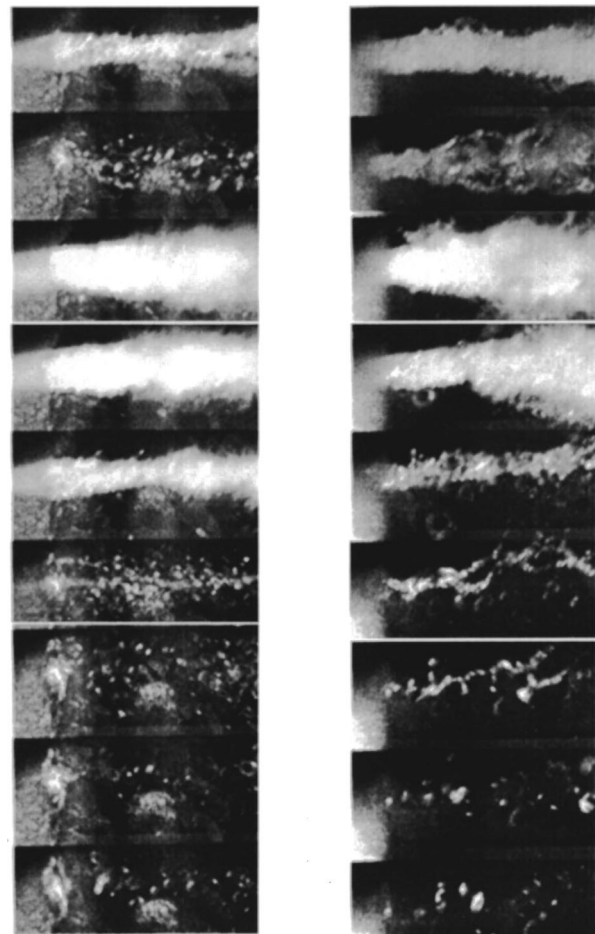


Fig. 42 End of injections of EUI system under various camshaft speeds and injection duration

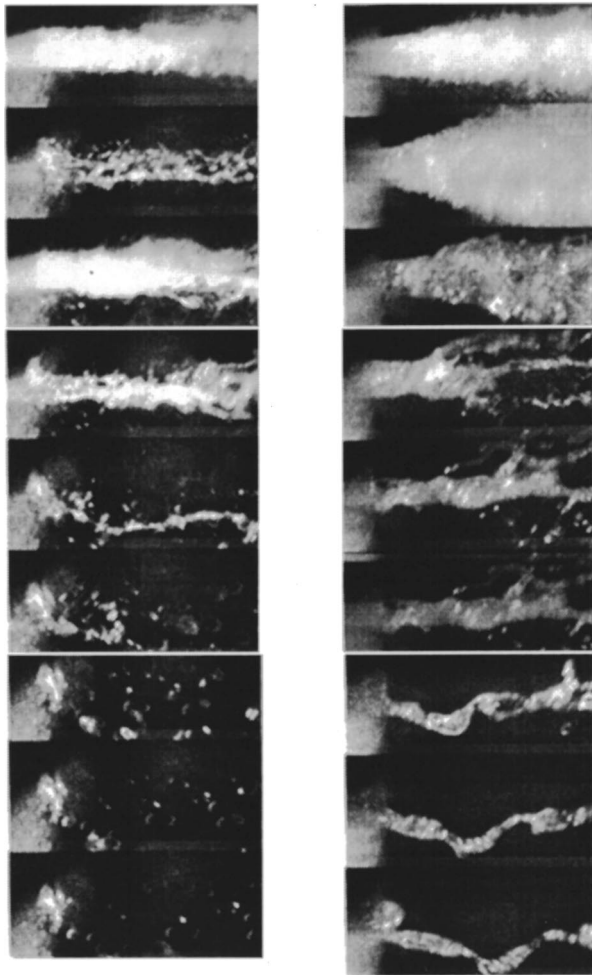
et al. [16]). The bottom side of the spray showed the formation of large droplets. The size of the droplets increased with increasing distance from the nozzle exit. Although some drops were not entirely in focus, their diameters could be estimated to be 10–20% of that of the nozzle hole, corresponding to the turbulent integral scale within the nozzle. In comparison, the top side of the sprays did not show a symmetric and corresponding distribution of large droplets, but instead suggested the formation of a very fine mist, in spite of possible light attenuation across the spray. The nozzle internal flow direction was from top to bottom; therefore, the top-side spray was directly downstream of the turnaround point, where the nozzle internal geometry dictates that the fuel negotiates a sharp turn into the VCO hole. The fine mist observed could



610 VCO nozzle, 98 MPa peak injection pressure & 1.7 ms duration

620 Mini-sac nozzle, 97 MPa peak injection pressure & 1.7-ms duration

Fig. 44 Effect of nozzle configuration on end of injection of HEUI system. (610 VCO versus 620 mini-sac), with common-rail pressure of 379 bar.



610 VCO nozzle,
69 MPa peak
injection pressure &
1.7 ms duration

620 Mini-sac nozzle,
71 MPa peak
injection pressure &
1.7-ms duration

Fig. 45 Effect of nozzle configuration on end of injection of HEUI system. (610 VCO versus 620 mini-sac), with common-rail pressure of 276 bar.

be a direct confirmation of a cavitation-enhanced breakup mechanism (Lai et al. [11]). More research is needed to verify these observations.

Spray Cone Angle and Oscillation. High-speed microscopic visualization of EUI sprays are shown in Fig. 37 for two injection conditions. The spray cone-angle oscillation phenomena were observed on both of the EUI and HEUI sprays. For the HEUI sprays, as shown in Fig. 38, a wider spray angle was observed at the early development of the injections, within 0.2 ms from start of injection, for injection pressures of 64, 80, and 124 MPa. Under the operating conditions for the data plotted in Fig. 10 (12-inch rate-shaping pipe), the time required for the needle to fully open was about 0.2 ms, which is consistent with the time period over which the wider spray cone angle was observed. Hence, it can be concluded that the wider spray cone angle during the early development of the spray is induced by needle opening. This result is also verified by Fig. 39, which shows that under the same pressure rising rate, even with different injection durations and types of nozzles, a wider spray cone angle forms during the early development of the sprays, during the 0.2-ms period after SOI. Similarly, as that for the HEUI spray, a wider spray cone angle was

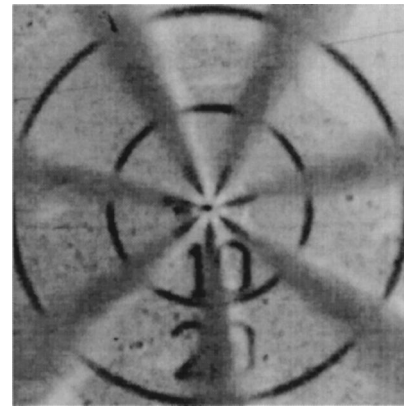


Fig. 46 Secondary injection (needle valve bouncing)

observed for the EUI spray at the early development as well as prior to the end of injection. This is shown in Figs. 40 and 41. The sprays started with an 80-deg spray cone angle. Within 0.2 ms after start of injection, the cone angle decreased to about 20 deg and stabilized at the same angle through the mid-injection period until the end of injections. At that point the cone angle jumped to about 30 deg. As a conclusion of the analysis on the spray cone angle oscillation of EUI and HEUI injection, it is suggested that the opening and closing of the needle induces the wide spray cone angle. In the mid-injection period, both EUI and HEUI sprays were devoid of any significant oscillation, which may be attributed to their quick needle opening and settling at the full open position.

Spray Characteristics at End of Injection. In the microscopic visualization, it was observed that the spray trickled down and formed larger drops or liquid ligaments at the end of injections. Figure 42 shows the end of injections of EUI sprays for four injection conditions. Figure 43 shows the captured images by a still camera taken just prior to the end of injection of two individual EUI injections at a 1500-rpm engine speed and a 10-deg duration. Both figures show that large drops are formed at the edges of the spray as well as in the spray. The maximum size of the larger drops is approximately 100 μm , moving with a speed as low as 12 m/s.

Figure 44 allows comparison of the end of injections of the mini-sac and VCO nozzles of the HEUI system. The mini-sac nozzle tends to produce larger ligaments and drops at the end of injection (and consequently higher HC emission in engine tests). As compared to the minisac nozzle the VCO nozzle showed some improvement. For both injection pressures of 70 and 98 MPa, secondary injection due to needle bouncing were observed. As a result, the period of injection with poor atomization was extended. As shown in Fig. 45, the width of the ligament formed at the end of injection of a mini-sac nozzle was about 110 μm , 60% of the size of the nozzle hole. On the average, the velocity of the drops formed at end of injection of HEUI injection is about 3 to 4 m/s. Figure 46 showed the spray penetration of a secondary injection caused by needle bounce. The maximum penetration of secondary injection could be as large as 5 mm.

Conclusions

1. The specific findings for the characterization of HEUI injection system can be summarized as follows:

- common-rail pressure and length of the injection rate-shaping pipe determine injection pressure, while pressure rising rate and injection duration determines peak injection pressure.
- nozzle flow area, common-rail pressure, and length of rate-

shaping pipe affect injection rate. The rate shape is affected mainly by common-rail pressure, especially the pressure rising rate, and length of rate-shaping pipe.

- injection response time is in the range of 0.1 to 0.18 ms and mainly depends on common-rail pressure, length of rate-shaping pipe, and shim thickness.
- dynamic discharge coefficients derived from measured upstream injection pressures and injection rates are about 6% lower than static discharge coefficients derived from static flow data.
- startup injection transient was observed. At system start-up, it took three to four injections to establish line pressure in the high-pressure section of the system. Afterward, stable and repeated injection was issued.
- the pressure drop across the nozzle seat flow area is in the range of 5 to 10 MPa and transportation lag between upstream and nozzle sac chamber is in the range of 0.1 to 0.14 ms, which are independent of common-rail pressure and injection duration.

2. Based on the study of HEUI and EUI sprays, both injection pressure and ambient pressure affect the spray tip penetration significantly. The penetration increases with increasing injection pressure or with decreasing ambient pressure.

3. The spray tip penetration model correlates fairly well with the measured data of HEUI sprays under various injection and ambient pressures. However, the model tends to over predict the early phase of the penetration and under predict that of the later phase.

4. The variation of spray penetration depends on type of injection system, nozzle configuration, and ambient pressure. The large variation observed on the HEUI sprays could be caused by eccentricity of the VCO nozzle. From the visualization results of the HEUI sprays, the variation of mini-sac nozzle is 50% less than that of the VCO nozzle.

5. The spray cone-angle oscillation phenomena was observed on both of the EUI and HEUI sprays. The testing suggests that the opening and closing of the needle induces the wide spray cone angle. In the mid-injection period, both EUI and HEUI sprays are devoid of significant oscillation, which may be attributed to their quick needle opening and settling at the full open position.

Acknowledgment

The financial supports from ARO (Grant DAAH04-96-1-045), Sandia National Laboratory (contract LF-5224), and University of Michigan Automotive Research Center to Wayne State University are gratefully appreciated.

Nomenclature

HEUI = hydraulic electronic unit injector
 EUI = electronic unit injector
 CR = common rail
 VCO = valve covered orifices
 C.R.P = common-rail pressure

PWM = pulse width modulation
 LVDT = linear variable differential transformer
 SOI = start of injection
 EOI = end of injection
 Q = volume flow rate, m³/sec
 A = nozzle flow area, m²
 P = injection pressure, MPa
 ρ = fuel density, Kg/m³
 Cd = discharge coefficients
 Cv = coefficients of effective injection velocity
 S = penetration
 ΔP = injection pressure
 do = diameter of nozzle hole
 1 MPa = 10 bar
 1 bar = 0.1 MPa

References

- [1] Han J. S., Wang, T. C., Xie, X. B., Lai, M.-C., and Henein, N. A., 2000, "Dynamics of Multiple-Injection Fuel Sprays in a Small-Bore HSDI Diesel Engine," *SAE Trans.*, **109**(3), pp. 1538–1554.
- [2] Han, J. S., Wang, T. C., and Lai, M.-C., 1999, "Common-Rail Diesel Fuel Injection System Dynamics and Spray Characterization," *ILASS AMERICAS '99*, Indianapolis, IN, pp. 201–205.
- [3] Harrington, D., and Lai, M.-C., 1998, "Characterization and Visualization of Hole-To-Hole Variation and Wall Impingement of Diesel Sprays," *ILASS AMERICAS '98*, Indianapolis, IN, pp. 106–110.
- [4] Pierpont, D. A., and Reitz, R. D., 1995, "Effects of Injection Pressure and Nozzle Geometry on D.I. Diesel Emissions and Performance," *SAE Paper No. 950604*.
- [5] Kato, T., Tsujimura, K., Shintani, M., Minami, T., and Yamaguchi, I., 1989, "Spray Characteristics and Combustion Improvement of D.I. Diesel Engine With High Pressure Fuel Injection," *SAE Paper No. 890265*.
- [6] Stockner A. R., Flinn M. A., and Camplin, F. A., 1993, "Development of the HEUI Fuel System — Integration of Design, Simulation, Test, and Manufacturing," *SAE Paper No. 930271*.
- [7] Wang, T. C., Han, J. S., Xie, X. B., Lai, M. C., and Henein, N. A., 1999, "Direct Visualization of High Pressure Diesel Spray and Engine Combustion," *SAE Paper No. 1999-01-3496*.
- [8] Bosch, W., 1966, "The Fuel Rate Indicator; A New Measuring Instrument for Display of the Characteristics of Individual Injection," *SAE Paper No. 660749*.
- [9] Sjoberg, H., Manneberg, G., and Cronhjort, A., 1996, "Long-Working-Distance Microscope Used for Diesel Injection Spray Imaging," *Opt. Eng. (Bellingham)* **35**(12), pp. 3591–3596.
- [10] Fath A., Munch K. U., and Leipertz, A., 1997, "Spray Break-up Process of Diesel Fuel Investigated Close to the Nozzle," *Proceedings of ICLASS - '97*, Seoul, Korea, Aug., pp. 513–520.
- [11] Lai, M.-C., Wang, T.-C., Xie, X., Han, J., Henein, N. A., Schwarz, E., and Bryzik, W., 1998, "Microscopic Characterization of Diesel Sprays at VCO Nozzle Exit," *SAE Trans.*, **107**(4), pp. 1283–1293.
- [12] Hiroyasu, H., Kadota, T., and Arai, M., 1983, "Development and Use of a Spray Combustion Modeling to Predict Diesel Engine Efficiency and Pollutant Emission," *Bull. JSME* **26**(214), pp. Apr.
- [13] Kuo, T. W., 1987, "Evaluation of a Phenomenological Spray-Combustion Model for Two Open-Chamber Diesel Engines," *SAE Paper No. 872057*.
- [14] Soteriou, C., Andrews, R., and Smith, M., 1995, "Direct Injection Diesel Sprays and the Effect of Cavitation and hydraulic Flip on Atomization," *SAE Paper No. 950080*.
- [15] Dan, T., Lai, M.-C., Wang, T.-C., and Xie, X., 1998, "Transient Characterization of High-Pressure Diesel Sprays," *COMODIA 98*, JSME Engine Division, pp. 471–477.
- [16] Lai, M.-C., Dan, T., Wang, T.-C., and Xie, X., 1998, "Correlating the Diesel Spray Behavior to Nozzle Design," *SAE Paper No. 982681*.

Development of Micro-Diesel Injector Nozzles via Microelectromechanical Systems Technology and Effects on Spray Characteristics

S. Baik¹

Department of Mechanical Engineering,
University of Wisconsin-Madison,
Madison, WI 53706

J. P. Blanchard

e-mail: blanchard@engr.wisc.edu

M. L. Corradini

e-mail: corradini@engr.wisc.edu

Department of Nuclear Engineering and
Engineering Physics,
University of Wisconsin-Madison,
1500 Engineering Drive,
Madison, WI 53706

Micromachined planar orifice nozzles have been developed using MEMS (micro-electro-mechanical systems) technology and tested with commercially produced diesel injection systems. Such a system, properly designed, may have the capability to improve the spray characteristics in DI diesel engines due to improved atomization and fuel-air mixing. To demonstrate this process, 14 microplanar orifice nozzles were fabricated with deep X-ray lithography and electroplating (LIGA) technology. The circular orifice diameters were varied from 40 to 260 microns and the number of orifices varied from one to 169. Three plates with noncircular orifices were also fabricated to examine the effect of orifice shape on spray characteristics. These nozzles were then attached to commercial diesel injectors and the associated injection systems were used in the study of drop sizes. The experiments were carried out at two different injection pressures (around 25 MPa and 80 MPa). Local drop sizes were measured by a laser diffraction technique, and the average drop sizes of the whole sprays were measured by a light extinction technique. The drop sizes were found to depend primarily on the total mass flow area. Coalescence droplet collisions among adjacent sprays were apparent for the multiple orifice nozzles. Nonplanar configurations are under development and may show improved performance.

[DOI: 10.1115/1.1559901]

Introduction

MEMS (micro-electro-mechanical systems) is a class of electromechanical systems that are fabricated to be very small; i.e., 1–100 micron sizes. These systems can have both electrical and mechanical components. MEMS originally used modified integrated circuit fabrication techniques and associated materials to create mechanical devices. Today there are many more fabrication techniques and material bases. Silicon-based systems are in the process of altering conventional use of sensors, actuators and miniature mechanical devices, [1]. It is a very versatile material but quite brittle under certain operating conditions.

Alternatively, microstructures can be fabricated from metals via the LIGA process, which is based on deep etch X-ray lithography, electroplating, and molding, [2–5]. The name “LIGA” comes from the German acronym for *Lithographie, Galvanoformung und Abformung*. The process involves preparation of a layer of X-ray resist, high-energy X-ray radiation and development to produce a plastic mold for electroplating. After the mold is filled with metals by electroplating, the mold is removed and a metal structure is obtained. The metal structure may be a final product or serve as a mold insert for precision plastic injection molding. The plastic mold, retaining the same dimension of the original resist structure, can be reproduced for mass production as part of an infinite loop, [6]. Worldwide research activities on LIGA have been initiated more recently, [3]. However, the LIGA process has not found a

large number of industrial applications as yet and only a few realizations in micro-optics are expected to rapidly find industrial outlets. Nevertheless, the fabrication of monolithic devices defined with a single deep X-ray lithographic step remains the most attractive applications of the LIGA process.

Based on the recent development of components for microfluid handling, there is a growing interest in research on these handling systems, [7], and the application of MEMS technology to the combustion and engine areas. Gardner et al. [8] fabricated silicon micromachined compound nozzles for SI engine fuel injectors. Micromachined port fuel injectors were also fabricated by Hamid et al. [9] using laser drilling technology. Sufficient hole-to-hole separation was considered to be critical in avoiding droplet coalescence in the multiple-hole micromachined injectors.

Snyder [10] developed a gas-efficient liquid atomization device using LIGA technology. One design of greater than 4000 holes at 7 microns produced average droplet sizes of less than 30 microns through gas assisted liquid film break up. Kobori et al. [11] developed a micro-hole nozzle which has orifices with diameters as small as 60 microns using laser drilling technology. Combustion tests were carried out using a rapid compression-expansion machine that had a DI diesel-type combustion chamber. There was a decrease in soot emission, whereas an increase in NO emission was observed.

For our work, micromachined planar orifice nozzles have been developed using the LIGA technique and tested with commercially produced diesel injection systems. The micro-nozzles have submicron resolution, and the reproducibility of the process is high. Such systems may have the capability to improve spray characteristics in direct injection diesel engines due to improved atomization and fuel-air mixing, [12].

¹Current address: University of Illinois-Urbana Champaign, 295 Roger Adams Laboratory, Bc-3, 600 S. Mathews Avenue, Urbana, IL 61801. e-mail: sbaik@scs.uiuc.edu

Contributed by the Internal Combustion Engine Division of THE AMERICAN SOCIETY OF MECHANICAL ENGINEERS for publication in the ASME JOURNAL OF ENGINEERING FOR GAS TURBINES AND POWER. Manuscript received by the ICE Division, November 2001; final revision received by the ASME Headquarters, April 2002. Associate Editor: D. N. Assanis.

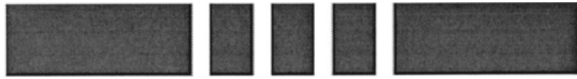


Fig. 1 Schematic view of nozzle cross section

Fabrication of Microplanar Orifice Nozzles Using the LIGA Technique

Research at the University of Wisconsin in the LIGA area has been conducted for many years. LIGA has many possible steps and the applied process sequence depends on the desired product. Detailed fabrication steps and nozzle designs are described in previous publications, [13–16].

The nozzles fabricated for this work are made of 78% nickel and 22% iron alloy, i.e., permalloy. The outer diameter of the circular plates is about 2.5 mm. As shown in Fig. 1, all the orifices have straight side walls and sharp inlet and outlet geometry. All the nozzles have the same thickness of about 300 microns, which is the practical maximum thickness for structural integrity, which can be achieved with high throughput at the University of Wisconsin-Madison. Therefore, the length-over-diameter ratio varied as the diameter of orifices varied. The effect of different length over diameter ratio on spray characteristics has not been investigated in this study.

Five plates that have a single orifice were fabricated to investigate the effect of orifice diameter on spray characteristics. The diameters were 40, 60, 80, 100, and 260 microns. The single 40-micron orifice nozzle is shown in Fig. 2. The spacing between multiple orifices was varied in three other plates that each have five 40-micron orifices, in order to investigate the effect of orifice spacing on interference between sprays. The spacing between orifices was 100, 150, and 200 microns. In addition, two plates that each have 41 orifices and 169 orifices, respectively, were fabricated. The orifices in these plates also have a diameter of 40 microns. The 41-orifice nozzle has the same flow area as that of the single 260-micron orifice nozzle, and the 169-orifice nozzle has the same flow area as that of the four 260 micron orifice nozzle. Figure 3 shows the 169-orifice nozzle. Finally, three plates with noncircular orifices were also fabricated to examine the effect of orifice shape on spray characteristics. A single cross-shaped orifice nozzle, a single triangular-shaped orifice nozzle and a four triangular-shaped orifice nozzle were fabricated. Figure 4 shows the magnified view of the four triangular shaped orifice nozzle. All three nozzles have the same flow area as that of the single 100-micron circular orifice nozzle.

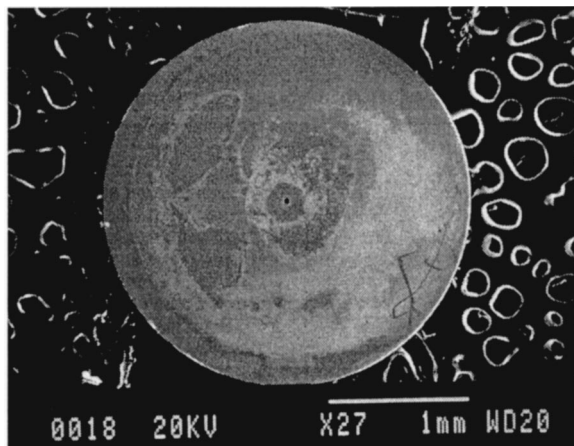


Fig. 2 The single 40-micron orifice nozzle

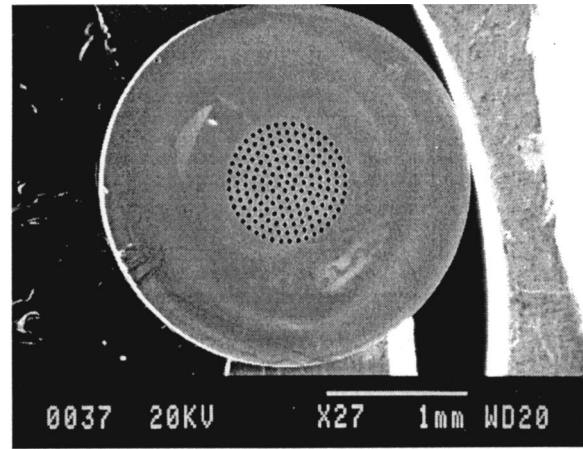


Fig. 3 The 169-orifice nozzle with an orifice diameter of 40 microns

Experimental Setup

The experiments were performed, at room temperature and under quiescent gas conditions, in a constant volume cylindrical chamber (185 mm inner diameter and 185 mm long) equipped with two quartz windows with a field of view 101 mm in diameter.

Measurements were performed on intermittent diesel sprays produced by a Bosch in-line fuel-injection pump. California diesel fuel ($\rho_f = 841 \text{ kg/m}^3$) was used. The pump was driven by a variable speed shunt DC motor through a semi-flexible coupling. Experiments were carried out for two different injection pressures and the associated conditions. Low-injection pressure profiles with maximum injection pressures of about 20–25 MPa were presented in previous publications, [14,16]. Figure 5 shows high injection pressure profiles during the initial 4 ms after start of injection for the single and 169-orifice nozzles with orifice diameters of 40 microns, which, respectively, have the minimum and maximum flow areas. An absolute pressure sensor was installed anterior to the inlet of the injector. The nozzles with smaller total mass flow areas produced slightly higher maximum injection pressures with the same rack position for the in-line fuel-injection pump. The maximum injection pressures were determined to be about 70–80 MPa. Argon gas was used to pressurize the chamber and the gas density inside the chamber was 18.9 kg/m^3 .

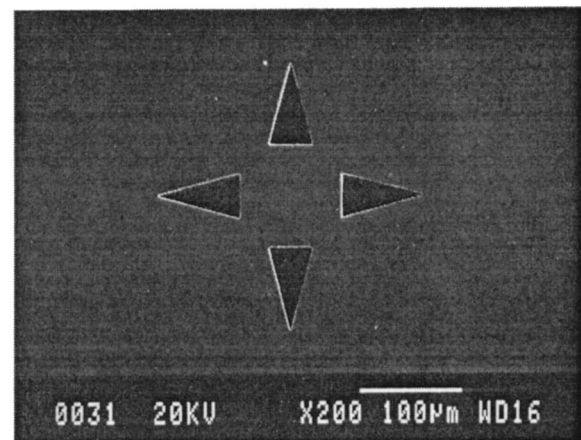


Fig. 4 Magnified view of the four triangular-shaped orifice nozzle

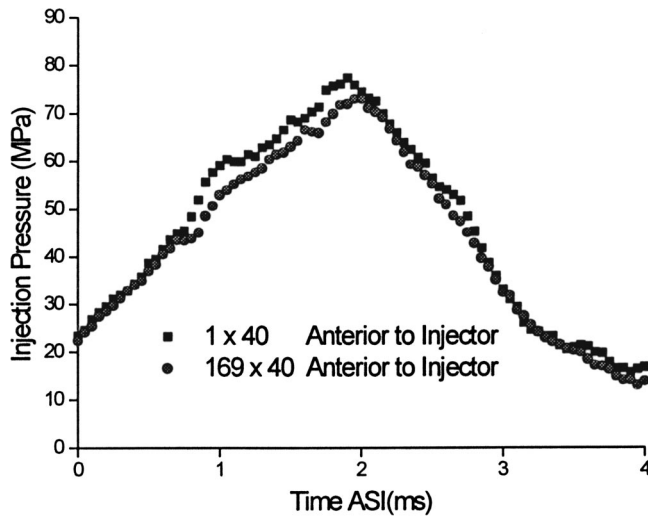


Fig. 5 Injection pressure profiles

A LucasVarity injector was used for the low-pressure experiments and a Bosch injector was used for the high-pressure experiments. The very end of the commercial nozzle was cut and the micro-nozzle was attached to that end using a mechanical retainer. As orifice diameter decreased, special care was needed to prevent plugging. Accordingly, a 7 micron filter was attached to the fuel line just before the Bosch in-line fuel-injection pump.

A laser diffraction-based commercial system from Malvern/Insitec, the Spraytec ST218, was used to measure local drop sizes. The receiver focal length was 200 mm. The laser incorporated in the Spraytec was a diode laser and the laser beam diameter was 10 mm. Data were extracted with a sampling period of 0.4 ms.

A light extinction technique was also used in order to measure the average drop sizes of the whole spray. The basic theory relates the attenuation of a collimated monochromatic laser that passes through a poly-disperse droplet field to the average droplet size of the whole spray. The final formulation for the Sauter mean diameter (SMD) is given in Eq. (1), and the detailed derivation is given in the references [17,18].

$$\text{SMD} = \frac{\sum N_i D_i^3}{\sum N_i D_i^2} = \frac{3M_f \overline{RQ_{\text{ext}}}}{2a_p \rho_f \sum_{j=1}^p (-\ln \tau_j)} \quad (1)$$

M_f is the total fuel mass in the instantaneous spray image, $\overline{RQ_{\text{ext}}}$ is the averaged corrected extinction coefficient, a_p is the cross-sectional area of each pixel, ρ_f is the density of fuel, and τ_j is the transmittance of the j th optical path inside the spray. A schematic of the setup including components for the light extinction technique is given in Fig. 6. A high-speed digital camera, made by the Eastman Kodak Company (model 4540), was used with 4500 frames/second for recording the injection event. The light source was a pulsed copper-vapor laser (Oxford) rated up to 14 kHz repetition rate and 2 mJ per pulse with 20–60 ns pulse duration. Absorptive neutral density filters were used to calibrate transmittance. The absorptive filters cause negligible reflection, and they can be overlapped to obtain added optical density values. Fourteen different transmittance values, ranging from 0 to 1, were used in this study. Mass flow rates were measured using the Bosch type rate of injection meter, [19].

Experimental Results

Fourteen microplanar orifice nozzles were divided into four groups in order to compare the spray characteristics systematically; i.e., single orifice nozzles, multiple orifice nozzles

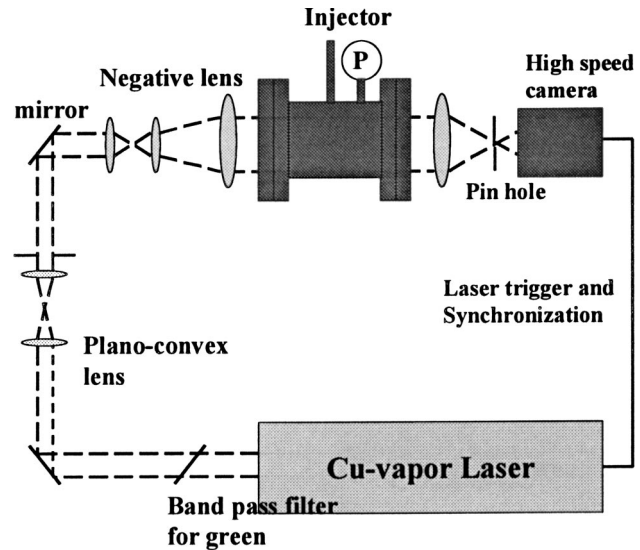


Fig. 6 Experimental setup

with noncircular orifices and shower head nozzles. Detailed test results about the spray tip penetration lengths and the spray cone angles were presented in previous publications, [14–16]. The drop size data at low and at high injection pressures measured by the laser diffraction technique and the light extinction technique will be mainly explained in this paper.

Single Orifice Nozzles

Five plates that have a single orifice were fabricated to investigate the effect of orifice diameter on spray characteristics. The diameters were 40, 60, 80, 100, and 260 microns.

The spray regimes are shown in Fig. 7, [20]. The data moved from the atomization regime to the second wind-induced regime near the borderline as the orifice diameter decreased. A decrease in the orifice diameter resulted in a decrease in the Reynolds number. A large decrease in the Reynolds number suggests a decrease in turbulence, which has a negative effect on atomization. However, the smaller orifice nozzles produced smaller drop sizes, as will be discussed shortly.

The spray tip penetrating speeds and the spray cone angles decreased as the orifice diameter decreased, [14–16]. Figure 8 shows ensemble averaged SMD values and standard deviations measured using Malvern. Data were obtained for a duration of 4 ms starting from when the spray arrived at the measurement loca-

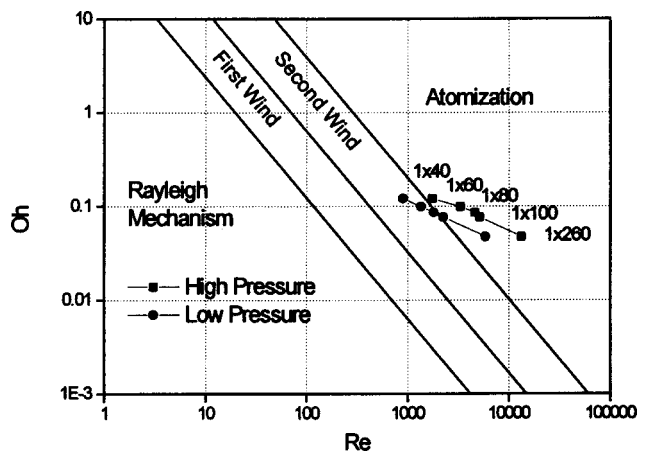


Fig. 7 Spray regimes

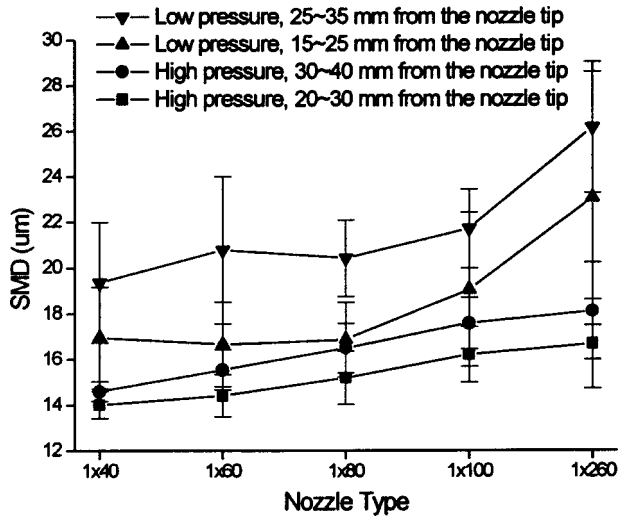


Fig. 8 Drop sizes of single orifice nozzles measured using Malvern

tions, with a sampling time of 0.4 ms, and the ensemble averaged data of five injections are presented in this paper. Drop size data measured using Malvern are reproduced from previous publications, [15,16]. Drop sizes at high injection pressures were measured at the middle of spray 20~30 mm away from the nozzle tip and 30~40 mm away from the nozzle tip. Drop sizes at low injection pressures were measured at the middle of spray 15~25 mm away from the nozzle tip and 25~35 mm away from the nozzle tip. Drop sizes could not be measured more closely to the nozzle tip because the Malvern receiver lens would be blocked by the spray chamber wall as the lens approached the nozzle tip. The SMD generally decreased as the orifice diameter decreased. The SMD measured downstream was larger than that upstream, possibly due to coalescence droplet collisions. The SMD at high injection pressures was smaller than that at low injection pressures.

Figure 9 shows the transmittances, the percentage of light that passes through the spray, of single orifice nozzles measured using Malvern. The transmittance generally decreased as the orifice diameter increased. The transmittance measured downstream was smaller than that upstream. The transmittance at high-injection pressures was smaller than that at low-injection pressures, possi-

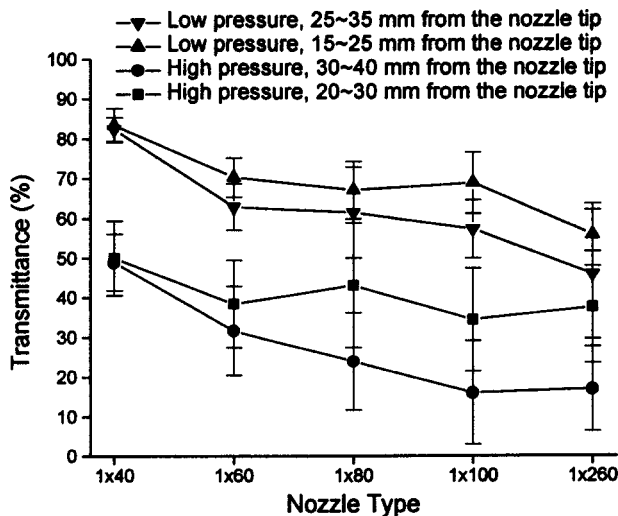


Fig. 9 Transmittances of single orifice nozzles measured using Malvern

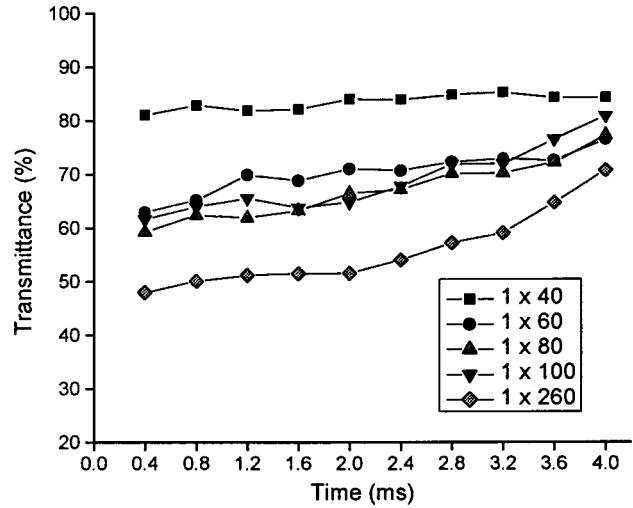


Fig. 10 Transmittances of single orifice nozzles measured at low injection pressures at a location 15~25 mm from the nozzle tip using Malvern

bly due to larger mass flow rates. A multiple scattering correction algorithm developed by Malvern/Insitac was used to more accurately measure drop sizes at low transmittances. Figure 10 shows transmittances as a function of time measured at low injection pressures, at a location 15~25 mm from the nozzle tip. The transmittances were obtained starting from when the spray arrived at the measurement location, for a duration of 4 ms. The spray was denser nearer the tip region and became less denser nearer the trailing edge.

Figure 11 shows ensemble averaged SMD values and standard deviations at high injection pressures measured by the two different techniques. The average drop sizes of the whole spray were measured by the light extinction technique. Drop sizes were obtained until the spray tip reached the end of the optical window or up to a duration of 4 ms after start of injection. Data were extracted with a sampling period of 0.22 ms. The two different measurement techniques gave qualitatively similar trends as the diameter of orifices changed. The quantitative differences may originate from the different measurement locations relative to different spray tip penetrations.

A spray image of the single 40-micron orifice nozzle at a time 4 ms after start of injection and a spray image of the single 260-

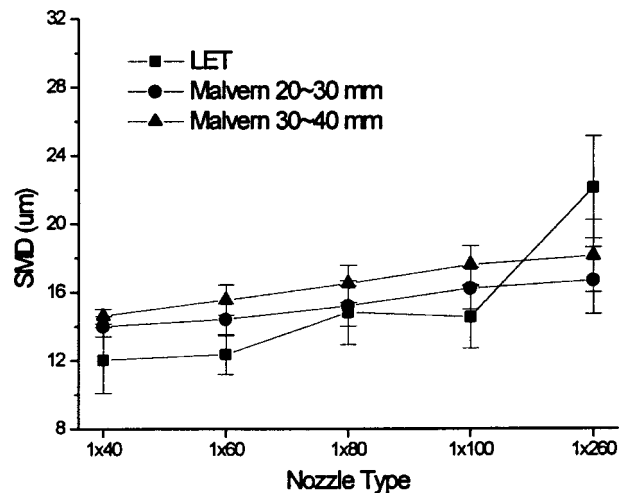


Fig. 11 Drop sizes of single orifice nozzles at high injection pressures

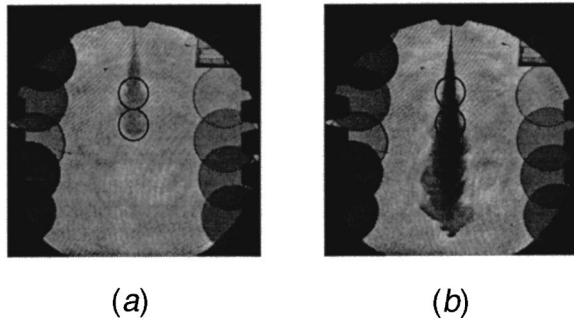


Fig. 12 Spray images at high injection pressures (a) single 40-micron orifice nozzle at 4 ms (b) single 260-micron orifice nozzle at 1.5 ms

micron orifice nozzle at a time 1.5 ms after start of injection, measured at high injection pressures, are shown in Fig. 12. The Malvern measurement locations are shown at the center of the spray. The spray from the single 260-micron orifice nozzle is one of the largest sprays. The laser beam, with a diameter of 10 mm, encompasses most of the sprays at the measurement locations, with a corresponding measurement area of 79 mm². However, it is possible that some of the drops at the periphery of the spray might not have been detected.

Comparing the images of Fig. 12, the smaller mass flow area nozzle with slower spray tip penetrating speed produced a short spray, which did not reach the end of the optical window, even after a duration of 4 ms had passed after the start of the spray. According to the Malvern measurements, drop sizes measured downstream in a spray were larger than those upstream. In Fig. 12, the drops at a location downstream relative to the center of the spray were measured using Malvern for the single 40 micron orifice nozzle. These drops downstream may be larger than the average drop size of the whole spray measured by the light extinction technique. On the other hand, drops located relatively upstream were measured using Malvern for the single 260-micron orifice nozzle. The drop sizes upstream may be smaller than the average drop size of the whole spray. This may be a reason for the switching in relative magnitude of the drop size between the Malvern and the light extinction technique results for the largest orifice nozzle shown in Fig. 11.

Alternatively, there might be some bias in drop size for the different measurement techniques. The limitations of the laser diffraction technique are summarized by Lefebvre [20]. One of the sources of error for the light extinction technique is inaccurate mass information. The averaged mass flow rate of thousands of injections was measured using the Bosch type rate of injection meter, and this measurement was used instead of measuring the mass flow rate for each spray. Therefore, shot-to-shot variation in mass flow rate was not considered.

Multiple Orifice Nozzles

For the multiple orifice nozzles, the number of 40 micron diameter orifices was varied from one to 169. The spacing between multiple orifices was also varied in three plates that each have five 40-micron orifices, in order to investigate the effect of orifice spacing on interference between sprays. For these multiple orifice nozzles, the spray tip penetrating speeds and spray cone angles increased as the number of orifices increased, [14–16].

The drop sizes measured using Malvern are shown in Fig. 13. The SMD increased as the number of orifices increased, and the SMD measured downstream was larger than that upstream. Higher injection pressures produced smaller SMD. However, there was no noticeable difference in SMD among the five 40-micron orifice nozzles with different spacings between orifices. In the nozzles fabricated for this study, all the orifices are aligned in the same

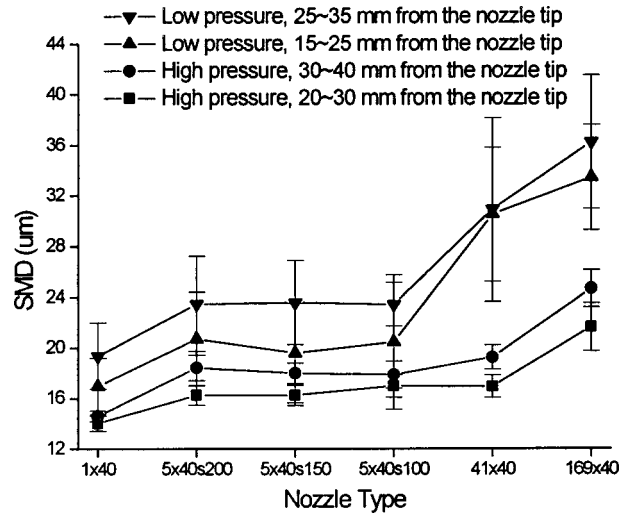


Fig. 13 Drop sizes of multiple orifice nozzles measured using Malvern

direction; i.e., zero injection angle. The maximum spacing that can be made at the end of the diesel injector nozzle tip is about 1 mm, compared to the sprays, which are in centimeter scales. The interference among adjacent sprays could not be avoided, which probably lead to coalescence droplet collisions. The different spacings between orifices within the range of our designs do not seem to affect drop sizes much.

As shown in Fig. 14, the transmittance generally decreased as the number of orifices increased. Similar to single orifice nozzles, the transmittance measured downstream was smaller than that upstream, and higher injection pressures produced smaller transmittance.

Figure 15 shows drop sizes measured at high injection pressures by the two different techniques. Similar to the single orifice nozzles, the average drop sizes of whole sprays of the smaller mass flow area nozzles were smaller than the local drop sizes measured using Malvern. For the larger mass flow area nozzles, 41 and 169-orifice nozzles, the average drop sizes were larger than the local drop sizes.

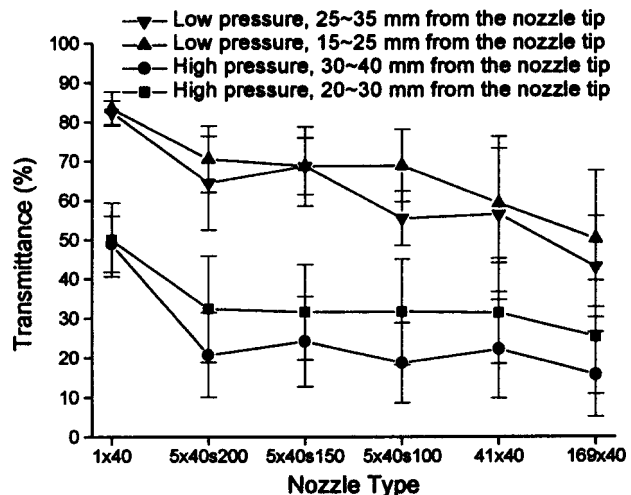


Fig. 14 Transmittances of multiple orifice nozzles measured using Malvern

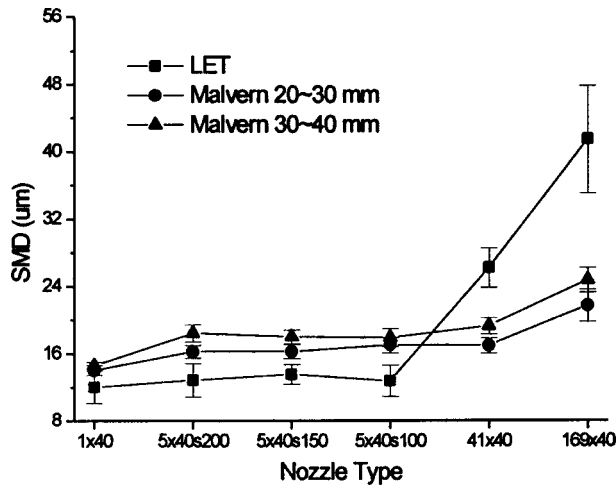


Fig. 15 Drop sizes of multiple orifice nozzles at high-injection pressures

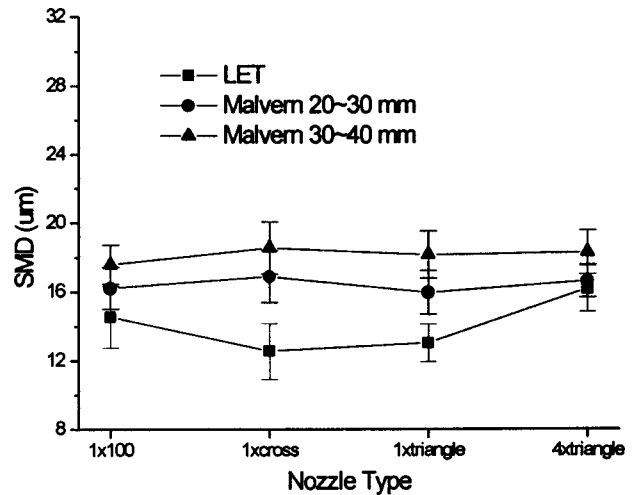


Fig. 17 Drop sizes of the single 100-micron circular orifice nozzle and the nozzles with noncircular orifices at high-injection pressures

Nozzles With Noncircular Orifices

Three plates with noncircular orifices were fabricated to examine the effect of orifice shape on spray characteristics. All the noncircular orifice nozzles have the same mass flow area as that of the single 100-micron circular orifice nozzle. There was no noticeable difference in spray tip penetrating speeds and cone angles, [14–16].

Drop sizes of the single 100 micron circular orifice nozzle compared with the nozzles with noncircular orifices are shown in Fig. 16 and Fig. 17. All the nozzles produced similar SMD except for the four triangular shaped orifice nozzle at low-injection pressures. A discussion of this result will be presented later. The different orifice shapes within the range of our designs do not seem to affect the spray characteristics much, as long as they are single-orifice nozzles, when measured at locations more than 15 mm away from the nozzle exit.

Shower Head Nozzles

The 41 orifice nozzle has the same flow area as that of the single 260 micron orifice nozzle, and the 169-orifice nozzle has the same flow area as that of the four 260-micron orifice nozzle.

Nozzles with the same flow areas produced similar penetrating speeds and cone angles regardless of single, multiple, or shower head designs, [14–16].

Drop sizes of shower head nozzles measured using Malvern are shown in Fig. 18. At low-injection pressures, the SMD of the 41-orifice nozzle was larger than that of the single 260-micron orifice nozzle at the two central measurement locations. The multiple orifice nozzle produced larger SMD than that of the single orifice nozzle with the same mass flow area. This suggests that a large number of coalescence droplet collisions may be occurring at the measurement locations. On the other hand, at high-injection pressures, the 41-orifice nozzle produced SMD similar to the single 260-micron orifice nozzle. This result will be discussed further later.

At low-injection pressures, the SMD of the 169-orifice nozzle was smaller than that of the four 260-micron orifice nozzle. A nozzle with a large number of small orifices produced smaller SMD than a nozzle with a few large orifices, having identical mass flow area. At high injection pressures, nozzles with the same flow area produced similar SMD.

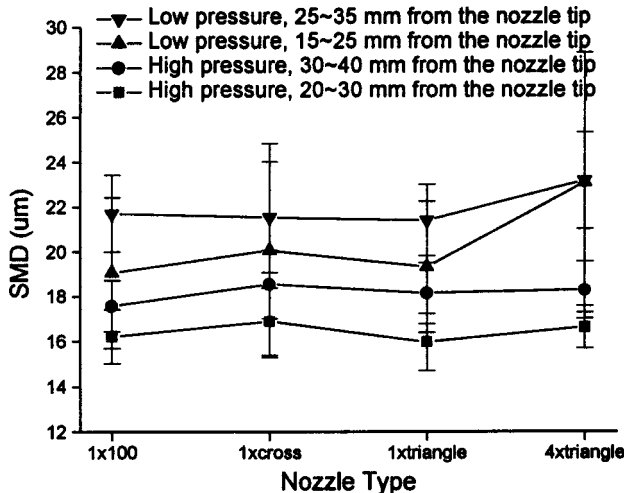


Fig. 16 Drop sizes of the single 100-micron circular orifice nozzle and the nozzles with noncircular orifices measured using Malvern

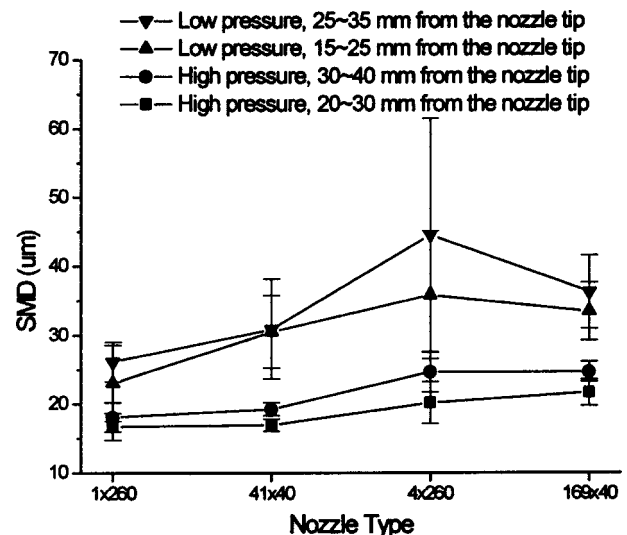


Fig. 18 Drop sizes of shower head nozzles measured using Malvern

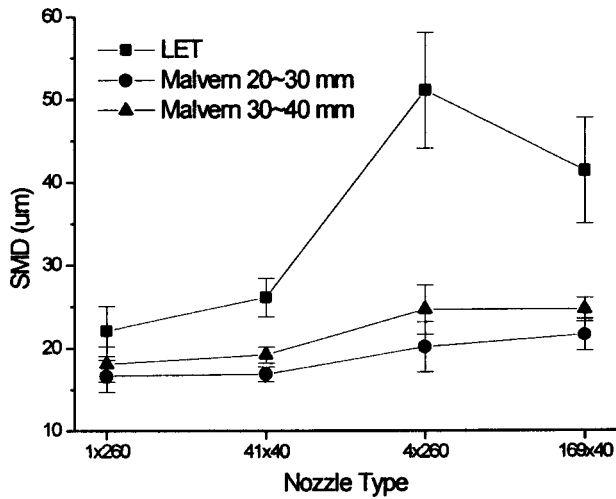


Fig. 19 Drop sizes of shower head nozzles at high-injection pressures

Drop sizes measured by the two different techniques are shown in Fig. 19. The trend in the average drop sizes at high injection pressures was similar to that in local drop sizes at low injection pressures. This will also be discussed further shortly.

Suggested Droplet Collision Dynamics

Schematic diagrams of sprays from the single and multiple orifice nozzles are shown in Fig. 20. From a macroscopic view point, the spray from the single orifice nozzle has an axial velocity component and radial diverging velocity components. Of course, there will be a large number of droplet collisions at microscopic scales. However, the diverging velocity components of adjacent sprays from the multiple orifice nozzle collide with each other even at macroscopic scales. The multiple orifice nozzle has a better chance of droplet collisions due to the interference among adjacent sprays.

The drop sizes of the single 260-micron orifice nozzle and the 41-orifice nozzle are shown again in Fig. 21. At low-injection pressures, the drop sizes of the 41-orifice nozzle were larger than those of the single 260-micron orifice nozzle at the two central Malvern measurement locations, which may be due to coalescence droplet collisions.

At high-injection pressures, the initial fuel-injection velocities will be faster than those at low-injection pressures due to greater pressure differences. The higher initial injection velocities will lead to higher relative collision velocities when droplet collisions

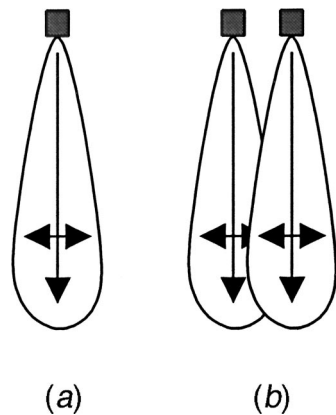


Fig. 20 Schematic diagrams of the sprays (a) single orifice nozzle (b) multiple orifice nozzle

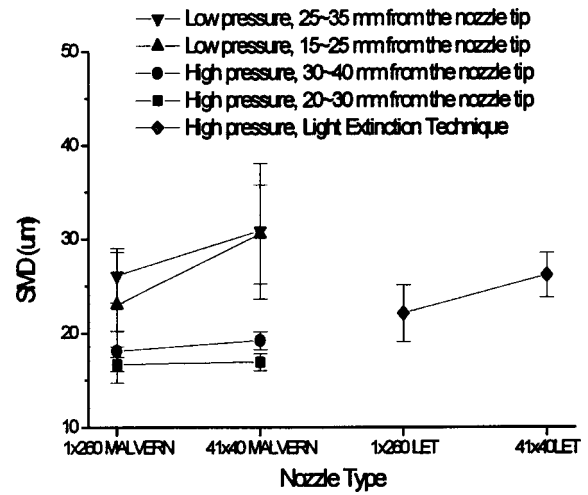


Fig. 21 Drop sizes of the single 260-micron orifice nozzle and the 41-orifice nozzle with an orifice diameter of 40 micrometers

occur at the two central Malvern measurement locations. The higher relative collision velocities will lead to less coalescence droplet collisions and more shattering. In a study of binary collisions of liquid drops carried out by Ashgriz and Poo [21], the probability of coalescence droplet collisions decreased significantly as the Weber number increased, depending on drop-size ratio, collision angle, and an impact parameter. The impact parameter was defined as the distance from the center of one drop to the relative velocity vector placed on the center of the other drop. The Weber number was defined using liquid drop density, surface tension, the diameter of the smaller drop and the relative velocity of the two drops. Accordingly, this may be a reason for the similar drop sizes at the two central Malvern measurement locations at high injection pressures.

However, even at high-injection pressures, the droplets will keep on colliding at the reduced velocities further downstream. This will lead to more coalescence droplet collisions further downstream, resulting in larger average drop sizes of the multiple orifice nozzle compared to those of the single orifice nozzle.

The drop sizes of the single triangular-shaped orifice nozzle and the four triangular-shaped orifice nozzle are shown again in Fig. 22. Similar trends in drop sizes could be observed for these nozzles as for the circular orifice nozzles in Fig. 21.

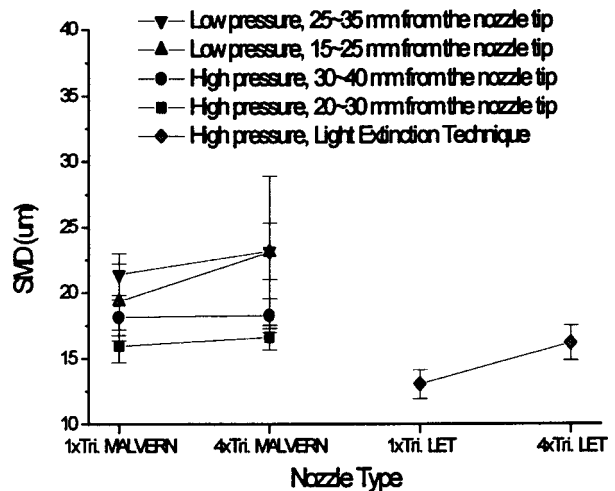


Fig. 22 Drop sizes of the single triangular-shaped orifice nozzle and the four triangular-shaped orifice nozzle

Conclusion

In this paper, micromachined diesel injector nozzles were fabricated using MEMS technology and tested with commercially produced diesel injection systems. This work showed that a LIGA technique can be used to fabricate nozzle tips of arbitrary shapes and sizes for real diesel injector nozzles. The availability of a LIGA processing sequence supported the construction of micro-diesel injector nozzles, and microsystems technology was also employed in our macro-instrumentation.

Drop sizes of 14 microplanar orifice nozzles were analyzed at two different injection pressures. Current test results show expected qualitative trends in drop sizes, but the quantitative magnitudes of the behavior are less dependent on geometry than first anticipated. The drop sizes were found to depend primarily on the total mass flow area. Three main observations were obtained within the range of our designs. First, the SMD decreased as the diameter of orifices decreased in a nonlinear fashion. Secondly, the SMD increased as the number of orifices increased, possibly due to agglomeration effects, and finally, the different geometry of single orifice nozzles did not affect the SMD as much as might be expected.

The next step in our investigation is to improve our MEMS fabrication technique coupled with structural and fluid mechanics analysis to optimize the micronozzle sizes and shapes for the required diesel spray conditions. Also, micronozzles with diverging orifices are being fabricated, and the results are forthcoming.

Acknowledgments

The authors would like to acknowledge the financial support of the Army Research Office and S. C. Johnson Wax and the technical assistance provided by the Wisconsin Center for Applied Microelectronics.

References

- [1] Peterson, K. E., 1982, "Silicon as a Mechanical Material," *Proc. IEEE*, **70**(5), pp. 420–457.
- [2] Guckel, H., Christenson, T., and Skrobis, K., 1992, "Metal Micromechanisms via Deep X-Ray Lithography, Electroplating and Assembly," *J. Micromech. Microeng.*, **2**, pp. 225–228.
- [3] Rogner, A., Eicher, J., Munchmeyer, D., Peters, R-P., and Mohr, J., 1992, "The

- LIGA Technique—What are the New Opportunities," *J. Micromech. Microeng.*, **2**, pp. 133–140.
- [4] Guckel, H., Skrobis, K., Christensen, T., and Klein, J., 1994, "Micromechanics for Actuators via Deep X-Ray Lithography," *Proc. SPIE's 1994 Symposium on Microlithography*, SPIE Press, San Jose, CA, pp. 39–47.
- [5] Guckel, H., 1995, "Deep X-Ray Lithography for Micromechanics and Precision Engineering," *Synchrotron Radiation Instrumentation (Invited)*, Advanced Photon Source, Argonne, IL.
- [6] Madou, M., 1997, *Fundamentals of Microfabrication*, CRC Press, Boca Raton, FL.
- [7] Gravesen, P., Branebjerg, J., and Jensen, O., 1993, "Microfluidics a Review," *J. Micromech. Microeng.*, **3**, pp. 168–182.
- [8] Gardner, R., Horn, W., Rhoades, M., Wells, M., and Yockey, S., 1989, "Silicon Micromachined Compound Nozzle," U.S. Patent Number 4828184.
- [9] Hamid, M., Kim, H., Im, K., Lai, M. Nuglisch, H., and Dressler, J., 2000, "Effect of Pressure Modulation on Micro-Machined Port Fuel Injector Performance," *Eighth International Conference on Liquid Atomization & Spray Systems*, IOP Publishing Ltd., Pasadena, CA, pp. 546–551.
- [10] Snyder, H., 1997, "Efficient Liquid Atomization Using Gas Flows and Novel Micro-Machining Techniques," Ph.D. thesis, University of Wisconsin, Madison, WI.
- [11] Kobori, S., Kamimoto, T., and Kosaka, H., 1996, "Ignition, Combustion and Emissions in a DI Diesel Engine Equipped With a Micro-Hole Nozzle," SAE Paper No. 960321.
- [12] Siebers, D., and Higgins, B., 2001, "Flame Lift-Off on Direct-Injection Diesel Sprays Under Quiescent Conditions," SAE Paper No. 2001-01-0530.
- [13] Baik, S., Goney, K. H., Kang, S., Murphy, J., Blanchard, J., and Corradini, M., 1999, "Development of Micro-Diesel Injector Nozzles via MEMS Technology and Initial Results for Diesel Sprays," SAE Paper No. 1999-01-3645.
- [14] Baik, S., Kang, S., Blanchard, J., and Corradini, M., 2000, "Development of Micro-Diesel Injector Nozzles via MEMS Technology and Effects on Spray Characteristics," *Eighth International Conference on Liquid Atomization & Spray Systems*, Pasadena, CA, pp. 782–789.
- [15] Baik, S., Blanchard, J., Corradini, M., 2001, "Development of Micro-Diesel Injector Nozzles via MEMS Technology and Effects on Spray Characteristics," SAE Paper No. 2001-01-0528.
- [16] Baik, S., 2001, "Development of Micro-Diesel Injector Nozzles via MEMS Technology and Effects on Spray Characteristics," Ph.D. thesis, University of Wisconsin, Madison, WI.
- [17] Goney, K. H., and Corradini, M., 2000, "Isolated Effects of Ambient Pressure, Nozzle Cavitation and Hole Inlet Geometry on Diesel Injection Spray Characteristics," SAE Paper No. 2000-01-2043.
- [18] El-beshbeeshy, M., Hodges, J., and Corradini, M., 1992, "Image Analysis of Diesel Sprays," SAE Paper No. 921628.
- [19] Bower, G., and Foster, D., 1991, "A Comparison of the Bosch and Zuech Rate of Injection Meters," SAE Paper No. 910724.
- [20] Lefebvre, A. H., 1989, *Atomization and Sprays*, Taylor and Francis, London.
- [21] Ashgriz, N., and Poo, J. Y., 1990, "Coalescence and Separation in Binary Collisions of Liquid Drops," *J. Fluid Mech.*, **221**, pp. 183–204.

Effect of Subgrid Modeling on the In-Cylinder Unsteady Mixing Process in a Direct Injection Engine

K. Sone

S. Menon

e-mail: suresh.menon@aerospace.gatech.edu

School of Aerospace Engineering,
Georgia Institute of Technology,
Atlanta, GA 30332

Fuel-air mixing in a direct injection spark ignition (DISI) engine occurs in a highly unsteady, turbulent and three-dimensional flow. As a result, any cycle-to-cycle unsteady variation in the mixing process can directly impact the performance of the DISI engine. To study the unsteady process in these engines, we have developed and implemented a large-eddy simulation (LES) approach with an innovative subgrid scalar mixing model based on the linear-eddy mixing (LEM) model into a commercial IC engine code (KIVA-3V). Time-averaged results of the simulations using the new LES version (KIVALES) are compared to the steady-state predictions of the original KIVA-3V. Significantly different in-cylinder turbulent fuel-air mixing is predicted by these two methods. Analysis shows that KIVALES resolves spatial features larger than the grid and that the subgrid kinetic energy adjusts to the LES resolution. As a result, KIVALES captures a highly unsteady, anisotropic fuel-air mixing process whereas a more diffused mixed field is predicted by the original KIVA-3V. This ability of KIVALES is attributed to the subgrid closure which scales the subgrid dissipation with the local grid size and thus, decreases the overall dissipation in the flow. [DOI: 10.1115/1.1501918]

Introduction

The direct-injection spark-ignition (DISI) engine has attracted more attention recently due to its potential for generating very low emission. In a DISI engine, liquid fuel is directly injected into the cylinder and rapid fuel-air mixing is employed to achieve an ignitable mixture. This approach ([1,2]) essentially combines diesel engine combustion with a spark engine ignition process. To achieve DISI engine's performance potential, very precise control of fuel injection, fuel-air mixing, and ignition processes will have to be demonstrated. For example, at light load a locally stratified fuel-air mixture with an easily ignitable composition at the spark plug (and at the ignition timing) is necessary ([1]). Furthermore, in order to achieve sustained performance, cycle-to-cycle variations have to be minimized or eliminated. However, in-cylinder fuel-air mixing process is known to be highly unsteady and subtle changes in the boundary and/or flow conditions can impact the mixing process drastically. This implies that temporal evolution of the mixing process is just as important as the spatial distribution of the mixed fluid for the DISI engine (and possibly, for other similar combustion systems).

Although experimental measurements continue to play a major role in understanding in-cylinder processes, they have well-known limitations in these complex and hostile (to in-situ measurements) flows. Therefore, a complementary numerical "experiment" is needed to provide additional insight into in-cylinder mixing and combustion processes. Since the numerical method has to maintain both spatial and temporal accuracy, Reynolds-averaged Navier-Stokes (RANS) method (in which only the time-averaged flow field is modeled), of which KIVA-3V code is typical example, is incapable of predicting the unsteady effects of fuel-air mixing. Note that, since the cylinder volume is changing during a cycle, the actual KIVA-3V solver is time-dependent. However, the turbulence model in the KIVA-3V code (the very popular $k-\epsilon$

model) employs a single velocity and a single length scale to represent all turbulent scales smaller than the mean motion. Thus, the modeled turbulent dissipation ϵ scales with the integral (or the largest) length scale. Furthermore, in complex flows with regions of recirculation and/or separation gradient diffusion models, such as the $k-\epsilon$ model, are known to be inapplicable.

In recent years, an unsteady simulation technique called large-eddy simulation (LES) has become very popular ([3]). In LES, all scales of motion larger than the computational grid are resolved in space and time accurately, and the effect of the small-scale fluctuations inside the grid is modeled using a subgrid model. The small scales in high Re flows are known to be more universal and nearly isotropic, and primarily provide dissipation of the energy transferred from the resolved scales. Thus, simple eddy viscosity type models (similar to the model used in the RANS) have been proposed. However, as discussed recently ([4]) and also noted below, there are some issues regarding subgrid closure that need to be reconsidered when attempting LES of high Reynolds number reacting flows.

For example, algebraic eddy viscosity models such as the Smagorinsky's model ([5]) require that equilibrium between kinetic energy production and dissipation occurs in the subgrid scales. This implies that a computationally impractical grid resolution is required for high Re flows. Gradient diffusion closure for scalar transport is also questionable for reacting flows since this approach ignores countergradient effects (that do occur in regions of high shear) and also ignores molecular diffusion process. This is a serious limitation since it is well known that turbulent mixing consists of two different processes that occur concurrently: turbulent convective stirring which wrinkles and increases the interface between initially unmixed species, and molecular diffusion which enable species to achieve molecular contact. It is important to distinguish between these two processes and treat them separately since they are fundamentally different, and experiments [6] have shown that both processes impact turbulent mixing, even in high Re flows. A subgrid scalar mixing model that explicitly includes both these effects has been developed in recent years ([7]), and is also used in the present study.

Contributed by the Internal Combustion Engine Division of THE AMERICAN SOCIETY OF MECHANICAL ENGINEERS for publication in the ASME JOURNAL OF ENGINEERING FOR GAS TURBINES AND POWER. Manuscript received by the ICE Division May 23, 2001; final revision received by the ASME Headquarters December 1, 2001. Associate Editor: D. Assanis.

This study employs the KIVA-3V as a baseline code. This code (in its many variant forms) is used extensively for IC engine studies by many researchers. For example, Han and Reitz [8] replaced the k - ϵ model by the Yakhot and Orszag's RNG k - ϵ version and showed good general agreement with experiments. More recently, Celik et al. [9] implemented the Smagorinsky eddy viscosity model and carried out some preliminary LES studies. Here, a new LES version of the KIVA code (denoted hereafter, as KIVALES) using a one-equation transport model for the subgrid kinetic energy ([10,11]) is developed and demonstrated. The KIVALES version is further extended to include the subgrid scalar mixing model (denoted hereafter, as KIVALES-LEM) and used to study spray mixing in IC engine flows.

Governing Equations for Large-Eddy Simulation (LES).

The compressible LES equations are obtained by spatial Favre filtering of the Navier-Stokes equations. The filter width is the grid scale, $\bar{\Delta}$ and a box filter is used since it is suitable for finite volume schemes (as in the KIVA code). The filtered LES equations consistent with the KIVA-3V formulation are ([11,4]):

$$\frac{\partial \bar{\rho}}{\partial t} + \frac{\partial \bar{\rho} \bar{u}_j}{\partial x_j} = \bar{\rho}^s \quad (1)$$

$$\frac{\partial \bar{\rho} \bar{u}_i}{\partial t} + \frac{\partial}{\partial x_j} [\bar{\rho} \bar{u}_i \bar{u}_j - \bar{\tau}_{ij} + \tau_{ij}^{sgs}] = \bar{F}_i^s \quad (2)$$

$$\frac{\partial \bar{\rho} \bar{e}}{\partial t} + \frac{\partial \bar{\rho} \bar{u}_j \bar{e}}{\partial x_j} = -\bar{p} \frac{\partial \bar{u}_j}{\partial x_j} - \frac{\partial h_j^{sgs}}{\partial x_j} - \frac{\partial \bar{q}_j}{\partial x_j} + \bar{\sigma}_{ij} \frac{\partial \bar{u}_i}{\partial x_j} + \Theta^{sgs} + \Pi^{sgs} + \bar{Q}^s \quad (3)$$

$$\frac{\partial \bar{\rho} \bar{Y}_m}{\partial t} + \frac{\partial}{\partial x_j} \left[\bar{\rho} \bar{u}_j \bar{Y}_m - \bar{D}_m \frac{\partial \bar{Y}_m}{\partial x_j} + \Phi_{j,m}^{sgs} \right] = \bar{\rho}_m^s \quad (4)$$

where $\bar{\tau}_{ij} = -\bar{p} \delta_{ij} + \bar{\sigma}_{ij} = -\bar{p} \delta_{ij} + 2\bar{\mu} \bar{S}_{ij} + \bar{\lambda} \bar{S}_{kk} \delta_{ij}$, and $\bar{q}_j = -\bar{\kappa} \partial \bar{T} / \partial x_j - \bar{p} \Sigma_{m=1}^N \bar{h}_m D_m (\partial \bar{Y}_m / \partial x_j)$. Chemistry terms are ignored at present, and spray terms (superscript s) follows the original models, and are not repeated here for brevity. In these equations, τ_{ij}^{sgs} , h_i^{sgs} , Θ^{sgs} , Π^{sgs} , and $\Phi_{i,m}^{sgs}$ all require closure. These terms represent, respectively, the subgrid stress tensor, subgrid heat flux, subgrid viscous work, subgrid velocity-pressure gradient correlation, and subgrid species mass flux.

The subgrid stress tensor τ_{ij}^{sgs} is modeled using the resolved strain rate \bar{S}_{ij} , and a subgrid eddy viscosity, ν_t which is, in turn modeled in terms of $\bar{\Delta}$ and a characteristic velocity obtained using the subgrid turbulent kinetic energy, $k^{sgs} = (1/2) [\bar{u}_i \bar{u}_i - \bar{u}_i \bar{u}_i]$. Thus, $\nu_t = C_\nu k^{sgs/2} \bar{\Delta}$, and this model differs from the Smagorinsky's model where the velocity scale is obtained using $\bar{\Delta}$ and \bar{S}_{ij} . An advantage of the present model is that it is capable of capturing the effect of nonequilibrium between production and dissipation of kinetic energy in the subgrid scales. This is particularly important when high-Re flows has to be simulated using relatively coarse grid resolution ([4]). In the present case, $\tau_{ij}^{sgs} = -2\bar{\rho} \nu_t (\bar{S}_{ij} - [1/3] \bar{S}_{kk} \delta_{ij}) + [2/3] \bar{\rho} k^{sgs} \delta_{ij}$ and the subgrid kinetic energy k^{sgs} is obtained by solving the following equation ([10]):

$$\frac{\partial \bar{\rho} k^{sgs}}{\partial t} + \frac{\partial \bar{\rho} \bar{u}_j k^{sgs}}{\partial x_j} = -\tau_{ij}^{sgs} \frac{\partial \bar{u}_i}{\partial x_j} - D^{sgs} + \frac{\partial}{\partial x_j} \left[\bar{\rho} \frac{\nu_t}{Pr_t} \frac{\partial k^{sgs}}{\partial x_j} \right] + \bar{W}^s \quad (5)$$

Here, $D^{sgs} = C_\epsilon \bar{\rho} k^{sgs 3/2} / \bar{\Delta}$ is the subgrid kinetic energy dissipation rate. In this k^{sgs} - $\bar{\Delta}$ model, C_ν and C_ϵ are coefficients that have to be assigned values *a priori*, or obtained dynamically ([11,12]) as a part of the solution. In the present study, values of $C_\nu = 0.067$ and $C_\epsilon = 0.916$ are chosen, based on a recent analytical derivation us-

ing the viscous-convective spectral form of high-Re turbulence ([13,14]). Finally, the source term \bar{W}^s is the (subgrid) turbulent energy production or depletion due to droplet-gas interactions. The closure of this term follows the original KIVA model ([15]) except that, in KIVALES it is determined as a function of k^{sgs} instead of k . A more formal LES closure, as described earlier ([16]) is also possible and this is an issue for future investigation. The species mass flux Φ^{sgs} is modeled by a gradient diffusion closure,

$$\Phi_{i,m}^{sgs} = -\bar{\rho} \frac{\nu_t}{Sc_t} \frac{\partial \bar{Y}_m}{\partial x_i} \quad (6)$$

in both KIVA-3V and KIVALES. However, in KIVALES-LEM this term does not have to be modeled since the scalar field evolves in a different manner which obviates the need for this closure. The subgrid velocity-pressure gradient correlation term, Π^{sgs} is ignored, following earlier studies ([17]).

Finally, the subgrid heat flux term, h_j^{sgs} is modeled as ([4,17])

$$h_j^{sgs} = -\bar{\rho} \frac{\nu_t C_p}{Pr_t} \frac{\partial \bar{T}}{\partial x_j} \quad (7)$$

and Θ^{sgs} which represents subgrid viscous work is modeled (following KIVA-3V closure) as $\Theta^{sgs} = D^{sgs} = C_\epsilon \bar{\rho} k^{sgs 3/2} / \bar{\Delta}$.

Linear-Eddy Mixing (LEM) Model

The LEM model offers a fundamentally different closure for the scalar fields within the context of LES. This model, originally developed by Kerstein [18] for stand-alone turbulent mixing studies, was extended into a subgrid model for LES ([7]). In LEM, subgrid turbulent mixing and molecular diffusion processes evolve concurrently in a one-dimensional domain within each LES cell. This one-dimensional domain represents an instantaneous slice through the local subgrid scalar structure and the resolution is fine enough to resolve the smallest eddy (e.g., Kolmogorov eddy, η), if warranted.

To describe the LEM model, the exact species conservation equations are rewritten in the following form:

$$\frac{\partial Y_m}{\partial t} + (\bar{u}_j + u_j'') \frac{\partial Y_m}{\partial x_j} - \frac{1}{\rho} \frac{\partial}{\partial x_j} \left[\rho D_m \frac{\partial Y_m}{\partial x_j} \right] = \frac{\dot{\rho}_m^s}{\rho} \quad (8)$$

where \bar{u}_j is the Favre-filtered velocity and $u_j'' = u_j - \bar{u}_j$ is the unresolved velocity fluctuation at the local cell face. Here, u_j'' is further decomposed into two parts: an isotropic subgrid fluctuation, u_j^{sgs} , obtained using the subgrid Reynolds number and an anisotropic fluctuation resolved on the LES grid, u_j^{LES} , obtained using k^{sgs} . Note that, the above species equation is not filtered unlike Eq. (4) and is solved in three phases (as in KIVA-3V), as follows:

$$\frac{Y_m^A - Y_m^n}{\Delta t} = \frac{\rho_m^s}{\rho} \quad (9)$$

$$\frac{Y_m^B - Y_m^A}{\Delta t} = \frac{1}{\rho} \frac{\partial}{\partial x_j} \left(\rho D_m \frac{\partial Y_m}{\partial x_j} \right) - u_j^{sgs} \frac{\partial Y_m}{\partial x_j} \quad (10)$$

$$\frac{Y_m^{n+1} - Y_m^B}{\Delta t} = -(\bar{u}_j + u_j^{LES}) \frac{\partial Y_m}{\partial x_j} \quad (11)$$

Superscripts n, A, B denote, respectively, the time level, the phase A (in which spray and chemistry are treated), and the phase B (in which Lagrangian fluid motion is carried out ([15])). Although combustion and heat release are not included in the present study, the extension of the LEM model to account for these effects has been demonstrated in the cited references.

Equation (11) is integrated on the resolved scale while Eq. (10) is implemented in the one-dimensional LEM domain in the following form:

$$\frac{\partial Y_m}{\partial t} = \frac{1}{\rho} \frac{\partial}{\partial s} \left[\rho D_m \frac{\partial Y_m}{\partial s} \right] + F_m^{\text{stir}}, \quad (12)$$

where s is the LEM coordinate direction which oriented in the flame normal direction. In these equations, molecular diffusion is implemented explicitly, as in a DNS, while the subgrid turbulent stirring, denoted as F_m^{stir} is modeled by a stochastic process. This is briefly discussed below, and more details can be found in Refs. [7], [13], [19].

Turbulent small-scale stirring is implemented by a series of rearrangements of the scalar field in the one-dimensional domain. Each rearrangement event physically represents the effect of a turbulent eddy of a given size l (within a range $\eta < l < \bar{\Delta}$) on the scalar field(s) and is determined by two parameters: a pdf of the eddy size distribution $f(l) = (5/3)(l^{-8/3}) / (\eta^{-5/3} - \bar{\Delta}^{-5/3})$ in the range $\eta < l < \bar{\Delta}$ ([18]), and an event frequency per unit length Λ :

$$\Lambda = \frac{54}{5} \frac{\nu \text{Re}^{sgs} (\bar{\Delta}/\eta)^{5/3} - 1}{\bar{\Delta}^3 [1 - (\eta/\bar{\Delta})^{4/3}]} \quad (13)$$

Here, the subgrid Reynolds number is defined as $\text{Re}^{sgs} = u' \bar{\Delta} / \nu$, and $u' = \sqrt{(2/3)k^{sgs}}$. Both $f(l)$ and Λ are determined using Kolmogorov scaling for three-dimensional inertial range turbulence and it is this feature of subgrid stirring that makes it feasible for the LEM model to capture three-dimensional turbulent stirring effects within a one-dimensional domain. The procedure for turbulent stirring requires determining the stirring time interval $\Delta t_{\text{stir}} = 1/\Lambda \bar{\Delta}$, choosing an eddy size from $f(l)$ and an event location (chosen randomly from a uniform distribution), and then implementing a mapping procedure (called triplet map) which “stirs” the scalar field. Additional details are given elsewhere ([18]).

To complete the LEM model, convection of the subgrid scalar field across the LES cell faces due to resolved-scale advection (Eq. (11)) has to be implemented. In this study, linear superposition of subgrid field according to the local cell-face volume flux ratio is implemented ([16,20]) since this method suits phase C of KIVA. In this method, each upwind side subgrid field is superimposed onto the adjacent downwind side subgrid field, and its ratio is determined by the local volume-flux ratio ($\mathbf{u} \cdot \mathbf{A} \Delta t / V$).

Large-Eddy Simulation (LES) of Temporal Mixing Layers

To investigate the mixing process, LES of temporally growing mixing layer using KIVALES is performed and the results are compared with predictions using KIVA-3V. The initialization for the temporal mixing layer problem follows the earlier DNS study by Metcalfe et al. [21], and the results are compared based on the same nondimensional time and Reynolds number based on the initial vorticity thickness ($\text{Re} = U_0 \delta_i / \nu = 400$, and $U_0 = \Delta U / 2$) reported in that study. Computational domain is nondimensionalized by initial vorticity thickness δ_i and is $2\pi^3$ in nondimensional space with periodic boundary condition applied in the streamwise direction while spanwise and transverse direction employs slip-wall condition. This setup is slightly different to the original case ([21]) where periodic boundary condition is also used in the spanwise direction. However, since only primarily two-dimensional modes are simulated, this change in spanwise boundary condition should not impact the overall results significantly. According to Riley and Metcalfe [22], it takes a nondimensional time (scaled by $\delta_i / \Delta U$) of around 8 for the fundamental mode to grow, roll up into a vortex, and saturate. Here, 32^3 and 64^3 grids are used for both KIVA-3V and KIVALES simulations.

Figure 1 shows the growth of fundamental energy mode as a function of time. KIVALES shows a similar trend as in Fig. 1 of Metcalfe et al.; however, KIVALES is more dissipative and eventually is not able to maintain a saturated state of vortex rollup. The initial linear energy growth rate, $\sigma = (dE/dt)/2E$, predicted by

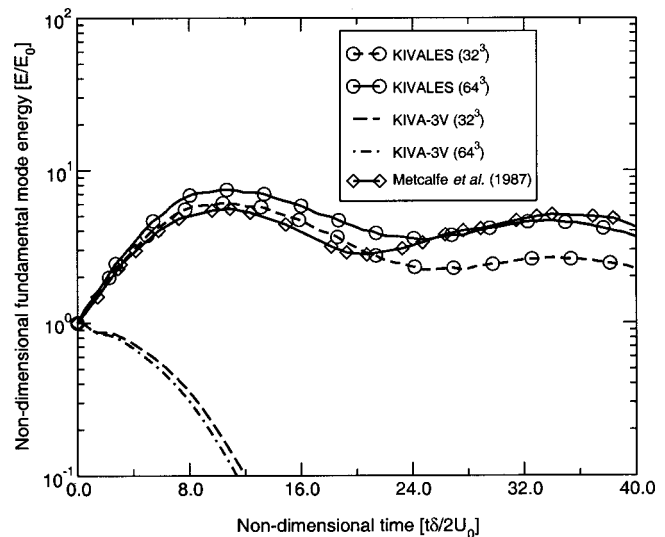


Fig. 1 Resolved scale fundamental mode energy growth. Growth rate of KIVALES is 0.19, which is also predicted by an earlier study by [23] whereas KIVA-3V rapidly dissipates.

KIVALES is 0.19, which matches the value of 0.19 predicted by linear instability analysis ([23]) and predicted by DNS ([21]). On the contrary, KIVA-3V shows immediate energy decay right after the start of the simulation.

The original KIVA-3V code has significantly high dissipation and the vortex is dissipated before it forms. On the other hand, the mixing layer rollup predicted by the KIVALES is much closer to that predicted by DNS, and the vortex rollup occurs in KIVALES at around the nondimensional time predicted by Metcalfe et al. [21]. This suggests that in the KIVALES code total dissipation is reduced when the $k-\epsilon$ model is replaced by the LES $k^{sgs}-\bar{\Delta}$ subgrid model. Increase in grid resolution also improves the LES prediction, as shown in Fig. 1. With 64^3 grid, the fundamental mode energy is better maintained and the “braid” regions are resolved better than in the 32^3 grid (not shown here). On the other hand, even when the finer grid is employed, KIVA-3V shows high dissipation. Even though the case presented here is not “real” turbulence but rather an idealized flow field, the ability to capture the growth and breakdown of large-scale structures is critical to predict accurate mixing. Thus, it appears from this study that time-averaged turbulence models such as the standard $k-\epsilon$ model may not be able to capture temporally varying mixing process in a DISI engine.

This study demonstrates that KIVALES is capable of capturing the time-accurate evolution of vortex rollup. Note that, since only a coherent two-dimensional mode growth is simulated, the three-dimensional temporal mixing layer should contain negligible subgrid kinetic energy (and this is confirmed from the data). Thus, the KIVALES implementation shows that the subgrid k^{sgs} model is behaving as expected and is not introducing additional dissipation when not required. In contrast, in the KIVA-3V code, the $k-\epsilon$ model introduces excessive dissipation regardless of the state of the flow field.

Large-Eddy Simulation (LES) of Flow Within a Piston-Cylinder Engine

As application to IC engines is of eventual interest, LES of flow in a motor-driven, fixed-valve piston cylinder engine configuration is conducted. This configuration has been studied experimentally ([24]), and more recently, numerically using an unstructured LES solver ([25]). Geometry used for this study follows the experimental setup ([24]). There is one fixed valve with a valve gap of 4 mm in a radial direction, opening at 30 deg from the axis. The

piston is driven as a simple harmonic motion at a rate of 200 rpm, which results in a mean piston velocity, $\bar{U} = 40$ cm/s, and a Reynolds number (based on the mean piston velocity and the bore diameter, 7.5 cm) of around 2000.

Computational grid used in this study incorporates $54 \times 54 \times 23$ computational cells in the cylinder part, totaling approximately 80,000 cells. The geometry is axisymmetric, but a full-sector mesh is used to investigate the effect of azimuthal variation of velocity field. The flow field around the inlet valve gap is of particular importance for port-fuel-injection IC engines, since fuel droplet atomization and transport process are affected by the flow field around the gap ([26]). This region is also important for DISI engines as it introduces swirl and tumble motion inside the cylinder. Therefore, the grid is clustered in this region.

Note that, the present resolution is much coarser (by a factor of three) than the resolution used by Haworth [25]. On the other hand, since a higher-order subgrid model (based on k^{sgs}) is used in KIVALES (compared to the algebraic model in the earlier study), it is expected that reasonably accurate predictions using relatively coarse grid will be possible. Similar observations were obtained in past studies ([11,27]) of both nonreacting and reacting flows.

Pressure boundary condition is specified at the inlet where atmospheric mean pressure and a small random fluctuation (of 5% of mean at most is specified). At all walls, no-slip and adiabatic conditions are imposed.

Shown in Fig. 2 are the mean and rms axial velocity profiles obtained on several planes perpendicular to the cylinder axis at the crank angle of 36 deg from TDC. The KIVALES results are obtained by averaging over all five cycles as well as averaging azimuthally. Computation using KIVA-3V is also performed for comparison purpose but only for one cycle. Mean velocity profiles predicted by KIVA-3V show generally good agreement. However, it underestimates the turbulence rms profiles considerably. Very good agreement is observed in the mean velocity profiles using KIVALES at every measurement location, ($x = 1.0, 2.0,$ and 3.0 from the cylinder head). The LES prediction of the rms profiles includes both the resolved and subgrid turbulence effects (i.e., $u' = \bar{u}'^{rms} + \sqrt{2/3k^{sgs}}$). Although the agreement with data is superior in KIVALES some deviation from experimental data is also observed, for example, at around $x = 2.0$. There are two possible reasons for this. Axial fluctuations might be larger than in other two directions, but the contribution from k^{sgs} is added assuming isotropy in the subgrid scales. Another reason may be the low spatial resolution used in present study. Haworth and Jansen obtained a better agreement in their LES study with a much finer grid. Increasing the resolution in KIVALES would result in significant increase in the computational cost unless parallel processing is carried out (as done by Celik et al. [9]). Parallel implementation of KIVALES is being considered but remains to be accomplished. Regardless, the present agreement with data is reasonable for the resolution employed.

Large-Eddy Simulation (LES) of Flow Within a Direct Injection Engine

The computational geometry used for this study is shown in Fig. 3. This geometry features two vertical valves, one for intake and one for exhaust, and a high compression ratio cylinder. A baseline grid of $40 \times 17 \times 56$ computational cells in cylinder part (at bottom dead center) with a total of around 51,000 cells is used. A coarser grid of 21,000 cells, and a finer grid of 96,000 cells are also used for some of the simulations; however, the results are discussed relative to the baseline case. RANS results obtained using the baseline resolution are indistinguishable from the higher resolution study indicating that grid independence is achieved. In LES, grid independence has a different interpretation since an increase in grid resolution will resolve more fine-scale structures which will, in turn, modify some of the turbulent features. However, in the time-averaged sense (where only mean and rms prop-

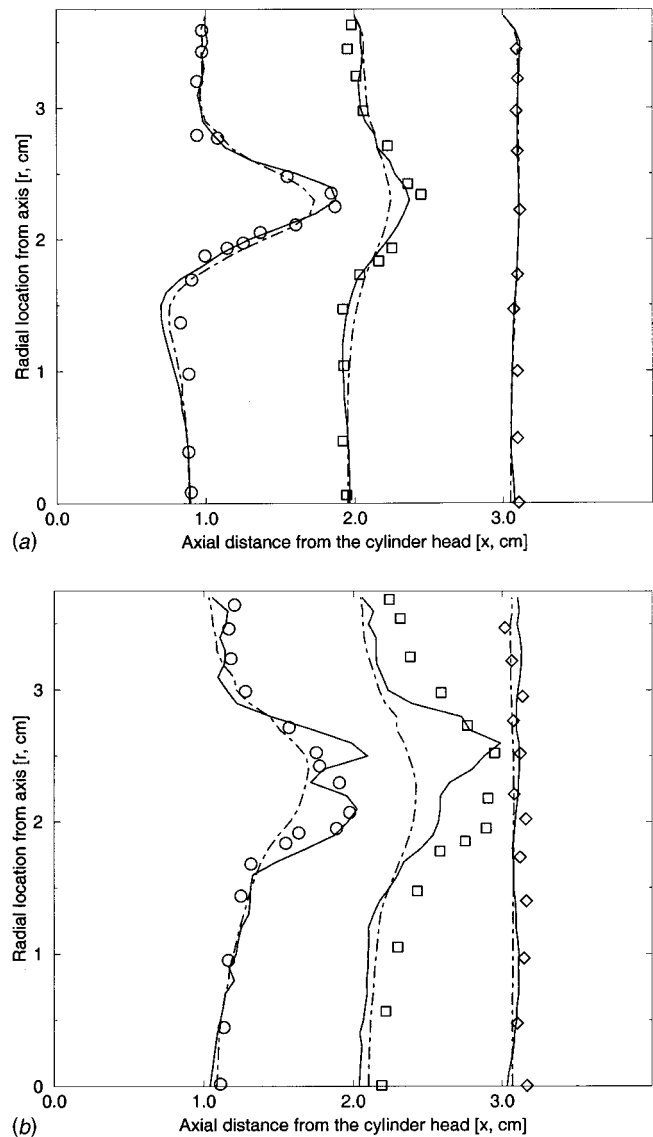


Fig. 2 Comparison of KIVA-3V and KIVALES predictions of turbulent mean and rms profiles in the experimental configuration. Symbols represent experimental data ([24]), solid lines and dot-dashed lines represent KIVALES and KIVA-3V, respectively. Scale of 1.0 on the x-axis corresponds to 400 cm/s in (a) and 1200 cm/s in (b), respectively. (a) Mean velocity profile at 36 deg crank angle. (b) rms velocity profile at 36 deg crank angle.

erties are of interest), LES predictions also reach stationarity as long as sufficient number of flow-through times are used. On the other hand, convergence of higher-order correlations is not likely unless very high resolution LES over many time cycles are conducted.

Some important initial conditions are summarized in Table 1. Simulations begin from the middle of an engine cyclic operation at a fixed revolution. Thus, initially, moderately high temperature, and remanent gaseous fuel and combustion products are assumed to be in the combustion chamber with an ignitable concentration. These conditions are obtained from earlier studies ([8]). Fuel is gasoline (C_8H_{17}) and injected directly into combustion chamber in a conical spray, and the spray vaporizes immediately after injection because of the high temperature in the cylinder. The fuel injector is located at the middle of the cylinder top.

RANS and LES studies of spray injection into the hot cylinder gas mixture are conducted and compared. The injected fuel drop-

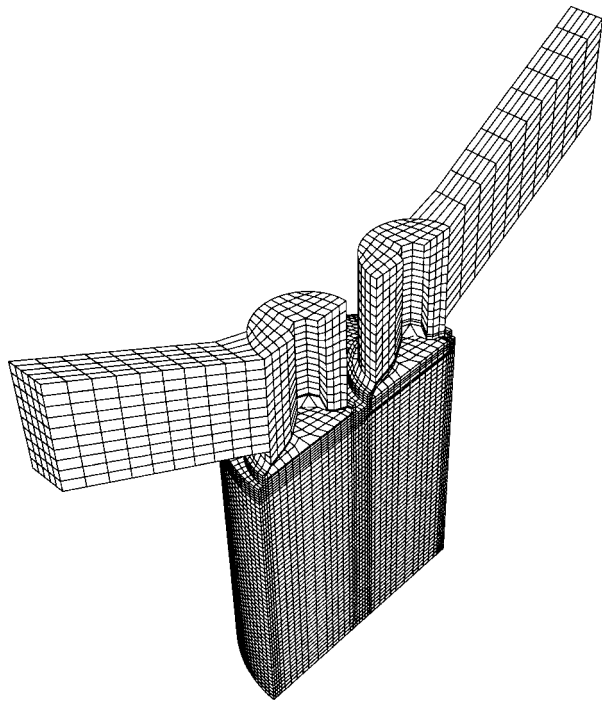


Fig. 3 Geometry used for the internal combustion engine simulations with two valves, one is the intake and the other is the exhaust. The symmetric boundary condition is employed on the plane of symmetry. The pictures shown here are the baseline geometry (51,000 cells).

lets vaporize and fuel-air turbulent mixing in the gas phase becomes a controlling parameter. Figures 4(a) and (b) show the vorticity field predicted by KIVA-3V and KIVALES, respectively, for the same grid resolution. Clearly, KIVALES shows a significantly different (and relatively more complex) turbulent structures than KIVA-3V. This demonstrates that dissipation in KIVALES is considerably reduced due to the $k^{sgs}-\Delta$ model. Increase in the resolution in LES (Fig. 4(c)) allows resolution of finer scales of motion (as noted earlier).

Figures 5(a)–(c) show the predicted gaseous fuel mass fraction and the stoichiometric surface at a crank angle of 210 deg. KIVA-3V shows a very diffused field with no significant three-dimensional structure, whereas both KIVALES and KIVALES-LEM show more complex three-dimensional fields. Interestingly, all models predict nearly the same spatial mean fuel mass fraction profile. However, KIVALES-LEM predicts a much larger scalar variance compared to the other two models (Fig. 6). This is a direct consequence of subgrid turbulent mixing that is explicitly included in the KIVALES-LEM approach (whereas, in the other approaches, a simple resolved-scale diffusion is modeled). On the other hand, as turbulence decays, all model predictions converge, as they should.

Table 1 Initial conditions for DI engine simulations

Engine speed (rpm)	1500
Intake gas temperature (K)	310
Residual gas temperature (K)	900
Fuel	gasoline (C_8H_{17})
Start-of-injection (deg)	none, 90, 180 (3 cases)
Injection duration (deg)	48
Sauter mean radius (cm)	1.0×10^{-3}
Spray angle (deg)	75
Overall fuel-air ratio	15

Further analysis reveals that the probability density function (pdf) of the fuel mass fraction predicted by LES and RANS are significantly different (Fig. 7). In particular, significant deviation of the LES results (interestingly, both KIVALES and KIVALES-LEM show similar results, thus indicating that the resolved large-scale mixing are captured consistently) from the RANS results is observed. Since there is no experimental data for comparison, these results can be considered only indicative of the predictive capability of the LES models.

Turbulent kinetic energy (TKE) field is also modified by fuel droplets. The injection timing study (using KIVA-3V) by Han et al. [28] showed considerable amount of turbulent intensity at a later fuel injection timing (SOI=180). However, this can be attributed to the higher dissipation in the KIVA-3V code which is confirmed here since our RANS predictions agrees with these earlier results ([28]). In contrast, LES predicts a 2.4% increase in turbulent intensity at SOI=180 degree (13.9% in Han et al.), and a 9.7% increase at SOI=90 deg (−3.7% in Han et al.) at TDC. The current RANS and LES predictions of TKE are shown in Fig. 8. Three key observations can be made: (i) RANS and LES results are self-consistent, (ii) as expected, RANS TKE is much higher than LES since RANS models all turbulent scales whereas in LES, only the TKE from the unresolved scales is modeled by k^{sgs} , and (iii) the peak TKE occurs earlier in LES (indicating that turbulence production and mixing by the resolved-scale velocity and scalar gradients is more resolved in the LES).

Figure 9 shows the instantaneous snapshots of turbulent kinetic energy and SGS kinetic energy. Besides the difference in the order of magnitude (as in Fig. 8), LES captures the fine-scale structure of turbulence. Note that, when multiple cycles of the LES fields are averaged it is likely that some of these fine-scale features will be smeared out. However, since mixing and combustion processes are local and time-dependent, the present results suggest that both KIVALES and KIVALES-LEM have the ability to capture local fine-scale (and time-dependent) features.

The computational cost of LES can be considerable since multiple cycles of the flow field must be simulated to obtain the time-averaged properties. For a half-cycle (0–360 deg) simulation on a SGI Origin 2000 (195 MHz) system for the baseline case, around 8 CPU hours are needed for KIVALES and around 30 CPU hours for KIVALES-LEM. KIVA-3V is only slightly more expensive than KIVALES (due to the two-equation model used in KIVA-3V compared to the one-equation model used in KIVALES). Regardless, KIVALES would be four to five times more expensive (since four to five cycles are needed for averaging) and the cost of KIVALES-LEM is even more (unless parallel implementation is carried out since LEM is uniquely parallel in its application). Thus, the increased cost associated with KIVALES-LEM cannot be justified unless it can be demonstrated that the predictions are significantly superior. This justification should be made within the context of reacting flows with heat release since it is in this type of flow where LEM has demonstrated its superior ability in the past. Nevertheless, it is clear from this study that LES is capable of capturing unsteady fuel-air mixing features over a wide range of length scales and with the LEM closure, additional differences are observed in the scalar mixing process.

Conclusions

Fuel-air mixing process in a DISI engine is simulated with RANS based code (KIVA-3V) and the LES-based code (KIVALES) with and without LEM. It is found that the unsteady features of fuel-air mixing are captured in the LES whereas the RANS version is unable to resolve these features. This observation is particularly important since the same numerical algorithm and spatial resolution are employed for both LES and RANS. The LES version of the code shows an ability to capture dynamically evolving fine-scale vortical and scalar structures. In contrast, these features are markedly absent in the RANS calculations due to turbulence model induced dissipation.

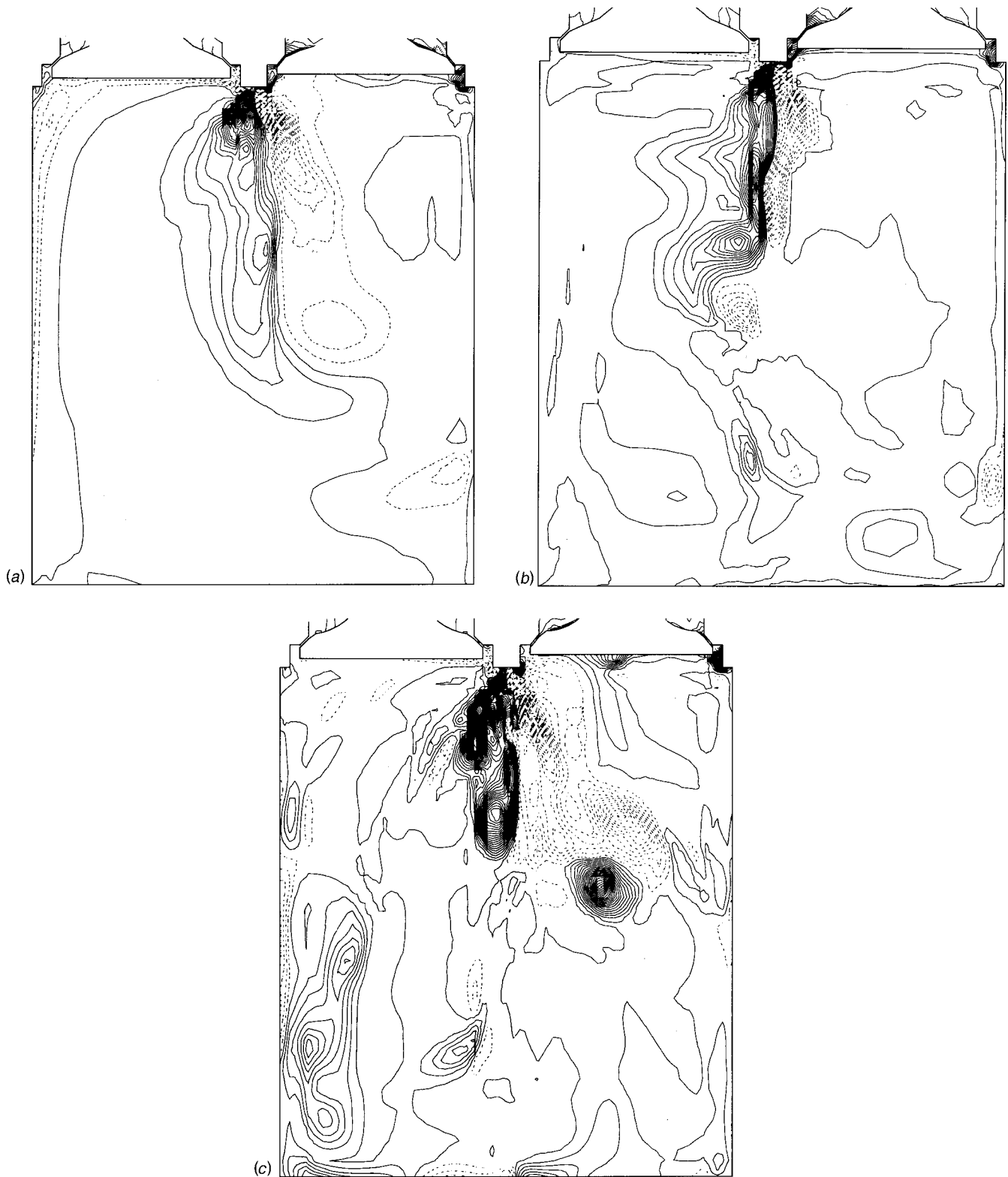


Fig. 4 Azimuthal vorticity at crank angle=210 (during injection). Contour intervals are fixed with $\Delta\omega=1000(\text{sec}^{-1})$. Solid contours show positive vorticity while dotted contours show negative vorticity. Even with fuel injection and vaporization, KIVALES still shows turbulent flow field. (a) KIVA-3V, start of injection=180, baseline grid. (b) KIVALES, start of injection=180, baseline grid. (c) KIVALES, start of injection=180, fine grid.

KIVALES predictions are also different for fuel spray vaporization and mixing in the DI engine. Since the spray model is unchanged, these differences may be due to changes to the droplet transport and fuel-air mixing caused by the presence of coherent

vortical structures. It is known that droplets tend to accumulate in low vorticity regions and that droplet motion depends upon the relative velocity between the two phases. With LES, fluctuations in the velocity field are resolved over a range of scales (both

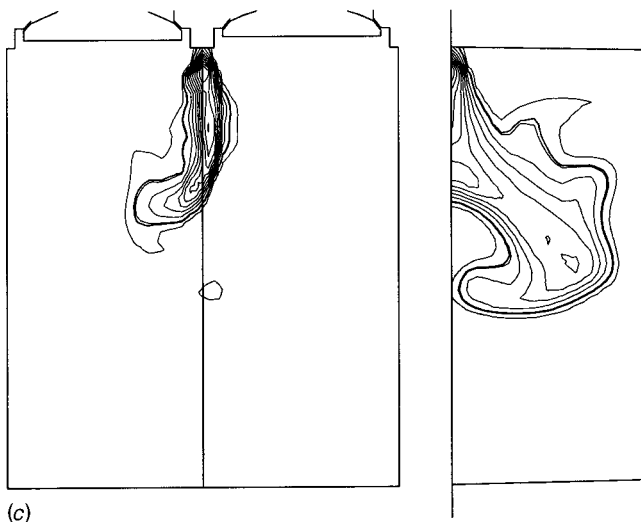
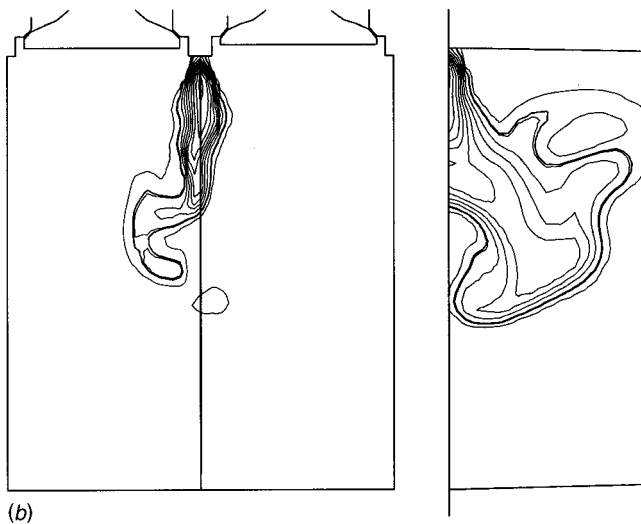
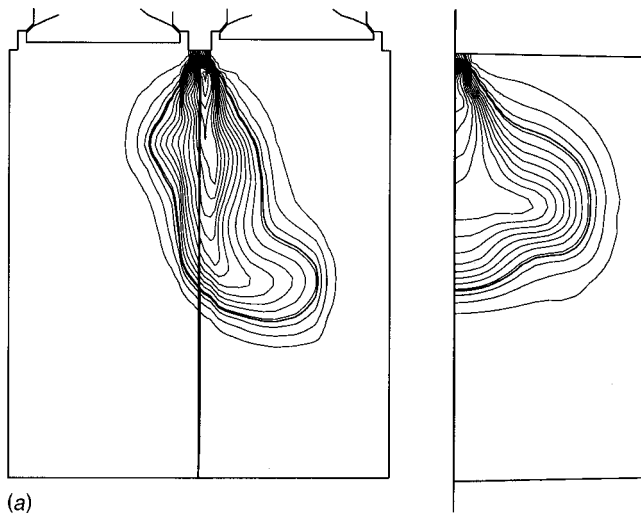


Fig. 5 Fuel mass fraction (gaseous) at crank angle=210. Contour intervals are $\Delta Y=0.03$. A bold line denotes the stoichiometric surface. Figures on the left show contours in the symmetric plane and the ones on the right show in the plane perpendicular to the symmetric plane (the location is shown as a line in the left figures). (a) KIVA-3V, (b) KIVALES, (c) KIVALES-LEM.

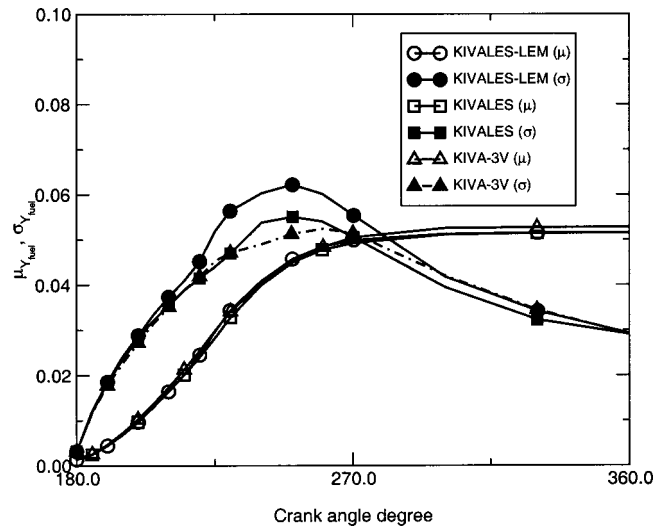


Fig. 6 Temporal evolution of scalar (fuel mass fraction) mean (μ) and the variance (σ^2) standard deviation (σ) is shown for comparison between gradient diffusion closure KIVALES and KIVALES-LEM. Light lines denote mean while black lines denote standard deviation. Note that the linear eddy model (LEM) predicts larger scale variance between bottom dead center and top dead center.

spatially and temporally) and this would directly impact droplet transport and hence, vaporized fuel mixing with air. Comparison of the two types of LES show that the gradient diffusion closure in KIVALES predicts smaller scalar variance than KIVALES-LEM although scalar mean profiles are almost similar. The implication of this effect will be more apparent in reacting flows and is being investigated. Finally, it remains to be demonstrated that there is an absolute need for the more expensive KIVALES-LEM closure for such flow problems. However, past simulations of turbulent mixing and reacting flows using LEM in gas turbine combustors and shear layers ([4]) have already demonstrated that LEM-based SGS model has the ability to capture the fine-scale substructure and predict flame-turbulence interactions more accurately. Thus, it is

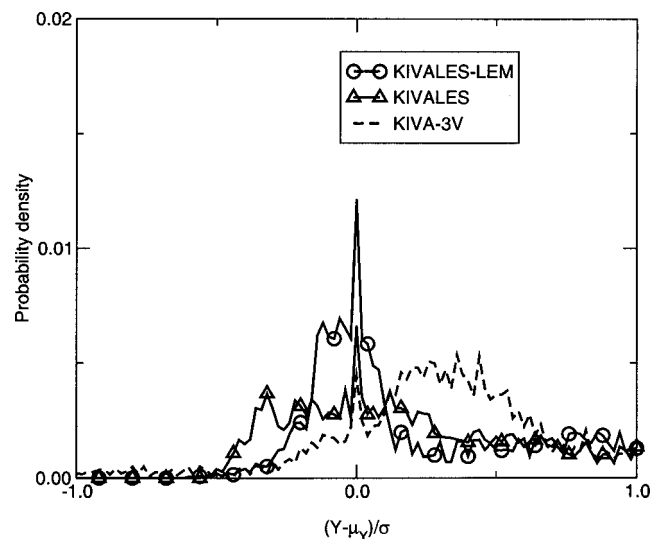


Fig. 7 PDF of fuel mass fraction normalized by the standard deviation at crank angle=360 where mean and variance are nearly same for all three cases while the shape of PDF is different in each case.

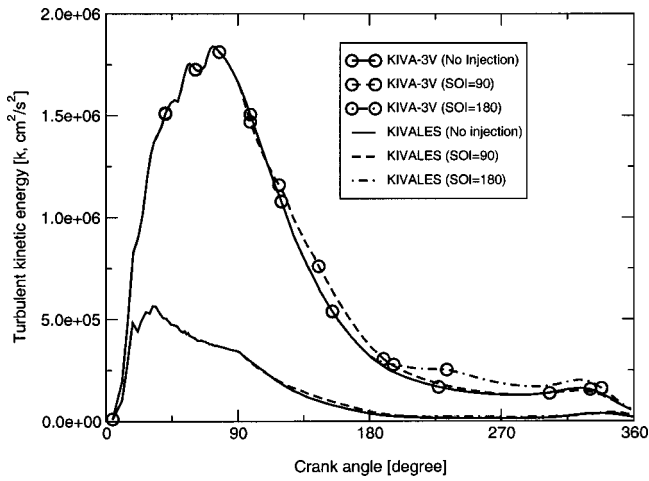


Fig. 8 Turbulent kinetic energy evolution with crank angle. Light lines indicate KIVA-3V while dark lines indicate KIVALES. KIVA-3V models are turbulent scales except the largest scale motions, therefore, the turbulent kinetic energy in KIVA-3V is larger than the subgrid scale turbulent kinetic energy in KIVALES.

anticipated that a parallel version of KIVALES-LEM could be an accurate and a reliable simulation tool to study complex flows as in the DISI engine.

Acknowledgment

This work is supported by Ford Motor Company and by National Science Foundation through a Connectivity Grant through the Engineering Research Center at Mississippi State University. The authors would like to acknowledge valuable comments by Dr. James Yi (Ford Motor Company) and Professor Daniel Haworth (Penn State University). We would also like to thank Professor Haworth for providing the experimental data for validation.

Nomenclature

- CA = crank angle (deg)
- DISI = direct-injection spark-ignition
- DNS = direct numerical simulation
- LEM = linear-eddy model
- LES = large-eddy simulation
- RANS = Reynolds-averaged Navier-Stokes (equations)
- SOI = start-of-injection (deg)
- SGS,
 - sgs = subgrid scale
 - D_m = molecular diffusivity of species m
 - e = specific internal energy
 - $f(l)$ = distribution function of eddy size l in a subgrid domain
 - k = turbulent kinetic energy
 - Pr_r = turbulent Prandtl number
 - Re = Reynolds number
 - Sc_t = turbulent Schmidt number
 - S_{ij} = rate-of-strain tensor
 - U_0 = reference velocity, $= \Delta U/2$ (used in mixing layer)
 - u_i = velocity
 - Y_m = mass fraction of species m
 - δ_i = initial vorticity thickness of mixing layer
 - δ_{ij} = Kronecker delta
 - η = Kolmogorov length scale
 - κ = thermal conductivity
 - Λ = event frequency per unit length in LEM
 - λ = the second coefficient of viscosity
 - ν_i = eddy viscosity

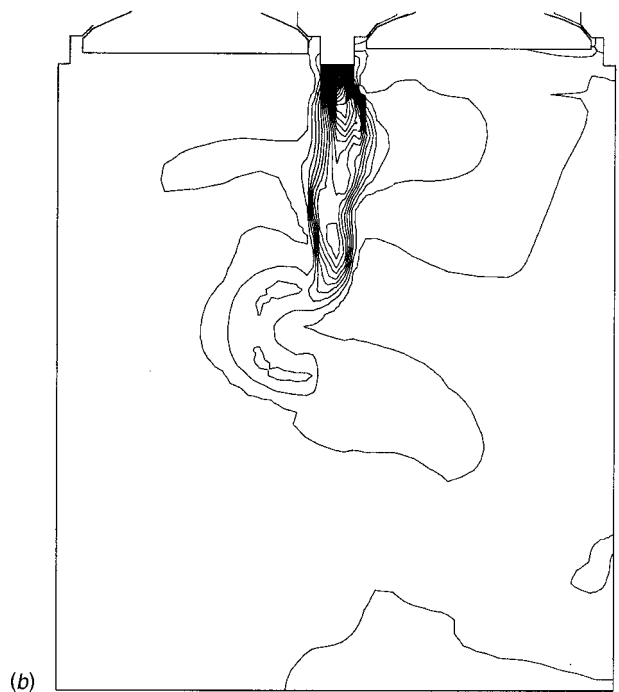
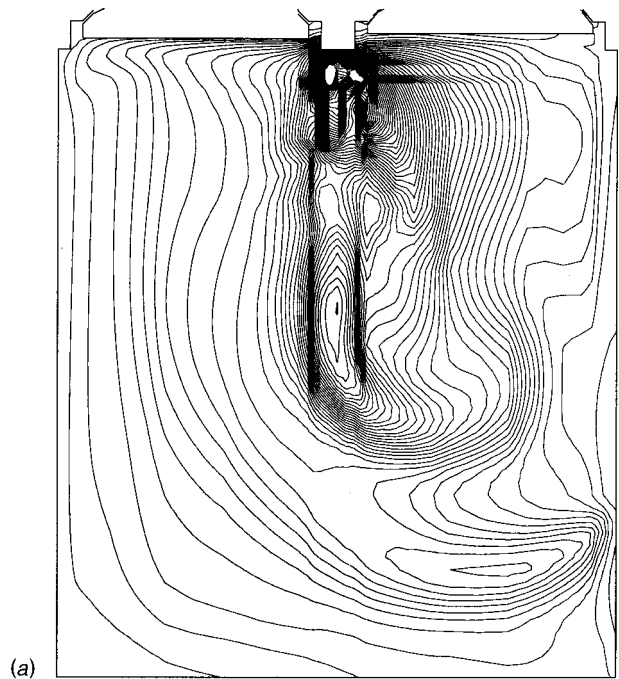


Fig. 9 Turbulent kinetic energy at crank angle=210. Contour intervals are fixed with $\Delta k=1.0 \times 10^5$ (cm²/sec²) for KIVALES and $\Delta k=2.0 \times 10^5$ (cm²/sec²) for KIVA-3V, which is twice the magnitude obtained with KIVALES. (a) KIVA-3V, start of injection=180. (b) KIVALES, start of injection, start of injection=180.

- ρ = density
- σ_{ij} = viscous stress tensor
- τ_{ij} = stress tensor

References

[1] Anderson, R. W., Yang, J., Brehob, D. D., Vallance, J. K., and Whiteaker, R. M., 1996, "Understanding the Thermodynamics of Direct Injection Spark Ignition (DISI) Combustion Systems: An Analytical and Experimental Investigation," SAE Paper No. 962018.

- [2] Iwamoto, Y., Noma, K., Nakayama, O., Yamauchi, T., and Ando, H., 1997, "Development of Gasoline Direct Injection Engine," SAE Paper No. 970541.
- [3] Galperin, B., and Orszag, S., eds., 1993, *Large Eddy Simulation of Complex Engineering and Geophysical Flows*, Cambridge University Press, New York.
- [4] Menon, S., 2000, "Subgrid Combustion Modelling for Large-Eddy Simulations," *Int. J. Engine Res.*, **1**(2), pp. 209–227.
- [5] Smagorinsky, J., 1963, "General Circulation Experiments With the Primitive Equations: I. The Basic Equations," *Mon. Weather Rev.*, **91**, pp. 99–164.
- [6] Mungal, M. G., and Dimotakis, P. E., 1984, "Mixing and Combustion With Low Heat Release in a Turbulent Shear Layer," *J. Fluid Mech.*, **148**, pp. 349–382.
- [7] Menon, S., McMurtry, P. A., and Kerstein, A. R., 1993, "A Linear Eddy Mixing Model for Large Eddy Simulation of Turbulent Combustion," *Large Eddy Simulation of Complex Engineering and Geophysical Flows*, B. Galperin and S. Orszag, eds., Cambridge University Press, New York, pp. 287–314.
- [8] Han, Z., and Reitz, R. D., 1995, "Turbulence Modeling of Internal Combustion Engines Using RNG $k-\epsilon$ Models," *Combust. Sci. Technol.*, **106**, pp. 267–295.
- [9] Celik, I., Yavuz, I., Smirnov, A., Smith, J., Amin, E., and Gel, A., 2000, "Prediction of In-Cylinder Turbulence for IC Engines," *Combust. Sci. Technol.*, **153**, pp. 339–368.
- [10] Menon, S., Yeung, P.-K., and Kim, W.-W., 1996, "Effect of Subgrid Models on the Computed Interscale Energy Transfer in Isotropic Turbulence," *Comput. Fluids*, **25**(2), pp. 165–180.
- [11] Kim, W.-W., Menon, S., and Mongia, H. C., 1999, "Numerical Simulations of Reacting Flows in a Gas Turbine Combustor," *Combust. Sci. Technol.*, **143**, pp. 25–62.
- [12] Kim, W.-W., and Menon, S., 1999, "A New Incompressible Solver for Large-Eddy Simulations," *Int. J. Numer. Methods Fluids*, **31**, pp. 983–1017.
- [13] Chakravarthy, V. K., and Menon, S., 2000, "Modeling of Turbulent Premixed Flames in the Flamelet Regime," *Combust. Sci. Technol.*, **162**, pp. 1–50.
- [14] Chakravarthy, V. K., and Menon, S., 2000, "Subgrid Modeling of Premixed Flames in the Flamelet Regime," *Flow, Turbul. Combust.*, **65**, pp. 131–161.
- [15] Amsden, A. A., O'Rourke, P. J., and Butler, T. D., 1989, "KIVA-II: A Computer Program for Chemically Reactive Flows With Sprays," Technical Report LA-11560-MS, Los Alamos National Laboratory, May.
- [16] Pannala, S., and Menon, S., 2000, "On Large Eddy Simulations of Reacting Two-Phase Flows," Technical Report CCL-00-006, Georgia Institute of Technology, Atlanta, GA, May.
- [17] Menon, S., and Calhoun, W., 1996, "Subgrid Mixing and Molecular Transport Modeling for Large-Eddy Simulations of Turbulent Reacting Flows," *Proc. Combust. Inst.*, **26**, pp. 59–66.
- [18] Kerstein, A. R., 1991, "Linear-Eddy Modelling of Turbulent Transport. Part 6. Microstructure of Diffusive Scalar Mixing Fields," *J. Fluid Mech.*, **231**, pp. 361–394.
- [19] Chakravarthy, V. K., and Menon, S., 2000, "Linear-Eddy Simulations of Schmidt and Reynolds Number Scaling of Scalar Mixing," *Phys. Fluids*, **13**, pp. 488–499.
- [20] Sone, K., Patel, N. V., and Menon, S., 2001, "KIVALES—Large-Eddy Simulations of Internal Combustion Engines. Part I: Theory and Formulation," Technical Report CCL-2001-008, Georgia Institute of Technology, Atlanta, GA.
- [21] Metcalfe, R. W., Orszag, S. A., Brachet, M. E., Menon, S., and Riley, J. J., 1987, "Secondary Instability of a Temporally Growing Mixing Layer," *J. Fluid Mech.*, **184**, pp. 207–243.
- [22] Riley, J. J., and Metcalfe, R. W., 1980, "Direct Numerical Simulation of a Perturbed, Turbulent Mixing Layer," AIAA Paper No. 80-0274.
- [23] Michalke, A., 1964, "On the Inviscid Instability of the Hyperbolic-Tangent Velocity Profile," *J. Fluid Mech.*, **19**, pp. 543–556.
- [24] Morse, A. P., Whitelaw, J. H., and Yianneskis, M., 1979, "Turbulent Flow Measurements by Laser-Doppler Anemometry in Motored Piston-Cylinder Assemblies," *J. Fluids Eng.*, **101**, pp. 208–216.
- [25] Haworth, D. C., and Jansen, K., 2000, "Large-Eddy Simulation on Unstructured Deforming Meshes: Towards Reciprocating IC Engines," *Comput. Fluids*, **29**, pp. 493–524.
- [26] Weclas, M., Melling, A., and Durst, F., 1998, "Flow Separation in the Inlet Valve Gap of Piston Engines," *Prog. Energy Combust. Sci.*, **24**, pp. 165–195.
- [27] Nelson, C., and Menon, S., 1998, "Unsteady Simulations of Compressible Spatial Mixing Layers," AIAA Paper No. 98-0786.
- [28] Han, Z., Fan, L., and Reitz, R. D., 1997, "Multidimensional Modeling of Spray Atomization and Air-Fuel Mixing in a Direct-Injection Spark-Ignition Engine," SAE Paper No. 970884.

Influence of the Injection Parameters on the Efficiency and Power Output of a Hydrogen Fueled Engine

R. Sierens

e-mail: Roger.Sierens@rug.ac.be

S. Verhelst

e-mail: Sebastian.Verhelst@rug.ac.be

Laboratory of Transporttechnology,
Ghent University,
Sint-Pietersnieuwstraat 41,
B-9000 Bent, Belgium

The advantages of hydrogen fueled internal combustion engines are well known, certainly concerning the ultra-low noxious emissions (only NO_x is to be considered). Disadvantages are the backfire phenomenon and the gaseous state of hydrogen at atmospheric conditions. A complete control of the mixture formation is necessary and therefore a test engine with sequential port injection was chosen. The tests are carried out on a single-cylinder CFR engine with the intention to use the results to optimize a 6 and 8-cylinder engine with multipoint injection. Different positions of the injector against the intake air duct are examined (represented as different junctions). A numerical simulation CFD code (FLUENT) is used under "stationary" conditions (continuous injection) for all geometries and under "real" conditions (sequential injection) for one situation. For each of the geometries the influences of the start of injection, the air/fuel equivalence ratio, injection pressure, and ignition timing on the power output and efficiency of the engine are analyzed. A comparison and discussion is given for all results. It is clearly shown that the start of injection for a certain engine speed and inlet geometry influences the volumetric efficiency and thus the power output of the engine due to the interaction between the injected hydrogen and the inlet pressure waves. Furthermore, the small influence of the injection pressure and the contradictory benefits of the different junctions between power output and fuel efficiency are measured. With retarded injection, so that cool air decreases the temperature of the "hot-spots" in the combustion chamber before the fuel is injected, backfire safe operation is possible. [DOI: 10.1115/1.1496777]

Introduction

Hydrogen is a "clean burning" fuel and has the features of a carbon-free fuel. Its combustion products are mainly water. It produces no toxic components such as hydrocarbons, carbon monoxide, carbon dioxide, oxides of sulphur, and organic acids. In the combustion products, only NO_x are formed. These can be reduced by the engine operation conditions. Furthermore, hydrogen does not have the problems associated with liquid fuels, such as vapor lock and cold wall quenching.

However, the mixing process of the gaseous hydrogen with the air must have the same flexibility and accuracy as liquid fuel injection. In the literature many injection systems are described (see [1–7]). Sequential multipoint injection of the gaseous hydrogen in each inlet channel before the inlet valve shows promising results. In this paper the influences of the injection parameters of an electromagnetic gas injector are examined. The same injectors are used on a multicylinder hydrogen-fueled engine ([8]).

Engine Setup

The test rig is shown in Fig. 1, and consists of a single-cylinder engine of the CFR type, connected to an electromotor. The characteristics of the CFR engine are given in Table 1. The single-cylinder engine runs at a constant speed of 600 rpm, due to its connection with the electromotor ([9]).

The air is admitted through a buffer vessel to obtain a constant air flow in the pipe before the vessel, in order to enable air mass flow measurements. Another flowmeter is installed in the fuel line

between the H₂ storage and the injector. The flowmeters (Nm³/h) are manufactured by Bronkhorst. The flowmeters allow measurement of the air/fuel ratio, which is also possible with the λ-sensor placed in the exhaust pipe.

The injector, located at 40 cm from the inlet valve of the engine, is made by Vialle and was designed to be able to deliver large volumes of gas. With an electronic circuit, the start of injection and the injection duration can easily be regulated. The injection pressure is regulated by a valve on the H₂ storage bottle. The injector is placed at different angles to the inlet air flow. Figure 2 shows the four examined inlet geometries (different junctions):

- Y-junction
- T-junction
- 45-deg junction
- 45-deg junction inverse

A high-pressure transducer is located in the cylinder head flush with the wall. A CAM sensor gives pulses at 1 deg ca (or with an interpolator at 0.5 deg; 0.25 deg; 0.1 deg ca). Another pressure transducer is located in the intake duct, at 8 cm from the inlet valve. The compression ratio is set at 8:1.

Numerical Simulation

A numerical simulation code (FLUENT 5.2.3) is used to calculate the mixing process in the inlet channel. More details on the code can be found in the documentation supplied by Fluent Inc. [10–12]. With the subprogram GAMBIT the geometry is drawn and the meshes are defined. These elements are imported in FLUENT. The boundary conditions for this application are calculated by Delborge and D'haveloose [13].

Contributed by the Internal Combustion Engine of THE AMERICAN SOCIETY OF MECHANICAL ENGINEERS for publication in the ASME JOURNAL OF ENGINEERING FOR GAS TURBINES AND POWER. Manuscript received by the ICE Division, May 29, 2001; final revision received by the ASME Headquarters, February 15, 2002. Editor: D. N. Assanis.

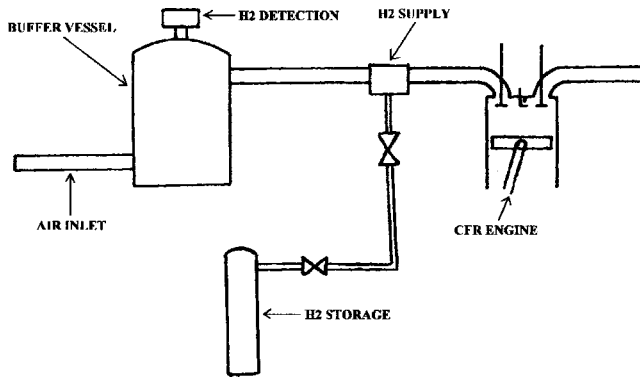


Fig. 1 Engine setup

Table 1 Engine characteristics

Type	CFR Single Cylinder, Four stroke
Bore	82.55 mm
Stroke	114.2 mm
Cylinder volume	612.5 cm ³
Engine speed	600 rpm
Compression ratio	variable

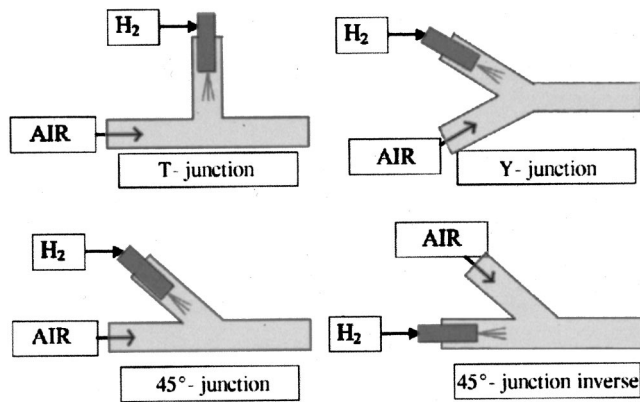


Fig. 2 Inlet geometries (position of the injector)

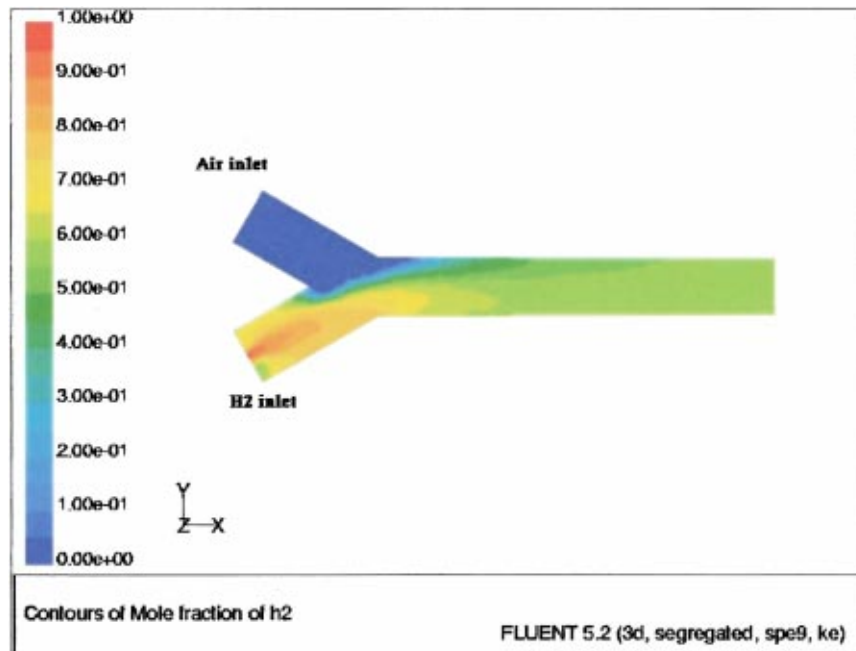


Fig. 3 Mole fraction of H₂ in the intake pipe (Y-junction, stationary condition, λ=2)

Under stationary conditions (continuous injection) the four junctions are simulated resulting in the mixture strength (given as the mole fraction H₂ in the air-fuel mixture) for the whole inlet configuration and at the end cross section of the junction, and resulting in the (total) pressure distribution at the end cross section of the junction. As an example the mole fraction of H₂ for the Y-junction is shown in Fig. 3.

A simulation of sequential injection is made for the Y-junction. As an example the mixture strength in the inlet channel at the moment the inlet valve closes (after three cycles of calculation) is shown in Fig. 4.

Figure 4 indicates that the concentration of H₂ in the injection channel is too high. This is due to a late injection timing (which benefits the power output) but mainly due to a too long injection channel (or the injector too far away from the air intake duct and inlet valve).

Experimental Results and Discussion

The influence of the injection parameters on the power output and efficiency are analyzed. Each time an overview of the results is given, followed by more experimental results and a discussion if necessary.

Definitions

Power Output. For a CFR engine, where the electromotor holds the one cylinder engine at a constant speed, the effective power output is difficult to obtain. Therefore the indicated power output is calculated from an averaged pressure diagram from 30 consecutive cycles following the formula

$$W_i = \sum_{i=1}^{720} p_i \times (V_i - V_{i-1})$$

and

$$P_i = W_i \times \frac{n}{2 \times 60}$$

For a good comparison of measurements taken at different conditions of atmospheric pressure and temperature (p_{atm} and T_{atm}), the normalized indicated power output is used:

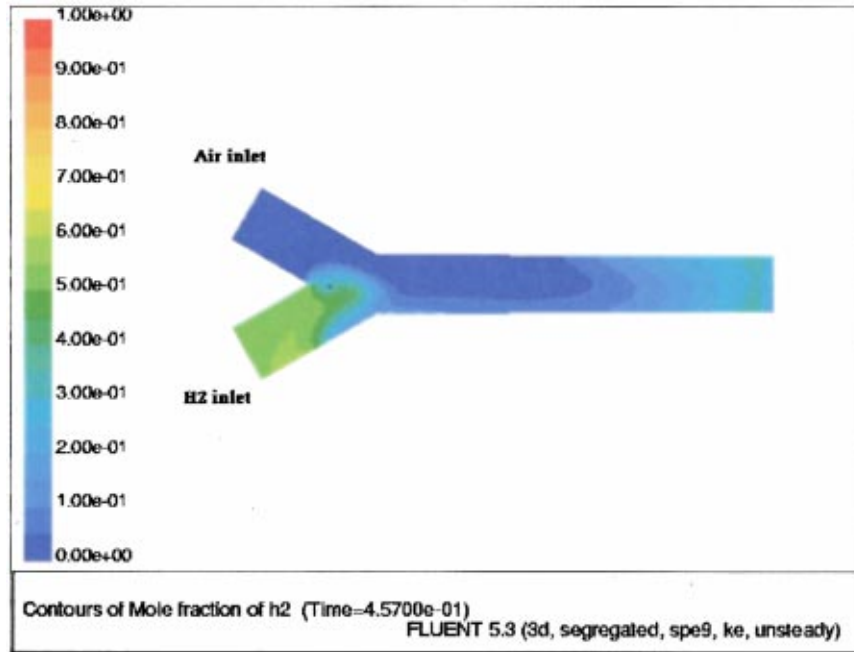


Fig. 4 Mole fraction of H₂ (sequential injection, third cycle, at IVC, λ=2)

$$P_{i,norm} = P_i \times \frac{101325}{p_{atm}} \times \sqrt{\frac{273 + T_{atm}}{273 + 20}}$$

Efficiency. The indicated efficiency is calculated from the measured fuel consumption:

$$\eta_i = \frac{P_{i,norm} \times 22,4}{Q_{H_2} \times H_{H_2} \times 1000}$$

with H_{H_2} the lower heat of combustion (241.8×10^3 J/mole).

Air/Fuel Equivalence Ratio $\lambda (= 1/\phi)$. From the exhaust gas composition with a calibrated λ -sensor and from the measured air and fuel flows,

$$\lambda = \frac{\text{mass flow air}}{\text{mass flow } H_2 \times L_s} = \frac{\rho_{air} \times Q_{air}}{\rho_{H_2} \times Q_{H_2} \times L_s} = 0,418 \times \frac{Q_{air}}{Q_{H_2}}$$

(normal conditions for the densities and volume flows).

Indicated Power Output

Influence of the Inlet Geometry and the Start of Injection (SOI).

Figure 5 shows the indicated power output for the different junc-

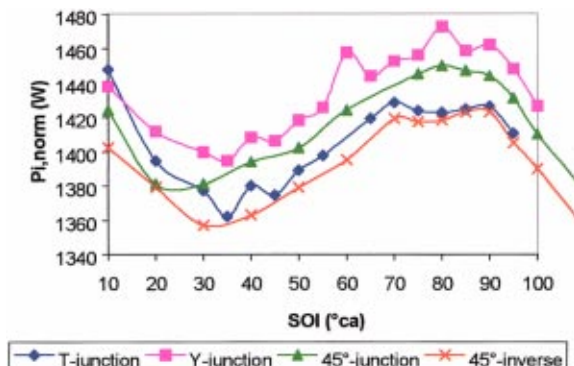


Fig. 5 Power output as a function of start of injection

tions as a function of the start of injection (in deg ca ATDC-gas exchange, for $\lambda=2$, IT=15 deg ca BTDC).

The Y-junction at a start of injection of 80 deg ca gives the highest output (and a minimum is reached at SOI=40 deg). The difference between the highest and lowest value is more than 10%. The importance of the start of injection can be seen in the air and fuel consumption in relation to the start of injection.

The air and fuel flows, as well as the pressure in the combustion chamber when the inlet valve closes, are maximum for the start of injection of 80 deg, and thus also the maximum cylinder pressure is the highest for this SOI, as can be seen in Fig. 6. This results in the highest volumetric efficiency (highest mass in the cylinder) and thus the highest power output. The explanation for this is the interaction between the injection stream of H₂ and the pressure waves in the intake duct (from the opening and closing of the inlet valve).

At the moment the inlet valve opens (18 deg ca ATDC) the cylinder pressure is somewhat lower than in the intake duct. The pressure in the intake pipe decreases and a pressure wave travels through the duct. If the injection starts when the inlet pressure

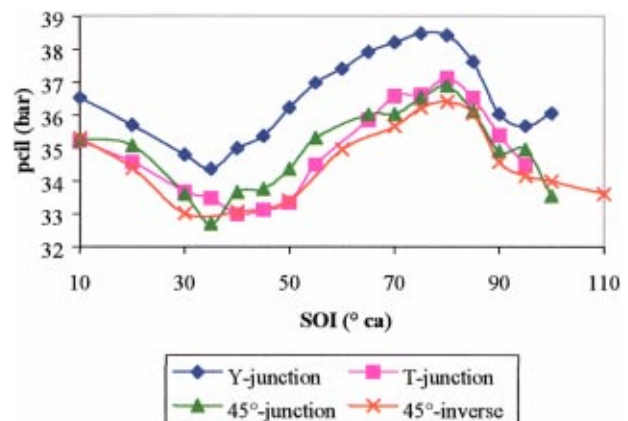


Fig. 6 Maximum cylinder pressure as a function of start of injection

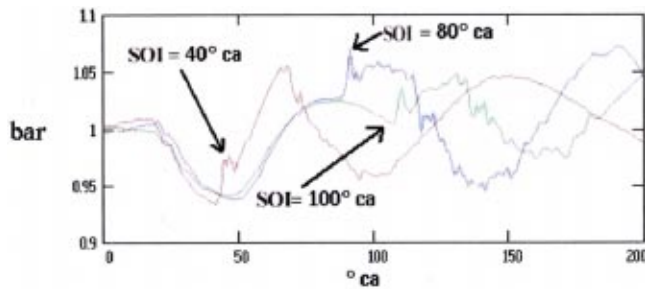


Fig. 7 Pressure development in the intake channel (at 8 cm from the inlet valve), for different SOI's

wave has a maximum value, the wave is strengthened and the pressure will increase. If the injection starts at a low pressure, the pressure wave will decrease in amplitude. This can be seen in Fig. 7 where the start of injection is optimal (80 deg ca), too early (40 deg ca) or too late (100 deg ca). The start of injection is seen by a sudden increase of the pressure signal. Not only the amplitude of the wave is influenced, but also the moment of the following pressure maximum is strongly changed. With the start of injection at 40 deg ca (lower power output) the maximum pressure is approximately at 150 deg ca, while for the start of injection of 80 deg ca (higher power output), the maximum pressure comes later. For a start of injection of 80 deg ca the maximum is also higher, the pressure still increases after 150 deg ca and at the moment the inlet valve closes there is a pressure of 1.1 bar in the cylinder. This results in a gain of 10% in the power output.

The influence of the junction on the power output is smaller than the start of injection, and all junctions have a maximum power output around SOI 80 deg (see Fig. 5.). The Y-junction has the highest power output and the 45 deg junction inverse has the lowest power output. In the latter the air flow (= highest flow) has to make the biggest bend in the junction, resulting in the highest pressure losses. Comparison of pressure measurements show (not given here) that for the Y-junction the pressure in the inlet pipe has a higher value than the cylinder pressure for a longer period and that the pressure difference is bigger than for the other junctions. Therefore the Y-junction gives the best filling for the engine.

Influence of the Air/Fuel Equivalence Ratio (λ) and the Ignition Timing (IT). Figure 8 shows the influence of the air/fuel equivalence ratio and the ignition timing on the indicated power output for two different SOI's (Y-junction). In the figure the ignition timing is regulated between 2 and 20 deg ca (BTDC). For an optimal ignition timing the power output changes linearly with the

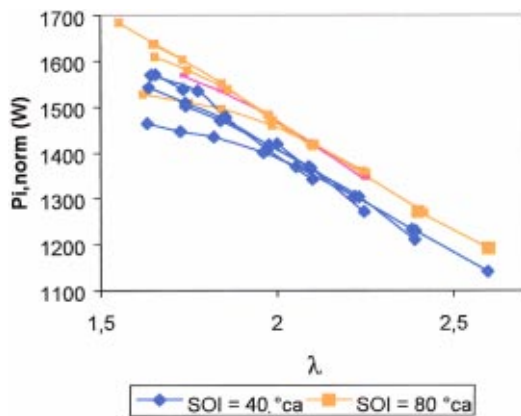


Fig. 8 Power output as a function of the air/fuel equivalence ratio, Y-junction (for different ignition timings—between 2 deg and 20 deg ca BTDC)

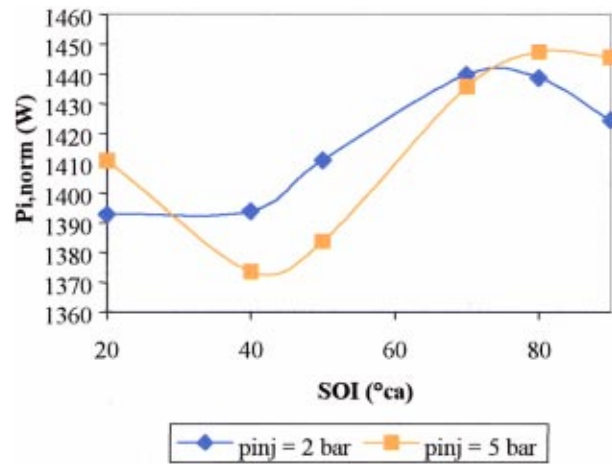


Fig. 9 Power output as a function of the start of injection for different injection pressures, Y-junction

air/fuel equivalence ratio (all tests at wide open throttle). But the optimal ignition timing strongly depends on the air/fuel equivalence ratio (ignition timing changing from 2 deg ca at $\lambda = 1.7$ to 20 deg ca at $\lambda = 2.5$). Again the influence of the start of injection is seen in the figure. It is also found (not all measurements given here) that for each λ -value the start of injection of 80 deg ca gives the highest power output.

Influence of the Injection Pressure (p_{inj}). All tests mentioned above are with an injection pressure of 3 bars. Figure 9 shows the influence of the injection pressure and the start of injection on the indicated power output for the 45-deg junction at $\lambda = 2$ and IT = 10 deg ca. Figure 9 shows that at a lower injection pressure the interaction between the injection and the inlet pressure waves decreases, which decreases the influence of the start of injection on the power output. The optimal start of injection occurs earlier for an injection pressure of 2 bars.

For a constant λ -value the injection duration will decrease by increasing the injection pressure. The relationship between the air/fuel equivalence ratio λ , the injection duration and injection pressure (given in bar) is shown in Fig. 10.

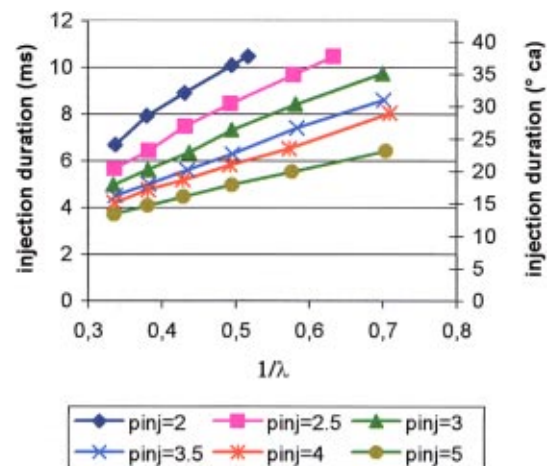


Fig. 10 Injection duration as a function of the air/fuel equivalence ratio for different injection pressures

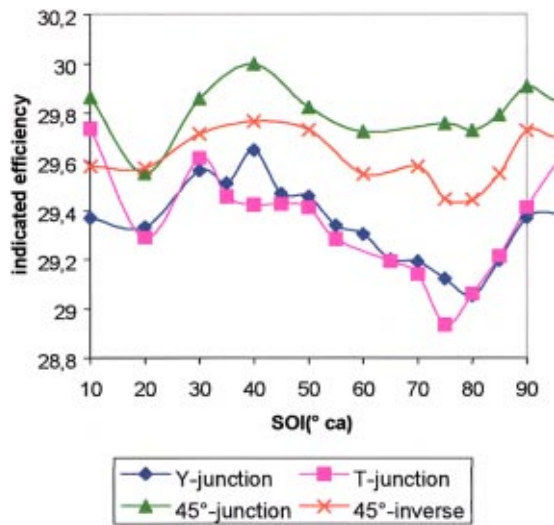


Fig. 11 Indicated efficiency as a function of the start of injection

Indicated Efficiency

Influence of the Inlet Geometry and the Start of Injection (SOI).

Figure 11 shows the indicated efficiency for the different junctions as a function of the start of injection (and for $\lambda=2$, $IT=15$ deg ca). The influence of the start of injection on the efficiency is less than on the power output. The 45-deg junction gives the best results for the efficiency. The highest efficiencies are now located around $SOI=40$ deg ca. A possible explanation is that for a start of injection of 40 deg ca the pressure wave is distorted, which gives an increase in the turbulence and a better mixing of the fuel and air.

With the CFD code FLUENT, the probable mixing process of the different junctions is calculated. A better mixing will result in a better combustion, thus a higher efficiency. Figure 12 shows the mole fraction of hydrogen at the end cross section of the different junctions (for a stationary condition, $8=2$).

The 45-deg junction shows the least difference in composition, as the best mixing and the highest efficiency can be expected (according to the real engine test). Also the 45-deg junction inverse shows a good mixing. With the two 45-deg junctions the smallest corner between fuel and air stream results in the best mixing.

Influence of the Air/Fuel Equivalence Ratio (λ) and the Ignition Timing (IT). Figure 13 gives the indicated efficiency for the different junctions as a function of the air/fuel equivalence ratio (and different ignition timings). Of course the highest efficiency is obtained for an optimized ignition timing (the same as to obtain the highest power output). The better efficiency for the 45-deg junction is shown again.

Influence of the Injection Pressure. The influence of the injection pressure on the efficiency is very small (less than 0.1% on total efficiency).

Backfire. In this study the attention was not given to the backfire problem. All tests were done at an air to fuel ratio $\lambda \geq 1.4$, and backfire never occurred. But it is well known that for rich mixtures (near stoichiometric), the hydrogen-air mixture in the intake manifold can explode before IVC.

In many studies, the causes of backfire have been reported to be excessive temperatures of large thermal mass combustion chamber surfaces such as the cylinder walls, valves, the piston or the

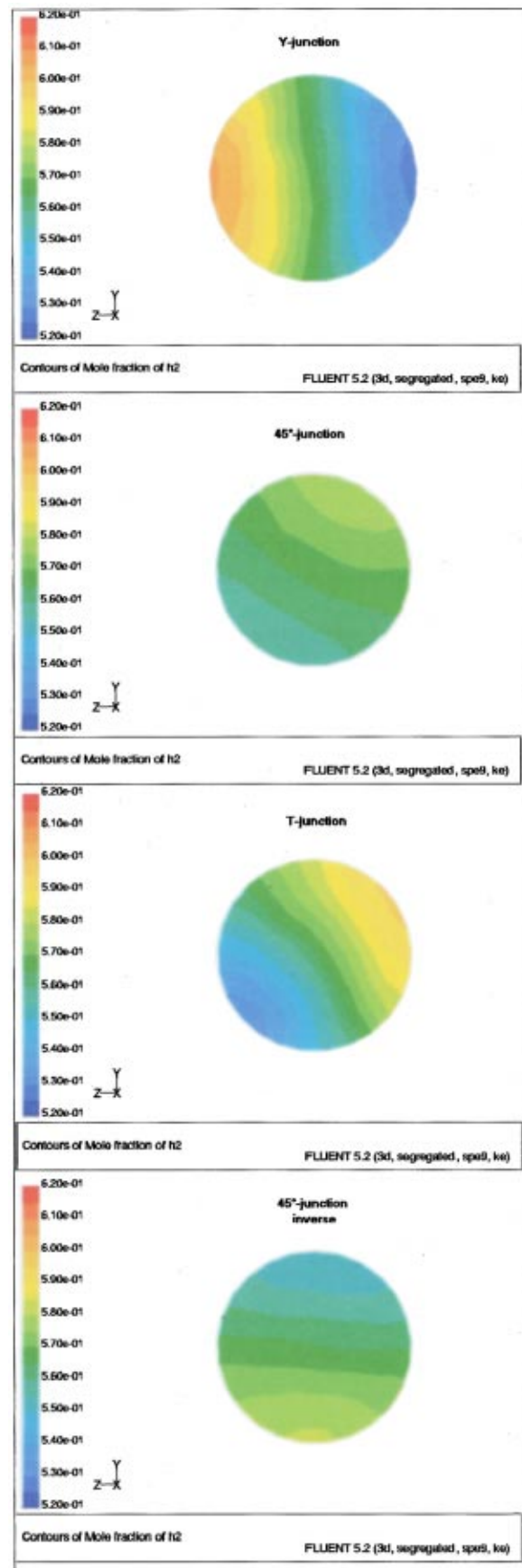


Fig. 12 CFD simulation: end cross section of different junctions (stationary condition)

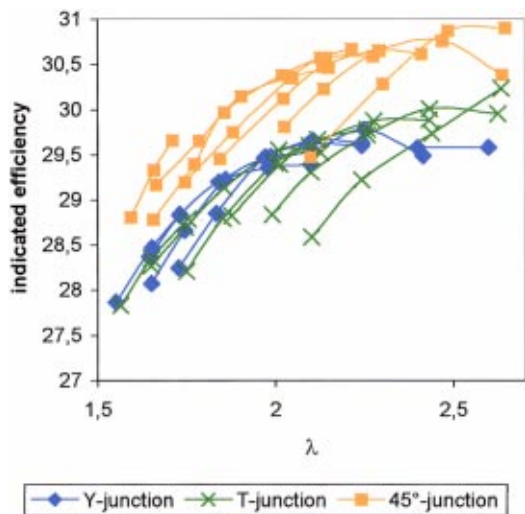


Fig. 13 Indicated efficiency as a function of the air/fuel equivalence ratio λ (for different ignition timings)

spark plug, or by low thermal mass sites with cyclically varying temperatures such as surface deposits, suspended pyrolysis products, or hot residual gases ([14]).

Timed fuel injection provides a means of delayed fuel delivery in order to pre-cool the small thermal mass sites and residual exhaust gases. In the described tests on the CFR engine there was no danger of backfire because of the small valve overlap of the engine, the air/fuel equivalence ratio was never at stoichiometric and mainly the retarded injection (relatively large injector for the speed of the engine).

Figure 10 shows that the maximum injection duration was 10 ms (= 36 deg ca). With an injection beginning at 80 deg ca ATDC (gas exchange) there is plenty of time to cool the cylinder gases and cylinder surfaces.

In a future study, the performance of the engine at stoichiometric conditions will be examined. But it is predictable that backfire-safe operation under these high load conditions is possible, because the injector can deliver enough fuel in a short time (the retarded injection can be optimized).

The same injectors are used for an 8-cylinder GM engine with a maximum engine speed of 4000 rpm. At high load conditions the injector has to be open nearly for the whole time the inlet valve is open. Retarded injection is not possible then.

Conclusions

A one-cylinder CFR engine is adapted for hydrogen fuel. The mixture formation is done with sequential injection of the hydrogen in the air inlet channel. Four different junctions of the injection position (fuel line) against the air flow are examined.

The influence of the start of injection, the injection duration (λ value at WOT), the injection pressure and the ignition timing on the indicated power output and efficiency are analyzed. With a CFD code (FLUENT) the mixing process is simulated mainly under stationary conditions.

The main conclusions of this study are

- The importance of the start of injection on the power output.
- The small influence of the injection pressure.
- The junction that gives the highest power output (Y-junction) is different from the junction that gives the highest efficiency (45-deg junction). A compromise may be taken.
- The well-known influence of the air/fuel equivalence ratio on the power output (at WOT) and of the ignition moment are confirmed.

More experimental results are given by Delborge and D'haveloose [13]. The tests are extended at the moment to another engine speed (900 rpm), different distances of the injector (junction) to the inlet valve and measurements of the exhaust gas composition (H_2 and NO_x mainly). After this, conclusions could be drawn for the optimization of different multicylinder engines with the same (multipoint) injection system.

Acknowledgments

The authors would like to thank the students Bart Delborge and Tom D'haveloose, for their contribution to this work, by conducting numerous experiments.

Nomenclature

- H = lower heat of combustion (J/mole)
 L_s = stoichiometric air/fuel ratio
 n = engine speed (rpm)
 p = pressure (Pa)
 P = power output (W)
 Q = volume flow (m^3/s)
 T = temperature ($^{\circ}C$)
 V = volume (m^3)
 W = work (J)
 ϕ = fuel/air equivalence ratio
 η = efficiency
 λ = air/fuel equivalence ratio
 ρ = density (kg/m^3)

Subscripts

- air = value concerning air
atm = atmospheric value
 H_2 = value concerning H_2
 i = indicated value
norm = normalized value

References

- [1] Tebelis, T., and Krepec, T., 1985, "A Concept of Electronically Controlled Hydrogen-Gas Injector for High Speed Compression Ignition Engine," *Proc. Hydrogen from Renewable Energy*, Cape Canaveral, FL, pp. 397–405.
- [2] Sorusbay, C., and Veziroglu, T. N., 1988, "Mixture Formation Techniques for Hydrogen-Fueled Internal Combustion Engines," *Proceedings of the 7th World Hydrogen Energy Conference*, Moscow, 3, pp. 1901–1921.
- [3] Green, C. J., and Wallace, J. S., 1989, "Electronically Actuated Injector for Gaseous Fuels," SAE Paper No. 89147.
- [4] Das, L. M., 1990, "Fuel Induction Techniques for a Hydrogen Operated Engine," *Int. J. Hydrogen Energy*, 15, pp. 823–842.
- [5] Furuhashi, S., 1995, "Problems of Forecasting the Future of Advanced Engines and Engine Characteristics of the Hydrogen Injection With LH_2 Tank and Pump," Calvin Rice Lecture, Apr. 23.
- [6] Lee, S. T., Yi, H. S., and Kim, E. S., 1995, "Combustion Characteristics of Intake Port Injection Type Hydrogen Fueled Engine," *Int. J. Hydrogen Energy*, 20, pp. 317–322.
- [7] Das, L. M., Gulati, R., and Gupta, P. K., 2000, "Performance Evaluation of a Hydrogen-Fueled Spark Ignition Engine Using Electronically Controlled Solenoid-Actuated Injection System," *Int. J. Hydrogen Energy*, 25, pp. 569–579.
- [8] Sierens, R., and Verhelst, S., 2000, "Experimental Study of a Hydrogen Fueled Engine," Paper No. 2000-ICE-285, ICE-Vol. 34-3, ASME, New York.
- [9] ASTM, 1964, *Manual for Rating Fuels by Motor and Research Methods*, Philadelphia, PA.
- [10] FLUENT Incorporated, 1998, *Fluent 5 User's Guide*, 1, till 4.
- [11] FLUENT Incorporated, 1998, *Fluent 5 Tutorial Guide*, 1, till 3.
- [12] FLUENT Incorporated, 1998, *Gambit I Tutorial Guide*.
- [13] Delborge, B., and D'haveloose, T., 2000, "Experimentele Studie en Optimalisatie van Waterstofinjectie in een CFR-Motor" (Experimental Study and Optimization of Hydrogen Injection in a CFR Engine—in Dutch), end of year thesis, Ghent University.
- [14] MacCarley, C. A., 1981, "A Study of Factors Influencing Thermally Induced Backfiring in Hydrogen Fueled Engines, and Methods for Backfire Control," *Proceedings 16th IECEC*, ASME, New York.

A Predictive Ignition Delay Correlation Under Steady-State and Transient Operation of a Direct Injection Diesel Engine

D. N. Assanis¹
Z. S. Filipi
S. B. Fiveland
M. Syrimis

W. E. Lay Automotive Laboratory,
University of Michigan,
1231 Beal Avenue,
Ann Arbor, MI 48109-2133

Available correlations for the ignition delay in pulsating, turbulent, two-phase, reacting mixtures found in a diesel engine often have limited predictive ability, especially under transient conditions. This study focuses on the development of an ignition delay correlation, based on engine data, which is suitable for predictions under both steady-state and transient conditions. Ignition delay measurements were taken on a heavy-duty diesel engine across the engine speed/load spectrum, under steady-state and transient operation. The dynamic start of injection was calculated by using a skip-fire technique to determine the dynamic needle lift pressure from a measured injection pressure profile. The dynamic start of combustion was determined from the second derivative of measured cylinder pressure. The inferred ignition delay measurements were correlated using a modified Arrhenius expression to account for variations in fuel/air composition during transients. The correlation has been compared against a number of available correlations under steady-state conditions. In addition, comparisons between measurements and predictions under transient conditions are made using the extended thermodynamic simulation framework of Assanis and Heywood. It is concluded that the proposed correlation provides better predictive capability under both steady-state and transient operation.

[DOI: 10.1115/1.1563238]

Introduction

Ignition delay in direct injection diesel engines is of great interest to researchers and engineers because of its direct impact on the intensity of heat release immediately following autoignition, as well as its indirect effect on engine noise and pollutant formation. The delay period is composed of a physical delay, encompassing atomization, vaporization, and mixing, coupled with a chemical delay, a result of pre-combustion reactions in the fuel/air mixture. The two time scales are not simply additive, but are occurring simultaneously. Detailed ignition models exist, e.g., Agarwal and Assanis [1], but due to the complexity of the in-cylinder physical and chemical processes, can only provide ignition delay trends for practical fields. Therefore, experiments and analytical studies are performed to enhance our understanding of the physical and chemical mechanisms in the pre-ignition phase, as well as to provide global correlations that capture the ignition event.

Numerous steady-state ignition delay correlations have been proposed based on experimental data in constant volume bombs, steady flow reactors, rapid compression machines and engines, e.g., Wolfer [2]; Stringer et al. [3]; Henein and Bolt [4]; Kadota et al. [5]; Hardenberg and Hase [6]; Watson et al. [7]; Spadaccini [8]; Ikegami et al. [9]; Spadaccini and TeVelde [10]; Hiroyasu et al. [11]; Itoh and Henein [12]; Callahan and Ryan [13]; and Fujimoto et al. [14]. Many of those correlations use an Arrhenius expression similar to that proposed by Wolfer [2], i.e.:

$$\tau_{id} = A p^{-n} \exp\left(\frac{E_a}{R_u T}\right) \quad (1)$$

¹To whom correspondence should be addressed.

Contributed by the Internal Combustion Engine Division of THE AMERICAN SOCIETY OF MECHANICAL ENGINEERS for publication in the JOURNAL OF ENGINEERING FOR GAS TURBINES AND POWER. Manuscript received by the ICE Division July 2000; final revision received by the ASME Headquarters Nov. 2002. Associate Editor: H. Nelson.

where p and T are pressure and temperature, E_a is activation energy, R_u is universal gas constant, and A , n are adjustable constants.

Pischinger et al. [15] noted that the inverse pressure-dependence in correlations of the form of Eq. (1) can be deduced from elementary reaction kinetics based on a single-stage reaction mechanism. In an attempt to further improve correlation with data, Kadota et al. [5] performed a fundamental study of fuel droplet autoignition in an elevated pressure/temperature environment and showed that ignition delay of hydrocarbon droplets can depend on the available oxygen content. Hiroyasu et al. [11] and Fujimoto et al. [14] also correlated combustion bomb data using a modified Arrhenius correlation that included an inverse function of equivalence ratio for diesel fuel and heavy oil, respectively. Lahiri et al. [16] modified Hiroyasu's correlation by replacing the equivalence ratio with the fuel-to-oxygen ratio, attempting to make it more suitable for studies of oxygen enriched combustion. Weisser et al. [17] considered low, intermediate, and high temperature chemistry in developing their ignition delay correlations intended for CFD applications; however, only the one for the intermediate temperature range included a dependency on the reciprocal of the equivalence ratio. Table 1 summarizes the empirical constants found in widely used correlations of form given by Eq. (1), used to calculate τ_{ID} in ms based on values for air pressure in bar and temperature in K.

When available steady-state correlations are applied to the estimation of ignition delay in direct-injection diesel engines, their predictiveness often proves to be rather limited. The most obvious reason is the fact that correlations are often applied outside the pressure/temperature range of their validity. Discrepancies can also be attributed to the fact that correlations developed in constant volume bombs cannot capture the dynamic variation in pressure and temperature during the delay period in real engine chambers. Furthermore, correlations that were developed for premixed environments (e.g., Spadaccini [8] and Spadaccini and TeVelde [10]) cannot account for the physical delay period that is present

Table 1 Summary of empirical constants employed by widely used ignition delay correlations

Correlation	Test Apparatus	Fuel	A	n	Ea/Ru
Wolfer	C.V. bomb	Cetane No.>50	0.44	1.19	4650
Kadota	single droplet	n-dodecane	6.58	0.52	4400
Spadaccini	steady flow	diesel No. 2	4.00×10^{-10}	1	20080
Stringer	steady flow	diesel, Cetane No.=49	0.0409	0.757	5473
Hiroyasu	C.V. bomb	diesel	$0.01 * \phi^{-1.04}$	2.5	6000
Fujimoto	C.V. bomb	Heavy oil, Cetane No.=52.5	0.134	1.06	5130
p<40 bar	-	-	0.136	0.615	4170
p>40	-	-	0.0081	1.14	7813
Pischinger	steady flow	diesel, Cetane No.=50	0.0081	1.14	7813
Watson	diesel engine	diesel	3.45	1.02	2100

in a DI diesel environment. Even the relatively few correlations that have been explicitly developed using diesel engine data under steady-state operating conditions (e.g., Watson et al. [7] and Hardenberg and Hase [6]), cannot track ignition delay under transients (Fiveland [18]). Their weakness is attributed to the fact that their functional form does not account for dependence on mixture quality, which varies dramatically during the turbocharger lag period.

The objective of our work is to develop an ignition delay correlation that is predictive under both steady-state and transient engine operating conditions. Our approach relies on the premise that ignition delay should be a function of pressure, temperature, and mixture composition during the ignition period as well as during the combustion process, an argument that is consistent with physical intuition and which can be deduced through approximate chemical kinetic considerations. The experimental techniques developed to measure reliably ignition delay under both steady-state and transient operating conditions are described first. Then, an Arrhenius expression that depends on pressure, temperature, and equivalence ratio is established based on our steady-state data, and subsequently compared against other available correlations. Finally, the predictive ability of the proposed correlation under transient conditions is explored. It will be shown that the proposed ignition delay correlation has enhanced potential for predicting ignition delay in modern, heavy-duty diesel engines under both steady-state and transient operation.

Experimental Setup

A modern, heavy-duty truck diesel engine has been setup in a computerized test cell in the Walter E. Lay Automotive Laboratory of the University of Michigan. The setup is capable of simultaneous measurements of engine system parameters, as well as cycle-resolved parameters in all cylinders during either steady-state or transient operation. In the studies reported in this work, emphasis is placed on exploring how fuel-air mixing and ignition delay during transients depart from standard, steady-state values.

The engine used in this study is a Detroit Diesel Series 60, 12.7 liter engine, commonly found in heavy-duty trucks. Engine specifications of the four-stroke, in-line, six-cylinder, turbocharged, intercooled, water-cooled, direct-injection diesel engine are listed in Table 2. An air-to-water intercooler with feedback control of intake air temperature was used in the test cell instead of the air-to-air unit found on the vehicle. The relatively quiescent combustion chamber employs a shallow "Mexican hat" bowl-in piston and very high injection pressures, delivered by unit injectors. The fuel injection timing and duration are electronically controlled. The pulse from the electronic control module energizes a solenoid that operates the spill valve on the fuel unit injector. As the fuel cam acts on the plunger while the spill valve remains closed, the fuel is pressurized and injection begins. Opening of the spill valve relieves the pressure and ends injection.

The diesel engine is coupled to a 500 hp motoring/600 hp absorbing electric dynamometer. To allow for transient capability, the dynamometer speed/load is controlled via a solid-state controller. The engine is fully instrumented for pressure, temperature, mass flow, rotational speed, torque, and exhaust composition mea-

surements. A "low speed" data-acquisition system is configured to record up to 120 channels as a function of time. A "high speed," Tektronix VXI-based system, capable of simultaneously acquiring 32 channels of data at up to 200 ks/second per channel, is dedicated to crank-angle resolved measurements. An optical shaft encoder provides an external trigger signal every 0.25 deg crank angle. The high-speed signals used in this study include cylinder pressure transducer signals, fuel injection pressure signals, and manifold pressures for precise pegging of cylinder pressure signals during transients.

Every cylinder in the engine is instrumented with a flush mounted, water-cooled, piezo-electric, Kistler 6067B pressure transducer. In order to measure the injection pressure and dynamic start of fuel injection, a fuel cam rocker arm is instrumented with a temperature-compensated 90-deg Rosette strain gage. This technique was chosen since the unit injector design makes internal instrumentation using a Hall effect sensor extremely difficult. The strain gage with its half-bridge circuit was mounted at the center location on the top side of the fuel rocker arm, as shown in Fig. 1. By measuring the strain gage voltage signal, and removing the component that stems from compressing the injector follower spring, the force on the plunger is obtained. For a known plunger diameter this directly yields the injection pressure. More details on the technique and the calibration procedure can be found in Filipi et al. [19] and Fiveland [18].

The LabVIEW programming environment has been utilized to control the data acquisition system and allow real time processing of raw signals. The additional post-processing routines for detection of the actual start of injection and combustion were developed in FORTRAN90.

Diagnostic Techniques

Experimental studies of ignition delay in direct injection diesel engines require accurate diagnostic techniques for detecting both the start of injection and start of combustion. In the work presented here, the dynamic start of injection is determined from the injection pressure profile and the needle opening pressure. The start of combustion is determined through mathematical analysis of the in-cylinder pressure trace. In addition, accurate measure-

Table 2 Engine specifications

Engine type	diesel, 4-stroke
Configuration	6-cylinder, in-line
Air intake	turbocharged, intercooled
Injector type	unit injector
Fuel type	diesel No. 2D
Fuel cetane #	40
Displacement	12.7 liter
Bore	13 cm
Stroke	16 cm
Con. rod. length	26.93 cm
Compression ratio	15
Rated power/speed	350 kW/2100 rpm

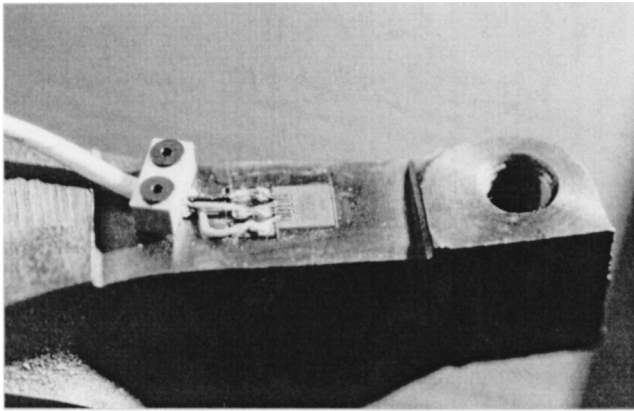


Fig. 1 Fuel injector rocker arm instrumented with strain gage

ment of the mass of air trapped in the cylinder per cycle, as well as the fuel mass injected per cycle during transients are very critical for our analysis. Techniques for inferring transient air and fuel flows based on measured intake manifold pressure traces and cyclic fuel injection profiles are reported by Assanis et al. [20].

Start of Fuel Injection. Determination of the dynamic start of injection (SOI) is inferred from measurement of the fuel injection pressure profile, obtained from processing of the rocker arm strain gage signals. As the fuel spill valve solenoid is energized and the valve closes, fuel pressure builds on the face of the needle. When this pressure buildup exceeds a threshold pressure required for needle opening, injection begins. While the injector manufacturer quotes an approximate value (345 bar with a tolerance band of 5%) for the needle lift pressure, a special *in situ* procedure had to be developed to determine accurately the actual threshold value for a given injector being exposed to the actual cylinder pressures.

The technique is based on the assessment that the fuel injection pressure will oscillate around the needle opening pressure when the engine is operated in a skip fire mode. In other words, the fuel controller is set exactly at the limit between motoring and firing operation. Figure 2 shows the peak cylinder pressures of 300 cycles during skip firing operation at 1800 rpm. Indeed, while the majority of the cycles are motored, there are intermittent firings indicated by 5–7 bar higher peak pressures. It is clear that in those firing cycles, the injection pressure was just high enough to overcome the spring force and lift the needle. Examination of fuel injection pressures versus in-cylinder peak pressures allows the

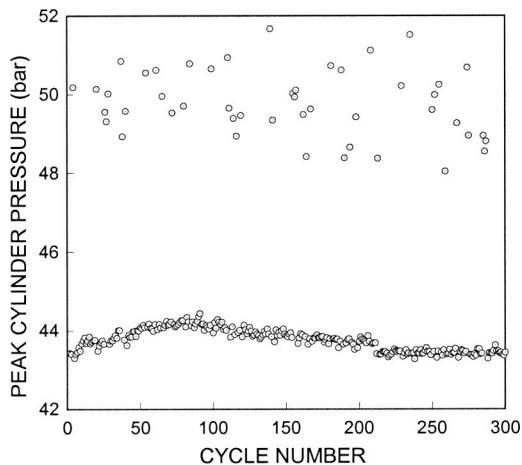


Fig. 2 Peak cylinder pressures measured during a series of “skip-fire” tests

identification of that threshold value of the injection pressure that separates cycles that did not receive any fuel from the firing cycles. This method was applied across the range of engine speeds, i.e., between 900 and 2100 rpm. Correlating fuel injection and peak cylinder pressures from 300 cycles for multiple operating points yielded an average value of 330 bar for the needle opening pressure for the given injector. Detection of the dynamic SOI then becomes only a matter of determining the crank angle corresponding to 330 bar on the fuel injection pressure profile of the cycle being analyzed.

Start of Combustion. Selection of a proper ignition criterion is probably the most controversial issue of ignition study [21]. Criteria that can be used to quantify the start of combustion (SOC) in diesel engines include the abrupt change in cylinder pressure gradient, or other pressure-based diagnostics; the light emission detected by a photocell; the temperature rise due to combustion; the combustion of a certain mass of fuel; and the change of slope in the heat release profile [4,22,23]. Of the techniques listed above, the pressure-based ones have been shown to be more reliable than the light emission technique. In particular, Heywood [23] indicates that a pressure change is often detected before the luminosity detector has noted the appearance of a flame.

For our work, a criterion is needed that is accurate and yet robust in order to allow automatic evaluation of SOC during post-processing of sets of data obtained for a large number of cycles. Given our objective, techniques that have been used to automatically characterize knock in a spark ignition engine are especially attractive due to its similarity to autoignition in a diesel engine. Barton et al. [24] tried to quantify knock as a function of the rate of pressure change. This makes physical sense, but the application presents several problems. One problem that this technique presents is that it is difficult to choose a characteristic magnitude of the pressure derivative over the full engine operating range. In other words, the criterion is load dependent and could introduce error in an automatic detection algorithm applied to transient operation.

Ando et al. [25] showed that “autoignition indices” derived from knocking heat release results correlated well with the intensity of knock. Their indices included the maximum and minimum slope of the net heat release rate, thus involving second-order derivatives of pressure with respect to crank-angle. The points of maximum and minimum slope are, consequently, the points of maximum and minimum acceleration of the net heat release rate, i.e., the combustion process. The maximum slope occurs slightly after the onset of autoignition, while the minimum slope occurs slightly before the end of the autoignition process. Syrimis et al. [26] showed that the higher the intensity of knock, i.e., the larger the amount of fuel that autoignites, the higher the maximum acceleration of the net heat release rate due to autoignition, and thus the higher the maximum slope of the net heat release rate curve.

Alternatively, Checkel and Dale [27] proposed that the third derivative be used as a knock indicator. Even though this gives a very clear indication that knock has occurred, their procedure does not provide an accurate indication of the timing. Syrimis et al. [26] have investigated all available options and have concluded that the second derivative of pressure actually always peaks at, or only slightly after the point of autoignition, in agreement with the work of Ando et al. [25]. The subsequent fluctuations of this signal after the initial peak quickly subside, thus making diagnostics based on the second derivative very reliable. An example of the results obtained when this technique was applied to the DDC diesel engine is presented in Fig. 3. The peak value of the second derivative of pressure clearly coincides with the sudden increase of cylinder pressure due to ignition. Furthermore, while the magnitude of the $dp/d\theta$ signal varies significantly with load and speed, the second derivative has proven to be much more consistent. It is for this reason that the second derivative of a cylinder pressure has been chosen for detection of the ignition point. The technique is robust, and it was found that it can be successfully applied even

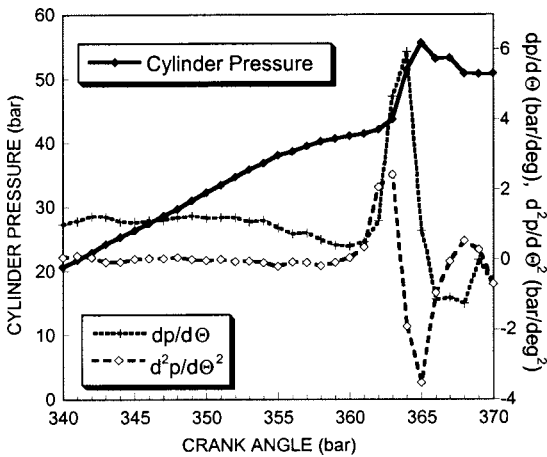


Fig. 3 Using the second derivative of the cylinder pressure to detect ignition

to unfiltered pressure signals. The algorithm for evaluating the position of the peak signal is incorporated in the post-processing diagnostic code.

Ignition Delay Measurements Under Steady-State Conditions

Using the above diagnostic techniques for identifying SOC and SOI, ignition delay was determined under a wide range of steady-state operating conditions from 5% to 100% load, and from 900 rpm to 2100 rpm. This was done in order to ensure that our experimental procedure yielded results that exhibited proper ignition delay trends and reasonable magnitudes. Furthermore, acquiring a comprehensive set of steady-state data is a prerequisite for developing an ignition delay correlation suitable for predictions under both steady-state as well as transient conditions.

The acquired ignition delay data over the load spectrum is shown in Fig. 4. Clearly, ignition delay was found to decrease as engine load increases, in accordance with published work [28]. The observed trend is a result of the effect that increasing injection pressures, in-cylinder pressures, and mean gas temperatures have on atomization, evaporation, and chemical reaction rates. Note that the higher thermodynamic state of the gas at the end of compression stroke is the consequence of increased boost pressure provided by the turbocharger at higher loads. Points on the graph represent the ensemble averaged values over 300 consecutive

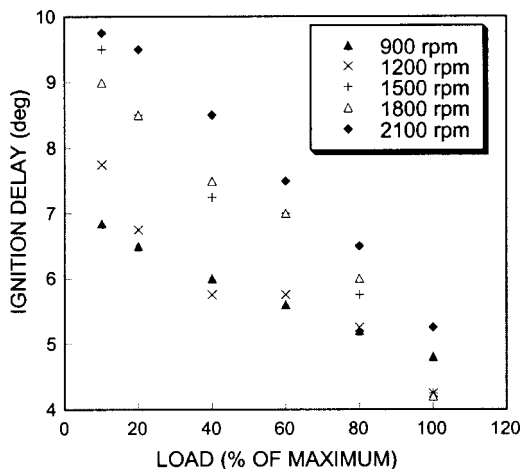


Fig. 4 Ignition delay measured at steady-state operating conditions

cycles. The coefficient of variance (COV) of the fuel injection pressure data was below 0.5%, the maximum variations of cylinder pressure at ignition were typically 0.3–0.6% [20], while the ignition delay COV was on the order of 2%. It should be noted that the ignition delay error band encompasses the variation of the raw rocker arm signal, the cylinder pressure signal, as well as the numerical routines to find the SOI and SOC indices. The low variability of the ignition delay data, and their consistency with other steady-state measurements reported in the literature made them a valid set for regression analysis. The functional form and empirical constants of the resulting ignition delay correlation, applicable of modern heavy-duty direct-injection diesel engines, are presented in the next section.

Ignition Delay Correlation

In accordance with the work of Kadota et al. [5], Hiroyasu et al. [11], Cowell and Liefebre [29], and Xia and Flanagan [30], our work sets out to correlate ignition delay due to physical and chemical processes with pressure, temperature, and equivalence ratio. It should be emphasized that the chemical reaction rate processes leading to the autoignition of diesel fuel are composed of many reactions that are not yet fully defined. Consequently, this work uses global reaction rate theory to find the functional dependence of the ignition delay correlation. The complex combustion event in a DI diesel engine is assumed to be described by a single-step mechanism with a reaction rate (RR) given by Cowell and Lefebvre [29] as

$$RR = \eta_{\text{coll}} \prod_{i=1}^N (C_{M_i})^{v_i} \exp\left(\frac{-E_a}{R_u T}\right) \quad (2)$$

where η_{coll} is the collision efficiency, C_M are global concentrations, and the exponential term is the Boltzmann factor, which specifies the fraction of collisions that have an energy greater than the activation energy [21].

Through manipulation of Eq. (2) involving the equation of state for an ideal gas, the definition of fuel-air equivalence ratio, and order of magnitude scaling, the forward reaction rate for the global, one-step fuel/air reaction can be rewritten to yield the dependence of reaction rate on pressure, temperature, and equivalence ratio (ϕ). Hence, the ignition delay, in ms, which is the inverse of the reaction rate of the global one-step mechanism can be cast in the following form:

$$\tau_{ID} = A \phi^{-k} P^{-n} \exp\left(\frac{E_a}{R_u T}\right) \quad (3)$$

Note that the functional dependence of pressure and temperature are consistent with Wolfer's expression [2]. By including the global equivalence ratio dependence, the authors are not assuming that the local fuel-air mixture in a DI diesel engine is perfectly mixed. Instead, it is postulated that the global equivalence ratio is a measure of the probability of finding local pockets of fuel-air mixture within flammability limits for autoignition sites to be promoted. Several parallels exist between our analysis and that conceptualized by Xia and Flanagan [30], the primary one being consideration of single-step kinetics to describe the pre-flame reaction rate.

The adjustable constants in Eq. (3) were fit in order to minimize the least-square error between measured and correlated ignition delay, as well as ensure that the latter would tend to zero at extremely high load. The ignition delay data were correlated as a function of the overall equivalence ratio and the mean pressure and temperature over the ignition delay interval. Use of the mean value over the ignition delay interval is consistent with Watson et al. [7]. Furthermore, it was felt that since the activation energy is dependent on the intensity of a molecular collision, it could not be used as a regression variable. Instead it was held constant, at a value equal to that given by Watson et al. [7] for a diesel fuel D2 mixed with air, i.e., $E_a/R_u = 2100$. The resulting expression is

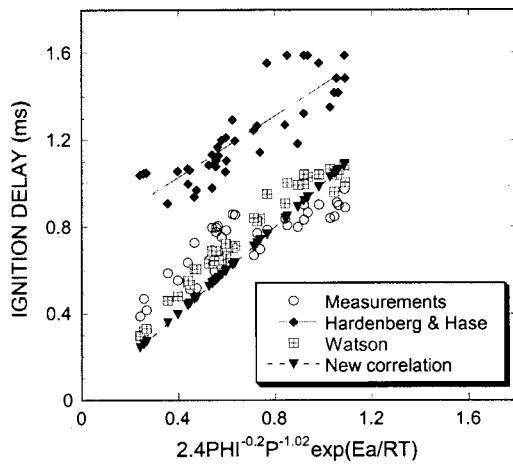


Fig. 5 Comparison of different ignition delay correlations applied to steady state operating points of the DDC series 60 diesel engine

$$\tau_{ID} = 2.4\phi^{-0.2}\bar{P}^{-1.02}\exp\left(\frac{E_a}{R_u\bar{T}}\right) \quad (4)$$

where pressure (P) and temperature (T) are measured in units of bar and Kelvin, respectively, and ignition delay is calculated in ms. It should be noted that the best fit produced the exponential pressure dependence of 1.02 found in the Watson correlation.

In order to validate and explore the potential of the proposed correlation, its predictions have been compared against those of selected, widely used empirical correlations (see also Table 1). Assanis and Heywood [31] previously assessed many of the available correlations, including [2,6,7,8,10]. Consistent with their findings, our proposed correlation was compared to the Watson et al. [7] correlation and the Hardenberg and Hase [6] correlation. These two correlations were specifically developed using diesel engine data, as opposed to others that were developed from measurements in combustion bombs and steady flow reactors (see also Table 1). Recall that the Watson correlation is described by Eq. (1). The Hardenberg and Hase correlation has an exponential temperature dependence, but is also a function of mean piston speed, and uses top dead center conditions to evaluate the reaction rates. Since the two alternative correlations have a different functional form than the proposed one, measured data and ignition delay predictions from each expression are plotted versus the ignition delay predicted from our expression in Fig. 5. The experimental data appear scattered around the line of our correlation, with the latter underpredicting shorter ignition delays, and overpredicting longer ones. The Watson correlation appears to predict values with similar accuracy to our correlation. Its main difference compared to our correlation is that it underpredicts shorter ignition delays to a lesser extent, but at the same time it overpredicts longer delays by a wider margin. On the other hand, the Hardenberg and Hase correlation consistently overpredicts the ignition delay. This is attributed to reduced physical delays found in newer engines, coupled with the fact that the chemical delay is reduced at higher loads.

In summary, both the Watson correlation and our proposed correlation capture satisfactorily ignition delay trends and magnitudes, under a wide range of steady-state conditions in a modern turbocharged direct-injection engine. Note, however, that, unlike Watson's correlation, our pre-exponential coefficient in Eq. (4) is a function of equivalence ratio, as illustrated in Fig. 6. For our tests, the coefficient ranges from 2.6 to 3.8, as opposed to the Watson correlation where it is fixed at 3.45 over all operating points. Interestingly, constant value used by Watson would translate into $\phi=0.116$ which might be close to the actual mean fuel/

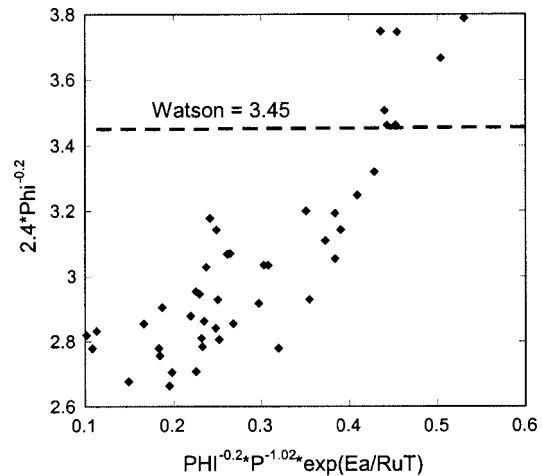


Fig. 6 Values of the dynamic coefficient that includes the dependency on the fuel air equivalence ratio under various steady-state operating conditions

air equivalence during the ignition delay period. Nevertheless, keeping this value constant fails to capture variations of local mixture composition as well as other factors indirectly affecting intensity of molecular collisions. The introduction of the overall equivalence ratio dependency makes the proposed correlation more dynamic, accounting for the ratio of fuel to air mass and its indirect effect on physical and chemical processes in the cylinder. Consequently, this has the potential to make the correlation more predictive during transients where conditions in the cylinder are often very different from steady state operation. This hypothesis will be investigated in the next section.

Transient Measurements and Validation

Transient engine operation is a major contributor to pollutant information as well as acoustic noise, a result of the sluggish response of the air intake system, which is commonly termed the turbocharger lag period. During this period, part of the exhaust enthalpy is used to overcome inertia and accelerate the rotor, hence the lag in the increase of boost pressure delivered by the compressor. The result is lower cylinder trapped air per unit of fuel, which can lead to transient excursions of the equivalence ratio and the ignition delay. Our tests have also indicated significantly longer ignition delays and higher pressure gradients during the initial phase of load transients [18].

The ignition delay correlation that was developed using steady-state data explicitly involves a dependency on equivalence ratio. Hence, provided that instantaneous values of the equivalence ratio are known during a transient, the proposed correlation has the potential to be more predictive under transients than correlations of the type of Eq. (1). Thus, this section focuses on a comparison of predicted and measured values of ignition delay during elementary transients in order to validate the correlation. A transient diesel engine simulation is used to facilitate the comparison by providing instantaneous values of temperature, pressure, and equivalence ratio throughout the transient.

Transient Diesel Engine Simulation. The foundation of the diesel engine cylinder model used in this work is the physically based, thermodynamic, zero-dimensional model developed by Assanis and Heywood [31]. In the parent model, the in-cylinder contents are represented by one continuous medium, uniform in pressure, temperature, and described by one equivalence ratio. During the engine cycle, the cylinder control volume is open to transfers of mass, enthalpy, and energy in the form of heat and work flows. Each of the in-cylinder processes is represented by a blend of more fundamental and phenomenological models of turbulence,

heat transfer, and combustion. The ignition model consists of an empirical correlation for ignition delay, which is being evaluated using instantaneous values of cylinder temperature and pressure until the ignition delay period has elapsed, following the procedure of Livengood and Wu [32], i.e.,

$$\int_{t_s}^{t_s + \tau_{ID}} \frac{dt}{\tau_{ID}(t)} \approx 1.0. \quad (5)$$

The use of this equation accounts for the effects that a variable volume combustion chamber will have on state properties over the ignition delay interval. The code predictions have been validated against engine data for heavy-duty turbocharged diesel engines [31]. Filipi and Assanis [33] added engine dynamics to create a nonlinear transient single cylinder code. The latter was modified in this work so that it could accept time-dependent input data for the intake manifold pressure, exhaust manifold pressure, mass of fuel injected and injection timing. Thus, the code was able to fully reproduce the transient experiment. The simulation now becomes a “test bed” for various ignition delay correlations by providing very realistic operating conditions in the cylinder for every cycle included in the transient.

Testing Methodology. The analysis was performed using a step change in load transient at constant speed. This type of transient produces typical effects important for evaluating engine response, such as turbocharger lag and associated corrections of the fueling strategy. At the same time, it minimizes uncertainties in the evaluation of the time derivatives by fixing the mean angular velocity of the crankshaft during the cycle. Furthermore, by decoupling speed from this elementary transient, it was hoped that a fundamental insight could be obtained without worrying about decreased residence time for heat transfer processes at higher speeds. Instead, the speed range was covered by repeating the test at three engine speeds: 900, 1200, and 1500 rpm.

The test starts with the engine idling at the selected crankshaft speed. Then the engine load controller initiates a step change of the signal to maximum torque demand. With each passing cycle, the injection pulse width and thus the mass of fuel injected increase; in response, the manifold and cylinder pressures increase until the engine reaches the next level of quasi-steady operation. Figure 7(a) shows the time history of the inlet manifold pressures during a load transient at 1200 rpm. The turbocharger lag period is very evident, as it takes roughly 15 seconds to reach the next steady-state value. Based on this signal for the available air, the electronic fuel control unit will limit the fuel. Hence, the fueling rate and indicated mean effective pressure (IMEP) values follow the same trend with the inlet boost pressure, as shown in Fig. 7(b). Note that the fuel mass injected per cycle during the transient was determined based on measured cyclic injection profiles, as reported by Fiveland [18]. Similarly to the behavior at 1200 rpm, turbocharger lag was very significant at 1500 rpm. However, at 900 rpm, the lag was very short due to the fact that the final values of turbocharger speed and boost pressure are relatively low.

Validation Under Transient Conditions. Ignition delay values have been determined experimentally using dynamic SOI and SOC measurements on each of the cycles throughout the elementary transient. For the same conditions as in the experiment, the computer simulation was successively run using the proposed ignition delay correlation, as well as the correlation introduced by Watson et al. [7]. Recall that both correlations were equally capable of capturing ignition delay under steady-state conditions. The issue therefore becomes to assess their predictive ability under transient conditions. Hence, measured and predicted ignition delays are compared for each of the transient tests in Fig. 8.

Results for the 900 rpm transient are presented in Fig. 8(a). Both correlations overpredict ignition delay very early into the transient. However, the proposed correlation quickly catches up with the experimental values, and eventually stabilizes after three

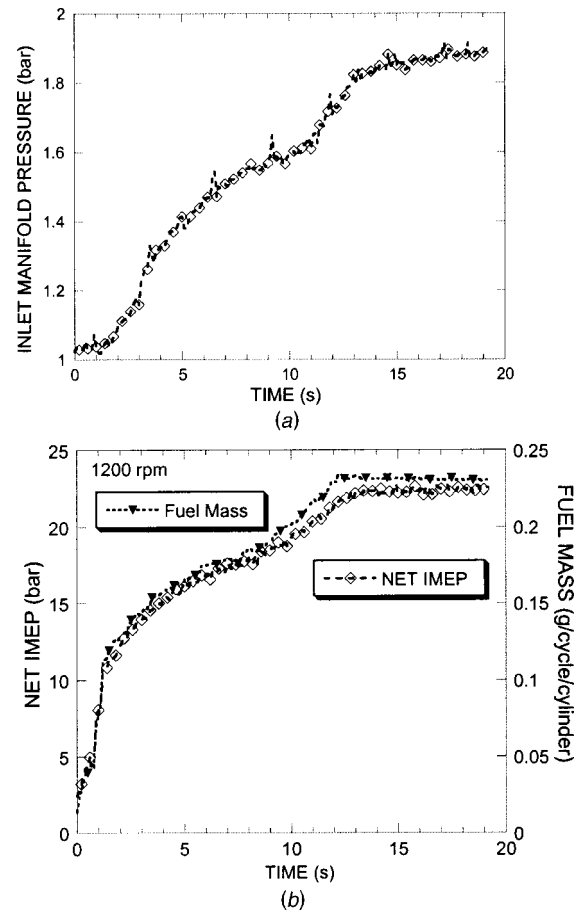


Fig. 7 Response of (a) boost pressure history and (b) fuel mass injected per cycle and net indicated mean effective pressure during a 0–100% load transient at 1200 rpm

sec at values somewhat smaller than, but close to the measured ones. In contrast, Watson’s correlation indicates an initial transient overshoot (after one sec), and eventually stabilizes at values higher (by approximately one degree) than the measured ignition delay. It should be noted that the period where transient effects are dominant is shorter than that at higher speeds (see Figs. 8(b) and 8(c)), since the variations of conditions in external engine components are the least dramatic of the three test runs.

Figure 8(b) shows the results at 1200 rpm. Initially, the measured ignition delay is somewhat higher than at 900 rpm (7 deg versus 6 deg). The truly transient conditions last longer, and a full load steady-state value of 3.5 deg of ignition delay is reached after 12 sec. The agreement between the proposed correlation and measurements is excellent, both in magnitude and trend. In contrast, Watson’s model is in agreement with measurements only at the initial steady state, while for the remainder of the test it consistently overpredicts ignition delay by one degree.

The 1500 rpm load transient seems to illustrate transient effects on ignition delay in the most explicit way (see Fig. 8(c)). Measurements once again show decreasing values of ignition delay as the result of the step increase of the engine load signal and gradual increase of the amount of fuel injected, as determined by the boost pressure history and controller calibration. Predictions obtained with the new correlation follow measurements very closely. In contrast, results calculated using Watson’s expression depart from measurements about two sec into the transient and from that point on continue to display a tendency to overpredict the ignition delay. Closer examination of curves given in Fig. 8(c) shows greatest departures of predictions obtained with Watson’s model be-

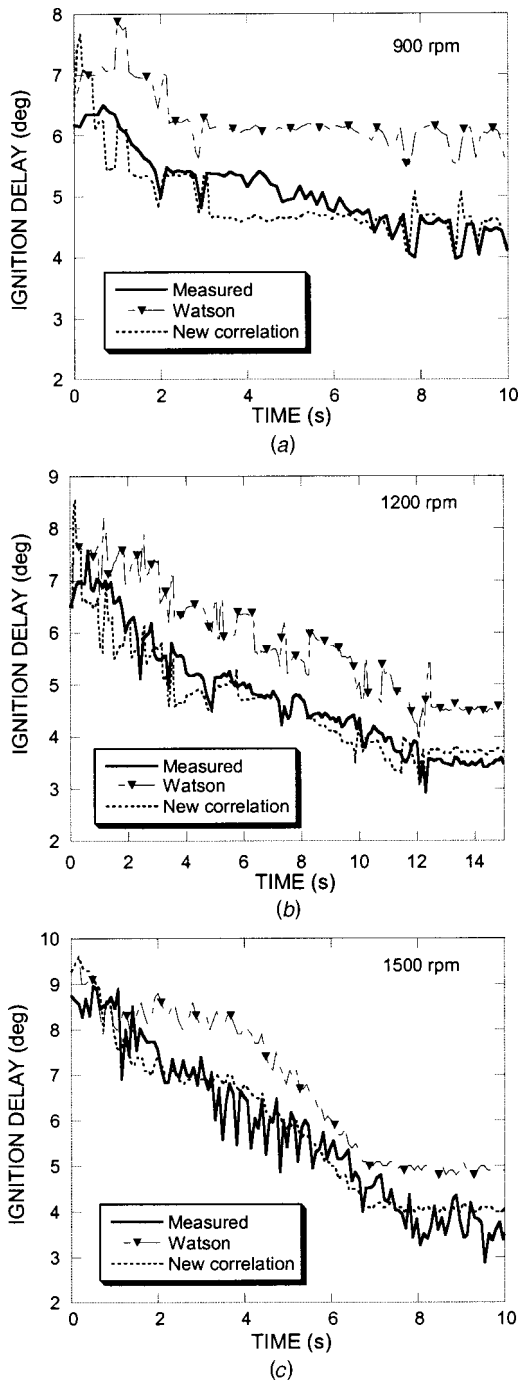


Fig. 8 Comparison of measured and predicted ignition delay histories during a 0–100% load transient at (a) 900 rpm, (b) 1200 rpm, and (c) 1500 rpm

tween two and six sec into the transient. This “hump” is attributed to the fact that, as a result of turbocharger lag and fuel control strategy, important cycle parameters depart far outside of usual limits associated with steady-state operation. During this time interval, as the amount of fuel is increased, the injection timing is advanced very rapidly, as documented in [20], simultaneously with rich excursions of the fuel air ratio. Hence, it can be hypothesized that Watson’s model overpredicts the effect of lower air temperatures at injection, while improved predictiveness of the new correlation stems from its ability to indirectly account for variations in mixing associated with transient enrichment of cylinder charge.

Overall, the deficiencies of Watson’s model during transients are attributed to the role of dramatic variations of equivalence ratio during that period, which are not captured by equations of the type of Eq. (1). The new correlation proposed in Eq. (4) explicitly considers the equivalence ratio dependency, and thus does prove to be predictive under both steady-state conditions, as well as transients.

Conclusions

In this study, a correlation was developed for predicting ignition delay in a typical, modern, heavy-duty, turbocharged, intercooled, direct-injection diesel engine, operating under both steady-state and transient conditions. Cycle-resolved cylinder pressure and rocker arm strain traces were recorded and analyzed for 300 cycles, at a number of steady-state operating points covering a wide range of engine loads and speeds. The dynamic start of injection was calculated by using a skip-fire technique to determine the dynamic needle lift pressure from a measured injection pressure profile. The dynamic start of combustion was determined from the second derivative of measured cylinder pressure traces. At each condition, ignition delay was determined as the difference between SOC and SOI. Application of global reaction rate theory yielded a correlation for ignition delay exhibiting a functional dependence of ignition delay on equivalence ratio, pressure, and temperature in the cylinder. The correlation has been compared against the Watson et al. [7] and the Hardenberg and Hase [6] correlations under steady-state conditions. The comparison showed that, at steady-state, only the expression published by Watson [7] provides a similar degree of accuracy as the new correlation derived in this work.

In addition, comparisons between measurements and predictions under load transients at a number of speeds have been made using the extended thermodynamic simulation framework of Asanis and Heywood [31]. The proposed correlation demonstrated very good predictive capabilities, as the agreement between the simulated and measured ignition delay histories was extremely close throughout the duration of transients. In contrast, the Watson et al. model consistently overpredicted the length of the ignition delay under transient conditions, even though the initial steady-state values were coinciding with the predictions of the new model. The primary cause for this behavior is attributed to the excursions of the fuel-air ratio and other operating parameters from the corresponding steady-state values resulting from the turbocharger lag effect and the response of the fuel control system. The new correlation is able to capture these effects by explicitly considering the fuel-air equivalence ratio as a measure of the probability of finding local pockets of fuel-air mixture within flammability limits. It is therefore concluded that the new ignition delay correlation significantly improves the overall predictiveness of the transient diesel engine system simulation, thus making it a more reliable tool for both performance and control strategy studies.

Acknowledgments

The authors would like to acknowledge the technical and financial support of the Automotive Research Center (ARC) by the National Automotive Center (NAC) located within the U.S. Army Tank-Automotive Research, Development and Engineering Center (TARDEC) in Warren, MI. The ARC is a U.S. Army Center of Excellence for Automotive Research at the University of Michigan, currently in partnership with University of Alaska-Fairbanks, Clemson University, University of Iowa, Oakland University, University of Tennessee, Wayne State University, and University of Wisconsin-Madison. The contributions of Profs. Arvind Atreya and David Dowling, Mr. Steve Hoffman, Mr. Sam Homsy, and Mr. Kevin Morrison are gratefully acknowledged.

References

- [1] Agarwal, A., and Assanis, D. N., 1998, "Multi-Dimensional Modeling of Natural Gas Ignition Under Compression Ignition Conditions Using Detailed Chemistry," SAE Paper No. 980136.
- [2] Wolfer, H. H., 1938, "Ignition Lag in Diesel Engines," VDI-Forschungsheft 392, translated by Royal Aircraft Establishment, Aug. 1959, *Farnborough Library No. 358, UDC 621-436.047*.
- [3] Stringer, F. W., Clarke, A. E., and Clarke, J. S., 1969, "The Spontaneous Ignition of Hydrocarbon Fuels in a Flowing System," *Proc. Inst. Mech. Eng.*, **184**, Pt. 3J.
- [4] Henein, N. A., and Bolt, J. A., 1969, "Correlation of Air Charge Temperature and Ignition Delay for Several Fuels in a Diesel Engine," SAE Paper No. 690252.
- [5] Kadota, T., Hiroyasu, H., and Oya, H., 1976, "Spontaneous Ignition Delay of a Fuel Droplet in High Pressure High Temperature Gaseous Environments," *Bull. JSME*, **19**(130), Paper No. 536.46, pp. 437–445.
- [6] Hardenberg, H. O., and Hase, F. W., 1979, "An Empirical Formula for Computing the Pressure Rise Delay of a Fuel From Its Cetane Number and From the Relevant Parameters of Direct-Injection Diesel Engines," SAE Paper No. 790493.
- [7] Watson, N., Pilley, A. D., and Marzouk, M., 1980, "A Combustion Correlation for Diesel Engine Simulation," SAE Paper No. 800029.
- [8] Spadaccini, L. J., 1977, "Autoignition Characteristics of Hydrocarbon Fuels at Elevated Temperatures and Pressures," *J. Eng. Power*, **99**, pp. 83–87.
- [9] Ikegami, M., Miwi, K., and Inada, M., 1981, "A Study of Ignition and Combustion of a Diesel Spray by Means of a Rapid Compression Machine," *Bull. JSME*, **24**(195), pp. 1608–1615.
- [10] Spadaccini, L. J., and TeVelde, J. A., 1982, "Auto-ignition Characteristics of Aircraft-Type Fuel," *Combust. Flame*, **46**, pp. 283–300.
- [11] Hiroyasu, H., Kadota, T., and Arai, M., 1983, "Development and Use of a Spray Combustion Model to Predict Diesel Engine Efficiency and Pollutant Emission," *Bull. JSME*, **26**(24), pp. 569–575.
- [12] Itoh, Y., and Henein, N. A., 1997, "Determination of Ignition Delay in Diesel Engines From Constant Volume Vessels Data," *Proceedings of ASME-ICE Spring Technical Conference*, ASME, New York, ICE-Vol. 28-1, pp. 29–34.
- [13] Callahan, T. J., and Ryan, T. W., 1988, "Engine and Constant Volume Bomb Studies of Diesel Ignition and Combustion," SAE Paper No. 881626.
- [14] Fujimoto, H., Shimada, T., and Sato, G., 1979, "Study of Diesel Combustion in a Constant Volume Vessel," *Trans. Jpn. Soc. Mech. Eng.*, **45**(392), pp. 599–609.
- [15] Pischinger, F., Reuter, U., and Scheid, E., 1988, "Self-Ignition of Diesel Sprays and Its Dependence on Fuel Properties and Injection Parameters," *ASME J. Eng. Gas Turbines Power*, **110**, pp. 399–404.
- [16] Lahiri, D., Mehta, P., Poola, R., and Sekar, R., 1997, "Utilization of Oxygen-Enriched Air in Diesel Engines: Fundamental Considerations," Paper No. 97-ICE-72, New York.
- [17] Weisser, G., Tanner, F., and Boulouchos, K., 1998, "Modeling of Ignition and Early Flame Development With Respect to Large Diesel Engine Simulation," SAE Paper No. 981451.
- [18] Fiveland, S. B., 1999, "Development of Engine Measurement Techniques With Applications to Steady State and Transient Ignition Delay and Heat Release Analysis in a Direct-Injection Diesel Engine," Master's thesis, The University of Michigan.
- [19] Filipi, Z. S., Homys, S. C., Morrison, K. M., Hoffman, S. J., Dowling, D. R., and Assanis, D. N., 1997, "Strain Gauge Based Instrumentation for In-Situ Diesel Fuel Injection System Diagnostics," *Proceedings of 1997 ASEE Annual Conference*, Milwaukee, WI, American Society for Engineering Education, Washington, DC.
- [20] Assanis, D., Filipi, Z. S., Fiveland, S. B., and Syrimis, M., 2000, "A Methodology for Cycle-by-Cycle Transient Heat Release Analysis in a Turbocharged Direct Injection Diesel Engine," *SAE Special Publication Series Volume SP-1530*, SAE Paper No. 2000-01-1185.
- [21] Kuo, K. K., 1986, *Principles of Combustion*, John Wiley and Sons, New York.
- [22] Lyn, W. T., 1962, "Study of Burning Rate and Nature of Combustion in a Diesel Engine," *Proceedings of Ninth International Symposium on Combustion*, The Combustion Institute, Pittsburgh, PA, pp. 1069–1082.
- [23] Heywood, J. B., 1988, *Internal Combustion Engine Fundamentals*, McGraw-Hill, New York.
- [24] Barton, R. K., Lestz, S. S., and Duke, L. C., 1970, "Knock Intensity as a Function Rate of Pressure Change," SAE Paper No. 700061.
- [25] Ando, H., Takemura, J., and Koujina, E., 1989, "A Knock Anticipating Strategy Based on the Real-Time Combustion Mode Analysis," SAE Paper No. 890882.
- [26] Syrimis, M., Shigahara, K., and Assanis, D. N., 1996, "Correlation Between Knock Intensity and Heat Transfer Under Light and Heavy Knock Conditions in a Spark-Ignition Engine," SAE Paper No. 960495.
- [27] Checkel, M. D., and Dale, J. D., 1986, "Computerized Knock Detection From Engine Pressure Records," SAE Paper No. 860028.
- [28] Wong, C. L., and Steere, D. E., 1982, "The Effects of Diesel Fuel Properties and Engine Operating Conditions on Ignition Delay," SAE Paper No. 821231.
- [29] Cowell, L. H., and Lefebvre, A. H., 1986, "Influence of Pressure on Autoignition Characteristics of Gaseous Hydrocarbon-Air Mixtures," SAE Paper No. 860068.
- [30] Xia, Y. Q., and Flanagan, R. C., 1987, "Ignition Delay—A General Engine/Fuel Model," SAE Paper No. 870591.
- [31] Assanis, D. N., and Heywood, J. B., 1986, "Development and Use of Computer Simulation of the Turbocompounded Diesel System for Engine Performance and Component Heat Transfer Studies," SAE Paper No. 860329.
- [32] Livengood, C. J., and Wu, C. P., 1955, "Correlation of Autoignition Phenomena in Internal Combustion Engines and Rapid Compression Machines," *Proceedings of Fifth International Symposium on Combustion*, The Combustion Institute, Pittsburgh, PA, pp. 347–356.
- [33] Filipi, Z. S., and Assanis, D. N., 2001, "A Non-Linear, Transient, Single Cylinder Diesel Engine Simulation for Predictions of Instantaneous Engine Sound and Torque," *ASME J. Eng. Gas Turbines Power*, **123**, pp. 951–959.

Experimental and Analytical Examination of the Development of Inhomogeneities and Autoignition During Rapid Compression of Hydrogen-Oxygen-Argon Mixtures

K. Chen
G. A. Karim¹

Department of Mechanical and
Manufacturing Engineering,
University of Calgary,
Calgary, Alberta, T2N 1N4, Canada

H. C. Watson
Department of Mechanical and
Manufacturing Engineering,
University of Melbourne,
Parkville, Victoria 3052, Australia

The reliable prediction of the processes leading to autoignition during the rapid compression of an initially homogeneous mixture of fuel and air requires the coupled modeling of multidimensional fluid dynamics and heat transfer together with a sufficiently detailed description of the chemical kinetics of the oxidation reactions. To satisfy fully such requirements tends at present to be unmanageable. The paper describes an improvised approach that combines multidimensional fluid dynamics modeling (CFD KIVA-3) with derived variable effective global chemical kinetic data. These were generated through a fitting procedure of the corresponding results obtained while using a detailed chemical kinetic scheme; albeit with uniform properties, at constant volume and an initial state similar to that existing during the ignition delay. It is shown while using such an approach that spatially nonuniform properties develop rapidly within the initially homogeneous charge due to piston motion, heat transfer and any preignition energy release activity. This leads autoignition to take place first within the hottest region and a reaction front progresses at a finite rate to consume the rest of the mixture. The present contribution examines the compression ignition of hydrogen-oxygen mixtures in the presence of argon as a diluent. Validation of the predicted results is made using a range of corresponding experimental values obtained in a single-shot pneumatically driven rapid compression apparatus. It is to be shown that the simulation which indicates the build up of temperature gradients during the compression stroke, predicts earlier autoignition than that obtained with a single-zone simulation. Good agreement between predicted and experimental results is achieved, especially for lean and stoichiometric mixtures under high compression ratio conditions. The CFD-based simulation results are found to be closer to the corresponding experimental results than those obtained with an assumed reactive system of uniform properties and using detailed reaction kinetics.

[DOI: 10.1115/1.1560710]

Introduction

Hydrogen has been long considered a possible alternative fuel for engines that may supplement depleting petroleum-based fuels. Its clean-burning characteristics with the absence of carbon-based pollutants and the ability to generate it from water through the expenditure of energy via electrolysis provide incentives for continued research into the potential limitations to its utilization as a fuel in engine applications. Until the fuel cell technology matures sufficiently, the conventional internal combustion engine, whether in the form of spark-ignition or compression ignition remains largely unchallenged. An interim measure is to consider using hydrogen as a fuel in mobile and stationary applications to meet the requirement for very low emissions while maintaining high efficiencies. Hydrogen-fueled compression ignition engines, whether of the dual-fuel type (e.g., [1–3]), direct gas injection type (e.g., [4–7]), or motored autoigniting piston engines (commonly known as homogeneously charged compression ignition engines,

H.C.C.I.), (e.g., [8]), received relatively less investigation than the premixed hydrogen-fueled spark-ignited engine (e.g., [9–11]). One of the major problems that limits the performance of engines operating on hydrogen as a fuel is that of pre-ignition and knock, [12]. At compression ratios similar to those normally used in engines fueled with fossil fuels, the hydrogen engine usually tends to suffer from rough running, knock, and sometimes misfiring. Accordingly, there is a need to investigate further the autoignition and knock characteristics of diluted hydrogen-oxygen mixtures both experimentally and analytically under closely controlled and well-defined conditions that are not commonly available when using practical engines.

The familiar phenomenon of knock in engines is associated with the autoignition of the “end gas” region of the charge. It is usually very difficult to obtain the transient properties of the cylinder charge which are governed to varying degrees by many factors such as the compression of the end gas due to piston motion, flame propagation, heat transfer effects, and any energy release due to preignition reactions. These effects combine to make the accurate prediction of the onset of autoignition in fired engines both difficult and uncertain requiring often numerous simplifying and deleterious assumptions.

There are typically three approaches to estimate the end gas

¹To whom correspondence should be addressed.

Contributed by the Internal Combustion Engine Division of THE AMERICAN SOCIETY OF MECHANICAL ENGINEERS for publication in the ASME JOURNAL OF ENGINEERING FOR GAS TURBINES AND POWER. Manuscript received by the ICE Division, October 2000; final revision received by the ASME Headquarters, July 2001. Associate Editor: D. N. Assanis.

temperature for the prediction of the onset of autoignition and knock in an engine that assume: (i) homogeneous gas with uniform properties, (ii) homogeneous adiabatic core, and (iii) exothermic centers or hot spots formation. The homogeneous gas and adiabatic core temperature assumptions represent a rough approximation of the state of the end gas. They permit the end-gas temperature to be estimated using the known measured cylinder pressure data. These simple approaches permit sufficiently comprehensive chemical kinetic schemes to be incorporated into analytical models to describe in depth the preignition chemical reaction activity. For example, Lee and Hochgreb [13,14], employed the homogeneous core gas temperature assumption in a two-zone thermodynamic model with a detailed chemical kinetic mechanism to predict the autoignition of hydrogen-oxygen mixtures in a rapid compression machine. Their model predicted throughout an earlier onset of autoignition than when measured experimentally, indicating an overestimate of the end-gas temperature.

The formation of exothermic centers or hot spots within the end gas has been hypothesized to take place mainly by the nonuniformities in temperature within the end gas. Autoignition is then assumed to take place first at those distinct high temperature regions. Their existence has been supported indirectly by experiments (e.g., [15–19]) that indicated autoignition in fired engines seldom occurs uniformly throughout the end gas region but originates randomly at localized centers which may then merge. This concept cannot be used readily to model at present the autoignition processes in fired engines mainly because of the complex coupling between chemistry, gas dynamics, and transport processes (e.g., [20,21]). Therefore, practical analytical approaches for predicting the onset of autoignition incorporates inevitably some necessary simplifications. For example, Chen and Karim [22–25] described an approach that combines multidimensional fluid dynamics modeling (CFD KIVA-3) with variable effective global chemical kinetic data for the prediction of methane-air autoignition in a rapid compression apparatus and a motored engine. These kinetic data were derived while using a fitting procedure from corresponding results obtained from the application of a detailed chemical kinetic scheme to a similar system of uniform properties and constant volume conditions for an initial state similar to that existing in the engine during the ignition delay. The results of such an approach produced very good agreement with those of the comprehensive kinetic scheme but for a zero-dimensional simulation with uniform properties. It was shown also while simulating methane autoignition within an engine environment in the absence of the application of a spark (i.e., H.C.C.I.), that spatially nonuniform properties developed rapidly before autoignition, due to piston motion, heat transfer, and pre-ignition energy release activity. These processes can produce significant temperature and velocity gradients that increase in severity with the progress of compression and lead to autoignition taking place first within the hottest region. In the absence of a spark, a fast reaction front then progresses at a finite rate to consume very rapidly the rest of the charge.

The present investigation examines the autoignition of diluted hydrogen-oxygen mixtures and compares predicted values to corresponding experimental measurements obtained while using a pneumatically driven rapid compression-expansion apparatus that is more amenable to control and analysis than running engines. Argon was used as the diluent, mainly to effect autoignition of lean mixtures while employing moderately low compression ratios. By incorporating derived variable global chemical kinetic data for hydrogen pre-ignition reactions into the CFD modeling, the development during compression of charge thermal inhomogeneity was established. Corresponding results were also obtained for comparison purposes while using a single-zone approach with a detailed chemical kinetic scheme that assumes a homogeneous charge throughout. Comparison of these two sets of predicted re-

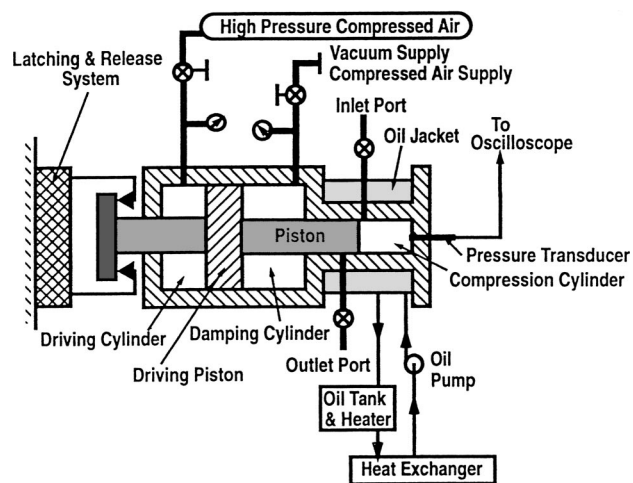


Fig. 1 Schematic diagram of the compression expansion machine with peripheral equipment

sults with the corresponding experimental values highlighted the important role of the development of charge nonuniformity in effecting autoignition within engines.

Experimental Approach

Rapid compression apparatus have been used (e.g., [26,27]) to study autoignition phenomena such as those taking place in the end gas of spark ignition engines as well as to examine chemical kinetic mechanisms for autoignition under similar conditions (e.g., [13,14]). A major motivation for the use of these devices is their providing of a relatively simple method for simulating the compression and expansion processes that take place in internal combustion engines but with a greater control over influencing parameters such as initial charge composition, temperature, pressure, and induction swirl. Charge leakage, contamination due to lubricants and residuals, and cylinder surface reaction activity are also amenable to closer control. Through the pneumatic control of piston motion, the stroke, clearance volume, and compression time can be altered to allow the compression ratio, piston speed, and density time to be varied independently.

In the present work, the autoignition following rapid compression of initially homogeneous hydrogen-oxygen-argon mixtures were conducted in a specially developed single-shot rapid compression-expansion apparatus involving a pneumatically driven piston in a flat-topped circular cylinder (50.8 mm bore, 342.9 mm maximum stroke). The apparatus was constructed to offer a continuously varying density system, with very close control over many of the experimental parameters (e.g., [22–24,28]). The apparatus permits a reactive mixture, once confined in a cylinder closed by a piston, to be compressed rapidly and then expanded. A flat-topped stainless steel piston with teflon rings was used to seal the unlubricated chrome-plated smooth test cylinder. Prior to compression, the charge usually was initially quiescent and homogeneous. The tests described in this contribution were conducted at the same compression time of 37.5 millisecond which corresponds to an equivalent engine speed of around 800 rev/min. The equivalence ratio of the test mixtures was varied widely from 0.15 to 2.50, with argon, having a high Cp/Cv, rather than nitrogen as the diluent to effect autoignition at lower compression ratios than required with nitrogen. A charge dilution ratio of 79:21 (argon:oxygen) by volume was used for all tests except those with a stoichiometric mixture when a higher dilution ratio of 90:10 was used to limit the resulting rates of pressure rise and peak cylinder pressures. A schematic diagram of the apparatus is shown in Fig. 1.

The cylinder pressure was measured using a precalibrated piezoelectric pressure transducer mounted centrally and flush with the flat and smooth cylinder head. The rapid piston displacement was determined employing a calibrated traversing potentiometer. The maximum cumulative error in pressure measurement was 1.1% and in piston displacement 1.8% at 30:1 compression ratio reducing to only 0.2% at the maximum piston displacement from the cylinder head. Initial mixture pressure, temperature, and composition were controlled to within an accuracy of 0.1%, 0.2%, and 1% respectively. In these tests, the mode of volume-time development effected pneumatically, may not be necessarily exactly the same as those in conventional engines where it is governed by the crank-connecting rod relationship.

Analytical Approach

Two different analytical approaches were employed to simulate the physical and chemical processes in the autoignition of $H_2/O_2/Ar$ mixtures. The first is a *single-zone approach* that incorporates detailed chemical kinetics but assumes a homogeneous mixture with uniform properties throughout, which is a key inadequacy of such an approach. The second (e.g., Chen and Karim [22–25]) is a *CFD approach* that combines multidimensional fluid dynamic modeling, (CFD, KIVA-3), [29], with derived variable effective global chemical kinetic data. This approach can indicate the development of dynamic and thermal inhomogeneities within the charge and represents more faithfully the physical and chemical processes that lead to autoignition.

The coupling of detailed chemical kinetics with multidimensional CFD simulation is a desirable objective that cannot be readily achieved at present. It has been restricted to applications where simplifications can be made such as when either the physical or chemical factors can be assumed to predominate. It is usual when using comprehensive multidimensional CFD simulation models to employ a highly simplified reaction kinetics that are often of the single-step Arrhenius form with fixed parameters to represent the oxidation reactions of the fuel. Such a simplified approach has been shown to be often inadequate and cannot predict accurately the reactions over the wide temperature and pressure ranges during compression that lead to autoignition. Chen and Karim [22–25] demonstrated that an assumed single-step oxidation reaction of the Arrhenius form may be employed in detailed CFD modeling procedures to represent mainly the thermal consequences of the chemical reaction. This is possible when the effective activation energy values are varied suitably with temperature so as to yield fuel depletion and energy release rates that are in full agreement with those obtained using sufficiently comprehensive chemical kinetic schemes but for a uniform property system.

A comprehensive kinetic scheme (e.g., [30]) was adopted. It consists, when excluding nitrogen-oxygen reactions, of 137 reaction steps and 32 chemical species. It was developed to describe the chemical reactions of common gaseous fuels, such as those in natural gases and contains 20 reaction steps relating to the oxidation of hydrogen for conditions relevant to engine operation. A homogeneous charge, single-zone model (e.g., [31]) incorporating the detailed kinetic scheme was employed to derive effective equivalent global kinetic data for the oxidation of hydrogen under adiabatic constant volume conditions with an initial temperature and pressure similar to those existing during the ignition delay in the cylinder during compression. A fitting procedure where the value of the activation energy E_a was adjusted continually with temperature while keeping the other Arrhenius kinetic coefficients unchanged to give a best overall match to the pressure and temperature histories predicted with the detailed chemical kinetic scheme, was employed. The resulting derived apparent activation energy values for hydrogen over a range of initial temperatures, are shown in Fig. 2. The corresponding values obtained for methane are also shown. These values are acknowledged to be artificial and have their limitations but they can offer an improved repre-

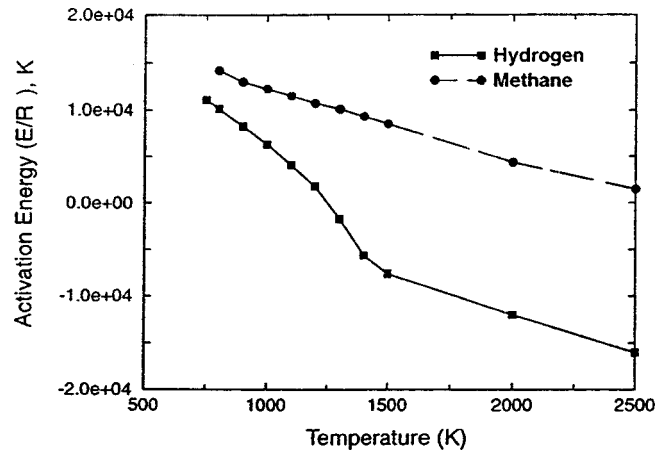


Fig. 2 Variations of the fitted activation energy value with initial temperature for stoichiometric H_2 -air and CH_4 -air mixtures in an adiabatic constant volume cylinder with initial pressure of 2.8 Mpa

sentation of the thermal consequences of the reaction activity than the fixed value approach and can be incorporated readily into the CFD KIVA-3 code. It can be noted that the derived activation energy values for hydrogen do not decrease linearly with temperature as for methane. The corresponding calculated times to autoignition, as shown in Fig. 3, are also not logarithmically linear with the inverse of temperature for hydrogen, which is consistent with the results of Lee and Hochgreb [13,14] and Lutz et al. [32]. These trends also indicate that it is not necessarily correct to assume a constant activation energy value for the oxidation reactions merely because of an apparent linear relationship between the logarithmic autoignition time and the inverse of absolute temperature. These derived variable effective activation energy values and the associated global kinetic parameters are strictly valid for representing the thermal consequences of the reactions only. Changes in pressure at constant temperatures had little effect on the values of the derived activation energy values.

The KIVA family of CFD codes (e.g., [29]) represents three-dimensional CFD software for chemically reactive, transient flows with fuel sprays developed originally for internal combustion engine applications. The numerics of KIVA include a combination of explicit and implicit solutions on a staggered mesh with moving

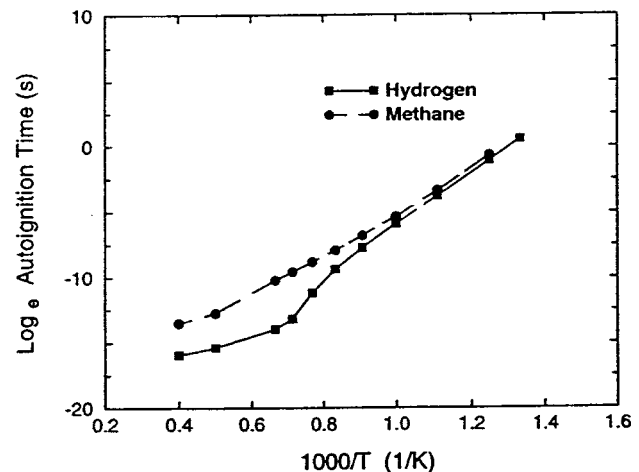


Fig. 3 Variations of the calculated logarithmic autoignition time with the inverse of initial temperature for stoichiometric H_2 -air and CH_4 -air mixtures in an adiabatic constant volume cylinder with initial pressure of 2.8 MPa

boundaries. For the present simulation studies, the code was suitably adopted to simulate the in-cylinder processes taking place within the confines of the rapid compression-expansion machine. The derived globally variable kinetic model for hydrogen described earlier was incorporated into the code. With the simple axisymmetric nature of the cylinder used, a two-dimensional simulation was chosen for computational economy. The cylindrical computational domain which was bounded by the cylinder head, walls and the piston face had a Cartesian two-dimensional computational grid whose spacing was uniform with 12 cells both for the radial and axial directions. The charge physical properties inside a computational cell were assumed to be homogeneous. However, every cell undergoes its own physical and chemical events throughout the simulation. The effects of turbulence were accounted for via the $k-\epsilon$ model. It was confirmed that the use of finer mesh would not have affected significantly the values of the computed results. The snapper in the code was turned off throughout the simulations so as to achieve a relatively higher spatial resolution when the piston approached top dead center (TDC). The wall shear stresses and heat transfer were accounted for (e.g., [33]). At the start of each simulation calculation, the cylindrical chamber contained initially a homogeneous, unless otherwise indicated, quiescent hydrogen-oxygen-argon mixture having known initial temperature, pressure and composition.

For comparative purposes, a single-zone model with the detailed chemical kinetic scheme (e.g., [31]) was also used to simulate the in-cylinder processes in the rapid compression-expansion machine. A heat transfer correlation derived from experimental observations in the same machine while using non-reactive mixtures, [22–24], were incorporated into the single-zone model to account for the apparent instantaneous heat flux at the gas wall interface.

Results and Discussion

An objective of the present experimental work was to validate the prediction of autoignition of hydrogen-oxygen mixtures within the confines of the closely controlled cylinder-moving piston assembly. At each fuel-oxidant mixture, the compression ratio was adjusted so that autoignition occurred within the first cycle. The experimental pressure and piston displacement-time records obtained were employed in the validation of the corresponding predicted values both when using the CFD and the single-zone approaches. Figure 4 shows the temporal variations of the experimentally measured cylinder pressure and the corresponding predicted mean values obtained when using both the CFD and single-zone approaches for stoichiometric $H_2/O_2/Ar$ mixtures with a very low O_2/Ar volumetric ratio of 0.10/0.90. Three relatively low compression ratios of 6.78, 6.82, and 7.38 were used. It can be seen that with a small increase in compression ratio, autoignition moved from the expansion stroke into the compression stroke with increased peak pressure and autoignition intensity. Both approaches predicted the experimental trends correctly except for the failure of the single-zone approach to predict autoignition occurrence at a compression ratio of 6.82 over the period examined. The CFD approach always predicted earlier autoignition. These differences result from the development of inhomogeneities within the charge due to piston motion, heat transfer and any preignition energy release activity.

Similarly, Fig. 5 shows the corresponding pressure-time development records for very lean mixtures with equivalence ratio of only 0.15 and an O_2/Ar volumetric ratio of 0.21/0.79 for three relatively low compression ratios of 6.49, 7.26, and 8.54. It can be seen that the onset of autoignition moved forward from the expansion stroke well into the compression stroke with the increase in compression ratio. Lower peak pressures and milder autoignition intensities were associated with these lean mixtures despite the lower dilution ratio employed than in the previous case. The CFD approach appeared again to predict earlier onset of autoignition than experimentally observed. Except for the highest compression

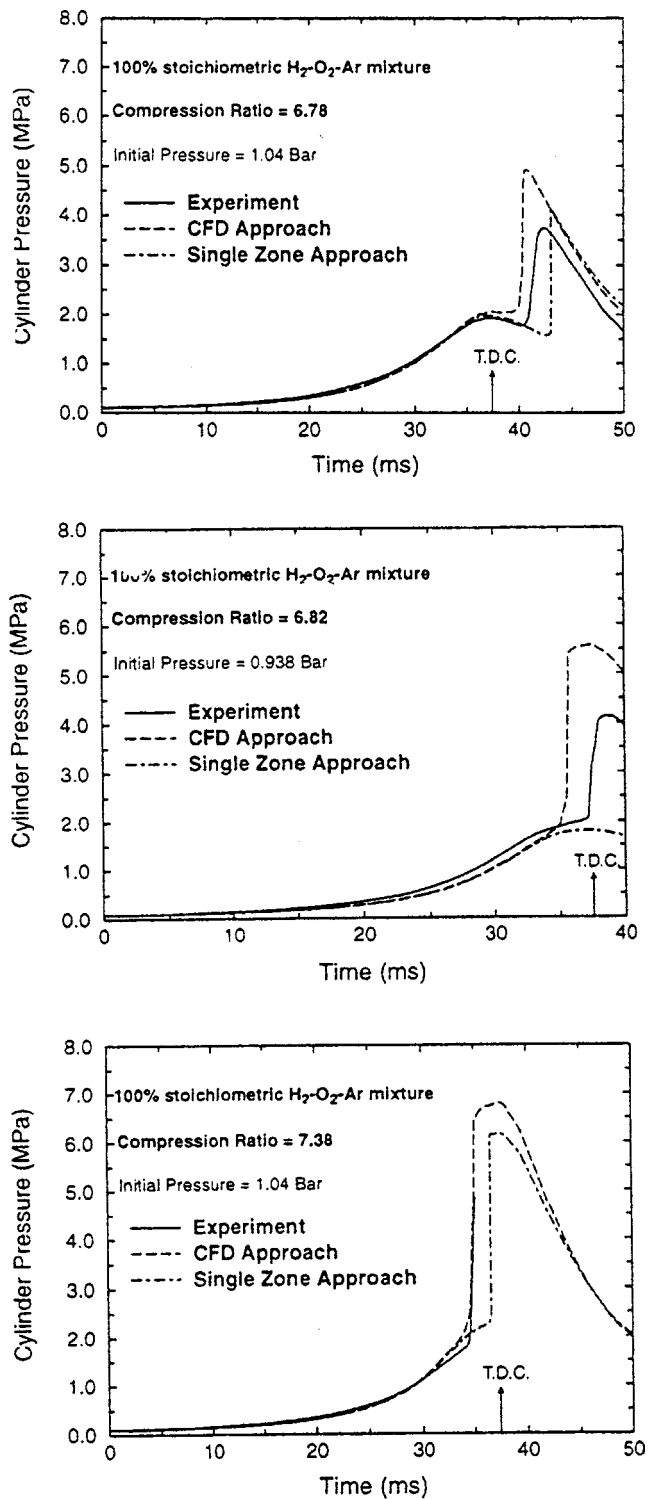


Fig. 4 Comparison between experimental and predicted pressure records using the CFD and single-zone approaches for a stoichiometric mixture and an O_2/Ar of 0.10/0.90

ratio employed of 8.54, the single-zone approach failed to predict autoignition altogether. This would indirectly indicate that for slow reactive lean mixtures, the temperature gradients developed within the cylinder charge can make all the difference between having autoignition or not.

Figure 6 shows similarly for rich mixtures with an equivalence ratio of 2.50 and an O_2/Ar volumetric ratio of 0.21/0.79 that significantly higher compression ratios of 9.93, 10.07, and 12.16

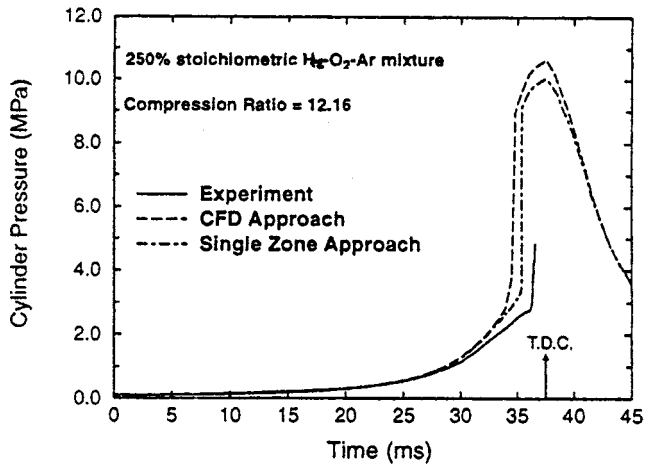
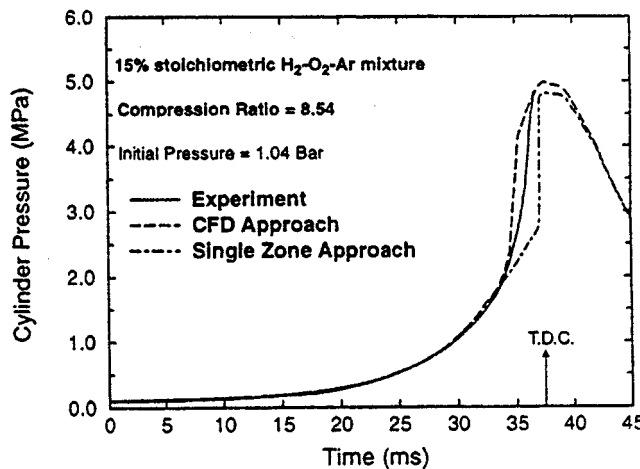
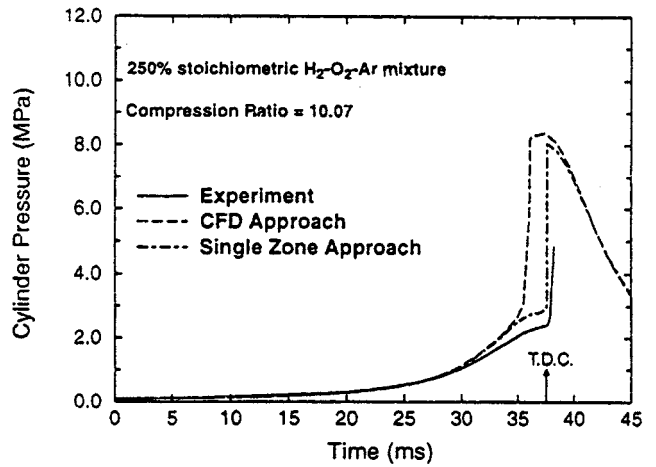
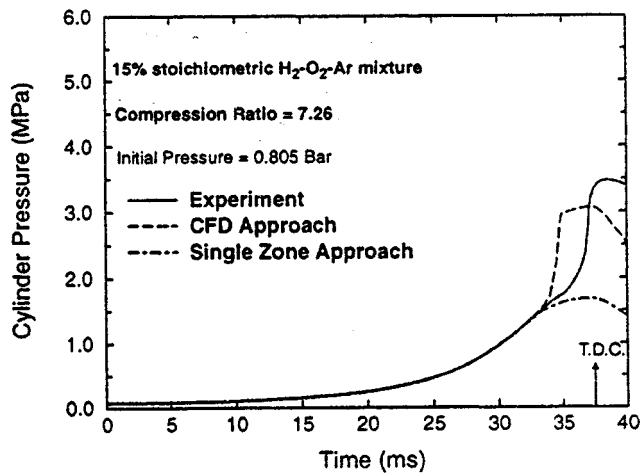
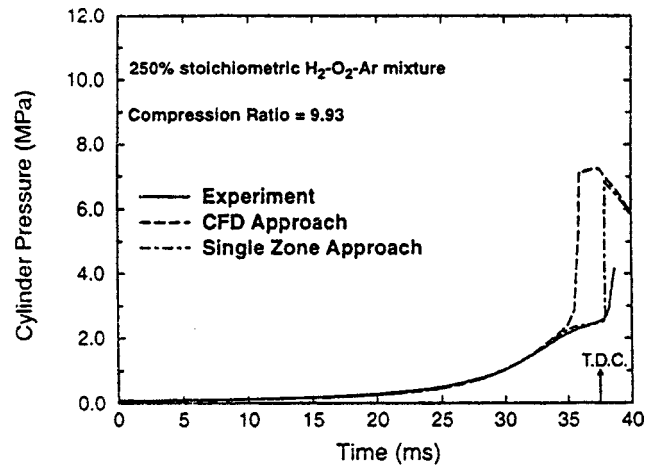
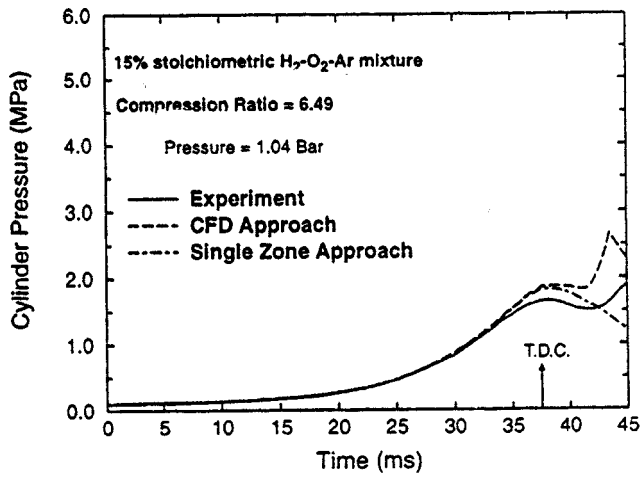


Fig. 5 Experimental and predicted pressure histories while using the CFD and single-zone approaches for a 15% stoichiometric hydrogen-oxygen-argon mixture for three different compression ratios, $T_{in}=353$ K and dilution 79:21 by volume

Fig. 6 Experimental and predicted pressure histories while using the CFD and single-zone approaches for a 250% stoichiometric hydrogen-oxygen-argon mixture for three different compression ratios, $P_{in}=0.89$ bar, $T_{in}=353$ K and dilution 79:21 by volume

than before were needed to effect autoignition. High peak pressures with intense autoignition that took place earlier are observed. With the gradual increase in compression ratio, both the CFD and single-zone approaches predicted qualitatively well the increase in peak pressure and autoignition intensity, but they predicted earlier autoignition. These differences may be in part due to the contribution of the development of cylinder charge inhomogeneities

during compression and the kinetic data employed may not have been representing the reactions of such fuel rich mixtures equally well.

The comparison of experimental and computational results for all the cases studied involving lean, stoichiometric, and rich mixtures shows that the CFD approach that accounts for the build up of temperature gradients and increased charge nonuniformity predicted earlier autoignition than with the single-zone approach.

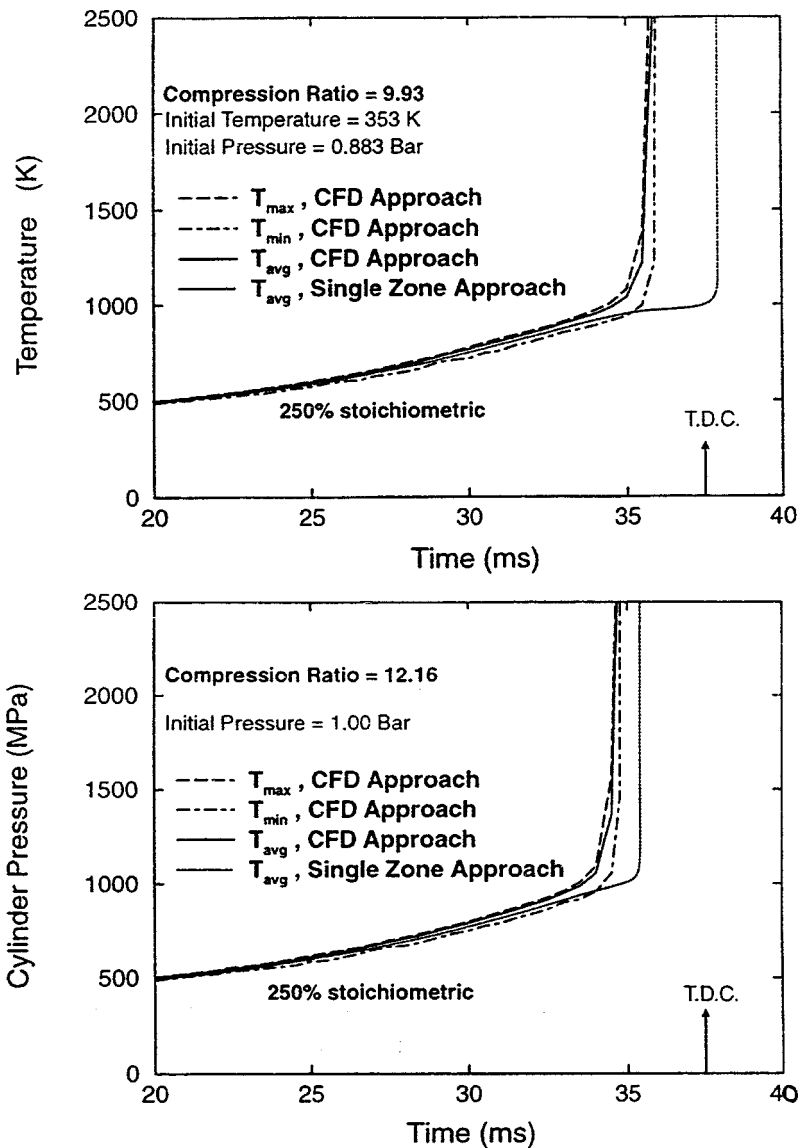


Fig. 7 Comparison of temporal variations of different temperatures while using the CFD approach and the single-zone approach for the 250% stoichiometric hydrogen-oxygen-argon mixture with two different compression ratios of 9.93 and 12.16

Also, good agreement between the predicted and experimental results was observed, especially for lean and stoichiometric mixtures under high compression ratio conditions. Superior agreement with the corresponding experimental results were observed with the corresponding CFD predicted values.

The observed differences between the predicted and measured values could be a reflection of lingering inadequacy of analytical approaches employed as well as the inevitable uncertainties, errors, and limitations associated with the experimental approach. Some contributory factors could have been the following:

- i. The derived characteristic values of the global chemical kinetic model may not have been sufficiently optimized to consider the use of Argon instead of nitrogen as the diluent. Although we have found only relatively small changes in these values with changes in pressure and equivalence ratio, the overlooking of these small differences could have nevertheless contributed to some of the observed differences.
- ii. The experimentally measured pressure values at the center of the cylinder head may not have corresponded exactly with the

calculated mean cylinder pressure, particularly during the rapid rise in pressure values during autoignition. Also, the experimentally determined piston displacement, especially near TDC position, needs to be known very precisely. Any associated errors with its determination could have a significant impact on the accuracy of the results.

iii. The initial experimental conditions despite the great care exercised, may not have been defined sufficiently precisely. There is a negligible extent of gas phase reaction activity before the commencement of compression. However, any initial flow disturbance within the mixture would have departed from the quiescent conditions assumed for modeling. Moreover, the initial composition of the charge needed to be known precisely. This is not easy to achieve, especially for the lean and stoichiometric mixtures when very low concentrations of hydrogen or oxygen are used in the presence of very high concentrations of the diluent.

iv. The turbulence modeling by the CFD KIVA-3 code is based on the standard $k-\epsilon$ turbulence model that has its limitations particularly for representing the wide range of turbulence scales ex-

isting within the engine environment. Similarly, the associated wall heat transfer modeling with the code based on the turbulent wall function has its inevitable limitations.

v. It was shown earlier that for stoichiometric mixtures only a little variation in compression ratio is needed to effect significant changes to the autoignition delay time compared to lean and rich mixture operations. Also, with the increase in compression ratio, the differences between predicted and measured results become smaller. The CFD approach always predicted earlier autoignition than experiment or the single-zone approach. It is possible that the increase in compression ratio and the associated reduction in the space containing the charge lead to enhanced mixing and a reduction in the extent of thermal nonuniformity. Figure 7 shows the temporal variations of the maximum, minimum, and average temperatures obtained using the two analytical approaches for two different compression ratios involving rich mixtures. The observed differences between the CFD predicted maximum and minimum cylinder temperatures indicate the extent of cylinder charge thermal inhomogeneity which leads to different autoignition times. It can also be seen that the maximum temperature curve is closer to that of the CFD predicted average values.

vi. Figure 8 shows the predicted temperature fields for two different compression ratio conditions at around the occurrence of autoignition, with normalized axial distance Z/Z_{min} . The predicted maximum, X , minimum N , and mass-averaged temperature, A , contours are shown. The symbols, H and L represent the closest temperature contours to the maximum and minimum local cell temperature points, respectively. Higher temperature levels were associated with the higher compression ratio condition. It can also be seen that a larger fraction of the cylinder volume encompassed (symbols of H) the high temperature region with a somewhat less apparent thermal inhomogeneity for the higher compression ratio condition. This resulted in a lower peak value of maximum temperature difference within the cylinder charge during autoignition because of the less time needed for the consumption of the rest of the unreacted mixtures after the initiation of autoignition from the high temperature region.

vii. A comparison of the temporal variations of the mean cylinder pressure and local cell pressure at the measurement position when predicted by the CFD approach showed negligible differences, indicating that any pressure inhomogeneity is insignificant in comparison to the development of thermal inhomogeneities.

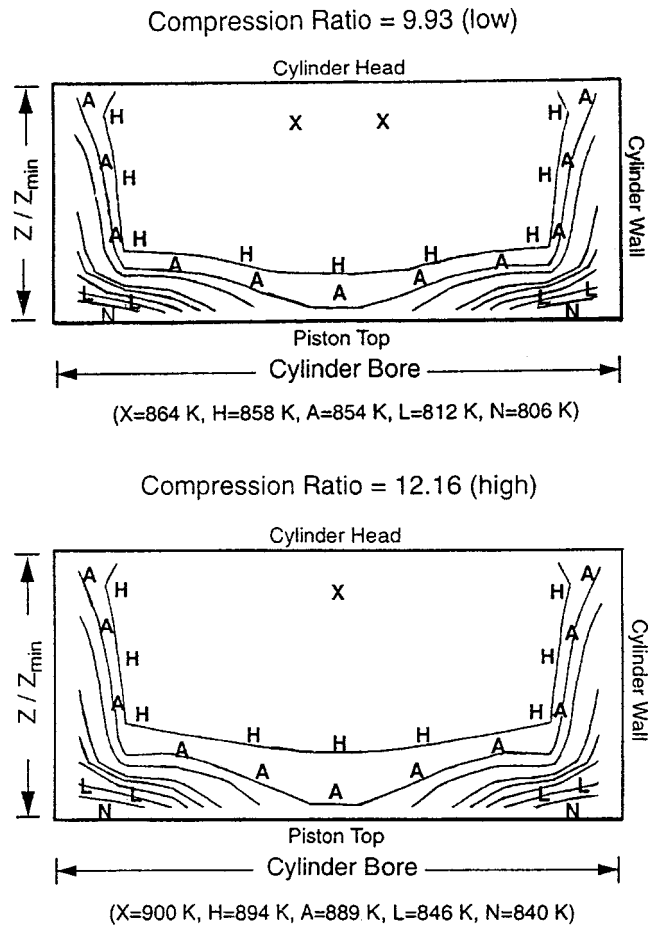


Fig. 8 Predicted cylinder temperature fields for low and high compression ratio conditions involving the 250% stoichiometric hydrogen-oxygen-argon mixture at time=32 ms that is near and before autoignition occurrence

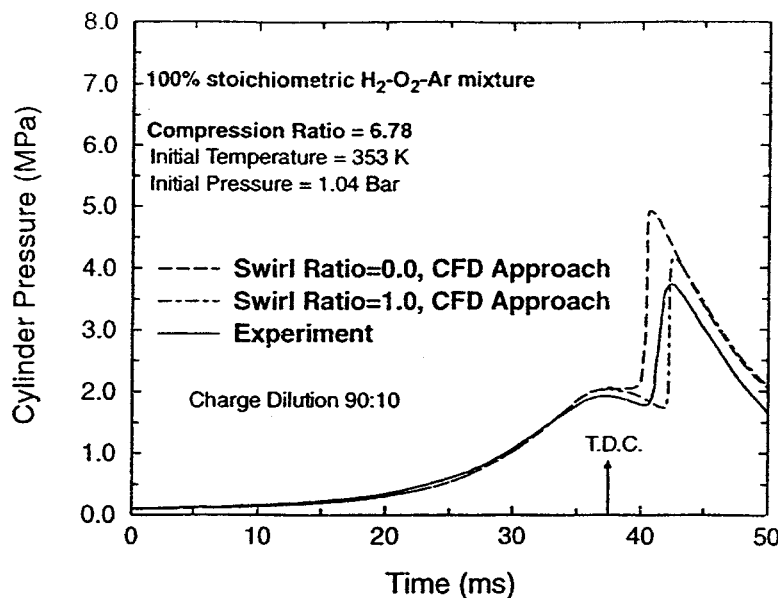


Fig. 9 Comparison of measured pressure variation with time with those predicted by the CFD approach for the 100% stoichiometric hydrogen-oxygen-argon mixture with two different swirl ratios

Any flow disturbance within the charge at the commencement of rapid compression would contribute to the observed differences between the measured and predicted values on the basis of an initially quiescent charge. When the results of simulation with an assumed initial swirl were compared with the corresponding values for the initially quiescent charge, Fig. 9 shows autoignition taking place later with a lower peak pressure value for the case with an initial swirl. The corresponding thermal inhomogeneity within the cylinder charge was decreased with the swirling flow and as a result of increased heat transfer, the general temperature levels tend to be lower and result in a later autoignition. This would indicate that the general temperature levels are more important than the extent of thermal inhomogeneity for the occurrence of autoignition. But for the same general temperature levels, the existence of thermal inhomogeneity will promote the occurrence of autoignition.

Conclusions

i. The derived activation energy values for hydrogen for the conditions considered, do not decrease linearly with temperature as for methane. The corresponding autoignition times with hydrogen do not vary logarithmically linearly with the inverse of temperature.

ii. Comparison of experimental and computational results showed that the CFD approach which allows for the buildup of temperature gradients and increased charge nonuniformity predicted earlier autoignition than the single-zone approach. Good agreement between the predicted and experimental results was observed especially for lean and stoichiometric mixtures under high compression ratio conditions.

iii. The differences in the predicted values of the time to autoignition when using the CFD and the single-zone approaches become smaller with the increase in compression ratio probably as a result of the reduction in the space containing the charge leading to improvement in mixing and a reduction in the extent of nonuniformity.

iv. The comparison of the temporal variations of mean cylinder pressure and local cell pressure at the point of measurement when predicted by the CFD approach showed only minor differences.

v. The existence of an initial swirl in the charge decreases the thermal inhomogeneity promoting heat transfer between the charge and cylinder walls and results in lower temperature levels leading to correspondingly later occurrence of autoignition. The general temperature levels are more important than the extent of thermal inhomogeneity for the occurrence of autoignition. At the same general temperature levels, the existence of thermal inhomogeneity will promote autoignition.

Acknowledgments

The authors wish to acknowledge PanCanadian Petroleum Limited and Canadian Pacific Limited for the awards of scholarships to the first author (K. Chen), and the financial support of the Natural Sciences and Engineering Research Council (NSERC) of Canada.

References

- [1] Karim, G. A., and Klat, S. R., 1975, "Experimental and Analytical Studies of Hydrogen as a Fuel in Compression Ignition Engines," ASME Paper No. 75-DGP-19.
- [2] Gopal, G., Rao, P. S., Gopalakrishnan, K. V., and Murthy, B. S., 1982, "Use of Hydrogen in Dual-Fuel Engines," *Int. J. Hydrogen Energy*, **7**(3), pp. 267–272.
- [3] Rao, B. H., Shrivastava, K. N., and Bhakta, H. N., 1983, "Hydrogen for Dual Fuel Engine Operation," *Int. J. Hydrogen Energy*, **8**(5), pp. 381–384.
- [4] Ikegami, M., Miwa, K., and Shioji, M., 1982, "A Study of Hydrogen Fuelled Compression Ignition Engines," *Int. J. Hydrogen Energy*, **7**(4), pp. 341–353.
- [5] Wong, J. K. S., 1990, "Compression Ignition of Hydrogen in a Direct Injection

- Diesel Engine Modified to Operate as a Low-Heat-Rejection Engine," *Int. J. Hydrogen Energy*, **15**(7), pp. 507–514.
- [6] Johnson, N. L., Amsden, A. A., Naber, J. D., and Siebers, D. S., 1995, "Three-Dimensional Computer Modeling of Hydrogen Injection and Combustion," High Performance Computing Conference, Society for Computer Simulation, Phoenix, AZ.
- [7] Naber, J. D., and Siebers, D. L., 1998, "Hydrogen Combustion Under Diesel Engine Conditions," *Int. J. Hydrogen Energy*, **23**(5), pp. 363–371.
- [8] Karim, G. A., and Watson, H. C., 1971, "Experimental and Computational Considerations of the Compression Ignition of Homogeneous Fuel-Oxidant Mixtures," SAE Paper No. 710133.
- [9] King, R. O., Hayes, S. V., Allan, A. B., Anderson, R. W. P., and Walker, E. J., 1958, "The Hydrogen Engine: Combustion Knock and the Related Flame Velocity," *Trans. Eng. Inst. Canada*, **2**(4), pp. 143–148.
- [10] Karim, G. A., and Taylor, M. E., 1973, "Hydrogen as a Fuel and the Feasibility of a Hydrogen-Oxygen Engine," SAE Paper No. 730089.
- [11] De Boer, P. C. T., and Hulet, J. F., 1980, "Performance of a Hydrogen-Oxygen-Noble Gas Engine," *Int. J. Hydrogen Energy*, **5**, pp. 439–452.
- [12] Das, L. M., 1990, "Hydrogen Engines: A View of the Past and a Look into the Future," *Int. J. Hydrogen Energy*, **15**(6), pp. 425–443.
- [13] Lee, D., and Hochgreb, S., 1998, "Rapid Compression Machines: Heat Transfer and Suppression of Corner Vortex," *Combust. Flame*, **114**, pp. 531–545.
- [14] Lee, D., and Hochgreb, S., 1998, "Hydrogen Autoignition at Pressures above the Second Explosion Limit (0.6–4.0 MPa)," *Int. J. Chem. Kinet.*, **30**(6), pp. 385–406.
- [15] Konig, G., and Sheppard, C. G. W., 1990, "End Gas Autoignition and Knock in a Spark Ignition Engine," SAE Paper No. 902135.
- [16] Konig, G., Maly, R. R., Bradley, D., Lau, A. K. C., and Sheppard, C. G. W., 1990, "Role of Exothermic Centres on Knock Initiation and Knock Damage," SAE Paper No. 902136.
- [17] Bauerle, B., Hoffmann, F., Behrendt, F., and Warnatz, J., 1994, "Detection of Hot Spots in the End Gas of an Internal Combustion Engine Using Two-Dimensional LIF of Formaldehyde," *25th Symposium (International) on Combustion*, The Combustion Institute, Pittsburgh, PA, pp. 135–141.
- [18] Bauerle, B., Warnatz, J., and Behrendt, F., 1996, "Time-Resolved Investigation of Hot Spots in the End Gas of an S. I. Engine by Means of 2-D Double-Pulse LIF of Formaldehyde," *26th Symposium (International) on Combustion*, The Combustion Institute, Pittsburgh, PA, pp. 2619–2626.
- [19] Stiebels, B., Schreiber, M., and Sakak, A. S., 1996, "Development of a New Measurement Technique for the Investigation of End-Gas Autoignition and Engine Knock," SAE Paper No. 960827.
- [20] Schreiber, M., Sadat, A., Poppe, C., Griffiths, J. F., Halford-Maw, P., and Rose, D. J., 1993, "Spatial Structure in End-Gas Autoignition," SAE Paper No. 932758.
- [21] Agarwal, A., and Assanis, D. N., 1998, "Multidimensional Modeling of Natural Gas Ignition Under Compression Ignition Conditions Using Detailed Chemistry," SAE Paper No. 980136.
- [22] Chen, K., and Karim, G. A., 1998, "An Examination of the Effects of Charge Inhomogeneity on the Compression Ignition of Fuel-Air Mixtures," SAE Paper No. 982614.
- [23] Chen, K., and Karim, G. A., 1998, "Evaluation of the Instantaneous Unsteady Heat Transfer in a Rapid Compression-Expansion Machine," *J. Power Energy*, **A**, **212**(A5), pp. 351–362.
- [24] Chen, K., and Karim, G. A., 1998, "Multidimensional Computer Modelling and Experimental Investigation of In-Cylinder Processes in a Rapid Compression-Expansion Machine in the Absence of Fuel Introduction," ASME Paper No. ETCE 98-4726.
- [25] Chen, K., and Karim, G. A., 1999, "The Effects of Charge Non-Uniformity on Autoignition in a Gas Fuelled Motored Engine," SAE Paper No. 1999-01-1179.
- [26] Park, P., and Keck, J. C., 1990, "Rapid Compression Machine Measurements of Ignition Delays for Primary Reference Fuels," SAE Paper No. 900027.
- [27] Griffiths, J. F., Halford-Maw, P. A., and Rose, D. J., 1993, "Fundamental Features of Hydrocarbon Autoignition in a Rapid Compression Machine," *Combust. Flame*, **95**, pp. 291–306.
- [28] Karim, G. A., and Watson, H. C., 1969, "Experimental and Analytical Studies of the Compression Ignition of Fuel-Oxidant Mixtures," *Proc. Inst. Mech. Eng.*, **183**, pp. 1–12.
- [29] Amsden, A. A., 1993, "KIVA-3: A KIVA Program with Block-Structured Mesh for Complex Geometries," Los Alamos National Laboratory Report LA-12503-MS.
- [30] Liu, Z., and Karim, G. A., 1995, "Knock Characteristics of Dual-Fuel Engines Fuelled with Hydrogen Fuel," *Int. J. Hydrogen Energy*, **20**(11), pp. 919–924.
- [31] Liu, Z., and Karim, G. A., 1994, "An Analytical Examination of the Preignition Processes Within Homogeneous Mixtures of a Gaseous Fuel and Air in a Motored Engine," SAE Paper No. 942039.
- [32] Lutz, A. E., Kee, R. J., Miller, J. A., Dwyer, H. A., and Oppenheim, A. K., 1988, "Dynamic Effects of Autoignition Centers for Hydrogen and C_{1,2}-Hydrocarbon Fuels," *22th Symposium (International) on Combustion*, The Combustion Institute, Pittsburgh, PA, pp. 1683–1693.
- [33] Launder, B. E., and Spalding, D. B., 1974, "The Numerical Computation of Turbulent Flows," *Comput. Methods Appl. Mech. Eng.*, **3**, pp. 269–289.

Homogeneous Charge Compression Ignition Engine: A Simulation Study on the Effects of Inhomogeneities

P. Maigaard

F. Mauss¹

e-mail: fabian.mauss@forbrf.lth.se

Division of Combustion Physics,
Lund University,
P. O. Box 118,
22100 Lund, Sweden

M. Kraft

Department of Chemical Engineering,
University of Cambridge,
Cambridge CB2 3RA, UK
e-mail: markus_kraft@cheng.cam.ac.uk

A stochastic model for the HCCI engine is presented. The model is based on the PaSPFR-IEM model and accounts for inhomogeneities in the combustion chamber while including a detailed chemical model for natural gas combustion, consisting of 53 chemical species and 590 elementary chemical reactions. The model is able to take any type of inhomogeneities in the initial gas composition into account, such as inhomogeneities in the temperature field, in the air-fuel ratio or in the concentration of the recirculated exhaust gas. With this model the effect of temperature differences caused by the thermal boundary layer and crevices in the cylinder for a particular engine speed and fuel to air ratio is studied. The boundary layer is divided into a viscous sublayer and a turbulent buffer zone. There are also colder zones due to crevices. All zones are modeled by a characteristic temperature distribution. The simulation results are compared with experiments and a previous numerical study employing a PFR model. In all cases the PaSPFR-IEM model leads to a better agreement between simulations and experiment for temperature and pressure. In addition a sensitivity study on the effect of different intensities of turbulent mixing on the combustion is performed. This study reveals that the ignition delay is a function of turbulent mixing of the hot bulk and the colder boundary layer.

[DOI: 10.1115/1.1563240]

Introduction

The homogeneous charge compression ignition (HCCI) engine is a promising alternative to the existing spark ignition (SI) engines and compression ignition (CI) engines. As in a diesel engine, the fuel is exposed to sufficiently high temperature for autoignition to occur, but for HCCI a homogeneous fuel/air mixture is used. The homogeneous mixture is created in the intake system as in a SI engine, using a low-pressure injection system or by direct injection with very early injection timing. To limit the rate of combustion, very diluted mixtures have to be used. Compared to the diesel engines, the HCCI has a nearly homogeneous charge and virtually no problems with soot and NO_x formation. On the other hand, HC and CO levels are higher than in conventional SI engines. Overall, the HCCI engine shows high efficiency and fewer emissions than conventional internal combustion engines.

The efficiency of the HCCI engine has previously been shown by a number of experiments. Parts of the experiments have been complemented by numerical studies modeling the engine as a plug flow reactor (PFR), [1,2]. In these simulations the ignition delay times for a set of different parameters were investigated. The results indicate that local inhomogeneities are responsible for differences between measurements and simulation results.

One way of accounting for these inhomogeneities is to use multiple zones to model boundary layer effects. Such work has recently been performed using a 10 zone-model for the HCCI engine, [3]. This model is not able to take fluctuations in the zones into account and the chemical source terms are calculated by using the means of temperature and gas composition in the zones. A more sophisticated way is to use a model that is based on the probability density function of the physical variables that are im-

portant in the combustion process. However, the numerical cost, to study chemical reactions together with all aspects of flow in detail, is high and simplifying assumptions have to be introduced. In this paper, we assume that chemical species and temperature are random variables with a probability density function (PDF) that does not spatially vary in the combustion chamber. As in the homogeneous PFR model the combustion chamber is modeled by only one zone, but the gas temperature and composition can fluctuate.

The purpose of this paper is to introduce a new simulation model featuring the partially stirred plug flow reactor (PaSPFR) as described in Refs. [4], [5]. Numerical simulations of the ignition process in the HCCI engine will be performed using a detailed chemical model for butane and lower alkanes in the framework of the PaSPFR. The reaction mechanism contains 53 chemical species and 590 elementary chemical reactions. A simple deterministic IEM model is used to describe the unclosed term for turbulent micromixing in the PaSPFR.

The PaSPFR model, taking fluctuations in temperature that are induced by the colder thermal boundary layer into account, will be used in an attempt to improve on previous numerical simulations of the HCCI process, [1,2]. The results of the new PDF-based model and the old PFR model are compared to experiments in Refs. [1,2]. Additionally, we perform a sensitivity study on the influence of turbulent mixing on ignition delay. The effect of different mixing intensities on the mean of temperature and pressure as well as their standard deviation (STD-DEV) will be discussed.

This discussion is limited to the effect of an assumed initial temperature inhomogeneity. The question how the mixing effects the development of the inhomogeneity will be matter of a later publication.

Previous Model and Experimental Results

The experimental data used in this work are the same as those described in [1]. The experimental setup is as follows: A six-cylinder Volvo TD100 series truck diesel engine has been modi-

¹To whom correspondence should be addressed.

Contributed by the Internal Combustion Engine Division of THE AMERICAN SOCIETY OF MECHANICAL ENGINEERS for publication in the ASME JOURNAL OF ENGINEERING FOR GAS TURBINES AND POWER. Manuscript received by the ICE Division July 2000; final revision received by the ASME Headquarters Aug. 2002. Associate Editor: D. Assanis.

Table 1 Volvo TD100 engine parameters

Displaced Volume	1600 cm ³
Bore	120.65 mm
Crank radius	70 mm
Stroke	140 mm
Connection rod	260 mm
Exhaust valve open	39 deg BBDC (at 1 mm lift)
Exhaust valve close	10 deg BTDC (at 1 mm lift)
Inlet valve open	5 deg ATDC (at 1 mm lift)
Inlet valve close	13 deg ABDC (at 1 mm lift)

fied for one-cylinder use, and converted to HCCI operation. The engine data are given in Table 1. The simplest possible combustion chamber geometry is used, i.e., a flat piston crown giving a pancake combustion chamber. Common, commercially available natural gas is used as fuel, [2]. The major compound of the natural gas is methane. The content of higher hydrocarbons such as ethane, propane, and butane (see Table 2 for details) is non-negligible. In Ref. [1] it was demonstrated that the amount of butane in the natural gas is the most sensitive parameter in HCCI combustion with natural gas.

The engine is run on natural gas at fuel-air ratios of $\phi=0.30$ –0.45. Four different engine speeds are used: 800, 1000, 1200, and 1400 rpm. These engine speeds are chosen as being representative for normal use considering that maximum torque for a normal CI-operating TD100-series diesel is achieved at 1400 rpm and the engine idle speed is 475–525 rpm. In this work we will focus on the operating conditions stated in Table 3, measured at 60 CAD BTDC.

The detailed reaction mechanism for natural gas that was used in the PFR model predicts the ignition timing correctly. This is shown in Fig. 1. The oscillations in the single cycle curve are due to pressure oscillations. The temperature profile has not been measured but was evaluated from the pressure transducer measurement. The origin of the pressure oscillations is not fully understood. The rate of combustion is most likely so fast that the pressure gradient in the cylinder generates vibrations in the engine structure. These then result in volume changes in the cylinder and hence in pressure oscillations (private communication with B. Johansson).

Modeling the Boundary Layer

As stated above, the assumption of homogeneity is responsible for the rapid temperature rise during ignition or in other words, very short combustion duration. In Ref. [1] it was found that the time of autoignition is mainly dependent on the fuel quality (octane number) and to a lesser extent on initial temperature and fuel/air equivalence ratio.

In Ref. [6] it has been shown that, for the engine under consideration in this paper, inhomogeneities in the fuel charge have only a modest effect on the combustion process. We therefore assume

Table 2 Natural gas components

Component	Mole-%	Mass-%
Methane	91.3	81.0
Ethane	5.0	7.9
Propane	1.8	4.2
<i>n</i> -butane+higher	1.0	4.7
Nitrogen	0.3	0.9
Carbon dioxide	0.6	1.2

Table 3 Initial values for the simulations of engine case (60 CAD BTDC)

ϕ	CR	T (K)	P (BAR)	RPM
0.368	17.30	664	4.40	1000

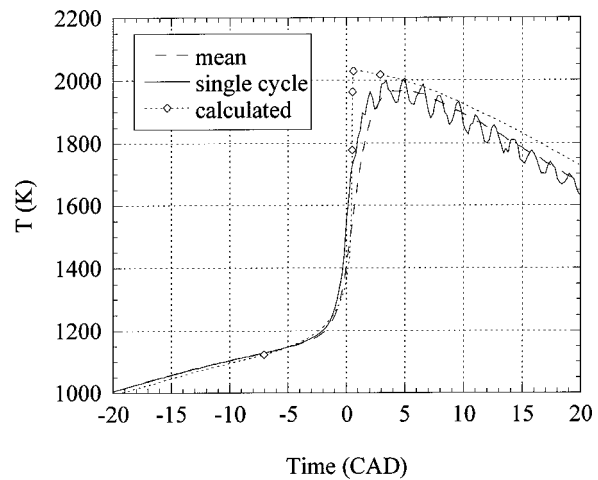


Fig. 1 Numerical results from the PFR model compared with experiments. The TD100 engine is in this case run at 1000 rpm and $\phi=0.368$. The jagged line represents results from a single experimental engine cycle and the broken line is its smoothed version.

that the inhomogeneity in the temperature field, caused by the mixing of the colder gases in the boundary layer into the bulk gas, is the most sensitive on the combustion duration. To investigate the influence of the temperature inhomogeneity we model the existence of a colder boundary layer of gas near the cylinder wall at a prescribed crank-angle degree (-60 CAD).

The thickness of this thermal boundary layer has been investigated experimentally on the TD100 series engine, [7]. These experiments suggest that the thickness of the boundary layer is approximately three millimeters. This result coincides with findings from Heywood [8] for the general case. For the current HCCI engine setup a boundary layer of 3 mm corresponds to approximately 15% of the displaced cylinder volume. Since the boundary layer is assumed to be significantly cooler than the bulk gasses, and the average density in the boundary layer is about twice that in the bulk, the total gas mass in the boundary layer will be about 15–20%. Additionally we have to account for colder fluid parcels in crevices.

The boundary layer can be described by applying theories for the flow of a fluid passing a solid surface. It is assumed that it consists of a thin film layer immediately adjacent to the cylinder wall plus a “buffer zone” between this and the turbulent bulk flow, [9]. The crevices are represented by the first five particles and the film layer corresponds to particle numbers 6 to 15 as illustrated in Fig. 2. Within the film layer we have a strong in-

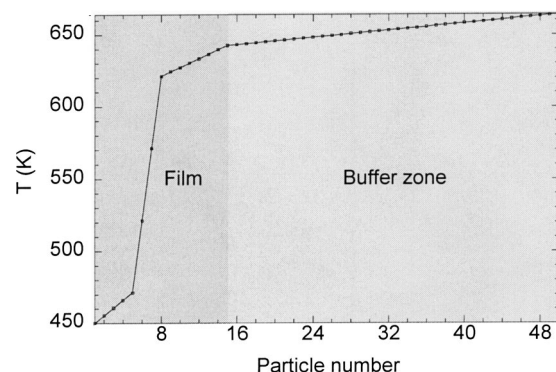


Fig. 2 Temperature distribution in the boundary layer. The temperature increases from the wall temperature and asymptotically approaches the bulk gas temperature.

crease in temperature. This is reflected by the large variance of temperature of the film layer particles. In the viscous sublayer, heat is transferred primarily through conduction.

As one approaches the bulk of the cylinder the temperature increases asymptotically towards the bulk gas temperature (illustrated by the "Buffer zone" in Fig. 2). In Fig. 2 the wall temperature is 450 K and the hot bulk gas is 650 K. The boundary layer is modeled using 50 fluid particles representing the 3 mm radius adjacent to the cylinder wall.

Turbulent Phenomena in the Engine

Experimental results performed on the Volvo TD100 series engine give a quantitative description of the turbulent flow characteristic in the cylinder, [10]. These experiments have been performed under inert or motored conditions and in lean SI mode. In the following we assume that the turbulence characteristics for the engine in HCCI mode are comparable to these results. This assumption is justified by the fact that the same pancake shaped combustion chamber is used in the two setups and that there is no influence on the flow from a propagating flame front in the motored case.

The fluctuating velocity component is defined by the turbulence intensity u' as

$$u' = \lim_{t \rightarrow \infty} \left(\frac{1}{t} \int_{t_0}^{t_0+t} u^2 dt \right)^{1/2}$$

and the integral length scale l_I is defined as

$$l_I = \int_0^{\infty} R_x dx,$$

where R_x is the autocorrelation coefficient of the fluctuating velocity. We assume that the turbulent scalar time scale is related to the fluctuating velocity component by a proportionality constant:

$$\tau_\phi = \frac{\tau}{C_\phi} = \frac{1}{C_\phi} \frac{l_I}{u'},$$

where C_ϕ is a model constant. The turbulent energy dissipation rate ε is given by

$$\varepsilon = \frac{(u')^3}{l_I}.$$

Measurements of turbulence intensity in the cylinder show fluctuations in the range of 0.5–0.9 m/s from 20 CAD BTDC to 20 CAD ATDC. The integral length scale is in the range of 10–18 mm. This gives a turbulence mixing time scale in the order of 0.01 s and a dissipation rate in the order of $10 \text{ m}^2/\text{s}^3$.

The Stochastic Reactor Model

As discussed in the Introduction, we use a stochastic reactor model PaSPFR-IEM from Ref. [4] to describe the influence of inhomogeneities on the combustion process. The assumption of homogeneity for species mass fractions and temperature that has been made previously in [1] is replaced by the assumption of statistical homogeneity. This means that the joint scalar PDF does not vary within the combustion chamber.

In the following, we distinguish between global and local quantities. Global quantities are mass m , volume $V(t)$, mean density $\langle \rho(t) \rangle$, and pressure $p(t)$. We assume that global quantities do not vary spatially in the combustion chamber. Local quantities are chemical species mass fractions $Y_i(t)$, $i = 1, \dots, S$ and temperature $T(t)$. They can vary within the combustion chamber and are assumed to be random variables. Their joint random vector is defined as

$$\Phi(t) = (\Phi_1, \dots, \Phi_{S+1}) = (Y_1, \dots, Y_S, T),$$

and the corresponding joint scalar mass density function (MDF) is given by $F_\Phi(\Psi_1, \dots, \Psi_{S+1}; t)$ assuming spatial homogeneity as proposed in the PaSPFR model. Its time evolution is given by the following MDF-transport equation:

$$\begin{aligned} \frac{\partial}{\partial t} F_\Phi(\Psi; t) + \frac{\partial}{\partial \Psi_i} (Q_i(\Psi) F_\Phi(\Psi; t)) \\ = \frac{\partial}{\partial \Psi_i} \left(\frac{1}{2} \frac{C_\phi}{\tau} (\Psi_i - \langle \Phi_i \rangle) F_\Phi(\Psi; t) \right), \end{aligned}$$

where the initial conditions are given as $F_\Phi(\Psi; 0) = F_0(\Psi)$. The brackets $\langle \cdot \rangle$ denote the mean according to F_ϕ and C_ϕ/τ is a measure for the intensity of scalar mixing. The model constant C_ϕ is set to 2.0, [11] and the turbulent time scale is estimated from the experiment as discussed above. The right-hand side of MDF-transport equation describes the mixing of the scalars by turbulent diffusion. This model is called IEM model and is known to have some deficiencies. It was chosen due to its simplicity and low numerical cost (see details in Ref. [4]). The term Q_i describes the change of the MDF due to chemical reactions, change in volume, and heat losses.

$$\begin{aligned} Q_i &= \frac{M_i}{\rho} \sum_{j=1}^R \nu_{i,j} \omega_j \quad i = 1, \dots, S \\ Q_{S+1} &= \frac{1}{c_v} \sum_{i=1}^S \left(h_i - \frac{RT}{M_i} \right) \frac{M_i}{\rho} \sum_{j=1}^R \nu_{i,j} \omega_j + \frac{p}{mc_v} \frac{dV}{dt} \\ &\quad - \frac{1}{mc_v} (\alpha A (T - T_w) + \sigma \hat{\varepsilon} (T^4 - T_w^4)) \end{aligned}$$

The convective heat transfer coefficient is obtained from the Woschni equation, [8], σ is the Stefan-Boltzmann constant and the radiation coefficient $\hat{\varepsilon}$ of water and carbon dioxide, [12], is used. Besides the MDF transport equation the time evolution of the global quantities has to be computed. The change of volume $V(\Theta(t))$ in terms of CAD is given by

$$V(\Theta(t)) = V_c + \frac{\pi \cdot B^2}{4} (l + a - a \cdot \cos(l^2 - a^2 \cdot \sin^2 \Theta(t)))^{1/2}$$

as in [8]. Mean density can be calculated as

$$\langle \rho(t) \rangle = \frac{m}{V(t)},$$

pressure is given by the ideal gas law

$$p(t) = \langle \rho(t) \rangle \frac{R \langle T \rangle}{\langle M \rangle},$$

where $\langle T \rangle$ is the mean temperature according to the MDF and $\langle M \rangle$ is the expected mean molecular weight. These equations as well as the transport equation of the MDF have to be solved simultaneously. For this work the stochastic reactor model is implemented into the existing code for the calculation of ignition processes in HCCI engines, [1,2], and in the end gas of SI engines as described in [13,14]. The solution procedure is based on a stochastically weighted particle method and a higher-order operator splitting technique. The stochastic particle ensemble approximates the MDF. Each stochastic particle is associated with certain temperature and fluid composition and is thereby related to a fluid particle. Details of the numerical procedure will be published separately.

Initial Conditions

The simulations for the autoignition process were made using initial values obtained from the experiments at 60 CAD BTDC described in Table 3. The species composition in the boundary layer and the bulk is assumed to be homogeneous at 60 CAD

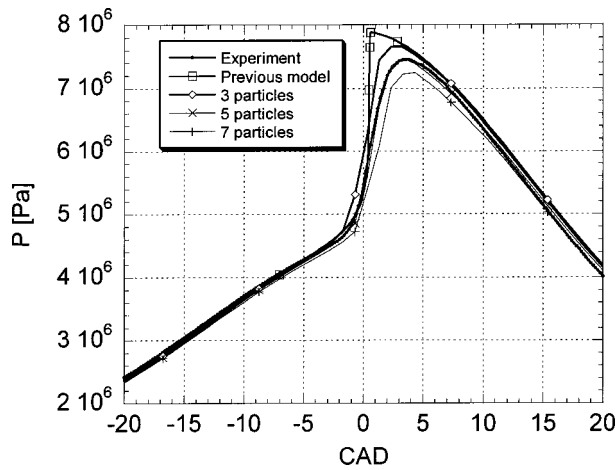


Fig. 3 Pressure history. Results from the new model with varying number of particles are compared to experimental data and a previous model result.

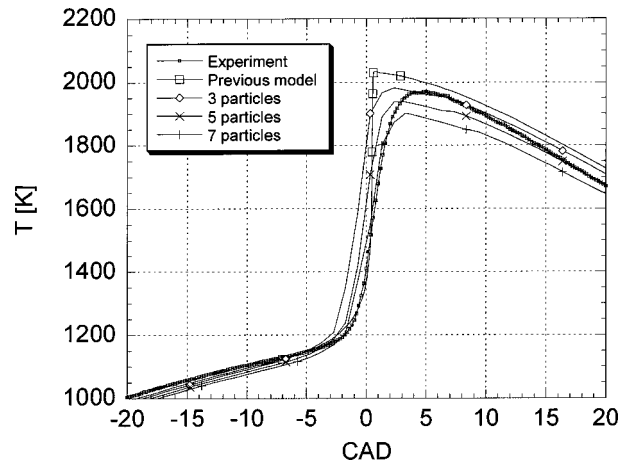


Fig. 4 Temperature history. Results from the new model with varying number of particles are compared to experimental data and a previous model result.

BTDC. During the process inhomogeneities will develop, caused by the inhomogeneous combustion process. The only scalar variable that is assumed to be inhomogeneous at 60 CAD BTDC is the temperature. The initial MDF is given by

$$F_0(\Psi) = \underbrace{\sum_{n=1}^{BL} w^{(n)} \delta(\Psi - \Psi^{(n)})}_{\text{BoundaryLayer BL}} + \underbrace{w^{(BL+1)} \delta(\Psi - \Psi^{(BL+1)})}_{\text{Bulk}}$$

The weights $w^{(n)}$ are chosen to be

$$w^{(n)} = \begin{cases} \frac{m_{BL}}{BL} : n = 1, \dots, BL \\ m_{Bulk} : n = BL + 1 \end{cases}$$

with $m = m_{BL} + m_{bulk}$ being the mass of the fuel-air mixture in the combustion chamber. The scalars $\Psi_j^{(n)}$ for $j = 1, \dots, S$ are the chemical species mass fractions and are all set to the same value to meet the conditions in Table 3. The temperature in the boundary layer (BL) $\Psi_{S+1}^{(n)} : n = 1, \dots, BL$ is set according to the temperature profile displayed in Fig. 2. The temperature in the bulk $\Psi_{S+1}^{(n)} : n = BL + 1$ is set to a value to match the initial mean temperature in the combustion chamber. For the present case we model the boundary layer by choosing a turbulent mixing time scale (τ) of 0.02s and 20% of the total gas mass in the boundary layer.

Results and Discussion

In the following section we demonstrate the capabilities of the new model and compare numerical results with experimental data and results from the previous homogeneous model described in [1]. In the reference case described in Table 3 the engine is operating at 1000 rpm with a fuel/air equivalence ratio of 0.368.

Figure 3 illustrates the pressure history for the reference case. The number of fluid particles representing the viscous sublayer of the film layer and the crevices is varied from three to seven. The shape of the ignition curve is independent of the number of cold particles in this part of the film layer but ignition timing and maximum pressure is affected. Choosing five fluid particles gives a simulated result nearly identical to the experimental results. The new model generally produces results significantly closer to the experiments than the previous model.

Figure 4 shows the temperature history for the same case. The experimental temperature history is not directly measured but calculated from the pressure measurements using a very simple one-

zone model. Therefore the simulated temperature is not directly comparable to the experimental results in this figure.

Figure 5 illustrates the standard deviation (STD-DEV) of the calculated temperature for the simulation. Again the number of fluid particles representing the viscous sublayer of the film layer is varied from three to seven. The STD-DEV is slowly decreasing during the first inert part of the compression stroke due to the temperature mixing of fluid parcels in the bulk and in the boundary layer. At around three CAD BTDC the bulk ignites which leads to a rapid increase of STD-DEV. While the ignition process is progressing the STD-DEV decreases until most of the boundary layer has ignited. The difference in STD-DEV between the time before ignition and after ignition indicates that not all parts of the boundary layer are fully burnt.

Generally one can conclude from these first results that the implementation of the SRM greatly improves the numerical simulation of the HCCI process. The IEM mixing model describes mixing adequately if the initial distribution of particles in crevices and boundary layer is sufficiently good. In the following sections five fluid particles are chosen to represent the laminar part of the film layer.

Sensitivity Study

In this section, we study the effects of varying the turbulence time scale (which is related to turbulence intensity) as predicted

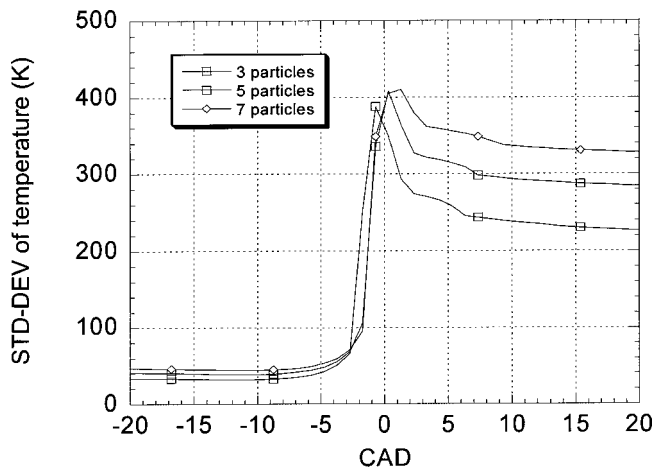


Fig. 5 STD-DEV of temperature history

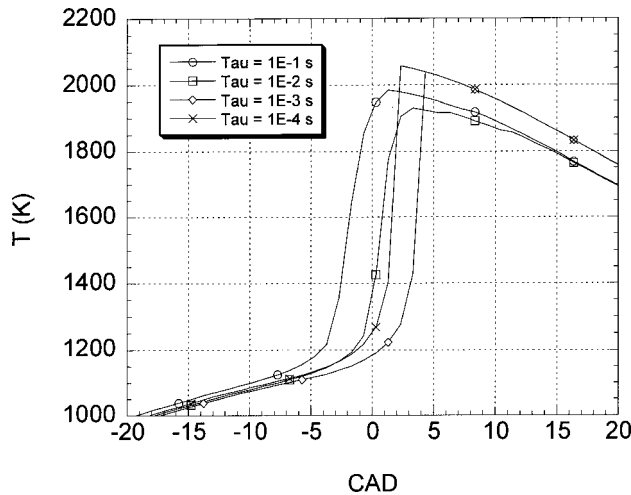


Fig. 6 Sensitivity study on turbulence mixing time scale (τ)

by the model. It is noted here that we study the influence of the mixing on an existing inhomogeneity. We do not study the development of inhomogeneities caused by the turbulent flow. This means we keep the temperature inhomogeneity at 60 CAD BTDC constant. We further assume that the ongoing cooling of the gas by the wall is not adding inhomogeneity. These assumptions do not hold and a refinement of a stochastic wall–gas interaction model will be matter of a further publication. It is expected that increased turbulent mixing will cause better cooling and thereby will raise the inhomogeneity of the temperature before ignition.

In Fig. 6, the turbulence mixing time scale is varied from 0.1 s to 0.0001 s. The result of this study shows that a very slow mixing ($\tau=0.1$ s) promotes early ignition of the hot spots in the cylinder since they do not mix with the cold spots. As one increases the influence of mixing by decreasing τ the ignition is delayed. At a value of τ of 0.001 s the mixing is now so efficient that a very large region of the fuel and air mixture will ignite simultaneously. At an even smaller value of τ the situation is in essence similar to the homogeneous case and a very steep slope on the ignition curve is observed. These results cannot explain the finding in engines that the combustion duration in engines raises with increasing turbulence in the cylinder, [15]. Again we expect that this finding is caused by the convective cooling of the in cylinder gases, leading to an increased temperature inhomogeneity.

By observing the STD-DEV of temperature for this study in Fig. 7, the mixing effects described above can be better understood. From this graph, it is evident that the bulk ignites earlier in the slow mixing cases as compared to that in fast mixing cases, because of less mixing with the colder boundary layer. As a consequence we find a decrease in the maximum value of the STD-DEV with increasing mixing intensity. As mixing becomes more efficient a time delay between ignition of the colder and hotter spots is noticed.

The effects of mixing in the fast mixing cases are shown in Fig. 8. For $\tau=0.001$ s the mixing is close to perfect before ignition and the STD-DEV is an order of magnitude smaller than for the two slow mixing cases. For $\tau=0.0001$ s the mixing is so fast that no STD-DEV reading is noticeable.

Conclusion

In the present work, a new model for the numerical simulation of the combustion process in the HCCI engine has been presented. This model is based on the PaSPFR-IEM model. It is capable of simulating the influence of inhomogeneities in the cylinder caused by the thermal boundary layer adjacent to the cylinder walls on the combustion process. The model predictions have been compared with engine measurements and numerical results from a

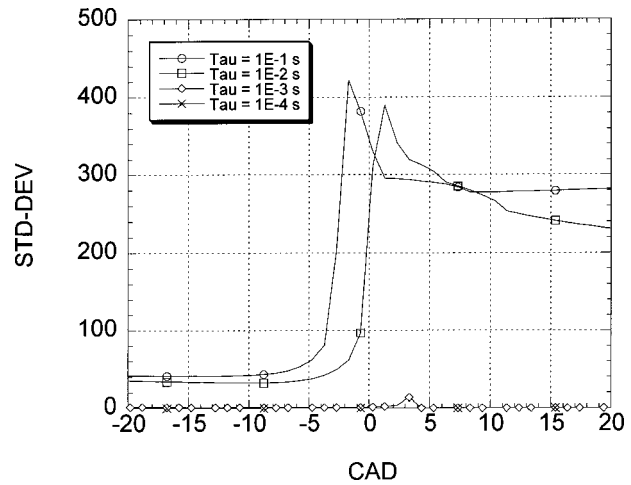


Fig. 7 STD-DEV of temperature histories for the sensitivity study on turbulence time scale

PFR model. Generally the new model shows promising results by significantly improving the quality of the agreement with experimental data compared to the previously used PFR model.

The calculated ignition time histories for temperature and pressure are in very good agreement with the experiments. The modeling of the boundary layer in the cylinder results in a “smoother” ignition curve as the cold and hot spots in the cylinder ignite at different times. In other words, in cylinder temperature inhomogeneities result in an increase of the combustion duration. The STD-DEV of temperature gives evidence that not all of the boundary layer is burnt. This explains the excess of unburnt hydrocarbons from the HCCI engine.

The sensitivity of the turbulent mixing on the combustion process has been investigated. Slow mixing will result in early ignition of the hot spots followed by a delayed ignition of the colder ones. Fast mixing results in almost homogeneous combustion. The weakness of the model is, that it is not able to calculate the origin of the temperature inhomogeneities. It is therefore not able to calculate the influence of different engine geometries on the combustion process.

Future work will discuss the implementation of a more detailed mixing model, e.g., the Curl mixing model. This will increase the demand on CPU time but will give a more accurate description of the mixing processes taking place in the cylinder. A stochastic

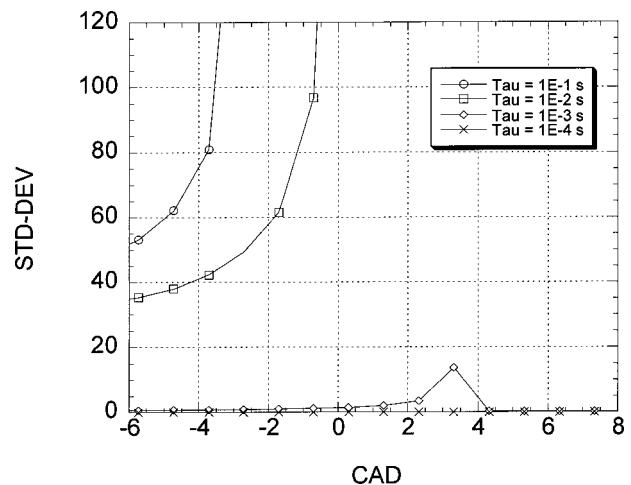


Fig. 8 STD-DEV of temperature. Closeup on the faster mixing cases

wall interaction model needs to be developed to allow the prediction of influence of turbulence intensity on the inhomogeneities in the gases.

Acknowledgments

We would like to thank Prof. B. Johansson, Division of Heat and Power, Lund Institute of Technology, for some very useful discussions on the turbulent characteristics of the HCCI engine. We further thank Mr. A. N. Bhawe, Department of Chemical Engineering, University of Cambridge, for the help in preparing this manuscript. Financial support from Caterpillar and EPSRC (Proposal GR/R53784) is kindly acknowledged.

Nomenclature

Abbreviations

HCCI	= homogeneous charged compression ignition
PFR	= plug flow reactor
PaSPFR	= partially stirred plug flow reactor
PDF	= probability density function
MDF	= mass density function
IEM	= interaction by exchange with the mean mixing model
STD-DEV	= standard deviation
ATDC	= after top dead center
BTDC	= before top dead center
BTDC	= before bottom dead center
CAD	= crank angle degree
CR	= compression ratio
RPM	= revolutions per minute
SRM	= stochastic reactor model

Arabic Symbols

a	= crank radius
A	= cylinder surface area
B	= bore
c_v	= specific heat at constant volume
C_ϕ	= proportionality constant
F_ϕ	= joint scalar mass density function
h_i	= specific enthalpy of species i
l	= connecting rod
l_i	= integral length scale
m	= mass
M	= mean molecular weight
M_i	= molecular weight of species i
p	= pressure
t	= time
T	= temperature
Q_i	= source term
R	= universal gas constant
R_x	= autocorrelation coefficient
V	= volume
V_c	= clearance volume
$w^{(n)}$	= mass weight for PDF
Y_i	= mass fraction of species i

Greek Symbols

α	= heat transfer coefficient
$\hat{\epsilon}$	= radiation coefficient
ϵ	= dissipation
ϕ	= equivalence ratio
Φ	= joint scalar random vector
Θ	= CAD
ν_{ij}	= stoichiometric coefficients
ρ	= density
τ	= turbulent velocity time scale
τ_ϕ	= turbulent scalar time scale
ψ	= joint scalar sample variable
ω_j	= rate of reaction j

Subscripts and Superscripts

BL	= index for boundary layer
Bulk	= index for bulk
i	= index for scalars
j	= index for reactions
n	= particle index
S	= number of chemical species
R	= number of reactions
w	= wall

References

- [1] Amneus, P., Nilsson, D., Mauss, F., Christensen, M., and Johansson, B., 1998, "HCCI Engine: Experiments and Detailed Kinetic Calculations," *COMODIA 98*, Japan Society of Mechanical Engineers, Tokyo, Japan, pp. 567–572.
- [2] Christensen, M., Johansson, B., Amneus, P., and Mauss, F., "Supercharged HCCI Engine," SAE Paper No. 980787.
- [3] Aceves, S. M., Flowers, D. L., Westbrook, C. K., Smith, J. R., and Pitz, W., 2000, "A Multi-Zone Model for Prediction of HCCI Combustions and Emissions," SAE Paper No. 2000-01-0327.
- [4] Kraft, M., 1998, "Stochastic Modelling of Turbulent Reacting Flow in Chemical Engineering," VDI Verlag, Fortschrittsberichte des VDI, Reihe 6(391).
- [5] Procaccini, C., Kraft, M., Fey, H., Bockhorn, H., Longwell, J. P., Sarofim, A., and Smith, K. A., 1998, "PIC Formation During the Combustion of Simple Hydrocarbons in Inhomogeneous Incineration Systems," *Proc. Combust. Inst.*, **27**, pp. 1275–1281.
- [6] Richter, M., Engström, J., Franke, A., Aldén, M., Hultqvist, A., and Johansson, B., 2000, "The Influence of Charge Inhomogeneity on the HCCI Combustion Process," SAE Paper No. 2000-FL-633.
- [7] Hultqvist, A., Christensen, M., Johansson, B., Franke, A., Richter, M., and Aldén, M., "A Study of the HCCI Combustion Process by Chemiluminescence Imaging," SAE Paper No. 1999-01-3680.
- [8] Heywood, J. B., 1989, *Internal Combustion Engine Fundamentals*, McGraw-Hill, New York.
- [9] Perry, R. H., *Perry's Chemical Engineers' Handbook*, 6th Ed., McGraw-Hill, New York.
- [10] Johansson, B., 1995, "On Cycle to Cycle Variations in Spark Ignition Engines," Doctoral thesis, Lund Institute of Technology.
- [11] Pope, S. B., 1985, "PDF Methods for Turbulent Reactive Flows," *Prog. Energy Combust. Sci.*, **11**, pp. 119–192.
- [12] Hottel, H. C., 1954, *Radiant Heat Transmission*, 3rd Ed., W. H. Adams, ed., McGraw-Hill, New York.
- [13] Hajireza, S., Mauss, F., and Sundén, B., 1997, "Investigation of End-Gas Temperature and Pressure Increases in Gasoline Engines and Relevance for Knock Occurrence," SAE Paper No. 971671.
- [14] Bood, J., Bengtsson, P.-E., Mauss, F., Burgdorf, K., and Denbratt, I., 1997, "Knock in Spark-Ignition Engines: End-Gas Temperature Measurements Using Rotational CARS and Detailed Kinetic Calculations of the Autoignition Process," SAE Paper No. 971669.
- [15] Christensen, M., Johansson, B., and Hultqvist, A., "The Effect of Combustion Chamber Geometry on HCCI Operation," SAE Paper No. 2002-01-0425.

Characteristics of Homogeneous Charge Compression Ignition (HCCI) Engine Operation for Variations in Compression Ratio, Speed, and Intake Temperature While Using n-Butane as a Fuel

M. Iida

Yamaha Motor Company,
2500 Shingai,
Iwata, Shizuoka 438-8501, Japan
e-mail: iidaminoru@yamaha-motor.co.jp

M. Hayashi

e-mail: mototoyo@aol.com

D. E. Foster

e-mail: foster@engr.wisc.edu

J. K. Martin

e-mail: martin@engr.wisc.edu

Engine Research Center,
University of Wisconsin,
1500 Engineering Drive,
Madison, WI 53706

In this paper, some basic properties of homogeneous charge compression ignition operation are reported. The effect of inlet temperature, compression ratio and engine speed on the homogeneous charge compression ignition (HCCI) operating ranges were evaluated in a CFR engine using n-butane as a fuel. The minimum and maximum loads for HCCI operation were determined using criteria of coefficient of variation of the indicated mean effective pressure and the derivative of in-cylinder pressure, respectively. Exhaust emissions, particularly hydrocarbons, were measured using a Fourier transform infrared spectrometer. The concentration of intermediate hydrocarbon species rapidly decreased as the magnitude of the energy release increased. Hydrocarbon emission at the maximum HCCI load mainly consists of the fuel itself, which is probably emitted from colder areas in the combustion chamber. Finally, the relationship between IMEPCOV and ISFC is discussed. [DOI: 10.1115/1.1501914]

Introduction

Driven by concern over potential petroleum shortages, greenhouse warming effects of carbon dioxide (CO_2), and acid rain and smog from nitrogen oxides (NO_x), demands for a power source with high efficiency and low environmental impact are increasing year by year. Spark ignition (SI) engines, with precise control of air fuel ratio and three-way catalysts, are proving to be a very clean power source. However, due to throttling losses, knock limit and lean flammability limits, their maximum practical efficiency is constrained. Another popular power source is the direct-injection Diesel engine (DI diesel), which is a very efficient power source. However, due to heterogeneous combustion, the diesel is hampered with the constraint of a tradeoff between NO_x emissions and particulate matter. Homogeneous charge compression ignition (HCCI) engines are being investigated for their potential of efficient energy conversion with low environmental impact. That is, HCCI engines have the potential for high efficiency like direct-injection Diesel engines ([1]), while emitting extremely low NO_x emission, and no smoke.

Many researchers have studied HCCI combustion during the last three decades. The earliest reported work ([2,3]) showed the basic characteristics of HCCI, which have been validated by subsequent researchers, namely: very little cyclic variation and no flame propagation. Noguchi et al. [3] conducted a spectroscopic study of HCCI combustion and observed many radicals in a specific sequence. These initial research efforts were done using two-stroke engines, with low compression ratios and very high residual gas in the cylinder. Najt and Foster [4] were the first to run a four-stroke engine in HCCI. They conducted fundamental studies in pursuit of understanding this combustion phenomenon.

They demonstrated that experimentally observed results could be understood in terms of global hydrocarbon kinetics and fuel autoignition phenomena.

Recently the interest in HCCI has been growing. HCCI combustion is fundamentally interesting because the energy release processes are governed by chemical kinetics, which in turn are influenced by the fluid mechanic and thermodynamic state history. Consequently, it represents a good research problem to which one can apply different experimental and analytical methods ([5–12]). Through these research efforts the relative importance of control parameters, such as the intake temperature, equivalence ratio, and internal exhaust gas recirculation (EGR) and their impact on the start of combustion (SOC) and heat release rates have been revealed.

On the other hand, some researches have focused on application of HCCI ([13–16]). They have shown the advantages and disadvantages of HCCI: high efficiency, an indicated thermal efficiency of up to 50% is possible, with only several ppm of NO_x being emitted from the cylinder in the exhaust gas. However, the maximum load achievable with HCCI has characteristically been much lower than in a typical SI and DI diesel. The authors believe that this is a characteristic of HCCI combustion. HCCI combustion is the same autoignition process as knocking combustion. Trying to achieve higher loads will likely result in very large rates of pressure rise and noisy operation, or shortened engine life. It is the authors' opinion that to minimize noise and keep rates of pressure rise to mechanically tolerable limits, HCCI will probably be limited to very lean operation and therefore lighter load operation. More usual SI or diesel combustion will most likely be needed for other operating regimes. Consequently, exhaust gas aftertreatment to reduce HC, CO, and NO_x emissions will probably still be required to meet emission regulations when the entire engine operational range is considered.

The main objective of this study was to investigate the opera-

Contributed by the Internal Combustion Engine Division of THE AMERICAN SOCIETY OF MECHANICAL ENGINEERS for publication in the ASME JOURNAL OF ENGINEERING FOR GAS TURBINES AND POWER. Manuscript received by the ICE Division, May 23, 2001; final revision received by the ASME Headquarters, December 1, 2001. Editor: D. N. Assanis.

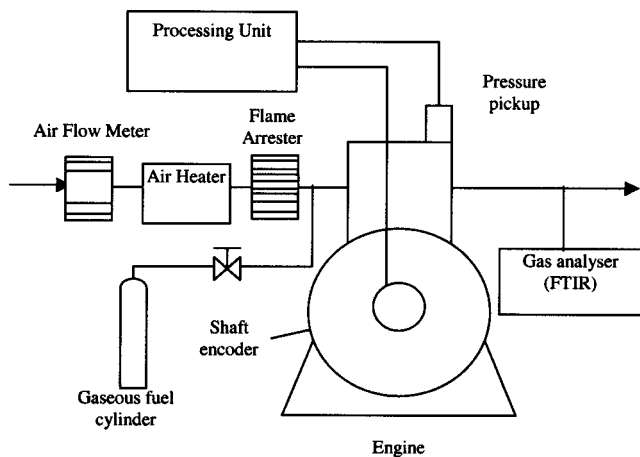


Fig. 1 Diagram of experimental setup

tional characteristics of HCCI combustion. In this work we first define the boundaries of the operational range of HCCI by considering a combination of the stability of the indicated mean effective pressure (IMEP) and the derivative of the pressure in the cylinder ($dP/d\theta$). Second, general properties of HCCI combustion are described, such as IMEP, fuel consumption, and exhaust emissions. Engine speed dependence is also described. Third, the effects of the intake air temperature and compression ratio are investigated as they relate to the operating range determined by the IMEP and ($dP/d\theta$).

Experimental Setup

Figure 1 shows a diagram of the complete engine test cell used in this study. A single-cylinder, four-stroke cycle, cooperative fuels research (CFR) engine was used because of its variable compression ratio mechanism and high durability. Properties of the engine are shown in Table 1. Not shown in the schematic is the surge tank in the intake line, which was used to dampen out flow oscillations caused by the periodic nature of the intake strokes. This engine is designed for the relatively low engine speed of 900 rpm. In this research the engine was run from 600 rpm to 2000 rpm. An intake valve shroud was installed instead of the shrouded valve to eliminate swirl effects on combustion. The compression ratio (CR) of the engine was controlled by vertically changing the relative position of the cylinder in a clamping sleeve. To precisely determine the CR, the clearance between head cylinder and piston at top dead center (TDC) was measured. This engine has a spark plug at the side of the combustion chamber, which was not used during the tests.

The air pressure in the intake system was maintained at 100 kPa by a pressure regulator. The temperature of the intake air was heated using a 3 kW CHROMALOX heater, which was controlled by an Omega series CN77000 temperature controller.

In the experiments reported in this paper, n-butane was used as fuel. n-butane was chosen as a fuel because it has an octane number similar to gasoline. Also, n-butane is considered to have ki-

Table 1 Engine specifications

Compression ratio	4~18
Bore	82.6 mm
Stroke	114.3 mm
Displacement	612 cc
Connecting rod length	254 mm
Exhaust valve open	ATDC140
Exhaust valve close	ATDC5
Intake valve open	ATDC10
Intake valve close	BTDC146

Table 2 Properties of n-butane

Chemical formula	$\text{CH}_3-\text{CH}_2-\text{CH}_2-\text{CH}_3$
Purity	99.5% min.
Molecular weight	58.12
Boiling point	-0.5°C
Lower heating value	45.72 MJ/kg
Heat capacity	1.67 kJ/kg-K
Autoignition temperature	365°C
Octane number	91.8(ROn)

netic similarity to gasoline, because it has a similar reaction scheme of hydrogen abstraction followed by β -scission. Moreover, the reaction schemes have been extensively studied ([17–19]), which will help in understanding what occurs in the combustion chamber through kinetic modeling. The properties of n-butane are shown in Table 2. The flow rate of the fuel was measured with a calibrated rotameter. The fuel was introduced into the intake pipe 180 mm upstream of the intake port.

After the exhaust surge tank, part of the exhaust gas was sampled and routed, through a heated filter and heated line, to a Fourier transform infrared spectrometer (FT-IR) for analysis. The following species were analyzed and recorded quantitatively: H_2O , CO_2 , CO , NO , NO_2 , N_2O , NH_3 , CH_4 (Methane), C_2H_2 (Acetylene), C_2H_4 (Ethylene), C_2H_6 (Ethane), C_3H_6 (Propylene), C_4H_{10} (n-butane), CH_3OH (Methyl alcohol), CH_2O (Formaldehyde), and CH_3CHO (Acetaldehyde). The NO_x concentration was calculated by taking the sum of concentrations of nitrogen oxide and nitrogen dioxide. The total Hydrocarbon (THC) concentration was calculated by summing the concentrations of all species containing carbon, excluding CO and CO_2 , and multiplying by the number of carbon atoms in each species.

The cylinder pressure was measured using a Kistler model 6061B water-cooled pressure transducer. The charge output from this transducer was converted to an amplified voltage using a Kistler model 5010B1 dual mode amplifier. The charge amplifier time constant was set to medium (1–10,000 seconds). The 720 pulses per rotation from a shaft encoder on the engine crankshaft were used as the data acquisition clocking pulses to acquire the pressure data.

Cylinder pressure data was recorded using DSP Technology combustion data acquisition equipment. Data was logged and post-processed with this equipment to obtain a complete set of combustion parameters, such as indicated mean effective pressure (IMEP), 10% to 90% burn duration (B1090), 10% burn location (CA10), maximum rate of pressure rise (MRPR), and coefficient of variation of IMEP (IMEPCOV). In this study, data for over 100 consecutive cycles were recorded, processed, and stored.

Result and Discussion

Operation Range in Homogeneous Charge Compression Ignition (HCCI) Mode. Examples of the pressure data of 100 consecutive cycles are shown in Fig. 2. Note that in both cases the load is very low (low equivalence ratio). For run conditions of higher load, such as shown in (a), the variation of the pressure curve from cycle to cycle was very small. The stability of operation was confirmed by the value of the coefficient of variation of the IMEP (IMEPCOV), which in this case is 1.2%. In addition, the rate of pressure increase ($dP/d\theta$) was very large. The rate of pressure rise ($dP/d\theta$ max) is considered an indicator of noise emitted from the engine and the violence of the combustion. Indeed, it was observed in experiments that the noise became larger as $dP/d\theta$ max increased. Moreover, very loud combustion, which we classified as knock, was often detected at the higher load and it correlated with high rates of pressure rise in the cylinder. Based on our experimental observations, we defined the maximum load limit for HCCI as the combustion condition for which $dP/d\theta$ max = 10[bar/deg].

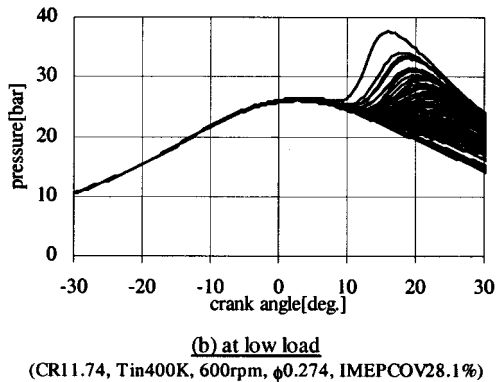
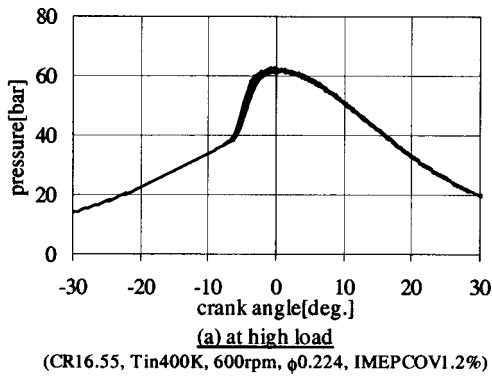


Fig. 2 Pressure data of consecutive 100 cycles

On the other hand, in the case of lower load, such as shown in Fig. 2(b), the IMEPCOV was large (28.1% for this operating condition). For this operating condition the operation of the engine was continuous. We could classify it as steady state. However, as seen in the figure, there was large variation in the combustion timing and energy release rate from cycle to cycle. The cylinder pressure varied significantly from cycle to cycle, within the envelope shown in Fig. 2(b). There could be many reasons for this behavior. For example, if the operating condition of the engine was right on the verge of allowing HCCI combustion, one could get one cycle that reacted very little. This would lead to a larger, cooler exhaust residual, which would be rich with partially reacted fuel and stable intermediates. This “enriched” residual could then promote the next cycle to yield “good” HCCI combustion. The good HCCI combustion would result in the subsequent residual fraction being absent of fuel fragments and stable intermediates, which in turn would result in a poor HCCI cycle that would then lead to a repeat of the sequence. The exact reason for this behavior is subject to conjecture and worthy of further study as one tries to understand the limits of HCCI operation. However, for this work, the observations of Fig. 2(b) led us to conclude that IMEPCOV could be used as a good indicator of combustion stability and a means for defining the lower limit of HCCI operation. Consequently, the minimum load limit for HCCI combustion was defined as being when IMEPCOV = 10%.

An example of the HCCI operating range is shown in Fig. 3. The lines shown on the figure are the upper and lower limit of operation as defined by $dP/d\theta$ max and IMEPCOV. It is clearly shown that the operating range lies on the very lean side of stoichiometric. This is one of the reasons for the high efficiency of HCCI. Though these limits depend on the operating condition, such as the engine speed, the intake air temperature and the compression ratio, the maximum equivalence ratio obtained in this

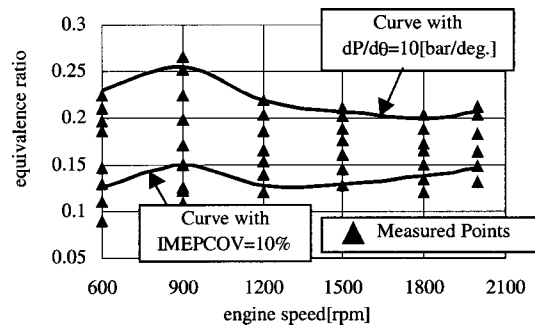


Fig. 3 Operation range (CR=16.55, T_{in} =400 K)

work was still quite lean, approximately 0.37. Such a low maximum equivalence ratio results in low power density. This clearly highlights one of the disadvantages of HCCI.

Indicated Mean Effective Pressure (IMEP), Fuel Consumption, and Exhaust Emission. The general characteristics of the HCCI combustion for fixed conditions will be described in this section. In the results reported below the intake air temperature was held constant at 400 K, the compression ratio was set to 16.55 and the coolant temperature was maintained at 353 K.

Contours of IMEP for these experiments are shown in Fig. 4. It is clearly seen that the maximum IMEP achieved is much lower than usual for SI or DI diesel engines. This is because the equivalence ratio is severely limited to avoid noisy combustion, which is represented by the constraint of $dP/d\theta$ max.

Contours of indicated specific fuel consumption (ISFC) are shown in Fig. 5. The best ISFC for this condition is 220[g/kW-hr]. At another operating condition, it decreases to 175[g/kW-hr]. Assessment of our data indicated that there was a tendency for the best ISFCs to be obtained at the highest load. In this figure, the ISFC at 1200 rpm is the best among the conditions observed. This

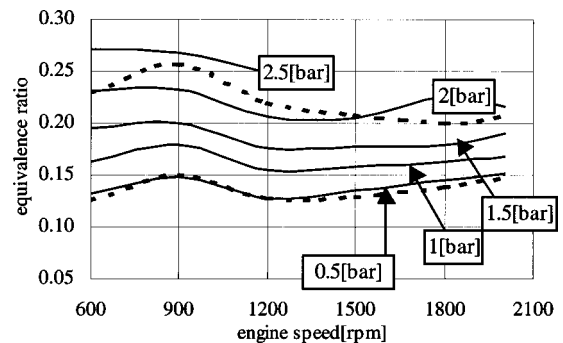


Fig. 4 Contour of IMEP (CR=16.55, T_{in} =400 K.) (Dotted lines show the upper and lower limit of operation.)

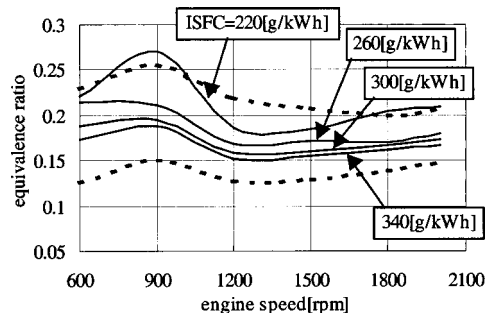


Fig. 5 Contour of ISFC (Cr=16.55, T_{in} =400 K.) (Dotted lines show the upper and lower limit of operation.)

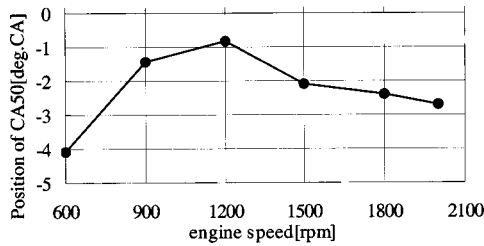


Fig. 6 Position of CA50 (CR=16.55, $T_{in}=400$ K, at maximum load)

can be explained by the position of the heat release. The position at which 50% of the heat release has occurred, CA50, is a good indicator of the relative position of the heat release. CA50 is shown in Fig. 6. It is seen that CA50 occurs before TDC in all conditions, which is probably not ideal, however, CA50 at 1200 rpm is the closest to TDC. This means that negative work of compressing against the reacting mixture is the smallest for the conditions at 1200 rpm. This observation confirms the importance of the position of heat release for thermal efficiency. It also opens up for speculation the possibility of even better fuel economy if the CA50 location could be controlled to a more optimal position after TDC. Since the energy release is controlled by the kinetics, which in turn are controlled by the thermodynamic state, the challenge of controlling HCCI combustion becomes self-evident. How does one obtain an optimal phasing of the energy release, in which the rate of pressure rise and the coefficient of variation are both acceptable, when we have relinquished direct control over the start of combustion?

Figure 6 shows the dependence of CA50 on the engine speed for the case of $T_{in}=400$ K, CR=16.55, maximum load. There is an unusual behavior, especially at speeds greater than 1200 rpm. Initially the position of 50% burned moves closer to TDC as the engine speed increases. Then for engine speeds over 1200 the 50% burned point recedes away from TDC with increases in speed.

The cylinder pressure and temperature histories are significant factors for the autoignition process. For a given pressure and temperature time history there will be a certain kinetic time delay before heat release starts. As the engine speed increases, the time period, in seconds, in which the temperature and pressure are made high by compression, becomes short. If the pressure and temperature history, in crank angles, were the same under all engine speeds, heat release would then occur at later crank angles for higher engine speed, as is the case for engine speeds between 600 and 1200 rpm. But this is not the case. The trend reverses for speeds over 1200 rpm, as shown in Fig. 6. One assessment of these observations would be that the interaction between the kinetics and the pressure and temperature histories, in crank angles, during the compression stroke are engine speed dependent.

The cylinder pressure and temperature histories are determined by the compression ratio, the exhaust residual, the engine speed and the pressure and temperature at intake valve closing (IVC). The pressure in the cylinder was measured in the experiment using a piezoelectric transducer, so it is not the absolute pressure. It is a relative value, referenced to a standard value that needs to be assessed at some point during the cycle. We took a reference value of 100 kPa (absolute) at IVC at 600 rpm. This is the pressure in the intake surge tank, which was controlled via a pressure regulator and quantified relative to the laboratory ambient condition.

The effects of gas dynamics on the value we assigned to the cylinder pressure at intake valve closing, and how it changed with changes in engine speed, were also considered. Gas dynamic effects are smallest at low engine speeds. To adjust for the variation of volumetric efficiency, and other gas dynamic effects, as the engine speed was increased, we adjusted the value of the pressure at intake valve closing, $P(IVC)$, by considering the change in pres-

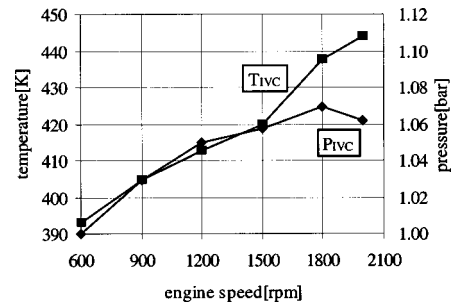


Fig. 7 Change of T_{IVC} and P_{IVC} on engine speed

sure during an early stage of the compression stroke. This was accomplished by normalizing the pressure change between intake valve closing and 90 deg before TDC for speeds greater than 600 to the observed pressure change over this same interval at 600 rpm. This became the adjustment factor for the cylinder pressure at intake valve closing relative to the manifold reference pressure. This procedure is shown below as an equation.

$$P(IVC)_{\text{mod}}^{N \neq 600} = 100[\text{kPa}] \frac{(P(-90)_{\text{obs}}^{N \neq 600} - P(IVC)_{\text{obs}}^{N \neq 600})}{(P(-90)_{\text{obs}}^{N=600} - P(IVC)_{\text{obs}}^{N=600})}$$

where

- N = engine speed (rpm),
- $P(\theta)$ = absolute pressure at crank angle of θ
- obs = observed data,
- mod = modified data,
- θ = crank angle (deg)

The temperature at IVC (T_{IVC}) was calculated using P_{IVC} and the volumetric efficiency, assuming that the gas was ideal. These estimated values of P_{IVC} and T_{IVC} are shown in Fig. 7. The results show that the pressure and temperature in our experiments increase as the engine speed increases. This is one of the phenomena that complicate the speed dependence of CA50, shown in Fig. 6. It is intriguing that the temperature at intake valve closing continues to rise through the entire speed range, while the pressure at intake valve closing continues to rise to a peak at 1800 rpm. The increase in temperature at intake valve closing over the speed range would be consistent with an advancing combustion. This is consistent with the advancing of combustion with increasing speed for engine speeds over 1200 rpm, as seen in Fig. 6. This does not offer an explanation for the retarding of the combustion for speed increases from 600 to 1200 rpm, also seen in Fig. 6. It appears that competing factors affect the start and duration of combustion as engine speed changes. Perhaps the shorter time at the higher temperatures is controlling the combustion initiation for speed increases from 600 rpm to 1200 rpm, at which point the continually increasing temperature starts to become dominant and causes the combustion to advance for speeds greater than 1200 rpm.

HC emission contours are shown in Fig. 8. For these experiments the smallest value of [HC] is 1400 [ppm]. This is a typical result for HCCI combustion, high-unburned hydrocarbon emissions. It was observed that there was a tendency for lower [HC] emissions at the higher load. This is believed to be the result of the combustion being quenched at the light loads and becoming progressively more complete as the load increased. This is consistent with an increase in CO concentrations at lower equivalence ratios (lighter loads).

Dependence of the hydrocarbon speciation on the equivalence ratio is shown in Fig. 9. The species found in the exhaust gas are methane (a very stable hydrocarbon), alkenes (such as ethane (C_2H_4), and propylene (C_3H_6), which are the products of the termination reactions in the oxidation mechanism), and aldehydes

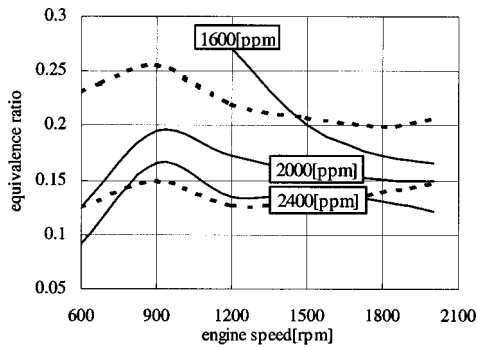


Fig. 8 Contour of HC emission (CR=16.55, $T_{in}=400$ K.) (Dotted lines show the upper and lower limit of operation.)

(formaldehyde (HCHO) and acetaldehyde (CH_3CHO), which have an important role in the oxidation mechanism), as well as n-butane, which is the fuel.

The concentration of intermediate species of combustion rapidly decreases as the equivalence ratio, i.e., load, increases. But the emission of n-butane changes very little with changes in equivalence ratio. At higher load, the amount of products of partial oxidation is small even though a considerable amount of n-butane is emitted. These observations imply that the n-butane emission is a result of crevice volume type storage phenomena. It appears that unreacted fuel is stored somewhere in the combustion chamber, such as in a crevice volume, where it is precluded from reaction. The fuel subsequently reenters the main combustion chamber on the expansion stroke, at a time when the temperatures are lower, and is then emitted from the chamber during the exhaust stroke. Colder areas in the combustion chamber, such as crevices and boundary layers near the wall are candidates for storage regions for the fuel. This assumption is supported by work of Aceves et al. [11], where by numerical analysis the hydrocarbon emission is predicted to come mainly from colder areas. During the operation at the lighter loads, we believe that partial oxidation of the fuel occurring in the bulk gas is responsible for the emission of the intermediate species. As can be seen in Fig. 10, the CO emission increases, as the load gets lighter, indicating progressively more incomplete combustion. The unreacted fuel that is emitted is believed to come from the same source as at higher load, namely cold unreacted regions.

Contours of the concentrations of CO emission are shown in Fig. 10. For these operating conditions the smallest value of [CO] was 3000 [ppm]. There is a similar trend to that observed for the hydrocarbon emissions, that smaller [CO] is obtained at higher load. As inferred in the discussion above, we believe that this is an indication of increased bulk quenching at the lower loads.

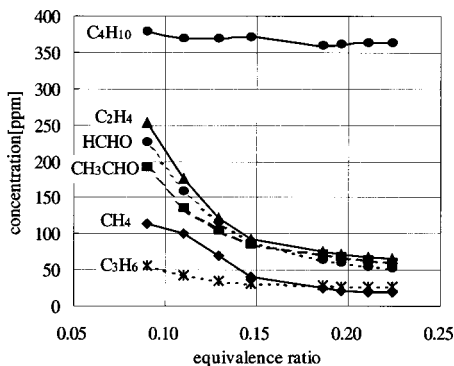


Fig. 9 Concentration of each HC species (CR=16.55, $T_{in}=400$ K, 600 rpm)

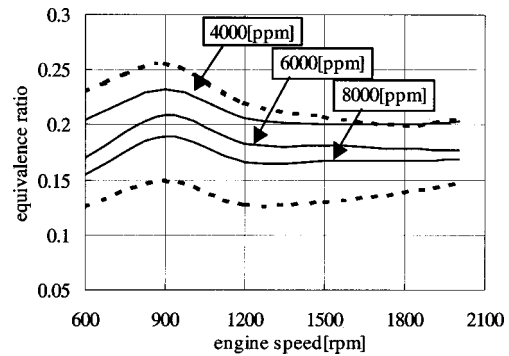


Fig. 10 Contour of CO emission (CR=16.55, $T_{in}=400$ K.) (Dotted lines show the upper and lower limit of operation.)

The dependence of the emission of CO on the equivalence ratio is shown in Fig. 11, along with the emission data for formaldehyde and n-butane. CO exhibits a more complicated dependence on load than n-butane and formaldehyde. This may be explained by the fact that CO emission is determined by the balance between production from hydrocarbon and consumption to CO_2 . However, the gross trend in the CO emission is one of decreasing levels with increasing load.

The NO_x in exhaust gas was below 10 ppm in all cases, which is the lower limit of detection by FTIR used. This suggests that the overall reaction occurs at low temperatures and there are no hot spots, which might be indicative of flame propagation.

Effect of the Compression Ratio. The operational range for different compression ratios is shown in Fig. 12. It is seen that for fixed inlet temperature, the acceptable operating range shifts in the direction of higher engine speed and lower equivalence ratios as

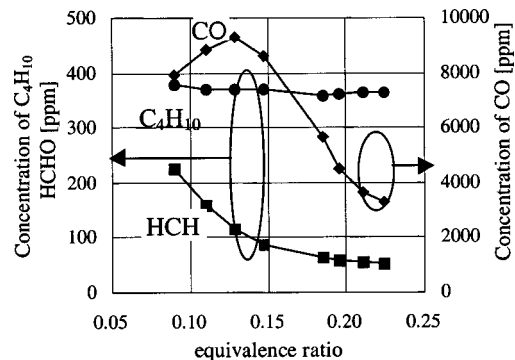


Fig. 11 Concentration of CO (CR=16.55, $T_{in}=400$ K)

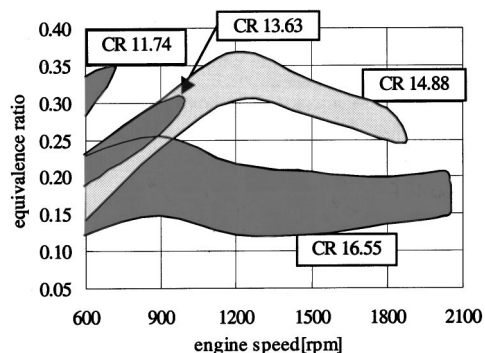


Fig. 12 Operation range with various compression ratio ($T_{in}=400$ K)

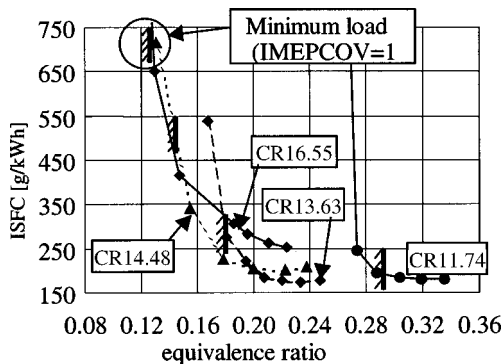


Fig. 13 Dependence of ISFC on equivalence ratio (CR = 16.55, T_{in} = 400 K, 600 rpm)

the compression ratio is increased. This tendency is not surprising, because the temperature and pressure around TDC are higher at higher compression ratios.

A comparison of ISFC for different equivalence ratios and compression ratios is shown in Fig. 13. In each case a value of 10% coefficient of variation in the IMEP (IMEPCOV) is used to mark the edge of the operating condition. It is seen in the figure that at this inlet temperature, lower ISFC is obtained with the higher equivalence ratio for each condition. One interesting point is that for operation with a high compression ratio, the regime in which the IMEPCOV is lower than 10% does not necessarily result in the best ISFC. However, for the low compression ratio of 11.74, low IMEPCOV is conducive to good ISFC. This is a result of the limited operating range for CR = 11.74.

One may view the combustion processes of n-butane very simplistically as a semi-global sequence of two steps: decomposition of the fuel through intermediates to CO and CO oxidation to CO_2 . In the first step, the fuel decomposes to smaller hydrocarbons. This decomposition continues and leads to a concentration of CO. This process is almost thermally neutral, that is only a small portion of the heat release occurs during this first sequence of reactions. It is in the second sequence, where CO oxidizes to CO_2 , that most of energy is released. The ISFC will be most closely linked to the extent to which CO completely oxidizes to CO_2 . If the CO is not completely oxidized the ISFC will be large, even though the reaction sequence may be repeatable, i.e., a low IMEPCOV.

In case of the higher compression ratios, the temperature around TDC is relatively high, which is conducive to initiation of the chemical reactions. However, the equivalence ratios for high compression ratio operation are quite lean. As a result, even as the fuel air mixture begins to react, the energy release will not be very large. Consequently the energy release of the CO oxidation may be only marginally effective in overcoming the cooling effect of expansion from the descending piston. The net result is a stable combustion process that is relatively long in duration. The observed engine results for this operation would be a small IMEPCOV without attaining a minimum in ISFC. It is concluded that when the compression ratio is high and the mixture is very lean, small IMEPCOV is necessary but not sufficient for a small ISFC.

In the case of operation with a low compression ratio, the temperature around TDC is low relative to the higher compression ratio operation. It is conceivable that HCCI operation under this condition is right on the threshold, even though the equivalence ratio is more fuel rich than for higher compression ratio operation. The sequence of the chemistry is the same, however, now slight variations in the compression temperature will have a much more profound impact on whether or not the autoignition chemistry is initiated. If the chemistry doesn't start, combustion fails and operation becomes intermittent, resulting in a high IMEPCOV.

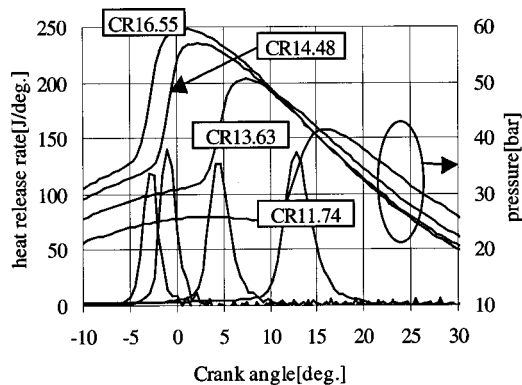


Fig. 14 Comparison of pressure and heat release rate (T_{in} = 400 K, 600 rpm)

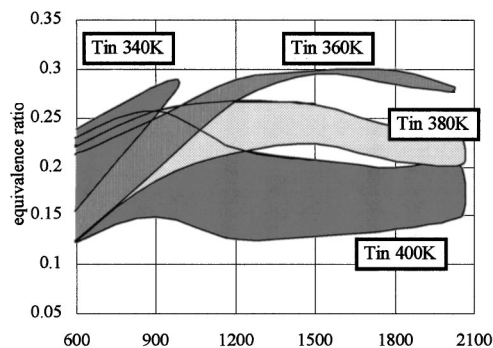


Fig. 15 Operation range with various intake air temperature (CR = 16.55)

Once the chemistry starts, the larger energy release from the higher fuel concentration results in a more optimal combustion duration. The net result is that when operating at the lower compression ratios, with richer equivalence ratios, conditions that lead to low IMEPCOV also result in low ISFC.

Another interesting point in Fig. 13 is that the best ISFC is attained with relatively low compression ratio (13.63) instead of the highest compression ratio. This is explained by the position of the heat release, shown in Fig. 14. In this figure, it is shown that the heat release is completed before TDC for the two higher compression ratio cases. This increases the negative work to the piston during compression. On the contrary, the majority of the heat release occurs after TDC for the operating conditions of the two lower compression ratios. Therefore, it is concluded that compression ratio plays a significant role in determining the efficiency of an HCCI engine through its impact on the start of combustion and the position of the heat release.

Effect of the Intake Air Temperature. The operational ranges with different intake air temperature are shown in Fig. 15. The operational range shifts in the direction of higher engine speed and lower equivalence ratio with an increase of the intake air temperature. This tendency is similar to that seen for the compression ratio. By observing the HCCI operating ranges that could be established through variation in compression ratio, Fig. 12 and through variation of intake temperature, Fig. 15, one concludes that the combination of variable compression ratio with variable intake temperature offers interesting possibilities for extending the HCCI operating range of an engine.

Conclusion

The characteristics of an HCCI engine for a range of intake temperatures, compression ratios and equivalence ratios were in-

vestigated experimentally in a CFR engine using n-butane as a fuel. After studying the data the following conclusions were reached:

(1) For the conditions studied, the HCCI operational range lies on the lean side of stoichiometric, and the range of equivalence ratios for satisfactory operation is very narrow. For example, the equivalence ratio range is between 0.12 and 0.26 for the conditions where the intake temperature is 400 K and compression ratio is 16.55.

(2) HCCI operation was achieved in the CFR engine at a relatively high engine speed, 2000 rpm, with a high compression ratio and a high intake air temperature, 16.55 and 400 K, respectively.

(3) The maximum IMEP obtained in HCCI mode was only 3.5 [bar], which is much lower than that usually obtained in an SI or DI diesel engine.

(4) The minimum ISFC was 175 g/kWh, which is comparable to a DI diesel.

(5) Over the HCCI operating ranges studied the exhaust emissions of HC and CO decreased as the load increased.

(6) The main component of the HC emissions under stable operation was n-butane, the fuel. It is assumed that the unreacted fuel was emitted from the cool areas in the combustion chamber.

(7) It appears that as the load is made lighter bulk quench, or incomplete combustion, is responsible for progressively increasing concentrations of intermediate hydrocarbon species.

(8) Exhaust emissions of NO_x were very low. Under no operating condition did they exceed 10 ppm.

References

- [1] Suzuki, H., Koike, N., Ishii H., and Odaka, M., 1997, "Exhaust Purification of Diesel Engines by Homogeneous Charge With Compression Ignition Part 1: Experimental Investigation of Combustion and Exhaust Emission Behavior Under Pre-Mixed Homogeneous Charge Compression Ignition Method," SAE Paper No. 970313.
- [2] Onishi, S., Jo, S. H., Shoda, K., Jo, P. D., and Kato, S., 1979, "Active Thermo-Atmosphere Combustion(ATAC)—A New Combustion Process for Internal Combustion Engines," SAE Paper No. 790501.
- [3] Noguchi, M., Tanaka, Y., Tanaka, T., and Takeuchi, Y., 1979, "A Study on Gasoline Engine Combustion by Observation of Intermediate Reaction Products during Combustion," SAE Paper No. 790840.

- [4] Najt, P., and Foster, D. E., 1983, "Compression-Ignited Homogeneous Charge Combustion," SAE Paper No. 830264.
- [5] Thring R. H., 1998, "Homogeneous-Charge Compression-Ignition (HCCI) Engines," SAE Paper No. 892068.
- [6] Takatsuto, R., Igarashi, T., and Iida, N., 1998, "Auto Ignition and Combustion of DME and n-Butane/Air Mixtures in Homogeneous Charge Compression Ignition Engine," *Proceedings of the Fourth International Symposium COMODIA 98*, JSME, Tokyo, pp. 185–190.
- [7] Furutani, M., Ohta, Y., Kono, M., and Hasegawa, M., 1998, "An Ultra-Lean Premixed Compression-Ignition Engine Concept and Its Characteristics," *Proceedings of the Fourth International Symposium COMODIA 98*, JSME, Tokyo, pp. 173–177.
- [8] Ohta, Y., 1998, "Fundamental Theory of HCCI Engines," *Proceedings of the 74th National JSME Conference*, VI, pp. 334–335 (in Japanese).
- [9] Igarashi, T., and Iida, N., 1998, "N-butane and DME Autoignition and Combustion Process in HCCI Engine," *Trans. Jpn. Soc. Mech. Eng., Ser. B*, **64**, pp. 605–612 (in Japanese).
- [10] Yamasaki, Y., and Iida, N., 2000, "Numerical Simulation of Auto-Ignition and Combustion of n-Butane and Air Mixtures in a 4-Stroke HCCI Engine by Using Elementary Reactions," SAE Paper No. 2000-01-1834.
- [11] Aceves, S. M., Flowers, D. L., Westbrook, C. K., Smith, J. R., Pitz, W., Dibble, R., Christensen, M., and Johansson, B., 2000, "A Multi-Zone Model for prediction of HCCI Combustion and Emissions," SAE Paper No. 2000-01-0327.
- [12] Fiveland S. B. and Assanis, D. N., 2000, "A Four-Stroke Homogeneous Charge Compression Ignition Engine Simulation for Combustion and Performance Studies," SAE Paper No. 2000-01-0332.
- [13] Christensen, M., Johansson, B., and Einewall, P., 1997, "Homogeneous Charge Compression Ignition (HCCI) Using Isooctane, Ethanol and Natural Gas—A Comparison With Spark Ignition Operation," SAE Paper No. 972874.
- [14] Christensen, M., Johansson, B., Amneus, P., and Mauss, F., 1998, "Supercharged Homogeneous Charge Compression Ignition" SAE Paper No. 980787.
- [15] Christensen, M., and Johansson, B., 1998, "Influence of Mixture Quality on Homogeneous Charge Compression Ignition," SAE Paper No. 982454.
- [16] Christensen, M., Hultqvist, A., and Johansson, B., 1999, "Demonstrating the Multi Fuel Capability of a Homogeneous Charge Compression Ignition Engine With Variable Compression Ratio," SAE Paper No. 1999-01-3679.
- [17] Kojima, S., and Suzuoki, T., 1993, "Autoignition-Delay Measurement Over Lean to Rich Mixtures of n-Butane/Air Swirl Conditions," *Combust. Flame*, **92**, pp. 254–265.
- [18] Kojima, S., 1994, "Detailed Modeling of n-Butane Autoignition Chemistry," *Combust. Flame*, **99**, pp. 87–136.
- [19] Warth, V., Stef, N., Glaude, P. A., Battin-Leclerc, F., Scacchi, G., and Come, G. M., 1998, "Computer Aided Design of Gas-Phase Oxidation Mechanism: Application to the Modeling of the Oxidation of n-butane," *Combust. Flame*, **114**, pp. 81–102.

Modeling the Initial Growth of the Plasma and Flame Kernel in SI Engines

H. Willems

e-mail: Hilde.Willems@hogent.be

R. Sierens

e-mail: Roger.Sierens@rug.ac.be

Laboratory of Transporttechnology,
Ghent University,
Sint-Pietersnieuwstraat 41,
B-9000 Ghent, Belgium

The initial size and growth of the plasma and flame kernel just after spark discharge in S.I. engines determines if the flame becomes self-sustainable or extinguishes. On the other hand, the development of the kernel during the initial phases has non-negligible influences on the further combustion. For example, cyclic variations often find their origin in the beginning of combustion and determine the working limits of the engine and the driving behavior of the vehicle. These factors demonstrate the crucial importance of the knowledge of the initial growth of the plasma and flame kernel in S.I. engines. A complete model is developed for the growth of the initial plasma and flame kernel in S.I. engines, which takes into account the fundamental properties of the ignition system (electrical energy and power, geometry of the spark plug, heat losses to the electrodes and the cylinder wall), the combustible mixture (pressure, temperature, equivalence ratio, fraction of residual gasses, kind of fuel), and the flow (average flow velocity, turbulence intensity, stretch, characteristic time and length scales). The proposed model distinguishes three phases: the pre-breakdown, the plasma, and the initial combustion phase. The model of the first two phases is proposed in a previous article of the same authors [1], the latter is exposed in this article. A thermodynamic model based on flamelet models and which takes stretch into account, is used to describe the initial combustion phase. The difference between heat losses to the electrodes and the cylinder wall is considered. The burning velocity varies from the order of the laminar velocity to the fully developed burning velocity. The evolution is determined as well by the life time as by the size of the kernel. The stretch (caused by turbulence and by the growth of the kernel), the nonadiabatic character of the flame, and instabilities have influence on the laminar burning velocity. Validation of this model is done using measurements of the expansion in a propane-air mixture executed by Pischinger [2] at M.I.T. The agreement seems very good.

[DOI: 10.1115/1.1501912]

Introduction

The expansion during the first moments after ignition in a S.I. engine determines if the flame becomes self-sustainable or extinguishes. On the other hand, the early development has also non-negligible influences on the further combustion. Cyclic variations often find their origin in the beginning of combustion and determine the working limits of the engine and the driving behavior of the vehicle. The knowledge of the initial growth of the plasma and flame kernel in S.I. engines is therefore of crucial importance.

For this purpose in this article a numerical model is presented which describes the initial growth of the plasma and flame kernel in S.I. engines.

The birth of the flame kernel is a very complex process. Different mechanisms stimulate the growth of the kernel. An electrical spark will cause breakdown in an isolating medium. A conductive plasma channel is formed with a high pressure and temperature. A shock wave and heat conduction and diffusion allow the kernel to expand before the combustion reactions take over and the combustion will become self-sustainable.

For the initial development of the kernel three phases can be distinguished: the pre-breakdown phase (closed by breakdown), the plasma phase (expansion determined by shock wave and heat conduction), and the initial combustion phase (expansion determined by exothermic combustion reactions).

Contributed by the Internal Combustion Engine Division of THE AMERICAN SOCIETY OF MECHANICAL ENGINEERS for publication in the ASME JOURNAL OF ENGINEERING FOR GAS TURBINES AND POWER. Manuscript received by the ICE Division May 2001; final revision received by the ASME Headquarters Feb. 2002. Associate Editor: D. Assanis.

Pre-breakdown phase

Initially the gas between the electrodes is a perfect isolator. If a voltage is applied between the electrodes, the electrons in the spark gap accelerate from the cathode and the anode. Collisions with gas molecules ionize these, new electrons are produced. If the number of electrons increases sufficiently to make the discharge self-sustainable, breakdown takes place and the pre-breakdown phase is closed. A very small conductive path is formed between the electrodes with a high pressure (around 20 MPa) and temperature (around 60,000 K).

A detailed description and the mathematical model for the pre-breakdown phase can be found in a previous article of the same authors [1].

Plasma Phase

At the end of the pre-breakdown phase the plasma channel is not in equilibrium. The very high pressure and temperature of the channel compared with the surrounding gas causes an immediate expansion of the channel, first by a shock wave and later by heat conduction.

In S.I. engines it is the purpose to study combustible mixtures. The question has to be posed if exothermic burning reactions don't have to be considered and if they cause expansion of the plasma. Indeed combustion reactions (self-ignition) take place at temperatures lower than the inversion temperature, so only at the

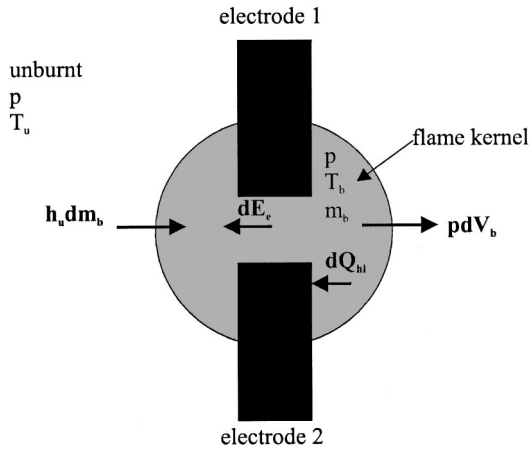


Fig. 1 Thermodynamic model of the flame kernel during the initial combustion phase

border of the plasma. In a very small channel with a high temperature the expansion is dominated by thermal conduction and the combustion reactions can be neglected. If the temperature decreases, these reactions become more and more important. If the expansion by these combustion reactions prevails, the plasma phase is closed and the initial combustion phase starts (transition from self-ignition to flame propagation).

A detailed description and the mathematical model for the plasma phase can be found in a previous article of the same authors [1].

Initial Combustion Phase

In the initial combustion phase the combustion reactions dominate the expansion of the kernel. The kernel is no longer a plasma kernel, but can be called a flame kernel. This kernel has to be sufficiently large, to make it possible that the burning reactions can gain the opposite effects of the heat losses and flame stretch to ignite the mixture successfully. Ignition takes place if the expansion becomes self-sustainable. The burning reactions are then sufficiently powerful to lead the expansion of the kernel without supplementary energy supply.

In this article the mathematical model for the initial combustion phase is described profoundly.

Equations. To model the initial combustion phase the following assumptions are made:

- The system is in thermodynamic equilibrium.
- The pressure is uniform in burned and unburned.
- The general gas law is applicable.
- The flame kernel is much smaller than the cylinder.
- The burned gas is in chemical equilibrium at each moment.
- The temperature of the kernel is sufficiently low. The burning reactions dominate the expansion of the kernel and the influence of thermal conduction and diffusion from the burned to the unburned is minimal.

The model starts from mass and energy conservation and from the first law of thermodynamics. The thermodynamic system of the flame kernel is given in Fig. 1.

The heat losses of the kernel to the surrounding unburned gas are not taken into account in the conservation of energy. This simplification is acceptable if the delivered chemical energy is much larger than the heat losses. Because the initial combustion phase is modeled and the plasma phase is already closed, the temperature of the kernel is sufficiently low, the simplification is justified.

The change in enthalpy of the system depends on the change in internal energy and the volume work:

$$\frac{d}{dt}(m_b h_b) = m_b \frac{dh_b}{dt} + h_b \frac{dm_b}{dt} = \frac{dU}{dt} + p \frac{dV_b}{dt} + V_b \frac{dp}{dt} \quad (1)$$

Mass conservation gives

$$\frac{dm_b}{dt} = \frac{d}{dt}(\rho_b V_b) = \rho_u A_b S_t \quad (2)$$

and energy conservation

$$\frac{dU_b}{dt} = \frac{dQ_{ch}}{dt} + \frac{dE_e}{dt} - \frac{dQ_{hl}}{dt} - p \frac{dV_b}{dt} \quad (3)$$

Taking the general gas law into account and the definition of the reaction heat

$$\frac{dQ_{ch}}{dt} = h_u \frac{dm_b}{dt}, \quad (4)$$

Eqs. (1), (2), and (3) deliver after some calculation the following set of equations to calculate the evolution of the temperature and the radius of the flame kernel with time:

$$\frac{dT_b}{dt} = \frac{1}{c_{p,b}} \frac{h_u - h_b}{\rho_b V_b} \rho_u A_b S_t + \frac{1}{c_{p,b} \rho_b V_b} \left(\frac{dE_e}{dt} - \frac{dQ_{hl}}{dt} \right) + \frac{1}{c_{p,b} \rho_b} \frac{dp}{dt} \quad (5)$$

$$\frac{dr_b}{dt} = \frac{\rho_u}{\rho_b} S_t + \frac{V_b}{A_b} \left(\frac{1}{T_b} \frac{dT_b}{dt} - \frac{1}{p} \frac{dp}{dt} \right) \quad (6)$$

Initial Conditions. The initial conditions to model the initial combustion phase follow out of the solution from the plasma phase [1]. But the exact moment of transition between these two phases (the moment at which combustion reactions can't be neglected anymore) still has to be fixed.

During the plasma phase self-ignition reactions are started where the temperature is lower than the inversion temperature. After a certain self-ignition delay combustion takes place. The expansion of the plasma is determined by a shock wave and a series of expansion waves caused by heat conduction and diffusion. As long as the expansion stays supersonic, a flame cannot be formed and the expansion by self-ignition is neglected. Flame propagation is a subsonic phenomena that can determine the expansion of the kernel only if the Mach number is smaller than 1.

The moment the combustion starts to dominate, is correlated in the model with the adiabatic flame temperature. That temperature is in fact a measure of the chemical energy that can be liberated by combustion. An average temperature of the kernel equal to the threefold of the adiabatic flame temperature

$$T_{tr} = 3T_{ad} \quad (7)$$

seems to agree with the moment the expansion velocity of the plasma becomes equal to the sound velocity. In the model this temperature is considered as the transition temperature between the plasma and initial combustion phase T_{tr} . At that moment the expansion of the kernel calculated with the plasma model is almost equal to the expansion calculated with the model of the initial combustion phase. The choice of the transition temperature is not really critical. Increasing or decreasing the transition temperature with some hundreds Kelvin, seems to have only a minimal effect on the further simulation of the combustion. Shen, Hinze, and Heywood [3] choose the same approach to determine the moment at which the combustion reactions start to dominate the expansion.

Numerical Solution Method. The purpose of this study is to integrate the simulation for the ignition in an existing simulation model of the total combustion cycle in S.I. engines developed at the Department of Flow, Heat, and Combustion Mechanics at the

University of Gent, Belgium [4]. The same solution method for the differential equations is chosen: a fourth-order Runge Kutta method.

Heat Losses to the Electrodes. The heat losses are calculated by

$$\frac{dQ_{hl}}{dt} = h_c A_c (T_b - T_w) \quad (8)$$

wherein the losses by radiation are neglected as generally accepted in S.I. engines. A detailed discussion about the difference in heat losses to the cylinder wall and the electrodes by one of the authors can be found elsewhere [7], the conclusion for the calculation of the convection coefficient to the electrodes is

$$h_c = \frac{\lambda_b}{3.25 \delta_l} \quad (9)$$

with the thickness of the laminar flame front δ_l

$$\delta_l = \frac{\alpha_u}{S_l} \quad (10)$$

Turbulent Burning Velocity. Herweg and Maly [5] adapted the normally used flamelet models to the beginning of combustion. At that moment the combustion is not yet influenced by the whole frequency spectrum of the turbulence in the flow. For a small flame kernel the integral length scale L of the turbulent flow is larger than the kernel, the kernel can only be affected by the high-frequency part of the turbulence spectrum. On the other hand, also a characteristic time scale seems to be necessary to wrinkle the flame front.

In laminar flamelet models the turbulent flame is composed of small flamelets, wherein the combustion is laminar but stretched. The turbulent burning velocity is normally determined by [6]:

$$S_t = 2\sqrt{D_t S} \quad (11)$$

To calculate the turbulent burning velocity in the beginning of combustion the laminar stretched burning velocity $S_{l,s}$ has to be taken into account:

$$S_t = S_{l,s} + 2\sqrt{D_t S} \quad (12)$$

or

$$S_t = I_s S_l + 2\sqrt{D_t S} \quad (13)$$

For very small kernels the second term is negligible compared with the first, for larger flame kernels the influence of turbulence increases. Herweg and Maly [5] indicate that the turbulent diffusion for a small flame kernel can be calculated with

$$D_t = \frac{u'(\bar{U}^2 + u'^2)^{\frac{1}{2}}}{(\bar{U}^2 + u'^2)^{\frac{1}{2}} + S_l} L \left[1 - \exp\left(-\frac{r_b}{L}\right) \right] \times \left[1 - \exp\left(-\frac{(\bar{U}^2 + u'^2)^{\frac{1}{2}} + S_l}{L} t\right) \right] \quad (14)$$

The reaction velocity S (per time unit) in flow fields in engines is [5]

$$S \approx \frac{u' I_s}{4L} \left(1 + \frac{4.4}{1 + 3.919(u'/S_l)} \right) \quad (15)$$

if

$$1 < \frac{u'}{S_l} < 10. \quad (16)$$

For

$$0 \leq \frac{u'}{S_l} \leq 5 \quad (17)$$

holds

$$\frac{u'}{S_l} \left(1 + \frac{4.4}{1 + 3.919(u'/S_l)} \right)^{\frac{1}{2}} \approx \left(\frac{u'}{S_l} \right)^{\frac{5}{6}} \quad (18)$$

This gives for the turbulent burning velocity

$$\frac{S_t(r_b, T_b, t)}{S_l} = I_s + I_s^{\frac{1}{2}} \left[\frac{(\bar{U}^2 + u'^2)^{\frac{1}{2}}}{(\bar{U}^2 + u'^2)^{\frac{1}{2}} + S_l} \right]^{\frac{1}{2}} \left[1 - \exp\left(-\frac{r_b}{L}\right) \right]^{\frac{1}{2}} \times \left\{ 1 - \exp\left[-\frac{(\bar{U}^2 + u'^2)^{\frac{1}{2}} + S_l}{L} t\right] \right\}^{\frac{1}{2}} \left(\frac{u'}{S_l} \right)^{\frac{5}{6}} \quad (19)$$

The influence of turbulence increases with the size and life time of the flame kernel. During the initial combustion the integral length scale is larger than the diameter of the kernel. Only the high-frequency spectrum of turbulence has influence on the growth of the kernel. The effective length scale can only be equal to the integral length scale, if the whole turbulence spectrum wrinkles the flame front. For smaller kernels the effective length scale L_b is only a fraction of the integral length scale L as can already be seen in (19):

$$L_b = L \left[1 - \exp\left(-\frac{r_b}{L}\right) \right] \quad (20)$$

The average flow velocity \bar{U} and the turbulence intensity u' influence the turbulent burning velocity via the characteristic time scale T_t

$$T_t = \frac{L}{(\bar{U}^2 + u'^2)^{\frac{1}{2}} + S_l} \quad (21)$$

Larger values of \bar{U} , u' and S_l and smaller values of L introduce a smaller characteristic time scale, the flame behaves sooner as a fully turbulent flame. The influence of turbulence is only complete after a period depending on the characteristic time scale combined with a minimal size of the flame kernel depending on the integral length scale of the flame. Two aspects are important to determine the influence of turbulence on combustion. First of all the size of the flame kernel determines in which measure turbulence can wrinkle the flame front but, on the other hand, wrinkling requires some time. Only if the time span that the flame kernel is exposed to the turbulence is sufficiently large, the turbulent flow can affect the kernel completely.

To calculate the turbulent burning velocity the model formula (19) is used, therefore it is necessary to know the laminar unstretched burning velocity S_l and the influence factor of stretch I_s . In the next paragraph the calculation of these factors is explained.

The Laminar Burning Velocity

The Laminar Burning Velocity Under Adiabatic, Unstretched, and Stable Conditions. Many formulas are derived from experimental research to calculate the laminar burning velocity. The measurements are not always done under adiabatic, unstretched, and stable conditions. This declares the spread in the results. One of the authors made a comparison between the formulas in the literature to calculate this velocity for propane, iso-octane, indolene, methane, and hydrogen [7]. For propane the formula of Metghalchi and Keck [8] is preferred:

$$S_l = S_{l0} \left(\frac{T_u}{298 \text{ K}} \right)^{\alpha} \left(\frac{p}{0.1 \text{ MPa}} \right)^{\beta} (1 - 2.1f) \quad (22)$$

with

$$\begin{aligned}\alpha &= 2.18 - 0.8(\phi - 1) \\ \beta &= -0.16 + 0.22(\phi - 1) \\ S_{l0} &= [0.3422 - 1.3865(\phi - 1.08)^2] \frac{m}{s}\end{aligned}\quad (22)$$

for an equivalence ratio ϕ between 0.8 and 1.5, a pressure p between 0.1 MPa and 5 MPa, a temperature of the unburned T_u between 350 K and 700 K, and a mass fraction of residual gas lower than 20%.

Influence of Stretch on the Laminar Burning Velocity. Three factors can cause stretch of a flame kernel [9,10]: aerodynamic stretch (caused by the variations in flow along the surface), the variation in curve of the surface and the growth of the flame. In the laminar flamelet model the combustion is supposed to be laminar, but stretched on the scale of the flamelets. On that scale the stretch caused by the curve of the flame front introduced by the surrounding flow can be neglected, only the influence of the flow along the surface and the growth of the flamelets have to be taken into account to calculate the influence of stretch. The stretch factor K is

$$K = \frac{1}{A} \frac{dA}{dt} + \frac{u'}{\lambda_T} \quad (23)$$

The first term is the laminar stretch and the second the aerodynamic stretch caused by turbulence. The dimensionless stretch factor or the Karlovitz number becomes

$$Ka = \frac{\delta_l}{S_l} K \quad (24)$$

The influence of stretch on the laminar burning velocity is represented by I_s :

$$S_{l,s} = I_s(Ka)S_l \quad (25)$$

Law [9] proves that the influence of stretch on the laminar burning velocity can be calculated from

$$I_s = 1 - \frac{Ka}{Le} + \left(\frac{1}{Le} - 1\right) \frac{KaT_a}{2T_{ad}} \quad (26)$$

Taking (5), (6), (23), (24) and [11]

$$\frac{\lambda_T}{L} = \sqrt{15} \left(\frac{u'L}{\nu}\right)^{-\frac{1}{2}} \quad (27)$$

into account, the stretch factor becomes

$$\sqrt{I_s} = \frac{-BCDS_l \pm \sqrt{(BCDS_l)^2 - 4(BE - F)(1 + BDS_l)}}{2(1 + BDS_l)} \quad (28)$$

with

$$B = n \frac{\delta_l}{S_l} \frac{1}{r_b} \left[\frac{1}{Le} + \left(\frac{Le-1}{Le}\right) \frac{T_a}{2T_{ad}} \right] \quad (29)$$

$$\begin{aligned}C &= \left[\frac{(\bar{U}^2 + u'^2)^{\frac{1}{2}}}{(\bar{U}^2 + u'^2)^{\frac{1}{2}} + S_l} \right]^{\frac{1}{2}} \left[1 - \exp\left(-\frac{r_b}{L}\right) \right]^{\frac{1}{2}} \\ &\times \left\{ 1 - \exp\left[-\frac{(\bar{U}^2 + u'^2)^{\frac{1}{2}} + S_l}{L} t\right] \right\}^{\frac{1}{2}} \left(\frac{u'}{S_l}\right)^{\frac{5}{6}}\end{aligned}\quad (30)$$

$$D = \frac{\rho_u}{\rho_b} + \frac{h_u - h_b}{T_b \rho_b c_{p,b}} \rho_u \quad (31)$$

$$E = \frac{V_b}{A_b} \left(\frac{1}{T_b} \frac{dE_e/dt - dQ_{hl}/dt}{\rho_b V_b c_{p,b}} + \frac{1}{T_b \rho_b c_{p,b}} \frac{dp}{dt} - \frac{1}{p} \frac{dp}{dt} \right) \quad (32)$$

$$F = 1 - \left(\frac{\delta_l}{15L} \right)^{\frac{1}{2}} \left(\frac{u'}{S_l} \right)^{\frac{3}{2}} \left[\frac{1}{Le} + \left(\frac{Le-1}{Le}\right) \frac{T_a}{2T_{ad}} \right] \quad (33)$$

Influence of the Nonadiabaticity on the Laminar Burning Velocity. The nonadiabatic character of the combustion has in the first place consequences on the electrical energy supply E_e and the heat losses Q_{hl} of Eqs. (5) and (6) but, on the other hand, there will be a change in the mass that's burned per time unit, because the temperature influences the burning velocity. From a comparison between different researchers [2,3,12,13] the authors define the influence of the nonadiabaticity on the laminar velocity as follows [7]:

$$S_{l,nad} = I_{nad} S_{l,ad} \quad (34)$$

with

$$I_{nad} = \sqrt{\frac{T_{mad}}{T_m}} \exp\left[-\frac{E_a}{2\mathfrak{R}} \left(\frac{1}{T_m} - \frac{1}{T_{mad}}\right)\right] \quad (35)$$

$$T_m = \frac{T_u + T_f}{2} \quad (36)$$

$$T_{mad} = \frac{T_u + T_{ad}}{2} \quad (37)$$

$$T_f = \frac{-b + \sqrt{b^2 - 4ac}}{2a} \quad (38)$$

$$\begin{cases} a = \rho_u c_{p,b} S_{l,ad} r_b \\ b = 2\lambda_b (T_{ad} - T_q) - \rho_u c_{p,b} S_{l,ad} (T_{ad} + T_q) r_b \\ c = -2\lambda_b (T_{ad} - T_q) T_b + \rho_u c_{p,b} S_{l,ad} T_{ad} T_q r_b \end{cases} \quad (39)$$

Instability of the Flame. Two types of instability can be distinguished. Aerodynamic stretch can lead to thermodiffusive instability. If the Lewis number is smaller than a critical value (smaller than 1), the flame gets a cellular structure that causes an exponential increase of the burning velocity. On the other hand, hydrodynamic instability is caused by the interaction of the flame and hydrodynamic disturbances, generated by the flame itself by thermal expansion. If the Lewis number is larger than the critical Lewis number, thermodiffusive effects hold the flame stable until a critical flame radius is reached. The critical Peclet number makes it possible to calculate this critical flame radius.

In S.I. engines under normal conditions thermodiffusive stable mixture are used and for sufficiently small kernel also hydrodynamic stability can be neglected. In this work the supposition is made that both kinds of stability's can be let out of consideration.

Experimental Validation of the Model

Description of the Experiments. To verify the model of initial plasma and flame growth in S.I. engines it is necessary to have detailed measurements of the initial flame growth. On the other hand, also the knowledge of the operation conditions of the engine, the flow around the spark plug, the energy supply, the shape of the spark plug,... are indispensable. The measurements done by Pischinger [2] at the Massachusetts Institute of Technology at the end of the 1980s are very interesting for this purpose because the initial flame growth is measured in a propane-air mixture under well-known working conditions and surrounding parameters.

A transparent visualization engine with a square piston is used for this purpose. During the initial phases of combustion the development of pressure by combustion is so small that it becomes difficult to get accurate information about the initial development

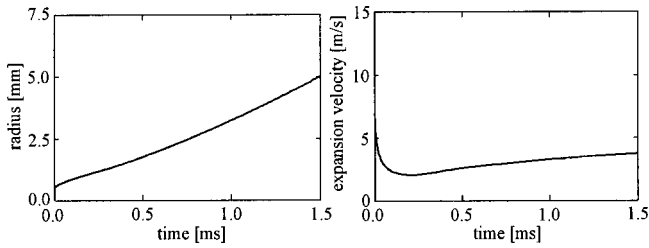


Fig. 2 Evolution of the radius and the expansion velocity of the flame kernel with time for working conditions MIT2te

of combustion out of pressure measurements. Conventional visualization techniques (direct or Schlieren photography) have another important disadvantage: a limited resolution along the vision line. To reduce this uncertainty, a special Schlieren setup is used which takes simultaneously two orthogonal images of the flame. The detailed description of the engine and the measurement equipment can be found elsewhere ([14,15]). The comparison between experimental and simulated results is done for two series of working conditions, each for three types of spark plug (MIT1te and MIT2te with the spark-plug with thin electrodes, MIT1bd and MIT2bd with a breakdown spark-plug, MIT1ps and MIT2ps with the spark-plug with a projecting surface gap). The description of the spark-plug and the working conditions can be found in [7].

Results. Before comparing simulation and experiment, the development of the radius of the flame kernel in time is discussed in detail for one series of working conditions. The conclusions are however generally applicable to simulation results of the same type.

In Fig. 2, respectively, the evolution of the radius of the plasma and flame kernel r_b and the expansion velocity S_b with time is seen for the second series of working conditions and with the use of spark plugs with thin electrodes (MIT2te). The expansion velocity is defined as

$$S_b = \frac{dr_b}{dt} \quad (40)$$

The evolution is characteristic for a normal kernel growth in a S.I. engine. The expansion velocity starts at very high values and decreases fast until a minimum is attained. The expansion velocity begins to increase. After a certain time it seems like a maximum is reached and the expansion velocity stays almost constant. This evolution is also seen during experiments.

Four different regimes can be discovered:

- Spark breakdown and kernel initiation: the expansion velocity falls down from very high values to a minimum at around $300 \mu\text{s}$ after breakdown and a radius of around 1.5 mm.
- Passing through a minimum in the expansion velocity: the survival of the flame kernel is controlled by the balance of the decreasing influence of the plasma, the increasing contribution of the combustion and the crossing effect of the flame stretch.
- Wrinkling of the flame front: after the minimum the surface of the flame is wrinkled by the turbulent flow field. The wrinkling is controlled by characteristic time and length scales, respectively, depending on the life time and the size of the kernel.
- Fully developed turbulent flame propagation: if the radius of the flame kernel exceeds the integral length scale, the flame velocity approaches the value of a freely expanding turbulent flame.

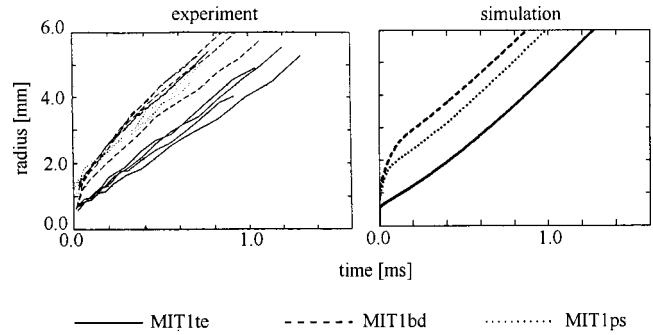


Fig. 3 Comparison between experimental and simulated flame growth for the first working conditions

It is possible that the flame doesn't become fully turbulent, but quenches. The expansion velocity decreases continuously until its value becomes zero. The heat delivered by the combustion reactions isn't sufficient to compensate heat losses.

On the other hand, if the supplied electrical energy is sufficiently high and the heat losses small, the expansion velocity becomes a monotonous function in time and doesn't show a minimum.

The results of the experiments and simulation can be found in Fig. 3 for the working conditions MIT1te, MIT1bd and MIT1ps and Fig. 4 for the working conditions MIT2te, MIT2bd, and MIT2ps. Each experiment is repeated about five times, the experimental evolution of the flame kernel is given about five times for each condition. Caused by cyclic variations a spread in the radius evolution can be seen on the figure. The correspondence between measurements and simulations seems to be good to very good.

The discussion shows that the proposed model is a valuable instrument to analyze the initial growth of the plasma and flame. Besides the example above proves that it's necessary to take the energy supply, the spark plug design, the local flow properties,... into account to get a correct image of the combustion. These characteristics determine the limits for successful combustion.

At the Department of Flow, Heat and Combustion Mechanics of the University of Gent a complete simulation model is developed for the thermodynamic and gasdynamic cycle of S.I. engines. The model of the combustion process is derived from the model of Tabaczynski. The study has the purpose to eliminate the ignition delay used in that model for the initial combustion phase. It is replaced by a more detailed model of the expansion of the plasma and the initial flame kernel. In reality the ignition delay in a S.I. engine has no physical meaning. There is no delay between the spark and the beginning of the growth of the plasma and the flame kernel. The ignition delay in the model of Tabaczynski is defined as the time between the spark and the moment of measurable heat production, which corresponds with the moment on which 1% of the cylinder mass is burnt. To calculate the ignition delay a pa-

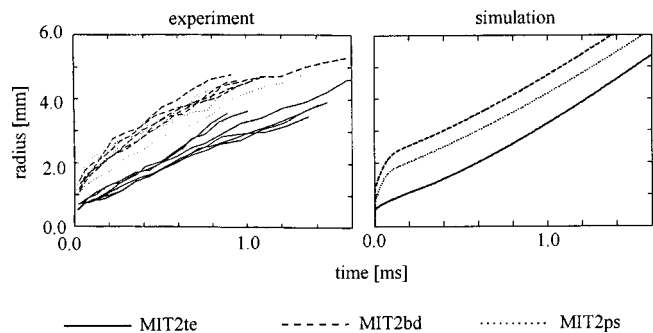


Fig. 4 Comparison between experimental and simulated flame growth for the second working conditions

parameter, which is said to be dependent of the engine, but independent of the working conditions, has to be determined by experiment. Willems [7] proves that this parameter can only be considered as constant for small variations of rotation speed and preignition. Also the equivalence factor and the ignition pressure can't sustain changes of more than 20%. The model developed in this study doesn't has these limitations. Above this model has the advantage that no parameter without physical meaning has to be determined. Conclusions for improving the combustion are therefore much easier derived than with a model which used an ignition delay.

Conclusion

In this article a relatively simple one-dimensional model is developed to simulate the growth of the plasma kernel and the initial flame in S.I. engines taking into account the detailed properties of the ignition system, the inflammable mixture and the flow, which means a big step forwards in the combustion of S.I. engines. This model starts from the very beginning, namely the plasma channel caused by spark breakdown and distinguishes three phases: the pre-breakdown phase, the plasma phase, and the initial combustion phase. Once and forever the notion ignition delay is thrown away for S.I. engines. In reality there is no ignition delay, so it has no sense to define that in models just to put some initial conditions. This is a big step forwards, because the influence factors on the initial expansion can now be adapted for an optimal combustion (increasing efficiency, decreasing fuel consumption, improving the quality of the exhaust gases,...).

Nomenclature

A	= surface
A_c	= contacting surface between the burned gas on one hand and the cylinder wall and/or electrodes on the other hand
b	= burned mass
c_p	= specific heat capacity at constant pressure
D_t	= turbulent diffusion
E_a	= activation energy
E_e	= electrical energy supplied by the electrodes
f	= mass fraction residual gas
h	= specific enthalpy
h_c	= convection coefficient
I_{nad}	= influence of the nonadiabaticity on the laminar burning velocity
I_s	= influence of stretch on the laminar burning velocity
K	= stretch factor
Ka	= Karlovitz number
L	= integral length scale
L_b	= effective length scale
Le	= Lewis number
m	= mass
n	= constant ($n=1$ for cylindrical, $n=2$ for spherical flame kernel)
p	= pressure
Q_{ch}	= reaction heat
Q_{hl}	= heat losses to the cylinder walls and the electrodes
r	= radius
\mathfrak{R}	= general gas constant

S	= reaction velocity (per time unit)
S_l	= laminar adiabatic unstretched burning velocity
$S_{l,nad}$	= laminar nonadiabatic burning velocity
$S_{l,s}$	= laminar stretched burning velocity
S_t	= turbulent burning velocity
t	= time
T	= temperature
T_a	= activation temperature
T_{ad}	= adiabatic flame temperature
T_f	= maximum temperature of the flame front
T_m	= average temperature
T_q	= quenching temperature
T_t	= characteristic time scale
T_{tr}	= transition temperature between the plasma and initial combustion phase
u	= unburned mass
u'	= turbulence intensity
U	= internal energy
\bar{U}	= average flow velocity around the spark plug
V	= volume
α	= thermal diffusivity
δ_l	= thickness of the laminar flame front
ϕ	= equivalence ratio
λ	= thermal conductivity
λ_T	= Taylor micro scale
ρ	= density

References

- [1] Willems, H., and Sierens, R., 1999, "Modeling the Initial Phases of Ignition in S.I. Engines," ASME Paper No. 99-ICE-168.
- [2] Pischinger, S., 1989, "Effects of Spark Plug Design Parameters on Ignition and Flame Development in an SI-Engine," Ph.D. thesis, Massachusetts Institute of Technology, Boston, MA.
- [3] Shen, H., Hinze, P. and Heywood, J., 1994, "A Model for Flame Initiation and Early Development in SI Engine and Its Application to Cycle-to-Cycle Variations," SAE Paper No 942049.
- [4] Vandevoorde, M., 1998, "Model voor de Thermodynamische en Gasdynamische Cyclus van Drukgevlude Gasmotoren," Ph.D. Thesis, Universiteit Gent, Belgium.
- [5] Herweg, R., and Maly, R., 1992, "A Fundamental Model for Flame Kernel Formation in S.I. Engines," SAE Paper No. 922243.
- [6] Bray, K., 1990, "Studies of the Turbulent Burning Velocity," Proc. R. Soc. London, Ser. A **431**, pp. 315–335.
- [7] Willems, H., 2000, "Model voor de Initiële Plasma- en Vlamgroei in Vonkontstekingsmotoren," Ph.D. thesis, Universiteit Gent, Belgium.
- [8] Metghalchi, M., and Keck, J., 1982, "Burning Velocities of Mixtures of Air with Methanol, Isooctane, and Indolene at High Pressure and Temperature," Combust. Flame **48**, pp. 191–210.
- [9] Law, C., 1988, "Dynamics of Stretched Flames," *Twenty-Second Symposium (International) on Combustion*, The C Combustion Institute, pp. 1381–1402.
- [10] Williams, F., 1985, *Combustion Theory, The Fundamental Theory of Chemically Reacting Flow Systems*, 2nd Ed., Addison-Wesley, Reading, MA.
- [11] Tabaczynski, R., Ferguson, C., and Radhakrishnan, K., 1977, "A Turbulent Entrainment Model for Spark-Ignition Engine Combustion," SAE Paper No. 770647.
- [12] Ferguson, C., and Keck, J., 1977, "On Laminar Flame Quenching and Its Application to Spark Ignition Engines," *Combustion and Flame*, **28**, pp. 197–205.
- [13] van Maaren, A., 1994, "One-step Chemical Reaction Parameters for Premixed Laminar Flames," Ph.D. thesis, Technische Universiteit Eindhoven, Holland.
- [14] Gatowski, J., Heywood, J., and Deleplace, C., 1984, "FlamePhotographs in a Spark-Ignition Engine," Combust. Flame **56**, pp. 71–81.
- [15] Namazian, M., Hansen, S., Lyford-Pike, E., Sanchez-Barsse, J., Heywood, J., and Rife, J., 1980, "Schlieren Visualization of the Flow and Density Fields in the Cylinder of a Spark-Ignition Engine," SAE Paper No. 80044.

S. H. Joo

P/T Test and Development Team,
Power Train Division,
Technical Center,
Daewoo Motor Co., Ltd.,
199 Cheongcheon-dong,
Bupyeong-gu, Incheon 403-714, Korea
e-mail: shjoo@bama.ua.edu

K. M. Chun

Department of Mechanical Engineering,
Yonsei University,
134 Shinchon-Dong,
Seodaemun-gu, Seoul 120-749, Korea
e-mail: kmchun@yonsei.ac.kr

Y. Shin

Department of Mechanical Engineering,
Sejong University,
98 Kunja-dong,
Kwangjin-gu, Seoul 143-747, Korea
e-mail: ygshin@sejong.ac.kr

K. C. Lee

Department of Mechanical Engineering,
The University of Alabama,
180 Hardaway Hall,
Tuscaloosa, AL 35487
e-mail: klee@bama.ua.edu

An Investigation of Flame Expansion Speed With a Strong Swirl Motion Using High-Speed Visualization

In this study, a simple linear superposition method is proposed to separate the flame expansion speed and swirl motion of a flame propagating in an engine cylinder. Two series of images of flames propagating in the cylinder with/without swirl motion were taken by a high frame rate digital video camera. A small tube (4 mm ID) was installed inside the intake port to deliver the fuel/air mixture with strong swirl motion into the cylinder. An LDV was employed to measure the swirl motion during the compression stroke. Under the assumption that flame propagates spherically from the each point of the flame front, a diameter of small spherical flames can be calculated from the two consecutive images of the flame without swirl motion in the cylinder. Using the normalized swirl motion of the mixture during the compression stroke and the spherical flame diameters, the flame expansion speed and swirl ratio of combustion propagation in the engine cylinder can be obtained. This simple linear superposition method for separating the flame expansion speed and swirl motion can be utilized to understand the flow characteristics, such as swirl and turbulence, during the combustion process. [DOI: 10.1115/1.1564067]

Introduction

In general, the flame images contain the various information of combustion and flow fields in an engine cylinder. A series of flame images may show the combined result of various phenomena such as chemical reaction, thermal expansion of the burned gas and the stretch of the flame front due to the flow fields, etc. Many research works have been conducted to separate the individual effect on the flame propagation from the in-cylinder flame images, [1–4]. Gadowski et al. [5] reported a flame propagation model which estimates the mean expansion speed of the burned gas and the flame front area under the assumption that the flame propagates spherically from the point of ignition through the fuel/air mixture without the significant swirl in the flow. Due to the various limitations, however, the model could not estimate the flame propagation characteristic through the flow field with significant swirl motion, which makes the flame front shape much different from the spherical configuration. Shen et al. [6] proposed a flame propagation model to examine the flame front in a significant swirl flow. They assumed that an elliptic flame front is formed in the high swirl flow field, and estimated the convective motion velocity by comparing the length of two major and minor axes of the elliptic flame front configuration. This model, however, still has its limitations to estimate the flame front configuration due to the lack of similarity between the flame configuration and the ellipse.

In spite of those intensive research works, a practical method to extract the individual information from flame images is still lack. A simple method to estimate the flame expansion speed and the

convective motion of the flame with the significant swirl motion in an engine cylinder is proposed and the experimental and analytical results are discussed in this study.

Assumptions and Definitions

There is a few effects which can be combined and affect on the flame propagation process in the cylinder. In this paper, the speeds related to the flame propagation are defined as follows:

- Mixture burning speed (flame speed): The velocity at which unburned gases move through the combustion wave (flame) in the direction normal to the wave surface under conditions of free expansion in an open flame.
- Burned gas expansion speed: The speed of flow induced by the thermal expansion of the hot burned gas in the combustion wave.
- Flame expansion speed: The sum of mixture burning speed and burned gas expansion speed. Consequently, the speed can be much higher than the mixture burning speed defined above.
- Flame propagation speed: The speed of the flame which propagates through the combustion chamber as a result of the interaction between the flame expansion and convective flow.

The method to estimate the flame expansion speed and swirl motion from the images of flame propagation is proposed based on the following assumptions:

1. Turbulence intensity of the unburned mixture ahead of the flame is spatially uniform and the mixture burning speed is proportional to the turbulence intensity: This assumption can be validated from the studies such as spherical flame propagation model, [7–10], and cycle-resolved turbulence measurement results, [11,12].

Contributed by the Internal Combustion Engine Division of THE AMERICAN SOCIETY OF MECHANICAL ENGINEERS for publication in the ASME JOURNAL OF ENGINEERING FOR GAS TURBINES AND POWER. Manuscript received by the ICE Division, March 2001; final revision received by the ASME Headquarters, June 2002. Associate Editor: D. Assanis.

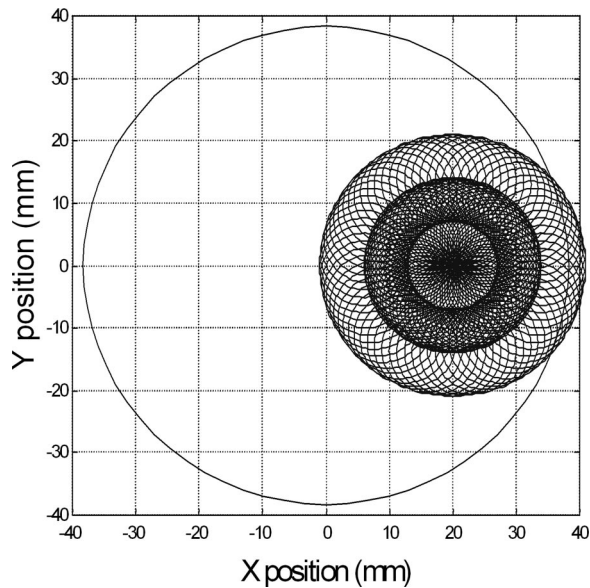


Fig. 1 An example of flame propagation calculated using a proposed flame propagation model for the case of no swirl

2. Burned gas expansion speed is spatially uniform. The expansion of the burned gas occurs in the combustion wave due to the raise of temperature in the combustion wave, and the thermal expansion occurs uniformly regardless of location.

3. The initial flame ignited by a spark plug, propagates spherically from the spark point. If the turbulence intensity and scale are spatially uniform, the mixture burning speed and burned gas expansion speed are uniform, and hence the flame propagates in spherical shape.

4. Linear superposition of the speed of the flame expansion and the speed of the flame center movement due to the convective flow motion can be applied. For the small time-step associated

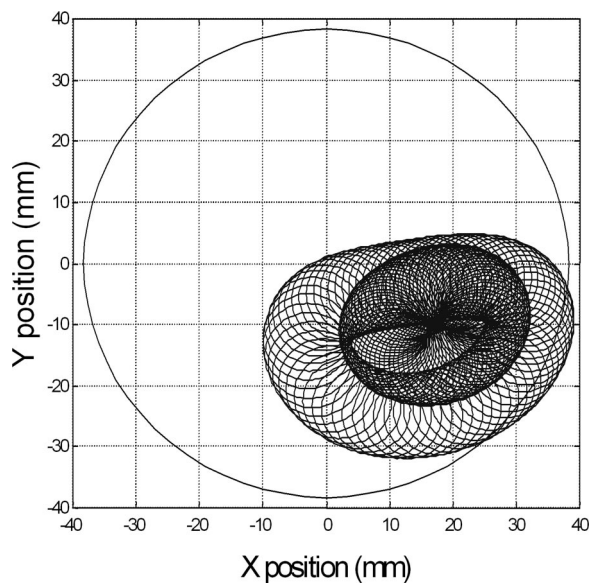


Fig. 2 An example of flame propagation calculated using a proposed flame propagation model for the case of swirl

with the geometric evolution of the flame front, the linear superposition can be useful for the quick estimation.

5. The flame shape consists of the loci of outer surfaces of the small spherical flames which propagate from the every point on the initial flame front surface.

The flame propagation model of a spherical shape flame, which consists of small spherical flames, is illustrated in Fig. 1. The initial flame is developed in a form of a small sphere. Every point of the initial flame surface plays a role as a new ignition point. At these infinite number of ignition points, the small spherical flames begin to propagate and the loci of outer intersection of these small spherical flames form a new large spherical flame. And on the surface of this newly formed spherical flame, the small spherical flames begin to propagate again and form a larger spherical flame.

The flame propagation in a strong swirl flow field is depicted in Fig. 2. The flame propagates in the same manner of no swirl case. A small spherical initial flame is developed when it is ignited. But the center of the initial flame is deformed by the swirl flow. Then, from the every point of the surface of the deformed initial flame, a small spherical flame is developed and propagated. The loci of outer intersection of these small spherical flames form a new large flame front, which is no longer spherical in shape due to the swirl motion.

With the velocity profile during the compression stroke, the flame expansion speed and swirl motion can be estimated from the series of flame images by determining the deformation of the shape of the flame front by the swirl motion and the radii of the small spherical flames developed from the points on the flame front surface of the previous time-step. The detail procedure and method of the estimation will be discussed in the following chapters.

Experiment

A schematic of the experimental setup is depicted in Fig. 3. A four-cylinder, two-valve SOHC, MPFI, pent-roof type production engine with 76.5 mm bore and 81.5 mm stroke was modified for

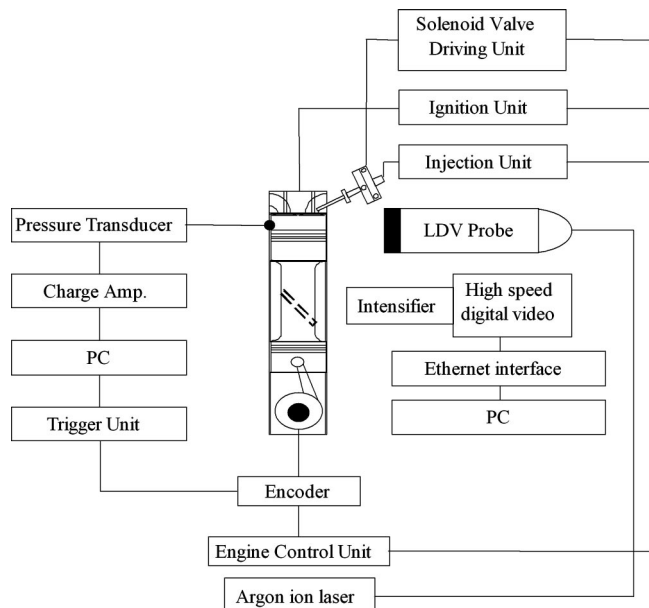


Fig. 3 Experimental setup

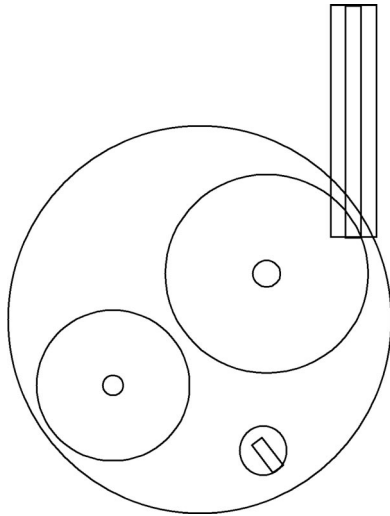


Fig. 4 A mixture supply system which generates the swirl flow

optical access through the flush mounted window in the flat piston. The displacement volume of the engine is 1498 cc, while the compression ratio is 8.6. A small tube (4 mm ID) was installed inside the intake port to generate strong swirl motion in the cylinder. To intensify the swirl motion in the cylinder, the tube was located in the circumferential direction of the intake valve as shown in Fig. 4. The fuel/air mixture was prepared and driven into the cylinder during the intake stroke and the amount of the mixture was controlled by a high speed solenoid valve, [4]. For this process, the intake manifold was blocked so that the mixture flew only through the tube into the cylinder. Though the mixture was not compressed by an extra device, the mixture which flew directly into the cylinder through the small tube and intake valve could induce a very strong swirl motion due to the pressure difference between cylinder and atmosphere. Since the solenoid

valve was open at the early stage (50° ATDC) of the intake stroke, the mixture at the end of the compression stroke in cylinder was considered to be homogeneous. For the case of the weak swirl motion in the cylinder, intake manifold was used for the air flow and fuel injected into the intake port. So, the fuel and air were mixed in the port and the mixture flew into the cylinder during the intake stroke. For the optical access, a quartz window was mounted on the piston. An aluminum-coated mirror was installed under the piston to reflect the flame images.

A high frame rate digital video camera equipped with an image intensifier was employed to take the flame propagation images. The resolution of the camera sensor is 512 pixels by 384 pixels and the maximum frame rate was 2000 frames per second (fps). The flame propagation process was pictured at the maximum frame rate of the camera (2000 fps) at the engine speed of 800 rpm and 0.8 bar IMEP.

An LDV system was used to measure velocity profile in the cylinder during the compression stroke. A quartz window was installed at 5 mm below the cylinder head for the laser beam access. The LDV system consists of a 5W Ar-ion laser, fiber optic probe, photomultiplier tube and a burst spectrum analysis (BSA) data acquisition (DANTEK). For the LDV measurement, the engine was motored at the same operating condition as the firing case. For this study, the engine was operated either in motoring or firing mode at 800 rpm with 10° BTDC of ignition timing, and the air/fuel ratio of 14.6.

Results and Discussion

Figure 5 shows the examples of the flame images, which were taken using a high-speed digital video with an image intensifier. Figure 5(a) is a flame image at 2.5 ms after the ignition without the swirl flow. The flame shape is nearly the spherical without swirl motion. The flame deforms from the spherical shape due to the strong swirl motion in Fig. 5(b). (See the Appendix for flame propagation behavior.) The swirl flow enhanced the flame propagation speed in one direction while retarded in other direction.

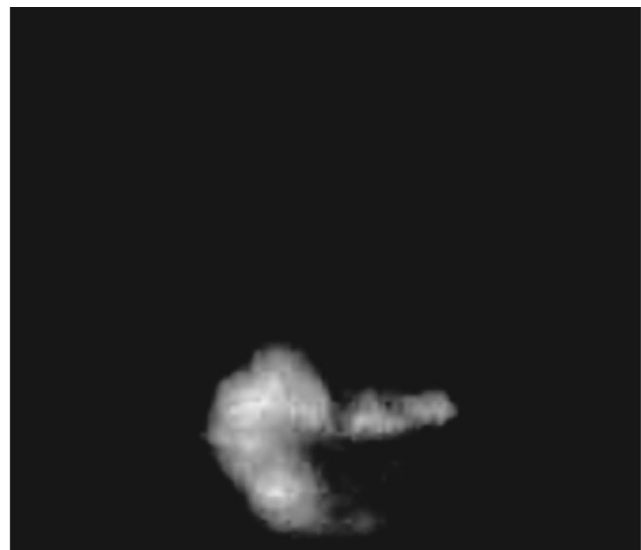
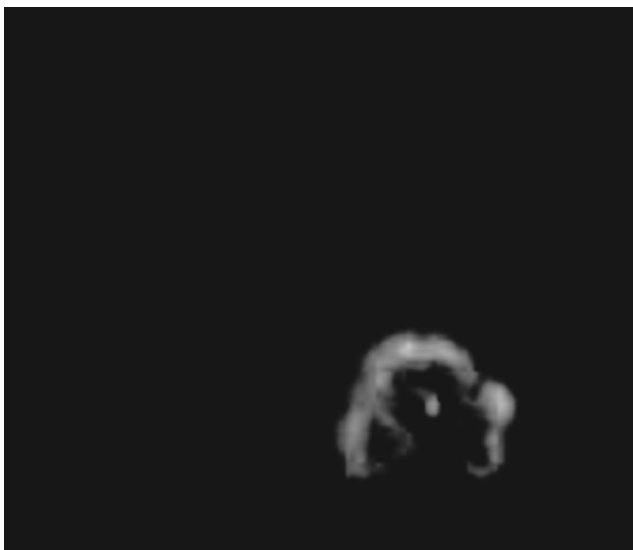


Fig. 5 Flame images at 2.5 ms after ignition; (a) without swirl motion and (b) with strong swirl motion

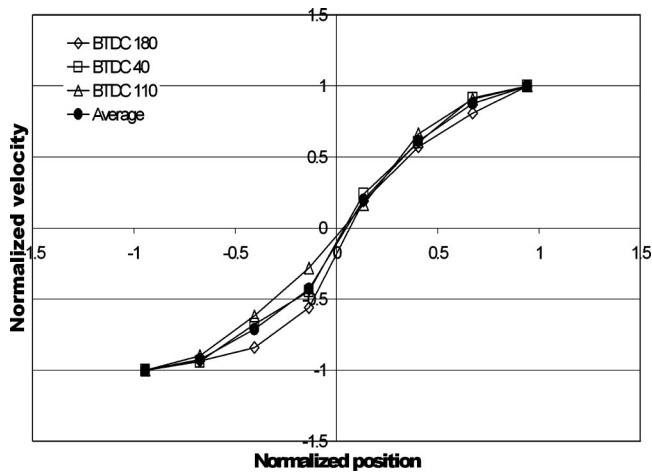


Fig. 6 Normalized velocity profile for the case of swirl during compression process measured by LDV

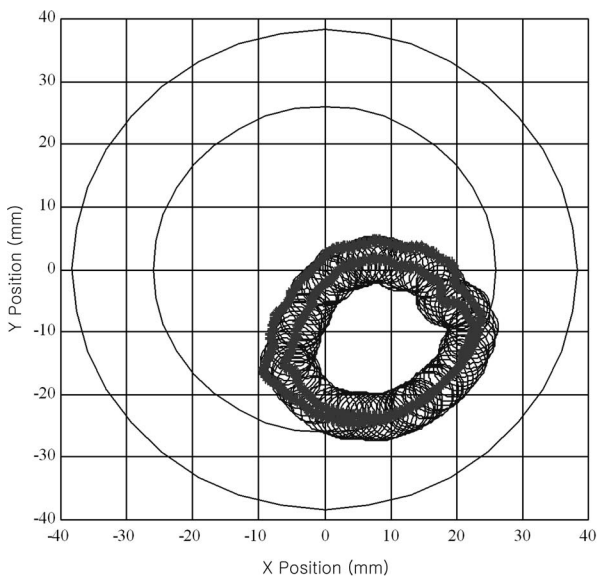
The normalized swirl motion in the cylinder at 180°, 110°, 40° BTDC during compression stroke are shown in Fig. 6. The velocity measurements were made along the horizontal axis (*X*-axis) with 7 mm increments at a plane of 5 mm below the top deck of the cylinder. After 40° BTDC crank angles the velocity measurement was not possible because the piston blocked the laser beams. The results were normalized with the maximum velocity of each measurement to compare the profile of the swirl motion. Even though the maximum velocity of each measurement was different from each other the normalized velocity profiles of the three crank angles showed that the axes of the rotational motions are very close each other and the curves are also very similar each other. Since the normalized results are nearly identical, it seems reasonable to represent a swirl motion by the normalized velocity and

scaling factor. To simplify the parameter, the average of these three normalized measured profiles was used for this study.

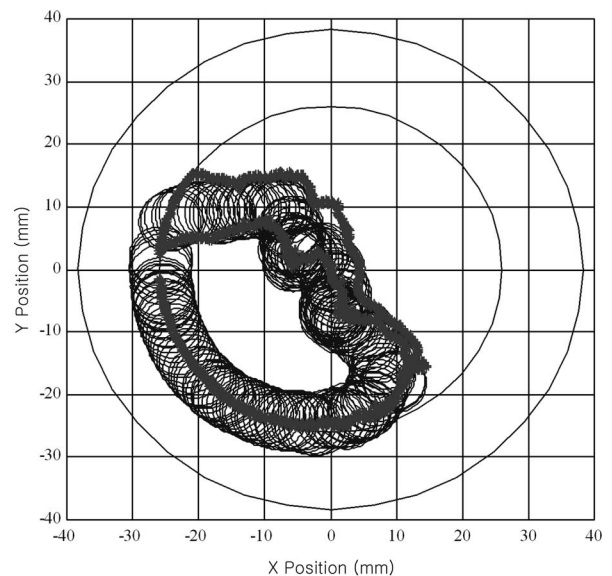
To separate the effects of flame expansion and swirl motion, the radius of the small spherical flames which develop from the every point on the flame front surface and the swirl scale factor from the averaged normalized swirl profile were determined by comparing the measured and the estimated flame fronts. The comparisons of the measured and the estimated flame fronts are shown in Fig. 7. The two consecutive flame images were superposed in Fig. 7(a) for the case of no swirl motion and in Fig. 7(b) for the case of strong swirl motion case. In the figures, the inner circle is the boundary of visible area through the window while the outer one presents the piston. The thick solid lines are the traces of the flame fronts from the images taken by the digital camera in 0.5 ms time interval.

The flame front surface can be recalculated with the swirl scale factor of the in-cylinder motion. Then, the new flame front surface can be constructed with the loci of the outer surfaces of the small spheres with same radius centered at the every point of the recalculated flame front surface. If the front side radii of the small spherical flames are smaller than those in rear side in circumferential direction (swirl direction), the swirl motion does not apply sufficient enough than the actual flame propagated. On the other hand, if the rear side radii of the small spherical flames are bigger than those in front side in the swirl direction, too much swirl effect is added to the calculation. This process was repeated until the constructed flame front by the small spherical flame surfaces located on the top of the second measured flame front. This iterative process took around five minutes for a pair of images and less than an hour for whole combustion process. One of the results of this method is shown in Fig. 7.

The swirl ratio during the combustion process and the flame expansion speed were calculated with the swirl scale factor and the radius of the small spherical flames. The radius of the small spherical flame is the distance of the flame expended by the mixture burning speed and hot burned gas thermal expansion during



(a)



(b)

Fig. 7 Examples of determining the flame expansion speed and swirl speed (3 msec after the start of ignition)

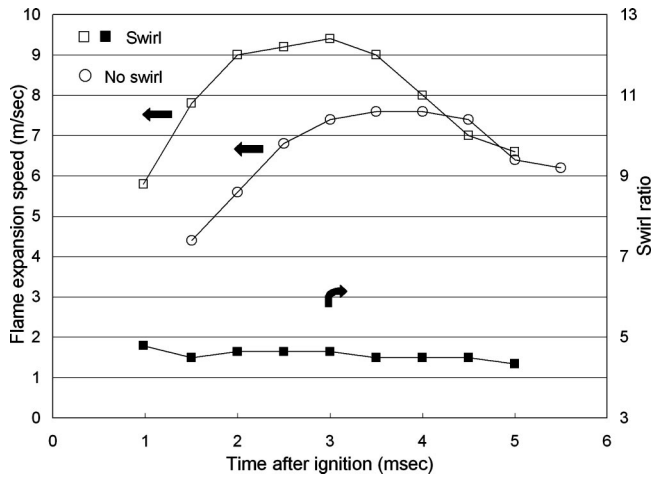


Fig. 8 Estimated flame expansion speed and swirl ratio determined from flame images

the period of the time step. The flame expansion speed can be obtained by the radius of the small spherical flame divided by the time-step interval. The calculation results are shown in Fig. 8. In both cases of with/without swirl motion, the flame expansion speed increases rapidly at the beginning combustion and maintains the constant for a while, finally slows down at the final stage of combustion process, [13]. The flame expansion speed with the strong swirl is faster than that without swirl during the combustion process. The flame propagation in the strong swirl motion is promoted earlier than without the swirl motion. It is a well-known fact that the flame expansion speed depends strongly on turbulence intensity. Therefore, this may explain that the strong swirl motion generates higher turbulence in in-cylinder flow motion and the higher turbulence affects on the flame expansion speed during the combustion process.

The swirl ratio during the combustion process reduces slowly from 4.8 to 4.3. During the first 0.5 ms, the swirl reduces almost 0.3 and then the rest of measured period, the swirl ratio remains almost constant. The rapid increase of the flame expansion speed might affect the swirl. During the period of the constant flame expansion speed, the swirl remains constant until the flame expansion speed reduces. This can be compared with the angular momentum loss due to the friction in cylinder, [14]. For the momentum loss calculation, the gas flow was assumed as a flow in a thin disk with a constant volume. During the studied period, 5.5 ms from the spark ignition, the piston moves up from the position at 10° BTDC and down to the 16.5° ATDC. During this period, the constant volume assumption can be applicable due to the small changes in cylinder volume.

Friction on the cylinder wall can be obtained as

$$\tau = \frac{1}{2} \rho \left(\frac{\omega_s B}{2} \right)^2 C_f \quad (1)$$

where ω_s is the equivalent solid-body swirl and B is the diameter of the cylinder (bore). The friction factor C_f over the flat plate is

$$C_f = 0.037 \lambda (\text{Re}_B)^{-0.2} \quad (2)$$

where λ is an empirical constant for the difference between the flat plate and cylinder wall ($\lambda \approx 1.5$) and Re_B is Reynolds number over the flat plate,

$$\text{Re}_B = \frac{\rho(B\omega_s/2)(\pi B)}{\mu} \quad (3)$$

For the calculation of the friction loss on the combustion chamber surface and the piston crown, in-cylinder flow was modeled as the fully developed flow between the two flat plates. For this calculation Eq. (1) was modified. Since the tangential velocity v_θ in the combustion chamber varies with radius, the shear stress should be integrated over the surface:

$$\tau = \int_0^R 2\pi r \cdot \tau(r) dr \quad (4)$$

and

$$\tau(r) = C_1 \frac{1}{2} \rho [v_\theta(r)]^2 \text{Re}^{-0.2} \quad (5)$$

with

$$\text{Re} = \frac{\rho v_\theta(r) r}{\mu} \quad (6)$$

here C_1 is an empirical constant (≈ 0.055).

The calculations resulted that angular momentum was 2.93×10^{-5} (kgm²/sec), the equivalent solid-body angular velocity was 381.83 (rad/sec), and the swirl ratio was 4.56. The angular momentum loss during combustion process was 6.97×10^{-7} (kgm²/sec). The calculation results showed that only 2.4% of angular momentum loss occurred during the combustion process. This small angular momentum loss results the swirl motion remains almost constant during the combustion process as shown earlier.

Conclusion

Flame propagation process with/without swirl motion in an engine cylinder was examined. With the careful examinations of the experiment results and analysis, the following conclusions were obtained:

1. The normalized velocity profiles at different crank angles during the compression stroke are very similar to each other in case of strong swirl.
2. The flame expansion speed and swirl motion was separated by calculating the flame front with the normalized swirl profile and the uniform flame propagation through the unburned mixture from the every point on the recalculated flame front surface. The predicted flame front surface configurations were well matched with the flame images taken by the digital camera.
3. The maximum flame expansion speed in the presence of significant swirl increases about 30% higher than that with no swirl during the combustion process.
4. It is found that the swirl ratio during the combustion process remains nearly constant due to the small friction loss during the combustion process.

Appendix

Flame Propagation Behavior in a Spark Ignition Engine
Figs. 9, 10, and 11 are the Appendix.

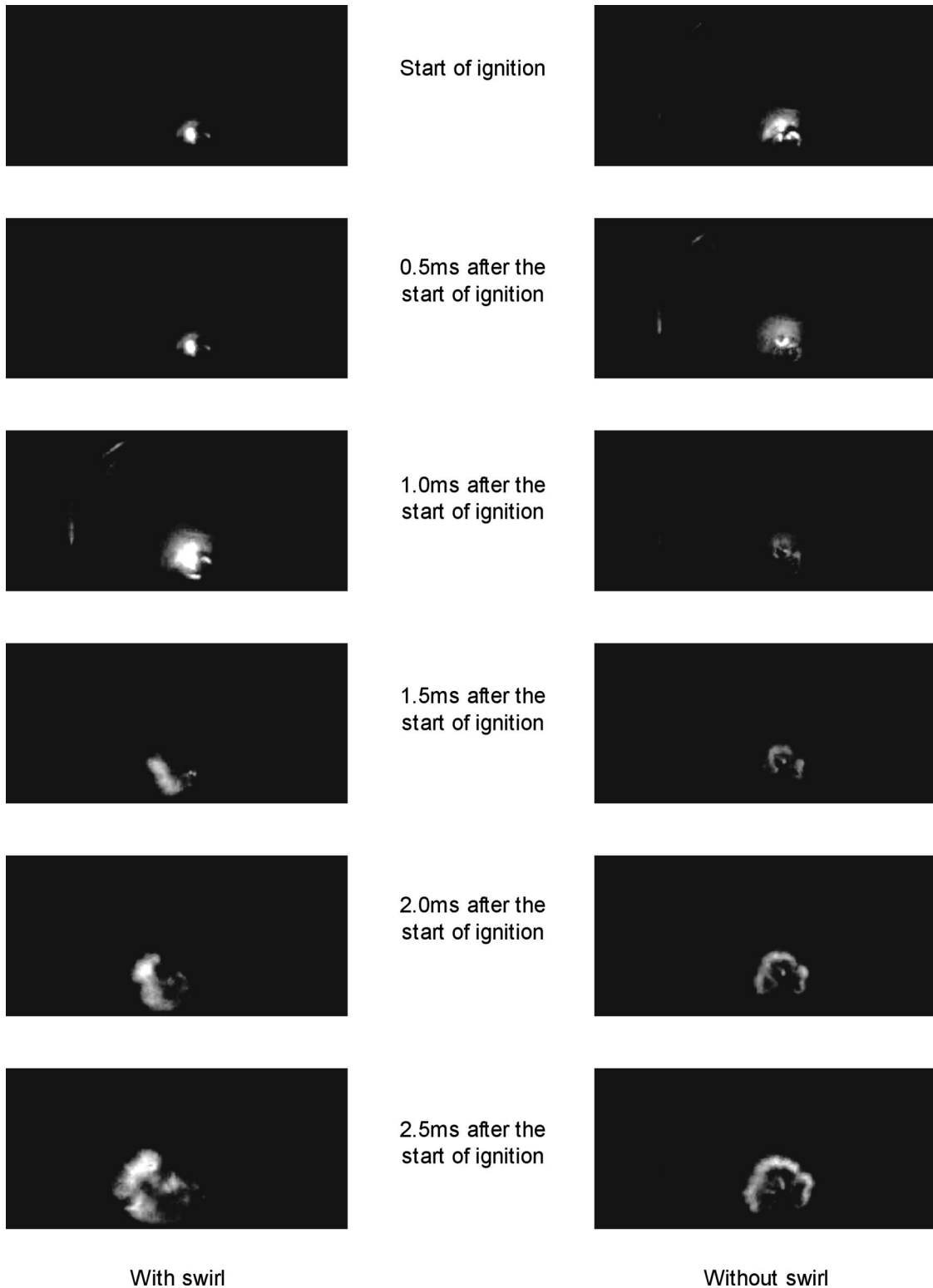
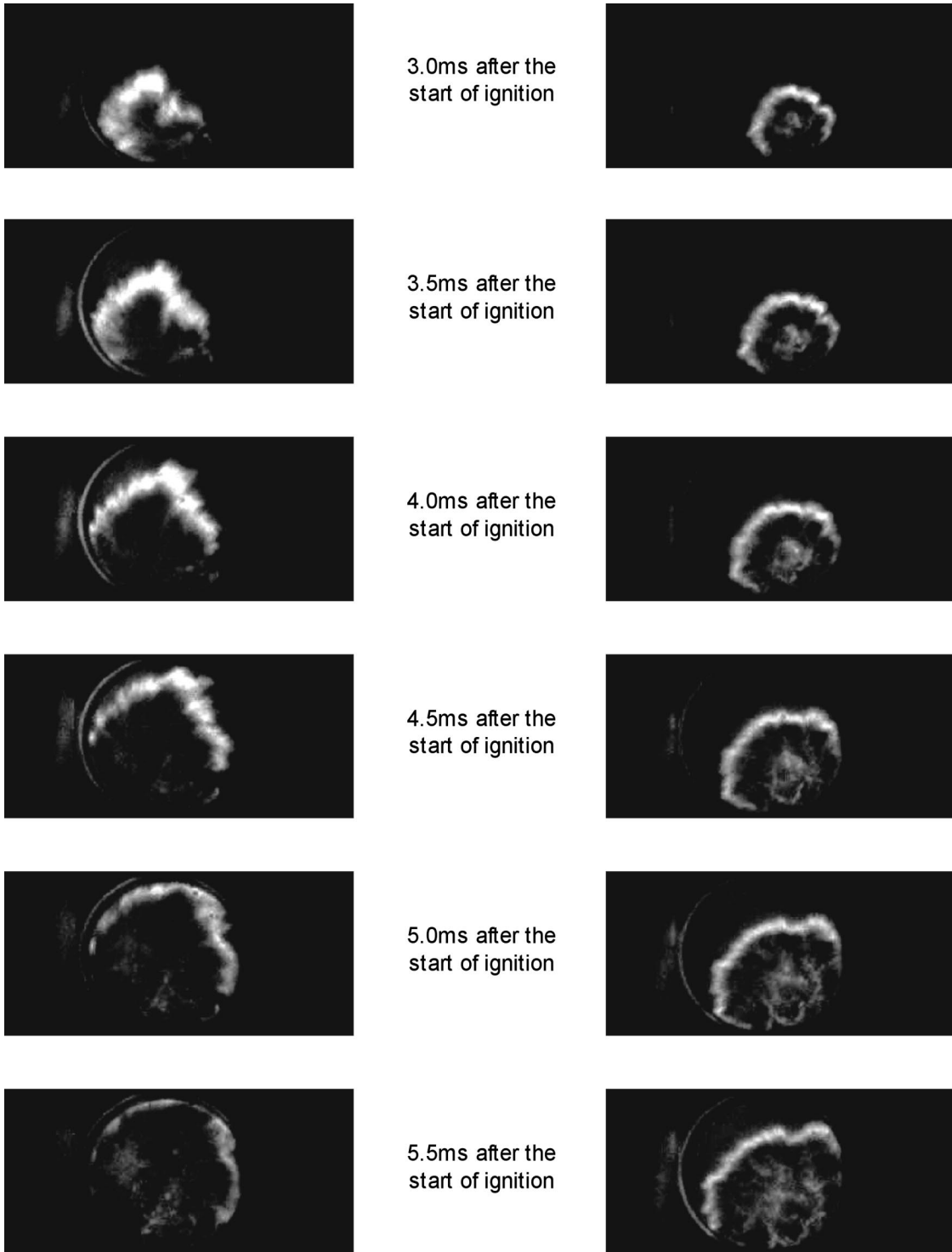


Fig. 9



With swirl

Without swirl

Fig. 10

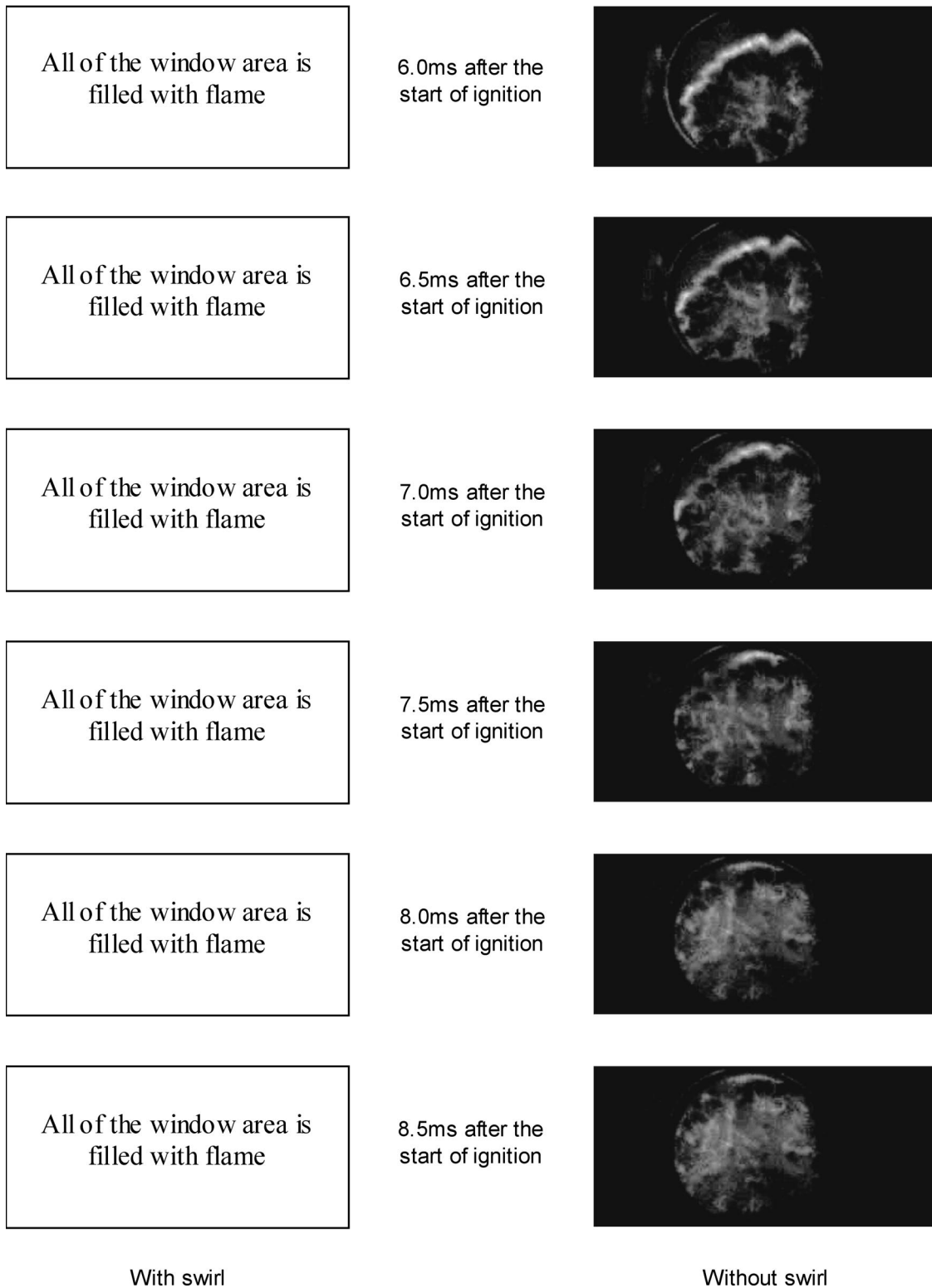


Fig. 11

References

- [1] Arcoumanis, C., Hu, Z., Vafidis, C., and Whitelaw, J., 1990, "Tumbling a Mechanism for Turbulence Enhancement in Spark-Ignition Engines," *SAE Paper No. 900060*.
- [2] Checkel, D., and Ting, S., 1993, "Turbulence Effects on Developing Turbulence Flames in a Constant Volume Combustion Chamber," *SAE Paper No. 930867*.
- [3] Arcoumanis, C., and Bae, C., 1993, "Visualization of Flow/Flame Interaction in a Constant-Volume Combustion Chamber," *SAE Paper No. 930868*.
- [4] Joo, S., and Chun, K., 1999, "Improvement of the SI Engine Idle Combustion Stability Using a Fuel/Air Mixture Injection Device," *JSAE Paper No., 9932566*.
- [5] Gatowski, A., and Heywood, J., 1985, "Effects of Valve-Shrouding and Squish on Combustion in a Spark-Ignition Engine," *SAE Paper No. 852093*.
- [6] Shen, H., Hinze, P., and Heywood, J., "A Model for Flame Initiation and Early Development in SI Engine and Its Application to Cycle-to-Cycle Variations," *SAE Paper No. 942049*.
- [7] Stone, C. R., Brown, A. G., and Beckwith, P., 1996, "Cycle-by-Cycle Variations in Spark Ignition Engine Combustion—Part II: Modeling of Flame Kernel Displacements as a Cause of Cycle-by-Cycle Variations," *SAE Paper No. 960613*.
- [8] Ma, F., Shen, H., Liu, C., Wu, D., Li, G., and Jiang, D., 1996, "The Importance and Initial Flame Kernel Center Position on the Cyclic Combustion Variations for Spark-Ignition Engine," *SAE Paper No. 961969*.
- [9] Blizard, N. S., and Keck J. C., 1974, "Experimental and Theoretical Investigation of Turbulent Burning Model for Internal Combustion Engines," *SAE Paper No. 740191*.
- [10] Tabaczynski, R. J., Trinker, F. H., and Shannon, B. A. S., 1980, "Further Refinement and Validation of a Turbulent Flame Propagation Model for Spark Ignition Engines," *Combust. Flame*, **39**, pp. 111–121.
- [11] Witze, P. O., and Mendes-Lopes, J. M. C., 1985, "Direct Measurement of the Turbulent Burning Velocity in a Homogeneous-Charge Engine," *SAE Paper No. 851531*.
- [12] Hall, M. J., Bracco, F. V., and Santavicca, D. A., 1986, "Cycle-resolved Velocity and Turbulence Measurements in an IC Engine With Combustion," *SAE Paper No. 86032*.
- [13] Berreta, G. P., Rashidi, M., and Keck, J. C., 1983, "Turbulent Flame Propagation and Combustion in Spark Ignition Engines," *Combust. Flame*, **52**, pp. 217–245.
- [14] Heywood, J. B., 1988, *Internal Combustion Engine Fundamentals*, McGraw-Hill, New York.

Knocking Cylinder Pressure Data Characteristics in a Spark-Ignition Engine

M. Syrimis

D. N. Assanis

W. E. Lay Automotive Laboratory,
University of Michigan,
Ann Arbor, MI 48109-2121

An experimental study of the knock initiation and development period was conducted in a single-cylinder research engine. Cylinder pressure was recorded at two locations in the combustion chamber using a high sampling frequency, thus allowing the identification of spatial and temporal pressure characteristics introduced by knock. It was found that substantial local pressure differences exist inside the chamber during the initiation of autoignition. In most cases, knock-induced pressure waves are of acoustic nature, but they can become weak shock waves in heavily knocking cycles. Waves appear first in the pressure trace of the transducer closer to the site of autoignition, and are subsequently detected by the other transducer. The results show evidence of multiple sites of autoignition, and indicate changes in the nature and the direction of propagation of pressure waves. Cylinder pressure signals sampled at locations closer to the center of the chamber show significantly smaller amplitude of pressure fluctuation, making them more suitable for further mathematical processing. [DOI: 10.1115/1.1560709]

Introduction

The autoignition of the end-gas mixture during knocking operation causes a local pressure increase in the combustion chamber, leading to the creation of traveling pressure waves. As the waves reflect at the walls of the chamber, they combine and form stationary pressure waves, i.e., the combustion chamber cavity is set into resonance. Metallic parts in the engine structure, e.g., the valve train, may also be set into resonance, causing the characteristic “ringing” noise associated with knock.

Cylinder pressure, a signature of the combustion process, thus acquires time-dependent spatial characteristics. The initial pressure disturbance induced by the onset of autoignition is not felt at other points in the chamber until the created pressure waves reach those locations. Once resonance sets in the chamber, the local pressure variation depends on the predominant resonant mode, the frequency of which also decides the time variation at each location.

Drapper [1] presented a theoretical estimation of the resonant mode frequencies in the cylinder cavity based on the analytical solution of the wave equation. The wavelengths of resonant modes, as high as the combined second azimuthal, second radial and second axial mode (2,2,2), were presented as ratios of the cylinder radius. This very early work provides a solid fundamental understanding of the different resonant modal shapes. Another, comprehensive presentation of the modal shapes in a cylindrical cavity is given by Zucrow and Hoffman [2].

While cylinder pressure is known to vary spatially upon autoignition, its knocking characteristics have not been studied extensively in the literature. A number of former studies presented cylinder pressure data at different locations in the chamber, without paying attention to the detailed differences in the pressure signal, especially those during the knock initiation period, [3–5]. More recently, Stiebels et al. [6] presented high-speed photographs of the end-gas zone along with cylinder pressure data at two locations in the chamber. While the study provided excellent insight into the initiation of knock and the flame propagation patterns during autoignition, it did not examine in detail the characteristics

of the cylinder pressure. Finally, a study by Brunt et al. [7] dealt entirely with the pressure signal during knock. The study employed four transducers in the combustion chamber and compared their signals in both the time and frequency domain. Conclusions were drawn regarding the effect of position and method of mounting of the probes on the knock index and the frequency of the recorded pressure oscillations. However, the characteristics of the knock initiation period were not explored in the study of Brunt et al.

Cylinder pressure is the most important classical diagnostic in engine studies, providing information on the burn rate and the overall engine performance. In knock studies in particular, cylinder pressure also provides measures of knock intensity. Such knock indicators include the amplitude of the pressure fluctuation, the rate of pressure rise, the third derivative of pressure, the burn duration, and the rate of change of net heat release rate, [8].

The objective of the present study is to develop an improved understanding of the phenomena occurring during the knock initiation and development period through the detailed study of cylinder pressure characteristics. A series of cylinder pressure data was simultaneously recorded at two chamber locations under heavy knocking conditions. Through this approach, the effects of sampling frequency and pressure transducer location on the recorded signal were investigated first. Subsequently, the spatial and temporal pressure differences introduced by knock were analyzed, thus shedding light into the nature of pressure waves upon autoignition. Furthermore, the study provides useful guidelines concerning the optimum placement of the pressure transducer to facilitate further mathematical processing of its signal, such as for computing rates of heat release and derivative-based knock indicators.

Experimental Setup and Method

A single-cylinder R52 Mitsubishi research engine in its extended piston configuration was used in this study. The engine is a four-valve, overhead camshaft, port-injected unit with a fuel injector in each intake port. The compression ratio is 9.78; the bore is 85 mm and the stroke is 88 mm yielding a displacement of 499 cc. Certain design features of the engine make it a very versatile research tool for studying knock. Three spark-plug ports are available, thereby allowing single or dual spark-plug operation. In single spark operation, the spark may be placed either centrally or on the side of the combustion chamber, with side spark operation

Contributed by the Internal Combustion Engine Division of THE AMERICAN SOCIETY OF MECHANICAL ENGINEERS for publication in the ASME JOURNAL OF ENGINEERING FOR GAS TURBINES AND POWER. Manuscript received by the ICE Division, July 2000; final revision received by the ASME Headquarters, November 2002. Associate Editor: H. Nelson.

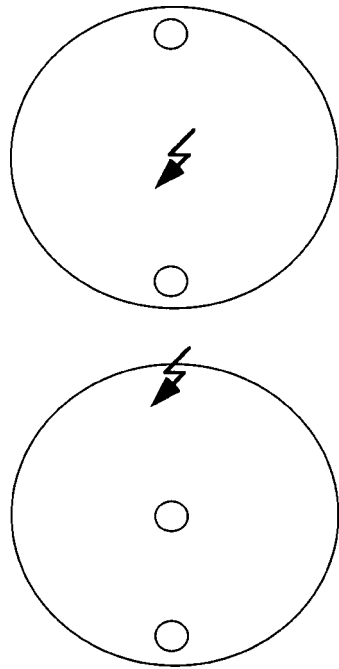


Fig. 1 Engine configurations used; center spark-plug, front and rear pressure transducers (top) and rear spark-plug, front and center pressure transducers (bottom)

being more susceptible to knock. The spark-plug ports can also be used as pressure transducer ports. Furthermore, the cylinder head has three separate cooling galleries, allowing independent control of the coolant temperature in each gallery. Finally, the extended piston configuration facilitates the measurement of piston surface temperatures using a mechanical linkage to route thermocouple wires. A detailed description of the engine setup is given by Syrimis et al. [9].

Data were taken with two different engine configurations, each placing the spark-plug at a different position while being instrumented with two flush-mounted AVL Q500ca pressure transducers. Specifically, the first configuration placed the spark-plug at the center and the two transducers at the front and rear of the combustion chamber, as shown in Fig. 1 (top). The second configuration had the spark-plug at the rear and the transducers at the center and the front of the chamber, Fig. 1 (bottom). The engine was run under a stoichiometric (14.6) air-fuel ratio, at a speed of 1000 rpm and a load corresponding to 75% volumetric efficiency. Heavy knock was obtained by advancing the spark 8° and 12° beyond the onset of trace knock for the center and rear spark-plug cases, respectively. These spark timings corresponded to 24 crank angle degrees before top dead center in both cases.

A single pressure signal was recorded first, using three sampling frequencies, namely 25, 50, and 100 kHz. For the test engine speed, the three sampling rates correspond to resolutions of approximately 1/4, 1/8, and 1/16 crank angle degree. The exact resolution is slightly higher, i.e., 24 kHz corresponds exactly to 1/4 crank angle degree resolution. Subsequently, data from both transducers were taken at 100 kHz to provide the highest possible spectral resolution.

An HP3852A data acquisition system with three high-speed 13-bit voltmeters (HP44702B) was used in this study. In the initial stage of this investigation, the buffer size of the high-speed voltmeters limited the number of cycles that could be recorded at 100 kHz to just 5. Later on, however, it became possible to circumvent this difficulty and record an unlimited number of cycles.

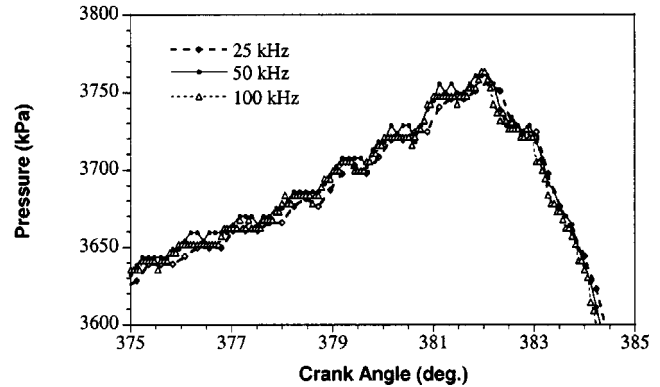
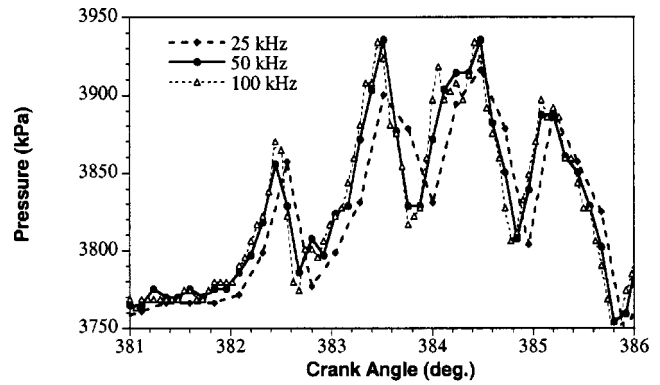


Fig. 2 Sampling frequency effects on recorded cylinder pressure for a heavy (top) and a light (bottom) knocking cycle. Rear spark, front transducer, 1000 rpm, 24° spark advance (trace knock +8°).

Results

Sampling Frequency Effects. Pressure signals recorded at three different sampling frequencies for a heavy and a light knocking cycle are shown in Fig. 2. The difference in knock intensity of the cycles is a result of the cyclic variability associated with knocking operation. In the heavy knocking cycle (Fig. 2, top), the 50 and 100 kHz signals are very similar, while the 25 kHz signal is quite different from the other two. The local peaks in the 25 kHz signal appear after the peaks in the other two signals, and they tend to be lower in magnitude. These effects are a result of “aliasing,” i.e., the existence of high frequency components in the signal which cannot be resolved with the 25 kHz sampling frequency, [10]. Unresolved components have frequencies higher than 12.5 kHz, the Nyquist frequency. The presence of the higher frequency components is obvious in the 50 and 100 kHz signals, where one identifies local peaks between the peaks of the dominant pressure oscillations.

However, in less heavily knocking cycles such as the one shown in Fig. 2 (bottom), using a higher than necessary sampling frequency introduces digitization noise, and thus deteriorates the quality of the signal. As the rate of pressure change is low, when the increase between successive data points is lower than the resolution of the analog-to-digital converter (approximately 7 kPa in our case), flat regions are produced in the digitized signal. Consequently, a lower sampling frequency produces a more physical representation of the pressure variation, in such light knocking cycles, even though it is susceptible to aliasing. Higher frequency components are still present in the signal, although at a much lesser extent than at heavy knock, as it can be seen on the 50 kHz

signal. In our more general study, it has been observed that the higher frequency modes tend to get excited at heavier knock intensities.

Given the inherent variability of knock, i.e., the succession of cycles with different knock intensity, one has to compromise on the selection of sampling frequency. Based on the observations made on the two cycles of Fig. 2, a sampling frequency of at least 50 kHz is necessary in order to retain the high frequency characteristics of the signal during both heavy and light knock.

Transducer Location Effects. Since knock sets the combustion chamber in resonance, the magnitude of the recorded pressure fluctuations depends on the location of the pressure transducer. A transducer located at a point where a pressure node exists will indicate a smaller amplitude of fluctuations than a transducer located further away from the pressure node, at all knock intensities. However, for the same reason, a cylinder pressure signal recorded at a nodal location will require considerably less smoothing and filtering prior to further mathematical processing. Consequently, the accuracy of quantitative results obtained from further numerical analysis of such pressure signals, e.g., instantaneous net heat release and burn rates, can be significantly improved.

Fluctuations are superimposed on the cylinder pressure trace once resonance occurs in the chamber following autoignition (see also following section), and thus do not affect instantaneous heat release rate at the onset of autoignition. Any possible effect on heat release will occur late in the combustion process, and it will be due to increased heat loss by convection due to the oscillating gas molecules. It has to be mentioned, however, that any such effect will be considerably less significant than the effect of autoignition-induced flame fronts passing over the surface and destroying the protective boundary layer, [9].

To assess the transducer location effects, data were taken for both engine configurations shown in Fig. 1. A sampling frequency of 100 kHz was used to obtain the highest possible resolution. Figure 3 shows the recorded pressure traces for a heavy knocking cycle in each of the two cases examined. In the center spark case (Fig. 3, top), resonance sets in the chamber shortly after the onset of autoignition, thus causing the pressure at each location to fluctuate. There is a phase difference of 180 deg between the pressure signals at the two locations, indicating that the transducers are located at different phase regions of the resonant mode. The amplitude of the fluctuations is very closely the same at each location. As the transducers are placed symmetrically about the axis of the cylinder, it is expected that a pressure node exists between the transducers.

In the rear spark-plug case, Fig. 3 (bottom), the pressure signal at the center of the chamber shows very small pressure fluctuations, while the front transducer shows significant fluctuations. The small magnitude of fluctuations indicates that a pressure node exists in the vicinity of the center transducer. The fluctuations in the signal of the center transducer have a higher frequency, approximately twice the frequency of the fluctuations at the front transducer. While the signal from the center transducer may not provide accurate knock intensity indices based on the amplitude of pressure fluctuations, it would be preferred for heat release analysis; in the latter, differentiation of a fluctuating cylinder pressure introduces numerical noise. Calculated values for net heat release rate, amount burnt by autoignition, and total amount burnt will be more accurate than corresponding values calculated from a highly fluctuating signal. The less fluctuating signal of the center transducer will also provide more accurate pressure derivative-based knock indices. Such indices are the third derivative index, suggested by Checkel and Dale [11], and the minimum rate of net heat release rate suggested by Ando et al. [12].

Calculation of the energy spectra of the two signals reveals the frequency of the resonant modes established in the chamber. The spectra of the front and rear transducers are quite similar, see Fig. 4 (top). Two modes are clearly identified in both signals, and are marked by arrows in Fig. 4, the first at 6.5 kHz and the other at

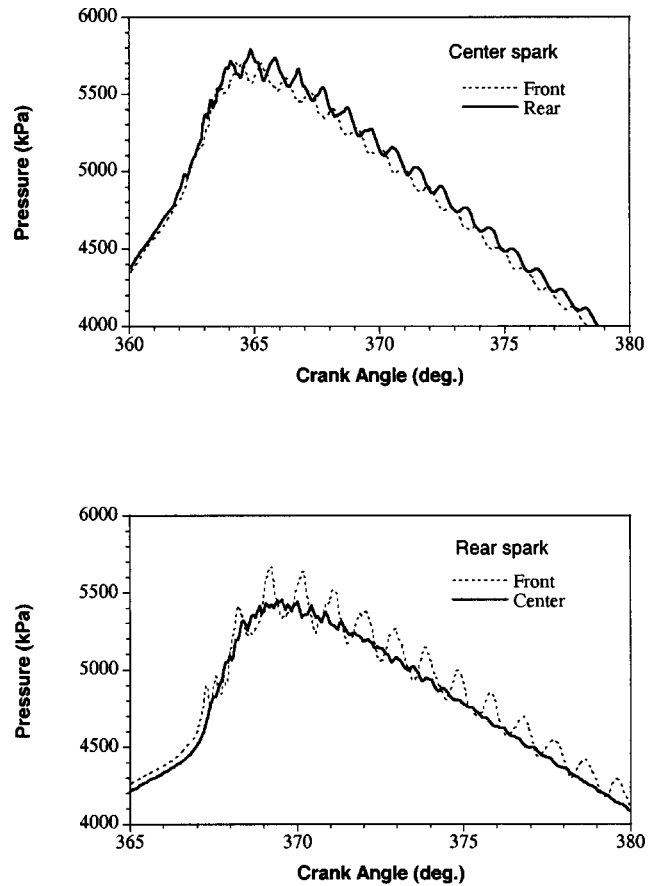


Fig. 3 Pressure transducer signals at different locations of the combustion chamber. Center spark, front and rear transducers (top); rear spark, center and front transducers (bottom).

11.5 kHz. A series of higher frequency modes exist in both signals. On the other hand, in the rear spark-plug engine configuration, the spectra of the transducers show very distinct differences, Fig. 4 (bottom). While the signal from the front transducer shows again the two modes, at 6.5 kHz and 11.5 kHz, the signal of the center transducer shows only one mode at 11.5 kHz. The absence of the first mode from the spectrum of the center pressure trace is simply caused by the fact that the transducer is located at the pressure node of that particular mode. The mode is indeed excited, as proven by the power spectrum of the front transducer. The excitation of a particular mode depends on the position of the excitation force, in this case the location of the autoignition site, and on the coupling mechanisms transferring energy between the modes, [13].

Assuming a speed of sound of 900 m/s in the chamber (based on 2000 K temperature and air properties) and using theoretical estimations of the frequencies of the resonant modes of a cylinder, [1], the 6.5 kHz mode corresponds to the first azimuthal (circumferential) resonant mode of the chamber. In this mode, there is a single pressure node containing one diameter and extending along the axis of symmetry of the cylinder. The 11.5 kHz mode is found to be the second azimuthal mode, with pressure nodes existing along two diameters of the cylinder. The actual frequencies of the two modes based on the analysis of Drapper [1] are 6.2 and 10.1 kHz, respectively. Such discrepancies between theoretical estimates and experimental values have also been reported by Puzinauskas [8] and Brunt et al. [7]. The differences are expected as Drapper [1] derived his analytical relationship for a simplified geometry, e.g., cylindrical combustion chamber. Identification of

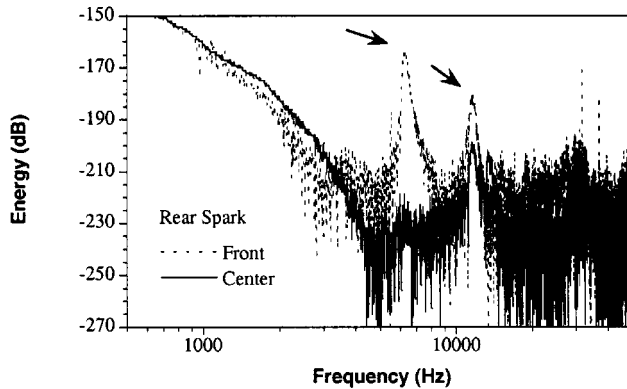
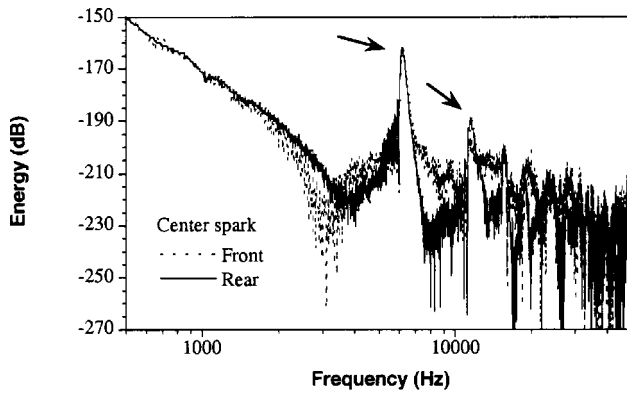


Fig. 4 Comparison of the energy spectra for a heavily knocking cycle recorded simultaneously by two pressure transducers at 100 kHz sampling frequency, 1000 rpm. (Top) front and rear transducers, center spark, 24° spark advance (trace knock +12°); (Bottom) front and center transducers, rear spark, 24° spark advance (trace knock +8°).

the higher frequency modes exhibited in the energy spectra of the transducers requires more detailed modal analysis which is beyond the scope of the current work.

Characteristics of the Knock Initiation Process. Cycles in which specific characteristics appear during the knock initiation period will now be presented for the center spark-plug test. In cycle 1, Fig. 5 (top), the wave caused by autoignition appears first in the rear transducer signal. The wave does not appear in the front transducer until 80 μ s (eight data points) later. The appearance of the wave in each signal is shown by the vertical arrows in Fig. 5 (top). Shifting the front pressure trace so that the first peaks coincide, Fig. 5 (bottom), indicates that the same pattern exists in both signals. The wave is reflected on the sides of the pent-roof chamber twice before resonance is reached. The amplitude of the wave is lower in the front pressure trace than in the rear one, due to energy dissipation occurring as the wave travels towards the front transducer.

Assuming a speed of sound of 900 m/s, the above mentioned 80 μ s difference corresponds to a traveled distance of 72 mm. It is thus deduced that the distance between the autoignition site and the rear transducer is 72 mm shorter than the corresponding distance to the front transducer. Taking into account that the bore diameter is 85 mm, it is concluded that the autoignition location must be very close to the rear probe.

Before the initiation of knock, some low amplitude fluctuation exists in the pressure trace of the front transducer, shown by the horizontal arrow in Fig. 5 (top). This must be caused by the normal flame propagation, showing that the flame propagates towards

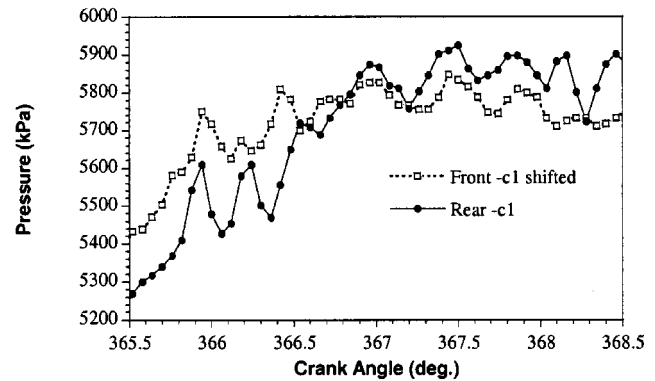
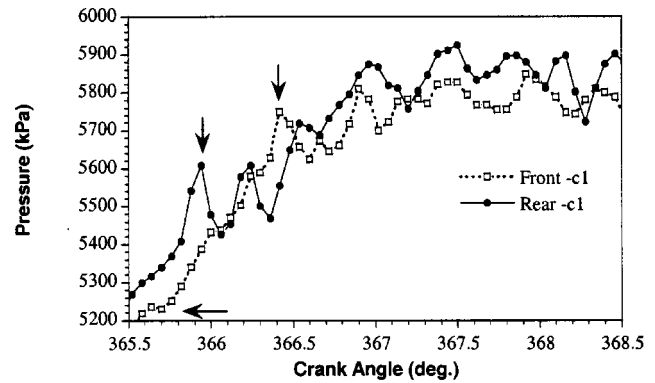


Fig. 5 Pressure traces from the front and rear transducers for cycle 1 (top) showing the knock initiation and propagation of the pressure waves in the chamber. Matching of the first peak in the two traces (bottom) shows that the initial fluctuations in each trace are caused by the same pressure wave. Center spark, 1000 rpm, 24° spark advance (trace knock +12°).

the front of the chamber first. The fluctuation is absent from the rear trace as it becomes undetectable in the presence of the much stronger autoignition wave. The suggested relation between the initial fluctuation in the front trace and the direction of flame propagation agrees with the fact that autoignition occurs near the rear transducer. The possibility that the weak fluctuation on the front pressure trace was caused by factors other than the primary flame front has to be discounted. The authors' experience with the experimental setup has shown the pressure signal to be free from electrical interference and flame-induced ion currents. Interference was only observed during fuel injection, valve events, and at spark timing.

In cycle 3, the pressure wave appears on the rear transducer first and about 40 μ s later on the front transducer, see Fig. 6 (top). The amplitude of the wave at the front transducer is higher than the initial wave seen at the rear probe, indicating that additional mixture autoignites as the wave travels towards the front transducer. Indeed this is supported by the appearance of another wave of even higher amplitude in the trace of the front transducer, shown by the arrow, immediately after the appearance of the first wave. Following the creation of the wave, there is a substantial pressure decrease in the proximity of the probe as the wave moves away from the transducer (rarefaction effect). At the other end, pressure increases rapidly and reaches a local maximum 50 μ s later. These observations indicate that multiple sites of autoignition occur during knocking combustion. This has been shown in the study of Stiebels et al. [6].

Cycle 5, shown in Fig. 6 (bottom), knocks severely. Following a weak autoignition, evidenced by pressure fluctuation at the front transducer, an extremely violent autoignition occurs near the rear

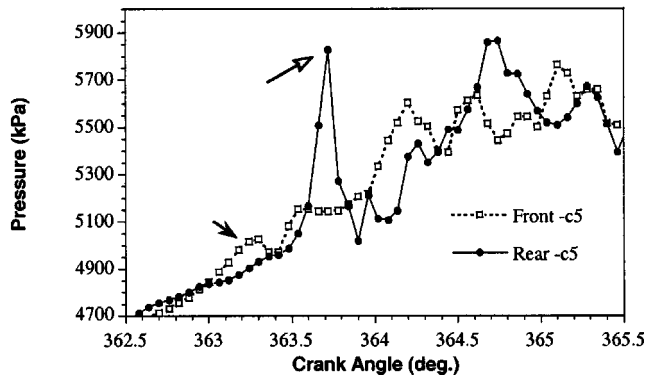
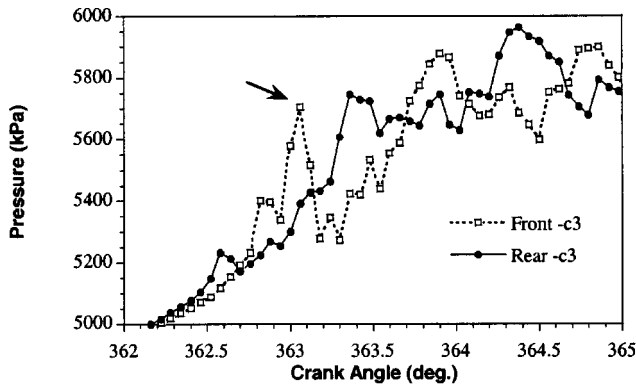


Fig. 6 Pressure traces from the front and rear transducers for cycle 3 (top) and cycle 5 (bottom). The increased amplitude of the initial pressure fluctuation in the second transducer-front transducer (top) and the rear transducer (bottom), indicates multiple sites of autoignition. Center spark, 1000 rpm, 24° spark advance (trace knock +12°).

transducer causing a pressure increase of 800 kPa. The initial stage of the second autoignition is felt first at the front transducer, where the pressure starts rising earlier than at the rear. However, once the violent autoignition occurs, additional mixture is rapidly consumed in the end-gas zone, thus causing the pressure at the rear transducer to increase to 800 kPa within 40 μ s. On the other hand, pressure at the front transducer remains momentarily constant before it rises rapidly, following the trend of the reflected waves at the rear transducer.

The period of approximately constant pressure at the front transducer is caused by the combination of two reasons. First, the rapid advancement of autoignition towards the rear where additional unburned mixture exists causes a rarefaction wave (decreasing pressure) moving towards the front transducer. The superposition of the rarefaction wave with the reflected pressure wave caused by the initial stages of autoignition maintains pressure temporarily constant at the transducer. Secondly, given the evidence of multiple autoignitions, the combination of the rarefaction wave with a pressure wave originating from another autoignition site causes pressure to remain constant near the front transducer.

Summarizing, it can be said that the violent autoignition is caused by multicentered autoignitions. It is initially sensed by both transducers, and then directionally propagates towards the rear. There is thus evidence of multiple autoignitions causing directional wave propagation. The pressure traces of cycle 5 are very similar to the ones shown in Fig. 13 of Stiebels et al. [6]. In their figure, evidence of a second autoignition was proven by high-speed photographs showing luminescence intensity differences in the flame. The aforementioned study was carried at sub-

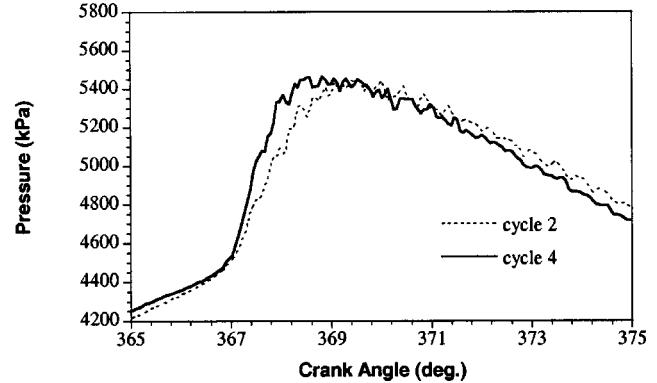
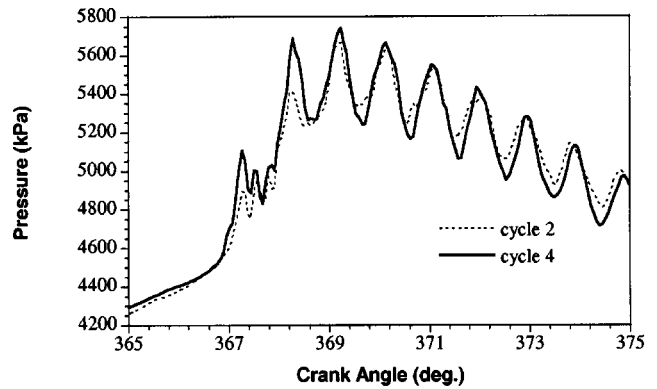


Fig. 7 Pressure traces from the front (top) and center (bottom) transducer for two cycles. Rear spark, 1000 rpm, 24° spark advance (trace knock +8°).

stantially heavier knock severity levels. In the particular cycle, the amplitude of pressure fluctuations was 10 bars, while the violent autoignition caused a 40 bar pressure increase.

Specific cycles for the rear spark-plug test are presented next. As has been shown in Fig. 3 (bottom) in this configuration, pressure fluctuations due to autoignition arise in the trace of the front transducer, but are almost absent from the trace of the center transducer. The pressure traces of cycles 2 and 4 are compared against each other in Fig. 7. Both the front and the center transducer signals for the two cycles are seen to be similar. The front transducer signals (Fig. 7, top) are almost identical, showing very closely the same timing of autoignition. The initial pressure fluctuations, immediately following autoignition, exist in the same number in both traces, proving that they are indeed caused by reflections of the initial wave on the walls. The center transducer traces, Fig. 7 (bottom), are also quite similar. The initial pressure rise caused by autoignition appears very clearly in the trace of the center transducer; however, evidence of pressure wave reflections does not exist.

Summary and Conclusions

An experimental study of the knock initiation and development period was conducted in a single-cylinder engine. The approach was based on simultaneously acquiring cylinder pressure data at two locations in the combustion chamber using a high sampling frequency, thus allowing the identification of spatial and temporal pressure characteristics introduced by autoignition. Two different transducer configurations were used. First, transducers were placed at the front and rear of the combustion chamber, and sec-

only at the front and the center of the chamber. Concerning the effects of transducer location and sampling frequency on the recorded signal, our conclusions are as follows.

- The location of the pressure transducer greatly affects the recorded pressure signal during knocking operation. During the initiation process, a transducer located far from the initiation region may not record the initial pressure disturbances. A transducer located at a pressure node of the resonant pattern, e.g., the center of the combustion chamber, records a much smaller amplitude of pressure fluctuations than the one recorded at locations close to the periphery.

- The cylinder pressure signal recorded at a pressure node of the resonant pattern will require less filtering and will provide more accurate net heat release analysis results. However, such a signal will also show a lower absolute value of knock intensity based on the amplitude of pressure fluctuations.

- A high sampling frequency (at least 50 kHz) is needed in the study of the knock initiation process in order to accurately capture the high frequency events occurring in the cylinder. Note, however, that using a higher than necessary sampling frequency introduces digitization error in light knocking cycles, and thus deteriorates the quality of the signal.

It can be concluded that a sufficiently high sampling frequency combined with the use of two transducers in the combustion chamber can provide valuable information on the knock initiation process. Such pieces of information include the approximate location of autoignition, the traveling speed and the direction of propagation of the waves, and the pressure ratio across them. More specifically, our work has shown the following:

- Normal flame propagation causes weak pressure waves which can only be detected by the pressure trace of a transducer close enough to their source. Such weak waves remain undetected in the presence of stronger fluctuations.

- The autoignition of the end-gas mixture causes substantial local pressure differences in the combustion chamber, leading to the creation of traveling pressure waves. In most cases, knock-induced pressure waves are of acoustic nature, and thus propagate in all directions inside the chamber.

- Multiple autoignitions in heavily knocking cycles cause pressure waves exhibiting directional propagation in the chamber. Directional properties arise from the combination of induced waves from different sites, but also from the combination between induced and reflected waves.

- Frequency analysis of recorded pressure data can provide the frequencies of the resonant modes of the chamber. The calculated frequencies for the first two resonant modes agree quite well with theoretically estimated frequencies.

Acknowledgments

This work was carried out at the Mechanical Engineering Department, University of Illinois at Urbana-Champaign and was supported by a grant from the Mitsubishi Motors Corporation. The contributions of Profs. Robert White, Lester Savage, and Alexander Vakakis of the University of Illinois and Mr. Kei Shigahara of the Mitsubishi Motors Corporation are greatly appreciated. The comments of an anonymous reviewer are also appreciated.

References

- [1] Drapper, C. S., 1938, "Pressure Waves Accompanying Detonation in the Internal Combustion Engine," *J. Aeronaut. Sci.*, **5**(6), pp. 219–226.
- [2] Zucrow, M. J., and Hoffman, J. D., 1976, *Gas Dynamics*, **2**, John Wiley and Sons, New York, pp. 69–111.
- [3] Lee, W., and Schaefer, H. J., 1983, "Analysis of Local Pressures, Surface Temperatures and Engine Damages under Knock Conditions," SAE Paper No. 830508.
- [4] Konig, G., and Sheppard, C. G. W., 1990, "End Gas Autoignition and Knock in a Spark Ignition Engine," SAE Paper No. 902135.
- [5] Konig, G., Maly, R. R., Bradley, D., Lau, A. K. C., and Sheppard, C. W., 1990, "Role of Exothermic Centers on Knock Initiation and Damage," SAE Paper No. 902136.
- [6] Stiebels, B., Schreiber, M., and Sadat Sakak, A., 1996, "Development of a New Measurement Technique for the Investigation of End-Gas Autoignition and Engine Knock," SAE Paper No. 960827.
- [7] Brunt, M. F. J., Pond, C. R., and Biundo, J., 1998, "Gasoline Engine Knock Analysis Using Cylinder Pressure Data," SAE Paper No. 980896.
- [8] Puzinauskas, 1992, "Examination of Methods Used to Characterize Engine Knock," SAE Paper No. 920808.
- [9] Syrimis, M., Shigahara, K., and Assanis, D. N., 1996, "Correlation Between Knock Intensity and Heat Transfer Under Light and Heavy Knocking Conditions," SAE Paper No. 960495.
- [10] Bendat, J. S., and Piersol, A. G., 1986, *Random Data Analysis and Measurement Procedures*, 2nd Ed., John Wiley and Sons, New York.
- [11] Checkel, M., and Dale, J., 1986, "Computerized Knock Detection from Engine Pressure Records," SAE Paper No. 860028.
- [12] Ando, H., Takemura, J., and Koujina, E., 1989, "A Knock Anticipating Strategy Based on the Real-Time Combustion Mode Analysis," SAE Paper No. 890882.
- [13] Meirovitch, L., 1976, *Elements of Vibration Analysis*, McGraw-Hill, New York.

Knock Rating of Gaseous Fuels

A. A. Attar

G. A. Karim¹

e-mail: karim@enme.ucalgary.ca

Department of Mechanical and Manufacturing
Engineering,
University of Calgary,
Calgary T2N 1N4, Canada

The knock tendency in spark ignition engines of binary mixtures of hydrogen, ethane, propane and n-butane is examined in a CFR engine for a range of mixture composition, compression ratio, spark timing, and equivalence ratio. It is shown that changes in the knock characteristics of binary mixtures of hydrogen with methane are sufficiently different from those of the binary mixtures of the other gaseous fuels with methane that renders the use of the methane number of limited utility. However, binary mixtures of n-butane with methane may offer a better alternative. Small changes in the concentration of butane produce almost linearly significant changes in both the values of the knock limited compression ratio for fixed spark timing and the knock limited spark timing for a fixed compression ratio. [DOI: 10.1115/1.1560707]

Introduction

Knock in spark ignition engines is an acknowledged barrier to the further improvement of efficiency, increased power, and the use of a wider range of fuels. The onset of knock, which is caused mainly by the autoignition of the unburned mixture in the end gas region of the charge, involves exceedingly rapid rates of combustion of the fuel-air mixture, increased heat transfer to the cylinder walls, excessively high cylinder pressure and temperature levels, and increased emissions which may lead to undesirable engine performance and the potential damage to engine components.

One of the most important factors in the consideration of knock is the resistance of the fuel to the incidence of knock. The terms *knock limit* and *knock rating* need to refer to a specialized and closely defined operating conditions. Over the years, a number of approaches have been established for the rating of gaseous fuels such as through the use of the *octane number* and the *methane number* (Ryan et al., [1], Leiker et al., [2], and Schaub and Hubbard [3]). These have their limitations (Klimstra et al. [4], and Kubesh et al. [5]) and there is still room for developing improved procedures for the knock rating of gaseous fuels in different engines and various operating and design conditions.

The present contribution examines experimentally the incidence of knock for binary mixtures of hydrogen, ethane, propane, and n-butane with methane in the CFR standard variable compression ratio spark ignited, research engine. It is suggested that n-butane and methane can be used as primary fuels for the knock rating of gaseous fuels instead of the use of other fuel combinations including the use of hydrogen and methane in the methane number.

Background

The octane number (ON), which uses iso-octane (2,2,4-trimethyl pentane) and n-heptane as the reference fuels and as defined by the ASTM procedure is primarily for the knock rating of liquid fuels. A lesser-known method for the rating of gaseous fuels is via the use of methane number (MN) (Lieber et al., [2]), which is based correspondingly on methane and hydrogen as reference fuels. A "100 MN" is given for pure methane and "zero MN" for pure hydrogen. A methane number is assigned to a gaseous fuel on the basis of the percentage by volume of methane in a blend of hydrogen and methane that exactly matches the knock intensity when using the fuel under a specified set of operating conditions in the test engine. Similarly a butane number (BN) (Ryan et al. [1]) was suggested to be based on a blend of methane and n-butane with pure methane assigned a value of zero while

n-butane a value of 100. Khalil and Karim [6], while using modeling methods suggested a *propane equivalent* for evaluating the knocking tendencies of natural gases. They assigned for the components of natural gas that are higher than butane an equivalent concentration of propane such that the modified and reduced in number of components, gas mixture had a similar knocking tendency as the original fuel under the same operating conditions.

Table 1 is a listing of the corresponding rating according to these differing methods for the common C1 to C4 normal paraffins, which make up most of natural gases and establish the combustion characteristics of a natural gas.

Leiker et al. [2] determined the methane number experimentally for a range of gaseous fuel mixtures and provided a correlation to predict the methane number of a gaseous fuel from a knowledge of its composition. Ryan et al. [1] examined different knock rating methods and found a linear relationship between the octane and methane numbers. They suggested that the "methane number appears to be the best choice for rating the knock sensitivity of natural gases." However, their spark timing was kept fixed and their results were based on the critical compression ratio for the knock limit. Their test conditions are listed in Table 2 for a naturally aspirated CFR engine. An approximately linear relationship was also found between the methane number and the compression ratio for the specified test procedure.

An alternative knock rating procedure employs a variable spark timing and presents the results on the basis of either the *knock limited spark timing* (KLST) for each compression ratio (Annand and Sulaiman [7]) or the *knock limited compression ratio* (KLCR) for a preset variable spark timing as a function of compression ratio, just as in the octane number rating method (Karim and Klat [8]). These procedures can be viewed to be closer to real engine operating conditions, chosen usually to obtain maximum power.

The problem remains that there are so many design and operating variables affecting the incidence of knock in an engine operating on a specific fuel. Conventional approaches proposed so far for knock rating do not give a reliable and universal classification of the knocking tendencies of gaseous fuels under practical operating conditions. Accordingly, this contributes to make experimental results from knock testing investigations somewhat confusing and producing sometimes conflicting statements.

Experimental Procedure

A number of approaches have been used to detect the onset of knock in spark ignition engines. In the present work, the incidence of knock was established directly from the observation of the cylinder pressure variations with time while using a flush mounted pressure transducer. The onset of knock, such as when the spark timing was advanced or the compression ratio increased from a knock-free setting could be identified by the appearance of high-frequency pressure oscillations near the beginning of the expansion stroke. These pressure oscillations would appear first in only

¹To whom correspondence should be addressed.

Contributed by the Internal Combustion Engine Division of THE AMERICAN SOCIETY OF MECHANICAL ENGINEERS for publication in the ASME JOURNAL OF ENGINEERING FOR GAS TURBINES AND POWER. Manuscript received by the ICE Division, October 1998; final revision received by the ASME Headquarters, September 2002. Associate Editor: D. N. Assanis.

Table 1 Knock Rating of C1 to C4 Normal Paraffins [1]

Gas	Motor ON	MN	BN
CH4	122	100	0.0
C2 H6	101	44	7.5
C3 H8	97	34	10
C5 H10	89	10	100

a small proportion of cycles. Increasing for example the compression ratio or the spark advance would increase the proportion of knocking cycles and the intensity of oscillations. In the present work, the knock boundary of operating conditions was taken when clearly perceptible pressure oscillations can be seen in 10 to 20% of the cycles. Once knock was detected the variations of the pressure with crank angle for 100 consecutive cycles were recorded by a data acquisition and computer system to confirm and record the condition for the knock limit with good accuracy.

The testing approach used in the present investigation, while using the CFR research variable compression ratio engine and fixed operating conditions, was based on employing a variable spark timing to establish the knock-free limit. Two constant values of compression ratio (8.5 and 11:1) and of equivalence ratio (0.80 and 1.00) were used. Once the required fuel composition and equivalence ratio were set, the spark timing was varied gradually up to the point of the onset of border line knock, established on the basis of the pressure-time records. Thus, the results can be presented in terms of *knock limited spark timing* for binary mixtures of the fuels, hydrogen, ethane, propane, and n-butane with methane, usually against the volumetric concentration of the gaseous fuel additive in the fuel mixture. This approach, which has been employed in the past by others (e.g. Annand and Sulaiman, [7]) tends to represent one of the operational procedures that is normally followed in practice to get out of a knocking condition in engines. However, mainly to compare our results with those of Leiker et al. [2], and those of Ryan et al. [1], some additional tests were carried out in the same engine at a fixed spark timing, as listed in Table 2, for two equivalence ratios of 0.80 and 1.00.

Knock Limited Spark Timing (KLST)

The variations of the knock limited spark timing (KLST) with the volumetric concentration of hydrogen, ethane, propane, and n-butane in binary mixtures with methane for two compression ratios and equivalence ratios of 0.80 and 1.00, are shown in Figures 1–4. The KLST decreases almost linearly with the volumetric concentration of hydrogen in the mixture, but begins to drop more significantly when the concentration of hydrogen increases beyond approximately 80%. This linear trend is a reflection of the nearly linear reduction of the combustion duration, while affecting the reactivity of the end gas mixture only little with increasing the hydrogen concentration in the mixture (Attar [9]). Values of the combustion duration are derived using the corresponding pressure-time records, as described by Bade Shrestha and Karim [10]. This is shown typically in Fig. 5. The change in equivalence ratio shown affects the KLST only little, especially for the higher compression ratio of 11:1. Retarding the spark timing somewhat towards the TDC position to avoid knock, increases the charge temperature during flame initiation and its subsequent propagation and speeds up the reactivity of the fuel mixture when it contains high concentrations of hydrogen. This produces a rapid drop in the

Table 2 CFR/RDH Engine Operating Conditions for Methane Number Rating

Equivalence ratio	1.0
Speed	900 rev/min
Spark timing	15° BTDC
Intake temperature	21°C

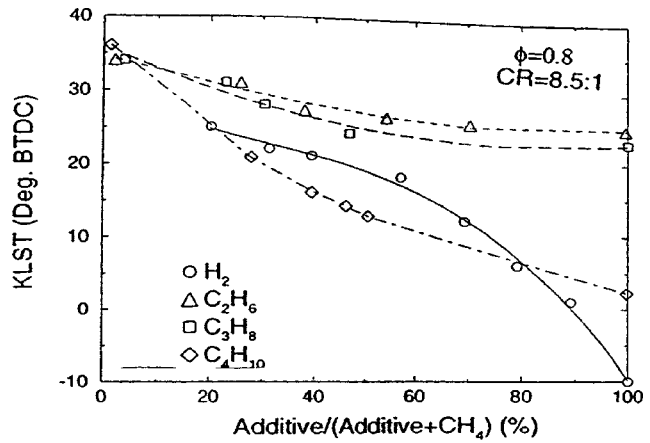


Fig. 1 Variation of the KLST with volumetric concentration of additive to methane at 900 rpm, CR=8.5:1, $\phi=0.80$, 87 kPa, and 27°C

KLST value. Excessive retardation of the spark timing beyond the TDC position will result in a substantial drop in power output.

The effect of changes in equivalence ratio on the KLST tends to become somewhat larger as the concentrations of ethane, propane, and butane increase in their binary mixtures with methane. There

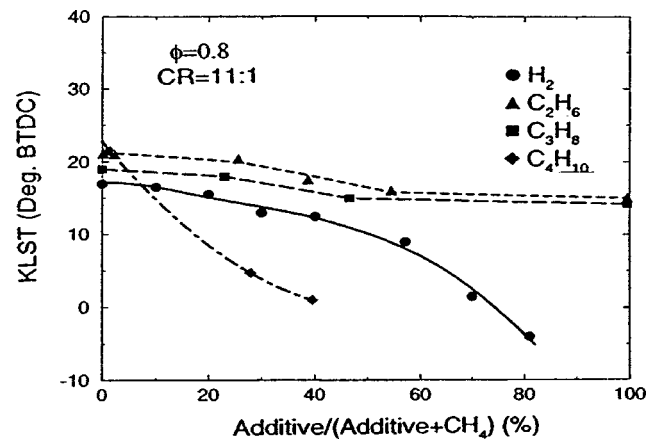


Fig. 2 Variation of the KLST with volumetric concentration of additive to methane at 900 rpm, CR=11:1, $\phi=0.80$, 87 kPa and 27°C

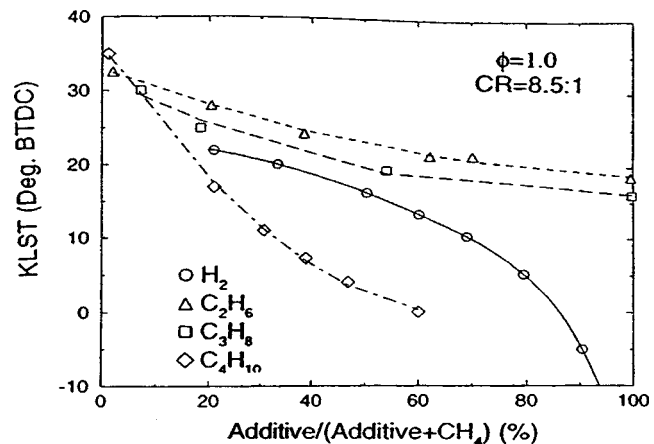


Fig. 3 Variation of the KLST with vol. concentration of additive to methane at 900 rpm, $\phi=1.0$, CR=8.5:1, 87 kPa and 27°C

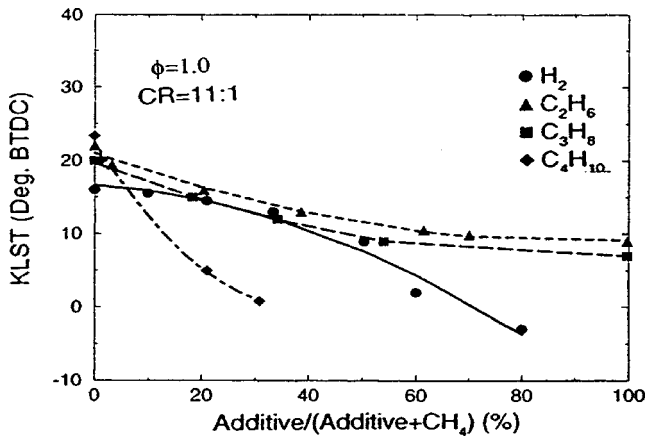


Fig. 4 Variation of the KLST with volumetric concentration of additive to methane at 900 rpm, $\phi=1.0$, CR=8.5:1, 87 kPa and 27°C

is an associated increase in the energy content of the mixture with increasing the concentration of these additive fuels, which produces higher temperature and pressure levels in the end gas. This is more pronounced for butane-methane mixtures. The figures show that increasing the extent of addition of ethane, propane and butane to the methane decreases the KLST throughout with its rate of drop decreasing as the concentration of the additive fuel is decreased except for hydrogen. This can be the result of the reduction of the effective polytropic index for compression in a fixed compression ratio engine, as the concentration of ethane, propane or butane increases in the mixture. Figure 6 shows the variation in the calculated value of the index with changes in the volumetric concentration of the fuel additive to methane in a stoichiometric methane-fuel additive fuel mixture in air. The drop in the value of the index with increased volumetric fraction of the additive fuel in the mixture results in a corresponding decrease in the average charge temperature at TDC, for a constant compression ratio and fixed intake conditions. In view of the exponential dependence of the reaction rate on temperature, this will slow down the autoignition reaction rates of the end gas and reduces the tendency to knock and its intensity. The associated relative reduction in the flame propagation rate is significantly less. In the

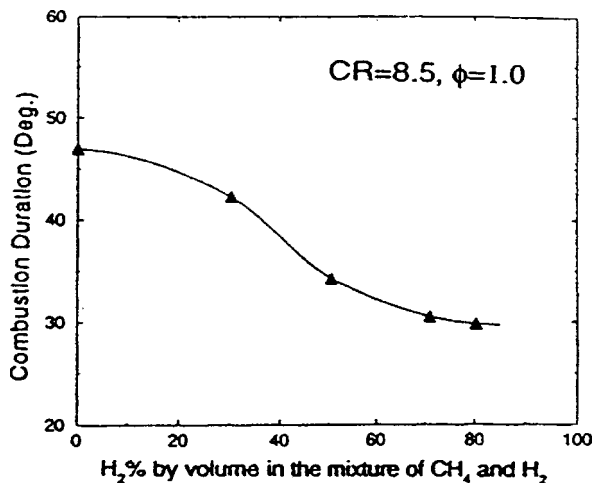


Fig. 5 Variation of the calculated combustion duration for mixtures of hydrogen and methane at 900 rpm, 20°BTDC, CR=8.5:1, $\phi=1.0$, 87 kPa and 27°C. Our own experimental points are shown

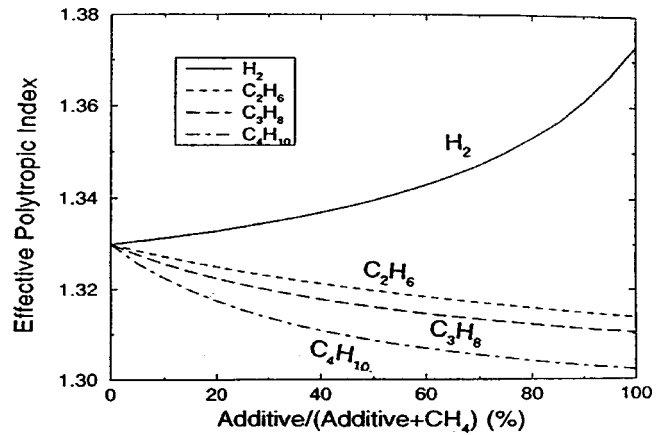


Fig. 6 Variation of effective polytropic index with volumetric concentration of additives in binary mixtures with methane at 900 rpm, CR=8.5:1, 87 kPa, and 27°C

case of hydrogen-methane mixtures, the charge temperature increases little due to the increase in the value of the corresponding effective polytropic index.

Under the same operating conditions, ethane addition to methane requires the most advance in KLST, while that for butane addition requires the least. The KLST for propane containing mixtures is less than that of the ethane mixtures but higher than that for hydrogen mixtures. The KLST for ethane and propane has the least sensitivity to their volumetric concentration in the fuel mixture. Changes in the composition of blends of hydrogen with methane showed no strong effect on the KLST, especially for the higher value compression ratio. Changes in the concentration of butane in butane-methane mixtures have a significant influence on the KLST throughout and can distinguish the knock intensity of the engine for the whole range of butane concentration in the mixture. This can indicate that butane-methane mixtures can provide a more sensitive indication of the knock rating of an unknown gaseous fuel mixture and may be considered as a good choice as reference fuel mixtures when compared to the other fuel mixture combinations examined.

Knock Limited Compression Ratio at Constant Mean Temperature at Top Dead Center (TDC)

An idealized procedure for comparing the reactivity of gaseous fuels in relation to the onset of knock may be considered under essentially similar effective temperature level during the flame propagation period. To have the value of the compression ratio kept constant while changing the fuel composition would not provide such a constant temperature condition. An alternative approach to the comparative testing of gaseous fuels in a variable compression ratio engine, such as the CFR, can be suggested. The value of the compression ratio can be suitably changed so as to retain the same mean temperature at top dead center (TDC) for all the fuel mixtures to be tested. The required compression ratio then will be given by the following relationship:

$$T_{TDC}/T_o = CR_m^{\gamma-1} = CR_{ref}^{\gamma_{ref}-1} \quad (1)$$

where $\gamma=Cp/Cv$ and CR is the compression ratio. T_o and T_{TDC} are the initial and the mean temperature at the end of compression, respectively. Subscript m stands for the fuel-air mixture, while ref stands for the methane-air mixture at the same equivalence ratio.

This observation highlights the difficulty of comparing the reactivity of different fuel mixtures in an engine in relation to the onset of knock. It points to the need for a proper link up between the thermodynamic conditions and the chemical kinetic aspects of the charge to assess the tendency of different fuel mixtures to knock in comparison to methane. Figure 7 shows the value of the

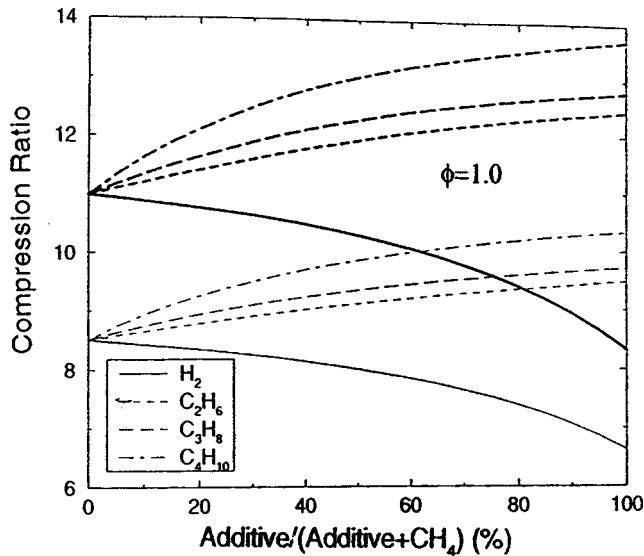


Fig. 7 Variation of the modified compression ratio, based on Eq. (1) with volume concentration of additive to methane at 900 rpm, $\phi=1.0$, CR=8.5:1, and 11:1

compression ratio needed to achieve the same mean temperature at TDC for different fuel additions to methane in air, for two values of compression ratios and stoichiometric mixtures. It can be seen that in order to maintain the same temperature level, the compression ratio needs to be adjusted increasingly upwards for the binary mixtures of ethane, propane, and butane with methane. For hydrogen mixtures the compression ratio needs to be reduced relatively substantially. These trends would indicate that the reactivity of a fuel mixture such as butane and methane in relation to knock in a certain constant compression ratio engine is normally moderated as the concentration of butane in the mixture is increased. This is a consequence of lowering the mean charge temperature due to the resulting changes to the thermodynamic properties of the charge. On the other hand, the corresponding reaction activity of hydrogen-methane mixtures is enhanced by the resulting increase in the mean temperature.

On the basis of retaining a similar effective temperature around the end of compression with changes in the volumetric concentration of the fuel additives to methane in binary mixtures through appropriate changes in the compression ratio in accordance with Eq. (1), the corresponding values of the KLST, as established

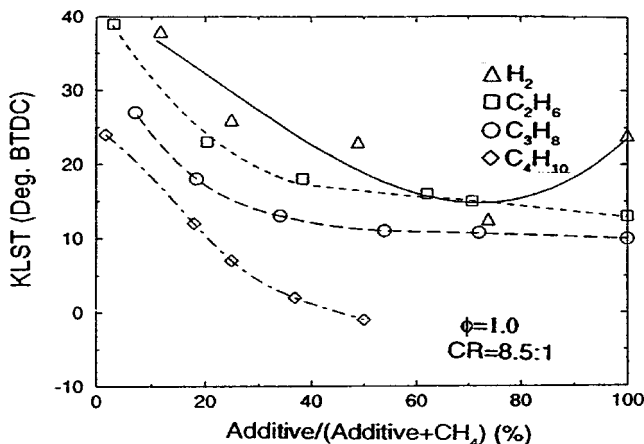


Fig. 8 Variation of the KLST with volume concentration of additive to methane with modified compression ratio at 900 rpm, $\phi=1.0$, CR=8.5:1, 87 kPa, and 27°C

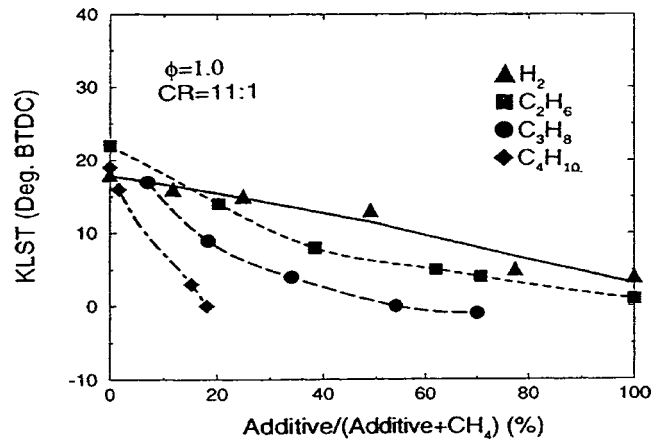


Fig. 9 Variations of the KLST with volume concentration of additive to methane with modified compression ratio at 900 rpm, $\phi=1.0$, CR=11:1, 87 kPa, and 27°C

experimentally, are shown in Figs. 8 and 9. These values are different from those determined earlier for the constant compression ratio engine case and shown in Figs. 1 to 4. Hydrogen has the highest value of KLST because of the lower compression ratio needed while butane-methane mixtures for example has the lowest values, because of the higher compression ratios needed. The resulting trends tend to be generally similar to those obtained at constant compression ratio, except for hydrogen-methane mixtures with the reference compression ratio of 8.5:1. The KLST then decreases with increasing the concentration of hydrogen in the binary fuel mixture but later on increases. This trend is due to the associated lowering of compression ratio. For blends of up to 40% ethane and propane, the KLST changes significantly with increasing the volumetric concentration of the additive fuel in the mixture. The spark timing is a convenient method for controlling the intensity of knock and its incidence in engines in general. The observed changes in KLST with changes in the composition of a binary fuel mixture serve to indicate that such fuel combinations can serve as a suitable basis for comparing the knock resistance qualities of fuel mixtures. However, it can be seen that a change in the concentration of butane in its binary mixture with methane has the strongest and virtually a linear effect on the KLST, which confirms them as a suitable candidate for use in the knock rating of fuel. On the other hand, the use of hydrogen-methane mixtures for this purpose has its complexities and thus limitations.

Knock Limited Compression Ratio (KLCR) at Constant Spark Timing

The variation in the knock limited compression ratio (KLCR) with the volumetric concentration of the fuel additive in a binary mixture with methane at a fixed spark timing of 15 deg BTDC are plotted in Figs. 10 and 11. The KLCR decreases with increasing the concentration of the additive in its blends with methane. The linear relationship, reported by Leiker et al. [2], for hydrogen-methane mixtures is shown, while ethane, propane, and butane blends with methane did not produce a similar linear variation. The linearity of the KLCR with hydrogen-methane mixtures is mainly due to an almost linear variation in the associated combustion period, while the corresponding relative variations in the reaction time to autoignition tend to be relatively somewhat small. Such a behavior is uncommon with the other fuel combinations. The corresponding combustion period variation for mixtures of other fuel additives with methane tends to be in comparison relatively small while the corresponding variations in the autoignition reaction time are much more substantial. For methane-butane

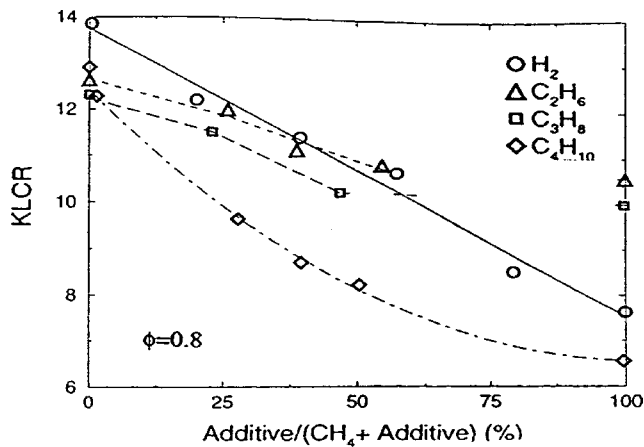


Fig. 10 Variation of the knock limited compression ratio with volume concentration of additive to methane at 900 rpm, 15 BTDC, $\phi=0.80$, 87 kPa, and 27°C

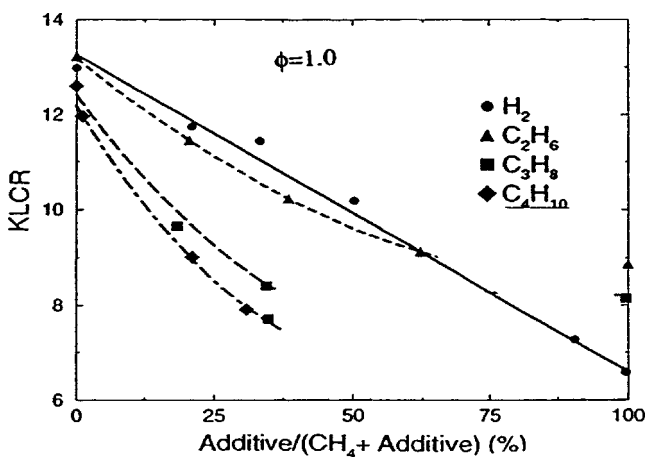


Fig. 11 Variation of the knock limited compression ratio with volumetric concentration of additive to methane at 900 rpm, 15° BTDC, $\phi=1.0$, 87 kPa, 27°C

mixtures, both the combustion period and reaction time to auto-ignition vary significantly with changes in the relative concentration of butane to methane.

Changes in the concentration of ethane and propane in their blends with methane do not show a significant effect on the KLCR for the lean mixture ($\phi=0.80$) investigated, while for hydrogen and butane, a more significant effect on the KLCR for different equivalence ratios can be observed. Therefore, when employing a constant spark timing procedure for establishing the knock-limited compression ratio, these trends would indicate again that a mixture of either hydrogen-methane or butane-methane are more suitable for the knock rating of a gaseous fuel than either ethane-methane or propane-methane mixtures. The equivalence ratio has almost a similar effect on the KLCR throughout for hydrogen-methane mixture, while its influence on the KLCR becomes greater when the concentration of butane in its mixture with methane increases. Consequently, butane-methane mixtures appear to be a more suitable fuel combination for determining the KLCR of an unknown fuel.

Summary and Conclusions

The KLCR and KLST decrease with increasing the concentration of ethane, propane, butane, and hydrogen in their binary mixtures with methane. Increasing the equivalence ratio for lean mixtures also decreases both the KLCR and KLST. The corresponding changes for ethane and propane additions have a relatively small effect on the KLCR and KLST, which make them less suitable for the knock rating of gaseous fuels. Hydrogen-methane mixtures show different influence on the KLCR and KLST based on the chosen knock rating procedure and the concentration of the hydrogen in the mixture. For constant spark timing, the variation of the KLCR with changes in the volumetric concentration of hydrogen in the mixture is linear, while the changes of KLST at constant compression ratio is not. Since the variations of KLCR and KLST with butane concentration in the mixture show a similar trend with sufficient sensitivity to the mixture composition, a butane-methane mixture may be considered to be a better alternative for the rating of gaseous fuels.

Acknowledgments

The financial assistance of Natural Science and Engineering Research Council (NSERC) of Canada, Alternative Fuel Systems (AFS) and the Ministry of Petroleum and Higher Education of Iran is gratefully acknowledged. The contribution to this work of Dr. Bade Shrestha is also acknowledged.

Nomenclature

- CR = compression ratio
- KLCR = knock limited compression ratio
- KLST = knock limited spark timing
- P = Pressure
- T = temperature
- TDC = top dead center
- ϕ = equivalence ratio
- θ = spark timing
- γ = heat capacity ratio

References

- [1] Ryan, T. W., Callahan, T. J., and King, S. R., 1993, "Engine Knock Rating of Natural Gases-Methane Number," *ASME J. Eng. Gas Turbines Power*, **115**, pp. 922-930.
- [2] Leiker, M., Christoph, K., Rankl, M., Cartellion, W., and Pfeifer, U., 1973, "Evaluation of Anti-Knock Property of Gaseous Fuels by Means of the Methane Number and Its Practical Application to Gas Engines," **72-DGP-4**, ASME, New York, pp. 1-15.
- [3] Schaub, F. S., and Hubbard, R. L., 1985, "A Procedure for Calculating Fuel Gas Blend Knock Rating for Large-Bore Gas Engines and Predicting Engine Operation," *Trans. ASME*, **107**, pp. 922-930.
- [4] Klimstra, J., Heranaez, A. B., Gerard, A., Karti, B., Quinto, V., Roberts, G., and Schollmeyer, H., 1999, "Classification Methods for Knock Resistance of Gaseous Fuels," *ASME Paper No. 99-ICE-214*.
- [5] Kubish, J., King, S. R., and Liss, W. E., 1992, "Effect of Gas Composition on the Octane Number of Gaseous fuels," *SAE Paper No. 922359*.
- [6] Khalil, E. B., and Karim, G. A., 2002, "A Kinetic Investigation of the Role of Changes in the Composition of Natural Gas in Engine Applications," *ASME J. Eng. Gas Turbines Power*, **124**, pp. 404-411.
- [7] Annand, W. J. D., and Sulaiman, S. J., 1970, "Knock Limits and Performance of Some Gaseous Fuels in a Supercharged Spark Ignition Engine," *Proc. Inst. Mech. Eng.*, **185-62/71**, pp. 857-867.
- [8] Karim, G. A., and Klat, S. R., 1966, "Knock and Autoignition Characteristics of Some Gaseous Fuels and Their Mixtures," *J. Inst. Fuel*, **39**, pp. 109-119.
- [9] Alizadeh Attar, A., 1997, "Optimization and Knock Modeling of a Gas Fueled Spark Ignition Engine," Ph.D. thesis, Mechanical Engineering, University of Calgary.
- [10] Bade Shrestha, O. M., and Karim, G. A., 2001, "An Experimental and Analytical Examination of the Combustion Period for Gas-Fuelled Spark Ignition Engine Applications," *Inst. Mech. Eng. J. Power Energy*, **215**, pp. 63-74.

Development of the Low-Emission GE-7FDL High-Power Medium-Speed Locomotive Diesel Engine

G. Chen

Department of Mechanical Engineering,
Gannon University,
Erie, PA 16541

P. L. Flynn

S. M. Gallagher

E. R. Dillen

GE Transportation Systems,
Erie, PA 16531

This paper summarizes the technical development of the low-emission GE-7FDL series locomotive diesel engine. The development focused on reducing the engine exhaust NO_x emission significantly while reducing and curbing other visible and nonvisible emissions with minimal adverse impact on the engine fuel efficiency and minimal changes to the engine system and components. Concepts were analyzed, and were investigated using a single-cylinder 7FDL research engine. A low-emission 16-cylinder 7FDL engine and a GE locomotive prototype were built and tested for performance demonstration, function evaluation, and design optimization. The GE low-emission 7FDL engines and locomotives have been in production. The newly developed low-emission locomotive engine meets the EPA Tier-0 levels without fuel efficiency penalty. This was accomplished with minimal changes to the engine system and components. The desired engine reliability performance is retained. The engines are interchangeable with the preceding 7FDL baseline models, and the upgrade of the existing baseline engines to the low-emission version is facilitated. [DOI: 10.1115/1.1563241]

Introduction

Medium-speed heavy-duty diesel engines are used as the motive power for present diesel electric locomotives. The Clean Air Amendments of 1990 directed the U.S. Environmental Protection Agency (EPA) to establish regulations on previously unregulated non-road mobile sources including rail locomotives. The EPA's final rule for locomotive exhaust emissions requires future manufactured or remanufactured domestic locomotives to meet standards at different stringency levels for both line-haul and switch locomotive duty cycles. This includes remanufactured locomotives to meet Tier-0 standards from 2001, newly manufactured locomotives to meet Tier-1 from 2002 through 2004, and newly produced locomotives to meet Tier-2 in 2005 and later, as shown by the regulation, [1]. The standards for the locomotive line-haul duty cycle shown by EPA [2] are given in Table 1. The regulations require locomotives to meet the standards over a wide range of environmental conditions. For instance, the standards of each Tier shown in Table 1 must be met from sea level up to 1219 meter (4000 ft) altitude by testing and up to 2134 meter (7000 ft) altitude by engineering analysis verification, as required by EPA [1].

The GE 7FDL series is one of the main engines for heavy duty locomotives in North America and worldwide. The engine's predecessor was designed by Cooper Bessemer and was adopted by GE in the late 1950s for entry into the heavy-duty locomotive market as a complete vehicle supplier. The 16-cylinder version was introduced at 1864 kW (2500 hp) in 1963 in the classic U25 locomotive. Over the next three decades the power grew successively to 2237, 2461, 2685, 2908, 3057, and 3356 kW (4500 hp) on the same bore and stroke format. This growth was made possible by the constant development of turbocharger, fuel injection, manifolds, power assemblies, and all other stressed components. The engine is the highest production medium speed diesel engine in the world, with over 1200 engines produced annually. The operating fleet numbers near 10,000 engines.

The engine has retained its original cross-section layout, as shown in Fig. 1, in spite of an almost 100% power growth. The individual power assemblies are carried on a low deck crankcase. The camshafts are driven by single reduction gears and are accessible through the crankcase doors. No separate camshaft openings and a deep skirt give the crankcase high bending and torsional rigidity. The crankshaft is supported in underslung, side bolted steel bearing caps. The connecting rod is a master-slave design which reveals its Cooper Bessemer heritage. This design provides one bearing for the full width of the crankpin for modest bearing loads. The piston pins are bolted to the rod ends which also provide full-width bearings. Pistons are composed of steel crowns bolted to aluminum skirts.

The electronic fuel injection system uses a solenoid-controlled pump mounted high on the cylinder and coupled by a short stiff fuel line to a low sac injector. The four-valve cross-flow head provides very little swirl to the quiescent combustion chamber. Two modular pulse converter exhaust manifolds feed a single turbocharger mounted on the free end of the engine. The turbo has been highly developed over the years in conjunction with GE Aircraft Engine and its high efficiency is largely responsible for the high power density and low fuel consumption of the engine. The basic specifications of the 7FDL engine baseline can be found in Table 2.

General levels of the exhaust gaseous emissions of the noncompliant 7FDL 16-cylinder engine equipped with an electronic fuel injection (EFI) system and split-intercooling system are included in Fig. 2 for comparison. This shows oxides of nitrogen (NO_x) is

Table 1 EPA Standards for line-haul locomotive duty cycle

	NO _x	CO	HC	PM	SMOKE (%OPACITY)		
					Steady state	30-sec peak	3-sec peak
					(g/hp-hr)		
Tier 0	9.5	5.0	1.0	0.60	30	40	50
Tier 1	7.4	2.2	0.55	0.45	25	40	50
Tier 2	5.5	1.5	0.30	0.20	20	40	50

Contributed by the Internal Combustion Engine Division of THE AMERICAN SOCIETY OF MECHANICAL ENGINEERS for publication in the ASME JOURNAL OF ENGINEERING FOR GAS TURBINES AND POWER. Manuscript received by the ICE Division, Oct. 2001; final revision received by the ASME Headquarters, June 2002. Associate Editor: D. Assanis.

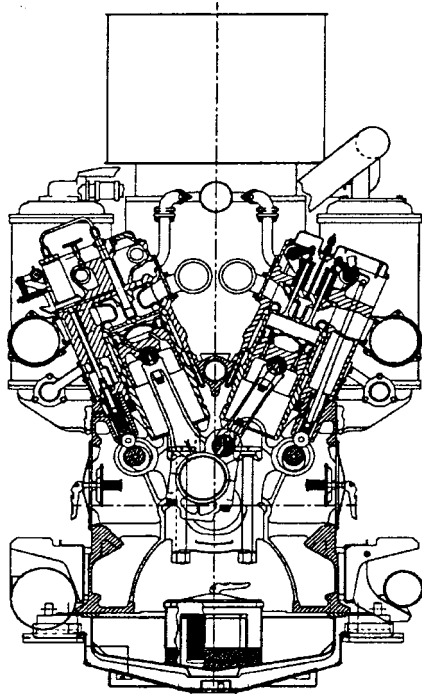


Fig. 1 Cross section of 7FDL engine baseline

a primary concern among the exhaust gaseous emissions of the baseline locomotive engine. The NO_x emission needed to be significantly reduced to meet the Tier-0 and further Tier-1 regulation standards while reducing and curbing other exhaust emissions such as smoke, particulate matters (PM) and carbon monoxide (CO). The adverse impact on the engine fuel efficiency needed to be avoided and minimized in the engine emission-reduction development. All of this needed to be realized with minimal changes to the existing baseline engine system and components in consideration of the interchangeability and upgrade from the baseline engines to the low-emission configuration.

Basic Technical Approach

The basic technical approach in the development was to meet the following objectives: (a) reduction in NO_x emission while reducing and curbing other visible and nonvisible emissions to comply with the regulations to meet the Tier-0 and further Tier-1 standards; (b) no or minimal loss in the engine fuel efficiency compared to the non-compliant baseline; (c) minimal changes in engine system and components; and (d) no adverse impact on any other desirable performance characteristics.

For NO_x reduction, one of the conventional effective means is to retard fuel injection timing. Nevertheless, using retarded injection timing to reduce NO_x results in lowering the cycle efficiency

Table 2 Specifications of GE-7FDL16 locomotive engine baseline configuration

Item	Specification
Configuration	V16, DI diesel, turbocharged, intercooled
Operating cycle	4-stroke
Bore	228.6 mm
Stroke	266.7 mm
Displacement volume	10.95 liter
Compression ratio (static)	12.2:1
Type of fuel injection system	Electronic fuel injection
Rated speed	1,050 rpm
Normal rated power	3,356 kW (4500 hp)

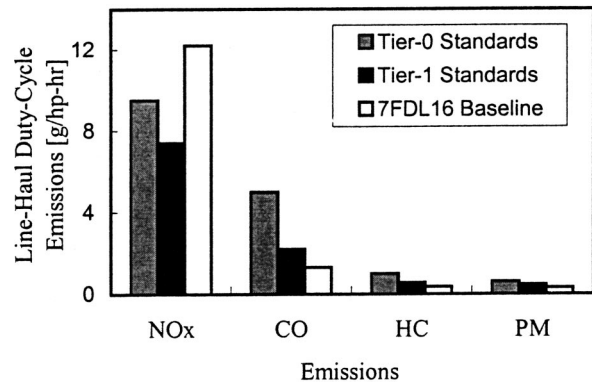


Fig. 2 Locomotive baseline emissions and comparison

and deteriorating the engine fuel efficiency. The mechanism can well be described by the low relative efficiency concept by Hsu [3]. The trend of change in the specific fuel consumption (SFC) of the 7FDL16 engine baseline in full load condition versus the NO_x reduction by only retarding fuel injection timing is shown in Fig. 3. Also, while the major noncompliant gaseous emission of the 7FDL16 baseline engine was NO_x , the additional concerns were on the exhaust emissions of smoke, CO, and PM. It was worth attention for the following reasons: (a) smoke, particularly transient smoke, of a turbocharged locomotive diesel engine may become a concern at some notch or notch-change operations; (b) retarding fuel injection timing to reduce NO_x would increase the fuel late burning and thus would usually increase CO, PM, and smoke; and (c) smoke and PM emissions may increase with time as the engine wears.

One of the measures to address the above concerns in this development was to increase the absolute cycle efficiency by raising the cylinder compression ratio (CR). Normally in a high-power medium-speed diesel engine, raising compression ratio is limited by the structurally allowable peak cylinder pressure. When injection timing is retarded, the engine peak cylinder pressure will decrease. Thus, coupled with retarding fuel injection timing, the CR can be increased to compensate for the efficiency loss brought by the timing retardation, while utilizing the maximum allowable structure capability without exceeding the peak firing pressure limit. For reducing NO_x without loss in the fuel efficiency, lowering intake manifold air temperature (MAT) can be effective as well. Lowering MAT reduces the initial combustion air temperature and therefore the peak cycle temperature is lower. The capability of lowering MAT in a diesel engine is generally limited by the intercooling system design and capacity. In addition, the late burning can be reduced with higher fuel injection rate due to the

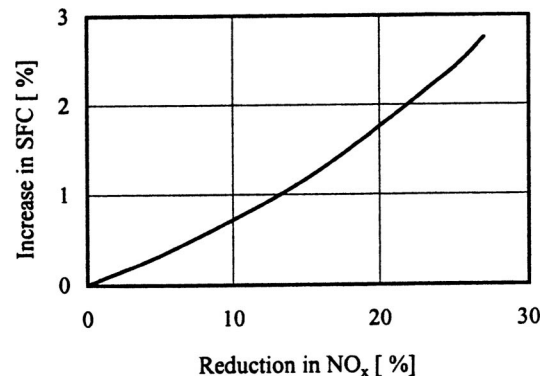


Fig. 3 Efficiency affected by solely retarding injection timing to reduce NO_x (estimated for 7FDL16 engine, full load)

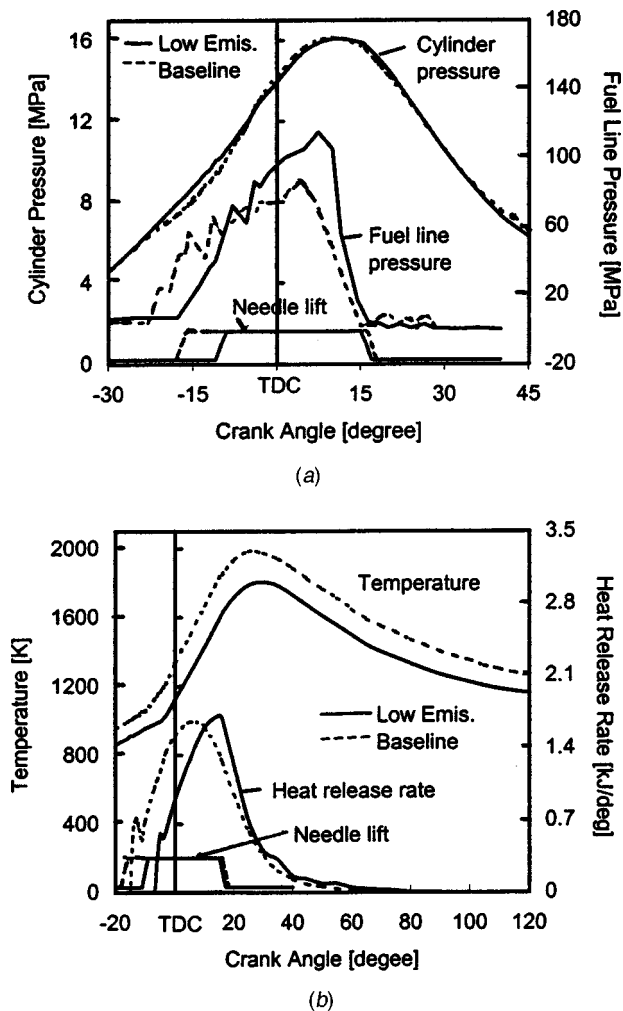


Fig. 4 Engine combustion analysis for the emission-reduction approach development; (a) cylinder pressure and fuel injection and (b) temperature and heat release

combined effect of increased timely heat release and shortened injection duration. Thus, sufficient soot burnoff time is maintained and the related emissions can be controlled. Higher fuel injection rates with higher injection pressures also have the added advantage of providing smaller fuel droplet size and higher fuel-air relative velocity for fast evaporation. In such case, the soot generation becomes less also.

Therefore, the technical approach to achieving the development objectives and the required emission reduction for the 7FDL locomotive engines is summarized as follows: modify fuel injection timing; increase compression ratio; increase fuel injection rate; optimize intake manifold air temperature based on the intercooling system capacity; improve turbocharger match and air boost; and optimize individual notch and duty-cycle operations.

The following underlying guidelines were followed in the development: maintain the baseline peak cylinder pressure, and the thermal loading on the engine components are not to exceed the previous production system. It is anticipated that much time can be saved for reliability development due to the consideration of these guidelines.

The in-cylinder combustion comparison analyzed using a set of test results is illustrated in Fig. 4. Relative to the nonsplit cooling 7FDL engine baseline (shown as baseline), the low-emission configuration (shown as low emis.) has a retarded fuel injection timing, raised compression ratio, increased injection pressure and lowered manifold air temperature. When the needle-lift start indi-

cating the fuel injection-start timing, is retarded from the baseline, the peak cycle temperature becomes lower. By lowering MAT, the cycle temperature is further reduced. As CR is raised with fuel injection timing retarded, the peak cylinder pressure can be maintained at the same level, as shown in the top part of Fig. 4. The higher injection rate due to the higher injection pressure in the low emission configuration results in the fuel injection ending earlier and thus injection duration is shorter. This means that for the 7FDL engine, by modifying the designs of a limited amount of engine components, the Tier-0 and possibly Tier-1 emissions requirements can be met by changing the combustion process.

Components Development and Design

In order to increase the compression ratio of the GE-7FDL engine with minimal impact on the overall engine configuration and with the interchangeability of the power-assembly components retained, the following engine components were investigated and redesigned, with the fundamental system consideration shown by Hsu and Chen [4] and by Hsu et al. [5].

Piston Crown Bowl Shape. Raising compression ratio was accomplished by simply reducing the top dead center (TDC) piston-to-cylinder head clearance volume. The piston crown with its top bowl contour was redesigned to reduce the TDC clearance volume, and to retain the required fuel injection jet flow behavior and combustion performance.

Cylinder Head Port Flow and Valve Event. The valve cam lift profiles for both the intake and exhaust valves were modified to accommodate the consequent smaller piston-to-valve bumping clearance when compression ratio was raised. With the high level of brake mean effective pressure (BMEP) at which medium-speed diesel engines operate, sufficient scavenging flow is necessary. The cylinder head of the engine was redesigned on the valve port throat bore for both intake and exhaust without changes to the valve seats. Thus, the required scavenging flow will be maintained or even improved while physically allowing sufficient piston-to-valve clearance after changing to the high compression ratio configuration.

Fuel Cam Profile. The fuel cam lift profile was changed from the baseline to obtain a higher cam lift velocity and consequently higher injection pressure. Achieving suitable match in phase between the cam lift velocity and injector needle lift duration was also included in the investigation and design. The higher-rate fuel cam, when used with the current EFI pump, is capable of delivering both the higher maximum and mean injection pressures. Analysis and experimental validation has shown that the cam loading is within the desired range and the desired reliability of the cam and driving components should be maintained.

Fuel Injector. As part of the combustion chamber design refinement and combustion process optimization, fuel injectors with different spray included angles were investigated in the development in response to the piston crown bowl shape change. As a result, the injector nozzle with a suitable spray included angle was determined.

Development With Single-Cylinder Research Engine

A single-cylinder 7FDL research engine was configured to verify the concepts and technical feasibility and capability. The engine has similar configuration parameters as the GE-7FDL series engine. The engine was supercharged with its intake manifold air pressure (MAP) and temperature (MAT) externally controlled. The exhaust back pressure could also be manually adjusted. A digital data acquisition and processing system, described in more detail by Hsu and Hoffman [6], was used to acquire and store outputs from transducers sensing the required parameters such as pressures, speed, torque, and injector needle lift. The in-cylinder combustion analysis and heat release

Table 3 Changes in emissions and efficiency with HCR crown design (single-cylinder engine, full load)

	Baseline	HCR Crown A	HCR Crown B
NO _x	+0%	-42.5%	-40.9%
SFC	+0%	+0.7%	+1.9%
Smoke (BSU)	+0	+0.02	+0.21

information were obtained through the computerized analysis and calculation based on the acquired data. The exhaust gaseous emissions and smoke were also measured.

Preliminary Investigation of Emission Reduction Capability

At the initial stage of investigation, various designs of the piston crown top contour were used to raise compression ratio, and tested to verify the desired emission reduction and performance capability. All test runs were at full load and compared at the same peak cylinder firing pressure. The comparison of two crowns to form the same increased compression ratio with the same level of MAT is shown in Table 3. The injection timing was retarded and the injection rate was modified from the baseline. For the reduction in NO_x, the fuel efficiency loss is considerably reduced with the HCR single-cylinder engine, compared to the engine solely retarding fuel injection timing. It is seen from Table 3 that the piston crown A is better in terms of NO_x reduction and fuel consumption, as well as smoke. It was chosen for the further development based on its better combustion results.

In the high-compression-ratio (HCR) configuration with the MAT unchanged and injection timing retarded without injection rate modification from a baseline, the NO_x reduction was the result of both lowering the peak cycle temperature and the smaller amount of fuel burned in the initial premixed stage immediately following fuel ignition. This is shown in the Fig. 5.

Intake Manifold Air Temperature Effect. The effect of MAT on the cylinder temperature of the 7FDL engine was investigated. The cylinder temperature history analyzed from the single-cylinder engine test results is shown in Fig. 6. As the MAT is decreased, the cylinder cycle temperature becomes lower, contributing to the NO_x reduction. This indicates if the HCR engine is run at a lower MAT, then the NO_x can be further reduced due to

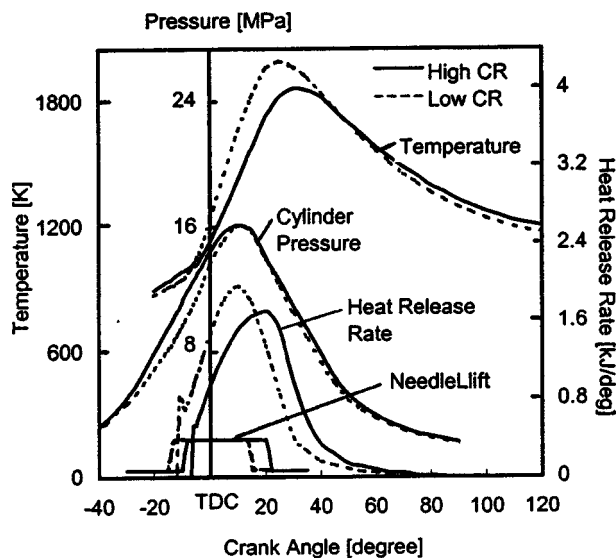


Fig. 5 Engine combustion analysis for increasing compression ratio coupled with modifying injection timing (single-cylinder engine)

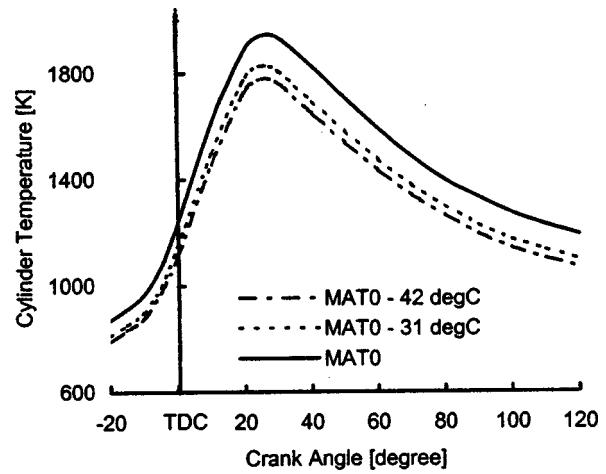


Fig. 6 Intake manifold air temperature effect on cylinder temperature

the further decreased cycle temperature. The comparison of the analyzed combustion process parameters is included in Fig. 4.

Fuel Injection Rate. The test was also conducted on the single-cylinder engine to verify that a higher fuel injection rate can be achieved with the modification in the fuel system. This is presented by the injection pressure trace shown in Fig. 7 from the single-cylinder research engine tested at the full load condition. With the modification, both the maximum and mean injection pressures are higher, and the injection duration is shortened.

Injector Tip Spray Included Angle Development. As part of the combustion chamber design refinement, injector tips with different spray included angles were experimentally investigated on the HCR single-cylinder engine. The spray included angle is illustrated in Fig. 8. The single-cylinder engine tests focused on the injectors with the spray angles (θ , $\theta+5^\circ$, $\theta+10^\circ$) for the detailed effect-on-combustion analysis, since the preliminary engine tests and analysis indicated a lower overall performance by injectors in the angle smaller than θ . Tests were run at full load. The θ spray included angle injector tip had the best fuel efficiency, highest NO_x emissions and lowest smoke level. All these indicators are summarized in Table 4. A typical cylinder firing pressure and heat release comparison of the θ and $\theta+5^\circ$ injectors is shown in Fig. 9. The cylinder pressure history of the $\theta+5^\circ$ injector tip drops down after the peak faster than the θ tip, as shown in the top part of the figure. The heat release comparison at the bottom depicts the initial heat release rates for the two injectors are about the same. Later the heat release of the $\theta+5^\circ$ tip

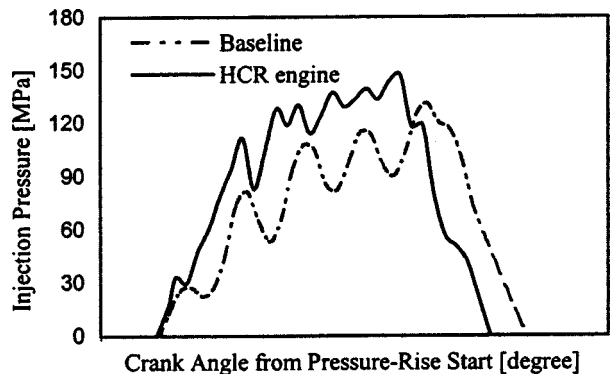


Fig. 7 Fuel injection pressure modification in the HCR engine configuration

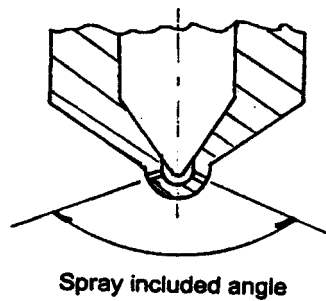


Fig. 8 Illustration of injector tip spray included angle

becomes slower and arrives at a lower peak value. Some degrees after TDC, the heat release rate for the $\theta+5^\circ$ tip becomes higher, signifying more late burning. The fuel efficiency loss is a direct consequence of this kind of untimely burning. The late burning shortens the time for soot burn off period and higher smoke emissions are the consequences. The θ° spray included angle injector tip was chosen.

Fuel Cam Phase Investigation. With retarding the fuel injection timing and modifying the fuel cam profile, the investigation and optimization of the fuel cam phase was needed. A shift in the phase of cam profile is illustrated in Fig. 10. Following preliminary analysis, two fuel cams with the modified profile and three-deg difference in the cam phase were tested and compared at about the same brake power. The measured engine performance results are summarized in Table 5. From Table 5, the phase-retarded cam has higher injection pressure and slightly lower indicated fuel consumption (ISFC) than the standard-phase cam. However, the higher injection pressure and lower ISFC did not yield lower brake fuel consumption (BSFC). Further data analysis

Table 4 Injector tip spray included angle comparison (single-cylinder engine, full load)

	θ° Angle	$\theta+5^\circ$ Angle	$\theta+10^\circ$ Angle
BSFC change	+0%	+2.1%	+2.4%
NO _x change	+0%	-10%	-8.4%
Smoke change (BSU)	+0	+0.28	+0.13

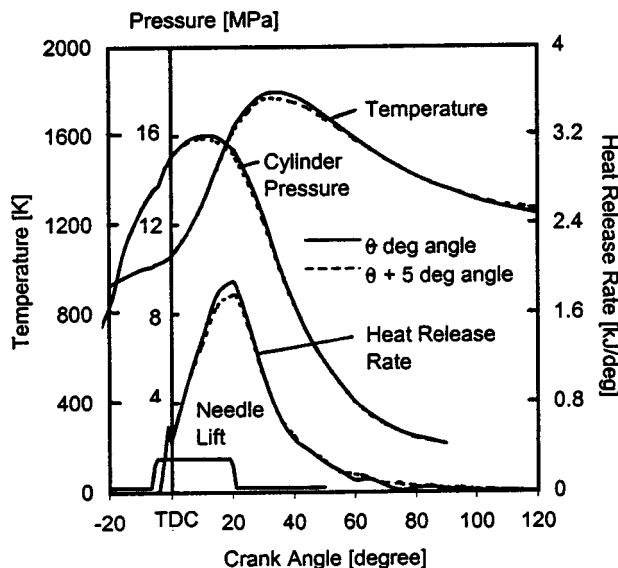


Fig. 9 Comparison of in-cylinder efficiency between two spray angle injector tips

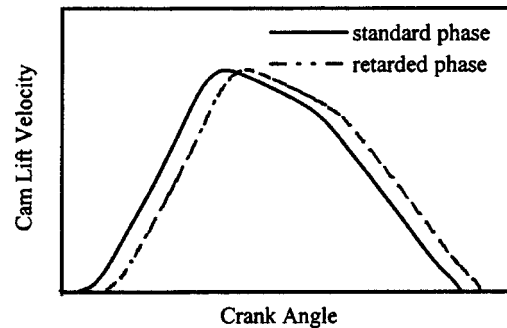


Fig. 10 Illustration of the fuel cam phase shift

had shown that, although the two cams were tested at about the same brake horsepower, the indicated power (IkW) for the phase retarded cam was higher than the standard-phase cam. The energy needed to drive the retarded cam was higher due to the higher mean injection pressure. However, the more efficient combustion with the phase-retarded cam cannot compensate for the greater amount of work needed to drive the fuel injection system, and consequently, the brake efficiency was lower. The change from the standard to the retarded phase may increase loading on the fuel injection components. In summary, the retarded-phase cam did not show much advantage over the standard-phase cam.

Development of 16-Cylinder Locomotive Engine

Following the single-cylinder engine testing, a 16-cylinder 7FDL locomotive engine (GE-7FDL16) in the HCR configuration was built and tested for design verification and optimization. Compared to the single-cylinder engine, the full-size engine was turbocharged and thus the turbocharger effect to the engine operation was included. During the full-size engine development, the compression ratio was incrementally changed from the engine baseline. The engine in various compression ratios was tested to optimize the engine design and performance.

The engine exhaust species measured during the tests included: CO₂, CO, NO_x, HC, smoke opacity, and PM. The exhaust emissions were measured by the equipment as follows: NO_x by a chemiluminescence analyzer, CO by a nondispersive infrared analyzer, HC by a heated flame ionization analyzer, PM by a split particulate tunnel, and smoke opacity by a full-flow opacity meter. For the purpose of evaluation and comparison, the measured NO_x emissions were corrected for inlet air temperature and humidity to a standard condition. The engine specific fuel consumption measured was also corrected to standard reference conditions of inlet air temperature and barometric pressure including the AAR reference condition. Results of the multi-cylinder engine development and investigation are summarized as follows.

Evaluation of Valve Overlap Flow. As one of the engine components changed to form the low-emission engine configuration, the cylinder heads were tested for comparison. The test was conducted on the 7FDL16 engine prior to raising the compression ratio. The difference between MAP and pre-turbine pressure

Table 5 Test results of fuel cam phase difference (single-cylinder engine, full load)

	Standard HCR Cam	Phase-Retard ed HCR Cam
Inj. pressure change	+0%	+1.2%
BSFC change	+0%	+0.6%
BkW	196.6	196.8
IkW	228.8	230.2
ISFC change	0%	-0.1%
Smoke change (BSU)	+0	-0.02

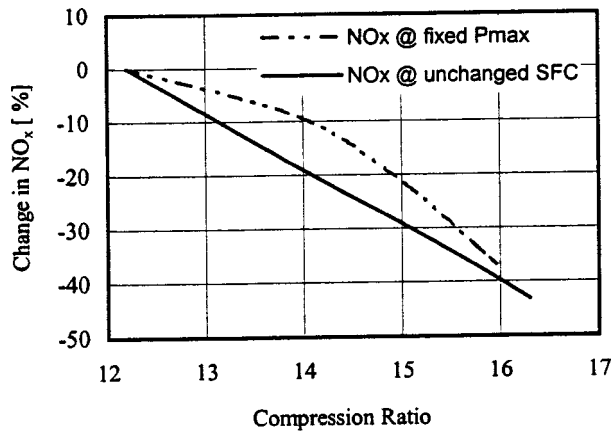


Fig. 11 Reduction in NO_x versus compression ratio (7FDL16 engine, full load)

(Δp_{ov}) was monitored as an indication of the valve flow efficiency during the valve overlap. The results compared with the baseline configuration and indicate that the Δp_{ov} became smaller as the modified head was applied. When both the modified cylinder heads and modified valve cam shafts were used, the Δp_{ov} was about the same as that of the engine baseline, meaning the required scavenge flow during the valve overlap was retained.

NO_x Reduction and Efficiency With Raising Compression Ratio at Full Load. Full-load operation of a locomotive engine generally consumes a major part of the total duty-cycle fuel and contributes a major part to the production of the duty-cycle NO_x and other gaseous emissions. The measured NO_x emissions versus compression ratio in the 16-cylinder engine full load condition are plotted in Fig. 11. As shown in the figure, with the averaged peak cylinder pressure remaining about the same, the NO_x emission decreases rapidly as the compression ratio increases from the baseline while the specific fuel consumption (SFC) remains below or the same as that of the baseline. The decrease in the NO_x emission was mainly due to the fuel injection timing retardation, and the retained engine fuel efficiency was mainly due to raising the compression ratio. The NO_x reduction versus raising compression ratio with SFC remaining unchanged is also shown in Fig. 11. All of this indicates, increasing compression ratio up to a certain level, coupled with retarding fuel injection timing allows the engine to achieve the NO_x reduction at full load condition without loss in the fuel efficiency within the allowable structure capability.

NO_x Reduction and Efficiency at Partial Load. The HCR engine test results showed the advantage of NO_x reduction at partial loads as well. Unlike the full-load operation at which the pressure p_{max} is dominating, partial load operation usually does not have a concern on the peak cylinder pressure limit. In partial loads, the peak cylinder pressure is always lower than the maximum allowable p_{max} and thus fuel injection timing may freely be set to achieve desired performance such as the exhaust emissions and the fuel efficiency. Figure 12 shows the reduction in NO_x of the tested 7FDL16 engine versus compression ratio without change in the fuel consumption at a half-load condition. As CR increases, the engine NO_x emission at the half-rated power also becomes lower under no penalty in SFC.

Duty-Cycle NO_x Reduction and Efficiency. In addition, the engine was also tested and evaluated through all of the locomotive notch conditions. Using the EPA defined locomotive line-haul duty-cycle weighting factors with the measured emissions, the line-haul duty-cycle NO_x reduction without sacrifice in the fuel efficiency compared to the baseline along with raising compression

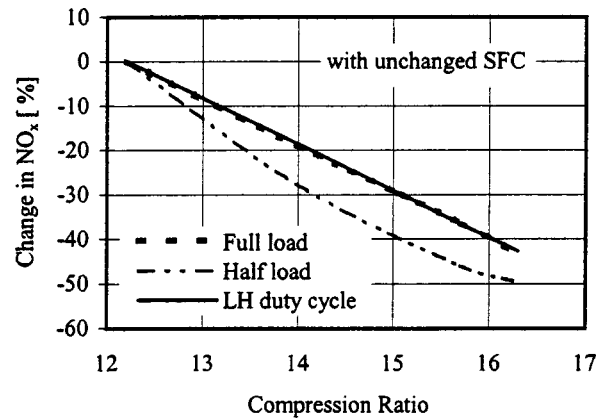


Fig. 12 NO_x reduction versus compression ratio with unchanged SFC (7FDL16 engine)

ratio is shown in Fig. 12 as well. The desired reduction in the duty-cycle NO_x emissions with retaining the desired fuel efficiency was achieved and demonstrated.

Effect of Manifold Air Temperature on NO_x Production. The full-size multicylinder locomotive engine was also tested under the full load condition over various intake MAT to investigate its effect on the NO_x generation. The MAT is the temperature of air in the intake manifolds after the turbocharger compressor and intercooler before the engine cylinders, and is different from the ambient temperature. The measured NO_x emission versus MAT is shown in Fig. 13. The main effect of MAT change was on NO_x , and the NO_x generation became lower as MAT was lowered.

Combustion and Heat Release Enhancement. The higher fuel injection rate accompanied with the higher compression ratio reduces the in-cylinder untimely combustion caused by retarding fuel injection timing. Thus the engine thermal loading and the exhaust emissions such as PM, smoke, and CO can be reduced. As a proper indication for the magnitude of late burning and untimely combustion, the temperature of exhaust gas at the location before the turbocharger-turbine entrance, usually called pre-turbine temperature, was measured. The full load results can be found in Fig. 14 in contrast with those from the engine baseline only retarding fuel injection timing to reduce NO_x . It is indicated that, as the fuel injection system with a higher injection pressure and improved atomization is applied to the engine with the raised compression ratio while injection timing is retarded, the increase in pre-turbine temperature compared to the engine baseline can be avoided and minimized.

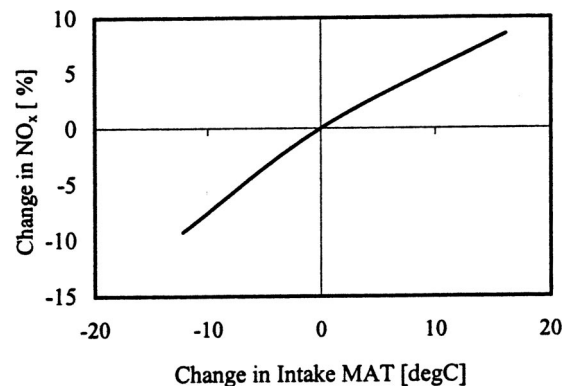


Fig. 13 Effect of MAT on HCR 7FDL16 engine NO_x

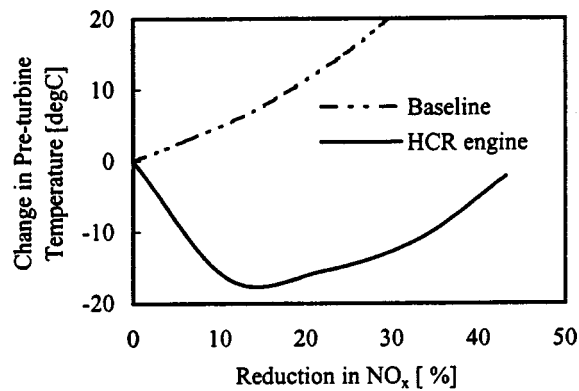


Fig. 14 Change in engine pre-turbine temperature (full load)

Fuel Cam Phase Optimization on 7FDL16 Engine. The fuel cam phase optimization was also verified on the HCR 7FDL16 engine. The results of performance comparison tests are shown in Fig. 15, which shows the differences in NO_x and SFC between the standard-phase and retarded-phase cam. It can be seen from Fig. 15 that the engine brake fuel efficiency with the standard-phase cam is better than that with the phase-retarded cam for the notches shown. The NO_x emission in the full-load condition with the standard-phase cam is also lower. The results confirm the indication from the single-cylinder research engine test. The fuel cam phase needs to be located to obtain a superior overall performance regarding the engine exhaust emissions and brake efficiency. The standard-phase cam provided better performance in the NO_x emissions and fuel efficiency.

Engine Operation Optimization and Smoke Control. With the engine configuration given, engine operation at each individual notch can be optimized to obtain the required duty-cycle NO_x reduction with reducing or curbing other visible and non-visible exhaust emissions. Steady-state and transient smoke during locomotive duty-cycle operation may become a concern. The exhaust emissions such as smoke, PM, and CO become higher as altitude increases. Thus, control of the exhaust emissions of smoke, PM, and CO caused by incomplete combustion was studied together with the NO_x reduction in the engine testing. Additional methods such as shown by Chen and Hsu [7] and by Chen et al. [8] for controlling engine operating parameters to reduce those emissions while achieving the desired duty-cycle NO_x reduction and maintaining the fuel efficiency were developed. During the investigation, the involved engine operating parameters

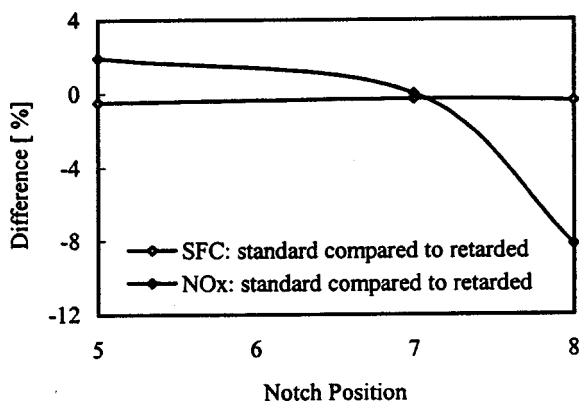


Fig. 15 Performance comparison over fuel cam phase (HCR 7FDL16 engine)

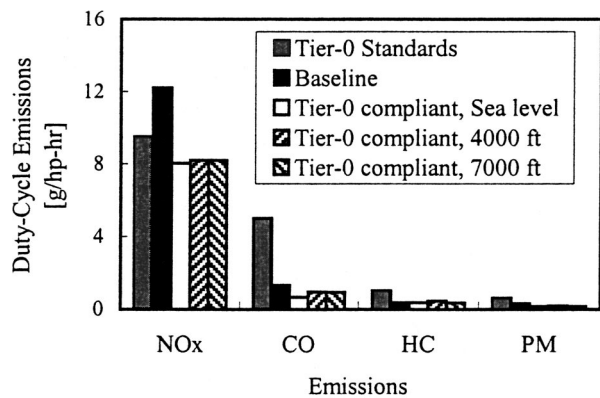


Fig. 16 Low-emission GE-AC4400 locomotive meeting Tier-0 standards (line-haul duty cycle)

affecting the formation of smoke and the other incomplete-combustion related emissions were experimentally verified and studied.

Locomotive Test and Control System Optimization

Following the successful engine development, a GE low-emission locomotive prototype was then built and tested for demonstration and complete function and performance evaluation. The locomotive demonstrated and tested was a GE-AC4400 locomotive using a 7FDL16 low-emission engine with the compression ratio determined based on the engine development results to achieve the Tier-0 emission reduction without loss in fuel efficiency versus the noncompliant baseline.

Exhaust Emissions and Performance. The locomotive was operated through all locomotive throttle notches during the demonstration and evaluation test. The exhaust emissions, operating parameters, and output performances were measured. The test followed the locomotive emissions test procedures by EPA [9]. The duty-cycle emissions were obtained by following the EPA locomotive throttle notch weighting factors. The emission results obtained are summarized in Fig. 16 versus the Tier-0 regulation standards. While achieving the duty-cycle emission reductions to comply with the regulations, no loss in the duty-cycle fuel efficiency compared to the locomotive baseline was demonstrated by the low-emission locomotive in the locomotive evaluation.

Control System Optimization and Smoke Reduction. Retarding fuel injection timing may contribute to an increase in smoke, especially the transient smoke during some notch changes. The engine control system optimization was investigated during the locomotive testing and development. The optimization focused on modifying the control strategies to achieve the desired duty-cycle NO_x reduction and fuel efficiency with the smoke opacity reduced to meet the EPA emissions standards.

The preceding engine development and initial locomotive investigation showed that transient smoke can be reduced through both load application delay and timing advance during a notch increase without affecting the overall load rate. The optimization of the load application and the transient timing advance was tested on the locomotive over a wide range of environmental conditions. A new speed schedule was developed at high altitude to raise the engine speed in lower notches. This reduced the steady-state smoke as well as reducing the transient smoke. The fundamental approach of these methods can be found in [7,8] and [10]. The locomotive was also tested with the new speed schedule to confirm the desired reduction in smoke and emissions. Finally, to further improve the transient smoke for low notch transitions at high altitude, the load rate at low notches was optimized. Figure 17 illustrates the 3-sec transient smoke reduction by the operation

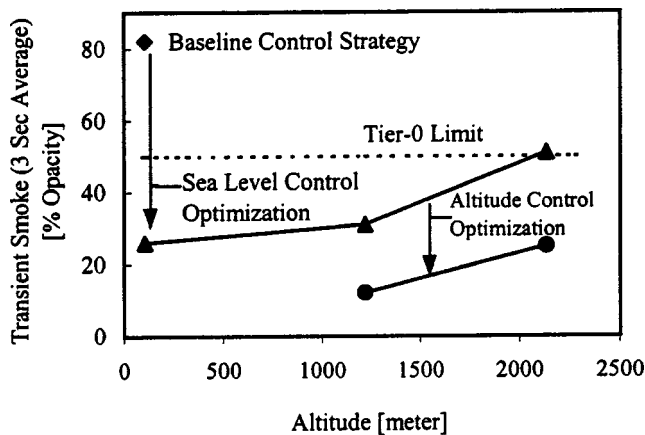


Fig. 17 Transient smoke optimization on tier-0 compliant locomotive

and control optimization developed for the emission-reduction locomotive during low notch transition. Applying these optimization strategies, the locomotive also demonstrated its ability to meet the steady state and transient smoke standards over a wide range of environmental conditions.

A “skip firing” control strategy as shown by Patel and Volpe [11] was also further developed to be implemented at idle notches to further reduce the steady-state smoke and optimize other gaseous emissions. Skip firing systematically skips cylinders from the normal firing sequence. The purpose is to raise injection pressure in the cylinders that are firing. Fuel injected at higher pressures atomizes better as it enters the combustion chamber, fostering complete burning and low smoke production. Applying the skip firing control strategy to the low-emission engine and locomotive, a significant reduction in smoke at idle notches was achieved. The skip firing mode was also validated by measuring smoke and emissions at various environmental and altitude conditions to ensure compliance.

Conclusions

The technical development of the low-emission GE 7FDL medium-speed locomotive diesel engine has been conducted. Conclusions drawn from the development described in this paper are summarized as follows.

1. High-power medium-speed diesel engines are used as the motive power for present diesel-electric locomotives. To comply with the EPA Tier-0 and further Tier-1 locomotive emission regulations, the exhaust NO_x emissions of the baseline locomotive engine needed to be significantly reduced while reducing and curbing other visible and non-visible exhaust emissions. The adverse impact on the engine efficiency needed to be avoided and minimized. All of this needed to be realized with minimal changes to the existing baseline engine system and components in consideration of the reliability, interchangeability and upgrade from the baseline engines to the low-emission configuration.

2. The low-emission GE-7FDL series locomotive engine has been successfully developed and produced. The main technical approach included increasing engine compression ratio coupled with modifying fuel injection timing, increasing fuel injection rate, and optimizing the notch and duty-cycle operations. The concepts were analyzed, and were investigated using the single-cylinder 7FDL research engine. The low-emission GE-7FDL16 engine and locomotive prototype were built and tested for performance and function evaluation and design optimization. The low-emission GE 7FDL engines and locomotives have been in production.

3. The development results have demonstrated that the newly developed low-emission GE-7FDL locomotive engine meets the EPA Tier-0 standards without fuel efficiency penalty versus the noncompliant baseline. The engine mechanical loading such as the peak cylinder firing pressure and thermal loading such as the cylinder exhaust temperature are maintained about the same as those of the engine baseline. The desired engine reliability performance can be retained. This was accomplished with the minimal changes to the engine system and components. The engine has been developed to be interchangeable with the preceding 7FDL baseline, and the upgrade of the baseline engines to the low-emission configuration is facilitated.

4. The development has established a base for the further engine development required for the locomotive diesel engines in accordance with further Tiers of regulation compliance.

Acknowledgments

The authors wish to thank General Electric Company for permission to publish this paper. The authors also would like to acknowledge the fundamental work performed by Dr. Bertrand Hsu as the precursor to this engine development.

Nomenclature

BSU	= Bosch smoke number
CO	= exhaust carbon monoxide
CR	= compression ratio
HC	= exhaust hydrocarbon
HCR	= high compression ratio
MAP	= intake manifold air pressure
MAT	= intake manifold air temperature
NO_x	= exhaust nitrogen oxides
PM	= exhaust particulate matters emission
p_{\max}	= peak cylinder pressure
SFC	= specific fuel consumption
TDC	= top dead center
T_{prt}	= pre-turbine temperature
Δp_{ov}	= difference between MAP and pre-turbine pressure

References

- [1] Environmental Protection Agency, 1998, “Emission Standards for Locomotives and Locomotive Engines,” 40 CFR, Part 85, 89, and 92.
- [2] Environmental Protection Agency, 1998, “General Provisions for Emission Regulations for Locomotives and Locomotive Engines,” 40 CFR, Part 92, Subpart A.
- [3] Hsu, B. D., 1984, “Heat Release, Cycle Efficiency and Maximum Cylinder Pressure in Diesel Engine—The Use of an Extended Air Cycle Analysis,” SAE Paper No. 841054.
- [4] Hsu, B. D., and Chen, G., 2001, “Increased Compression Ratio Diesel Engine Assembly for Retarded Fuel Injection Timing,” U.S. Patent 6,318,308, assigned to General Electric Company.
- [5] Hsu, B. D., Chen, G., and Cryer, R. D., 2002, “High Injection Rate, Decreased Injection Duration Diesel Engine Fuel System,” U.S. Patent 6,349,706, assigned to General Electric Company.
- [6] Hsu, B. D., and Hoffman, J. G., 1985 “The Effect of Diesel Fuel Properties on the Combustion of a Medium Speed Diesel Engine,” ASME Paper No. 85-DGP-14.
- [7] Chen, G., and Hsu, B. D., 2000, “Reduced Emissions Elevated Altitude Speed Control for Diesel Engines,” U.S. Patent 6,158,416, assigned to General Electric Company.
- [8] Chen, G., Hsu, B. D., and Cryer, R. D., 2001, “Apparatus and Method for Suppressing Diesel Engine Emissions,” U.S. Patent 6,325,044, assigned to General Electric Company.
- [9] Environmental Protection Agency, 1998, “Test Procedures,” 40 CFR, Part 92, Subpart B.
- [10] Dillen, E. R., Gallagher, S. M., Dunsworth, V. F., and Orinko, J. T., 2002, “Locomotive Transient Smoke Control Strategy Using Load Application Delay and Fuel Injection Timing Advance,” U.S. Patent 6,341,596, assigned to General Electric Company.
- [11] Patel, S. A., and Volpe, R., 1998, “Diesel Engine Cylinder Skip Firing System,” U.S. Patent 5,826,563, assigned to General Electric Company.

Exhaust Particulate Matter Emission Factors and Deterioration Rate for In-Use Motor Vehicles

B. Ubanwa

Texas Natural Resource Conservation
Commission,
13219 Marrero Drive,
Austin, TX 78729

A. Burnette

S. Kishan

Eastern Research Group,
5608 Parkcrest Drive, Suite 100,
Austin, TX 78731

S. G. Fritz

Principal Engineer,
Department of Emissions Research,
Southwest Research Institute,
6220 Culebra Road,
San Antonio, TX 78238-5166

Recent measurements and modeling of primary exhaust particulate matter (PM) emissions from both gasoline and diesel-powered motor vehicles suggest that many vehicles produce PM at rates substantially higher than assumed in the current EPA PM emission factor model, known as "PART5." The discrepancy between actual versus modeled PM emissions is generally attributed to inadequate emissions data and outdated assumptions in the PART5 model. This paper presents a study with the objective of developing an in-house tool (a modified PART5 model) for the Texas Natural Resource Conservation Commission (TNRCC) to use for estimating motor vehicle exhaust PM emissions in Texas. The work included chassis dynamometer emissions testing on several heavy-duty diesel vehicles at the Southwest Research Institute (SwRI), analysis of the exhaust PM emissions and other regulated pollutants (i.e., HC, CO, NO_x), review of related studies and exhaust PM emission data obtained from literature of similar types of light and heavy-duty vehicle tests, a review of the current PART5 model, and analysis of the associated emission deterioration rates. Exhaust PM emissions data obtained from the vehicle testing at SwRI and other similar studies (covering a relatively large number and wide range of vehicles) were merged, and finally, used to modify the PART5 model. The modified model, which was named PART5-TX1, was then used to estimate new exhaust PM emission factors for in-use motor vehicles. Modifications to the model are briefly described, along with emissions test results from the heavy-duty diesel-powered vehicles tested at SwRI. Readers interested in a detailed understanding of the techniques used to modify the PART5 model are referred to the final project report to TNRCC (Eastern Research Group 2000). [DOI: 10.1115/1.1559904]

Introduction

The revision of the National Ambient Air Quality Standards (NAAQS) for PM raise concerns as to whether the existing mobile source inventory of PM emissions is acceptably accurate. Studies and modeling of primary PM emissions from motor vehicles, including both gasoline and diesel powered light-duty (LD) and heavy-duty (HD) vehicles, indicate most vehicles produce PM at rates which are substantially higher than assumed in the current PM emissions inventory model (PART5). Technically, the model in its current form assumes there is no deterioration of the engine or emission control equipment as the vehicles age. This assumption is misleading, since it implies that vehicle PM emissions always remain at the same level throughout the vehicle's lifetime.

Current research efforts indicate that part of the deficiency of the PART5 model is the fact that the model assumptions are based upon very little "in-use" data. Consequently, since the mid 1990s, there have been an increased number of studies geared toward measuring in-use PM emissions from mobile sources and updating the PART5 model (Cadle [1], Norbeck [2], Whitney [3], Graboski [4], Mulawa [5], Darlington [6], and Weaver [7]). This update is especially necessary now, considering the new and stricter ambient PM standards which will likely result in many more metropolitan areas being out of compliance.

Two recent studies were focused on improving the PART5 model (Darlington [6] and Weaver [7]). They were especially helpful in providing insight for PART5 improvements and lists of

previous PM emissions data collection research. The first of these two studies focused on assessing the sources of inaccuracies in the EMFAC (California's mobile source PM model) and EPA PART5 models regarding modeling PM from catalyst equipped, light-duty, gasoline-fueled vehicles (Darlington [6]). The study found several shortcomings of the current PART5 model. In general, they stem from the lack of sufficient data or the use of inappropriate data to support the assumptions. For example, PM emission factors for catalyst-equipped vehicles are based upon data from prototype and first-generation three-way catalysts from the early 1980s.

The second of these two studies evaluated whether the deterioration module in EMFAC was appropriate for developing a heavy-duty vehicle deterioration module for the PART5 model, and to compile light-duty PM emissions data from previous studies (Weaver [7]). The report is currently in the EPA review process.

In spite of the several recent research projects aimed at light-duty and heavy-duty vehicle exhaust PM emission characterization, and the contribution of these vehicles to total mobile source PM, there are no studies clearly targeted towards providing data adequate to assess the overall contribution of the light and heavy-duty vehicles to the total PM inventory, and enabling revision of the PART5 model.

With this in mind, the Texas Natural Resource Conservation Commission (TNRCC) contracted with the Coordinating Research Council (CRC) for a study on measurement of primary exhaust PM emissions from light-duty motor vehicles (Whitney [3]). The study provided TNRCC with information leading to a conclusion that further PM emissions test data was needed, particularly in the area of PM emissions from HD diesel vehicles, to begin to adequately address the issue of exhaust PM emission characteriza-

Contributed by the Internal Combustion Engine Division of THE AMERICAN SOCIETY OF MECHANICAL ENGINEERS for publication in the ASME JOURNAL OF ENGINEERING FOR GAS TURBINES AND POWER. Manuscript received by the ICE Division July 2000; final revision received by the ASME Headquarters March 2002. Associate Editor: D. Assanis.

Table 1 Test vehicles

Model Year	Vehicle Type	Engine	GWR (lb) [kg]
1996	Carpenter 3800 School Bus	Navistar 7.3L T444E	29,000 [13,000]
1998	City Transit Bus	DDC Series 50	42,000 [19,000]
1998	Class 8 Truck	Caterpillar C-12	80,000 [36,000]
1998	Class 8 Truck	Caterpillar C-12	80,000 [36,000]

tion from motor vehicles. TNRCC recently began an effort to fill the gaps in the currently available data of PM emissions from HD vehicles, as well as developing an in-house revision of PART5 model based on Texas fleet data, to be called PART5-TX1. The modified PART5 model will be an in-house tool for modeling exhaust PM emissions from highway vehicles.

Major aspects of the work included:

- performing exhaust emissions testing of four heavy-duty diesel vehicles,
- examining PM exhaust emissions data from the previous CRC contract and similar studies related to light and heavy-duty diesel and gasoline powered vehicles,
- updating the PART5 model to incorporate the PM exhaust emissions data from (a) and (b) for use in modeling exhaust PM emissions from motor vehicles, and
- developing exhaust PM emissions factors for motor vehicles.

Heavy-Duty Vehicle Testing

Four heavy-duty vehicles were tested specifically for this project. Because the database of in-use PM data is quite sparse, every good data point is a significant contribution. These data points are especially significant for the database of Texas heavy-duty diesel vehicle emissions. This section of the paper contains a description of the test vehicles, test fuel, and test procedures used during this program.

Test Vehicles. Four heavy-duty diesel vehicles were obtained from public and private fleets. The test vehicles are identified in Table 1, along with the applicable engine and the gross combined vehicle weight rating (GVW).

The 1996 Carpenter 3800 series school bus, shown in Fig. 1, had a GWR of 29,000 pounds (13,154 kg), and was powered with a Navistar 7.3 liter, V-8, T444E diesel engine rated at 190 bhp



Fig. 1 1996 Carpenter school bus installed on SwRI heavy-duty chassis dynamometer



Fig. 2 Capital Metro bus no. 7464

(141 kW) at 2300 rpm. The bus was equipped with an Allison AT-500 four-speed automatic transmission, and had accumulated 46,420 miles (74,704 km) before testing in the current program.

The total dynamometer simulated inertia (test weight) of the school bus was 14,600 pounds (6622 kg), and the total theoretical road load at 50 mph (80 km/h) was 52 hp (38.8 kW). This theoretical road load was calculated by considering a rolling resistance of 17 hp (12.7 kW) and aerodynamic influences of 35 hp (26 kW), as outlined in an EPA recommended test procedure, [8,9].

The second vehicle tested was a 1998 model year urban transit bus (Fig. 2). The bus was equipped with a 1998 model year DDC Series 50, 8.5L, I-4 diesel engine with a rated power of 320 (239 kW) at a speed of 2100 rpm. It was equipped with an oxidation catalyst.

The simulated inertia weight used for the Capital Metro bus was 41,450 pounds (19,050 kg), which was selected based on the empty weight of the bus, plus an estimated 23 passengers and a driver weighing 150 pounds (68 kg) each. The theoretical road load was calculated by considering rolling resistance of 51.1 hp (38 kW) and aerodynamic influences of 39.3 hp (29.3 kW). Therefore, the resulting total theoretical road load at 50 mph (80 km/h) was 90.4 hp (67.4 kW).

The third and fourth vehicles, provided by H. E. Butt Grocery Company (HEB) in San Antonio (Fig. 3), were 1998 Sterling Class 8 tractors. Both trucks were equipped with a 1998 model year Caterpillar C12 diesel engine. This 12.0L, I-6 engine had a rated power of 355 hp (264.8 kW) at a governed speed of 2100 rpm. The trucks were equipped with a Rockwell 10-speed manual transmission.



Fig. 3 HEB truck no. 7242

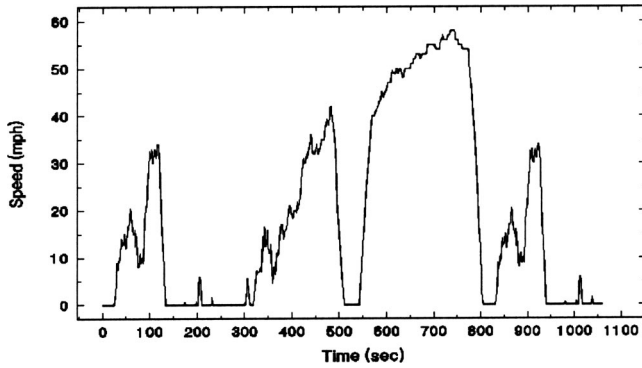


Fig. 4 Heavy-duty chassis cycle

The simulated inertia weight used for both HEB trucks was 56,000 pounds (25,400 kg), which was selected based on 70% of the 80,000 lbs (36,287 kg) gross vehicle-trailer combined weight rating. The theoretical road load was calculated by considering rolling resistance of 61 hp (45.5 kW) and aerodynamic influences of 70 hp (52.2 kW). Therefore, the resulting total theoretical road load for each of the HEB trucks at 50 mph (80 km/h) was 131 hp (97.9 kW).

Exhaust Emissions Test Procedures. The four vehicles were tested using SwRI's heavy-duty chassis dynamometer. The diesel fuel used for testing met EPA specifications for emissions certification of heavy-duty diesel engines, as given in the U.S. Code of Federal Regulations (CFR), Title 40, §86.1313-98. Tests were performed in accordance with procedures outlined in an EPA report titled, "Recommended Practice for Determining Exhaust Emissions From Heavy-Duty Vehicles Under Transient Conditions (France [8])."

For this test program, emissions were measured over triplicate hot-start runs using two different driving cycles, and during idle operation. One driving cycle, the EPA Urban Dynamometer Driving Schedule (UDDS) for Heavy-Duty Vehicles, also known as the heavy-duty chassis cycle (HDCC), is illustrated in Fig. 4. The duration of the HDCC is 1060 seconds, and the cycle covers a distance of 5.55 miles (8.94 km). The official use of this cycle is for preconditioning heavy-duty gasoline-fueled vehicles before an evaporative emissions test. However, the HDCC is commonly used for exhaust emissions testing of heavy-duty vehicles for research purposes, and was based on the engine speed and load conditions which were used to compile the EPA heavy-duty diesel engine transient test cycle specified for heavy-duty diesel engine emissions certification.

The second driving cycle used for this program is known as the Central Business District (CBD) cycle. The CBD cycle is one of four transit coach operating profile duty cycles adopted by the Federal Transit Administration (FTA) of the U.S. Department of Transportation. For this project, the "CBD-14" cycle was comprised of 14 repetitions of the basic cycle, which includes idle, acceleration to 20 mph (32.2 kph), cruise, and a sharp deceleration to a stop. The CBD-14 cycle used in this work, shown in Fig. 5, was 580 seconds in duration and covered a distance of 2.0 miles (3.2 km).

Emissions were also measured during idle operation. Two 20-minute idle tests were run, with the transmission in neutral. Before the hot-start tests, the vehicles were operated at 50 mph (80.5 km/h) and the road load on the dynamometer was set. One practice cycle was run, followed by a 20-minute soak, then the planned tests were run.

The analytical procedures used to measure the emissions produced and the fuel consumed during the tests are given in the EPA recommended practice for heavy-duty chassis testing and in the CFR description of heavy-duty diesel engine testing using the

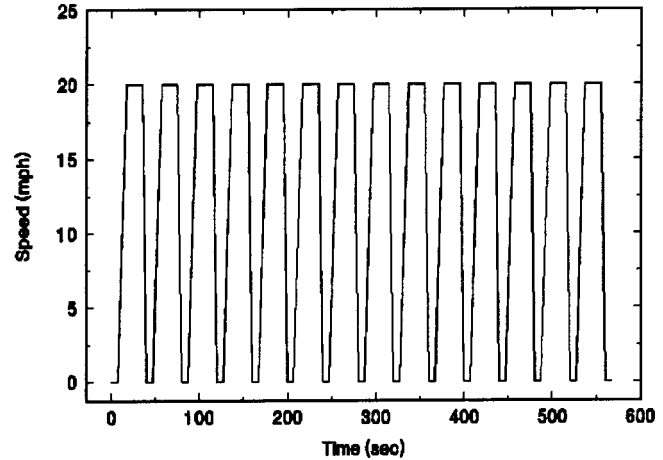


Fig. 5 Central business district (CBD) cycle

transient Federal Test Procedure (FTP). Total hydrocarbon and NO_x concentrations were continuously monitored in the dilute exhaust over each test, and the integrated results used in computing emissions. NO_x correction factors for engine intake air humidity were applied as specified in the transient FTP for diesel-fueled engines. Concentrations of CO and CO_2 in the proportional dilute exhaust bag samples were determined by nondispersive infrared (NDIR) instruments. Concentrations of HC, CO, CO_2 , and NO_x were processed along with CVS flow parameters and vehicle operating parameters to compute mass emissions on the basis of distance (g/mi). These computations were based on equations specified in the CFR. Exhaust PM emissions were measured using dilute sampling techniques as specified in the transient FTP for diesel fueled engines.

Heavy-Duty Engine Emission Test Results. The average exhaust emissions during idle, as well as the CBD and HDCC cycles, for the all the HD vehicles studied are summarized in Tables 2 and 3. Note that like the other vehicles tested, the idle tests on the city bus were performed with the transmission in neutral. However, the bus was equipped with an automatic air conditioning system that was not disabled during testing. This was thought to provide a more realistic measure of in-use emissions from the city bus.

Exhaust Particulate Emissions Data Collected From Other Studies

Included in the TNRCC study was a compilation of PM emission data obtained from other studies. Test results from a total of about 1000 vehicles were obtained from various other studies. There were a total of about 300 heavy-duty diesel vehicles in the mix. The bulk of useful data came from the National Renewable

Table 2 Average idle exhaust emissions

Vehicle Type	HC (g/hr)	CO (g/hr)	NO_x (g/hr)	PM (g/hr)	Fuel Consumption (g/hr)
School Bus	13.0	40.6	45.1	1.53	1,110
Metro Bus	0.84	26.0	495.1	0.32	4,380
Truck 1	3.3	15.9	79.6	1.18	1,250
Truck 2	1.8	14.8	69.3	0.90	1,084

Table 3 Average exhaust emissions from driving cycles

Vehicle Type	Test Cycle	HC (g/mi) [g/km]	CO (g/mi) [g/km]	NO _x (g/mi) [g/km]	PM (g/mi) [g/km]	Fuel Econ. (mpg) [km/L]
School Bus	CBD-14	0.81 [0.50]	3.8 [2.4]	14.0 [8.7]	0.22 [0.14]	7.8 [3.3]
	HDCC	0.62 [0.39]	2.3 [1.4]	11.9 [7.4]	0.19 [0.12]	8.4 [3.6]
Capital Metro Bus	CBD-14	0.00 [0.00]	4.2 [2.6]	41.8 [25.9]	1.02 [0.63]	3.2 [1.4]
	HDCC	0.10 [0.062]	3.0 [1.9]	36.1 [22.4]	0.60 [0.37]	5.3 [2.3]
Heavy-Duty Truck 7238	CBD-14	0.73 [0.45]	9.2 [0.57]	19.4 [12.0]	1.59 [0.99]	3.1 [1.3]
	HDCC	0.53 [0.33]	4.4 [2.73]	14.2 [8.82]	0.74 [0.46]	4.6 [2.0]
Heavy-Duty Truck 7242	CBD-14	0.97 [0.60]	9.3 [5.78]	17.3 [10.7]	1.61 [1.00]	3.1 [1.3]
	HDCC	0.61 [0.38]	4.6 [2.86]	12.5 [7.76]	0.76 [0.47]	4.9 [2.1]

Energy Laboratory Database and the following references: Cadle [1,10,11] Norbek [2], Whitney [3], Graboski [4], Fritz [12,13], and Mulawa [5]. Vehicle or engine certification data were not used.

This analysis was designed to only consider emissions measurements from vehicles used in commercial or private service, and using only chassis dynamometer techniques for both light-duty and heavy-duty vehicles. Therefore, certification emissions values reported by vehicle and engine manufacturers to the EPA were not used in this analysis. The certification levels are obtained using vehicles that have been aged under tightly controlled conditions, and for a limited amount of miles or engine hours. Those data were not considered applicable to this analysis.

For data from most sources, it was necessary to convert heavy-duty chassis dynamometer measurements from a “grams per mile” (g/mi) basis to a “grams per brake-horsepower hour” (g/bhp-hr) basis for convenience, and to help normalize the effect of different drive cycles on emissions results. Using this technique means that the PART5-TX1 model (like EPA’s MOBILE model) is appropriate for estimating PM emissions from large, diverse fleets of vehicles, but not for individual vehicles. This was only necessary for heavy-duty vehicles since they are often tested using a variety of driving different cycles and their standards are set in g/bhp-hr units. Further, none of the chassis cycles used for heavy-duty diesels have been approved by EPA as representative of actual driving patterns. Using this technique means that the PART5-TX1 model (like EPA’s MOBILE model) is appropriate for estimating PM emissions from large, diverse fleets of vehicles, but not for individual vehicles. All light-duty vehicles in the database use similar cycles and their standards are set in units of g/mi.

The equation used to convert heavy-duty chassis dynamometer data from “g/mi” basis to “g/bhp-hr” basis was as follows:

$$\begin{aligned} &\text{Conversion Factor (bhp-hr/mi)} \\ &= \text{Fuel Density (lb/gal)} / \text{BSFC (lb/bhp-hr)} \\ &\quad \times \text{Fuel Economy (mi/gal)} \end{aligned}$$

where diesel fuel density 7.10 lb/gal and BSFC is the average brake-specific fuel consumption for each vehicle weight class. This calculation method for brake-specific fuel consumption

(BSFC) and average fuel density was obtained from an EPA report used in developing the new MOBILE6 model (Arcadis [14]).

The Concept and Application of Emission Deterioration Rate

One assumption in the PART5 model is that no vehicles ever emit PM emissions more than they were certified to emit. A drive down the highway suggests that this assumption may not be correct. It appears that many of the vehicles on the road might not pass their “new engine” certification tests. A problem with this assumption is the adverse effect it has on model predictions as the vehicle fleet gets cleaner (as newer models enter the fleet and older ones are scrapped). Many technologies introduced in response to strict emissions standards newer emission control technologies rely upon relatively fairly complicated equipment systems to achieve their low, “new engine” emission levels (e.g., turbochargers or computer controlled fuel systems). Although the equipment seems reliable, it is probably unreasonable to assume that a significant fraction won’t deteriorate during their useful regulatory life. Failure of new generation equipment will usually result in a larger percentage increase of emissions compared to similar failures in older technology vehicles. A model that neglects these issues will, for example, tend to overpredict the reduction of PM emissions as new vehicles enter the fleet and old vehicles are scrapped.

Recent studies sponsored by TNRC, CRC, and others, indicate that the current PART5 model generally underestimates exhaust PM, and that deterioration which causes higher emissions occurs in vehicle PM emission control systems (Cadle [1], Norbek [2], and Whitney [3]). The SwRI study for the CRC (Whitney [3]) indicated that light-duty vehicle PM emissions increase with vehicle mileage (especially over 100,000 miles), and that actual PM emissions are 3 to 11 times higher than those predicted by PART5.

One of the main objectives of this project was to utilize the in-use vehicle PM emissions database to develop new PM emission factors for the PART5 model. These new emission factors take into account the PM deterioration of vehicle emission control equipment with time—and the resulting increase in PM emissions. This required introducing the concepts of “zero mile level” or ZML and “deterioration rate” or DET into the new model. ZML is the emission rate of a vehicle when it is new (expressed here in terms of g/mi (g/km)), and DET is the rate at which a vehicle’s emissions increase with mileage or time (expressed here in terms of g/mi/yr (g/km/yr)).

Using “real-world” data and techniques like those employed by EPA in developing the MOBILE models, ZML and DET were estimated for the various vehicle groups from empirical data. The concepts of ZML and DET are summarized in the hypothetical graph in Fig. 6. When a vehicle is new, its emissions should be at or below the certification standards. As a vehicle ages, its emissions systems equipment will often deteriorate, operating less and less efficiently, and causing the emissions to rise.

The ZML and DET were determined, wherever possible, for each type of vehicle represented in the model and for each emissions technology group. Emissions technology groups were defined by assuming the vehicles that conform to the same standards use similar technologies. This concept is summarized below, under the Model Year Groups section. When insufficient data existed for a specific vehicle type, engineering judgment was used to determine the technology group and an appropriate ZML or DET. As new data are collected to fill these data gaps, the assumptions of this model update can easily be replaced using empirical results.

Model Year Groups. In determining ZML emission rates and DET rates from the empirical data, it was useful to group vehicles for increased sample sizes. It is standard practice to group vehicle model years according to when the emission standards were established or changed, based on federal emission standards—the

Hypothetical Case: How Vehicle PM Emissions Increase as Emissions Equipment Deteriorates

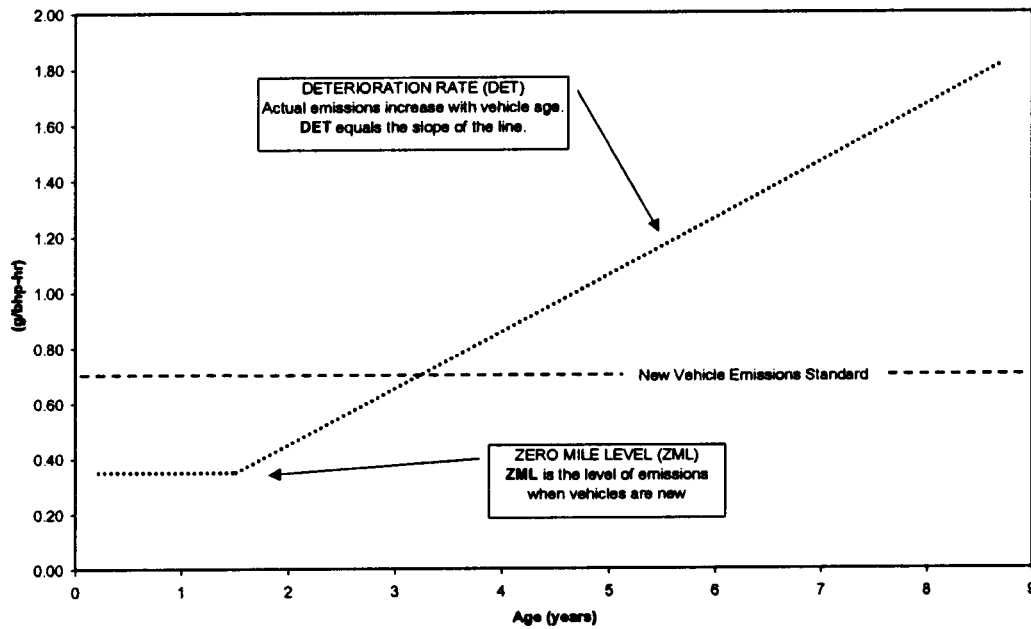


Fig. 6 Concepts of zero mile level (ZML) and deterioration rate (DET) for particulate matter (PM) emissions

driving force behind emission control technologies. These model year groups are used in the light and heavy-duty vehicle analyses of this project. The cutoff years used for the light-duty vehicle model year groups are when Tier-1 PM standards came into effect for the majority of light-duty vehicles. These groups are listed in Table 4.

Determining the Zero Mile Levels (ZMLs) and Deterioration Rates (DETs)

The trends in PM emissions within the in-use vehicle database were analyzed to determine deterioration rates for each technology group (model year group). It was determined that it was best to express deterioration in terms of vehicle age instead of vehicle

mileage. This is because of the uncertainty in vehicle mileage data (due to uncounted “rollover” of odometers) and because vehicle age is more commonly reported than mileage. In any case, the mileage accumulation data was not entirely ignored. It was an important tool in verifying the age-based deterioration factors and in determining vehicle technology group ZMLs, especially for newer vehicle groups. The overall method for determining ZML and DET for a given technology group was as follows:

1. Determine ZML by using emission factors for newer vehicles in the group. Cutoff levels for vehicle technology groups with no deterioration were set at 25,000 miles (40,000 km), or one year for gasoline vehicles, and 50,000 miles (80,500 km) or two years for diesel vehicles.
2. Using the ZML determined in step 1, calculate the age-based deterioration rate for each vehicle in the technology group using $DET = (\text{measured emission} - ZML) / \text{age}$.
3. The technology group DET is calculated as the average DET for all vehicles in the technology group. It is necessary to verify that data outliers do not unduly influence the average DET.

Using the general method above, ZML and DET for diesel and gasoline vehicle technology groups were calculated. Figures 7 and 8 give examples of data to which the preceding method was applied. As the plot in Fig. 8 shows, the data suggest that after a certain age, PM emissions no longer increase. Using this assumption, each vehicle type was assigned two DETs. DET1 represents the time period when PM deterioration is occurring, and DET2 represents the stabilized deteriorated level. At this stage of model development DET2 has been set to always equal zero. However, if later data prove otherwise, then DET2 can be easily changed for future revisions.

For most technology groups, the age when emissions stop increasing is hard to determine from the current data set. In those instances, one study recommended to EPA that the end of the vehicle’s useful regulatory life seems a reasonable “flex-point” for the DET (Weaver [7]). This means that the deterioration has increased linearly from the “zero-mile level” (DET1) until the vehicle reaches the DET “flexpoint” age. At that point, the dete-

Table 4 U.S. highway particulate matter (PM) standards (model year groups)

HDDV Model Year Groups (Except Bus)	Federal PM Standards (g/bhp-hr) [g/kWh]
1990	0.60 [0.80]
1991 – 1993	0.25 [0.34]
1994 and newer	0.10 [0.13]
Urban Bus Model Year Groups (g/bhp-hr) [g/kWh]	
1990	0.60 [0.80]
1991-1992	0.25 [0.34]
1993	0.10 [0.13]
1994 – 1995	0.07 [0.09]
1995 and newer	0.05 [0.07]
LDDV Model Year Groups (g/mi) [g/km]	
1994 and older	0.20 [0.27]
1995 and newer	0.08 [0.11]

PM Emissions, '94 & Younger HDDV

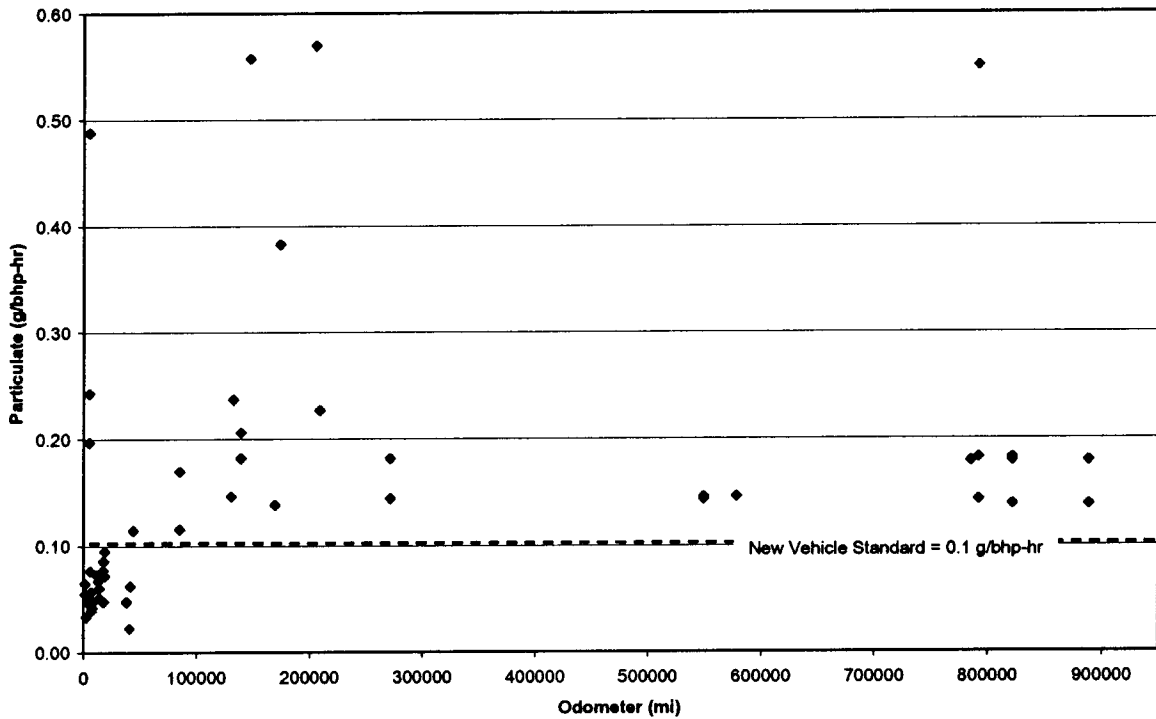


Fig. 7 Heavy-duty diesel truck particulate matter (PM) emissions, 1994 and Younger Technology Group

PM Emissions, '94 & Older LDGV/T

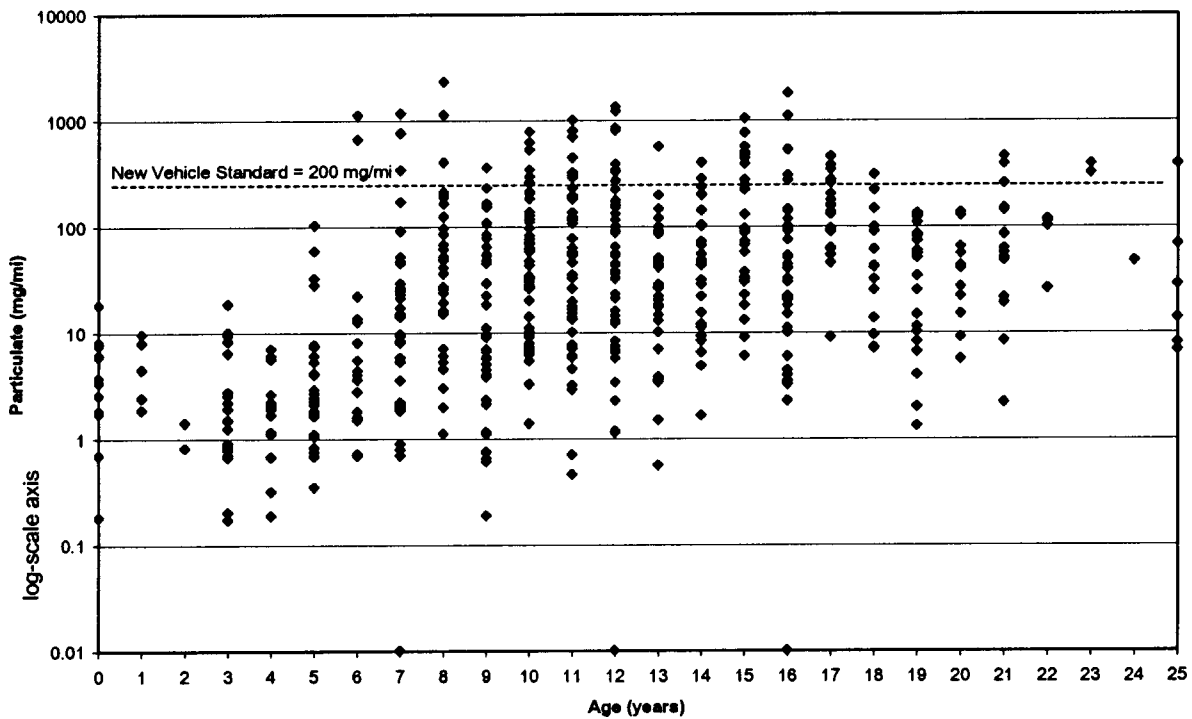


Fig. 8 Light-duty gasoline vehicle particulate matter (PM) emissions, 1994 and older

Table 5 ZML and DET1 values for PART5-TX1

HDDV Model Year Groups (Except Urban Bus)	ZML (g/bhp-hr)	DET1 (g/bhp-hr)/yr	Flex Point Age (yr)	Sample Size for this Project
≤1990	0.35	0.0250	13	27
1991 – 1993	0.18	0.00436	5	33
≥1994	0.08	0.0357	3	67
Urban Bus Model Year Groups				
≤1992	0.30	0.0137	9	94
1993	0.05	0.0133	9	33
1994 – 1995	0.05	0.0133	9	3
≥1996	0.06	0.0363	9	24
LDDV Model Year Groups				
≤1994	0.193	0.0376	9	52
≥1995	0.135	0.00612	9	3
LDGV Model Year Groups				
≤1994	0.00497	0.00856	10	659
≥1995	0.00413	0.00336	10	46

rioration rate is currently modeled to become zero (DET2). The emissions no longer increase as the vehicle ages. Table 5 lists the final ZMLs and DET1s for the technology groups defined in this paper. As noted above, the DET2 values are all zero for each technology group as of this writing, either as indicated by the database or at the end of the technology group’s useful regulatory life.

The three graphs following Table 5 (Figs. 9, 10, and 11) show the ZML and DET values for several major vehicle categories in graphical form. These graphs were derived from the information in Table 6, and show how projected emissions of the vehicle technology groups rise as vehicles age. As these graphs demonstrate, the in-use vehicle PM data indicate that deterioration has a major influence on emissions as vehicles age. Another interesting result is the fact that older diesels tend to emit substantially less than their certification standard until well into their useful lives, while new technology diesels tend to exceed their standard after a few years of use.

These ZML and DET values were applied to the vehicle groups defined in the PART5-TX1 model. For those vehicle groups that were not well represented in the emissions database, an engineering judgment was used to extrapolate ZMLs and DETs in the updated PART5-TX1, revision 1 (early Dec. 1999). The reader should keep in mind that these ZML and DET values can be easily updated as new data becomes available, and TNRCC plans to update the model as new data dictate.

In addition to modifying the basic assumptions in the PART5 model, this project also tried to make the model more useful as a planning tool and easier to keep current with the latest in-use emissions data. Table 6 summarizes relevant features of the PART5 model and how they were modified in PART5-TX1.

Comparisons of PART5 to PART5-TX1

The results of the modifications to the PART5 model were compared to those of the new model, PART5-TX1. The differences are significant, especially when vehicle individual categories are compared to each other. This section first presents the overall results for a typical fleet of vehicles, followed by results for some of the major vehicle groups. The analysis discussed here only covers model predictions of primary exhaust PM. This does not include model predictions of secondary PM or brake, tire, or re-entrained road dust.

Figure 12 summarizes predictions from PART5-TX1 and PART5 over a ten-year period beginning in 1995. Shown is a hypothetical vehicle fleet, typical for a large metropolitan area. Relative to the PART5 model, empirical data indicate that fleet emissions will probably not decrease as rapidly as previously predicted. This is probably due to the assumption in PART5 that new

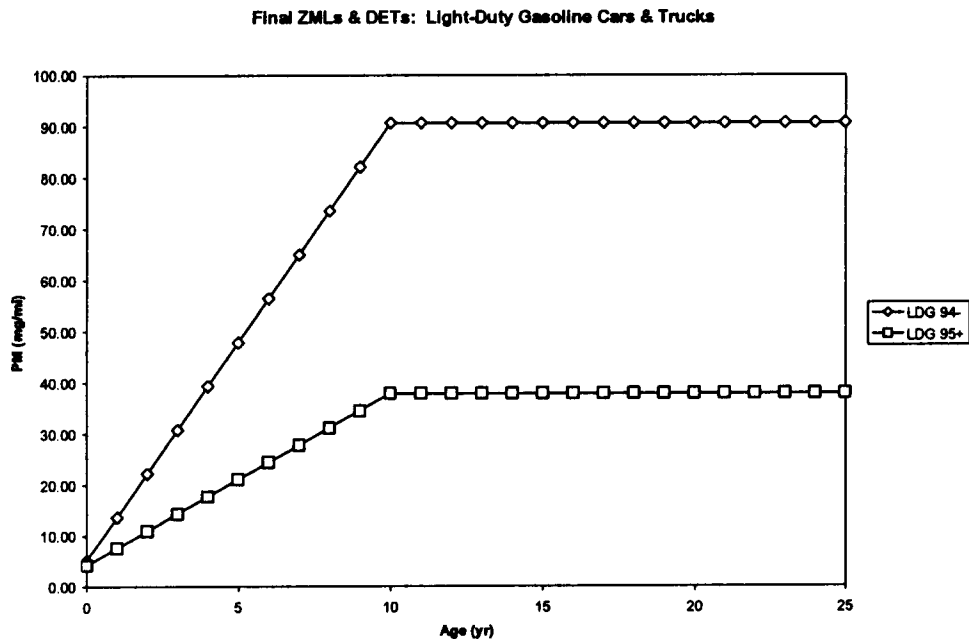


Fig. 9 Light-duty gasoline vehicle zero mile level (ZML) and deterioration rate (DET) curves

Final ZMLs & DETs: HDDTruck

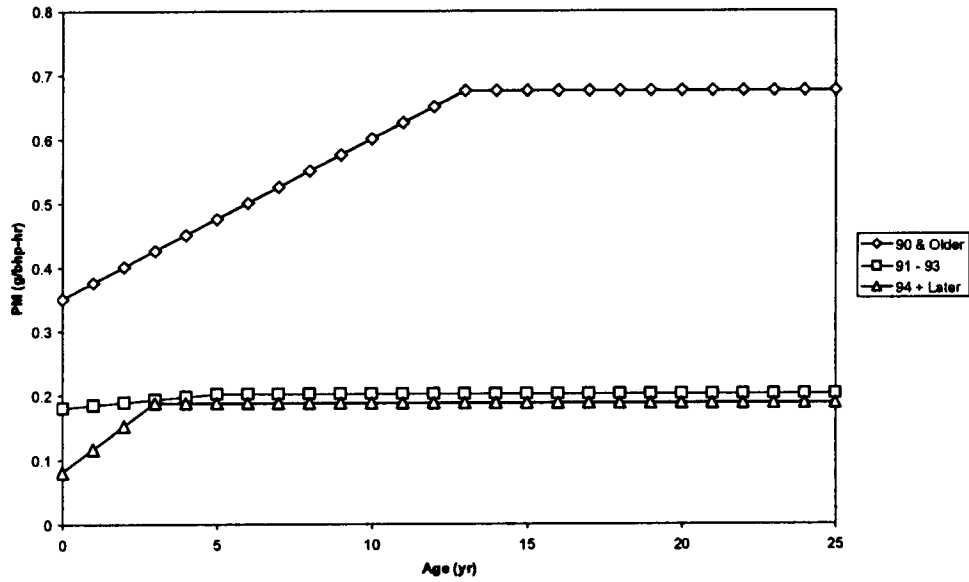


Fig. 10 Heavy-duty diesel truck zero mile level (ZML) and deterioration rate (DET) curves

vehicles stay clean throughout their useful life. We know from the in-use data that PM emissions from new vehicles increase over a certain period, depending upon the vehicle type. This observed trend decreases the “cleansing” influence of cleaner, newer technology vehicles entering the fleet and dirtier, old technology vehicles leaving the fleet with time.

As the graph in Fig. 12 demonstrates, the change in modeled predictions from the PART5 to the new PART5-TX1 model is apparent when looking at overall results for a fleet. However, this masks some of the more striking differences, which are revealed by comparing results for certain vehicle groups. Figure 13 compares the PART5 prediction for light-duty gasoline passenger cars (LDGVs) to those from the PART5-TX1 model. Because PART5-

TX1 included recently developed empirical data, the comparison of results for LDGVs parallels the conclusions of recent studies: PART5 underpredicts PM emissions from LDGVs (Cadle [1], Norbek [2], and Whitney [3]). For LDGVs, the effect of including real-world data was to increase the predicted emissions.

In-use data had a different effect on heavy-duty diesel vehicle predictions. Figure 14 compares PART5 to PART5-TX1 predictions for heavy-duty diesel trucks (HDDVs) and buses. The trend shows that during the late 1990s, PART5-TX1 predicts heavy-duty fleet emissions similar to the EPA PART5 model. After 2000, PART5-TX1 predicts higher PM emissions than the PART5 model. This effect is probably due to the high deterioration rates observed in newer model year HDDVs and buses.

Final ZML/DET Curves: HDDBus

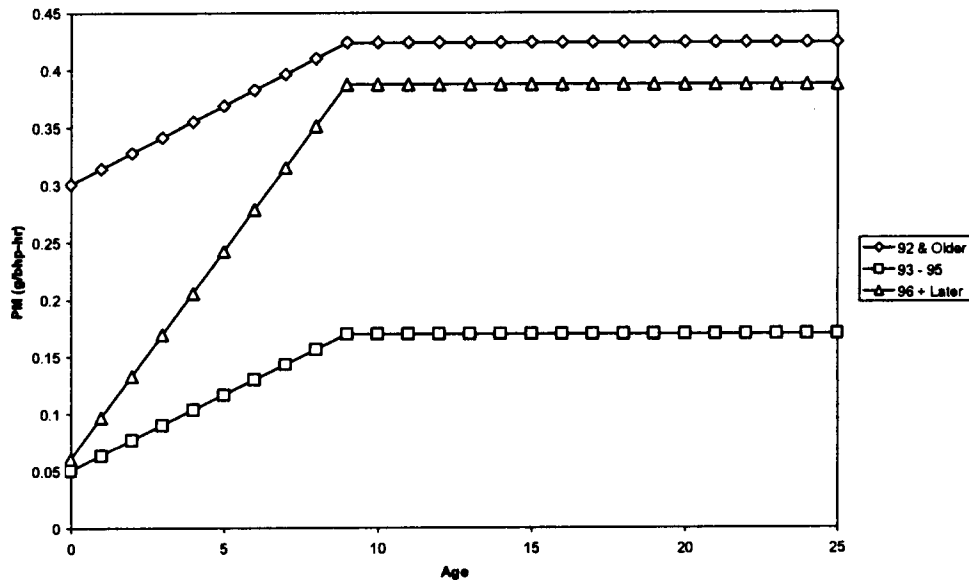


Fig. 11 Diesel bus zero mile level (ZML) and deterioration rate (DET) curves

Table 6 Comparison of features between PART5 and PART5-TX1

Feature	PART5	PART5-TX1
Estimation of primary exhaust PM emission factors	Based primarily upon certification data.	Based primarily upon in-use data and augmented with newer data (much larger data set).
Assumptions to improve estimates for vehicle classes with little empirical data	Mainly relies upon certification data. Little projection between vehicle classes	Augmented using engineering judgement to project emission factors from vehicle classes with ample data to those with few data.
Accounting for emitter categories to allow estimation of I/M benefits	None	Allowance for high and low emitters (smokers and non-smokers for gasoline vehicles).
Estimation of tire, brake, and fugitive dust	Based upon AP42.	Unchanged.
Estimation of Secondary PM Emission Factors	Based upon assumptions derived from studies of early- to mid-1980s.	Unchanged.
Main method For Updating The Model	Change the source code.	Update comma delimited text files which are called by the program.

Summary

PART5-TX1 was developed for the TNRCC as an “in-house” tool for modeling exhaust PM emissions from motor vehicles. The model was modified based on in-use data acquired from more than 1000 gasoline and diesel in-use vehicles. Assumptions in the new model are based upon empirical, in-use data (versus mainly certification data in the PART5 model). Thus, PART5-TX1 is a more appropriate planning tool for helping reduce mobile source PM emissions. It is prepared such that it can be kept current or revised as the latest in-use emission data become available. The new model, PART5-TX1, predicts that current mobile source exhaust PM emissions are higher and will not decrease as rapidly as the PART5 model predicts.

Conclusions

Comparison of results from PART5-TX1 to PART5 validates the concerns raised by others about PART5. Overall, the PART5-TX1 model predicts that vehicles will emit more exhaust PM in the future than the PART5 model predicted. This difference is especially significant when looking at only light-duty gasoline vehicles.

Some of the zero-mile emission levels and deterioration rates calculated from the empirical data are quite unexpected. For example, new diesel trucks appear to deteriorate more quickly than expected. It is difficult at this point to definitively determine if these results are due to sample bias in the heavy-duty chassis dynamometer emissions data set, or due to actual deterioration of the equipment in the vehicles.

The new model is designed to be easily updated as new chassis dynamometer data are collected, and TNRCC will update the model as appropriate.

P5 vs P5-TX1: Fleet

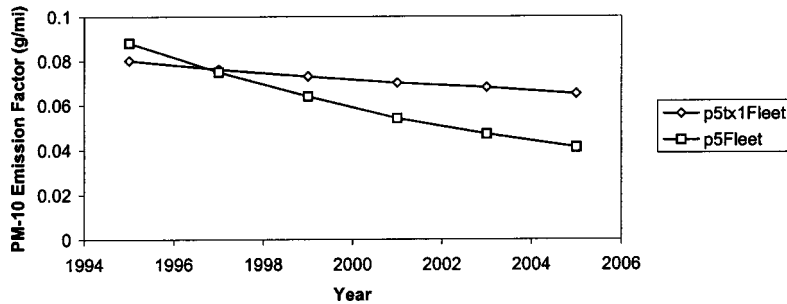


Fig. 12 PART5 and PART5-TX1 typical fleet predictions, 1995 to 2005

P5 vs P5-TX1: LDGVs

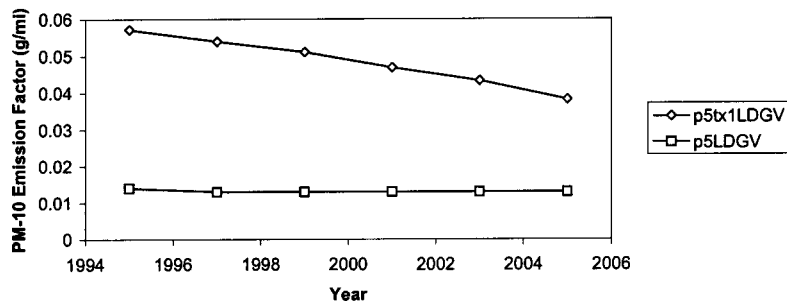


Fig. 13 PART5 and PART5-TX1 predictions for light-duty gasoline vehicles from calendar year 1995 to 2005

P5 vs P5-TX1: Heavy HDVs & Buses

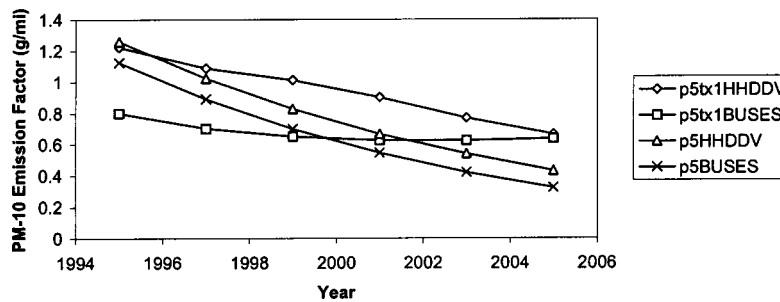


Fig. 14 PART5 and PART5-TX1 predictions for heavy-duty diesel trucks and buses for calendar years 1995 to 2005

Recommendations

It was evident as the new model was developed that the data set is still small for many vehicle types. The authors welcome any data which may have been missed in this analysis.

It is important that new PM emissions studies be designed to fill areas of the in-use PM emissions database that are currently deficient. Areas with a particularly small data set currently are: recent model years of all vehicle types (especially 1997 and newer), older diesel trucks, and medium heavy-duty diesel trucks (Class 6 & 7). As these new data are collected, PART5-TX1 can be easily updated.

It would be helpful to have more information about the duty cycles of various classes of heavy-duty vehicle. That information could be used to develop driving cycles that better represent on-road conditions for data collection on chassis dynamometers.

It may be appropriate to incorporate the effects of altitude, temperature, and humidity into future versions of the model. More data are needed to answer these and other related questions arising from this study.

Viewing the scatter plots in Figs. 7 and 8 gives rise to the question of data uncertainty. It is beyond the scope of this project to rigorously address data uncertainty. It was felt that since PART5-TX1 is an initial step to improve the prediction of in-use fleet particulate emissions, the larger issue of vehicle equipment deterioration was the most important. By including the concepts of ZML and DET into the model and basing the model upon in-use data, the basis for future improvements has been established. It may be appropriate to address data uncertainty in future refinements to the model.

Acknowledgments

The authors gratefully acknowledge TNRCC, SwRI, Radian International, and ERG for their support of this project. Also, we would especially like to thank the organizations who donated heavy-duty vehicles for chassis dynamometer tests, namely, San Antonio Northeast Independent School District, Capital Metro of Austin, Texas, and HEB, Inc. of San Antonio, Texas.

Nomenclature

bhp = brake horsepower
 BSFC = brake-specific fuel consumption
 CBD = central business district
 CFR = U.S. Code of Federal Regulations
 CO = carbon monoxide
 CO₂ = carbon dioxide
 CRC = Coordinating Research Council
 CVS = constant volume sampling
 DET = deterioration rate
 EPA = U.S. Environmental Protection Agency

ERG = Eastern Research Group
 FTP = Federal Test Procedure
 FTA = U.S. Federal Transit Administration
 g = gram
 gal = gallon
 GVW = gross vehicle weight
 HC = hydrocarbons
 HD = heavy duty
 HDCC = heavy-duty chassis cycle
 hp = horsepower
 hr = hour
 kg = kilogram
 km = kilometer
 kW = kilowatt
 L = liter
 lb = pound
 LD = light duty
 mi = mile
 MOUDI = micro-orifice uniform deposit impactor
 NAAQS = National Ambient Air Quality Standards
 NDIR = nondispersive infrared
 NO_x = oxides of nitrogen
 PM = particulate matter
 rpm = revolutions per minute
 SwRI = Southwest Research Institute
 TNRCC = Texas Natural Resource Conservation Commission
 UDDS = urban dynamometer driving schedule
 yr = year
 ZML = zero mile level
 μm = micrometer

References

- [1] Cadle, S. H., et al., 1998, "Measurement of Exhaust Particulate Matter Emissions from In-Use light-Duty Motor Vehicle in the Denver, Colorado Area," Final Report, CRC Project E-24-1.
- [2] Norbeck, J. M., et al., 1998, "Measurement of Primary Particulate Matter Emissions From Light-Duty Motor Vehicles," Final Report, CRC Project No. E-24-2.
- [3] Whitney, K. A., 1998, "Measurement of Primary Exhaust Particulate Matter Emissions From Light-Duty Motor Vehicles," Final Report, CRC Project No. E-24-3.
- [4] Graboski, M. S., et al., 1998, "Heavy-Duty Diesel Vehicle Testing for the Northern Front Range Air Quality Study," Final Report, Colorado State University Project.
- [5] Mulawa, P. A., et al., 1995, "Characterization of Exhaust Particulate Matter From 1986 through 1990 Model Year Light-Duty Gasoline Vehicles," GM Research and Development Publication 8456.
- [6] Darlington, T., et al., 1996, "Exhaust Particulate Emissions from Gasoline-Fueled Vehicles," 96WCC018, presented at World Car Conference.
- [7] Weaver, C., et al., 1998, "Modeling Deterioration in Heavy-Duty Diesel Particulate Emissions," EPA report under contract No. 8C-S112-NTSX.
- [8] France, C. J., et al., 1979, "Recommended Practice for Determining Exhaust Emissions From Heavy-Duty Vehicles Under Transient Conditions," Technical Report SDSA 79-08, EPA.

- [9] Urban, C. M., 1984, "Dynamometer Simulation of Truck and Bus Road Horsepower for Transient Emissions Evaluations," SAE Paper No. 840349.
- [10] Cadle, S. H., et al., 1995, "PM-10 Dynamometer Exhaust Samples Collected From In-Service Vehicles in Nevada," GM Research and Development Publication 8464.
- [11] Cadle, S. H., et al., 1997, "Particulate and Speciated HC Emission Rates from In-Use Vehicles Recruited in Orange County, CA," *Environ. Sci. Technol.*, **31**, p. 3405.
- [12] Fritz, S. G., et al., 1992, "Emissions From Heavy-Duty Trucks Converted to CNG," ASME 92-ICE-10.
- [13] Fritz, S. G., et al., 1993, "Emissions From Heavy-Duty Trucks Converted to Compressed Natural Gas," SAE 932950.
- [14] Arcadis Geraghty & Miller, Inc., 1998, "Update Heavy-Duty Engine Emission Conversion Factors for MOBILE6: Analysis of BSFC and Calculation of Heavy-Duty Engine Emission Conversion Factors," EPA Report No. 420-P-98-015, Mountain View, CA.

Reduction of NO_x and Particulate Emissions by Using Oxygen-Enriched Combustion Air in a Locomotive Diesel Engine

R. B. Poola

e-mail: ramesh.poola@gm.com

Electro-Motive Division,

General Motors Corporation,

9301 W. 55th Street,

LaGrange, IL 60525

R. Sekar

e-mail: rsekar@anl.gov

Argonne National Laboratory,

9700 South Cass Avenue,

Building 362,

Argonne, IL 60439-4815

This paper discusses operational and emissions results obtained with a locomotive (two-cylinder, EMD 567B) research diesel engine when oxygen-enriched combustion air is used. An operating regime was identified in which particulates and NO_x could be reduced simultaneously when the concentration of intake air oxygen, fueling rate, and injection timing were optimized. Using oxygen from an external source, particulates were reduced by approximately 60% and NO_x emissions were reduced by 15–20% with the optimal operating strategy. Higher gross power, lower peak cylinder pressures, and lower brake-specific fuel consumption were also observed. Gross power was increased by about 15–20% at base peak combustion pressure, and gross brake-specific fuel consumption was decreased by 2–10% with load. The effect of achieving oxygen enrichment by means of an air separation membrane is beyond the scope of the current study.

[DOI: 10.1115/1.1563236]

Introduction

Research efforts worldwide are focused on improving the diesel engine's performance and emissions characteristics by using numerous combustion and exhaust after-treatment techniques. With stricter emissions regulations, the focus has been narrowed toward in-cylinder combustion enhancements. Although the emphasis is on emissions research, performance improvements for diesels are also sought, particularly for large diesel engine applications (such as locomotives). Higher power density (power-to-displacement volume), higher smoke-limited brake torque with lower transient power demands, and lower brake specific fuel consumption (bsfc) are desired to sustain the dominance of diesel engines. Among many operating and design variables of diesel combustion, fueling strategies offer wide benefits, particularly significant reductions in exhaust emissions without reductions in performance.

To further improve performance and lower exhaust emissions, one of the least-exploited variables has been oxygen concentration in the combustion air, which is the subject of the current study. The use of oxygen-enriched intake air can significantly reduce particulate emissions, improve power density, lessen ignition delay, and allow the use of lower-grade fuels.

Air delivered to engines can be enriched in oxygen by selective permeation through a nonporous polymeric membrane, [1]. The basic principle of membrane operation and various designs and operating characteristics are described in Poola et al. [2]. The success of oxygen-enriched air utilization depends on the availability of a reliable, compact, and economical membrane that is able to produce the desired air composition onboard, depending on engine demands. Early attempts, [3,4] to use membranes to supply oxygen-enriched combustion air for diesel engines had limited success because of large driving force requirements and the membrane.

With advances in the development of newer membrane materials and coating techniques, module size and driving power requirements have been significantly reduced over the last few years and are now becoming attractive for combustion engines. The

authors have demonstrated the feasibility of a small-size prototype membrane for light-duty applications, [5], but scaling up to bigger modules that are appropriate for large diesel engines is still in the research phase. Membranes need to be further developed and optimized to adapt to diesel engine intake conditions (low pressure drop and pressure differential across the module). Nevertheless, the potential of intake air oxygen-enrichment needs to be further explored to eliminate its key drawback, which is high NO_x. The present study was aimed at re-examining key operating parameters and finding ways to obtain favorable NO_x-particulates and NO_x-bsfc tradeoffs.

Oxygen-Enriched Combustion. A few studies were made in the past evaluating the effects of oxygen-enrichment (oxygen concentration up to 35% by a few studies were made in the past evaluating the effects of oxygen-enrichment (oxygen concentration up to 35% by volume)) on both direct-injection and indirect-injection diesel engines, [6–13]. These studies have been carried out with the objective of reducing smoke, particulates, hydrocarbons, and carbon monoxide emissions. A majority of these studies report significant reductions in exhaust emissions, except for NO_x emissions. With the increased oxygen content in the combustion air, additional fuel can be burned to increase the indicated power. Oxygen enrichment of combustion air allows ignition with minimum amounts of premixed fuel, because it reduces the ignition delay and premixed combustion period, [8,14–16]. Nonetheless, with higher oxygen levels in the combustion air, the flame temperatures are higher, which increases in-cylinder formation of NO_x emissions. The reduction in the ignition delay period helps retard injection timing (without adversely affecting power and particulate emissions) so that NO_x emissions can be reduced to a certain extent, but it is difficult to attain the baseline NO_x levels. In the past, water-emulsified fuels, [17], low-grade fuels, [18], and water addition in the intake air, [19], were attempted to reduce accompanying NO_x emissions, but success was limited. In the current work, key operating variables (such as concentration of oxygen in the combustion air, fueling rate, and injection timing) were systematically evaluated in an effort to minimize particulate and NO_x emissions and yet maintain superior performance.

Oxygen-Enrichment Strategies. Air quality can best be described by the ratio of mole fraction of nitrogen to oxygen. Be-

Contributed by the Internal Combustion Engine Division of THE AMERICAN SOCIETY OF MECHANICAL ENGINEERS for publication in the ASME JOURNAL OF ENGINEERING FOR GAS TURBINES AND POWER. Manuscript received by the ICE Division November 2001; final revision received by the ASME Headquarters May 2002. Associate Editor: D. Assanis.

cause of changes in oxygen concentration associated with oxygen-enriched air, the standard mixture-quality terms, such as air-to-fuel ratio, equivalence ratio, and excess air factor, are misleading. To better characterize oxygen-enriched combustion under different oxygen concentration and fueling rates, and to compare those rates with those associated with using standard ambient air for combustion, the oxygen-to-fuel ratio is more indicative of mixture quality. For a given engine displacement and amount of intake air delivered, three different operating regimes exist, on the basis of the contents of oxygen and fuel in a cylinder, as given below:

1. *Rich oxygen-to-fuel ratio*: For a constant fuel input, increasing the oxygen content in the air such that

$$\left(\frac{\text{oxygen}}{\text{fuel}}\right)_{\text{amb}} < \left(\frac{\text{oxygen}}{\text{fuel}}\right)_{\text{OE}}$$

2. *Constant oxygen-to-fuel ratio*: Increasing both the oxygen content in the air and the fuel input such that

$$\left(\frac{\text{oxygen}}{\text{fuel}}\right)_{\text{amb}} = \left(\frac{\text{oxygen}}{\text{fuel}}\right)_{\text{OE}}$$

3. *Lean oxygen-to-fuel ratio*: Increasing the oxygen content of air and disproportionately increasing the fuel input such that

$$\left(\frac{\text{oxygen}}{\text{fuel}}\right)_{\text{amb}} > \left(\frac{\text{oxygen}}{\text{fuel}}\right)_{\text{OE}}$$

(The subscripts amb and OE stand for conditions with ambient and oxygen-enriched combustion air, respectively.)

Many previous oxygen-enrichment studies used the first operating strategy listed above, and the benefits (such as lower smoke and particulates) were well documented from those studies. Unfortunately, this strategy offers unfavorable NO_x-particulates and NO_x-bsfc tradeoff characteristics, which will be discussed later. For a given excess air factor, adding oxygen to the combustion air can influence high-temperature kinetics, but the resulting overall emissions and performance benefits are less attractive. Altering the oxygen-to-fuel ratio, as described in cases 2 and 3, is important to further exploit kinetically controlled combustion. The start of fuel injection timing is another independent variable, which can be combined with delineated cases to achieve potential benefits of the oxygen-enriched combustion air. The authors have examined the potential of strategies 1 and 2 by using an analytical model, and the results were reported in other work, [14,20].

In this paper, the results of using all three possible oxygen-enrichment strategies, along with the combination effect of injection timing, are reported. Unlike many previous attempts, the maximum oxygen concentration was limited to 27% by volume. Previous studies, [3,9,10,18], have shown that oxygen concentration higher than 27% offered marginal reductions in smoke and particulates, but NO_x emissions were higher by a factor of 2 to 4 from base levels.

Experimental Setup and Test Procedure

The test engine for the current study was a two-cylinder two-stroke EMD 567 locomotive diesel engine. An appropriate research diesel engine, representing current production locomotives, was unavailable at the time this study was conducted. Instead, an older version, the 567 series engine, was employed. Previously, this test engine was configured for conducting silver lubricity tests. For the current studies, the engine's hardware was upgraded appropriately with adequate instrumentation for conducting performance and emissions research. The major specifications of the test engine are shown in Table 1.

The oxygen-enrichment system consists of an external source of liquid oxygen, pressure regulators, a flow control valve, an evaporator, and oxygen sensors. Special pressure regulators were employed to handle the liquid oxygen. The liquid oxygen from an external mobile tank was bought in to the test cell by a flexible hose at a regulated pressure of about 5 bar (70 psi). Subsequently, the oxygen pressure was reduced to 0.35 to 0.7 bar (5 to 10 psi) by

Table 1 Technical specifications of the test engine

Parameter	Value
Bore, mm (in.)	216 (8.5)
Stroke, mm (in.)	254 (10)
Connecting rod length, mm (in.)	584.2 (23)
Displacement, liters (cubic in.)	9.3 (567)
Compression ratio	16:1
Rated speed, rpm	835
Rated brake power, kW (bhp)	140 (188)
Cycle	two-stroke
No. of cylinders	2
No. of exhaust valves/cylinder	4
No. of intake ports/cylinder	18
Fuel injector	mechanical unit injector
Beginning of fuel injection	16.5° BTDC @ full load

using another pressure regulator and sent to an evaporator. The liquid oxygen was vaporized in the evaporator, and then introduced at the engine's air filter section. Since the test engine was fitted with a Roots blower for supercharging, both the ambient air and pure oxygen in the gaseous state were drawn simultaneously into the blower unit, compressed, and delivered into the intake manifold (air box). The oxygen concentration of the combustion air was monitored by using an oxygen sensor in the exhaust and by sampling into the emissions bench from the air box section. The flow rate of the liquid oxygen was adjusted to maintain a constant (desired) oxygen concentration level in the combustion air. Oxygen concentration and suction pressure were also monitored in the crankcase to ensure safety.

The cylinder head was instrumented with a combustion pressure transducer by using the existing cylinder relief valve (CRV) port access. A strain gauge was mounted on the injector rocker arm to sense the dynamic injection timing. The test fuel was standard no. 2 diesel. The engine was connected to a generator for steady-state testing. The test engine was instrumented to measure the temperature, pressure, and flow rate of air intake, exhaust, water, lube oil, and fuel systems. A laminar-flow element was used to measure the intake airflow, and a Micro Motion-type device was used to measure the fuel mass flow rate. The Horiba emissions bench (THC/FID, CO and CO₂/NDIR, NO_x/CLD, O₂/paramagnetic) was employed to measure various gaseous emissions that include THC, CO, CO₂, O₂, and NO_x. The THC sample lines were heated to maintain a constant 175°C. Steady-state particulates were measured on a gravimetric basis by using a mini-dilution tunnel and EPA-recommended 70-mm filter papers. The diluted exhaust sample was analyzed for CO₂ composition.

Steady-state engine tests were conducted at eight different throttle settings that correspond to locomotive notch schedule, with each one providing a constant amount of torque at a governed engine speed. Nominal oxygen concentrations of 21%, 23%, 25%, and 27% by volume in the combustion air were employed in the current tests. To maintain a constant oxygen-to-fuel ratio, the fueling rate was predetermined for a given oxygen concentration level and adjusted by controlling the throttle at a constant speed (unlike the standard engine test condition, the torque output was not controlled). Since the test engine was equipped with a mechanical unit injector, changing the mechanical settings varied fuel injection timing. Baseline performance and emissions corresponded to engine intake air with ambient air of 21% oxygen concentration and the prescribed injection timing and fueling rate per manufacturer's recommendations. Since the test engine was originally manufactured prior to the locomotive emissions regulation, injection timing and fueling rate were optimized for only performance (horsepower and brake specific fuel consumption) at each throttle notch position. Therefore, the recommended injection timing and fuel rate settings at each throttle notch position may not be optimal for both performance and emissions, but were

considered as “baseline” for the present study. Obviously, any attempt to alter these prescribed settings would change the performance and/or emissions.

In the present study, no attempts were made to optimize the engine with respect performance or emissions before it was subjected to the studies on oxygen-enriched combustion air. Injection timing retard tests were conducted with ambient air (21% oxygen concentration) to establish the NO_x and particulates tradeoff characteristics and also to compare with oxygen-enriched combustion air cases. Injection timing sweeps with oxygen enrichment were conducted only at full load to develop optimal timing so that lower NO_x and particulate emissions could be achieved while maintaining the base fuel consumption. A nominal 25% oxygen concentration (selected arbitrarily) was tested by using a lean oxygen-to-fuel-ratio strategy. Because of limitations on the fuel pump and the maximum safe power output of the test engine, the fueling rate was increased to only 10% (above the fueling rate at which a constant oxygen-to-fuel ratio is maintained) to maintain a lean oxygen-to-fuel ratio. Because of the limitation on the maximum fueling rate at full load, neither a true constant or lean oxygen-to-fuel ratio at 27% oxygen-enriched air was attained.

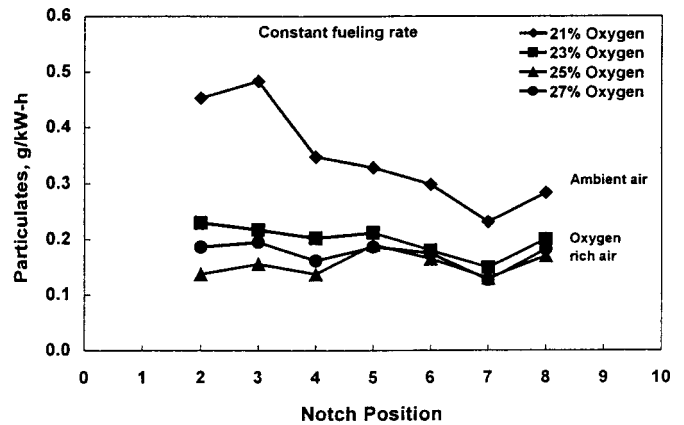
Results and Discussion

The test results are discussed in the order of the three different mixture qualities of oxygen-enriched combustion. Particulates and NO_x emissions are selected to illustrate the emissions characteristics, and peak cylinder pressure was compared to depict the combustion between ambient air and oxygen-enriched combustion air conditions. Throughout the paper, oxygen concentrations were expressed by percent volume. With oxygen-enrichment cases, brake power was referred to as gross brake power because the oxygen source was external.

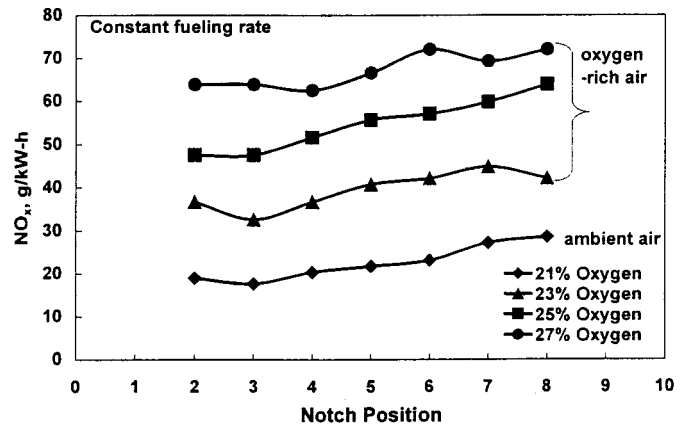
Rich Oxygen-to-Fuel Ratio. The effects of oxygen-enriched combustion air at a rich oxygen-to-fuel ratio (constant fueling rate) on exhaust emissions are engine-specific, but the qualitative trends were well established in many earlier studies. Figure 1 shows the results obtained from the test engine when 21% (ambient air), 23%, 25%, and 27% oxygen-enriched air was used in the engine intake. The fueling rate was maintained constant for both ambient air and oxygen-enriched air conditions. As a result of using oxygen-enriched air, particulates were significantly lower (30–70%) and NO_x emissions were much higher (50–150%) at all of the notch positions, compared with using ambient air. The reductions in particulates were more significant at part load than at full load, whereas the increase in NO_x was more uniform across the load. Qualitatively, these trends corroborate very well with test data available in the literature. Not surprisingly, power output was minimally affected by the different oxygen concentration levels because of the constant fueling rate. The net outcome of variations in combustion and heat transfer changed the power output very little.

The higher combustion temperatures with oxygen-enrichment were reported on the basis of adiabatic stoichiometric flame temperature calculations, [16,20], and in-cylinder combustion temperature measurements, [21,22]. It is believed that the high-temperature combustion resulted in higher soot oxidation and NO_x formation reactions. When oxygen concentration was increased from ambient air, 21% to 23% by volume, particulates were reduced considerably. Further increases in oxygen concentration to 25% or 27% resulted in a marginal decrease in particulates. On the other hand, NO_x emissions continued to increase with an increase in oxygen concentration. NO_x formation is a strong function of temperature; higher oxygen concentrations led to higher combustion temperatures and thus higher NO_x emissions.

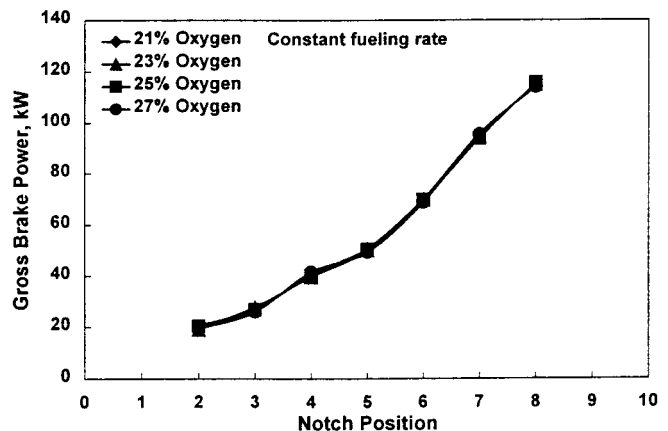
The majority of the combustion processes in diesel engines are often described as (fuel-air) mixing-controlled combustion, but the local temperature and oxygen and fuel concentrations dictate the combustion kinetics, in particular, the kinetics of soot formation/oxidation. The total particulates measured from the en-



(a)



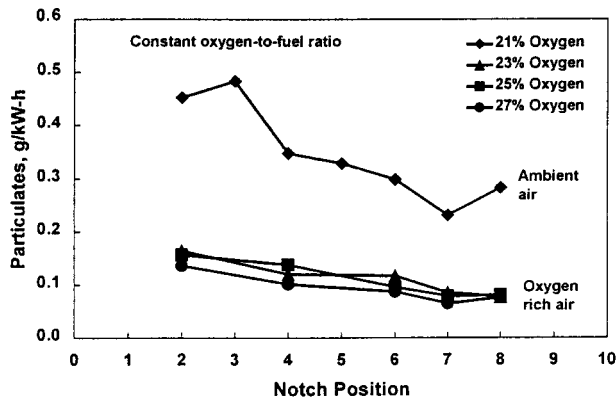
(b)



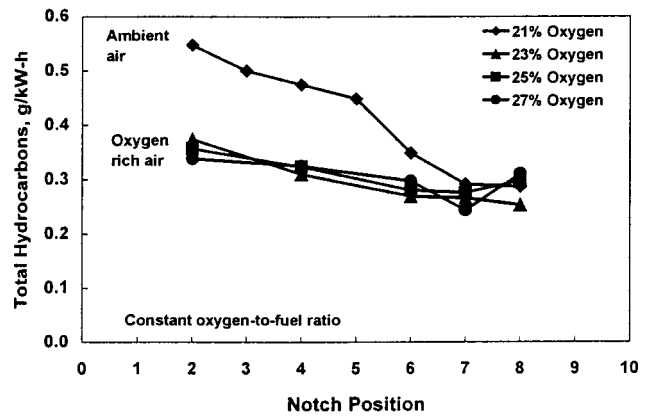
(c)

Fig. 1 Effects of intake air oxygen-enrichment at a rich oxygen-to-fuel ratio (constant fueling rate) on emissions and brake output

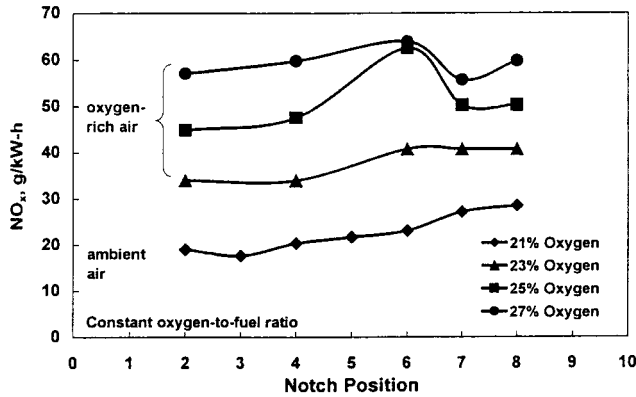
gine consist of volatile organic fractions and soot. The engine-out soot levels depend on the resulting soot formation and oxidation reactions occurring simultaneously during the combustion process. Several fundamental studies on soot (carbon) oxidation phenomena with respect to oxygen concentration exist in the literature, [e.g., [23–26]]. For example, Bews et al. [26] have studied the intrinsic kinetics of small carbon particles in different mixtures of O_2 and N_2 at temperatures up to about 1300 K and reported that carbon oxidation kinetics is half-order in O_2 . On the other hand, many reports were cited in the Ref. [26] on the order of reaction,



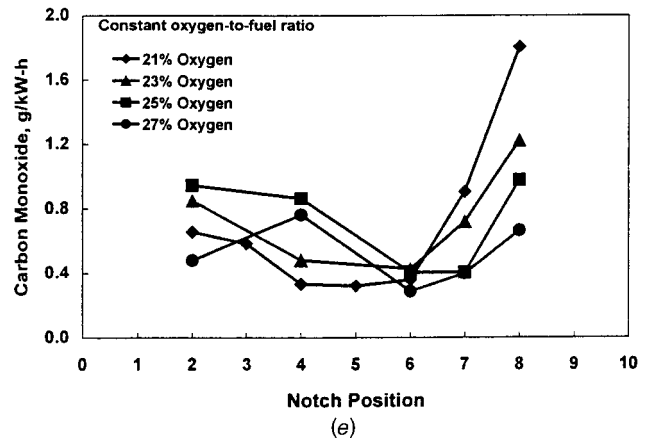
(a)



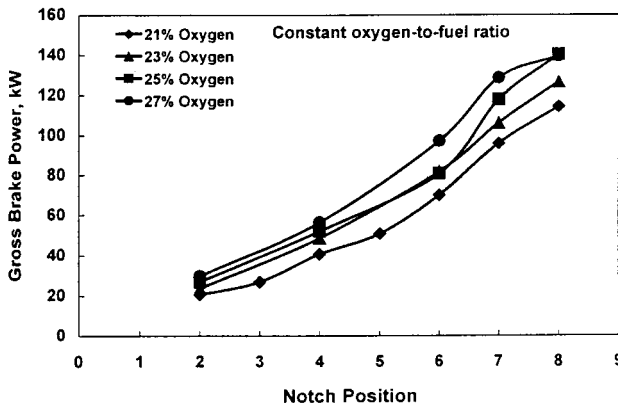
(d)



(b)



(e)



(c)

Fig. 2 (Continued)

Fig. 2 Effects of constant oxygen-to-fuel ratio on particulate, NO_x , THC, and CO emissions and brake power

which falls between zero and one. In the above cited studies, the findings on the kinetic order are influenced by the variables that were investigated, including temperature, oxygen concentration, carbon structure, and the presence of other chemical constituents (which might interact and/or alter carbon and oxygen oxidation reactions). The variations in structure and chemical constituents of soot being generated in diesel combustion add further complexity to knowing for certain about the order of reaction between oxygen and soot.

In the combustion studies relevant to diesel engines, higher soot oxidation reaction rates were reported by Iida [21] using a rapid compression machine with oxygen-enriched air. More recently, Donahue and Foster [22] have noticed that engine in-cylinder temperatures were higher (K-L factors were lower) within the

mixing-controlled portion of the combustion cycle when 23% oxygen-enriched air was used. Ignition delay is another important measured parameter in engine studies from which soot formation can be inferred. Many previous diesel engine studies demonstrated that ignition delay is shorter with oxygen-enriched air, [8,14–16]. The shorter ignition delay (thus lower soot formation), the higher in-cylinder temperatures during mixing-controlled combustion and the higher soot oxidation rates are believed to be responsible for such a drastic reduction in the observed particulate emissions when oxygen concentration is increased from 21% (ambient) to 23%. However, the reductions in particulate emissions were marginal with oxygen concentrations higher than 23%. These findings corroborate well with Argonne's previous findings, [3,9,18], and others, [10], on oxygen-enrichment for diesel engines, but contradict with few others, [7], who reported first-order reaction of soot with oxygen concentration. Among these diesel engine studies, the variations in combustion chamber characteristics and operating conditions led to some discrepancies in the reported total particulate emissions reductions with different intake air oxygen concentrations. This further confirms the complex interactions of mixing and local stoichiometry in diesel combustion, which lead to different engine-out soot levels with oxygen concentration. For the conditions tested in the test engine, an oxygen concentration of about 23–25% seems to be optimal to achieving lower engine-out soot levels across the load range. Incidentally, these moderate oxygen-enrichment levels will trigger drastic increases in NO_x formation. When nominal 23% oxygen-enriched air is used under the conditions of full engine load, particulates are reduced by about 30% and NO_x is increased by about 50% with no change in brake power. A 50% increase in NO_x , however, is not favorable. From a practical viewpoint, a rich

oxygen-to-fuel ratio yields particulate reduction at the expense of high NO_x emissions and loss of power to drive the membrane.

Constant Oxygen-to-Fuel Ratio. The additional oxygen concentration in the combustion air can be utilized to burn more fuel, thus producing more indicated power. The other known methods to increase the indicated power for a given displacement volume are increased turbocharging, oxygenated fuels, and higher compression ratios. Higher charge densities with increased turbocharging, oxygen-enriched combustion air, and oxygenated fuel are similar in increasing the availability of oxygen in the cylinder for combustion. But differences exist in the physical and operating requirements for such increased oxygen concentrations.

For example, in the case of turbocharging, both nitrogen and oxygen in the air are compressed to a higher pressure, and so the work involved in compressing nitrogen is clearly a drawback. Also, there are practical limits to boosting the intake manifold pressure before the complexity and losses associated with compressing the air are increased considerably (e.g., need for multi-stage turbocharging and intercooling). On the other hand, with an oxygenated fuel, a certain amount of energy is required in both adding and/or breaking oxygen molecules from hydrocarbon fuel, and there is a limit on the amount of oxygen that can be added. In comparison, oxygen enrichment via an air separation membrane offers an effective way to increase the overall oxygen (available in its free form) concentration for combustion.

To maintain a constant oxygen-to-fuel ratio for both ambient and oxygen-enrichment cases, the fueling rate was increased in proportion to the oxygen enrichment. Figure 2 shows the results obtained on the test engine with 23%, 25%, and 27% oxygen-enriched air cases compared with those obtained using ambient air. When a constant oxygen-to-fuel ratio was maintained, particulates and NO_x trends were quite similar, but gross power output was considerably different from that obtained by using a rich oxygen-to-fuel ratio (constant fueling rate). With a constant oxygen-to-fuel ratio, the gross brake power was increased by 11–22% when oxygen concentration was raised from 23% to 27%. Such an increase in power is expected because of differences in the fueling rate and resulting mixture quality. Like the rich oxygen-to-fuel ratio case, the maximum reductions in particulates were obtained when 23% oxygen-enriched air was used. Particulates changed little with further increases in oxygen concentration from 23% to 25% or 27%.

With a constant oxygen-to-fuel ratio, NO_x emissions exhibit similar trends with those obtained by using a rich oxygen-to-fuel ratio, although the increase in NO_x was slightly lower. For example by using 23% oxygen-enriched air, NO_x was increased by about 43% and 50% when the oxygen-to-fuel ratio was maintained constant and rich. For similar particulate and NO_x characteristics, achieving higher gross power was a beneficial outcome of applying a constant oxygen-to-fuel ratio. If the membrane's parasitic load offsets the power improvements, applying a constant oxygen-to-fuel ratio results in lower particulates at the expense of higher NO_x , which is still unattractive for current diesel engines. If using an exhaust after-treatment technique reduces NO_x emissions, the advantages of higher indicated power and lower particulates with oxygen-enriched air are imperative.

The total hydrocarbons (THC) and carbon monoxide emissions obtained with different oxygen-enrichment cases were compared with those of baseline and are shown in Fig. 2. The total hydrocarbon emissions were significantly reduced at engine part loads when oxygen concentration increased from 21% to 23%, but thereafter there was no change in the observed THC levels. The THC trends were similar to those for particulate emissions when higher than 23% oxygen concentrations were utilized. On the other hand, CO emissions were considerably lower at higher loads but marginally higher at part loads with different oxygen-enrichment levels when compared to the ambient air case. The variations in part-load CO emissions are marginal to establishing a definitive relationship with oxygen concentration.

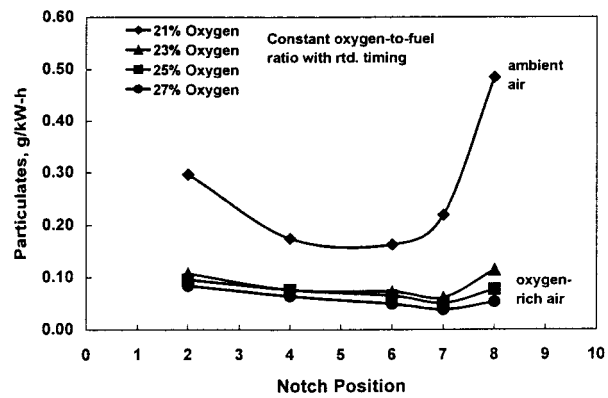
Constant Oxygen-to-Fuel Ratio With Retarded Injection Timing. Fuel injection timing can influence the NO_x -particulates tradeoff, which is an established behavior. Few attempts have been made to study injection-timing effects while using oxygen-enriched combustion air at rich oxygen-to-fuel ratio conditions, [3,9,17]. The underlying idea was to exploit the short ignition delays encountered with rich oxygen-to-fuel ratios so that NO_x could be lowered. But earlier studies showed little promise in achieving the base NO_x levels. Also, no timing sweep studies were made at a constant oxygen-to-fuel ratio.

In the current work, timing sweeps were conducted at engine full load by using 23% and 25% oxygen-enriched air while maintaining a constant oxygen-to-fuel ratio. Injection timing was kept retarded (results are not shown) such that the brake specific fuel consumption (bsfc) was no more than that with the ambient air at standard timing. From these tests, it was found that timing retarded by 7 deg from the baseline yielded a favorable NO_x -particulates and NO_x -bsfc tradeoff at both oxygen-enrichment levels tested. For all the subsequent tests at full load, injection timing was retarded (fixed) by 7 deg from the standard timing. The injection timings at other lower throttle positions were uniformly retarded, but the actual timing retarded (in degrees crank angle) followed the load-dependent timing settings incorporated within the mechanical unit injection (MUI) system. In locomotive diesel engines, typically, injection timing is advanced from top dead center with engine load.

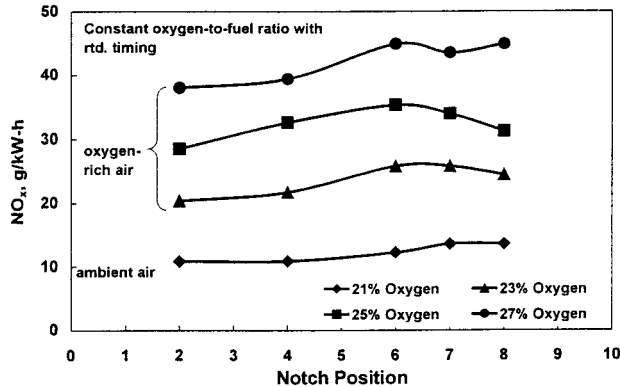
Figure 3 shows the results when injection timing was retarded by 7 deg while constant oxygen-to-fuel ratios of 21%, 23%, 25%, and 27% oxygen were maintained. Overall, particulates, NO_x , and gross brake power exhibited qualitative trends that were similar to those obtained at standard timing. By using ambient air at retarded timing, NO_x was reduced, but particulates increased, which corroborates with a known behavior. Conversely, particulates were significantly reduced with oxygen-enriched air, even at retarded injection timing. These reductions were about 50–75% and were quite significant at both part load and full load (notches 2 and 8, respectively). Like in previous cases, the maximum reduction in particulates was obtained with 23% oxygen-enriched air, and thereafter it changed little. However, quantitatively, particulates were relatively higher than those obtained at standard timing. For example, at 23% oxygen-enriched air, the amount of particulates increased from 0.077 to 0.11 g/kW-h when timing was changed from standard to 7 deg retard. Noticeably, the amount of particulates from oxygen-enriched air at retarded timing was much lower than that obtained by using ambient air at standard timing at all throttle conditions. The shorter ignition delay and higher soot oxidation reaction rates (higher temperatures) during the later part of the combustion cycle are believed to be responsible for such low engine-out particulate emissions.

As expected, NO_x emissions were relatively lower with ambient air at retarded timing, but when oxygen-enriched air is used, they were higher, and these trends were quite similar with those obtained at standard timing. Since the combustion temperatures were expected to be lower at retarded timing, NO_x emissions were relatively lower than those obtained at standard timing (compare Figs. 1(b) and 2(b)).

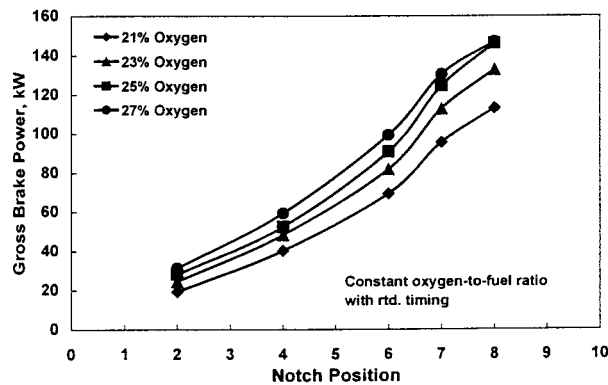
With oxygen-enriched air and at retarded timing, the gross brake power was higher by about 17–30% when compared with ambient air. The percentage gain in output was relatively higher at retarded timing than at standard timing (compare Figs. 2(c) and 3(c)). The promotion of late-cycle soot burn out could lead to higher energy conversion rates and thus increased power. As expected, the gross power increased with an increase in oxygen concentration in the combustion air, except at notch-8, where 27% oxygen-enriched air was used. The power output when using 27% oxygen-enriched air did not reflect the increase in power because a true constant oxygen-to-fuel ratio was not maintained. The limit on the fuel pump and the safe operating power limit on the engine



(a)



(b)



(c)

Fig. 3 Effects of constant oxygen-to-fuel ratio with retarded fuel injection timing on particulates, NO_x , and brake power

prevented the attainment of such a mixture quality; otherwise, the power output would be higher when compared with 25% oxygen-enriched air.

Attempts to achieve higher indicated power from a given displacement volume were constrained by the mechanical and thermal limits of the components, as well as by emissions limits. Before the material's limits are reached, emissions (visible smoke and particulates) will generally limit the maximum attainable output. Although particulates were not an issue while obtaining higher outputs with higher oxygen levels, it is important to examine the peak combustion pressures, which often represent an engine's mechanical and thermal threshold. The gross brake power attained with different oxygen-enriched levels was compared against respective peak cylinder pressures and is shown in Fig. 4. At both standard and retarded injection timings, peak cylinder

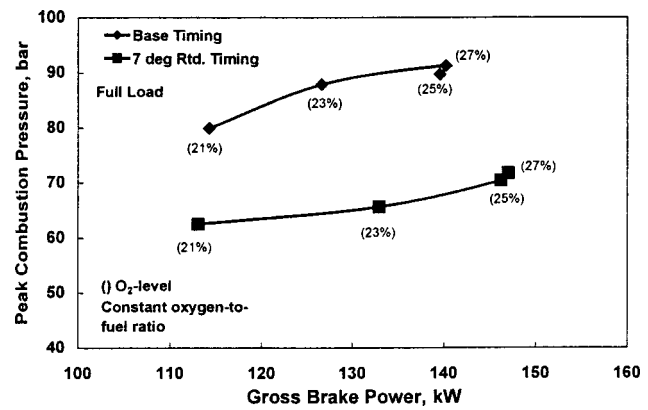


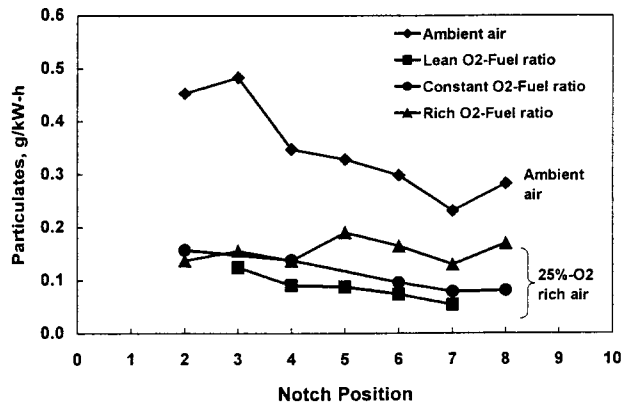
Fig. 4 Comparison of cylinder peak combustion pressures obtained while increasing the brake output using oxygen-enriched air

pressure increases with an increase in oxygen concentration and thus brake power. However, the increase in peak cylinder pressure was not proportional to the increase in brake power.

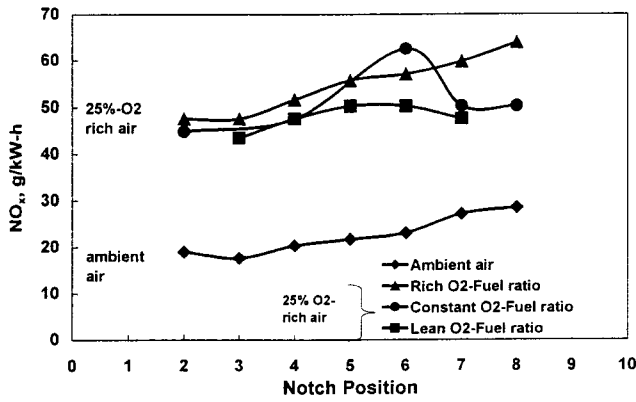
For example, at standard injection timing, when the brake output was increased by 22%, the peak cylinder pressure was increased by only 12%. Using other methods of increasing power, such as increased turbocharging or increased displacement volume, the cylinder pressures would have increased proportionately, [20]. The smaller increase in peak cylinder pressures is clearly an advantage associated with using oxygen-enrichment to increase cylinder output. This outcome is achievable primarily because of the shorter ignition delay and premixed combustion duration, [15,16].

Retarding the injection timing can further reduce peak cylinder pressures. As shown in Fig. 4, by retarding the injection timing by 7 deg crank angle, higher cylinder outputs were attained at any oxygen-enrichment level, and the respective peak cylinder pressures were considerably lower than those obtained at ambient air and standard injection timing. Compared with using ambient air, 30% more power can be generated by using appropriate oxygen concentration, fueling rate, and injection timing without exceeding the base peak cylinder pressure. Such a benefit is difficult to attain by using any other known practical techniques. In addition, recovering part of the increased exhaust energy (normally associated oxygen-enriched air) through a bottoming cycle can further boost the power output at the base peak cylinder pressure limit. The authors have analytically examined the potential of enhancing the power output by about 10–20% by using a heat recovery system, [20]. For a given limit on peak cylinder pressure, the benefit of higher power output achieved by using oxygen-enriched combustion rather than increasing boost with turbocharging was evident. Therefore, the use of oxygen-enriched air can be considered as an alternative or a complementary method to boost the power output without exceeding mechanical and/or thermal limits.

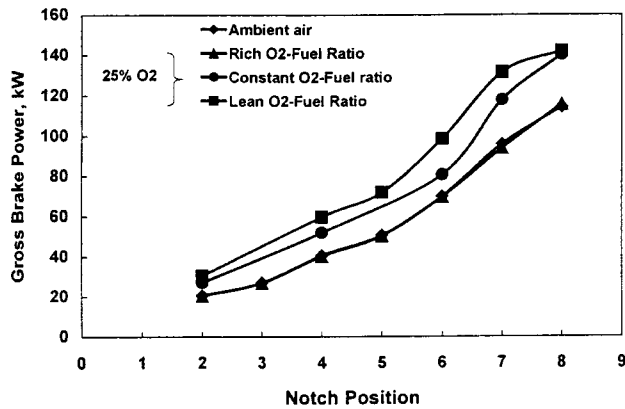
Lean Oxygen-to-Fuel Ratio. In consideration of lower particulates and higher power with a constant oxygen-to-fuel ratio, it is imperative to add more fuel using higher oxygen levels in the combustion air. The results obtained by using such a lean oxygen-to-fuel ratio strategy at standard injection timing are shown in Fig. 5. For comparison, 25% oxygen-enriched air was used for all the three operating strategies (rich, constant, and lean oxygen-to-fuel ratio). Noticeably, the power output was significantly higher with a lean oxygen-to-fuel ratio when compared with either a rich or constant oxygen-to-fuel ratio. The increase in power was a function of fueling rate at a given oxygen content. When compared with a constant oxygen-to-fuel ratio, a 10% increase in fueling rate resulted in a 10–20% increase in brake power. Theoretically, fueling rate could be further increased to attain a higher power



(a)



(b)

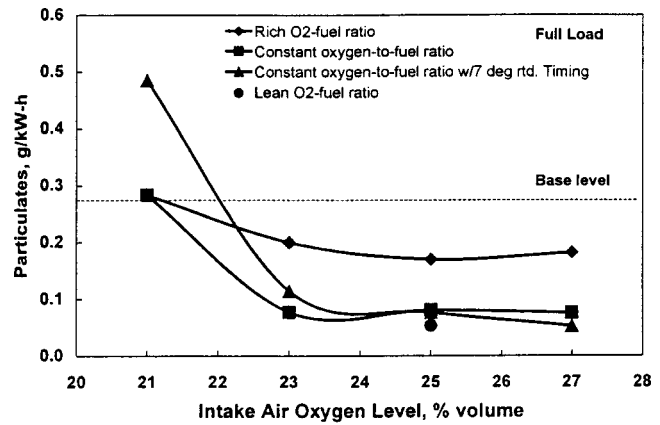


(c)

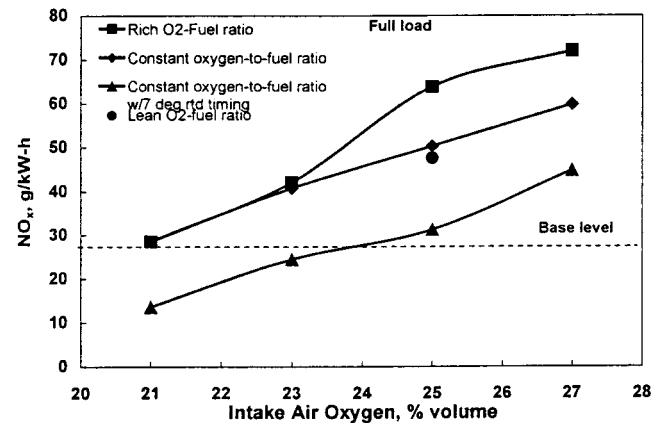
Fig. 5 Power and emissions characteristics with three different oxygen-enrichment strategies

output by using all of the oxygen available in the cylinder, but mechanical, thermal, and emissions limits will prevent such (between lean to stoichiometric) oxygen-to-fuel ratios.

The resulting particulates and NO_x emissions exhibit characteristics similar to those seen in the previous cases. Interestingly, both were relatively lower than the other two cases at 25% oxygen-enriched air. The lower particulates demonstrate the dominance of soot oxidation reactions under these lean oxygen-to-fuel ratio conditions. Although, relatively speaking, it is a lean oxygen-to-fuel ratio condition; the amount of oxygen available in the cylinder is much higher than the stoichiometric requirement for the fuel to burn completely. It is believed that the available temperature window for soot oxidation is much longer, and so soot ox-



(a)



(b)

Fig. 6 Comparison of performance and emissions with different oxygen concentration, fueling, and injection-timing strategies

idation reactions increase. However, it may be difficult to achieve complete combustion due to mixing-limited combustion, in particular at the tail end of combustion cycle. A lean oxygen-to-fuel ratio (at a fueling rate 10% higher than that at a constant oxygen-to-fuel ratio) has greater potential for lower particulate emissions and optimal brake power than at a rich or constant oxygen-to-fuel ratio, however, timing studies were conducted only at constant oxygen-to-fuel ratio. As discussed previously, combustion temperatures were higher with oxygen-enriched air and thus higher NO_x emissions. Except at notch 6, NO_x emissions were quite similar under both lean and constant oxygen-to-fuel ratios. However, because of the relatively fuel-rich conditions, the rate of NO_x formation was slower, but it was much higher than the rate of NO_x formation under ambient air conditions.

Performance and Emissions Tradeoff. It is worthwhile to compare the performance and emissions tradeoff when considering all of the operating parameters that were investigated (i.e., oxygen concentration, fueling rate, and injection timing) under different operating strategies simultaneously. For the current discussion, only results at notch 8 (full load) were compared. Incidentally, the full-load operating point is very important for locomotive diesel engines with respect to performance and emissions because the emissions at full-load contribute to the majority of the federal emissions duty-cycle average, particularly for line-haul locomotives. Additionally, the full-load performance is critical for railroad operators serving major line-haul locomotive operations.

Figure 6 shows the particulates and NO_x emissions when oxygen concentration, fueling rate, and injection timing were varied

to maintain rich, lean, and constant oxygen-to-fuel ratios. Between rich and constant oxygen-to-fuel ratios, the latter was more beneficial at obtaining lower particulate and NO_x emissions at any oxygen-enrichment level. This again explains the maximum potential of combustion enhancements by altering the chemical kinetics under mixing-limited combustion. At retarded injection timing with a constant oxygen-to-fuel ratio, particulates were significantly reduced and, surprisingly, NO_x emissions were also lower with certain oxygen concentration levels. Beyond 23–24% oxygen enrichment, there was no change in particulate emissions, but NO_x emissions were higher than the base level. An operating regime exists in which both particulates and NO_x could be simultaneously lowered. For the test engine, such a window was identified between 21% and 24% oxygen-enriched air while a constant oxygen-to-fuel ratio is maintained and injection timing is retarded by 7 deg from the base level. Such a window of simultaneous reduction of particulates and NO_x could be identified in any diesel engine, provided that the key operating variables—oxygen concentration, fueling rate, and injection timing—were properly optimized. In light of these findings, it was further confirmed that changing the oxygen concentration alone was not a preferred approach in the overall aim of lowering both particulates and NO_x and the potential to obtain higher indicated power.

On the basis of current experimental investigations on the test engine, an optimum oxygen-enrichment strategy was identified that is beneficial with respect to particulate emissions, NO_x emissions, brake power, and peak cylinder pressure. This strategy involves using 23% oxygen-enriched air with optimum fueling rate and timing (a constant oxygen-to-fuel ratio with 7 deg retarded injection timing). The results obtained from using such an optimum strategy were directly compared with those from a base engine (using ambient air at standard timing). It is reasonable to compare these results with those obtained by using ambient air by simply retarding the injection timing, which is a common practice.

Figure 7 compares NO_x -particulate emissions and NO_x -bsfc tradeoff characteristics between ambient air and an optimum oxygen-enrichment strategy. From these tradeoffs, it is evident that while lowering NO_x emissions, both bsfc and particulate emissions were significantly affected by simply retarding the injection timing on a base engine. At standard injection timing, oxygen-enriched air did influence both particulate emissions and bsfc more favorably, but the resulting NO_x was higher. But with an optimum oxygen-enrichment strategy, the NO_x -particulate emissions and NO_x -bsfc tradeoff curves were shifted to more favorable positions. By using this optimum oxygen-enrichment strategy, many simultaneous benefits were realized: particulate emissions were reduced by about 60%, NO_x emissions were reduced by about 14%, bsfc was reduced by about 2%, gross power was increased by 16% (not shown), and peak cylinder pressure was reduced by about 18% (not shown). These benefits, however, quantitatively different at other engine loads. But full-load performance and emissions benefits are quite relevant from the locomotive perspective. Also, a new strategy has evolved from the current studies that can contain NO_x emissions to base levels or even lower across the entire load range when oxygen-enriched air is used in diesel engines.

From Fig. 8, a reduction in observed bsfc was also evident in the entire operating range of the engine. The reductions in bsfc were more significant at part loads; they were about 10% by using the optimum strategy. The net bsfc improvements, however, are expected to be lower than reported here, if membrane parasitic loads had been considered. Beyond this window of the operating regime, the results follow conventional tradeoffs, which were not favorable for consideration. For example, if oxygen concentration is increased to 25% oxygen-enriched air, which is a deviation from “optimum operating strategy,” an increase in NO_x from the baseline is evident. The net benefits that can be realized from the optimum operating strategy would also change, if the membrane operating power (supplying 23% oxygen-enriched air) was con-

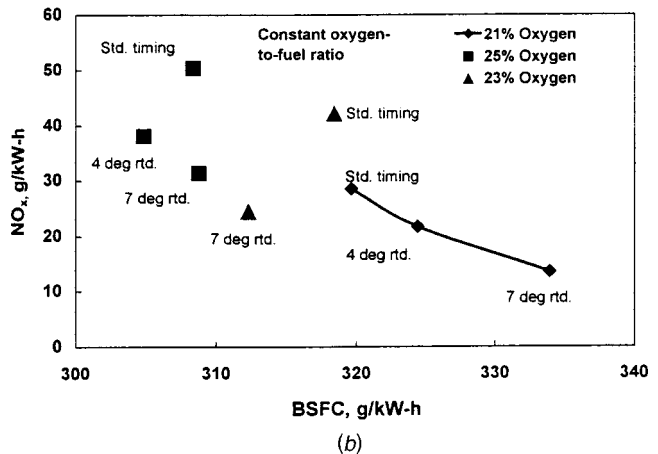
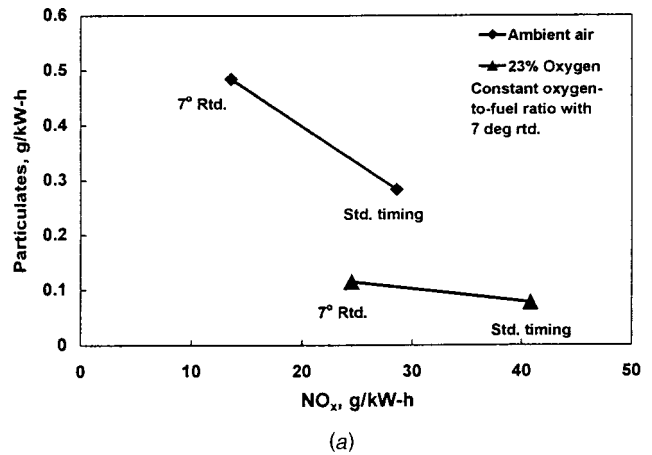


Fig. 7 Tradeoff between emissions and bsfc at engine full load using optimum oxygen-enrichment strategy

sidered. The difference between gross and net benefits is a function of power requirements and flow efficiency of an air separation membrane. If part of the higher exhaust enthalpies available as a result of oxygen enrichment is recovered, the power requirements of the air separation membrane can be met, resulting in substantial net benefits [20]. The sensitivity of oxygen concentra-

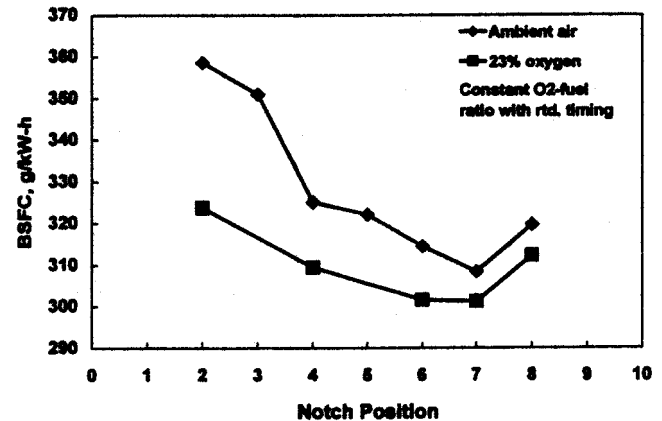


Fig. 8 Reductions in observed brake specific fuel consumption by using optimum oxygen-enrichment strategy

tion, fueling rate, and injection timing, which are engine specific, need to be evaluated on a given engine to realize such wide benefits.

On the basis of reported results obtained from the test engine, it is difficult to forecast such delineated benefits on a modern diesel engine. Nevertheless, the key operating parameters (oxygen concentration, fueling rate, and injection timing) and a methodology to combine these parameters (a constant oxygen-to-fuel ratio with retarded injection timing) were identified in the current work.

Conclusions

On the basis of current experimental investigations on a two-stroke locomotive research diesel engine, the following conclusions are drawn when oxygen concentration, fueling rate, and injection timing were evaluated by using different operating strategies.

1. To better describe the mixture quality associated with the use of oxygen-enriched combustion air and to compare the results with those obtained using ambient air, the term "oxygen-to-fuel ratio" was defined. With respect to ambient air, three different mixture qualities—rich, lean, and constant oxygen-to-fuel ratio—were examined by using oxygen-enriched combustion air.

2. Adding more oxygen in the combustion air while keeping the fueling rate (leading to a rich oxygen-to-fuel ratio) and injection timing constant offers the fewest benefits, in terms of lower particulate emissions at the expense of a much higher NO_x and operating power requirement for supplying oxygen-enriched air. From a practical standpoint, this strategy does not offer the full potential of oxygen enrichment, and so it is less attractive.

3. A constant oxygen-to-fuel ratio and/or a relatively lean oxygen-to-fuel ratio at standard injection timing can lower the particulates significantly at higher NO_x levels. The resulting NO_x emissions were much higher than those obtained by using ambient air. However, this strategy has much potential to generate higher gross power.

4. When injection timing is retarded by 7 deg from the base timing and a constant oxygen-to-fuel ratio is maintained, an operating regime was identified between 21% and 24% in which particulate and NO_x emissions were reduced simultaneously. Also, the corresponding gross brake power was higher and peak cylinder pressure and brake specific fuel consumption were lower compared with operation using ambient air.

5. By using an optimum oxygen-enrichment strategy (23% oxygen-enriched air, a constant oxygen-to-fuel ratio, and 7 degrees retarded injection timing), particulate emissions were reduced by about 60%, NO_x emissions were reduced by about 14%, gross power was increased by about 16%, peak cylinder pressure was reduced by 18%, and bsfc was reduced by about 2% at engine full load. Such wide benefits demonstrate the potential of the oxygen-enrichment technique.

6. It is possible to envision such an operating regime in any diesel engine where the simultaneous reduction of particulates and NO_x could be achieved by optimizing oxygen concentration, fueling rate, and injection timing, but the net benefits attainable depend on the membrane and its operating requirements to supply the desired oxygen-enriched air.

Acknowledgments

Work supported by the U.S. Department of Energy, Office of Energy Research—Laboratory Technology Research, under contract W-31-109-Eng-38. Work performed under a cooperative research and development agreement (CRADA) between the U.S. Department of Energy and Association of American Railroads and the Electro-Motive Division (EMD) of General Motors Corporation. The authors are grateful to all the CRADA-Program Managers, including Ted Vojonovich and Sam Barish, the U.S. Department of Energy, Office of Science; Deborah Clayton, Argonne National Laboratory; James Lundgren, Transportation Technology

Center, Inc.; and Charles Horton, EMD, for their interest and support of this program. The authors wish to acknowledge Pat McPartlin, John D'Auben, Rodney Trembczynski, Jo Goodwin, Ralph Appleby, Frank Tataro, Nicolette Lopez, and Jerry Schaus of AutoResearch Laboratories, Inc., for providing testing services and technical support during the experiments. The first author wishes to thank Richard Lill, EMD, for providing combustion instrumentation, Richard Tupek and Michael Goetzke, EMD, for their support in publishing this work.

References

- [1] Winston Ho, W. S., and Sirkar, K. K., 1992, *Membrane Handbook*, Chapman and Hall, New York.
- [2] Poola, R. B., Stork, K. C., Sekar, R. R., Callaghan, K., and Nemser, S., 1998, "Variable Air Composition with Air Separation Membrane: A New Low Emissions Tool for Combustion Engines," *SAE Trans.*, **106**, pp. 332–346.
- [3] Sekar, R. R., Marr, W. W., Cole, R. L., and Marciniak, T. J., 1991, "Experimental Evaluation of Oxygen-Enriched Air and Emulsified Fuels in a Single-Cylinder Diesel Engine," Technical Report, Argonne National Laboratory, ANL/ESD/TM, Vol. 1 & 2.
- [4] Rigby, G. R., and Watson, H. C., 1994, "Application of Membrane Gas Separation to Oxygen Enrichment of Diesel Engines," *J. Membr. Sci.*, **87**, pp. 159–169.
- [5] Sekar, R. R., and Poola, R. B., 1997, "Demonstration of Oxygen-Enriched Combustion System on a Light-Duty Vehicle to Reduce Cold-Start Emissions," Thirtieth International Symposium on Automotive Technology and Automation (ISATA), Florence, Italy, *Proceedings of the Motor Vehicle and the Environment—Entering a New Century*, Paper No. 97EN038, pp. 301–310.
- [6] Karim, G. A., and Ward, G., 1968, "The Examination of the Combustion Processes in a Compression-Ignition Engine by Changing the Partial Pressure of Oxygen in the Intake Charge," *SAE Paper No. 680767*.
- [7] Ghojel, J., Hilliard, J. C., and Levensis, J. A., 1983, "Effect of Oxygen-Enrichment on the Performance and Emissions of I.D.I. Diesel Engines," *SAE Paper No. 830245*.
- [8] Iida, N., Suzuki, Y., Sato, G. T., and Sawada, T., 1986, "Effects of Intake Oxygen Concentration on the Characteristics of Particulate Emissions From D.I. Diesel Engine," *SAE Paper No. 861233*.
- [9] Sekar, R. R., Marr, W. W., Schaus, J. E., Cole, R. L., and Marciniak, T. J., 1990, "Diesel Engine Experiments with Oxygen Enrichment, Water Addition and Lower-Grade Fuel," *Proceedings of the 25th Intersociety Energy Conversion Engineering Conference*, Vol. 4.
- [10] Watson, H. C., Milkins, E. E., and Rigby, G. R., 1990, "A New Look at Oxygen Enrichment, I, The Diesel Engine," *SAE Paper No. 900344*.
- [11] Virk, K. S., Kokturk, U., and Bartles, C. R., 1993, "Effects of Oxygen-Enriched Air on Diesel Engine Exhaust Emissions and Engine Performance," *SAE Paper No. 931004*.
- [12] Reader, G. T., Bowen, C. E., Maier, P., Potter, I. J., and Gustafson, R. W., 1995, "The Effects of Oxygen/Nitrogen Ratios on the Performance and Emissions of an IDI Diesel Engine," Third Asian-Pacific International Symposium on Combustion and Energy Utilization.
- [13] Li, J., Chae, J. O., Park, S. B., Paik, H. J., Park, J. K., Jeong, Y. S., Lee, S. M., and Choi, Y. J., 1997, "Effect of Intake Composition on Combustion and Emission Characteristics of DI Diesel Engine at High Intake Pressure," *SAE Paper No. 970322*.
- [14] Sekar, R. R., Marr, W. W., Assanis, D. N., Cole, R. L., Marciniak, T. J., and Schaus, J. E., 1991, "Oxygen-Enriched Diesel Engine Performance: A Comparison of Analytical and Experimental Results," *ASME J. Eng. Gas Turbines Power*, **113**, pp. 365–369.
- [15] Assanis, D. N., Karvounis, E., Sekar, R. R., Marr, W. W., 1993, "Heat Release Analysis of Oxygen-Enriched Diesel Combustion," *ASME J. Eng. Gas Turbines Power*, **115**, pp. 761–768.
- [16] Lahiri, D., Mehta, P. S., Poola, R. B., and Sekar, R. R., 1997, "Utilization of Oxygen Enriched Air in Diesel Engines—Fundamental Considerations," *ASME Fall Technical Conference*, Vol. 3, Paper No. 97-ICE-72, ASME, New York, pp. 119–128.
- [17] Sekar, R. R., Marr, W. W., Cole, R. L., and Marciniak, T. J., 1991, "Effects of Oxygen Enrichment and Fuel Emulsification on Diesel Engine Performance and Emissions," *ASME Meeting on Fuels, Controls, and After Treatment for Low-Emissions Engines*, ICE-Vol. 15, ASME, New York, pp. 21–28.
- [18] Marr, W. W., Sekar, R. R., Cole, R. L., Marciniak, T. J., and Longman, D. E., 1993, "Oxygen-Enriched Diesel Engine Experiments with a Low-Grade Fuel," *SAE Paper No. 932805*.
- [19] Cole, R. L., Sekar, R. R., Stodolsky, F., and Marciniak, T. J., 1990, "Technical and Economic Evaluation of Diesel Engine With Oxygen Enrichment and Water Injection," *ASME Energy Sources Technology Conference and Exhibition*, New Orleans, Paper 90-ICE-1.
- [20] Assanis, D. N., Poola, R. B., Sekar, R. R., and Cataldi, G. R., 2001, "Study of Using Oxygen-Enriched Combustion Air for Locomotive Diesel Engines," *ASME J. Eng. Gas Turbines Power*, **123**, pp. 157–166.
- [21] Iida, N., 1993, "Surrounding Gas Effects on Soot Formation and Extinction—Observation of Diesel Spray Combustion Using a Rapid Compression Machine," *SAE Paper No. 930603*.

- [22] Donahue, R. J., and Foster, D. E., 2000, "Effects of Oxygen Enhancement on the Emissions from a DI Diesel via Manipulation of Fuels and Combustion Chamber Gas Composition," SAE Paper No. 2000-01-0512.
- [23] Smith, I. W., 1982, "The Combustion Rates of Coal Chars: A Review," Nineteenth Symposium (Int'l) on Combustion, The Combustion Institute, Pittsburgh, pp. 1045–1065.
- [24] Nagle, J., and Strickland-Constable, R. F., 1962, "Oxidation of Carbon between 1000–2000°C," *Proceedings of Fifth Carbon Conference*, Vol. 1, pp. 154–164.
- [25] Park, C., and Appleton, J. P., 1973, "Shock-Tube Measurements of Soot Oxidation Rates," *Combust. Flame*, **20**, pp. 369–379.
- [26] Bews, I. M., Hayhurst, A. N., Richardson, S. M., and Taylor, S. G., 2001, "The Order, Arrhenius Parameters, and Mechanism of the Reaction Between Gaseous Oxygen and Solid Carbon," *Combust. Flame*, **124**, pp. 231–245.

A Nonequilibrium Turbulence Dissipation Correction and Its Influence on Pollution Predictions for DI Diesel Engines

F. X. Tanner

Department of Mathematical Sciences,
Michigan Technological University,
Houghton, MI 49931-1295
e-mail: tanner@mtu.edu

G.-S. Zhu

Detroit Diesel Corporation,
13400 W. Outer Drive,
Detroit, MI 48239-4001
e-mail: guangsheng.zhu@detroitdiesel.com

R. D. Reitz

Engine Research Center,
University of Wisconsin-Madison,
Madison, WI 53706-1572
e-mail: reitz@engr.wisc.edu

A correction for the turbulence dissipation rate, based on nonequilibrium turbulence considerations from rapid distortion theory, has been derived and implemented in combination with the RNG k - ϵ model in a KIVA-based code. This correction reflects the time delay between changes in the turbulent kinetic energy due to changes in the mean flow and its turbulence dissipation rate, and it is shown that this time delay is controlled by the turbulence Reynolds number. The model correction has been validated with experimental data in the compression and expansion phase of a small diesel engine operated in motored mode. Combustion simulations of two heavy-duty DI diesel engines have been performed with the RNG k - ϵ model and the dissipation rate correction. The focus of these computations has been on the nitric oxide formation and the net soot production. These simulations have been compared with experimental data and their predictions are explained in terms of the turbulence dissipation effect on the transport coefficients for mass and heat diffusion. It has been found, that the dissipation correction yields consistent results with observations reported in previous studies. [DOI: 10.1115/1.1501917]

Introduction

A widely used turbulence model, based on the eddy-viscosity approach, is the linear, two-equation k - ϵ model, where the turbulence kinetic energy, k , and the turbulence dissipation rate, ϵ , are described by appropriate transport equations (cf. [1–3]). This model has been successfully tested in a wide variety of steady-state flows occurring in technical applications. However, one of the model's shortcomings is in transient flows where the equilibrium turbulence assumption, that turbulence production balances dissipation at any instant, is not satisfied. In fact, due to piston movement, the fuel injection and the combustion process, the flows in DI diesel engines are transient in nature and therefore, the hypothesis of equilibrium turbulence is violated.

Various approaches have been investigated by numerous researchers in order to remedy the shortcomings of the linear k - ϵ -based turbulence models. Improvements of this model, based on the theory of re-normalization groups (RNG), have been achieved by Yakhot et al. [4] and successfully introduced to spray combustion simulations by Han et al. [5]. However, uncertainties in the dissipation transport equation still remain and have been investigated in a recent study by Bianchi et al. [6]. In this investigation, the change of the molecular viscosity, predicted by the rapid distortion theory, have been integrated into the ϵ equation. This is a further development of a study by Coleman and Mansour [7], where an additional closure relation has been developed to account for rapid distortion effects.

In a recent investigation, Tanner et al. [8] have implemented a nonequilibrium turbulence correction to the dissipation rate by changing the dissipation source terms in the RNG k - ϵ turbulence model equations. This study focused on the behavior of the turbulence characteristic combustion time of the two heavy-duty DI diesel engines, the Caterpillar 3406 (CAT) and the Sulzer S20 (S20) which operate under comparable conditions. It was found that the dissipation rate correction resulted in a more realistic

prediction of the turbulence length scales during the compression phase, and in an improved combustion performance due to the better fuel-air mixing.

The dissipation rate correction (ϵ correction) utilized in the present study models the delay between the turbulence kinetic energy and its dissipation rate in transient flow conditions by imposing an additional constraint on the dissipation rate. This constraint considers the local change of the turbulence Reynolds number and directly influences the turbulence viscosity. An improvement of this implementation and its effect on the turbulence length and time scales, as well as the performance of the characteristic time combustion model for the CAT and the S20, have been reported in [9]. In the present study, this ϵ correction has first been validated with experimental data of the turbulence length scale of a small experimental Lombardini engine operating in motored mode. The remaining investigations focus on the pollution formation of the CAT and the S20 engines. Particular attention has been given to the influence of this ϵ correction on the soot and nitric oxide formation for various operating conditions. The effect of the ϵ correction is discussed in view of the turbulence viscosity and its effect on the transport coefficients for the heat conduction and the species diffusion.

Aspects of Turbulence

The turbulence energy transfer occurs via the well-known Kolmogorov dissipation cascade (cf. [10]): The mean flow induces a wide spectrum of eddy sizes, where the larger eddies feed smaller ones by a vortex stretching mechanism, until the smallest eddies finally dissipate at the Kolmogorov cutoff scale. The largest length scale is the integral length scale, L_I , which describes the size of the largest eddies and is determined by the geometric configuration of the flow. The dissipation occurs at the Kolmogorov dissipation scale, L_η , which is a measure for the smallest observable flow structures. The Taylor microscale, L_λ , is the length scale which relates the local strain rates (i.e., the dissipation) and the turbulence intensity, q . The macrolength scale, L_ϵ , is a characteristic length scale of the dissipation cascade and is a measure for the "average" eddy sizes. L_ϵ is obtained from the turbulence parameters k and ϵ via the relation $L_\epsilon \propto k^{3/2}/\epsilon$. Note that L_I and L_ϵ

Contributed by the Internal Combustion Engine Division of THE AMERICAN SOCIETY OF MECHANICAL ENGINEERS for publication in the ASME JOURNAL OF ENGINEERING FOR GAS TURBINES AND POWER. Manuscript received by the ICE Division May 2001; final revision received by the ASME Headquarters November 2001. Associate Editor: D. Assanis.

are both “energy-containing” length scales, but L_ε is computed using the turbulence equilibrium assumption, as is discussed below. Associated with L_ε is the macro time scale, $\tau_\varepsilon = L_\varepsilon/q$, which characterizes the “average” eddy turnover time.

Equilibrium and Nonequilibrium Turbulence. The equilibrium hypothesis, which states that the instantaneous turbulence production rate equals the turbulence dissipation rate, is one of the fundamental assumptions in eddy viscosity-based turbulence models. Based on this assumption, equating the dissipation rate with the turbulence production rate leads to

$$\varepsilon_{eq} \propto q^3/L_I \quad (1)$$

where $q = \sqrt{2k/3}$ is the turbulence intensity and the subscript eq denotes equilibrium. For equilibrium turbulence it is assumed that $L_I \propto L_\varepsilon$ which yields the relation

$$\varepsilon_{eq} = C_\varepsilon k^{3/2}/L_\varepsilon \quad (2)$$

where C_ε is a constant. Note, if only one length scale is used to characterize turbulence, say L_ε as in the case of the two-equation k - ε model, then this length scale represents all the length scales of the turbulence, and the turbulence can be described as being in equilibrium. In this case, the turbulence is self-similar since all scales adjust to flow changes at the same rate.

For highly transient flows, however, the equilibrium turbulence assumption is likely to be violated, and Eq. (2) does not hold. In fact, the energy dissipation cascade adjusts to changes in the mean flow with some delay and different length scales adjust at different rates. Therefore, a nonequilibrium formulation for the dissipation is required.

Wu et al. [11] performed direct Navier-Stokes computations for flows under rapid compression conditions. They found that the Taylor length scale, L_λ , and the integral length scale, L_I , remain proportional to each other during a rapid compression. A similar observation has been made experimentally by Dinsdale et al. [12] in engine measurements. The result is also consistent with that obtained from a rapid distortion analysis of isotropic compressed turbulence given by Reynolds [13] and Wu et al. [11].

For isotropic, homogeneous turbulence, the dissipation can be expressed by the Taylor relation (cf. [10], p. 67)

$$\varepsilon = 10\nu_o k/L_\lambda^2 \quad (3)$$

where ν_o is the molecular (kinematic) viscosity and L_λ denotes the Taylor micro scale. Using the fact that for rapid compression flows $L_I \propto L_\lambda$, Eq. (3) becomes

$$\varepsilon \propto \nu_o k/L_I^2. \quad (4)$$

From Eqs. (2) and (4) Han et al. [14] derived the relation

$$L_\varepsilon \propto Re_t L_I \quad (5)$$

where $Re_t = qL_I/\nu_o$ is the turbulence Reynolds number. Equation (5) states that a rapid change in the turbulence behavior, caused for instance by a rapid change in the turbulence intensity, is reflected in an appropriate change of L_ε via Re_t . Therefore, in turbulence models where L_ε is the only length scale used to express the eddy size of the turbulence spectrum, a change from turbulence equilibrium is reflected by an appropriate change in L_ε via Re_t .

Comparison of formulas (1) and (4) yields the following relation between the equilibrium and nonequilibrium dissipation rates:

$$\varepsilon \propto \varepsilon_{eq}/Re_t. \quad (6)$$

Equation (6) is the key in the interpretation of the time delay between a change in the turbulence kinetic energy, k , and its dissipation rate ε . A change in the mean flow results in an immediate change in k , whereas the turbulence dissipation, which takes place on the smallest length scale, occurs with some delay. In fact, this delay lies in the order of one eddy turnover time given by τ_ε

$= L_I/q$. The relation between this time delay and the turbulence Reynolds number is given by the time-scale ratio

$$Re_t = qL_I/\nu_o = \tau_m/\tau_\varepsilon \quad (7)$$

where $\tau_m = L_I^2/\nu_o$ is the molecular diffusion time scale, which is independent of the turbulence behavior. According to Eq. (7), a change in the eddy turnover time τ_ε results directly in a change of Re_t and consequently, Eq. (6) is the statement that the delay in the dissipation rate is controlled by the turbulence Reynolds number.

Influence on the Transport Coefficients and Re_t . In eddy viscosity-based turbulence models, the turbulence viscosity, ν_t is modeled in analogy to the molecular viscosity in the kinetic theory of gases, as $\nu_t \propto u_c L_c$, where u_c and L_c represent a characteristic velocity and a characteristic length scale, respectively. It follows from dimensional analysis that $u_c \propto \sqrt{k}$ and $L_c \propto k^{3/2}/\varepsilon$, which leads to the well-known relation

$$\nu_t = c_\mu k^2/\varepsilon \quad (8)$$

where the constant $c_\mu = 0.09$ in the present study.

The turbulence viscosity influences the (turbulence) heat conduction (heat diffusion) coefficient, K , and the (turbulence) mass diffusion coefficient, D , as follows:

$$K = \rho \nu c_p / Pr \quad (9)$$

$$D = \nu / Sc \quad (10)$$

where ρ is the gas density, $\nu = \nu_o + \nu_t$ is the total viscosity, ν_o ($\ll \nu_t$) the molecular viscosity, c_p the specific heat at constant pressure and Pr and Sc represent the Prandtl and Schmidt numbers, respectively. Consequently, a change in the turbulence viscosity leads to proportional changes in K and D .

It follows that an increase in the mass diffusion leads to an increased mixing between the species, which, in a mixing controlled combustion, leads to an increased rate of heat release and consequently to higher (local) temperatures. In contrast, an increase in the heat conduction coefficient, K , leads to an improved local heat diffusion, and results in a reduction of the local temperatures and hence, counteracts the higher temperatures caused by the increased mixing. Therefore, it is not at all clear that an increased turbulence viscosity leads to higher local temperatures (and, therefore, to higher nitric oxide formations). The net effect of an increased turbulence viscosity will depend on the specific situation at hand. If, for instance, there is another limiting factor for the mixing (e.g., the gas is already fully mixed), then an increase in D will have little effect on the combustion rate and therefore, only the heat diffusion will be increased, which leads to lower local temperatures. On the other hand, if the local heat transport in the reaction zone is dominated by other means than the heat diffusion coefficient (e.g., near a boundary), then an increase in ν_t will primarily result in an increased mixing, hence in an increased heat release and consequently, in higher local temperatures.

The turbulence Reynolds number, $Re_t = qL_I/\nu_o$, depends on the integral length scale L_I which can be expressed in terms of the local variables via Eq. (4) as $L_I \propto \sqrt{\nu_o k/\varepsilon}$. This leads to $Re_t \propto \nu_o^{-1/2} k/\sqrt{\varepsilon}$ and, after identifying $\sqrt{\nu_t} \propto k/\sqrt{\varepsilon}$, using Eq. (8), one obtains

$$Re_t \propto \sqrt{\nu_t/\nu_o}. \quad (11)$$

Note that this expression is different from the one obtained under the assumption of equilibrium turbulence, where $Re_t \propto \nu_t/\nu_o$.

Models

The computations presented in this study have been performed with an enhanced version of the KIVA code [15]. This code is equipped with many new or improved models including the wave atomization and drop breakup model as originally developed for Kelvin-Helmholtz instabilities by Reitz [16], with further modifi-

Table 1 Specifications for the simulated engines

	Lombardini	Caterpillar 3406	Sulzer S20
Bore(mm)×stroke(mm)	86×75	137×165	200×300
Engine speed (rev/min)	1500 (motored)	1600	1000
Inlet valve closure (deg TDC)	-100	-147	-144
Orifices×diameter(mm)	-	6×0.259	12×0.285
Swirl ratio	-	0.67	-
Injection system	-	common rail	conventional
Injection pressure (avg.) (MPa)	-	90	95
Cells at TDC: rad.×azym.×height	30×51×14	24×30×14	23×13×14

cations incorporating the Rayleigh-Taylor instability as reported in Su et al. [17] and Ricart et al. [18]. Additional improvements include the wall heat transfer model of Han and Reitz [19], the Shell ignition model of Halstead et al. [20] as implemented by Kong et al. [21], and the characteristic time combustion model of Abraham et al. [22] as adapted to diesel combustion by Kong et al. [21]. For the low-temperature chemistry ($T < 1000$ K) the chemical reactions are described with the Shell ignition model, whereas for the medium and high-temperature range ($T \geq 1000$ K) the characteristic time combustion model takes effect.

The employed turbulence model is the RNG $k-\varepsilon$ turbulence model as implemented by Han and Reitz [5], together with Eq. (6) which accounts for the nonequilibrium turbulence effects discussed in the previous section. The details of this implementation are given in the next subsection.

Nonequilibrium Turbulence Modeling. A rapid change in the fluid flow leads to an immediate change of the turbulence production (via the mean flow) on the integral end of the turbulence spectrum. The turbulence dissipation, which occurs on the other end of the spectrum, is adjusting to such a flow change with some time delay. As discussed in the previous section, this delay is controlled by the dependence of the turbulence dissipation rate on the turbulence Reynolds number, i.e., $\varepsilon(\text{Re}_t)$, given in Eq. (6).

For equilibrium flow conditions, there are no changes in Re_t and hence, $\varepsilon = \varepsilon_{eq}$. Therefore, if the constant of proportionality in Eq. (6) is chosen to be Re_t from the previous time step, then this equilibrium limit is satisfied. Hence, Eq. (6) can be restated as

$$\varepsilon(t_k) = \text{Re}_t(t_{k-1})\varepsilon_{eq}(t_k)/\text{Re}_t(t_k) \quad (12)$$

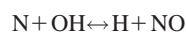
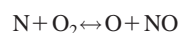
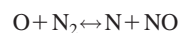
where t_k is the time corresponding to the time step k and t_{k-1} is the time of the preceding time step $k-1$.

Now, the nonequilibrium dissipation rate, $\varepsilon(t_k)$, is computed by simultaneously solving the transport equations for the RNG $k-\varepsilon$ model together with the algebraic relation given in Eq. (12). These equations are solved iteratively in each time step, where $\text{Re}_t(t_k)$ is computed via Eq. (11) using Eq. (8), while $\text{Re}_t(t_{k-1})$ from the previous time step serves as the proportionality constant. The nonequilibrium dissipation rate ε and the turbulent kinetic energy k are thus obtained once the iteration process has converged. These values are then used as initial values for the iteration procedure of the next time step.

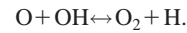
Finally, it should be remarked that if the flow is not subject to accelerations, then there are no changes in the turbulence Reynolds number and, therefore, the model reduces to the standard RNG $k-\varepsilon$ model.

Emission Models. In the following the emission models used in the computations are summarized. Further details can be found in the cited publications.

Nitric Oxide Formation. The nitric oxide formation is modeled with the extended Zeldovich mechanism



together with the equilibrium reaction for the involved hydrogen radicals



As described in [23], the above reactions together with a steady state assumption for nitrogen, N, lead to a single rate equation for the production of NO. More details and the values for the rate constants are documented in [24,25].

Soot Formation. The soot formation is based on the soot production-oxidation model of Hiroyasu et al. [26]. In this model the mass of the resulting soot formation, m_s , is given by

$$\dot{m}_s = \dot{m}_{sp} - \dot{m}_{sO}$$

where \dot{m}_{sp} is the soot production rate and \dot{m}_{sO} the soot oxidation rate. The soot production rate is proportional to the fuel vapor mass, m_{fv} , where the proportionality constant, K_p , is given by an Arrhenius type expression:

$$\dot{m}_{sp} = K_p m_{fv}$$

$$K_p = A_{sp} p^{0.5} \exp(-E_{sp}/RT)$$

A_{sp} and E_{sp} are constants, p is the gas pressure [bar], T denotes the temperature and R is the universal gas constant. Similarly, the soot oxidation rate is proportional to the soot mass and is described by the two equations

$$\dot{m}_{sO} = K_O m_s$$

$$K_O = A_{sO} X_{O_2} p^{1.8} \exp(-E_{sO}/RT) \quad (13)$$

where A_{sO} and E_{sO} are constants, p is the gas pressure and X_{O_2} is the oxygen mole fraction.

The Hiroyasu model has been modified by replacing the Arrhenius global oxidation rate coefficient, K_O , in Eq. (13) with the experimentally based oxidation rate of Nagle et al. [27] given by

$$K_O = \frac{6\dot{W}}{\rho_s D_{nom}}$$

In this equation \dot{W} denotes the soot mass oxidation rate per unit surface area, D_{nom} is a nominal spherical soot particle size, taken to be 25 nm, and the soot density, ρ_s , is taken to be 2.5 g/cm³. Further details about this soot model can be found in [24,25].

Computational and Experimental Details

In this section the computational details and aspects of the experimental setup are summarized. The engine specifications relevant for this study are listed in Table 1.

Experimental Data. The experimental data used for the validation of the ε -correction model have been obtained from a modified single-cylinder Lombardini diesel engine with a bore-stroke ratio of 86 mm to 75 mm and a volumetric compression ratio of 21:1. This engine features a 6 mm off-center cylinder bowl, and it is optically accessible to perform the LDV in-cylinder measurements of the turbulence integral length scales. The measurements

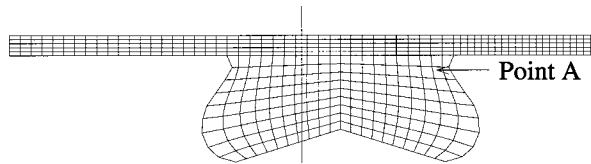


Fig. 1 Cross section at TDC of the experimental Lombardini engine showing the observation point A 5 mm below the cylinder head and 20 mm from the cylinder axis. The 6 mm piston bowl off-set is indicated by the cylinder axis (vertical line).

have been conducted in motored operation at 1500 rpm. Details of the experiments are reported in [14] and a cross section of the engine, indicating the measurement location 5 mm below the cylinder head and 20 mm from the cylinder axis as point A, is shown in Fig. 1.

The CAT engine is a single-cylinder research engine, modified from the production version to accommodate the various measurement devices. This engine has been extensively researched during the past decade and the methods used and the results obtained have been reported in numerous publications (e.g., [25,28–30]).

The experimental data from the S20 engine have been obtained from a nine-cylinder production engine and are reported in [31]. The nitric oxides have been measured by the principle of chemical illumination and then converted into mass specific units. The soot has been determined with a Bosch smoke meter in terms of Bosch smoke units (BSU). In order to permit comparisons with the mass specific units obtained from the simulations, the experimental soot data have been scaled by a factor of 27 to match the simulated values of the standard S20 computations obtained with the RNG k - ε model.

Computational Aspects. Validations of the ε -correction model have been performed with the experimental data obtained from the modified Lombardini diesel engine described above.

The combustion computations have been performed for the CAT and the S20 with the standard RNG k - ε model and with the ε correction, and have been compared with experimental results. The effect of the ε correction has been investigated for the soot and nitric oxide formation for different operating conditions. The CAT simulations have been performed at 75% full load (high load case) and at 25% full load (low load case). The S20 computations have been carried out at 100%, 75%, and 50% of the full load. In addition, different injection timings have been investigated for both engines to illustrate the consistency of the ε correction for the soot- NO_x tradeoff.

For the combustion computations without the ε correction, the coefficient of the turbulence characteristic time, C_M , had to be adjusted in order to match the experimental cylinder peak pressure. These values were found to be $C_M=0.25$ for the CAT and $C_M=2.5$ for the S20. In the corresponding computations with the dissipation correction, these values have been kept at $C_M=2.0$ for both engines.

Results and Discussion

The effect of the ε correction on the cylinder pressure of the CAT and the S20 has already been investigated in [9]. In this study considerable improvements in the performance of the characteristic time combustion model, as well as in the prediction of the turbulence length and time scales, have been obtained. The focus of the present study is the effect of the turbulence dissipation rate correction on the emission predictions of the CAT and the S20.

The problem of sufficient spatial resolution in the simulation of spray-combustion using the discrete droplet model approach, as is the case in this study, has been addressed in a previous paper [8]. In fact, the choice of the mesh resolution has been a compromise between CPU time and accuracy, where the latter has been mea-

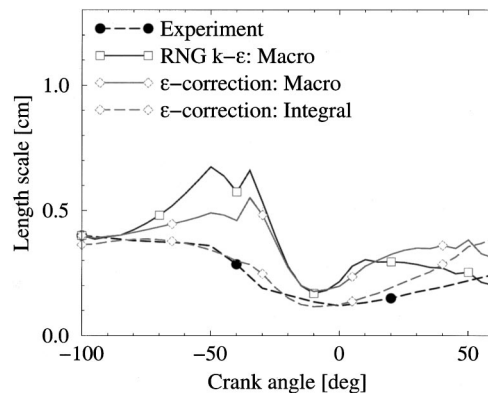


Fig. 2 Measured and computed integral and macro length scales at the observation point A

sured in terms of the relevant quantities under investigation, the average cylinder pressure and the average turbulence time and length scales. It has been found that the mesh resolution employed in these investigations is adequate and therefore, the same mesh resolutions have been used in the present study.

Model Validation. As discussed in the previous section, the ε -correction model has been validated during the compression and expansion phase in a modified single-cylinder Lombardini engine operating in motored mode. Particular attention has been given to the behavior of the integral and macro length scales, L_I and L_ε , respectively. In the compression phase, the mean gas velocity is induced by the piston movement, which results in the formation of a squish flow whose intensity is increasing with decreasing cylinder volume.

Recall that in nonequilibrium flows the integral length scale is assumed to be proportional to the Taylor length scale, and the latter can be computed by means of Eq. (3). Therefore, the integral length scale can be obtained from the Taylor length scale by multiplication of an appropriate proportionality constant. In order to compare the experimental and the computed integral length scales over the entire crank angle interval of interest, this proportionality constant has been determined by matching the computed Taylor length scale to the experimental integral length scale at the beginning of the computation. Its value has been found to be 6.0.

The behavior of the length scales at the observation point A (cf. Fig. 1) are presented in Fig. 2. The integral length scale computed with the ε correction reflects the experimental data very well. This behavior is consistent with the fact that the size of the largest eddies, which are determined by the geometry of the flow, start to decrease in the late compression phase due to the decrease in the cylinder volume. There is no apparent reason for the largest eddy sizes to increase in the compression phase, and therefore, the integral length scale predicted with the ε correction is more realistic than the one obtained by means of the RNG k - ε model, where $L_I \propto L_\varepsilon$.

The macro length scales, obtained with and without the ε correction, are also shown in Fig. 2. Note that for nonequilibrium turbulence, an increase in L_ε during the compression phase can be explained by Eq. (5) in terms of the increase of the turbulence Reynolds number, Re_t , which is illustrated in Fig. 3. In contrast, L_ε computed for equilibrium turbulence is assumed to be proportional to L_I , and since the latter is decreasing in the compression phase (L_I is determined by the geometry of the flow), the macro length scale would have to decrease also in this case.

Note that the length scales in Fig. 2, computed with and without the ε correction, are almost identical at the end of the compression phase. This is not surprising given the fact that the piston speed is almost zero and therefore, the nonequilibrium turbulence effects are minimal.

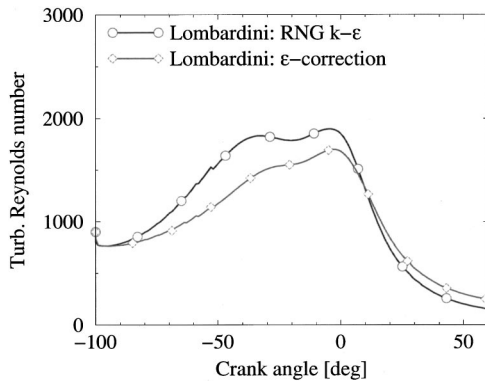


Fig. 3 Turbulence Reynolds number of the Lombardini for computations obtained with and without the dissipation correction

It can be concluded that the prediction of the turbulence length scales in the Lombardini engine is improved with the employed dissipation correction.

Soot and NO_x Formation. The turbulence viscosity, ν_t , for the CAT and the S20, computed with and without the ϵ correction, are shown in Fig. 4. Both engines show the same behavior: In the compression phase the ϵ correction shows a flatter trend in comparison with the standard RNG $k-\epsilon$ model, whereas during the combustion phase, the turbulence viscosity of the ϵ correction shows higher values. By virtue of Eqs. (9) and (10) the transport coefficient for the heat conduction, K , and mass diffusion, D , behave accordingly. Therefore, during the combustion phase an increase of K (relative to the RNG $k-\epsilon$ prediction) leads to an increase in the local heat diffusion, which results in the decrease of the local temperature. On the other hand, the increase in D results in an improved mixing of the fuel and air, which leads to an increase in the reaction rate, hence an increase in the heat release and therefore, results in higher local temperatures. Consequently, these opposing effects on the local temperature tend to neutralize the nitric oxide production, provided the heat conduction or the mass diffusion are not limited by other means. Therefore, the net effect on the nitric oxide formation due to an increased turbulence viscosity will depend on the particular flow.

As is shown in Fig. 5 for the CAT high load case, the ϵ correction results in a higher cylinder temperature throughout the combustion phase, which explains the higher NO_x formation shown in Fig. 6. This suggests that the net effect of the heat and the mass diffusions is dominated by the latter, which results in the higher cylinder temperature. On the other hand, the higher cylinder tem-

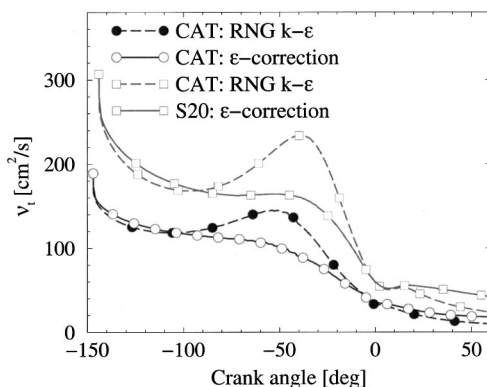


Fig. 4 Turbulence viscosity of the Caterpillar 3406 at high load and the Sulzer S20 at full load for computations obtained with and without the dissipation correction

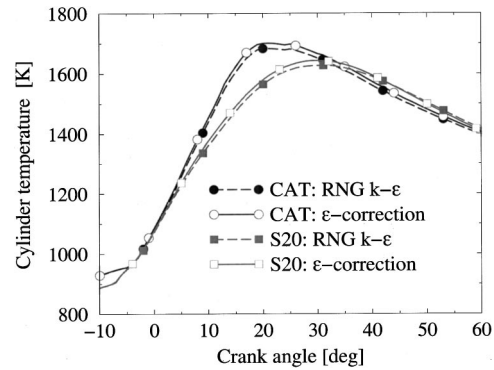


Fig. 5 Cylinder temperature of the Caterpillar 3406 at high load and the Sulzer S20 at full load for computations obtained with and without the dissipation correction

peratures of the CAT lead to an increased soot oxidation which results in a decrease of the net soot production. This behavior is illustrated in Fig. 7.

The S20 at full load shows a different temperature behavior than the CAT, as is seen in Fig. 5. The cylinder temperature of the ϵ correction lies above the one obtained by means of the RNG $k-\epsilon$ model until approximately 40 CA after TDC. After 40 CA the ϵ correction temperature falls below the one computed with the RNG $k-\epsilon$ model. Consequently, because the maximum NO_x level is already reached at 40 CA, the nitric oxide production is slightly

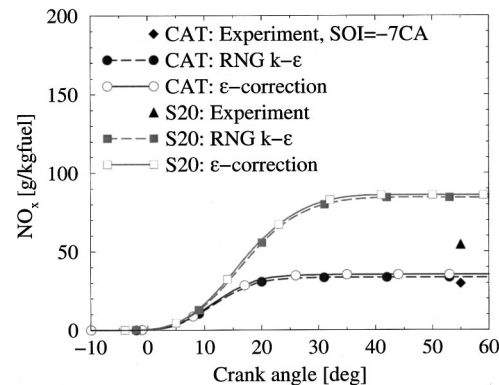


Fig. 6 Nitric oxide of the Caterpillar 3406 at high load and the Sulzer S20 at full load for computations obtained with and without the dissipation correction

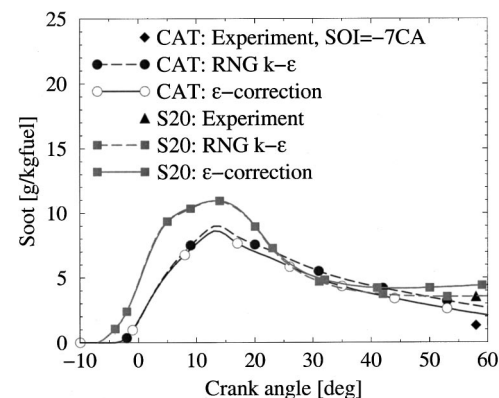


Fig. 7 Soot values of the Caterpillar 3406 at high load and the Sulzer S20 at full load for computations obtained with and without the dissipation correction

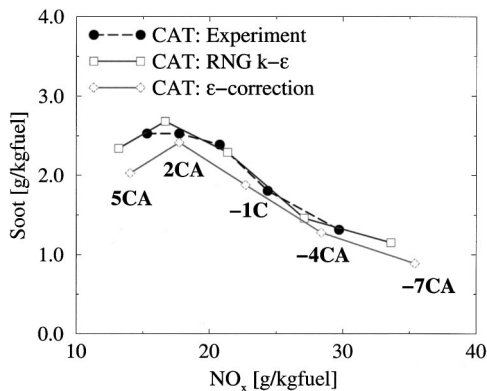


Fig. 8 Soot- NO_x tradeoff of the Caterpillar 3406 at high load for various injection timings. The computational data have been obtained with and without the dissipation correction.

increased, as is illustrated in Fig. 6. The relative decrease in the cylinder temperature of the ϵ -correction after 40 CA results in a decrease of the soot oxidation, hence an increase in the net soot formation, as is seen in Fig. 7.

For the S20, it appears that the counteracting effects on the local temperature by the increased heat conduction and mass diffusion coefficients are approximately in balance, i.e., the NO_x formation is almost unchanged by the combined effects of the increased heat and mass diffusions. After the injected fuel has been burned, an increase in the mass diffusion coefficient cannot increase the local temperature any further (there is no fuel left), while the increase in K continues to enhance the local heat diffusion. Consequently, the hot spots in the cylinder cool down and the soot oxidation is reduced accordingly, which results in the observed higher soot formation. This mechanism also explains the relative drop of the cylinder temperature of the ϵ correction case after 40 CA observed in Fig. 5.

The black dots in Figs. 6–7 are measured values and are shown for reference purposes only. It should be remarked that the pollution models, as utilized in this study, have been tuned to the performance of the RNG k - ϵ model, and therefore, the predictive capability of the ϵ -correction is not reflected by the presented data.

The soot- NO_x tradeoff for the CAT high load and the S20 full load cases for various injection timings are shown in Figs. 8 and 9, respectively. For the CAT, the ϵ correction yields a higher NO_x value and lower soot concentrations in all cases. For the S20, the ϵ correction leads to a lower net soot production for all injection

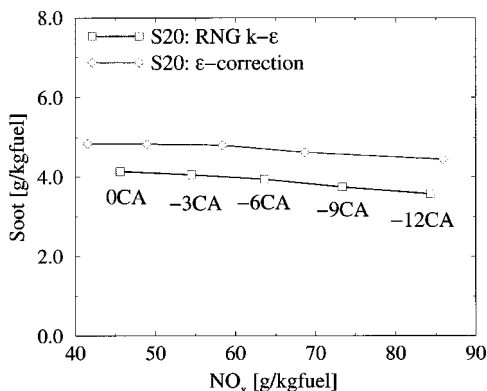


Fig. 9 Soot- NO_x tradeoff of the Sulzer S20 at full load for various injection timings. The computational data have been obtained with and without the dissipation correction.

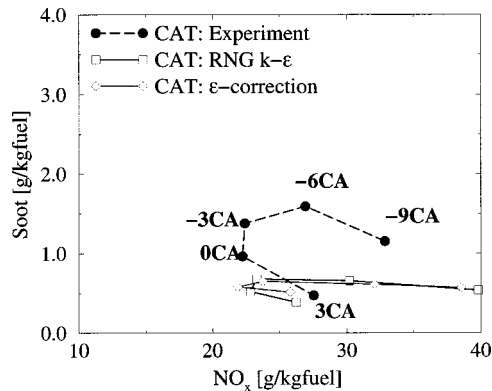


Fig. 10 Soot- NO_x tradeoff of the Caterpillar 3406 at 25% load for various injection timings. The computational data have been obtained with and without the dissipation correction.

timings. Except for the standard case with start of injection at -12.5 CA, the nitric oxide values are slightly decreased in comparison with the RNG k - ϵ computations.

The soot- NO_x tradeoff for the CAT low load is shown in Fig. 10 for various injection timings. Both, the ϵ correction and the RNG k - ϵ model are capable of predicting the horse shoe shape of the experimental soot- NO_x tradeoff curve. The soot and the NO_x predictions are almost identical for all injection timings. This suggests, that the effects of the ϵ correction on the pollution formation via the transport coefficients D and K are neutralized by each other, as has been discussed above.

Finally, the soot- NO_x tradeoff behavior for the S20 at full load and 75% and 50% partial load are shown in Fig. 11. As in the full load cases, the ϵ correction predicts higher soot values and slightly higher NO_x concentrations, which are in better agreement with the experimental data. These improved predictions can again be explained in terms of the opposing effects of the transport coefficients K and D on the local gas temperatures, which, for the S20, are independent of the engine operating condition.

Summary and Conclusions

A correction for the turbulence dissipation rate, based on non-equilibrium turbulence considerations from rapid distortion theory, has been derived and implemented in combination with the RNG k - ϵ turbulence model in a KIVA-based code. In particular, the turbulence dissipation rate has been adjusted via the turbulence Reynolds number by $\epsilon \propto \text{Re}_t^{-1} \epsilon_{eq}$. This model correction has been validated with experimental data in the compression and expansion phase of a small, high-compression engine in motored

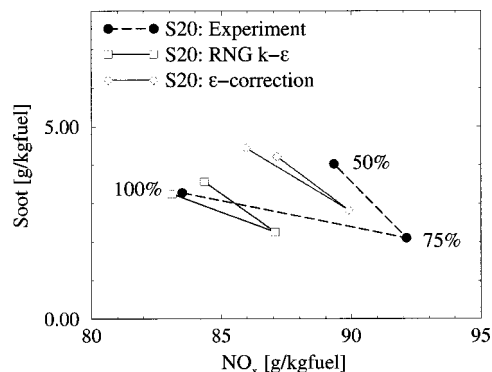


Fig. 11 Soot- NO_x tradeoff of the Sulzer S20 for 100%, 75% and 50% load. The computational data have been obtained with and without the dissipation correction.

mode. The resulting prediction of the integral length scale agreed well with the experimental values, and showed considerable improvements over the integral length scale obtained with the RNG $k-\varepsilon$ model.

Combustion computations have been performed for two heavy-duty DI diesel engines with a focus on the emission prediction capability of the ε correction. In particular, the influence of the ε correction on the transport coefficients for mixing and heat conduction has been studied. The ε correction lead to an improved mixing which resulted in an increased heat release and consequently, in higher local temperatures. Therefore, the production of thermal NO_x has been increased. On the other hand, the ε correction has lead to an increase in the local heat conduction which, in general, lead to a reduction in the local temperatures and thus opposed the nitric oxide formation. The two phenomena can neutralize the NO_x production, as is almost the case for the S20, or, if the limiting process is the local heat transfer, as in the CAT high load cases, the improved mixing can lead to an increased nitric oxide formation.

These observations are consistent with the net soot production of the two engines. The increased mixing in case of the CAT has lead to an increase in the soot oxidation and hence resulted in a reduction in the net soot formation. For the S20, the increased local heat dispersion in the very late combustion phase has lead to a decrease in the local temperature and hence a decrease in the soot oxidation, and finally, has resulted in an increase of the net soot production.

The soot- NO_x tradeoffs for the CAT and the S20 have been qualitatively well reproduced by the ε correction. The increased NO_x and the decreased soot predictions for the CAT have been consistent for the injection timing variations at high load. A corresponding statement holds for the S20 injection timing variations at full load.

For the CAT low load cases, however, the effect of the ε correction is almost not detectable which can be attributed to the opposing effects of the local mass and heat diffusions on the pollution formation. Also, the S20 75% and 50% partial load computations with the ε correction showed the same trend as in the full load cases. Further, a slightly improved soot- NO_x tradeoff behavior has been observed over the ones of the RNG $k-\varepsilon$ computations.

In conclusion, the ε correction results in an improved prediction of the turbulence length scales, and the effect on the transport coefficients yields consistent results with the emission data of the two heavy-duty DI diesel engines.

Acknowledgment

This research has been supported by the NSF grant EIA-9871133, and the DOE/Sandia Collaboratory 2000.

References

- [1] Jones, W., and Launder, B., 1972, "The Prediction of Laminarization With a Two-Equation Model of Turbulence," *Int. J. Heat Mass Transf.*, **15**, pp. 301–314.
- [2] Launder, B. E., and Spalding, D. B., 1974, "The Numerical Computation of Turbulent Flows," *Comput. Methods Appl. Mech. Eng.*, **3**, pp. 269–289.
- [3] Celik, I., 1999, "Overview of Turbulence Modeling for Industrial Applications," ASME Paper No. MAE-IC-99-01 970641.
- [4] Yakhot, V., and Smith, L. M., 1992, "The Renormalization Group, the ε -Expansion and Derivation of Turbulence Models," *J. Sci. Comp.*, **7**, pp. 35–61.
- [5] Han, Z., and Reitz, R., 1995, "Turbulence Modeling of Internal Combustion Engines Using RNG $k-\varepsilon$ Models," *Combust. Sci. Technol.*, **106**, pp. 267–295.
- [6] Bianchi, G., Michelassi, V., and Reitz, R., 1999, "Modeling the Isotropic Turbulence Dissipation in Engine Flows by Using the Linear $k-\varepsilon$ Model," ASME Paper No. 99-ICE-244.
- [7] Coleman, G., and Mansour, N., 1991, "Modeling the Rapid Spherical Compression of Isotropic Turbulence," *Phys. Fluids A*, **3**(9), pp. 2255–2259.
- [8] Tanner, F. X., Zhu, G., and Reitz, R. D., 2001, "Non-Equilibrium Turbulence Considerations for Combustion Processes in the Simulation of DI Diesel Engines," *SAE Trans.*, **109**(3), pp. 707–717.
- [9] Tanner, F. X., Zhu, G., and Reitz, R. D., 2000, "A Non-Equilibrium Turbulence Dissipation Correction of the $k-\varepsilon$ Model Applied to Combustion Simulations of DI Diesel Engines," *Proc. 8th International Conference on Liquid Atomization & Spray Systems*, Pasadena, CA, July.
- [10] Tennekes, H., and Lumley, J. L., 1972, *A First Course in Turbulence*, The MIT Press, Cambridge, MA.
- [11] Wu, C.-T., Ferziger, J., and Chapman, D., 1985, "Simulation and Modeling of Homogeneous Compressed Turbulence," Department of Mechanical Engineering, Technical Report No. TF-21, Stanford University.
- [12] Dinsdale, S., Roughton, A., and Collings, N., 1988, SAE Technical Paper 880380.
- [13] Reynolds, W., 1984, "Physical and Analytical Foundations, Concepts and New Directions in Turbulence Modeling and Simulation," *Proc. Turbulence Models and Their Applications*, 2, EYROLLES, Paris.
- [14] Han, Z., Reitz, R., Corcione, F., and Valentino, G., 1996, "Interpretation of $k-\varepsilon$ Computed Turbulence Length-Scale Predictions for Engine Flows," *Twenty-Sixth Symposium (International) on Combustion*, The Combustion Institute, Pittsburgh, PA, pp. 2717–2723.
- [15] Amsden, A. A., O'Rourke, P. J., and Butler, T. D., 1989, "KIVA II: A Computer Program for Chemically Reactive Flows With Sprays," Tech. Rep. LA-11560-MS, Los Alamos National Laboratory, Albuquerque, NM, May.
- [16] Reitz, R. D., 1987, "Modeling Atomization Processes in High-Pressure Vaporizing Sprays," *Atomisation Spray Technol.*, **3**, pp. 309–337.
- [17] Su, T. F., Patterson, M. A., Reitz, R. D., and Farrell, P. V., 1996, "Experimental and Numerical Studies of High Pressure Multiple Injection Sprays," SAE Technical Paper 960861.
- [18] Ricart, L., Xin, J., Bower, G. R., and Reitz, R. D., 1997, "In-Cylinder Measurement and Modeling of Liquid Fuel Spray Penetration in a Heavy-Duty Diesel Engine," SAE Technical Paper 971591.
- [19] Han, Z., and Reitz, R., 1997, "A Temperature Wall Function Formulation for Variable Density Turbulent Flows With Application to Engine Convective Heat Transfer Modeling," *Int. J. Heat Mass Transf.*, **40**(3), pp. 613–625.
- [20] Halstead, M., Kirsh, L., and Quinn, C., 1977, "The Autoignition of Hydrocarbon Fuels at High Temperatures and Pressures—Fitting of a Mathematical Model," *Combust. Flame*, **30**, pp. 45–319.
- [21] Kong, S.-C., Han, Z., and Reitz, R. D., 1995, "The Development and Application of a Diesel Ignition and Combustion Model for Multidimensional Engine Simulation," SAE Technical Paper 950278.
- [22] Abraham, J., Bracco, F., and Reitz, R., 1985, "Comparisons of Computed and Measured Premixed Charge Engine Combustion," *Combust. Flame*, **60**, pp. 309–322.
- [23] Heywood, J. B., 1988, *Internal Combustion Engine Fundamentals*, McGraw-Hill, New York.
- [24] Han, Z., Uludogan, A., Hampson, G., and Reitz, R., 1996, "Mechanism of Soot and NO_x Emission Reduction Using Multiple-Injection in a Diesel Engine," SAE Technical Paper 960633.
- [25] Patterson, M., Kong, S.-C., G. J., H., and Reitz, R., 1994, "Modeling the Effects of Fuel Injection Characteristics on Diesel Engine Soot and NO_x Emissions," SAE Technical Paper 940523.
- [26] Hiroyasu, H. and Nishida, K., 1998, "Simplified Three-Dimensional Modeling of Mixture Formation and Combustion in a D.I. Diesel Engine," SAE Technical Paper 890269.
- [27] Nagle, J., and Strickland-Constable, R., 1962, "Oxidation of Carbon between 1000–2000 C," *Proceedings of the Fifth Carbon Conference*, **1**, Pergamon Press, Tarrytown, NY, p. 154.
- [28] Nehmer, D., and Reitz, R., 1994, "Measurement of the Effect of the Injection Rate and Split Injections on Diesel Engine Soot and NO_x Emissions," SAE Technical Paper 940668.
- [29] Patterson, M., and Reitz, R., 1998, "Modeling the Effects of Fuel Spray Characteristics on Diesel Engine Combustion and Emission," SAE Technical Paper 980131.
- [30] Pierpont, D., Montgomery, D., and Reitz, R., 1995, "Reducing Particulate and NO_x Using Multiple Injections and EGR in a D.I. Diesel," SAE Technical Paper 950217.
- [31] Stebler, H., 1998, "Luft- und brennstoffseitige Massnahmen zur internen NO_x -Reduktion von schnelllaufenden direkteinge-spritzten Diesel Motoren," Ph.D. thesis, Swiss Federal Institute of Technology (ETH), Diss. ETH Nr. 12954.

Response Surface Method Optimization of a High-Speed Direct-Injection Diesel Engine Equipped With a Common Rail Injection System

T. Lee

R. D. Reitz

Engine Research Center,
Department of Mechanical Engineering,
University of Wisconsin-Madison,
1500 Engineering Drive,
Madison, WI 53706

To overcome the tradeoff between NO_x and particulate emissions for future diesel vehicles and engines it is necessary to seek methods to lower pollutant emissions. The desired simultaneous improvement in fuel efficiency for future DI diesels is also a difficult challenge due to the combustion modifications that will be required to meet the exhaust emission mandates. This study demonstrates the emission reduction capability of EGR and other parameters on a high-speed direct-injection (HSDI) diesel engine equipped with a common rail injection system using an RSM optimization method. Engine testing was done at 1757 rev/min, 45% load. The variables used in the optimization process included injection pressure, boost pressure, injection timing, and EGR rate. RSM optimization led engine operating parameters to reach a low-temperature and premixed combustion regime called the MK combustion region, and resulted in simultaneous reductions in NO_x and particulate emissions without sacrificing fuel efficiency. It was shown that RSM optimization is an effective and powerful tool for realizing the full advantages of the combined effects of combustion control techniques by optimizing their parameters. It was also shown that through a close observation of optimization processes, a more thorough understanding of HSDI diesel combustion can be provided.

[DOI: 10.1115/1.1559900]

Introduction

The direct injection (DI) diesel engine is a prime candidate for future transportation needs because of the increasing threat of limited oil resources and global warming due to CO₂ emissions. On the other hand, DI diesel engines emit more particulate and NO_x emissions than their gasoline counterparts. Many countries are focusing their regulatory efforts on reducing emissions of fine particles and ozone precursors (NO_x and hydrocarbons) from all sources, including diesel vehicles due to their possible adverse effects on health and the environment, [1]. Therefore, DI diesel engines will be strongly challenged by the emission standards expected in the 2004–2005 period, such as the Tier II/ULEV and EC Stage IV.

It is well known that due to the NO_x and particulate tradeoff relation it is difficult to reduce these two pollutants simultaneously. Therefore, researchers have been studying the combined effects of high pressure injections, boost pressure, multiple injections, and EGR to reduce particulate and NO_x emissions at the same time. Without EGR, Tanin et al. [2] found an increase in premixed burn fraction and an increase in NO_x emissions with high injection pressure. But with EGR, Montgomery [3] could decrease the premixed burn fraction and NO_x levels with high injection pressure. Also, he achieved a 30% reduction in particulate emissions using multiple injections with a 20% EGR rate, even though EGR is often thought to have a detrimental effect on particulate emissions.

However, it has been found that careful optimization of the operating conditions is required in order to get the full benefit of

the combined effects. Tow et al. [4] pointed out that the dwell between injection in split injections was very important to control soot production and there would exist an optimal dwell at a particular engine operating condition. Pierpont et al. [5] examined the combined effects of EGR and multiple injections. They found significant reductions in both NO_x and particulate emissions when EGR was used in combination with optimized double and triple injections with only a slight increase in BSFC. Tanin et al. [2] studied boost pressure effects in a single-cylinder version of a heavy-duty diesel engine. They found that particulate emissions decreased significantly with increased boost pressure when injection timing was adjusted to keep brake-specific NO_x emissions constant. They also assert that there is an optimum combination of injection pressure and boost pressure.

Realizing the importance and necessity of optimization, it is essential to have an efficient tool for finding optimized operating parameters of diesel engines with multiple injection, EGR, and flexible boosting capabilities. Montgomery [3] applied an RSM (response surface method) to the optimization of operating parameters for a heavy-duty diesel engine, and demonstrated that RSM optimization could be an effective and efficient method for optimizing engine operating parameters. Under 80 individual engine experiments were required to identify an optimum calibration of six independent variables at one engine operating condition.

Experimental Setup

The test engine is a single-cylinder HSDI diesel engine. The engine is capable of producing 21 kW at a rated speed of 4200 rev/min. The block is a Hydra from Ricardo Research. The cylinder head, piston, and other important engine parts were manufactured by FIAT. Table 1 shows the engine specifications, and the engine laboratory setup used in the present experiments is shown

Contributed by the Internal Combustion Engine Division of THE AMERICAN SOCIETY OF MECHANICAL ENGINEERS for publication in the ASME JOURNAL OF ENGINEERING FOR GAS TURBINES AND POWER. Manuscript received by the ICE Division, November 2001; final revision received by the ASME Headquarters, April 2002. Editor: D. N. Assanis.

Table 1 Engine specifications

Engine Type	Single cylinder diesel Direct injection Four valves Ricardo Hydra block
Bore x Stroke	82.0 x 90.4 mm
Compression Ratio	18.79:1
Displacement	477 cm ³
Squish Clearance Volume	26.84 cm ³
Piston Type	Reentrant bowl
Intake Ports	1 Helical shaped 1 Directed shaped
Intake Valve Opening	10° BTDC
Intake Valve Closing	38° ABDC
Exhaust Valve Opening	38° BTDC
Exhaust Valve Closing	8.5° ATDC

schematically in Fig. 1. Simulated turbocharging with intercooling is accomplished by metering compressed air into a temperature controlled intake surge tank and controlling back pressure in the exhaust surge tank. EGR is accomplished by a direct link between exhaust and intake surge tanks. Back pressure in the exhaust surge tank is raised above the intake pressure to get exhaust gas to flow into the intake surge tank when EGR is desired. In order to damp out pressure fluctuations and mix EGR with the fresh intake air, two ten-gallon pressure tanks were used as the intake and exhaust surge tanks.

The emission data recorded during the experiments included NO_x, CO, CO₂, THC, and smoke. NO_x and CO were measured with a Nicolet Rega model 7000, FTIR emissions analyzer. The samples were taken from the exhaust surge tank and run to the FTIR analyzer by a heated line after passing through a heated filter. With the use of the heated filter and line, the sample was kept above 170°C to help prevent any emissions species from condensing. Exhaust smoke levels were sampled with a Bosch model RTT100 smoke opacimeter. Note that the Bosch Smoke Opacimeter measures the visual opacity and absorption coefficient that can be converted into mass concentration through the use of the internal conversion table. This mass concentration specifies

the amount of particulate matter with units of mg/m³, is presented as PM (particulate matter) level in this paper by being converted into units of g/kW-hr. THC was measured with a flame ionization detector (FID), and CO₂ was detected with the use of a Horiba PIR-9000 infrared gas analyzer.

The fuel used during the present testing was #2 diesel obtained from a commercial fuel vendor. The cetane number of the fuel was 44.1. The injection system used for this study was a prototype Fiat/Bosch common-rail injection system. The system is capable of injection pressures up to 135 MPa. The injector used in the experiments was an electro-hydraulically controlled unit injector. The common-rail injection system specifications are summarized in Table 2.

A PC-based data acquisition system was used to take cylinder pressure averaged over 25 cycles at 1/2 crank angle degree increments. Cylinder pressure data, along with other engine operating parameters, were then analyzed to calculate the apparent heat release rate using the First Law of Thermodynamics.

Response Surface Method

The response surface method is a collection of mathematical and statistical techniques that are useful for modeling and analysis of problems in which a response of interest is influenced by several factors and the objective is to optimize this response, [6]. RSM uses experimental designs to identify important factors by characterizing the response surface by a polynomial model. Once the important factors are identified, the model is used to indicate the direction of future exploration for the likely optimum, [7]. The relationship between the response variable Y and the factors X_1, X_2, \dots, X_k in RSM applications is generally expressed as, [7],

$$Y = f(X_1, X_2, \dots, X_k) + \epsilon \tag{1}$$

where ϵ is the noise or error observed in the response Y .

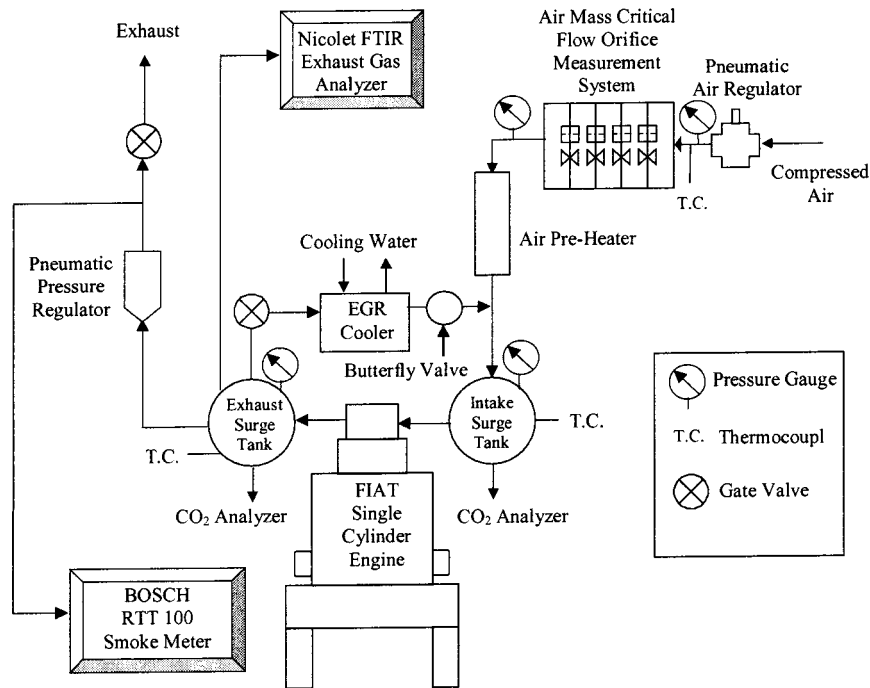


Fig. 1 Engine laboratory setup

Table 2 Common-rail system specifications

Injector Type	Electro-hydraulically controlled injector
Injection Pressure	Electronically set 135 MPa maximum
Nozzle Type	Dual guided VCO nozzle
Number of Nozzle Holes	6
Hole Diameter	160 μm
Hole L/D Ratio	6.25
Included Spray Angle	145°

Table 3 Control factors for optimization starting point

Injection Pressure [MPa]	100 ± 10
Boost Pressure [kPa]	152.4 ± 2.8
SOI [CA° ATDC]	-2 ± 1
Intake CO ₂ [%]	0.5 ± 0.3

f is the response surface.

The function f in expression (1) corresponds to the relationship between a response variable and the factors which is generally unknown. Thus, the first step in RSM is to find a suitable approximation of f . The simplest approximating function describing the relation between a response variable and the factors is the linear model.

$$Y = \beta_0 + \sum_{i=1}^k \beta_i X_i + \varepsilon \quad (2)$$

It is known that the linear response surface model is not always adequate because a few factors might interact with each other, [8]. This is handled in the model by adding terms consisting of the product of the interacting factors to the linear model given in expression (2).

Orthogonal designs associated with fitting linear response surface models include two-level factorial designs and two-level fractional factorial designs. Two-level factorial designs are generally used to study the effect of k factors on a response, each factor set at two levels usually denoted as “low” and “high.” Factorial designs allow an experimenter to evaluate not only effects of factors, but also any interaction effects between factors. Each level of every factor is tested with each level of every other factor resulting in all 2^k treatment combinations being tested. Therefore, the number of experimental runs for two-level factorial designs can become impractical when the number of factors is large. However, if certain assumptions can be met, the use of fractional factorials is the most efficient technique to reduce the number of observations and still obtain the desired information. For example, for a six-factor experiment, the full 2^6 factorial experiment requires 64 runs, but a 2^{6-2} fractional factorial experiment (resolution IV design) requires only 16 runs. With this resolution IV design, main effects still can be estimated separately, but two-factor interactions may not be estimable independently. A resolution III design can be used when only main effects are of interest.

At the center point, all the factors have a value that is the average of the high and low values used in the factorial experiments. The replication of the center points gives an independent estimate of the standard deviation of the experimental results that can be used in an analysis of variance to evaluate the probability (P) that the effects of the factors and interactions are caused by experimental error. Also, if the experiments must be conducted on different days (a blocked experiment), a center point is run at the beginning and end of each block so that block effects can be evaluated, [9].

The purpose of using RSM techniques here was to rapidly and efficiently reach the vicinity of the optimum. Therefore, the sim-

plest form of the model, i.e., the linear model was used. Also any interaction between factors was assumed to be negligible, and only main effects were considered.

Results of Response Surface Optimization

To use RSM as an optimization tool, a mathematical statement of goal must be defined in the form of an objective function. Montgomery [3] suggested an efficient objective function as follows:

$$f(X) = \text{Merit} = \frac{1000}{\left(\frac{\text{NO}_x}{\text{NO}_{x_t}}\right)^2 + \left(\frac{\text{PM}}{\text{PM}_t}\right)^2 + \frac{\text{BSFC}}{\text{BSFC}_t}} \quad (3)$$

where

$X = \{x_1, x_2, \dots, x_k\}$ array of factors (SOI, boost pressure, etc.),

NO_x and PM = are the measured emission levels,

BSFC is = the fuel consumption,

NO_{x_t} and PM_t = are the target emission levels, and

BSFC_t is = the target fuel consumption.

This function has been shown to be useful in engine optimization studies, [3,10]. With the power constants for NO_x and PM being greater than that for BSFC , Eq. (3) says that emission targets have a higher priority. But, if the target levels for emissions are reached, a decrease in BSFC will be more attractive than a further decrease in emissions. The target emissions for NO_x and PM were chosen as 0.79 and 0.32 g/kW-hr, respectively. Wickman et al. [10] derived these specific emissions targets from the EPA tier II 2004 automotive diesel mandates using the vehicle road power requirements and an assumption of 40% brake thermal efficiency (approximately 60 miles/gallon diesel fuel). The target BSFC is taken as 210 g/kW-hr (i.e., 40% brake thermal efficiency).

Engine testing was done at 1757 rev/min, 45% load. This speed was used because engine parameters were available from the manufacturer. The temperature of the intake surge tank was kept at 40°C. EGR was cooled by a water-cooled heat exchanger. EGR rates were controlled by varying the position of a butterfly valve which was located between the EGR cooler and the intake surge tank.

Table 3 shows the factor levels for the first factorial experiment. The values given after the \pm symbol indicate the deviation from the centerpoints that were used to define two levels, “high” and “low.” The factors used in the optimization process included injection pressure, boost pressure, SOI, and EGR rate. EGR rates are expressed using the following equation:

$$\% \text{ EGR} = \frac{\% \text{ CO}_2(\text{intake}) - \% \text{ CO}_2(\text{ambient})}{\% \text{ CO}_2(\text{exhaust}) - \% \text{ CO}_2(\text{ambient})} \times 100. \quad (4)$$

It should be noted that CO_2 percentage of the intake surge tank was chosen as a control factor for convenience instead of using EGR rate directly. But the final results are presented in terms of EGR rate.

The first experiment was conducted by using a 2^{4-1} fractional factorial design in two blocks (two days), which is a resolution III design. The centerpoint was run at the beginning and end of block, and this resulted in a total of 12 runs. Also, to protect against drift, the noncenter point experiments were randomized within the block. Table 4 shows the coefficients for the linear response surface model fit to the data gathered from the first factorial experiment. Since the response surface model is a linear equation, the gradient is the direction of the steepest ascent indicated by a movement of each factor in a step proportional to that factor’s coefficient. The P values in Table 4 indicate the probability that the observed difference could have occurred by chance alone. Therefore, the numerically high (approaching 1.0, the maximum)

Table 4 Coefficients and P values for the first two-level fractional factorial and results for optimization starting point

Term	Coefficient	P
Constant	36.25	
Injection Pressure	-2.25	0.276
Boost Pressure	1.75	0.184
SOI	9.00	0.006
Intake CO ₂	7.00	0.013
Averaged Center Point Emissions, BSFC, and Merit Value		
NO _x [g/kW-h]	4.07	
PM [g/kW-h]	0.327	
BSFC [g/kW-h]	266	
Merit	35	

Table 5 Control factors for second two-level fractional factorial experiment

Injection Pressure [MPa]	89 ± 10
Boost Pressure [kPa]	154.4 ± 2.8
SOI [CA° ATDC]	-1 ± 1
Intake CO ₂ [%]	1.5 ± 0.3

Table 6 Coefficients and P values for the second two-level fractional factorial and results for the center point

Term	Coefficient	P
Constant	111.25	
Injection Pressure	3.50	0.492
Boost Pressure	5.50	0.307
SOI	12.00	0.075
Intake CO ₂	13.00	0.063
Averaged Center Point Emissions, BSFC, and Merit Value		
NO _x [g/kW-h]	1.74	
PM [g/kW-h]	0.450	
BSFC [g/kW-h]	265	
Merit	123	

Table 7 Control factors for third two-level fractional factorial experiment

Injection Pressure [MPa]	90 ± 5
Boost Pressure [kPa]	155.1 ± 2.8
SOI [CA° ATDC]	-1 ± 1
Intake CO ₂ [%]	2.2 ± 0.2

P values mean that the corresponding factors are not significant. In this study, any factor effect that has a P value bigger than 0.25 was assumed to be negligible.

The NO_x level at the center point in the first factorial experiment given in Table 4 is over five times bigger than the target value, while PM level nearly meets the target. Therefore, it is expected that the RSM should focus on improving NO_x emission, and the coefficients in Table 4 are consistent with the strategies for a reduction in NO_x, those corresponding to increasing EGR rate, retarding injection timing, and decreasing injection pressure.

The first ascent experiment was conducted along the steepest ascent indicated by the gradient of the linear response surface model established with the first factorial experiment results until a maximum merit value was found. The maximum merit point determined in the first ascent experiment was used as the center point for the second factorial experiment set. The second factorial experiment was conducted at this point specified in Table 5 and the results are given in Table 6.

The NO_x level at the center point in the second factorial experiment is still over twice the target value, even though it was reduced by 57% through the first ascent experiment. Therefore, intake CO₂ and SOI are still the most active factors, and it indicates

Table 8 Coefficients and P values for the third two-level fractional factorial and the results for the center point

Term	Coefficient	P
Constant	155.75	
Injection Pressure	9.75	0.528
Boost Pressure	2.30	0.880
SOI	40.80	0.059
Intake CO ₂	11.75	0.454
Averaged Center Point Emissions, BSFC, and Merit Value		
NO _x [g/kW-h]	1.09	
PM [g/kW-h]	0.774	
BSFC [g/kW-h]	264	
Merit	114	

that further increase in EGR rate and retarding injection timing are required to reduce the still unacceptable NO_x level.

The second ascent experiment was conducted according to the coefficient values given in Table 6. Injection pressure and boost pressure were not varied in the second ascent experiment, because their high P values indicated that they were not significant factors anymore.

The second ascent experiment gave the center point of the third factorial experiment in Table 7. The third factorial experiment was conducted, and the results are given in Table 8. As can be seen in Table 8, the NO_x level was reduced by 73% through the two sets of ascent experiments, and the NO_x level exceeds the target value by 38%. But the PM level was increased due to the increased EGR rate and retarded injection timing, which ended up at over twice the target level. Therefore, it is expected that the strategy of the third ascent experiment should be different from those of the previous two ascent experiments in order to concentrate on a reduction in PM emissions. Surprisingly, the results of the third factorial experiment shown in Table 8 indicated that SOI was only the active factor, and that the injection timing should be retarded.

The third ascent experiment consisted of 4 steps. Since all factors were not active except SOI, only SOI was varied by a step size of 0.5 CA degree. Each step was measured twice and 8 runs were randomized. The results of the third ascent experiment are shown in Fig. 2. Figure 2 shows that gradually retarding the injection timing dramatically improved PM emissions. In order to verify the optimum, a fourth factorial experiment should have been conducted by using the point of step 4 in the third ascent experiment as a center point. However, since further retardation of injection timing was found to deteriorate the engine stability significantly with misfire, the fourth factorial experiment could not

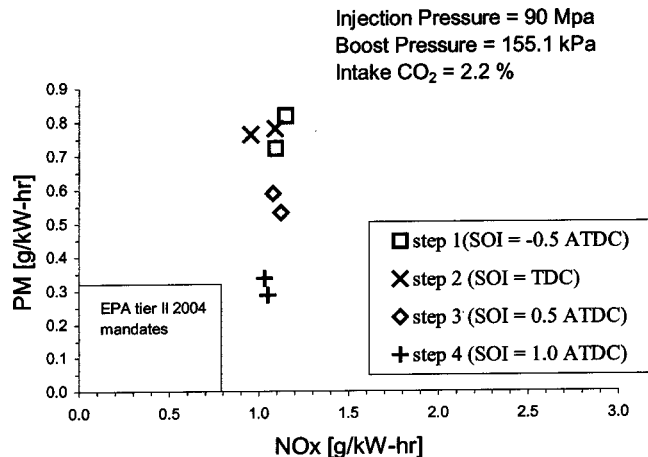


Fig. 2 PM versus NO_x results from the third ascent experiment

Table 9 The results of the RSM optimization

Operating Parameters	Starting point	Optimized
Injection Pressure [MPa]	100	90
Boost Pressure [kPa]	152.4	155.1
SOI [CA° ATDC]	-2.0	1.0
EGR rate [%]	4.4	21.4
NO _x [g/kW-hr]	4.07	1.04
PM [g/kW-hr]	0.327	0.313
BSFC [g/kW-hr]	266	274
Merit	35	250

be accomplished. Therefore, the best point in the third ascent experiment, i.e., step 4 was declared to be the final optimized point at this engine operating condition.

Table 9 shows the operating parameters, emission levels, and BSFC for the optimization start point and the optimized point. NO_x emissions were reduced by 74%, and even with heavy EGR and retarded injection timing, it was possible to keep PM emissions and BSFC at nearly the same levels. As can be seen in Fig. 2, NO_x emission still needs to be reduced in order to meet the target, but the PM emission is consistent with EPA tier II 2004 mandates.

As the optimized point was approached during the optimization process, more concern about total hydrocarbon emissions (THC) was necessary because of the increased EGR rate and the retarded injection timings. Also, CO was carefully monitored. At the optimized operating conditions CO and THC emissions were 4.79 and 0.21 g/kW-hr, respectively. These levels are within the EPA tier II 2004 automotive diesel mandates (6.72 g/kW-hr CO and 0.49 g/kW-hr THC) that can be obtained by using the same assumptions as those of the NO_x and PM target level calculations.

It is interesting to compare the combustion characteristics of the optimized point and the optimization start point. Figure 3 shows the cylinder pressure, rate of injection, and heat release of the optimization start point. The heat release rate of the optimization start point shows an ordinary two-stage profile, a premixed burn fraction followed by a diffusion burn. Figure 4 shows the cylinder pressure, rate of injection, and heat release of the optimized point. The heat release rate curve shows a single stage of entirely premixed combustion with gradual heat release in the initial combustion period, which characterizes the heat release rate of so-called modulated kinetics (MK) combustion, [11]. At the optimized point, almost all the fuel was injected prior to ignition as can be seen in Fig. 4. And this long ignition delay is due mainly to the retarded injection timing and makes it possible for the fuel and air to be mixed more thoroughly. This results in avoiding diffusion

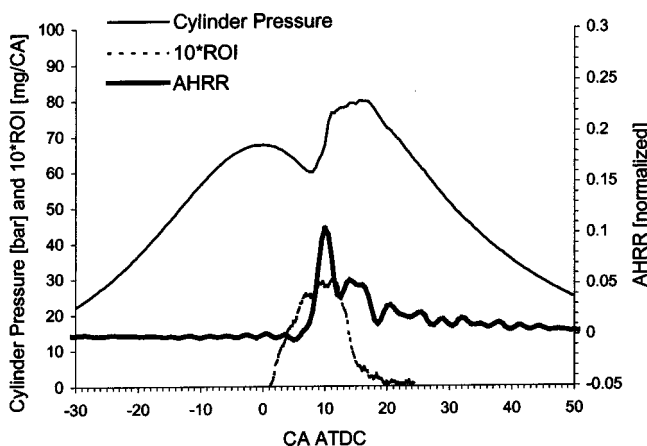


Fig. 3 Combustion data for the start point

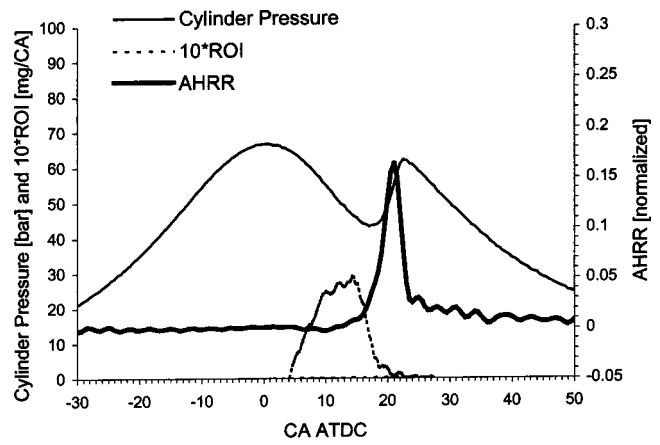


Fig. 4 Combustion data for the optimized point

burn, which explains the decrease in PM emissions seen by retarding the injection timing during the third ascent experiment.

The present impressive results could be achieved since the RSM optimization led the engine operating parameters to reach overall lean, low-temperature and premixed combustion characteristics, i.e., the MK combustion region. But, the RSM optimization found independently by exploiting the modern combustion control techniques provided in this study, such as cooled EGR and the common rail injection system. Kimura et al. [11] applied MK combustion to a high-load condition by using EGR gas cooling and high pressure injections. In the high load region, it is difficult to achieve MK combustion because of the shortened ignition delay due to the higher EGR gas temperature and the prolonged injection duration due to the increased fuel quantity. Thus, they used an EGR gas cooler to prolong the ignition delay and a common rail injection system to shorten the injection duration in the high load range. It should be noted that the engine running condition in this study was 1757 RPM, 45% load, which also corresponds to a high load region in their study.

Summary and Conclusions

A response surface optimization was performed to demonstrate the emission reduction capability of EGR on a HSDI diesel engine equipped with a common rail injection system. The factors used in the optimization process included injection pressure, boost pressure, SOI, and EGR rate. Engine testing was done at 1757 rev/min, 45% load. The RSM optimization led optimum operating

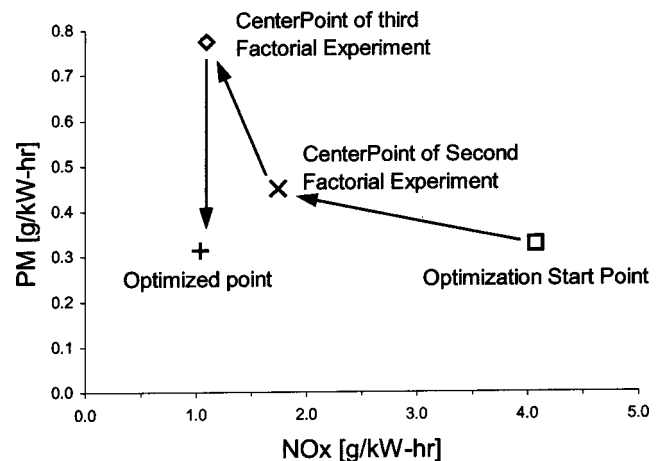


Fig. 5 PM versus NO_x emissions during RSM optimization

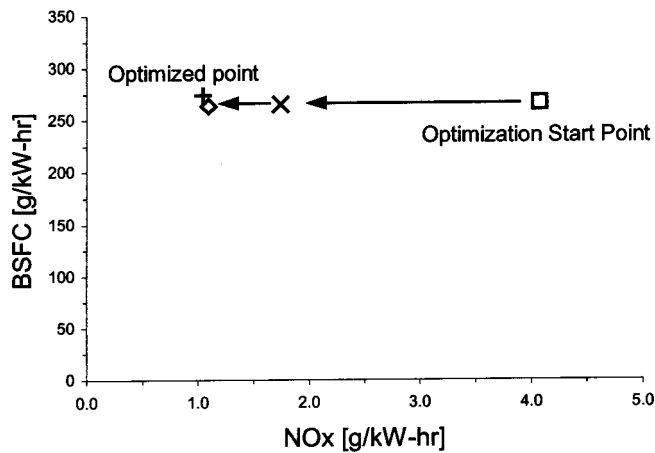


Fig. 6 BSFC versus NO_x emissions during RSM optimization

parameters to low-temperature and premixed combustion characteristics, i.e., the MK combustion region, resulting in simultaneous reductions in NO_x and PM emissions without sacrificing BSFC.

The emissions and fuel consumption improvements achieved during the optimization process are summarized in Figs. 5 and 6. The optimization proceeded by mainly increasing the EGR rate and retarding the injection timing until the center point of third factorial experiment was reached. Heavy use of EGR in the optimum scheme is responsible for the significant reduction in NO_x emissions. Also, decreased injection pressure and retarded injection timing helped the NO_x emission decrease further. However, following this path caused an increase in PM, while retaining BSFC. This exciting result of noncompromised BSFC might be attributed to the effect of cooling loss reduction, since heat loss to the cylinder walls would be reduced by the significantly decreased burned gas temperature with increased EGR, [12]. The third ascent progressed with a further retardation of the injection timing. Long ignition delays could be achieved with the retarded injection timing during the third ascent experiment, and produced the conditions for MK combustion, and resulted in 60% reduction in PM emissions with only a slight increase in BSFC.

It can be concluded that RSM optimization is an effective and powerful tool for realizing the full advantages of the combined effects of combustion control techniques by optimizing their parameters. It was also shown that through a close observation of optimization processes, a more thorough understanding of HSDI diesel combustion can be provided.

Acknowledgments

The authors thank the Ford Research Center in Aachen—Germany (FFA), and DOE/Sandia National laboratories for supporting this work. The authors also thank Hanho Yun for his assistance with data collection and all the other individuals at the University of Wisconsin-Madison Engine Research Center who were involved in making this work possible.

Nomenclature

AHRR = apparent heat release rate
 ATDC = after top dead center
 BSFC = brake specific fuel consumption
 CA = crank angle
 EGR = exhaust gas recirculation
 ROI = rate of injection
 THC = total hydrocarbons

References

- [1] Walsh, M. P., 1998, "Global Trends in Diesel Emissions Control—A 1998 Update," SAE Paper No. 980186.
- [2] Tanin, K. V., Wickman, D. D., Montgomery, D. T., Das, S., and Reitz, R. D., 1999, "The Influence of Boost Pressure on Emissions and Fuel Consumption of a Heavy-Duty Single-Cylinder D.I. Diesel Engine," SAE Paper No. 1999-01-0840.
- [3] Montgomery, David T., 2000, "An Investigation into Optimization of Heavy-Duty Diesel Engine Operating Parameters When Using Multiple Injections and EGR," Ph.D. thesis, University of Wisconsin-Madison.
- [4] Tow, T. C., Pierpont, A. and Reitz, R. D., 1994, "Reducing Particulates and NOx Emissions by Using Multiple Injections in a Heavy Duty D.I. Diesel Engine," SAE Paper No. 940897.
- [5] Pierpont, D. A., Montgomery, D. T., and Reitz, R. D., 1995, "Reducing Particulate and NOx Using Multiple Injections and EGR in a D.I. Diesel," SAE Paper 950217.
- [6] Montgomery, Douglas C., 1991, *Design and Analysis of Experiments*, John Wiley and Sons, New York.
- [7] Gardiner, W. P., and Gettinby, G., 1998, *Experimental Design Techniques in Statistical Practice*, Horwood Publishing.
- [8] Lorenzen, Thomas J., and Anderson, Virgil L., 1993, *Design of Experiments: A No-Name Approach*, Marcel Dekker, New York.
- [9] Box, G. E. P., Hunter, W. G., and Hunter, J. S., 1978, *Statistics for Experimenters*, John Wiley and Sons, New York.
- [10] Wickman, D. D., Senecal, O. K., and Reitz, R. D., 2001, "Diesel Engine Combustion Chamber Geometry Optimization Using Genetic Algorithms and Multi-Dimensional Spray and Combustion Modeling," SAE Paper No. 2001-01-0547.
- [11] Kimura, Shuji, et al., 1999, "New Combustion Concept for Ultra-Clean and High-Efficiency Small DI Diesel Engines," SAE Paper No. 1999-01-3681.
- [12] Heywood, J. B., 1988, *Internal Combustion Engine Fundamentals*, McGraw-Hill, New York.

Dynamic Response of Automotive Catalytic Converters to Variations in Air-Fuel Ratio

T. Shamim

V. C. Medisetty

Department of Mechanical Engineering,
The University of Michigan,
Dearborn, MI 48128-1491

The automotive catalytic converters, which are employed to reduce engine exhaust emissions, operate in transient conditions under all modes of operation. The fluctuation in air-fuel ratio is a major contributor to these transients. The consideration of these transients is essential in accurate modeling of catalyst operation during actual driving conditions. In this work, a numerical investigation is carried out to comprehend the dynamic response of three-way catalytic converters subjected to changes in air-fuel ratio. The mathematical model considers the coupling effect of heat and mass transfer with the catalyst reactions as exhaust gases flow through the catalyst. The converter dynamic response is studied by considering a converter operating under steady conditions, which is suddenly subjected to air-fuel ratio variations. Two types of imposed fluctuations (sinusoidal and step changes) are considered. The catalyst response is predicted by using a detailed chemical mechanism. The paper elucidates the effect of air-fuel modulations on the catalyst HC, CO, and NO conversion efficiencies. [DOI: 10.1115/1.1564065]

Introduction

Catalytic converters are employed to reduce engine exhaust emissions, and are an integral component of engine emission control systems. A three-way catalytic converter is designed to simultaneously convert carbon monoxide (CO), hydrocarbon (HC), and oxides of nitrogen (NO_x). The efficient operation of three-way catalysts requires that they be operated at or very near a stoichiometric air-fuel ratio (A/F). This is ensured by employing a closed-loop control fuel supply system. However, the control system's response lag causes the A/F to oscillate around the stoichiometric value. In addition to these fast oscillations, which have frequencies of 0.5 to 4 Hz, the catalysts are subjected to several slow fluctuations during a typical driving cycle, [1]. These slower changes, which have frequencies of 1 Hz and less, occur as a result of acceleration and deceleration, and cause fluctuations in gas flow rates, temperatures, and compositions. The influence of these dynamic conditions makes the catalyst behavior differ significantly from that under steady-state conditions, [1–5].

Due to its practical importance, many previous studies, [1–10], investigated the influence of fluctuating A/F on the catalyst behavior. In many studies, the enhancement of conversion due to fluctuating A/F is attributed to the washcoat oxygen storage capacity. However, Schlatter and Mitchell [11] explained the enhancement of CO conversion on the basis of temporarily increased activity of the water-gas shift reaction. They obtained the CO conversion enhancement by varying feed gas composition in cycled and step changes. The enhancement of catalyst's activity or selectivity has been reported in many other studies, [12–14]. Herz [2] showed the evidence that A/F influences the oxygen content of a base metal-containing three-way catalysts. The magnitude and rates of change of oxygen content measured after abrupt changes in A/F were sufficiently large to affect the performance of the catalyst under dynamic operating conditions. In a later study, Herz and co-workers, [7], presented a detailed analysis of CO conversion response of three-way catalysts following step-changes in engine A/F and during individual cycles. In order to identify ways toward possible improvement in the cyclic performance of automotive

catalysts, Cho and West [15] experimentally investigated the effect of feed composition cycling on catalyst performance as a function of operating temperature. In a later experimental work, Cho [16] examined the influence of A/F oscillation, and found the favorable effect of the feed composition oscillation on the conversion of three pollutants.

Schlatter et al. [9] used a simulated automotive exhaust with a Pt/Rh catalyst to examine how modulating the A/F affects CO, HC, and NO conversions at 550°C and a space velocity of 52,000 hr^{-1} . Their results show the influence of cyclic frequency and amplitude on CO and NO conversion over a range of A/Fs. The oscillation increases the CO conversion in the fuel rich zone, and has similar effect on NO conversion on the lean side. The conversion is improved by decreasing the frequency or increasing the fluctuation amplitude. At the stoichiometric value, the oscillation in A/F was found to decrease the CO and NO conversions. Similar conclusions were reported by Koltsakis and Stamatelos [5] in their recent experimental and computational study. In contrast to many previous studies that were performed under laboratory conditions, Silveston [4] investigated the influence of periodic fluctuations of A/F on the catalyst under real driving conditions. He found that frequency modulation was more beneficial in reducing emission at low temperatures. Hence, its influence during the cold start period will be greater. However, with an increase in temperature, the conversion enhancement was found to be reduced.

A review of the past studies shows that most of them are limited to experimental work. The use of mathematical modeling and numerical simulations in analyzing the catalyst dynamic behavior has been limited. Some studies used laboratory conditions for experiments, (e.g., [17]), which may not be directly applicable to catalysts operating under severe transient modes. Furthermore, the effect of fluctuation on catalyst efficiency is not clear and there are still contradicting views expressed in the literature, [5]. The present study is motivated by realizing the existing gaps in the literature. This study employs a mathematical model to investigate the influence of A/F modulations on the dynamic behavior of catalysts.

Mathematical Formulation

The governing equations were developed by considering the conservation of mass, energy, and chemical species. Using the

Contributed by the Internal Combustion Engine Division of THE AMERICAN SOCIETY OF MECHANICAL ENGINEERS for publication in the ASME JOURNAL OF ENGINEERING FOR GAS TURBINES AND POWER. Manuscript received by the ICE Division Nov. 2001; final revision received by the ASME Headquarters July 2002. Associate Editor: D. Assanis.

assumptions and notations listed elsewhere, [18], the governing conservation equations for a typical single channel may be written as follows:

the gas phase energy equation:

$$\rho_g C_p \left(\varepsilon \frac{\partial T_g}{\partial t} + v_g \frac{\partial T_g}{\partial z} \right) = -h_g G_a (T_g - T_s) \quad (1)$$

the gas phase species equations:

$$\left(\varepsilon \frac{\partial C_g^j}{\partial t} + v_g \frac{\partial C_g^j}{\partial z} \right) = -k_m^j G_a (C_g^j - C_s^j) \quad (2)$$

where the superscript j varies from 1 to 7 representing, respectively, the following gas species: CO, NO, NH₃, O₂, C₃H₆, H₂ and C₃H₈. The effect of homogeneous reactions in gas phase is very small and is, therefore, neglected.

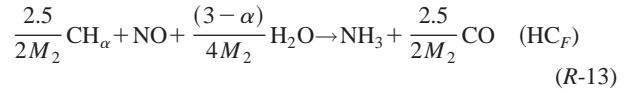
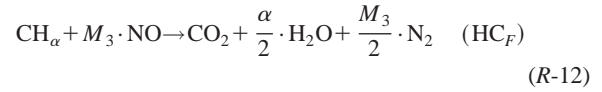
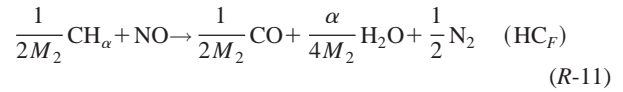
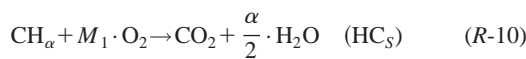
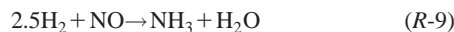
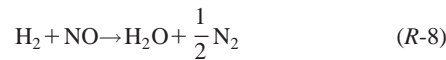
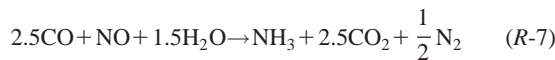
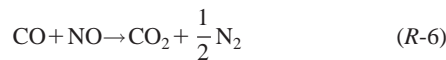
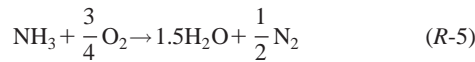
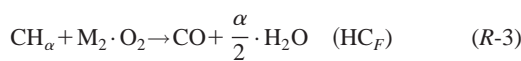
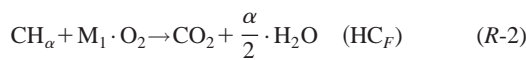
The surface energy equation:

$$(1 - \varepsilon) \rho_s C_p \frac{\partial T_s}{\partial t} = (1 - \varepsilon) \lambda_s \frac{\partial^2 T_s}{\partial z^2} + h_g G_a (T_g - T_s) - h_{\infty} S_{\text{ext}} (T_s - T_{\infty}) + G_a \times \sum_{k=1}^{n_{\text{reaction}}} R^k (T_s, C_s^1, \dots, C_s^{N_{\text{species}}}) \cdot \Delta H^k \quad (3)$$

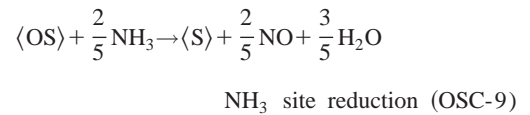
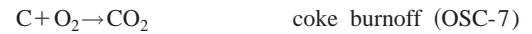
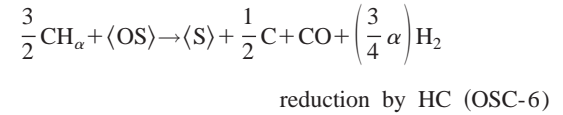
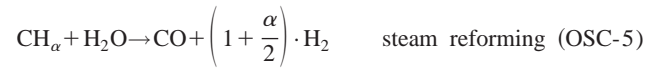
The surface species equations:

$$(1 - \varepsilon) \frac{\partial C_s^j}{\partial t} = k_m^j G_a (C_g^j - C_s^j) - G_a R^j (T_s, C_s^1, \dots, C_s^{N_{\text{species}}}) \quad (4)$$

Here superscript j varies from 1 to 7, representing the surface species in the same order as the gas species. Note that the radial variations of species and temperatures, which are much smaller than the axial variations, are neglected. The effect of heat loss to the ambient is, however, included in the surface energy equation. The heat and mass transfer coefficients in the above equations are calculated from the conventional correlations of Nusselt and Sherwood numbers, [19]. The heterogeneous surface chemistry is modeled by using the following 13-step chemical mechanism:



where α =hydrogen-to-carbon ratio; HC_F=fast burning HC; HC_S=slow burning HC; and $M_1=[1+\alpha/4]$; $M_2=[1/2+\alpha/4]$; $M_3=[2+\alpha/2]$. In the present study, propylene, and propane represent the fast and slow burning hydrocarbons respectively. In addition to the catalyst's substrate kinetics, the catalyst's oxygen storage capacity was modeled by using a nine-step mechanism of Otto [20], which is listed below:



where α is hydrogen-to-carbon ratio of the hydrocarbon.

The details of the chemical mechanisms and the corresponding kinetic data are given elsewhere, [18]. The governing equations were discretized by using a nonuniform grid and employing the control volume approach with the central implicit difference scheme in the spatial direction. A standard tridiagonal matrix algorithm with an iterative successive line under relaxation method was used to solve the finite difference equations. A sensitivity study was performed to select the optimum spatial node and time step sizes, [18]. For the present study, the spatial node size ranging from 0.1693 mm to 19.32 mm and the time step of 0.001 second were employed. Details of the solution procedure are described elsewhere, [18].

Results

The numerical model's performance under actual transient driving conditions was assessed by using experimental measurements across the front catalyst brick from a 4.6L 2V Lincoln Town car as it was driven during the federal test procedure (FTP). The difference between the pollutant conversion efficiencies as determined by the model and experimental measurements was compared in our previous paper and was found to be less than 5%, [18]. The

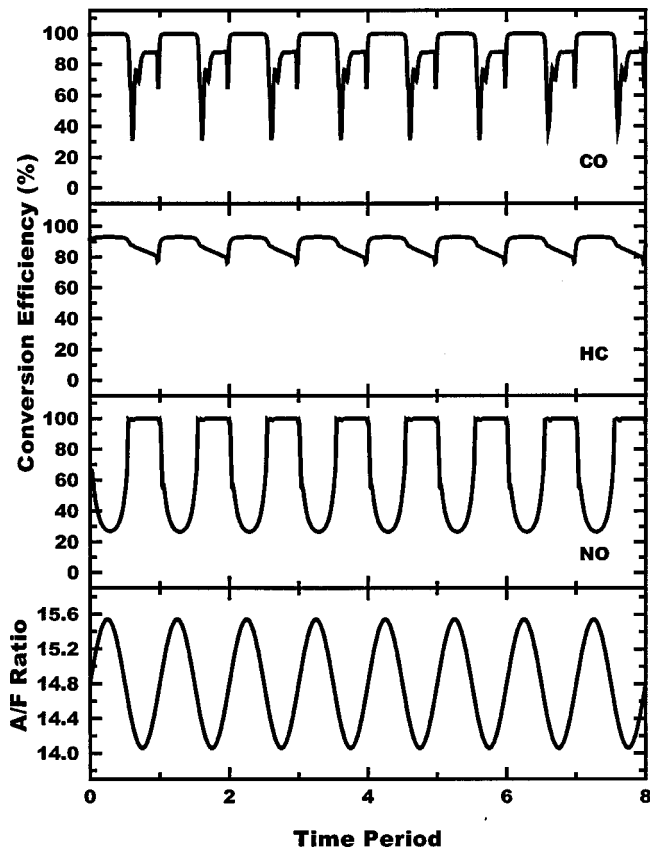


Fig. 1 Catalyst response to sinusoidal modulations in A/F near stoichiometric operating conditions (mean A/F=14.8, frequency=1 Hz, amplitude=5%)

catalyst used for the present study was palladium-based and had a length of 3 cm, cross-sectional area of 86.0254 cm², cell density of 62 cells/cm², and wall thickness of 0.1905 mm. The gas mass flow rate was 1.417×10^{-2} kg/s with 9.9205×10^{-7} kg/s CO, 8.0834×10^{-8} kg/s total HC, and 1.0282×10^{-6} kg/s NO. The feed gas temperature was 297°C. The variation in air fuel ratio through both sinusoidal and step changes are considered.

Response to Sinusoidal Variation in Air-Fuel Ratio. These results were obtained by considering the catalysts, which were initially at steady-state conditions and were suddenly subjected to sinusoidal modulations in A/F. During these modulations, other inlet conditions and the concentrations of CO, HC, and NO remained unchanged. The A/F was varied by changing the oxygen concentration. Figure 1 shows the CO, HC, and NO conversion efficiencies as a function of imposed fluctuation time period. The A/F, initially set at 14.8 (stoichiometric value of A/F is 14.51), is varied sinusoidally with a frequency of 1 Hz and amplitude of 5%. The A/F ranges between 14.06 and 15.54, and the catalyst undergoes a transition between rich and lean operating conditions during each fluctuation time period. The catalyst responds to A/F modulations with a time delay.

Figure 1(a) shows the CO conversion efficiency as a function of the fluctuation time period. The initial CO conversion efficiency, due to lean operating conditions, is very high. The results show that, with the imposed fluctuations in A/F and the corresponding transition to the rich zone, the CO conversion decreases. It starts increasing again after reaching a minimum value. Interestingly, the CO conversion efficiency drops much lower than the steady-state value corresponding to the lower value of A/F. Near the stoichiometric conditions, the CO conversion performance exhibits a discontinuous behavior and a sharp decrease in the efficiency.

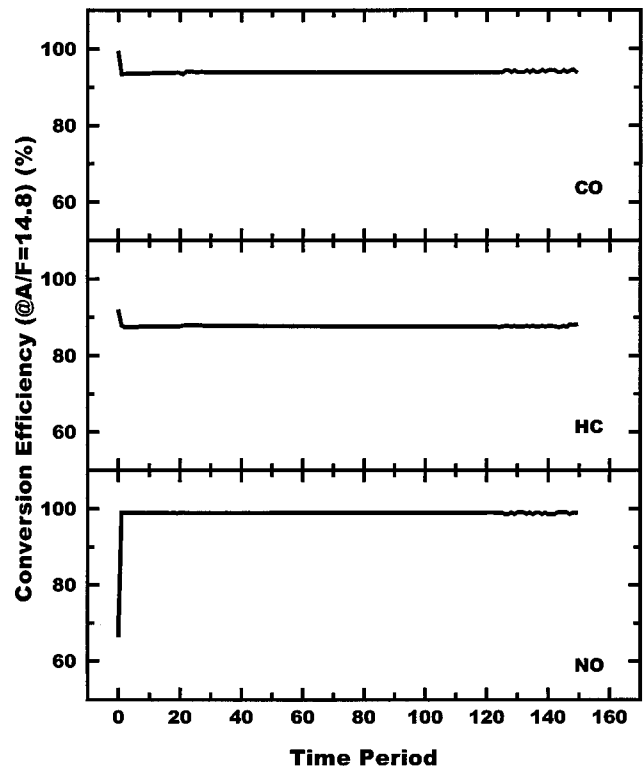


Fig. 2 Catalyst conversion efficiencies corresponding to A/F of 14.8 (when reached from rich side) during sinusoidal modulations in A/F (mean A/F=14.8, frequency=1 Hz, amplitude=5%)

The efficiency increases again as the A/F increases beyond stoichiometric value. During the initial time periods, the catalyst response is unsteady periodic. The response becomes steady periodic after a long time, as shown in Fig. 2 and is further discussed in the following section. The discontinuous and unsteady periodic behavior is due to some kinetic effect as this behavior was not observed with a simpler four-step kinetics, [21].

Figure 1(b) depicts the HC conversion efficiency as a function of the fluctuation time period. The results show that the HC conversion efficiency of the catalyst responds to the sinusoidal modulations in A/F in a periodic manner. However, the response is not truly sinusoidal. The increase in A/F increases the HC conversion efficiency. The conversion efficiency reaches a maximum value (~93%) corresponding to the maximum value of A/F. After reaching the maximum value, the HC conversion decreases. The decrease in HC conversion continues in the rich zone as the A/F crosses the stoichiometric value. The HC conversion efficiency attains a minimum value (~76%) before the A/F reaches its minimum value. The conversion efficiency then increases. The increase is relatively sharp near the stoichiometric A/F. Beyond the stoichiometric value, the HC conversion efficiency continues to increase until the maximum value is attained. After the first cycle, the catalyst HC response exhibits a cyclic pattern. Similar to CO response, the result shows a drop in the mean value around which the conversion efficiency oscillates. This indicates that, near the stoichiometric point, the A/F modulation causes a reduction in CO and HC conversions.

Figure 1(c) shows the NO conversion efficiency as a function of fluctuation time period. Compared to HC conversion efficiency, the response of NO conversion to the sinusoidal fluctuations is relatively more sinusoidal and more substantial. The initial steady-state NO conversion efficiency corresponding to initial A/F of 14.8 is approximately 66.8%. The NO conversion responds to the change in A/F with a slight time delay. The conversion efficiency

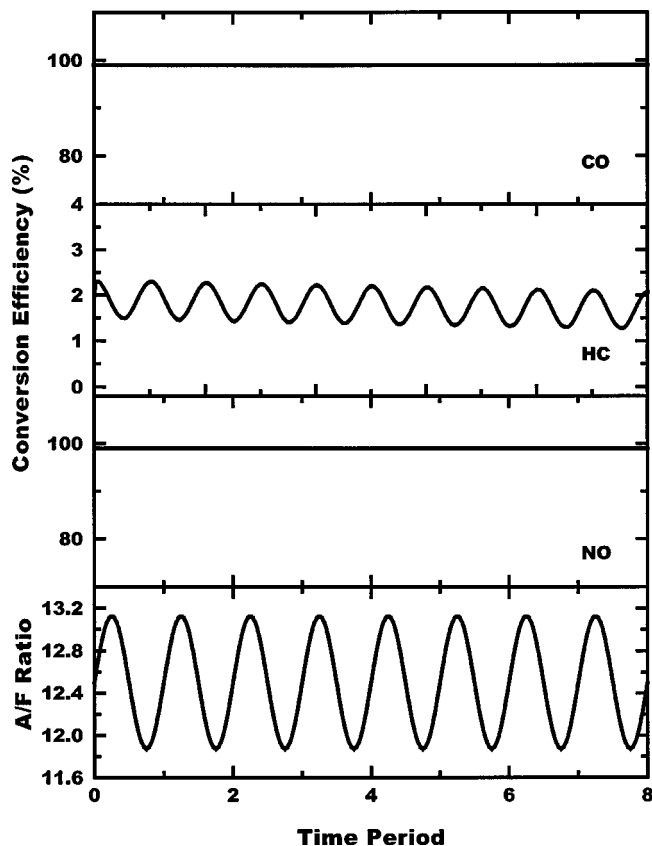


Fig. 3 Catalyst response to sinusoidal modulations in A/F near rich operating conditions (mean A/F=12.5, frequency=1 Hz, amplitude=5%)

decreases due to an increase in the A/F. The efficiency attains a minimum value ($\sim 27\%$) corresponding to the maximum value of A/F, following which it starts increasing again. The conversion efficiency increases sharply with a decrease in the A/F near the stoichiometric conditions in the rich zone. As expected, in most of the rich region, the NO conversion efficiency is very high and is close to 100%. The conversion efficiency remains high even when the A/F is increased beyond the stoichiometric value and into the lean zone. The efficiency starts decreasing after the A/F is increased further in the lean zone. The catalyst's periodic response continues as long as the fluctuating A/F field is maintained. Contrary to the CO and HC cases, the A/F modulation has positive impact on NO conversion, which is improved from a steady state value of 66.8% to 67.3%.

The steadiness of periodic response can be better judged from Fig. 2. In this figure, the conversion efficiencies corresponding to A/F of 14.8 (approaching from the rich side) are plotted as a function of time period. The initial drop in CO and HC conversion efficiencies is due to lag in catalyst response to the imposed fluctuations. The catalyst CO and HC conversion corresponding to A/F of 14.8 (which is slightly on the lean side) is high as shown by the initial values. However, during the fluctuations, the catalyst conversion at any instant does not correspond to the A/F value of that instant and lags behind. Hence, at any time period, when the A/F of 14.8 is reached from the rich side, the conversion efficiency at that instant correspond to an A/F less than 14.8 (a value in the rich region) and is therefore lower than the initial value. The response lag is also responsible for the initial rise in NO conversion. Small fluctuations in the conversion efficiency at A/F of 14.8 indicates unsteady periodic behavior in the catalyst response, which does not disappear completely even after a long time.

The effects of sinusoidal fluctuations in rich and lean zones

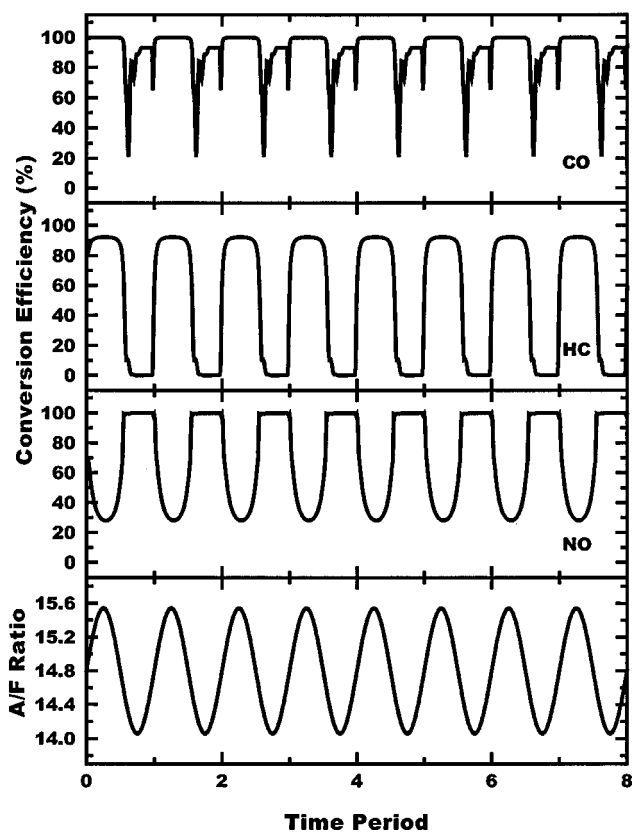


Fig. 4 Catalyst response to sinusoidal modulations in A/F without oxygen storage capacity (mean A/F=14.8, frequency=1 Hz, amplitude=5%)

away from the stoichiometric value are presented next. The rich zone results, as shown in Fig. 3, were obtained by initially setting the A/F at 12.5. The catalyst is subjected to sinusoidal modulations in the A/F with a 1 Hz frequency and 5% amplitude. The resulting A/F ranges between 11.88 and 13.13. The effect of fluctuation on the CO conversion is found to be insignificantly small. The HC conversion, on the other hand, is found to be relatively more affected. Due to rich conditions throughout, the initial HC conversion efficiency is very small ($\sim 2.1\%$). The results show that, in contrast to the case of transition zone, the conversion response is truly sinusoidal. There is no delay in catalyst response to A/F variations. Owing to rich conditions throughout the fluctuation periods, the NO conversion remains very high and is not influenced by the imposed modulations. The lean zone results, not shown here, depict no influence on CO conversion and insignificantly small influence on HC conversion. The NO conversion efficiency shows relatively larger influence of A/F modulations. These results clearly show that the effects of A/F modulations are different under different operating conditions.

Effect of Oxygen Storage Capacity. From many prior experiments and calculations, the oxygen storage capacity (OSC) has been found to improve the catalyst conversion efficiencies during rich operating condition, [18]. The effect of this mechanism on the catalyst response to A/F modulations, however, is not well studied. In the present work, we investigated this effect by simulating the catalyst response to A/F modulations without using the oxygen storage mechanism. The results depict that the catalyst conversion response to the imposed A/F modulations is relatively larger in the absence of the OSC (see Fig. 4). The response amplitudes of CO and HC conversion efficiencies are 79% and 92.2%, respectively, which are higher than those of the OSC case (having response amplitudes of 69.1% and 17.4%, respectively). NO conversion, on

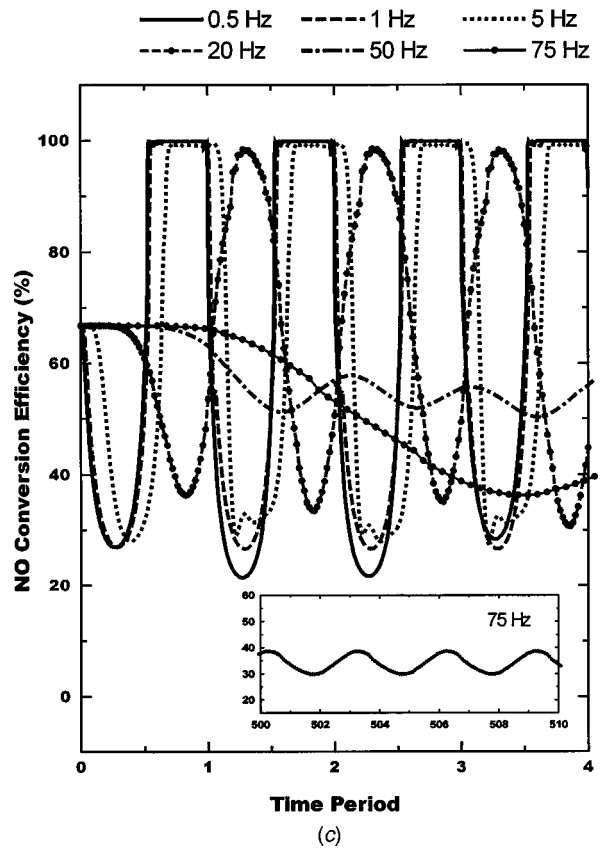
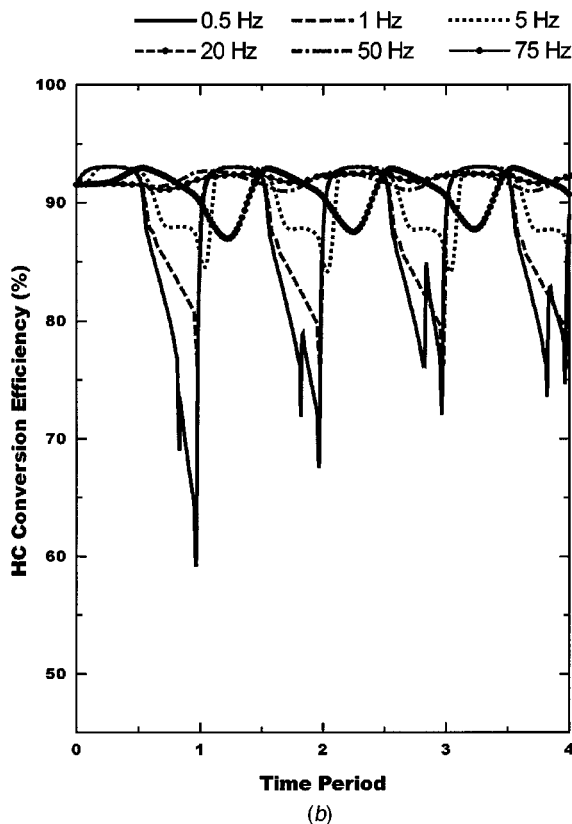
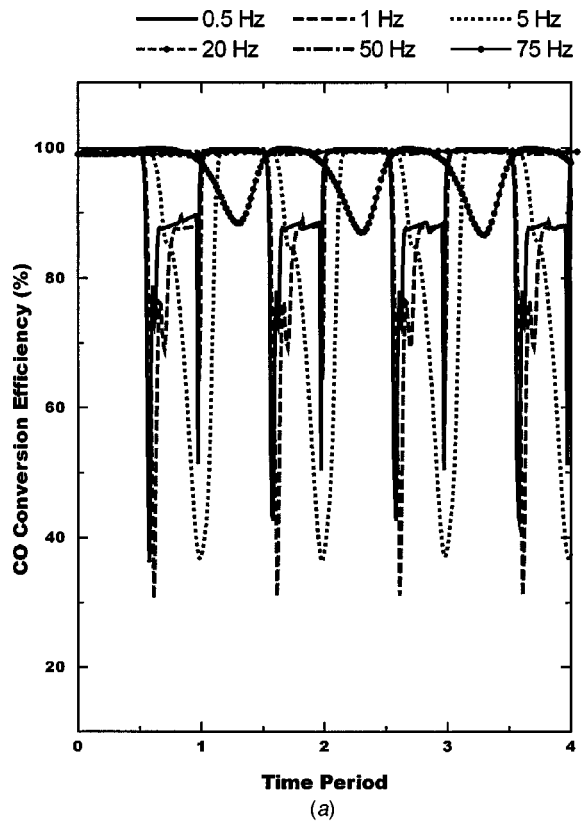


Fig. 5 (continued)

Fig. 5 Catalyst response to sinusoidal modulations in A/F: effect of oscillation frequencies (a) CO conversion efficiency; (b) HC conversion efficiency; (c) NO conversion efficiency (mean A/F=14.8, amplitude=5%)

the other hand, is relatively less influenced by the absence of the OSC. The NO conversion response amplitude for the non-OSC case ($\sim 71.8\%$) is slightly less than that for the OSC case ($\sim 73.1\%$). Overall, the results show that the catalyst is more sensitive to A/F modulations in the absence of the OSC, which is in agreement with the prior findings, [22].

Effect of Oscillation Frequency. Figure 5 presents the CO, HC, and NO conversion efficiencies as a function of imposed modulation time period for different frequencies. All these results are for catalysts, initially operating at A/F of 14.8, and subjected to sinusoidal oscillation in A/F of 5% amplitude. The figure depicts, as expected, that the catalyst response to imposed oscillation is maximum at low frequencies and its amplitude decreases with an increase of the imposed frequency. With an increase in frequency, the catalyst response becomes relatively more sinusoidal. Higher frequencies also increase the initial phase lag in the catalyst response to imposed modulations. The catalyst becomes insensitive to imposed fluctuations at high frequencies. The catalyst's "insensitivity" is due to effective neutralization of high frequency fluctuations by diffusion processes over the time period required to convect them to the reaction sites. The cutoff frequency corresponding to the catalyst's insensitivity is different for CO, HC, and NO. For the conditions studied, the cutoff frequency is lower for CO (less than 50 Hz) than that for HC and NO (~ 100 Hz). At higher frequencies, which are lower than the cutoff value, NO exhibits an increase in response time period. For example, the NO response time period is three times larger than that of the imposed modulation at 75 Hz. The effect of frequency on the catalyst response is also found to be different for different pollutants in different frequency ranges as shown in Fig. 6, where the catalyst average response amplitude is plotted as a function of the imposed frequency. The results show that HC response is very sensitive to the imposed modulation frequency at very low fre-

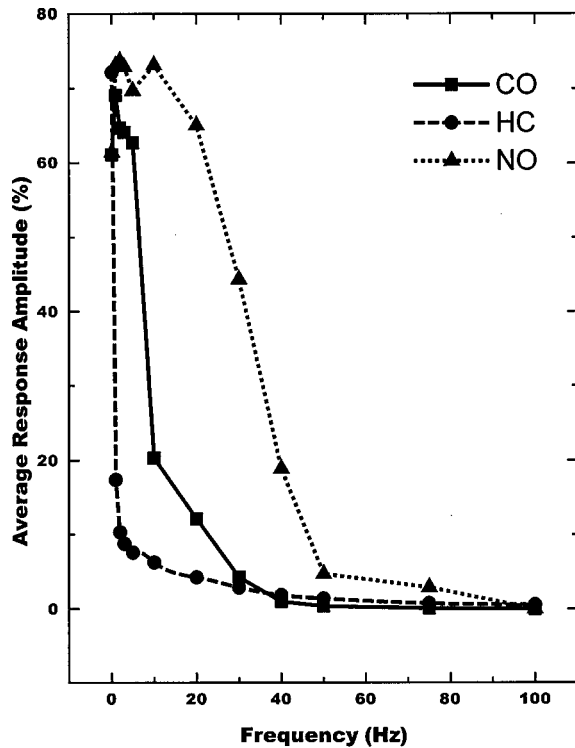


Fig. 6 Catalyst CO response to sinusoidal modulations in A/F for different oscillation frequencies (mean A/F=14.8, amplitude=5%)

quencies (below 1 Hz), whereas the CO and NO responses are not much sensitive to the modulation frequencies up to 5 and 20 Hz, respectively. At very low frequencies (e.g., 0.1 Hz), the CO and NO response amplitudes are lower than those at higher frequencies (e.g., 1 Hz). This may be explained by considering that, at very low frequencies, the catalyst performance is similar to that of the steady state conditions. So, the catalyst response at these frequencies corresponds to the difference between the two steady state values. Recall that, during the transient conditions, the catalyst performance may drop lower than that of the corresponding steady-state conditions. Hence, the response amplitude at 1 Hz (influenced by the transient behavior) becomes higher than that at 0.1 Hz (exhibiting steady-state behavior).

Effect of Oscillation Amplitude. Figure 7 shows the catalyst conversion efficiencies as a function of oscillation time period for different amplitudes of A/F modulations. These results are for catalysts, which are initially operating at A/F of 14.8 and are subjected to sinusoidal fluctuations in A/F of 1 Hz frequency. The results show that the increase of oscillation amplitude generally increases the catalyst response. The relative effect of amplitude on NO conversion is higher than that on other pollutant conversion. The relative effect of increasing the modulation amplitude from 5% to 10% is higher than that from 10% to 15%. For all amplitudes, the catalyst response exhibits some unsteady periodic behavior. At higher amplitudes, the catalyst is found to take much longer time before exhibiting a repeating response pattern. For the conditions studied, where all fluctuation amplitudes cause the catalysts to go through a transition from lean to rich zone, other than the response amplitude, the fluctuation amplitude has insignificant influence on any other aspect of the catalyst response. However, the fluctuation amplitude will have greater influence on the catalyst response when their values determine whether or not the catalyst will undergo a transition.

Response to Step Change in Air-Fuel Ratio. The response

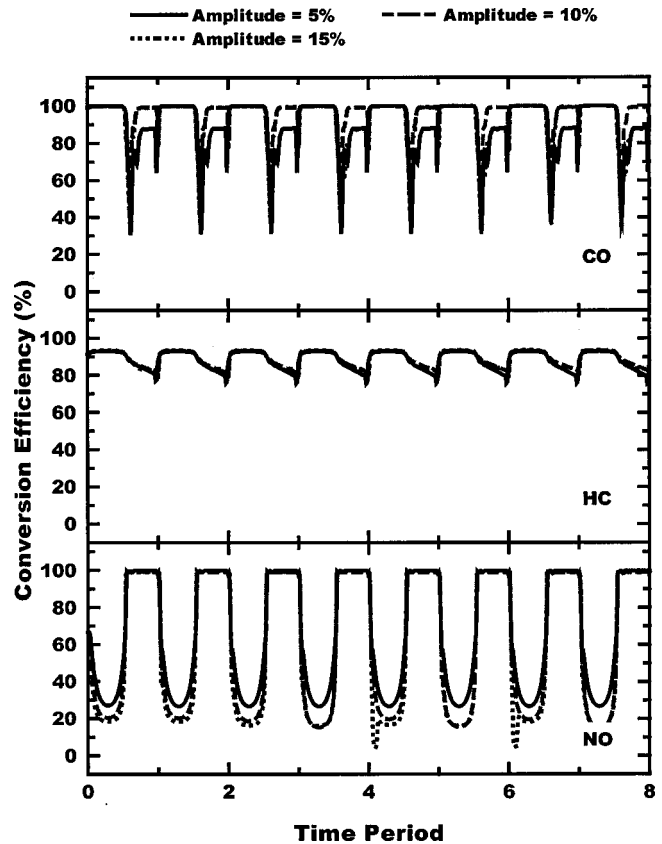


Fig. 7 Catalyst response to sinusoidal modulations in A/F: effect of oscillation amplitudes (mean A/F=14.8, frequency=1 Hz)

to step change in A/F is investigated by considering the catalysts initially operating at steady state, and which are subjected to step changes in A/F. During the step change, the other inlet conditions remain unchanged. Figure 8 shows the effect of step change in A/F from a value of 15 (lean condition) to a value of 14 (rich condition). The figure shows that CO conversion efficiency, which is initially 99.7%, responds to the step change and the efficiency drops to 39.3%. The low CO conversion performance lasts only a very short period and the conversion efficiency increases to values over 90%. While steady-state value of 93% is reached slowly, most major changes take place in the first second of the step change. For the conditions studied, the step change in A/F brings about a significant change in HC conversion performance. The efficiency drops from 92.7% to 2%. It takes a long time (~25 seconds) before the final steady state value is reached. The response of NO conversion to step change in A/F, on the other hand, is very fast. It takes 0.3 second to attain the final steady-state value. The NO conversion efficiency increases from 4.3% (in the lean zone) to 99.9% (in the rich zone).

The effect of step changes in transition from rich to lean conditions is considered next. Figure 9 shows the results of this transition, in which the A/F is changed from 14 (rich condition) to 15 (lean condition). The CO conversion is not much influenced (from 99.2% to 99.7%) by the step change in A/F. In this case, the initial CO conversion efficiency (99.2%) is higher than that obtained for the similar value of A/F of 14 in the previous case of step change from lean to rich. This difference is due to a slightly higher NO conversion corresponding to A/F of 14 in the previous case than in the present case. This difference in NO conversion performance is discussed further later in this section. There is also a small drop in the CO conversion for a very short period as the catalyst is subjected to step change. The drop is immediately followed by an

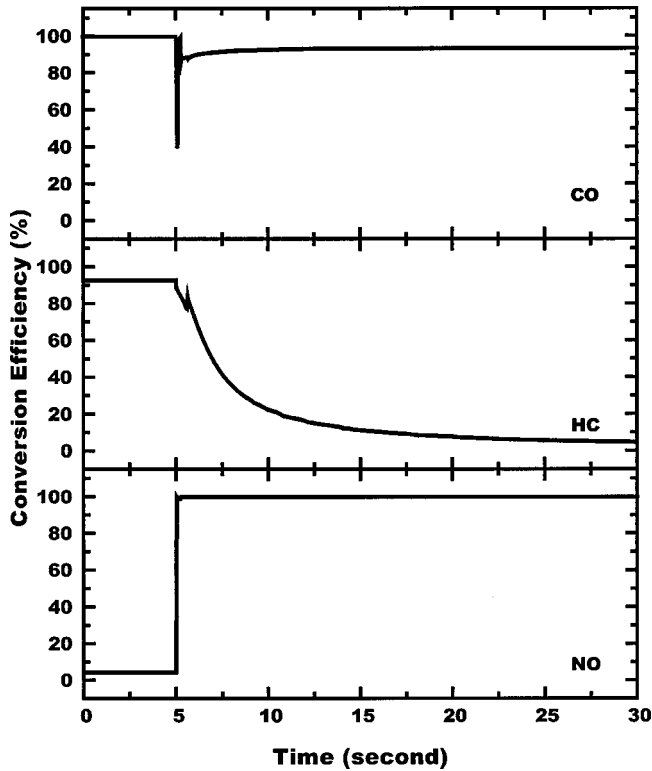


Fig. 8 Catalyst response to step change in A/F: from lean to rich zone (A/F=15 to 14)

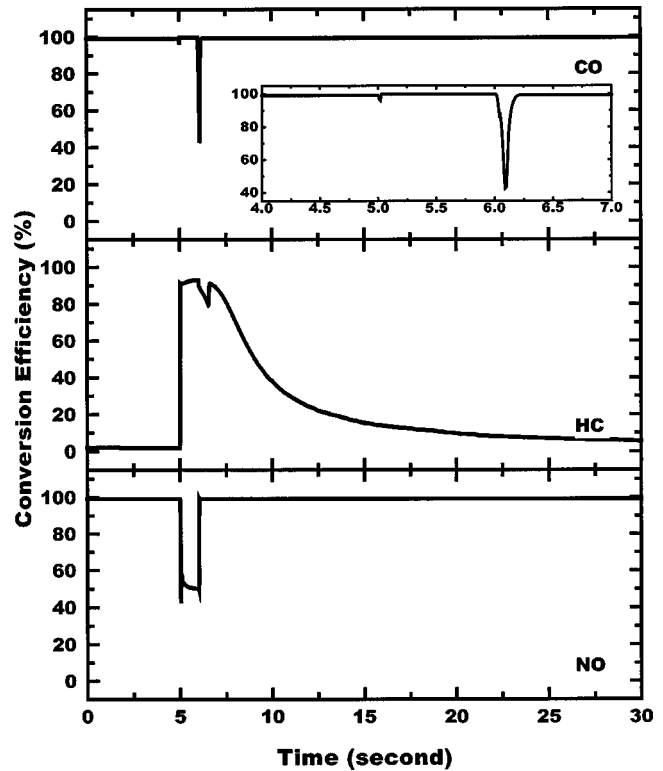


Fig. 10 Catalyst response to double-step change in A/F: lean excursion for 1 second (A/F=14 to 15 to 14)

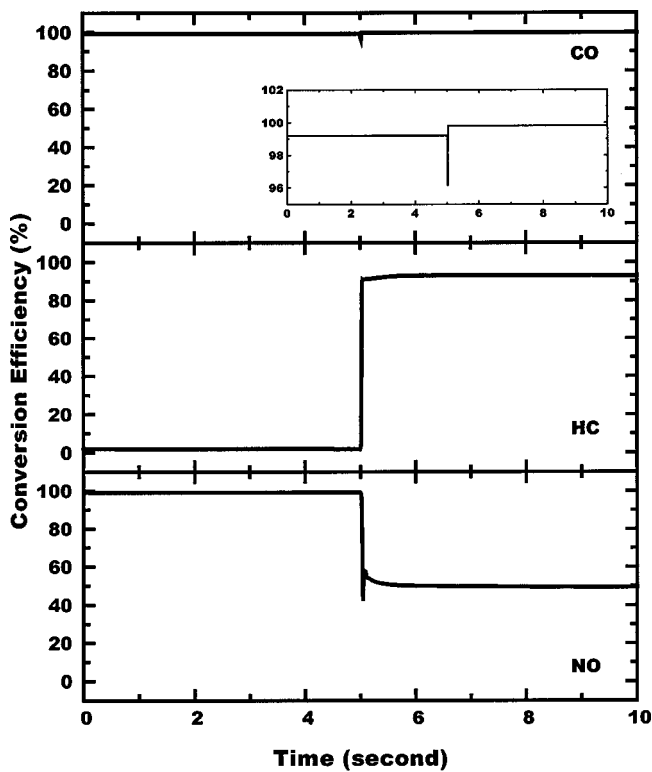


Fig. 9 Catalyst response to step change in A/F: from rich to lean zone (A/F=14 to 15)

increase in conversion. As in the previous case, the HC conversion is significantly affected by the step change. The conversion efficiency increases from 2% to 92.7%. The step change causes the NO conversion efficiency to decrease from 99.2% to a lower value of 42.3%. The efficiency then increases to 49.3% corresponding to A/F of 15. Note that this efficiency is much higher than the steady-state value of 4.3% corresponding to A/F of 15, which was obtained in the previous case. This increase in NO efficiency indicates a hysteresis effect. Thus the catalyst NO conversion efficiency corresponding to a value of A/F depends, not only on the value of the A/F, but also on the path by which that value is reached. Higher efficiency is obtained when a particular A/F is reached from the rich zone than the case when it is reached from the lean side. The hysteresis in NO conversion is due to the OSC effect as this behavior is not observed in the non-OSC case.

Double Step Change. The effect of double step change in A/F is investigated by considering a catalyst, initially operating at steady state, which is subjected to a step change in A/F for 1 second and then returns back to its original operating point. Figure 10 shows the results of double step change from the A/F of 14 (rich condition) to 15 (lean conditions) for one second, and then back to the value of 14 (rich condition). The results depict that the CO conversion is changed from 99.2% to 99.8%, which is followed by a drop of efficiency to a lower value of 42.6%. After reaching a minimum value, the CO conversion starts increasing until it attains the final steady value of 99.2%. The steady state is achieved in roughly less than 2 seconds. Similar to the case of a single step change, the effect on HC conversion efficiency is significant. The conversion efficiency increases from 2.1% to 93.1%, followed by a drop to the initial value. The steady-state conditions are achieved very slowly.

The NO conversion efficiency responds similar to that of the combination of two step changes. The efficiency drops from 99.2% to a lower value of 42.3%, followed by an increase to 49.8% (steady state value corresponding to A/F of 15 as discussed

earlier). The efficiency then increases further back to the initial value corresponding to the decrease of A/F to 14. Compared to the HC case, the steady-state conditions for CO and NO are reached faster.

Conclusions

During dynamic operation, the catalyst behavior is very different from that under the steady-state conditions. The behavior is also greatly influenced by the operating conditions and chemical kinetics. Near stoichiometric conditions, the A/F modulation decreases the CO and HC conversion and improves the NO conversion. The effect on HC conversion is relatively small. For these conditions, the response of conversion efficiencies is not truly sinusoidal to sinusoidal modulations. At higher modulation frequencies, however, the response becomes sinusoidal. Under lean and rich conditions, the A/F modulations have relatively insignificant effects on the catalyst conversion performance.

Near stoichiometric conditions, the oxygen storage capacity is found to make the CO and HC conversion less sensitive and NO conversion slightly more sensitive to A/F modulations. The catalyst response to imposed modulation is generally high at low frequencies and its amplitude decreases with an increase of the imposed frequency. The effect of imposed frequency on the catalyst response is different in different frequency ranges for different pollutants. At higher frequencies, the catalyst becomes "insensitive" to imposed modulations. The cutoff frequency corresponding to the catalyst's insensitivity is different for CO, HC, and NO. The increase of oscillation amplitude increases the response of catalyst. The step changes in A/F show that the HC conversion responds very slowly to a transition from lean to rich conditions. The response of NO conversion to step changes is very fast. Due to the effect of the oxygen storage capacity, the NO conversion efficiency exhibits a hysteresis effect. This causes the NO conversion efficiency corresponding to a value of A/F to depend, not only on the value of the A/F, but also on the path by which that value is reached. Higher efficiency is obtained when a particular A/F is reached from the rich zone than the case when it is reached from the lean side.

Acknowledgments

The financial support from the Ford Scientific Research Laboratory, Oak Ridge National Laboratory and the Center for Engineering Education and Practice (CEEP) of the University of Michigan-Dearborn is greatly appreciated. The technical discussion with Dr. C. S. Daw of Oak Ridge National Laboratory is also gratefully acknowledged.

Nomenclature

C_g^j	= gas phase concentration of species j , mol/m ³
C_s^j	= surface concentration of species j , mol/m ³
Cp_g	= specific heat of gas, J/(kg·K)
Cp_s	= specific heat of substrate, J/(kg·K)
G_a	= geometric surface area, m ² /m ³
ΔH^k	= heat of reaction of species k , J/mol
h_g	= heat transfer coefficient between flow and substrate, J/(m ² ·s·K)
h_∞	= heat transfer coefficient between substrate and atmosphere, J/(m ² ·s·K)
k_m^j	= mass transfer coefficient for species j , m/s
R^k	= reaction rate of k th reaction, mol/(m ² ·s)

S_{ext}	= external surface to volume area ratio, m ² /m ³
t	= time, s
T_∞	= ambient temperature, K
T_g	= gas temperature, K
T_s	= substrate temperature, K
v_g	= gas flow velocity, m/s
z	= coordinate along catalyst axis, m
α	= hydrogen-to-carbon ratio in the fuel
ε	= void volume fraction
λ_s	= thermal conductivity of substrate, J/(m·s·K)
ρ_g	= gas density, kg/m ³
ρ_s	= substrate density, kg/m ³

References

- [1] Herz, R. K., 1987, "Dynamic Behavior of Automotive Three-Way Emission Control System," *Catalysis and Automotive Pollution Control*, Elsevier, Amsterdam, pp. 427–444.
- [2] Herz, R. K., 1981, "Dynamic Behavior of Automotive Catalysts: 1. Catalyst Oxidation and Reduction," *Ind. Eng. Chem. Process Des. Dev.*, **20**, pp. 451–457.
- [3] Silveston, P. L., 1995, "Automotive Exhaust Catalysis Under Periodic Operation," *Catalysis Today*, **25**, pp. 175–195.
- [4] Silveston, P. L., 1996, "Automotive Exhaust Catalysis: Is Periodic Operation Beneficial?" *Chem. Eng. Sci.*, **51**, pp. 2419–2426.
- [5] Koltsakis, G. C., and Stamatelos, A. M., 1999, "Dynamic Behavior Issues in Three-Way Catalyst Modeling," *AIChE J.*, **45**, pp. 603–614.
- [6] Shulman, M. A., Hamburg, D. R., and Throop, M. J., 1982, "Comparison of Measured and Predicted Three-Way Catalyst Conversion Efficiencies Under Dynamic Air-Fuel Ratio Conditions," *SAE Paper No. 820276*.
- [7] Herz, R. K., Kleta, J. B., and Sell, J. A., 1983, "Dynamic Behavior of Automotive Catalysts: 2. Carbon Monoxide Conversion Under Transient Air/Fuel Ratio Condition," *Ind. Eng. Chem. Process Des. Dev.*, **22**, pp. 387–396.
- [8] Taylor, K. C., and Sinkevitch, R. M., 1983, "Behavior of Automobile Exhaust Catalysts With Cycled Feed Streams," *Ind. Eng. Chem. Process Des. Dev.*, **22**, pp. 45–50.
- [9] Schlatter, J. C., Sinkevitch, R. M., and Mitchell, P. J., 1983, "Laboratory Reactor System for Three-Way Automotive Catalyst Evaluation," *Ind. Eng. Chem. Process Des. Dev.*, **22**, pp. 51–56.
- [10] Matsunga, S.-I., Yokota, K., Muraki, H., and Fujitani, Y., 1987, "Improvement of Engine Emissions Over Three-Way Catalyst by the Periodic Operation," *SAE Paper No. 872098*.
- [11] Schlatter, J. C., and Mitchell, P. J., 1980, "Three-Way Catalyst Response to Transients," *Ind. Eng. Chem. Process Des. Dev.*, **19**, pp. 288–293.
- [12] Cutlip, M. B., 1979, "Concentration Forcing of Catalytic Surface Rate Processes," *AIChE J.*, **25**, pp. 502–508.
- [13] Abdul-Kareem, H. K., Silveston, P. L., and Hudgins, R. R., 1980, "Forced Cycling of the Catalytic Oxidation of CO Over a V₂O₅ Catalyst—1," *Chem. Eng. Sci.*, **35**, pp. 2077–2084.
- [14] Silveston, P. L., Hudgins, R. R., Adesina, A. A., Ross, G. S., and Feimer, J. L., 1986, "Activity and Selectivity Control through Periodic Composition Forcing Over Fischer-Tropsch Catalysts," *Chem. Eng. Sci.*, **41**, pp. 923–928.
- [15] Cho, B. K., and West, L. A., 1988, "Cyclic Operation of Pt/Al₂O₃ Catalysts for CO Oxidation," *Ind. Eng. Chem. Fundam.*, **25**, pp. 158–164.
- [16] Cho, B. K., 1988, "Performance of Pt/Al₂O₃ Catalysts in Automobile Engine Exhaust With Oscillatory Air/Fuel Ratio," *Ind. Eng. Chem. Res.*, **27**, pp. 30–36.
- [17] Hoebink, J. H. B. J., Marin, G. B., and Huinink, J. P., 1997, "A Quantitative Analysis of Transient Kinetic Experiments: The Oxidation of CO by O₂ Over Pt," *Appl. Catal., A*, **160**, pp. 139–151.
- [18] Shamim, T., Shen, H., Sengupta, S., Son, S., and Adamczyk, A. A., 2002, "A Comprehensive Model to Predict Three-Way Catalytic Converter Performance," *ASME J. Eng. Gas Turbines Power*, **124**, pp. 421–428.
- [19] Montreuil, C. N., Williams, S. C., and Adamczyk, A. A., 1992, "Modeling Current Generation Catalytic Converters: Laboratory Experiments and Kinetic Parameter Optimization—Steady State Kinetics," *SAE Paper No. 920096*.
- [20] Otto, N. C., 1984, private communication.
- [21] Shamim, T., and Medisetty, V. C., 2001, "Dynamic Response of Automotive Catalytic Converters: The Role of Chemical Kinetic Mechanisms," *Proceedings of the Second Joint Meeting of the U.S. Sections of the Combustion Institute*, Combustion Institute, Pittsburgh, PA, Paper No. 274.
- [22] Moore, W. R., and Mondt, J. R., 1993, "Predicted Cold Start Emission Reductions Resulting From Exhaust Thermal Energy Conservation to Quicken Catalytic Converter Lightoff," *SAE Paper No. 931087*.

Numerical Analysis of Unsteady Exhaust Gas Flow and Its Application for Lambda Control Improvement

K. Yoshizawa

K. Mori

K. Arai

A. Iiyama

Powertrain Research Laboratory,
Nissan Research Center,
Nissan Motor Co., Ltd.,
1 Natsushima-cho,
Yokosuka 237-8523, Japan

A multidimensional computational fluid dynamics (CFD) tool has been applied to analyze the exhaust system of a gasoline engine. Since gas flow in the exhaust manifold is affected by exhaust pulsations, prediction methods based on steady flow are not able to predict gas flow precisely enough. Therefore, a new multidimensional calculation method, called pulsation flow calculation, has been developed. A one-dimensional gas exchange simulation and a three-dimensional exhaust gas flow calculation are combined to simulate gas flow pulsations caused by the gas exchange process. Predicted gas flow in the exhaust manifold agreed with the experimental data. With the aim of reducing emissions, the pulsation flow calculation method has been applied to improve lambda feedback control using an oxygen sensor. The factors governing sensor sensitivity to the exhaust gas from each cylinder were clarified. The possibility of selecting the oxygen sensor location in the exhaust manifold on the basis of calculations was proved. The effect of an exhaust manifold with equal-length cylinder runners on achieving uniform sensor sensitivities was made clear. In addition, a new lambda feedback control method for an exhaust manifold with different-length cylinder runners is proposed. [DOI: 10.1115/1.1473149]

Introduction

In recent years, continuing concerns about air quality have necessitated further reductions of automotive emissions such as hydrocarbons (HCs) and nitrogen oxides (NO_x). Increasingly tighter regulatory standards are scheduled to be enforced in the future. In addition, recent growing concerns about the greenhouse effect caused by carbon dioxide (CO_2) emissions have resulted in the enforcement of stricter fuel economy standards. At the same time, there have been large expectations for engine power improvements to meet consumer demands for better drivability. In this regard, it is essential to use computational fluid dynamics (CFD) tools to develop new engine systems that can strike a balance between engine power and emission standards. Design and development lead time must also be shortened in order to meet consumers' rapidly changing needs. Hence, there have been strong expectations for the development of simulation methods for predicting performance in the design stage.

Progress has been made in applying multidimensional CFD tools to the intake system, including to the intake port design for larger mass flow ([1,2]) and for optimization of in-cylinder flow ([3–6]). There are some reports about gas flow optimization in underfloor catalytic converters with CFD tools ([7–9]). However, there have been few reports about CFD application to the exhaust manifold. The complex shape of the exhaust system requires considerable time to create computational grids. The exhaust manifold is characterized by high flow velocities and elevated temperatures, making it difficult to obtain sufficient calculation convergence. Recently, three-dimensional computer-aided design (CAD) software has developed rapidly and also CFD software codes have been greatly improved. It is now becoming possible to apply CFD tools to exhaust systems.

In this study, a multidimensional CFD tool was used to analyze the flow in the exhaust manifold of a gasoline engine. Initially, a

steady flow simulation was attempted. However, because the gas flow in the exhaust manifold is greatly affected by exhaust pulsations, prediction methods based on steady flow are not able to predict gas flow precisely enough. There are a few reports about unsteady flow simulation methods which consider the effect of exhaust pulsations ([10,11]). In those simulations, the inlet velocities obtained experimentally were used as boundary conditions. Because it takes a great deal of time to obtain inlet velocities through experiments, those simulation methods have not found application as design tools.

In this work, a new multidimensional calculation method, called pulsation flow calculation, has been developed. A one-dimensional gas exchange simulation ([12]) and a three-dimensional exhaust gas flow calculation are combined to simulate gas flow pulsations caused by the gas exchange process. This pulsation flow tool makes it possible to simulate unsteady exhaust gas flow in the exhaust manifold.

With the aim of reducing emissions, the pulsation flow calculation method has been applied to improve lambda feedback control using an oxygen sensor. Improvement of lambda control accuracy is important for effective utilization of three-way catalysts. In this regard, the oxygen sensor must be placed so that it has uniform sensitivity to the exhaust gas from each cylinder, i.e., the exhaust from each cylinder must pass through the sensor location equally. To date, time-consuming experimental work has been the only way to evaluate sensor sensitivities. Therefore, the pulsation calculation method was applied to select the optimum sensor location.

The exhaust gas flow around the oxygen sensor was first analyzed by running a pulsation flow simulation. The factors governing sensor sensitivities to the exhaust gas from each cylinder were made clear. As a result, the possibility of selecting the optimum oxygen sensor location in the exhaust manifold on the basis of calculations was demonstrated.

Next, the gas concentrations at the oxygen sensor location were analyzed thoroughly and the effect of an exhaust manifold with equal-length cylinder runners on achieving uniform sensor sensitivities was investigated. In addition, a new lambda feedback con-

Contributed by the Internal Combustion Engine Division of THE AMERICAN SOCIETY OF MECHANICAL ENGINEERS for publication in the ASME JOURNAL OF ENGINEERING FOR GAS TURBINES AND POWER. Manuscript received by the ICE Division January 2000; final revision received by the ASME Headquarters August 2000. Associate Editor: D. Assanis.

control method for an exhaust manifold with different-length cylinder runners was examined. It was found that uniform sensor sensitivities are difficult to achieve in an exhaust manifold with cylinder runners of different lengths. In this regard, a method of detecting the exhaust air-fuel ratio of each cylinder by using an observer has been reported ([13]). This method takes into account the exhaust gas volume ratio of each cylinder and uses the observer theory to detect the exhaust air-fuel ratio from each cylinder. It is said that the air-fuel ratio of the exhaust gas from each cylinder can be controlled to stoichiometric proportions with one oxygen sensor. However, this method is also based on an exhaust manifold with equal-length cylinder runners. Therefore, it would be difficult to control the air-fuel ratio precisely for an engine having an exhaust manifold with different-length cylinder runners. To overcome that problem, a new lambda feedback control method for such an exhaust manifold is presented.

Experimental Validation of Exhaust Gas Flow by Steady Flow Simulation

Qualitative Validation. Experimental validation was the first task undertaken in order to determine the possibility of applying a CFD tool to exhaust systems. A steady flow simulation was run to predict the exhaust gas flow. Figure 1 and Table 1 show the computational grids and flow analysis conditions, respectively. The model was one of a close-coupled catalyst of a V-6 engine. The general STAR-CD code was used to perform the calculations ([14]). The flow was assumed to be compressible. The conservation equations of mass, momentum, and energy, the transportation equations of turbulence energy, and its dissipation ($k-\epsilon$ turbulence model) were used. The law of the wall was used in the wall boundary. The differencing scheme was upwind.

First, the computational grid size dependency was examined. The computational grid type used in this simulation was all hexahedron as shown in Fig. 1. A steady flow simulation was conducted with different computational grid sizes to examine numerical accuracy and grid size dependency. Figure 2 shows the calculation results for normalized flow coefficients. The larger the computational grid sizes are, the smaller the flow coefficients become. Namely, calculation error increases with a larger grid size. This is because, as the grid size becomes larger, the cross-section area becomes smaller where the section is round. In addition to

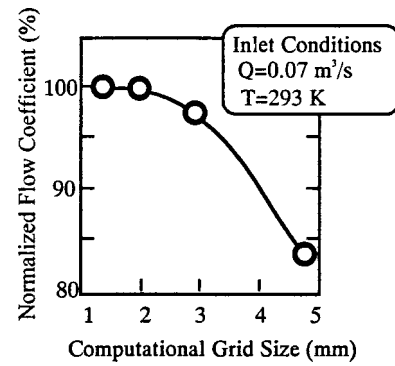


Fig. 2 Computational grid size dependency

that, the law of the wall is not applicable with a large grid size. Therefore, in this simulation, a grid size of about 2 mm was selected taking into account the calculation time. The calculation error was less than 1%, as shown in Fig. 2.

The gas flow distribution at the catalyst inlet (exhaust manifold outlet) was examined to validate the flow prediction qualitatively. A steady flow bench test was conducted using a close-coupled catalyst. An ink injector was placed upstream of the exhaust manifold. Atomized ink was injected into the air and mixed with it. The air mixed with the ink flowed from the exhaust manifold inlet of each cylinder (#2, #4, and #6) in succession. The ink thickness distribution at the catalyst inlet (Fig. 1) was examined.

A steady flow simulation was then conducted using the same inlet air flow volume as in the experiment. It was assumed that the atomized ink concentration in the air was uniform and that the ink thickness at the catalyst inlet would be proportional to the air flow rate. A comparison was made between the measured ink thickness distribution and the calculated velocity distribution.

Figure 3 compares the predicted and measured catalyst inlet gas flow. In the experimental results, the ink thickness was large at the #6 cylinder side when the gas flowed in from the #2 cylinder. In the calculation results under the same conditions, the velocities were large at the #6 cylinder side and their distribution agreed well with the experimental data. In the other two cases (#4 and

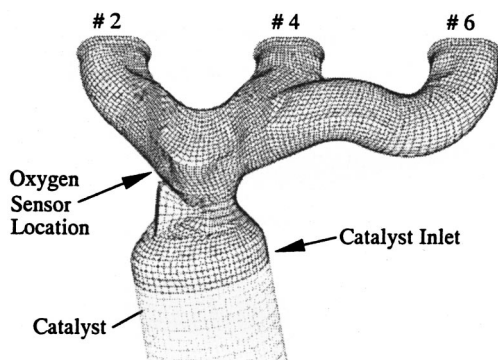


Fig. 1 Computational grids for a close-coupled catalytic converter system

Table 1 Flow analysis conditions

Program	STAR-CD
Flow	Compressible standard $k-\epsilon$
Wall boundary	Law of the wall
Differencing scheme	Upwind

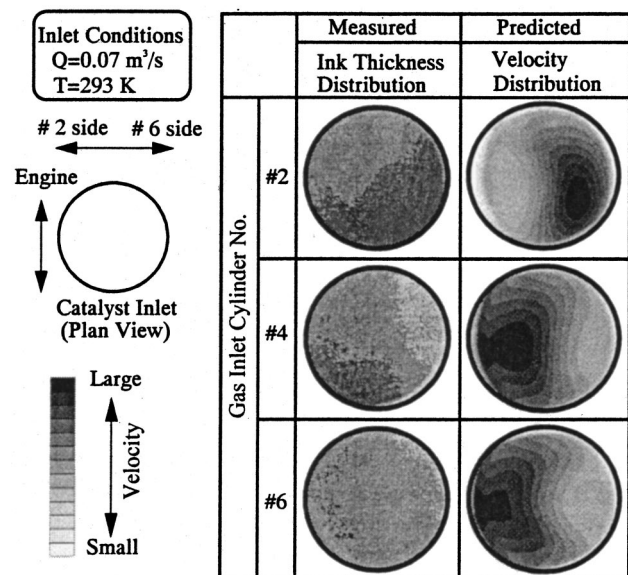


Fig. 3 Comparison of predicted and measured gas flow at catalyst inlet

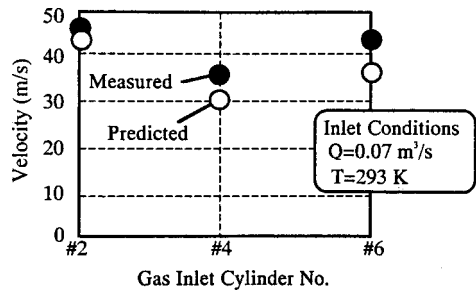


Fig. 4 Comparison of predicted and measured velocities at oxygen sensor

#6), the predicted velocities were large where the ink thickness was large in the experiment. These results confirmed qualitatively the validity of the exhaust gas flow calculation and showed that it is possible to make qualitative predictions of the gas flow in the exhaust manifold by simulation.

Quantitative Validation. A quantitative validation was then conducted by comparing the velocities at the oxygen sensor, which was located at the confluence point of the exhaust manifold (Fig. 1). Again, a steady flow bench test was conducted. The air flowed successively from the exhaust manifold inlet of each cylinder, just as in the qualitative validation. A hot-wire anemometer was placed at the sensor location and the velocities at the sensor top were measured. The computational grids shown in Fig. 1 were used in the calculation. The same inlet air flow volume as in the experiment was applied and the velocity at the sensor top was computed.

Figure 4 compares the predicted and measured velocities at the top of the oxygen sensor. The predicted velocities of the gas from each cylinder tended to agree well with the experimental results. The absolute values of the predicted velocities were in good agreement with the experimental results, though the calculated velocities were a little lower. Because, a grid size of 2 mm was used in this calculation model, the pressure drop was slightly higher than in the experimental results. That is the reason why the predicted velocities were a little lower than the measured ones. These results confirmed quantitatively the validity of the exhaust gas flow calculation, indicating that the gas flow in the exhaust manifold can be predicted quantitatively by simulation.

Oxygen Sensor Sensitivity

In a gasoline engine, lambda feedback control with an oxygen sensor is essential to utilize three-way catalysts effectively by keeping the air-fuel ratio as close to stoichiometric proportions as possible. However, the quantity of fuel injected into each cylinder of a multicylinder engine tends to differ. There is also some dispersion of the air flow volume distribution in each cylinder. For these reasons, the air-fuel ratio is not precisely equal in each cylinder, causing the oxygen concentration in the exhaust gas from each cylinder to differ. In this regard, the oxygen sensor must be placed where it can detect the exhaust gas from each cylinder equally in order to control the overall air-fuel ratio to stoichiometric proportions. In other words, the oxygen sensor must be uniformly sensitive to the exhaust gas from each cylinder. Time-consuming experimental work has been the only way so far to evaluate sensor sensitivities. It takes a lot of trial-and-error experimentation and development time to find the optimum sensor location. An attempt was made to overcome this problem by applying CFD simulation to select the optimum sensor location.

Figure 5 shows an example of the oxygen sensor sensitivities measured experimentally. In the experiment, the fuel injection quantity was forcibly reduced in one cylinder and the overall air-fuel ratio downstream of the confluence point was measured. In the case of sensor 1, sensitivity to the #2 cylinder exhaust gas was

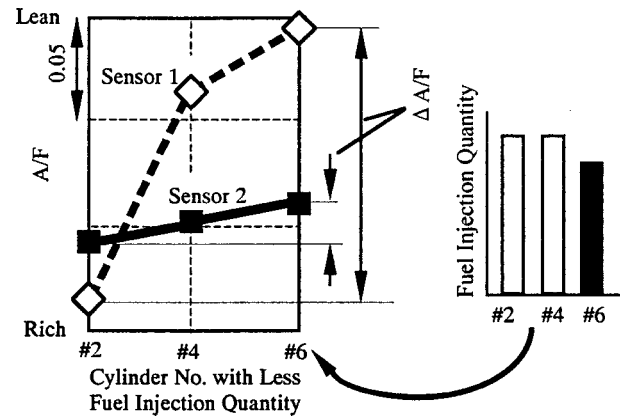


Fig. 5 Oxygen sensor sensitivity

high, indicating that the sensor detected the #2 cylinder exhaust gas more than that from the other cylinders. Hence, it would detect the lean exhaust gas of the #2 cylinder when the quantity of fuel injected into that cylinder was reduced. As a result, the fuel injection quantity would be increased for all three cylinders to control the air-fuel ratio to stoichiometric proportions, resulting in an overall rich air-fuel ratio. On the other hand, the sensor would detect the stoichiometric exhaust gas of the #2 cylinder even when the quantity of fuel injected into the #6 cylinder was reduced. In this case, the fuel injection quantity would not be changed to keep the air-fuel ratio at stoichiometric proportions, thus resulting in an overall lean air-fuel ratio.

As mentioned earlier, the oxygen sensor must be uniformly sensitive to the exhaust gas from each cylinder to ensure effective use of the catalyst. Accordingly, a sensor location that yields a uniform air-fuel ratio must be chosen. Based on a comparison of the experimental results in Fig. 5, the position of sensor 2 would be better.

Oxygen Sensor Sensitivity Prediction by Steady Flow Simulation

First, the possibility of predicting oxygen sensor sensitivity by steady flow simulation was examined. The model used was that of a close-coupled catalyst of a V-6 engine (Fig. 1). In the steady flow simulation, the gas flowed from the exhaust manifold inlet of each cylinder (#2, #4, and #6) in succession. Three different engine operating conditions were selected for making sensitivity predictions. The boundary condition of the simulation was the inlet velocity having an equivalent air flow volume to that of an actual engine. It was assumed that oxygen sensor sensitivity correlates with the exhaust gas flow from each cylinder at the sensor location. Therefore, the exhaust gas velocities from each cylinder at the sensor location were examined.

In comparing the experimental and calculated results, the following indices of sensor sensitivity were used. The index $\Delta A/F_{ave}$ was used for the experimental results. First, A/F_{ave} , the average overall air-fuel ratio for all three cylinders, was calculated by

$$A/F_{ave} = [A/F(\#2) + A/F(\#4) + A/F(\#6)]/3. \quad (1)$$

Then, $\Delta A/F_{ave}$, the deviation from A/F_{ave} of each cylinder was calculated by

$$\Delta A/F_{ave}(\text{cyl.}\#) = [A/F_{ave} - A/F(\text{cyl.}\#)]. \quad (2)$$

Sensor sensitivity increases in proportion to the value of A/F_{ave} .

The index ΔV_{ave} was used for the calculated results. First, the velocity of the exhaust gas from each cylinder at the sensor location was examined. V_{ave} , the average velocity for all three cylinders, was then calculated by

$$V_{ave} = [V(\#2) + V(\#4) + V(\#6)]/3. \quad (3)$$

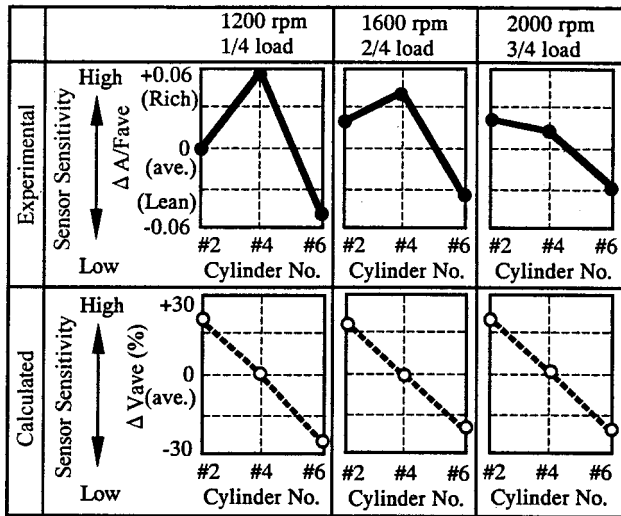


Fig. 6 Comparison of calculated and measured sensor sensitivities

Then, ΔV_{ave} , the normalized deviation from V_{ave} of each cylinder was calculated by

$$\Delta V_{ave}(\text{cyl.}\#) = [V(\text{cyl.}\#) - V_{ave}] / V_{ave} \quad (4)$$

Sensor sensitivity increases in proportion to the value of ΔV_{ave} .

Figure 6 compares the measured and calculated oxygen sensor sensitivities. Under a high load condition, the measured ($\Delta A/F_{ave}$) and calculated (ΔV_{ave}) results showed similar tendencies. However, the tendencies of the calculated sensor sensitivities (ΔV_{ave}), i.e., the gas flow velocities at the sensor location, were almost the same for all three operating conditions. These results suggest that the Reynolds number was large enough in these steady flow calculations and that the similarity law of flow was operating ([15]). On the other hand, the measured sensitivities ($\Delta A/F_{ave}$) of each cylinder varied depending on the engine operating conditions. The results indicate that it is difficult to predict oxygen sensor sensitivities on the basis of steady flow calculations. Since the gas flow in the exhaust manifold is affected by exhaust pulsations, gas flow predictions based on steady flow are not sufficiently accurate.

Pulsation Flow Simulation

A flow calculation procedure that takes into account the gas exchange process is needed to consider the effects of pulsation flow in the exhaust manifold. That requires a model of the entire engine system, including the intake and exhaust systems. However, it would be impractical to simulate the gas flow in the entire engine system with a three-dimensional model. Therefore, a new calculation method, called pulsation flow calculation, has been developed to simulate pulsation flow caused by the gas exchange process. In this pulsation flow simulation, a one-dimensional gas exchange simulation and a three-dimensional exhaust gas flow calculation are combined. An in-house gas exchange simulation code has been adopted for performing one-dimensional calculations and the STAR-CD code is used for three-dimensional calculations.

Figure 7 shows an outline of the pulsation flow simulation method. In the one-dimensional calculation, the entire engine system model is described as a combination of one-dimensional pipes and dimensionless containers. In the three-dimensional calculation, an exhaust system model that includes the exhaust ports, exhaust manifold, catalyst, and defuser is used. Therefore, the boundary conditions are set at both the inlet of the exhaust ports and outlet of the defuser, since the gas flow in the exhaust manifold is largely affected by the configurations of the exhaust ports and the defuser. First, a one-dimensional gas exchange simulation

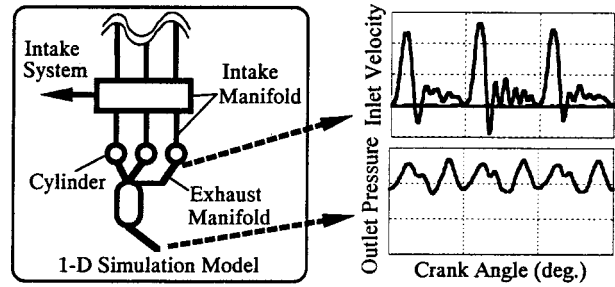


Fig. 7 Simulation method for exhaust gas pulsation due to the gas exchange process

is run to obtain velocity, pressure, temperature, and density data at both the inlet of the exhaust ports and outlet of the defuser for one cycle (720 crank angle degrees). Next, a three-dimensional calculation is executed using the results of the one-dimensional calculation as the boundary conditions.

Experimental Validation of Pulsation Flow Simulation

Experiments were conducted to validate the pulsation flow simulation method. First, the pressures at the oxygen sensor location were compared. In the experiment, a piezoelectric pressure sensor was placed at the oxygen sensor location to measure the change in pressure at each crank angle. Two different engine operating conditions, namely, low and high load conditions, were selected for experimental validation. The computational grids in Fig. 1 were used in the calculations, and a pulsation flow simulation was conducted to compute the pressure at the sensor location.

Figure 8 compares the predicted and measured pressure waveforms at the oxygen sensor location. The predicted peak pressure locations agree well with the experimental data, although the calculated peak pressures are a little smaller. A comparison of the results for the two different load conditions indicates that the measured pressure oscillations are much larger under the high load condition than under the low load condition. The same tendency is observed for the calculated results.

A gas flow visualization was then performed to compare the exhaust gas flow in the close-coupled catalyst. The visualization area was between the exhaust manifold and the catalytic converter, and the flow pattern of the tracer gas bubbles was examined. The predicted flow pattern in the visualization area agreed well with the experimentally measured pattern.

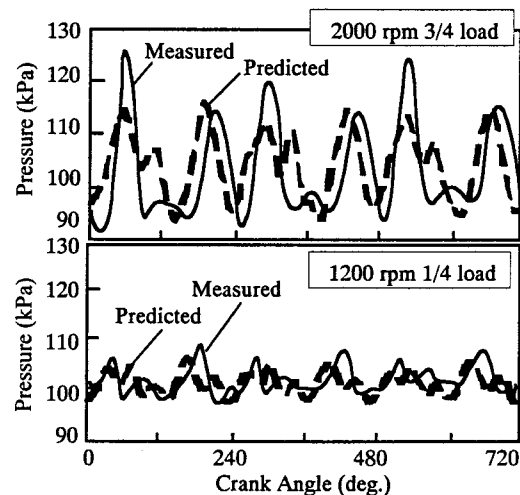


Fig. 8 Comparison of predicted and measured pressure at oxygen sensor

These results confirmed the validity of the pulsation flow simulation method, indicating that the pulsation gas flow caused by the gas exchange process in the exhaust manifold can be predicted by pulsation flow simulation.

Oxygen Sensor Sensitivity Prediction by Pulsation Flow Simulation

The possibility of predicting oxygen sensor sensitivity by pulsation flow simulation was then examined. The model used was that of the close-coupled catalyst of a V-6 engine (Fig. 1), which was employed in the predictions by steady flow simulation. Three different engine operating conditions were again selected for making sensor sensitivity predictions. In the calculation, the exhaust gas from each cylinder was marked to determine which cylinder gas passed the oxygen sensor location.

Figure 9 shows an example of the pulsation flow simulation results for an engine speed of 2000 rpm at a 3/4 load. The figure shows the velocities and concentrations of the exhaust gas from each cylinder at the oxygen sensor location. Due to the high load condition, blow down at an open exhaust valve had a large effect on gas flow. It created a main exhaust gas flow and three velocity peaks in the exhaust gas from each cylinder during one cycle. After the main gas flow passed the sensor location, its gas concentration was dominant, although the reverse flow of the exhaust gas from the previous cylinder also had some effect. The velocities at the sensor location were always larger than 1 m/s, which is the minimum velocity for the sensor to detect the oxygen concentration in the gas. Therefore, it is presumed that the sensor was detecting the oxygen concentration constantly. In this regard, the gas concentrations of each cylinder were analyzed.

In comparing the experimental and calculated results, the following indices of sensor sensitivity were used, as in the predictions by steady flow simulation. The index $\Delta \text{CONC}_{\text{ave}}$ was used

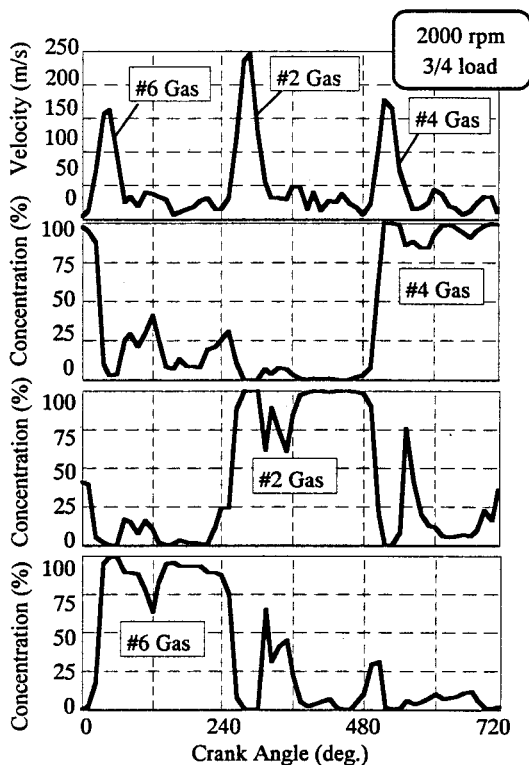


Fig. 9 Calculated velocities and gas concentrations at oxygen sensor

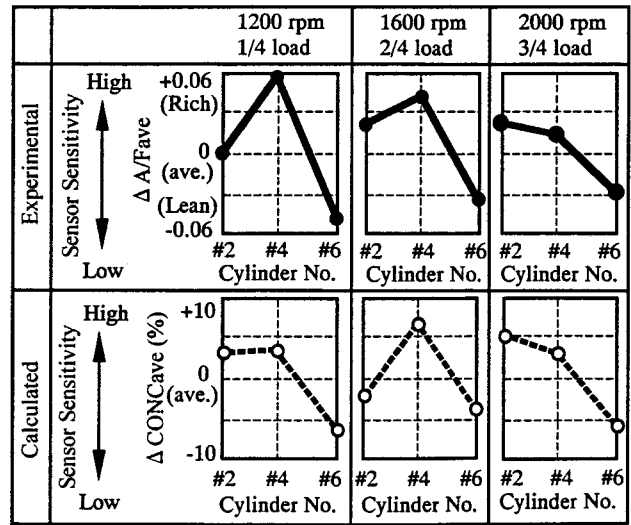


Fig. 10 Comparison of calculated and measured sensor sensitivities

for the calculated results. First, CONC , the average concentration of the exhaust gas from each cylinder at the sensor location in one cycle, was calculated by

$$\text{CONC}(\text{cyl.}\#) = \sum_{i=1}^{720} \text{concentration}(\text{cyl.}\#) / 720 \quad (5)$$

Then, CONC_{ave} , the average concentration for all three cylinders, was calculated by

$$\text{CONC}_{\text{ave}} = [\text{CONC}(\#2) + \text{CONC}(\#4) + \text{CONC}(\#6)] / 3. \quad (6)$$

Next, $\Delta \text{CONC}_{\text{ave}}$, the normalized deviation from CONC_{ave} of each cylinder, was calculated by

$$\text{CONC}_{\text{ave}}(\text{cyl.}\#) = [\text{CONC}(\text{cyl.}\#) - \text{CONC}_{\text{ave}}] / \text{CONC}_{\text{ave}}. \quad (7)$$

Sensor sensitivity increases in proportion to the value of $\Delta \text{CONC}_{\text{ave}}$.

The index $\Delta A/F_{\text{ave}}$ was used for the experimental results, as in the prediction by steady flow simulation (Fig. 6).

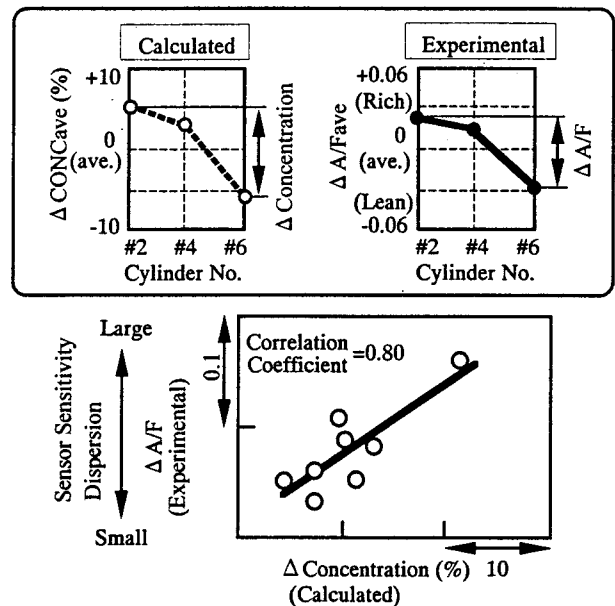


Fig. 11 Correlation between calculated and experimental sensor sensitivity dispersion

Figure 10 compares the experimental and calculated oxygen sensor sensitivities. As mentioned earlier, it is assumed that sensor sensitivity increases in proportion to the exhaust gas concentration. The experimental ($\Delta A/F_{ave}$) and calculated ($\Delta CONC_{ave}$) sensor sensitivities show nearly the same tendencies in all three cases. These results confirm the possibility of predicting oxygen sensor sensitivities by pulsation flow simulation.

The oxygen sensor sensitivity predictions were then validated quantitatively. Figure 11 shows dispersion indices of the experimental and calculated oxygen sensor sensitivities. The index Δ concentration was used for the calculated results. The Δ concentration was calculated by

$$\Delta \text{Concentration} = \Delta CONC_{ave}(\text{max}) - CONC_{ave}(\text{min}). \quad (8)$$

The index $\Delta A/F$ was used for the experimental results and was calculated by

$$\Delta A/F = A/F_{ave}(\text{max}) - A/F_{ave}(\text{min}). \quad (9)$$

The correlation between the dispersion indices of the calculated and experimental oxygen sensor sensitivities is also shown in Fig. 11. A relatively strong correlation is seen between the calculated (Δ concentration) and experimental results ($\Delta A/F$). The coefficient of correlation is approximately 0.8. These results verify that dispersion of sensor sensitivities can be predicted by simulation. This means that the optimum sensor location for uniform sensor sensitivity can be selected on the basis of calculations.

Selection of Optimum Oxygen Sensor Location

The optimum oxygen sensor location was selected using the foregoing simulation method. The optimum location was chosen among four possible positions allowed by the layout of the exhaust manifold in Fig. 1. Figure 12 shows the reduced sensor sensitivity dispersion at the optimum location. Sensor sensitivity dispersion indices were averaged for several engine operating conditions both in the calculation and in the experiment. Based on the calculated results, sensor location B was selected since it showed the smallest dispersion of sensor sensitivities among all the locations. The experimental data indicate that the dispersion of sensor sensitivities was reduced by 60% at location B. These results thus verify the possibility of selecting the optimum location for the oxygen sensor in the exhaust manifold on the basis of calculations.

Factor Governing Oxygen Sensor Sensitivity

An analysis was made of the factors governing oxygen sensor sensitivities. As seen in Fig. 10, sensor sensitivities to the exhaust gas from each cylinder ($\Delta A/F_{ave}$) vary depending on the engine operating conditions. It is thought that sensor sensitivities have a relatively strong correlation with the gas concentrations at the sensor location. Therefore, the gas concentrations at the sensor location were thoroughly analyzed.

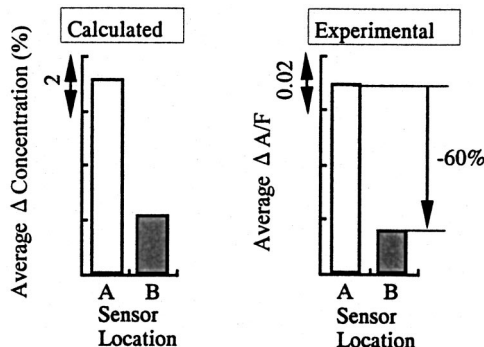


Fig. 12 Selection of optimum oxygen sensor location based on calculations

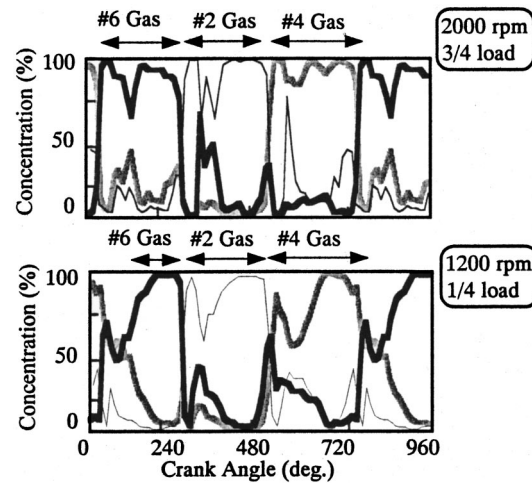


Fig. 13 Comparison of gas concentration from each cylinder at oxygen sensor

Figure 13 shows the exhaust gas concentration of each cylinder at the oxygen sensor location for one cycle. The period of time that the exhaust gas from each cylinder was present at the sensor location was investigated. Under the high load condition, the exhaust gas from each cylinder was present for nearly the same length of time. On the other hand, under the low load condition, the #4 cylinder exhaust gas was present for a longer period of time while the #6 cylinder exhaust gas was present for a shorter duration. This explains why the average concentration of the #4 cylinder exhaust gas was higher and that of the #6 cylinder was lower under the low load condition.

This difference originates in the shape of the exhaust manifold runners. The runner length from the exhaust port to the oxygen sensor location is different for each cylinder, which means the exhaust gas from each cylinder travels a different distance. For example, the exhaust manifold runner of the #6 cylinder is longer than that of the other two cylinders. Hence, it takes more time for the #6 cylinder exhaust gas to reach the sensor location than the exhaust gas from the other two cylinders, especially when the gas velocities become smaller under the low load condition. Therefore, in the low load condition, the #2 cylinder exhaust gas (#2 fires after #6) arrives soon after the #6 cylinder gas reaches the sensor location. Hence, the #6 cylinder gas stays at the sensor location for a shorter period of time. On the other hand, the #4 cylinder gas stays longer at the sensor location, since it takes more time for the #6 cylinder gas to reach the sensor. Therefore, it is assumed that the change in oxygen sensor sensitivities depending on the engine operating conditions is caused by the different lengths of the cylinder runners.

Uniform Oxygen Sensor Sensitivity

A way of achieving uniform oxygen sensor sensitivities is discussed here in reference to the foregoing results. It was found that the factors governing sensor sensitivity are the gas flow velocity and the average concentration of the exhaust gas from each cylinder at the sensor location in one cycle. The first condition is that the exhaust gas from each cylinder must be present at the sensor location in an equal concentration. Therefore, the oxygen sensor must be placed where the exhaust gases from all cylinders pass equally. Secondly, the exhaust gas from each cylinder must be present at the sensor location in the same time period to achieve uniform sensitivity. This means that the runner lengths from the exhaust port to the oxygen sensor location must be equal for all cylinders.

Figure 14 shows the effect of the cylinder runner length on the period of gas presence for two different engine operating condi-

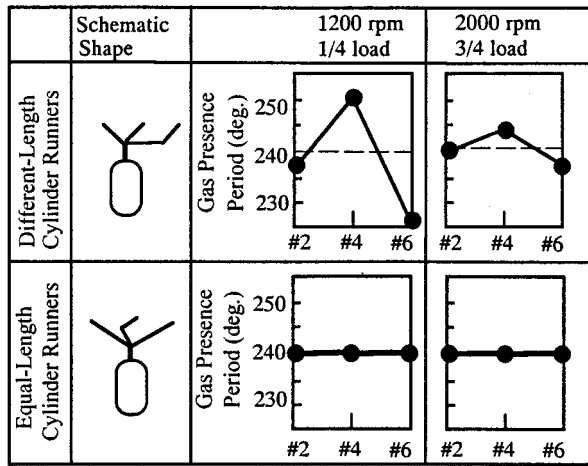


Fig. 14 Effect of cylinder runner length on period of gas presence

tions. These results were obtained by a one-dimensional gas exchange simulation. For the manifold with equal-length cylinder runners, the period of gas presence was equal for all three cylinders under both conditions. This indicates it is possible to achieve uniform sensor sensitivities when the oxygen sensor is placed where exhaust gas from each cylinder passes equally. On the other hand, for the manifold with different-length cylinder runners, the period of gas presence differed for each cylinder under both operating conditions. That would make it difficult to obtain uniform oxygen sensor sensitivities under all operating conditions.

With some engine types, it is difficult to adopt equal-length cylinder runners due to layout limitations. Therefore, for such engines, it is more practical to apply a new lambda feedback control method than to use hardware approaches, such as changing the exhaust manifold shape or using several oxygen sensors. In addition, V-8 engines with an eccentric ignition timing require a new lambda control method. Figure 15 shows the ignition timing and sensor sensitivities of a V-8 engine. The interval between one ignition timing and the next differs for each cylinder when each bank has its own lambda control. For example, in the left bank, the #8 cylinder has the longest interval to the next ignition timing of all the cylinders. The experimental results in the figure show that the oxygen sensor was most sensitive to the exhaust gas from the #8 cylinder as was expected. These results indicate that the periods of gas presence are not always equal for every cylinder in the case of an exhaust manifold with different-length cyl-

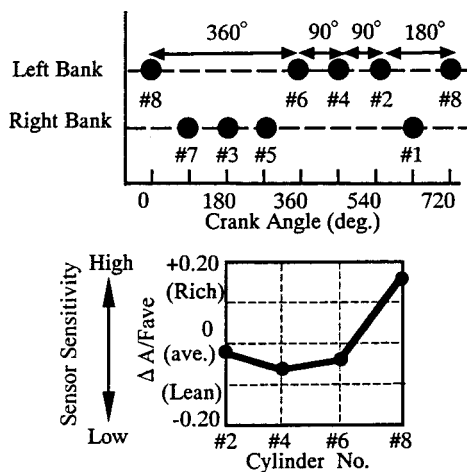


Fig. 15 Ignition timing and sensor sensitivity of V-8 engine

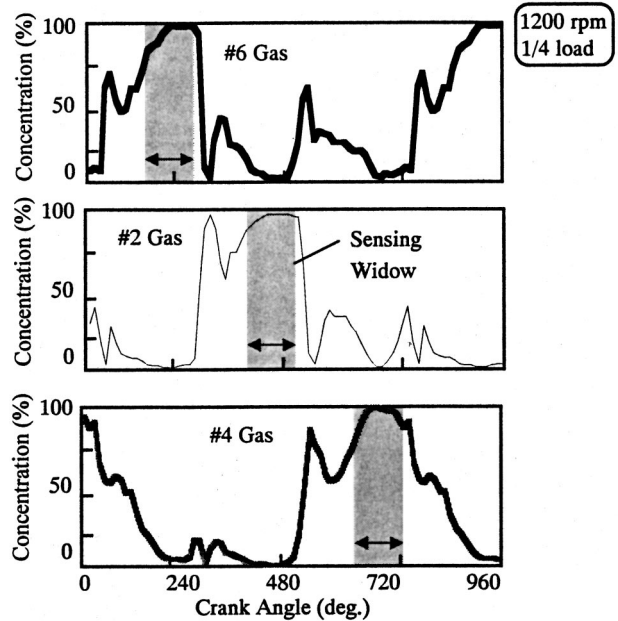


Fig. 16 Lambda control method for an exhaust manifold with different-length cylinder runners

inder runners or a V-8 engine. Therefore, it is difficult to achieve uniform sensor sensitivities with the present lambda control method.

A new lambda control method is therefore needed to detect the oxygen concentration of the exhaust gas from each cylinder in the same time period. It could be achieved by providing a window for oxygen concentration detection in order to cope with the difference in the period of gas presence depending on the engine operating conditions. Figure 16 illustrates a new lambda control method. The figure shows the maximum concentrations of each cylinder gas at the oxygen sensor location under a low load condition. The period of gas presence is not equal for each cylinder due to the different cylinder runner lengths. The new lambda control method provides a window for oxygen concentration detection in order to cope with differences in the period of gas presence. Namely, at high loads, the oxygen sensor signal can be used for lambda control at all times, since the period of gas presence is sufficiently equal for all cylinders, as shown in Fig. 13. On the other hand, at low loads, the oxygen sensor signal would be used when the exhaust gas from each cylinder passes the sensor location, since the exhaust gas concentrations of each cylinder become sufficiently high. In this way, the oxygen sensor could detect the oxygen concentration of the exhaust gas from each cylinder equally even if the period of gas presence differs from one cylinder to another.

The detection timing, which varies depending on the engine operating conditions, could be determined on the basis of pulsation flow simulation results, as indicated in Fig. 16. Namely, an optimum window timing that enables detection of each cylinder gas for an equal time period can be estimated by pulsation flow simulation. In this way, the necessary control parameters for the new lambda control method can be obtained even in the design stage.

As explained here, this lambda feedback control method with a window for oxygen concentration detection would allow equal detection of the oxygen concentration in the exhaust gas from each cylinder for an exhaust manifold with different-length cylinder runners. As a result, it would facilitate more precise air-fuel ratio control to stoichiometric proportions.

In addition to being applicable to an exhaust manifold with different-length cylinder runners, the new lambda feedback con-

trol method also has the potential to control the air-fuel ratio more precisely. With this new lambda control method, the oxygen concentration of each cylinder gas can be detected separately and the air-fuel ratio of each cylinder can be measured. Therefore, the fuel injection quantity of each cylinder can be controlled separately. In that case, the overall air-fuel ratio can be controlled to stoichiometric proportions even if the flow rates of the injectors vary. Further work will be done to clarify the control logic of this new lambda control method for production engine application.

Conclusion

A multidimensional computational fluid dynamics (CFD) tool has been applied to analyze the exhaust system of a gasoline engine. With the aim of reducing emissions, the gas flow around the oxygen sensor was analyzed to improve lambda control using an oxygen sensor. The following results were obtained in this study.

1. A new multidimensional simulation method, called pulsation flow simulation, has been developed. In this simulation, a one-dimensional gas exchange simulation and a three-dimensional exhaust gas flow calculation are combined to simulate gas flow pulsations caused by the gas exchange process.
2. Pulsation flow simulation makes it possible to predict unsteady gas flow caused by the gas exchange process in the exhaust manifold.
3. It was found that the principal factor governing sensor sensitivity is the average concentration of the exhaust gas from each cylinder at the sensor location in one cycle.
4. By examining the exhaust gas concentration dispersion at the oxygen sensor location, the optimum oxygen sensor location in the exhaust manifold can be selected on the basis of calculations.
5. The effect of an exhaust manifold with equal-length cylinder runners on achieving uniform oxygen sensor sensitivities was made clear.
6. A new lambda feedback control method for an exhaust manifold with different-length cylinder runners was proposed.
7. With this new lambda feedback control method, the detection timing, which varies depending on the engine operating conditions, can be determined efficiently on the basis of pulsation flow simulation results.

Nomenclature

- A/F ratio = air/fuel ratio
 A/F_{ave} = average A/F ratio for all cylinders
 $\Delta A/F_{ave}$ = deviation from A/F_{ave}

- $\Delta A/F$ = dispersion of $\Delta A/F_{ave}$
 CONC = average gas concentration in one cycle
 $CONC_{ave}$ = average CONC for all cylinders
 $\Delta CONC_{ave}$ = normalized deviation from $CONC_{ave}$
 Δ Concentration = dispersion of $\Delta CONC_{ave}$
 V = flow velocity at the sensor location
 V_{ave} = average V
 ΔV = normalized deviation from V_{ave}

References

- [1] Aita, S., Tabbal, A., Munck, G., Fujiwara, K., Hongoh, H., Tamura, E., and Obana, S., 1990, "Numerical Simulation of Port-Valve-Cylinder Flow in Reciprocating Engines," SAE Paper No. 900820.
- [2] Godrie, P., and Zellat, M., 1994, "Simulation of Flow Field Generated by Intake Port-Valve-Cylinder Configurations—Comparison with Measurements and Applications," SAE Paper No. 940521.
- [3] Naitoh, K., Fujii, H., Urushihara, T., Takagi, Y., and Kuwahara, K., 1990, "Numerical Simulation of the Detailed Flow in Engine Ports and Cylinder," SAE Paper No. 900256.
- [4] Trigui, N., Affes, H., and Kent, J. C., 1994, "Use of Experimentally Measured In-Cylinder Flow Field at IVC as Initial Conditions for CFD Simulation of Compression Stroke in I.C. Engine—A Feasibility Study," SAE Paper No. 940280.
- [5] Khalighi, B., El Tahry, S. H., Haworth, D. C., and Huebler, M. S., 1995, "Computation and Measurement of Flow and Combustion in a Four-Valve Engine with Intake Variations," SAE Paper No. 950287.
- [6] Kuo, T.-W., and Reuss, D. L., 1995, "Multidimensional Port-and-Cylinder Flow Calculations for the Transparent-Combustion-Chamber Engine," *Engine Modeling ICE-Vol. 23*, ASME, New York.
- [7] Lai, M.-C., Kim, J.-Y., Cheng, C.-Y., Chui, G., and Pakko, J. D., 1991, "Three-Dimensional Simulations of Automotive Catalytic Converter Internal Flow," SAE Paper No. 910200.
- [8] Wendland, D. W., Kreucher, J. E., and Andersen, E., 1995, "Reducing Catalytic Converter Pressure Loss with Enhanced Inlet-Header Diffusion," SAE Paper No. 952398.
- [9] Kuo, T.-W., and Khalighi, B., 1995, "Numerical Study on Flow Distribution in T-Junctions and a Comparison With Experiment," *Engine Modeling, ICE-Vol. 23*, ASME, New York.
- [10] Park, S.-B., Kim, H.-S., Cho, K.-M., and Kim, W.-T., 1998, "An Experimental and Computational Study of Flow Characteristics in Exhaust Manifold and CCC (Close-Coupled Catalyst)," SAE Paper No. 980128.
- [11] Cho, Y.-S., Kim, D.-S., Han, M., Joo, Y., Lee, J.-H., and Min, K.-D., 1998, "Flow Distribution in a Close-Coupled Catalytic Converter," SAE Paper No. 982552.
- [12] Takeyama, S., Ishizawa, S., Yoshikawa, Y., and Takagi, Y., 1987, "Gas Exchange Simulation Model for Improving Charging Efficiency of 4-Valve Internal Combustion Engine," I.M.E. the First Conference of the Computers in Engine Technology.
- [13] Hasegawa, Y., Akazaki, S., Komoriya, I., Maki, H., Nishimura, Y., and Hirota T., 1994, "Individual Cylinder Air-Fuel Ratio Feedback Control Using an Observer," SAE Paper No. 940376.
- [14] *STAR-CD Version 3.05 Manual*, 1998, Computational Dynamics, Ltd.
- [15] Chikahisa, T., and Murayama, T., 1990, "Theoretical and Experimental Study on Combustion Similarity for Different Size Diesel Engines," *COMODIA*, **90**, pp. 571–576.

Manifold Gas Dynamics Modeling and Its Coupling With Single-Cylinder Engine Models Using Simulink

G. Q. Zhang
D. N. Assanis

Department of Mechanical Engineering
and Applied Mechanics,
University of Michigan,
Ann Arbor, MI 48109-2121

A flexible model for computing one-dimensional, unsteady manifold gas dynamics in single-cylinder spark-ignition and diesel engines has been developed. The numerical method applies an explicit, finite volume formulation and a shock-capturing total variation diminishing scheme. The numerical model has been validated against the method of characteristics for valve flows without combustion prior to coupling with combustion engine simulations. The coupling of the gas-dynamics model with single-cylinder, spark-ignition and diesel engine modules is accomplished using the graphical MATLAB-SIMULINK environment. Comparisons between predictions of the coupled model and measurements shows good agreement for both spark ignition and diesel engines. Parametric studies demonstrating the effect of varying the intake runner length on the volumetric efficiency of a diesel engine illustrate the model use. [DOI: 10.1115/1.1560708]

Introduction

Fluid flow processes play an essential role in determining the volumetric efficiency and therefore the performance of an internal combustion engine throughout its operating range. Traditionally, engines have been tuned experimentally to achieve peak torque at a target speed, [1,2]. However, present and future engines increasingly utilize multivalved heads, variable valve events, and dual-tuned intake systems to gain maximum torque at both low and high-speed operation. Since the additional variables involved in designing an optimum system increases the number of experiments, the use of computer simulations to aid in manifold design is imperative. Comprehensive simulation programs should include the prediction of pressure waves in intake and exhaust systems, and should be able to handle various engine configurations, such as spark or compression ignited, four-stroke or two-stroke, etc.

While three-dimensional effects can be important in manifold gas dynamics, [3], most practical simulations of intake and exhaust manifolds are based on one-dimensional compressible flow equations and ideal gas behavior. The classical method of attack to solve the one-dimensional unsteady governing equations is through the use of the method of characteristics (MOC), e.g., [4–10]. With this technique, the partial differential equations are transformed into ordinary differential equations that apply on characteristic lines. The transformed equations are commonly solved numerically by linear interpolation onto a rectangular mesh. Although the MOC approach can yield exact solutions in simpler problems, its numerical accuracy is first order in both space and time and it requires the use of a large number of computational points to resolve short wavelength signals, [11].

As an alternative to the MOC approach, numerical techniques based on either the finite difference method (FDM) or the finite volume method (FVM) are being increasingly used due to their higher order accuracy and flexibility. A comprehensive review of numerical schemes that have been used to solve one-dimensional engine gas dynamic problems is presented in [12]. Only select representative approaches will be briefly summarized here. For instance, Lakshminarayanan et al. [13] presented an FDM ap-

proach based on central spatial differences and an explicit Runge-Kutta temporal integration. Takizawa et al. [14] used a two-step, explicit Lax-Wendroff FDM procedure to model the gas exchange processes. However, the two-step Lax-Wendroff method requires the use of artificial viscosity to prevent nonphysical short wavelength oscillations of large gradients and thereby reverts to a first order scheme. Meisner and Sorenson [15] presented an FDM based on the two-step explicit MacCormack scheme, [16].

Chapman et al. [11] presented an explicit method for the solution of the gas dynamic equations in the inlet and exhaust system based on the FRAM (filtering remedy and methodology) algorithm of Chapman [17]. This procedure allows the use of a higher-order finite difference scheme in the regions where the flow is smooth, and introduces a minimal amount of dissipation only in those regions where a higher-order algorithm would produce non-physical oscillations. Morel et al. [18] presented an explicit FVM approach using a staggered mesh and a quasi-second-order donor cell representation. Peters and Gosman [19] presented an unconditionally stable, implicit, FVM technique using the noniterative PISO algorithm, a staggered grid, and a second-order hybrid upwind/central differencing scheme.

Kirkpatrick et al. [20] presented an experimental evaluation of various one-dimensional computer codes for the simulation of unsteady gas flow through engines using (i) both homentropic and nonhomentropic MOC [10]; and (ii) FDM with two-step Lax-Wendroff scheme with flux correction transport, [21–23] or FDM with Harten-Lax-VanLeer upstream difference technique, [24]. As expected, when there are significant entropy changes, such as in exhaust flows, the MOC is less accurate. The various FDM approaches had comparable accuracy and were in good agreement with measurements. On the other hand, Morel et al. [25] also showed that their FVM approach compared well with measurements in a 2.2 liter Chrysler engine. Peters and Gosman [19] have concluded that while both FDM and FVM methods can compute manifold flows within 95% accuracy and are in principle equally good, the FVM scheme makes it easier to ensure conservation of all variables.

The objective of the present effort is to adopt a numerical method for solving the unsteady one-dimensional manifold gas dynamics equations with fast time-marching characteristics for nonshock problems, and with good shock-capturing ability for problems with discontinuity. While there are generally no shock

Contributed by the Internal Combustion Engine Division of THE AMERICAN SOCIETY OF MECHANICAL ENGINEERS for publication in the ASME JOURNAL OF ENGINEERING FOR GAS TURBINES AND POWER. Manuscript received by the ICE Division April 1999; final revision received by the ASME Headquarters November 2002. Associate Editor: H. Nelson.

phenomena in the intake process, shocks may form during the exhaust process, especially in exhaust pipes with diffusers. Classical shock capturing schemes which apply the same numerical algorithm throughout the flow field, tend to either diffuse discontinuities, if first-order accurate, or give rise to spurious oscillations in their vicinity, if second-order accurate [12]. In order to best capture discontinuities, several total variation diminishing TVD schemes [26–31] have recently been applied to the solution of engine manifold gas dynamic problems, [12,32]. In general, such TVD schemes use a higher order scheme as much as possible in the smooth region, while adding sufficient dissipation in the localized sharp gradient regions to damp any possible numerical oscillations. Considering tradeoffs between robustness, accuracy, and computational intensity, we have implemented an explicit FVM method using the (TVD) scheme of Chakravarthy and Osher [26]. The explicit form of the TVD scheme has first-order accuracy in time and third-order accuracy in space. For ease of implementation of the higher-order scheme, a collocated (rather than staggered) grid arrangement is used.

An important goal of our work is to couple the gas dynamic model with comprehensive, thermodynamic engine cycle simulations. In order to increase user-friendliness and be able to couple with different engine models (four-stroke or two-stroke, spark-ignition or diesel, etc.) without reprogramming, the graphical programming environment MATLAB-SIMULINK has been adopted. Our manifold gas dynamics model is converted into a module within the MATLAB-SIMULINK environment and connected with single-cylinder spark-ignition or diesel engine modules, also implemented within the same environment. This approach marries the accuracy features of coupled thermodynamic and gas dynamic models with the symbolic capabilities of a graphical environment to achieve a high fidelity, flexible, reconfigurable engine simulation. Furthermore, the extension of the single-cylinder engine-gas dynamics modules to multicylinder simulation can be readily accomplished with the aid of the graphical programming environment, [33].

This paper is arranged as follows. First, the numerical method for solving the one-dimensional manifold gas dynamic equations is presented. Next, the method is validated against MOC solutions for simple pipe problems without combustion. Subsequently, the manifold model is coupled with SI and diesel engine cycle simulation modules using MATLAB-SIMULINK. Finally, validation and illustrative parametric studies are conducted using the coupled manifold dynamics and engine codes for both SI and diesel engines. Hence, the manifold gas dynamics effects on intake port pressure, exhaust port pressure, cylinder pressure, and volumetric efficiency are explored.

Manifold Gas Dynamic Model

The governing equations to be solved are the quasi-one-dimensional Euler equations. Quasi-one-dimensional means that the area along the flow direction may change. If the area is constant, A will be canceled from Eq. (1).

$$\begin{aligned} \frac{\partial(\rho A)}{\partial t} + \frac{\partial(\rho u A)}{\partial x} &= 0 \\ \frac{\partial(\rho u A)}{\partial t} + \frac{\partial(\rho u^2 A)}{\partial x} &= -A \frac{\partial p}{\partial x} \\ \frac{\partial(\rho e_t A)}{\partial t} + \frac{\partial(\rho u e_t A)}{\partial x} &= - \frac{\partial(p u A)}{\partial x} \end{aligned} \quad (1)$$

where

$$\begin{aligned} e_t &= C_v T + 0.5u^2 \\ p &= \rho RT = \rho(\gamma - 1)(e_t - 0.5u^2) \end{aligned}$$

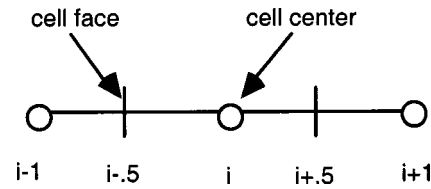


Fig. 1 Cell center and cell faces

The numerical method adopted to solve the set of Eqs. (1) is the finite volume method (FVM) using the collocated grid arrangement of Fig. 1, i.e., all variables (ρ, u, p, e_t) are stored in the cell centers.

The discretized FVM form for the system of Eqs. (1) is

$$\begin{aligned} \frac{(\rho A)_i^{n+1} - (\rho A)_i^n}{\Delta t} + \frac{(F_{i+0.5}^n - F_{i-0.5}^n)}{\Delta x} &= 0 \\ \frac{(\rho u A)_i^{n+1} - (\rho u A)_i^n}{\Delta t} + \frac{(G_{i+0.5}^n - G_{i-0.5}^n)}{\Delta x} &= A_i \frac{p_{i-1} - p_{i+1}}{2\Delta x} \\ \frac{(\rho e_t A)_i^{n+1} - (\rho e_t A)_i^n}{\Delta t} + \frac{(H_{i+0.5}^n - H_{i-0.5}^n)}{\Delta x} \\ &= u_{i-0.5} \frac{(p A)_i + (p A)_{i-1}}{2\Delta x} - u_{i+0.5} \frac{(p A)_i + (p A)_{i+1}}{2\Delta x}. \end{aligned} \quad (2)$$

The cell face fluxes are calculated according to the TVD scheme of Chakravarthy and Osher [26] which uses a second-order central difference scheme for the high-order flux and a first-order upwind scheme for the low-order flux, weighted with a flux limiter function:

$$F_{i+0.5}^{CO} = F_{i+0.5}^{FOU} + \phi(r)[F_{i+0.5}^{CN} - F_{i+0.5}^{FOU}]. \quad (3)$$

The ratio r is defined as

$$\begin{aligned} r &= \frac{u_{i+0.5} - \sigma \Delta_{i+0.5}}{u_{i+0.5} \Delta_{i+0.5}} \\ \sigma &= \text{sign}(u_{i+0.5}) \end{aligned} \quad (4)$$

and the limiter function $\phi(r)$ is

$$\phi(r) = \frac{3 - \eta}{4} \min \left(i \text{ mod } \left(\frac{r}{\omega}, 1 \right) + \frac{1 + \eta}{4} \min \left(i \text{ mod } (1, r\omega) \right) \right) \quad (5)$$

where ω is a compressive parameter defined as

$$1 \leq \omega \leq \frac{3 - \eta}{1 - \eta}. \quad (6)$$

The spatial accuracy of the scheme is controlled by the parameter η , which may take one of the following values:

$$\begin{aligned} \eta = -1 & \text{ fully upwind scheme} \\ \eta = \frac{1}{3} & \text{ third-order scheme} \\ \eta = \frac{1}{2} & \text{ second-order scheme} \\ \eta = 1 & \text{ central difference.} \end{aligned}$$

A segregated solution approach [34] is used to solve the discretized set of Eqs. (2), i.e., the three equations are decoupled and solved sequentially. In order to be able to use a collocated grid in conjunction with the segregated approach, the cell face velocity $u_{i+0.5}$ is calculated using nonlinear (NLI) cell face interpolation.

By relating the cell face velocity to *adjacent* pressures, “checker-board” pressure oscillations are avoided [3,34]. The appropriate NLI expression is

$$u_{i+.5}^{n+1} = u_{i+.5}^n + \Delta t \left(\frac{1}{\rho_{i+.5}} \frac{p_i - p_{i+1}}{\Delta x} - u^+ \left[\frac{u_{i+.5}^n - u_i^n}{.5\Delta x} \right] - u^- \left[\frac{u_{i+1}^n - u_{i+.5}^n}{.5\Delta x} \right] \right) \quad (7)$$

where

$$u^+ = \frac{u_{i+.5} + |u_{i+.5}|}{2} \quad \text{and} \quad u^- = \frac{u_{i+.5} - |u_{i+.5}|}{2}.$$

An explicit scheme is used for time marching; the time step is limited by the CFL criterion:

$$\Delta t \leq \frac{\Delta x}{a + |u|} \quad (8)$$

where a is the speed of sound, $a = \sqrt{kRT}$.

Boundary Conditions

Typical one-dimensional gas dynamic problems are illustrated in Fig. 2. In Fig. 2(a), a pipe exposed to an open end is connected to a single cylinder through a valve (partially open) end. The pipe can be either intake or exhaust, depending on the cylinder release pressure. If the cylinder pressure is higher than the open end pressure, the pipe is the exhaust one, otherwise, it becomes an intake one. Figure 2(b) shows a cylinder discharge process through a nozzle with a constant area less than the pipe’s cross-sectional area. Figure 2(c) combines the nozzle end with the intake/exhaust pipe. For all the above one-dimensional problems, there are essentially two types of boundary conditions, one applying to the open end, and the other for the partially open end.

Open End. The boundary condition of Lakshminarayanan [13] is adopted here for flows into and out of the manifold, as follows:

If fluid flows into the manifold ($P_p < P_o$):

$$\begin{aligned} P_{\text{end}} &= P_p, \\ u_{\text{end}} &= a_o \sqrt{\frac{2}{k-1} \left[1 - \left(\frac{P_{\text{end}}}{P_o} \right)^{(k-1)/k} \right]}, \\ T_{\text{end}} &= T_o - \frac{k-1}{2kR} u_{\text{end}}^2, \\ \rho_{\text{end}} &= \frac{P_{\text{end}}}{RT_{\text{end}}}. \end{aligned} \quad (9a)$$

If fluid flows out of the manifold ($P_p > P_o$):

$$\begin{aligned} P_{\text{end}} &= P_o, \quad u_{\text{end}} = u_p, \\ T_{\text{end}} &= T_p, \quad \rho_{\text{end}} = \rho_p. \end{aligned} \quad (9b)$$

Partially Open End. Benson’s constant pressure model [10] is adopted for flows between the manifold and the cylinder, as follows:

For flow out of the manifold into the cylinder ($P_{\text{cyl}} < P_p$):

$$\left(\frac{u_{\text{end}}}{a_{\text{end}}} \right)^2 = \frac{2}{k-1} \times \frac{\pi^2}{\frac{\pi^{4/(k-1)}}{\phi^2} - 1} \quad (10a)$$

where

$$\phi = \frac{A_v}{A_p}, \quad \pi = \left(\frac{P_p}{P_{\text{cyl}}} \right)^{(k-1)/2k} \quad (10b)$$

When the flow becomes choked i.e.,

$$P_{\text{cyl}}/P_p < \left(\frac{2}{k+1} \right)^{k/(k-1)}$$

then

$$\frac{u_{\text{end}}}{a_{\text{end}}} = \phi \left(\frac{a_v}{a_{\text{end}}}_{cr} \right)^{(k+1)/(k-1)} \quad (10c)$$

and $(a_v/a_{\text{end}})_{cr}$ is related to ϕ by the following relation:

$$\phi^2 = \left\{ \frac{k+1}{k-1} - \frac{2}{k-1} \left(\frac{a_{\text{end}}}{a_v} \right)_{cr}^2 \right\} \left(\frac{a_{\text{end}}}{a_v} \right)_{cr}^{4/(k-1)}. \quad (10d)$$

For flow into the manifold from the cylinder ($P_{\text{cyl}} > P_p$):

$$\frac{\phi}{\pi} \left\{ \frac{2}{k-1} \left(\frac{1}{\pi^2} - 1 \right) \right\}^{0.5} = \frac{\frac{u_{\text{end}}}{a_{\text{end}}}}{1 - \frac{k-1}{2} \left(\frac{u_{\text{end}}}{a_{\text{end}}} \right)^2} \quad (11a)$$

$$P_{\text{end}} = P_{\text{end}-1},$$

$$T_{\text{end}} = T_{\text{end}-1}, \quad \rho_{\text{end}} = \frac{P_{\text{end}}}{RT_{\text{end}}}. \quad (11b)$$

When the flow becomes choked, i.e.,

$$\frac{P_p}{P_{\text{cyl}}} < \left(\frac{2}{k+1} \right)^{k/(k-1)},$$

the velocity u_{end} is determined by

$$\pi^{2k/(k-1)} = \phi \left(\frac{2}{k+1} \right)^{(k+1)/2(k-1)} \left(\frac{1 - \frac{k-1}{2} \left(\frac{u_{\text{end}}}{a_{\text{end}}} \right)^2}{\frac{u_{\text{end}}}{a_{\text{end}}}} \right)^2. \quad (11c)$$

Validation of Manifold Gas Dynamics Model

In order to validate the accuracy of the manifold gas dynamics model prior to coupling with engine simulation codes, our numerical predictions are compared against MOC computations for three test cases of the type illustrated in Fig. 2.

Gradual Discharge From a Cylinder. The first test case deals with predicting a gradual discharge process from a cylinder through a nozzle (Fig. 2(b)). A cylinder of 0.152 m length, with gas at an initial pressure of 5.0 bar and a temperature of 289 K

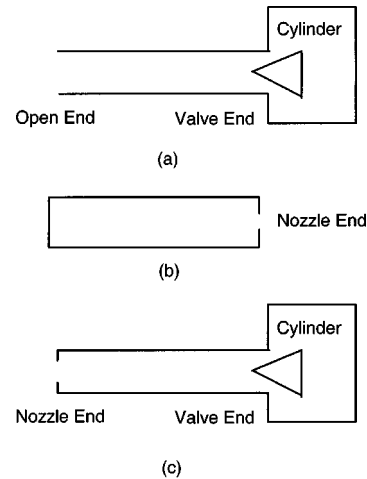


Fig. 2 Typical one-dimensional gas dynamic problems with different boundary conditions

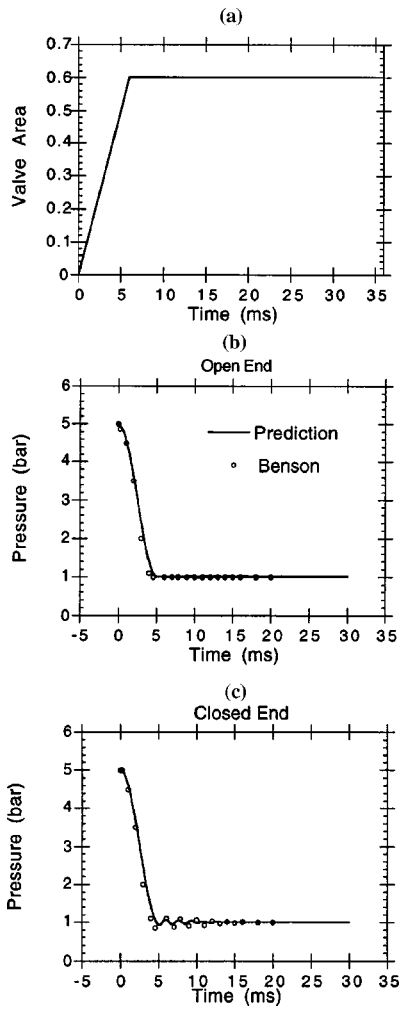


Fig. 3 The gradual discharge problem: (a) valve area diagram, (b) pressure at open end, and (c) pressure at closed end

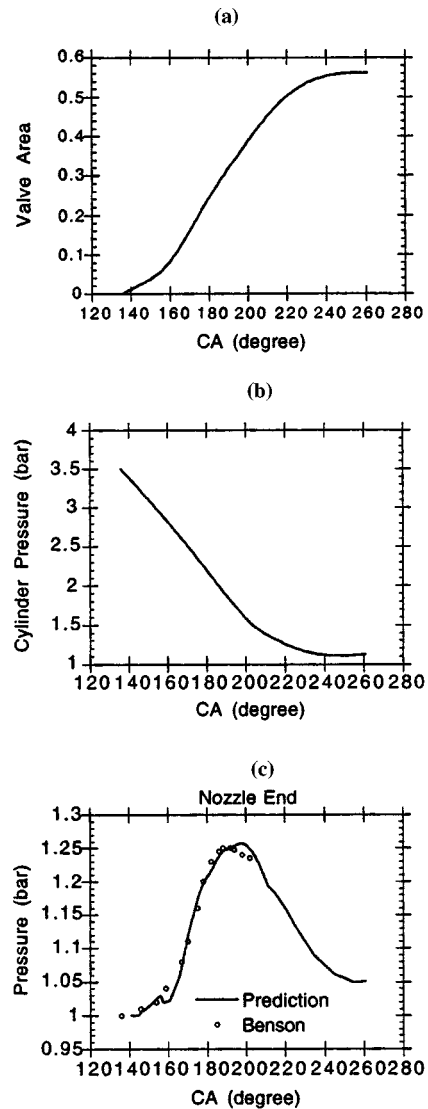


Fig. 4 Simulation of exhaust process from a cylinder with valve opening and closing to a pipe with end nozzle: (a) valve area variation, (b) cylinder pressure variation, (c) predicted pressure diagram in pipe's nozzle end, and (d) predicted pressure diagram in pipe's cylinder end

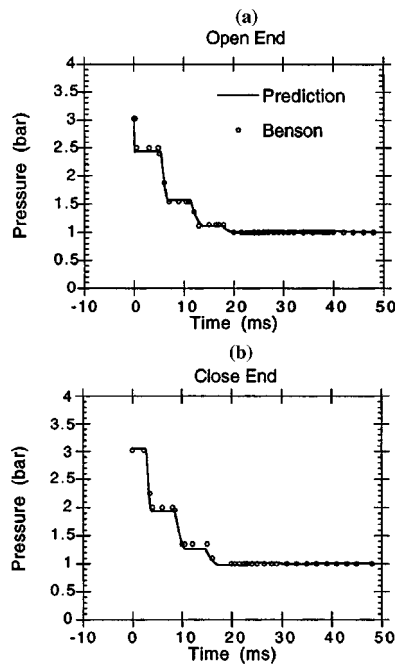


Fig. 5 The sudden discharge problem (a) open end pressure, and (b) closed end pressure

will be considered. The ambient pressure is 1 bar. The port at one end is opened linearly with time from its shut position, until it reaches an area equal to 60% of the cylinder cross-sectional area in 6 ms. This time is equivalent to a duration of 36 crank angle degrees at an engine speed of 1000 rpm. After the port reaches its maximum area, the opening remains constant. The port area, ex-

pressed as a fraction of the cylinder cross-sectional area, is shown in Fig. 3(a). The problem is to obtain the pressure-time diagram at the open and closed ends at a time period of 30 ms from the start of port opening. As shown in Figs. 3(b) and 3(c), respectively, the predicted pressure diagrams at the open and closed ends compare well with the MOC predictions. At the open end, the pressure decreases rapidly, reaches the ambient pressure in about 5 ms, and subsequently remains constant. At the closed end, both the MOC prediction and our method indicate a fluctuating, wave action after the pressure reaches the ambient pressure (Fig. 3(c)).

Sudden Discharge From a Cylinder. The second test case is selected to assess the shock capturing ability of our method by predicting a sudden discharge from a cylinder. When sudden discharge happens, shock waves are typically generated in the cylinder. A cylinder of 1.219 m long, with an opening of area equal to one quarter of the cylinder cross-sectional area, contains air at an initial pressure of 3.041 bar and temperature of 300 K. The cylinder is suddenly opened to atmospheric pressure (1 bar). Subsequently, the pressure changes with respect to time at both the closed and open ends. Our predictions are compared with Benson's MOC results, [10], in Fig. 4. It can be clearly seen that strong pressure shocks occur in both the open end and the closed end in the first 20 ms. Furthermore, it can be concluded that the TVD method captures the shocks almost as accurately as the MOC solution.

Exhaust Process From a Cylinder. The third test case simulates the exhaust process from a single cylinder into a single exhaust pipe (see Fig. 2(c)). The valve area opening and closing diagram is prescribed in Fig. 5(a). The exhaust pipe is 0.5 m long by 5 cm diameter, and is fitted at the outlet end with a nozzle of effective area one half of the cross-sectional area of the pipe. At an engine speed of 1000 rpm, and for a release pressure and temperature at exhaust valve opening equal to 3.5 bar and 1072 K, the cylinder pressure-crank angle diagram for the first 120 deg after valve opening is shown in Fig. 5(b). Upon exhaust valve opening, the initial pressure and temperature in the exhaust pipe are set to be 1.0 bar and 750 K, respectively. Figures 5(c) and 5(d) compare pressure profiles at the nozzle and cylinder ends, as predicted from our gas dynamics model and Benson's MOC computations [10]. At the nozzle end, the pressure reaches a maximum

value at about 190 deg crank angle, while at the cylinder end, the pressure profile exhibits a double humping. Overall, the predictions at both the nozzle end and the cylinder end are in good agreement with MOC.

Coupling the Gas Dynamics Model With Engine Simulations Using SIMULINK

In purely thermodynamic, engine simulations of the emptying and filling type, e.g., [35,36], the intake and exhaust manifolds are treated as plenums at uniform pressures. The instantaneous pressure difference between the manifold and the cylinders drives the mass flow rate into and out of the cylinder during the intake and exhaust strokes. However, to make such engine simulations more accurate, and to optimize the intake and exhaust pipe design, it is necessary to couple them with gas dynamics models for the flow in the intake and exhaust systems.

In order to achieve the coupling, the standard quasi-steady compressible flow computation of intake and exhaust flow rates needs to be replaced with appropriate gas dynamics subroutines. However, computation of the engine cycle along with manifold gas dynamics presents some challenges, as waves exist in the manifolds even after the cylinder has executed its intake or exhaust process [3]. Advanced graphical environments, such as MATLAB-SIMULINK, can make it possible, however, to compute in parallel both cylinder and manifold processes. In addition, such environments include powerful pre-processing and post-processing features, and can be readily reconfigured with different engine or manifold modules without reprogramming. Simply, FORTRAN or C source codes can be converted into MATLAB-MEX modules for linking in SIMULINK.

Figure 6 shows the SIMULINK structure of a single-cylinder engine simulation coupled with intake and exhaust gas dynamic modules. There are five blocks, i.e., input, output, intake, in-cylinder, and exhaust. The input block contains some important parameters that the user can change for parametric studies. The output block contains some output parameters that can be displayed to scope windows for monitoring during the simulation, or to the workspace for plotting after the simulation. The intake and exhaust blocks contain the gas dynamics simulation for intake and exhaust pipes, which use an open end as one boundary and a

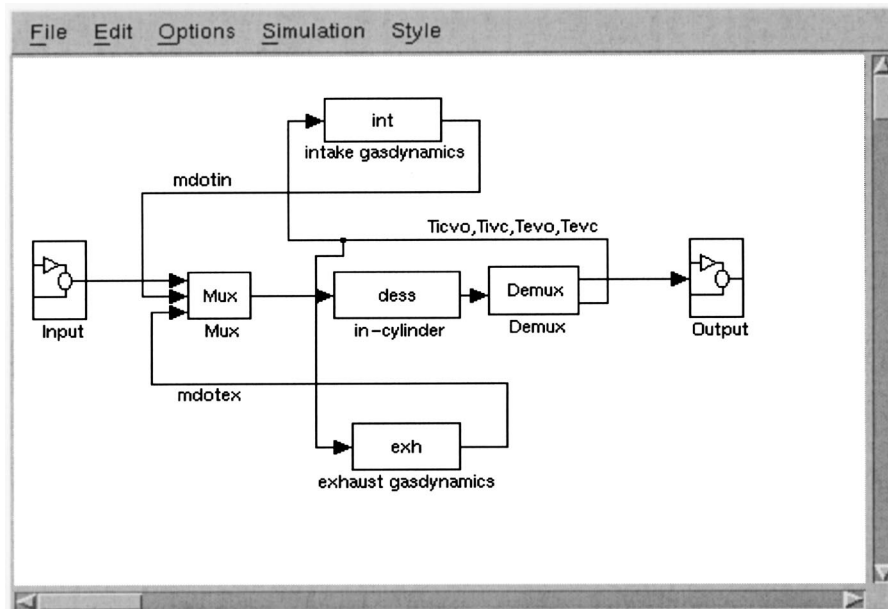


Fig. 6 Block diagram of gas dynamic models of the intake and exhaust manifolds coupled with a single-cylinder engine simulation in SIMULINK

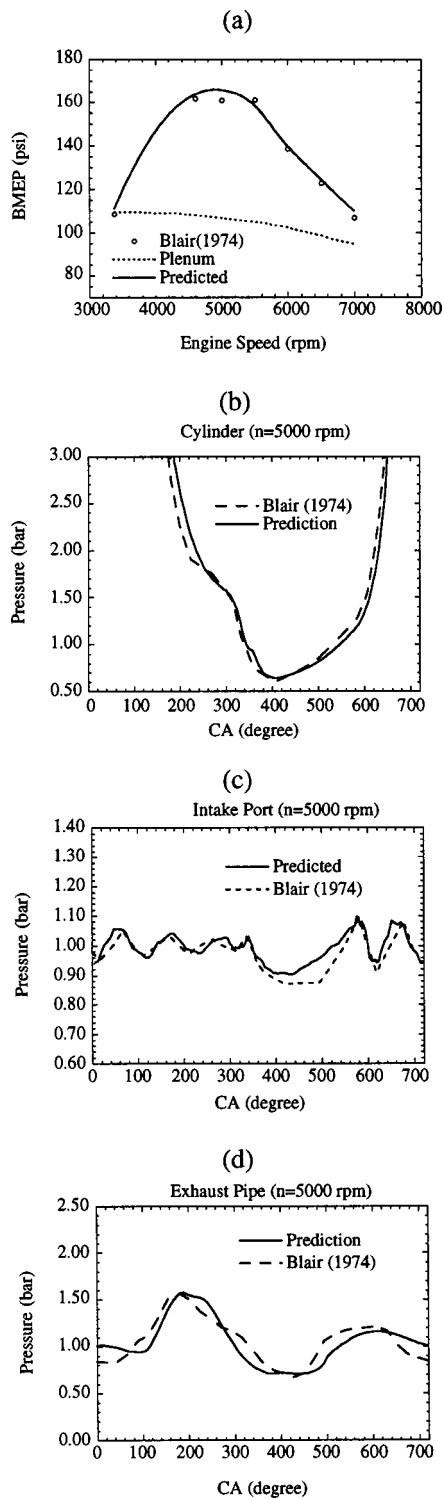


Fig. 7 Comparison of predictions and measurements for a single-cylinder spark-ignition engine: (a) BMEP for a range of speeds, (b) cylinder pressure, (c) intake port pressure, and (d) exhaust port pressure at a speed of 5000 rpm

partially open end as the other boundary at the intake or exhaust valve end. The in-cylinder block calculates the gas exchange and in-cylinder thermodynamic processes during intake, compression, combustion, and exhaust. For all modules (intake, cylinder, exhaust), boundary conditions at the cylinder-manifold interface feature crank-angle resolved state properties in the cylinder and the port, i.e., the numerical grid cell in the manifold adjacent to the

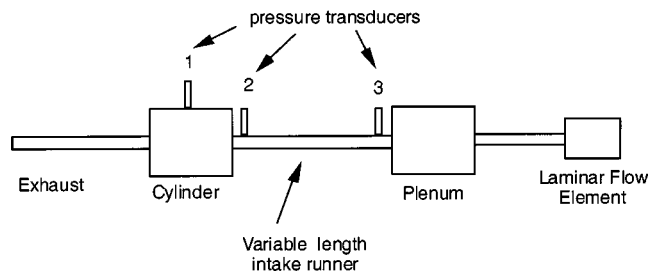


Fig. 8 Experimental setup with variable length intake runner for validation of manifold gas dynamics models coupled with single-cylinder direct injection diesel engine model

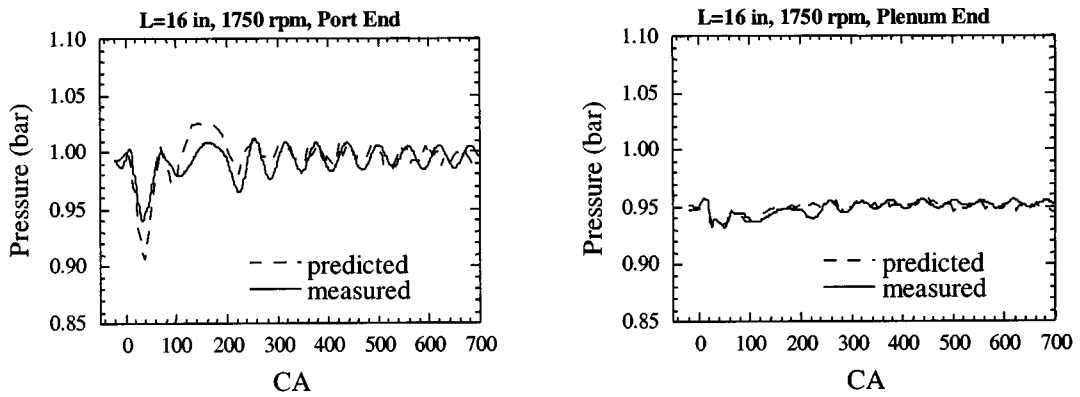
intake or the exhaust valve. Starting with initial guesses for the values of the state properties in the manifolds and the cylinder, computations are iterative until a converged, cyclic-periodic solution is achieved. The criterion that is used to establish convergence is that the residual fraction in the cylinder is within 99% of the value computed in the previous engine cycle. In general, three to four cyclic iterations are required to achieve a converged, steady-state solution for the cylinder and the manifolds.

Applications

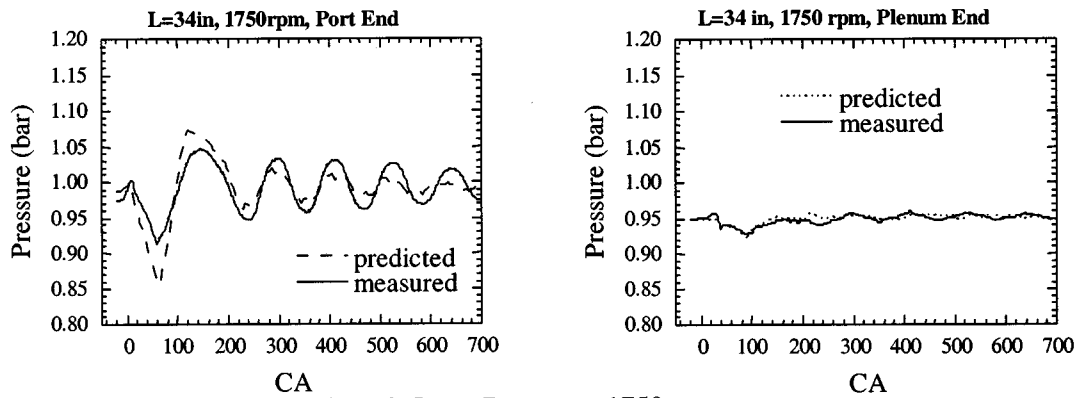
Coupling of Manifold Gas Dynamics Modeling With Single-Cylinder Spark-Ignition Engine. The single-cylinder, spark-ignition model used for coupling with gas dynamics models of the intake and exhaust manifolds is based on the quasi-dimensional simulation described by Filipi and Assanis [36]. The engine cycle simulation incorporates the comprehensive friction model to Patton et al. [37] in order to convert the predicted indicated quantities to brake quantities for comparison with dynamometer measurements. In order to explore the validity of the coupled SIMULINK model, we simulated a single-cylinder, spark-ignition engine for which experimental measurements have been published by Blair and McConnell [38]. The engine used was a 500 cm³ Victor, with a bore of 84 mm, a stroke of 90 mm, and a compression ratio of 10.

Computations of several engine cycle and manifold parameters are compared with the measurements in Fig. 7. The measured and predicted brake mean effective pressure (BMEP) values are in good agreement for stoichiometric, wide open throttle operation over a range of engine speeds. Note that unlike plenum models, gas-dynamics models integrated with engine simulations can capture the effects of intake system tuning, and the trend of BMEP with engine speed. A detailed comparison of the predicted cylinder pressure, and intake and exhaust port pressure waves at a speed of 5000 rpm with the measurements of Blair and McConnell [38] also displays favorable agreement. Note that for the purpose of the simulation, the location where port pressures were predicted was the numerical grid cell next to the intake or the exhaust valve.

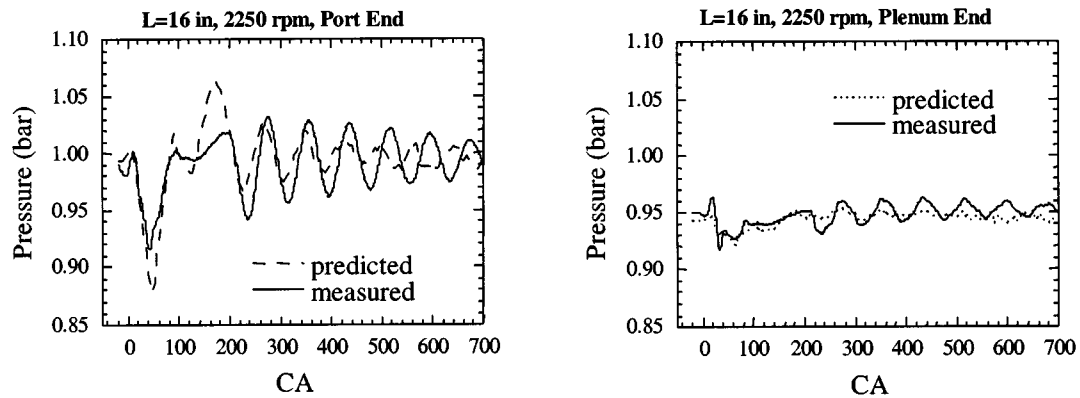
Coupling of Manifold Gas Dynamics Modeling With Single-Cylinder Diesel Engine. The zero-dimensional, thermodynamic diesel model of Assanis and Heywood [35] is used for SIMULINK coupling with gas dynamic models of the intake and exhaust manifolds. In order to validate our coupled gas dynamics-diesel engine simulation, a single-cylinder naturally aspirated, compression ignition Yanmar engine was set up at the W. E. Lay Automotive Laboratory with the capability of altering the intake runner length (see Fig. 8). The engine bore and stroke were 84 mm and 70 mm, respectively, and the compression ratio was 18.9. The manifold gas dynamics were tracked by measuring the crank angle resolved pressure at the intake port (location 2) and close to the plenum end of the runner (location 3). Experiments were conducted for intake runner lengths of 0.406 m (16 in.) and 0.762 m



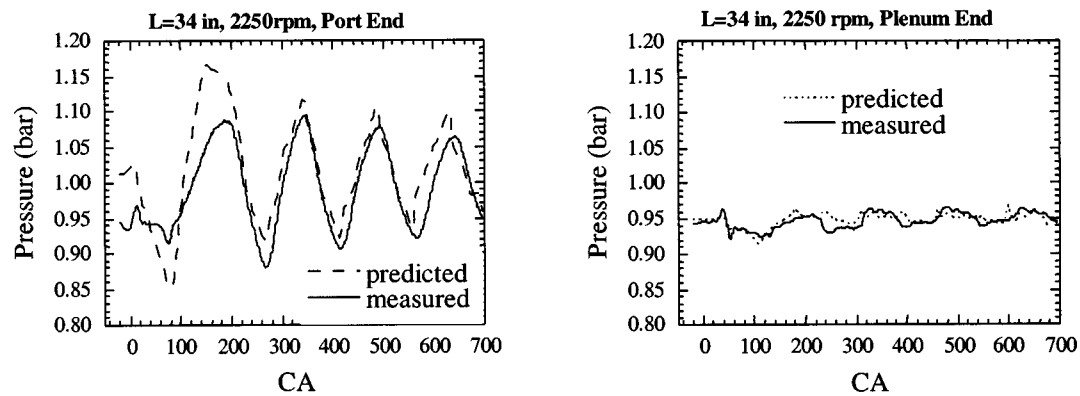
(a) Case 1: Short Runner at 1750 rpm



(b) Case 2: Long Runner at 1750 rpm



(c) Case 3 Short Runner at 2250 rpm



(d) Case 3 Long Runner at 2250 rpm

Fig. 9 Effect of runner length and engine speed on manifold gas dynamics

(30 in.) at two engine speeds, i.e., 1750 and 2250 rpm. A comparison of predicted and measured gas pressures at locations 2 and 3 is illustrated in Fig. 9. In general, the model can predict the observed wave dynamics trends at the intake port very well in terms of phasing, and satisfactorily in terms of magnitude. At a given engine speed, the shorter intake runner generates a higher frequency but lower amplitude pressure wave versus the longer intake runner, as can be readily concluded from comparing case 1 with case 2, or case 3 with case 4. This is in agreement with previously published studies which demonstrate that reducing the length of the primary intake runner increases the natural frequency of the system, [39]. On the other hand, for a given runner length, lower engine speeds result in higher frequency and lower amplitude waves, as inferred from comparing case 1 with case 3, or case 2 with case 4. Note that wave dynamic effects practically die out at the plenum end (location 3), where measurements and predictions are in excellent agreement.

A common manifold design technique to improve volumetric efficiency of high speed engines is to use variable length intake runners, so as to best tune the natural frequency of the system to the forcing frequency, as engine speed varies [1]. Through this approach, the intake port pressure is maintained at a level higher than the cylinder pressure between bottom dead center and the closing of the intake valve, thus increasing the trapped mass of air and hence volumetric efficiency. As an illustration, the model was used to conduct a parametric study of the effect of intake runner length on the volumetric efficiency of a high speed, turbocharged diesel engine. The engine bore and stroke were 84 and 90 mm, respectively, and the compression ratio was 18.5, [32]. Figure 10 shows computed volumetric efficiency curves as a function of engine speed for four intake runner lengths. Note that intake runner length is defined as the distance between the open end and the valve, as shown in Fig. 2(a). Clearly, for the shortest runner (0.2 m), the engine has lower volumetric efficiencies at low speed, but higher ones at high speed. As explained in Fig. 9, shorter runners generate higher frequency and lower magnitude pressure waves which tend to shift resonance to higher speeds. In contrast, for the longest runner (1.2 m), the engine has higher volumetric efficiencies at low speed, but lower ones at high speed. The intermediate length runners can yield resonance peaks at speeds in between the extremes achieved with the shortest and longest runners. It can be concluded that a variable length intake system can yield an optimum volumetric efficiency characteristic at all speeds; such a characteristic is the envelope of the individual curves shown in Fig. 10 for different runner lengths.

Additional simulation results demonstrating the impact of gas dynamics on the intake and exhaust processes of a larger bore, heavy-duty turbocharged diesel engine, in both single-cylinder and multicylinder configurations, as well as a comparison with corresponding plenum results for the same engine geometry can be found in Zhang and Assanis [3,32].

Conclusions

This paper presents a state-of-the-art methodology for computing one-dimensional unsteady gas dynamics in intake and exhaust manifolds coupled with single-cylinder engines. The numerical method is based on an explicit, finite volume formulation and the shock-capturing TVD scheme of Chakravarthy and Osher [26]. The model has been validated satisfactorily against both MOC predictions for flows without combustion, and with experimental measurements from a single-cylinder spark-ignition engine. The effects of gas dynamics on intake port pressure, exhaust port pressure, cylinder pressure, and volumetric efficiency have been demonstrated clearly. The following more general conclusions can be drawn from our work:

- Inclusion of a high-order shock-capturing scheme for discretization, such as the TVD scheme, is important for accurate computations of exhaust flows.

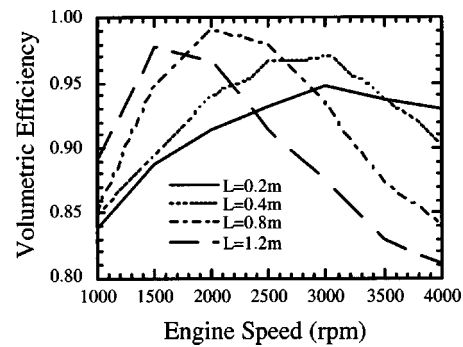


Fig. 10 The gas dynamics effect of intake runner length on the volumetric efficiency of a representative high-speed direct-injection diesel engine

- Thermodynamic cycle simulations using uniform pressure, intake, and exhaust plenums and quasi-steady-state assumptions for the gas exchange processes can introduce substantial error in both the magnitude and the trend of computed volumetric efficiency and BMEP with speed.
- The MATLAB-SIMULINK graphical interface provides a flexible and modular tool for coupling engine cycle simulations with gas dynamic models.
- Overall, a thermodynamic engine simulation coupled with a one-dimensional gas dynamics model provides a useful tool for studying and optimizing flow distribution for different intake runner lengths, and for analyzing the implications that gas exchange can have on engine cycle parameters and combustion.

Acknowledgments

The SIMULINK coupling of manifold gas dynamic models with single-cylinder, spark-ignition, and diesel engine modules has been pursued as part of the activities of the Automotive Research Center (ARC), a consortium of five universities directed by the University of Michigan. The authors would like to acknowledge the technical and financial support of the Automotive Research Center (ARC) by the National Automotive Center (NAC) located within the U.S. Army Tank-Automotive Research, Development, and Engineering Center (TARDEC) in Warren, MI.

Nomenclature

- A = area
- a = speed of sound
- Δt = time step
- Δx = grid size
- e_t = internal energy
- F = mass flux
- G = momentum flux
- H = energy flux
- k = ratio of specific heats
- p = pressure
- ρ = density
- t = time
- u = velocity
- x = coordinate in the flow direction
- π = pressure ratio
- η = scheme accuracy control parameter

Subscripts

- end = pipe end
- o = stagnation state
- p = pipe
- cr = critical
- v = valve
- cyl = cylinder

References

- [1] Engelman, H. W., 1953, "The Tuned Manifold: Supercharging Without a Blower," ASME Paper No. 53-DGP-4.
- [2] Engelman, H. W., 1973, "Design of a Tuned Intake Manifold," ASME Paper No. 73-WA/DGP-2.
- [3] Zhang, G., and Assanis, D. N., 1996, "Application of 1-D and 3-D Gas Dynamics Modeling to Engine Manifolds," 29th ISATA Proc., Florence, Italy, June 3–6.
- [4] Benson, R. S., 1955, "The Effect of Excess Scavenge Air on the Pressure Drop in the Cylinder of a Two-Stroke Engine During Exhaust Blowdown," J. Aero. Soc. Tech. Notes, **59**, pp. 773–778.
- [5] Wallace, F. J., and Boxer, G., 1956, "Wave Action in Diffusers for Exhaust Pipe Systems, With Special Reference to the Scavenging of Two-Stroke Engines," Proc. Inst. Mech. Eng., **170**, pp. 1131–1150.
- [6] Benson, R. S., and Woods, W. A., 1960, "Wave Action in the Exhaust System of a Supercharged Engine Model," Int. J. Mech. Sci., **1**, pp. 253–281.
- [7] Benson, R. S., Gary, R. D., and Woollatt, D., 1964, "A Numerical Solution of Unsteady Flow Problems," Int. J. Mech. Sci., **6**, pp. 117–144.
- [8] Blair, G. P., and Johnson, M. B., 1968, "Unsteady Flow Effects in Exhaust Systems of Naturally Aspirated Crankcase Compression Two Cycle Internal Combustion Engines," SAE Paper No. 680594.
- [9] Low, S. C., and Baruah, P. C., 1981, "A Generalized Computer-Aided Design Package for I.C. Engine Manifold System," SAE Paper No. 810498.
- [10] Benson, R. S., 1982, *The Thermodynamics and Gas Dynamics of Internal-Combustion Engines*, Vol. I, Oxford University Press, New York.
- [11] Chapman, M., Novak, J. M., and Stein, R. A., 1982, "Numerical Modeling of Inlet and Exhaust Flows in Multi-Cylinder Internal Combustion Engines," ASME Winter Annual Meeting, Phoenix, AZ, Nov. 14–19.
- [12] Winterbone, D. E., and Pearson, R. J., 2000, *The Theory of Engine Manifold Design: Wave Action Methods for IC Engines*, SAE Press, Warrendale, PA.
- [13] Lakshminarayanan, P. A., Janakiraman, P. A., Gajendra Babu, M. K., and Murthy, B. S., 1979, "Prediction of Gas Exchange Process in a Single Cylinder Internal Combustion Engine," SAE Paper No. 790359.
- [14] Takizawa, M., Uno, T., and Tadayoshi, Y., 1982, "A Study of Gas Exchange Process Simulation of an Automotive Multi-Cylinder Internal Combustion Engine," SAE Paper No. 820410.
- [15] Meisner, S., and Sorenson, S. C., 1986, "Computer Simulation of Intake and Exhaust Manifold Flow and Heat Transfer," SAE Paper No. 860242.
- [16] MacCormack, R. W., 1981, "A Numerical Method for Solving the Equations of Compressible Viscous Flow," AIAA Paper No. 81-0110.
- [17] Chapman, M., 1981, "FRAM-Nonlinear Damping Algorithms for the Continuity Equations," J. Comput. Phys., **44**, pp. 84–103.
- [18] Morel, T., Morel, J., and Blaser, D. A., 1991, "Fluid Dynamic and Acoustic Modeling of Concentric-Tube Resonators Silencers," SAE Paper No. 910072.
- [19] Peters, B., and Gosman, A. D., 1993, "Numerical Simulation of Unsteady Flow in Engine Intake Manifolds," SAE Paper No. 930609.
- [20] Kirkpatrick, S. J., Blair, G. P., Fleck, R., and McMullan R. K., 1994, "Experimental Evaluation of 1-D Computer Codes for the Simulation of Unsteady Gas Flow Through Engines—A First Phase," SAE Paper No. 941685.
- [21] Lax, P. D., and Wendroff, B., 1960, "Systems of Conservation Laws," Commun. Pure Appl. Math., **15**, pp. 217–237.
- [22] Book, D. L., Boris, J. P., and Hain, K., 1975, "Flux-Corrected Transport II: Generalization of the Method," J. Comput. Phys., **18**, pp. 248–283.
- [23] Niessner, H., and Bulaty, T., 1981, "A Family of Flux-Correction Methods to Avoid Overshoot Occurring with Solutions of Unsteady Flow Problems," *Proceedings of GAMM 4th Conf.*, pp. 241–250.
- [24] Harten, A., Lax, P. D., and VanLeer, B., 1983, "On Upstream Differencing and Gudunov-Type Schemes for Hyperbolic Conservation Laws," SIAM Rev., **25**, pp. 35–61.
- [25] Morel, T., Flemming, M. F., and LaPointe, L. A., 1990, "Characterization of Manifold Dynamics in the Chrysler 2.2 S. I. Engine by Measurements and Simulation," SAE Paper No. 900697.
- [26] Chakravarthy, S. R., and Osher, S., 1985, "A New Class of High Accuracy TVD Schemes for Hyperbolic Conservation Laws," Paper No. AIAA-85-0363.
- [27] van Leer, B., 1973, *Towards the Ultimate Conservative Difference Scheme I. The Quest of Monotonicity* (Lecture Notes in Physics, 18), Springer-Verlag, New York, pp. 163–168.
- [28] van Leer, B., 1974, "Towards the Ultimate Conservative Difference Scheme II. Monotonicity and conservation Combined in a Second Order Scheme," J. Comput. Phys., **14**, pp. 361–376.
- [29] Roe, P. L., 1985, "Some Contributions to the Modeling of Discontinuous Flows," *Lecture Notes in Applied Math.*, 22, Springer-Verlag, New York, pp. 163–193.
- [30] Davis, S. F., 1984, "TVD Differencing Schemes and Artificial Viscosity," NASA CR 172373.
- [31] Davis, S. F., 1987, "A Simplified TVD Finite Differencing Scheme via Artificial Viscosity," SIAM (Soc. Ind. Appl. Math.) J. Sci. Stat. Comput., **8**, pp. 1–18.
- [32] Zhang, G., and Assanis, D. N., 1997, "Manifold Gas Dynamics Modeling and Its Coupling With Single Cylinder Engine Models Using SIMULINK," ASME Paper 97-ICE-7, ICE-Vol. 28-1, pp. 51–60.
- [33] Zhang, G., Filipi, Z. S., and Assanis, D. N., 1997, "A Flexible, Reconfigurable, Transient Multi-Cylinder Diesel Engine Simulation for System Dynamics Studies," Mech. Struct. Mach., **25**(3), pp. 357–378.
- [34] Zhang, G., Assanis, D. N., and Tamamidis, P., 1996, "Segregated Prediction of 3-D Compressible Subsonic Fluid Flows Using Collocated Grids," Numer. Heat Transfer, Part A, **29**, pp. 757–775.
- [35] Assanis, D. N., and Heywood, J. B., 1986, "Development and Use of a Computer Simulation of the Turbocompounded Diesel System for Engine Performance and Component Heat Transfer Studies," SAE Paper No. 860329.
- [36] Filipi, Z., and Assanis, D. N., 1991, "Quasi-Dimensional Computer Simulation of the Turbocharged Spark-Ignition Engine and Its Use for 2 and 4-Valve Engine Matching Studies," SAE Paper No. 910075.
- [37] Patton, K. J., Nitschke, R. G., and Heywood, J. B., 1989, "Development and Evaluation of a Friction Model for Spark-Ignition Engines," SAE Paper No. 890836.
- [38] Blair, G. P., and McConnell, J. H., 1974, "Unsteady Gas Flow Through High Specific Output 4-Stroke Cyclic Engines," SAE Paper No. 740736.
- [39] Winterbone, D. E., and Pearson, R. J., 1999, *Design Techniques for Engine Manifolds: Wave Action Methods for IC Engines*, SAE Press, Warrendale, PA.

The Use of Neural Nets for Matching Fixed or Variable Geometry Compressors With Diesel Engines

S. A. Nelson II

Z. S. Filipi

D. N. Assanis

Department of Mechanical Engineering,
The University of Michigan,
Ann Arbor, MI 48109-2133

A technique which uses trained neural nets to model the compressor in the context of a turbocharged diesel engine simulation is introduced. This technique replaces the usual interpolation of compressor maps with the evaluation of a smooth mathematical function. Following presentation of the methodology, the proposed neural net technique is validated against data from a truck type, 6-cylinder 14-liter diesel engine. Furthermore, with the introduction of an additional parameter, the proposed neural net can be trained to simulate an entire family of compressors. As a demonstration, a family of compressors of different sizes is represented with a single neural net model which is subsequently used for matching calculations with intercooled and nonintercooled engine configurations at different speeds. This novel approach readily allows for evaluation of various options within a wide range of possible compressor configurations prior to prototype production. It can also be used to represent the variable geometry machine regardless of the method used to vary compressor characteristics. Hence, it is a powerful design tool for selection of the best compressor for a given diesel engine system and for broader system optimization studies. [DOI: 10.1115/1.1563239]

1 Introduction

It is common practice for diesel engine manufacturers to modify ratings of an existing engine to meet a range of different operating needs and market niches. One convenient and efficient method of enhancing engine performance involves selecting different compressor and turbine pairs in order to admit a larger mass of air into the cylinder for combustion. This procedure is referred to as engine-turbocharger matching. Such matching calculations using comprehensive engine cycle simulations are particularly valuable in the initial design stages, when many options have to be assessed, as described by Watson and Janota [1]. Through these numerical experiments, expensive prototype building and testing is only left for final verification of the selected turbocharger-engine combination.

In the context of turbocharged diesel engine simulations, turbomachinery is typically represented by steady-flow maps that interrelate efficiency, pressure ratio, mass flow rate, and rotor speed. During the course of matching calculations, digitized versions of these maps need to be linearly interpolated in a two-dimensional fashion (see, for instance, Assanis and Heywood [2]), in order to obtain characteristics exactly at a given operating point. Even though this technique has proven to be effective in dealing with a known compressor-turbine combination, using digitized maps is fairly limiting if new options are going to be evaluated, since a new map has to be provided a priori for every new case. In the concept evaluation stage these new options typically involve either a new engine design/geometry or a new turbocharging system configuration for an existing engine. While the turbocharger manufacturer will readily recommend a family of turbochargers suitable for the new application, a specific map corresponding to the narrow segment within the range that an engine designer would like to evaluate may not be available at this stage.

The need for new maps more often than not goes beyond just

variation of compressor or turbine size. As an example, variations of inducer or exducer blade angles, diameter ratios, scroll housing size, or casing treatment can all produce significant changes of the compressor map. In addition, the designer of a turbocharging system may decide to utilize the variable geometry (VG) machine by applying a swing blade [3], or moving sidewall design [4]. The simulation of a VG system effectively creates a need for an infinite number of maps within a range. Variation of turbomachinery characteristics with this type of geometry changes is nonlinear, thus making use of scaling laws [1], or linear interpolation between maps inappropriate. Hence, there is a need for a more flexible, adaptive turbomachinery modeling technique. This paper investigates such an alternative technique with the primary goal of exploring how to represent families of compressors or compressor trims, thus making it a useful tool for design studies of conventional or VG systems.

Artificial neural networks (ANN) have been introduced in a multitude of fields as both decision making methods [5], and functional approximation methods [6]. In the automotive field, they have been used in areas as diverse as fault recognition [7], emissions models [8], and engine management and control [9,10]. In the turbomachinery area neural networks were utilized for monitoring, diagnostics and prognostics of gas turbine engines [11–13]. In the context of turbocharging diesel engines, Ludwig and Ayoubi [14] selected neural nets as one of the two model based methods for turbocharger fault detection. More recently, Nelson et al. [15] demonstrated the potential of neural nets for modeling a whole family of compressors, while Kessel et al. [16] proposed an approach where a special type of neural network (LoLiMoT) is trained using predictions of the physical model rather than maps.

This work approaches development of an alternative, neural network based technique for modeling compressor flow characteristics in two steps. First, the potential of ANN as a technique able to replace the two-dimensional map interpolation is investigated and validated. Then, an additional input parameter is introduced in the neural net, in an attempt to capture multiple maps representing a compressor family with a single neural net. In this way the neural net could be used to simulate a range of nonexisting turbo-

Contributed by the Internal Combustion Engine Division of THE AMERICAN SOCIETY OF MECHANICAL ENGINEERS for publication in the JOURNAL OF ENGINEERING FOR GAS TURBINES AND POWER. Manuscript received by the ICE Division July 2000; final revision received by the ASME Headquarters Nov. 2002. Associate Editor: H. Nelson.

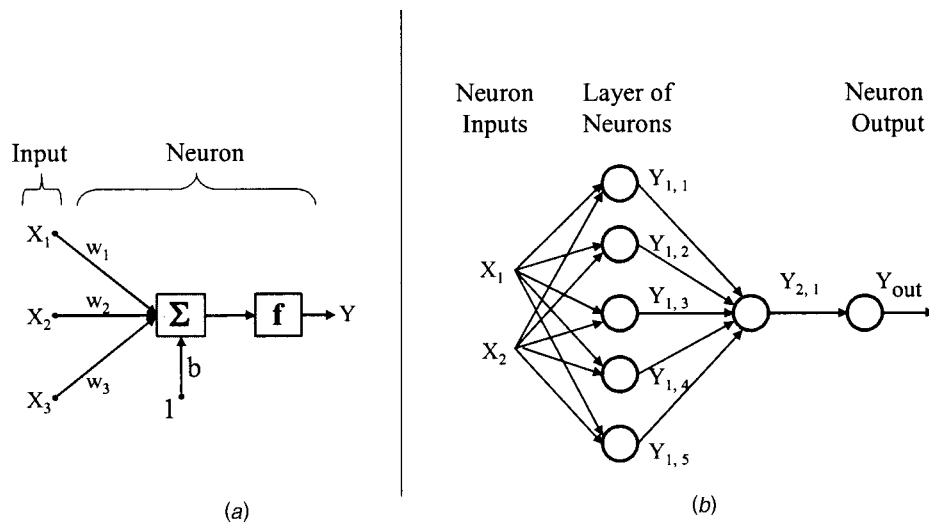


Fig. 1 Neural nets: (a) diagram of a single neuron with three inputs; and (b) a two input neural network with a single hidden layer of five neurons, each one having the inner structure resembling diagram (a)

machinery, thus becoming a powerful aid in the process of evaluating new “virtual” turbocharged engine configurations prior to the existence of physical prototypes. Alternatively, the extended neural network model could provide flow characteristics of a variable geometry compressor for any given blade position, thus becoming a powerful tool for simulating turbocharging system transient operation.

This paper is organized as follows. An overview of neural net models is given in Section 2. Section 3 summarizes the turbocharged diesel engine simulation used in this work, along with a description of the standard and proposed turbomachinery models, and the engine-turbomachinery matching process. Next, the validation of the neural net approach is given in Section 4. Finally, the extension of neural nets to determine the effects of design changes (within a compressor family) on diesel engine performance is presented in Section 5, followed by the summary and conclusions.

2 Neural Net Models: A Brief Overview

Neural nets are often used as a generic curve fitting and modeling technique when a straightforward algebraic form expressing relationships among variables is not obvious [6,17]. For compressors, their characteristics are usually represented in the form of maps that interrelate mass flow rates, efficiencies, rotor speeds, and pressure ratios. Such characteristics are typically obtained through flow rig experiments or through fairly computationally intensive CFD computations. As an alternative to maps, the interrelationships among the performance characteristics can be approximated by a nonlinear function known as a neural net. There are two primary ideas behind the use of neural nets to model relationships between sets of data. The first involves the concept of a *neuron*, and how neurons are abstracted and connected to each other in order to work together. The second concept is *training*, where a neural net is taught to model the relationships between two sets of data. Each of these concepts is explained in the following paragraphs.

A neural net consists of several interconnected neurons or modes, which are mathematical abstractions of the neurons in biological sciences. As shown in Fig. 1(a), the output of an individual neuron depends on inputs x_1, x_2, \dots, x_n —the mathematical equivalent of stimuli. The weighted sum of inputs and the bias is an argument of the transfer function f . In principle, each neuron must behave in a simple manner, by providing an output between zero and one, depending on the weighted sum of the inputs. If the weighted sum is greater than a certain bias (which is different for

every neuron), then the output will be greater than 1/2 (on), otherwise the output is less than 1/2 (off). One method of modeling an individual neuron uses the sigmoid transfer function given by Eq. (1) and portrayed in Fig. 2.

$$y = \text{sigmoid}(x_1, x_2, \dots, x_n) = \frac{1}{1 + \exp\left(b - \sum_{i=1}^n w_i x_i\right)} \quad (1)$$

In order to model complex functions, several neurons are strung together as in Fig. 1(b). The inputs to this neural net model are x_1 and x_2 . Each neuron has its own set of weights and biases, and the output of each neuron depends only on its own inputs. The output of the neural net, y_{out} , is calculated via Eqs. (2), (3), and (4).

$$(1 + \exp(b_{1,1} - w_{1,1,x_1}x_1 - w_{1,1,x_2}x_2))^{-1} = y_{1,1}$$

$$(1 + \exp(b_{1,j} - w_{1,j,x_1}x_1 - w_{1,j,x_2}x_2))^{-1} = y_{1,j} \quad (2)$$

$$(1 + \exp(b_{1,5} - w_{1,5,x_1}x_1 - w_{1,5,x_2}x_2))^{-1} = y_{1,5}$$

$$\left(1 + \exp\left(b_{2,1} - \sum_{i=1}^5 w_{2,1,y_{1,i}}y_{1,i}\right)\right)^{-1} = y_{2,1} \quad (3)$$

$$b_{3,1} - w_{3,1,y_{2,1}}y_{2,1} = y_{\text{out}} \quad (4)$$

Note that $y_{1,i}, i = \{1 \dots 5\}$ and $y_{2,1}$ are intermediate values, so that the outputs from some of the neurons are used as input to other neurons. The middle layer of neurons that produce the intermediate values makes up the hidden layer, so that the structure of the neural net in Fig. 1(b) is described as a *neural net with a single hidden layer consisting of 5 nodes*. Since the sigmoid function limits output values between 0 and 1, the last weight ($w_{3,1,y_{2,1}}$) and bias ($b_{3,1}$) are used to scale the output to a more useful domain, but are not truly associated with any neurons.

In the work presented here, a neural net is used to approximate functions that do not have a simple closed form readily available. The weights ($w_{1,i,j}$ and $w_{2,1,j}$) and biases ($b_{1,i}$ and $b_{2,1}$) determine the shape of the function, so their values must be found before the neural net is used. The process of finding these weights and biases is known as *training* the neural net. Like all fitting techniques, it is necessary to know some of the points on the function to be approximated. Suppose that the function to be approximated is a

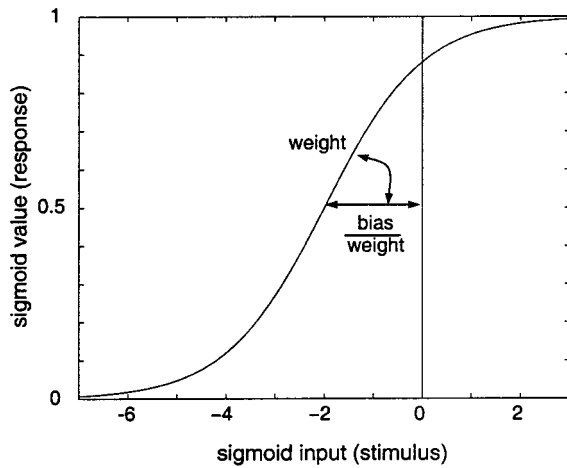


Fig. 2 Sigmoid function

multivariable single-valued function, and that there are m known points on the function, with the k th denoted $(x_1^k, x_2^k, \dots, x_n^k, y^k)$. The neural net is trained to respond with the output y^k when the inputs are $(x_1^k, x_2^k, \dots, x_n^k)$. The extent to which the neural net reproduces the data is measured by some form of error (ϵ), usually the sum of the square of the errors as given by Eq. (5):

$$\epsilon = \sum_{k=1}^5 (y^k - y_{\text{out}}(x_1^k, x_2^k, \dots, x_n^k))^2 \quad (5)$$

The squared error of a neural net model is then a function of weights and biases, thus it can be minimized by adjusting the weights and biases in an iterative process. During each iteration (sometimes called an *epoch*), $\partial\epsilon/\partial w_{i,j,k}$ and $\partial\epsilon/\partial b_{i,j}$ are calculated, and some correction for $w_{i,j,k}$ and $b_{i,j}$ is formulated in order to decrease ϵ . The specific form of modification to $w_{i,j,k}$ and $b_{i,j}$ determines the method of training, which vary from steepest descent (Rumelhart et al. [18,19]), to adaptive learning rate methods (Jacobs [20]). The iterations are continued until ϵ is sufficiently small or $\partial\epsilon/\partial w_{i,j,k}$ and $\partial\epsilon/\partial b_{i,j}$ suggest that no further improvement can be made. In fact, given enough nodes in the hidden layer, a neural net can model any function to within an arbitrarily small amount of error.

One noteworthy advantage of neural nets over a piecewise linear interpolation is the fact that $x_1^k, x_2^k, \dots, x_n^k$ need not be in a regular grid. The "training" data need only be reasonably spread over the range of interest.

3 Turbomachinery and the Diesel Simulation

Diesel Engine Simulation. The merits of the proposed neural net approach for matching turbomachinery with engines will be assessed using a modified version of the comprehensive turbocharged diesel engine simulation developed by Assanis and Heywood [2]. The thermodynamic model combines quasi-steady flow models of the compressor, turbines, manifolds, and intercooler with a zero-dimensional, multicylinder diesel reciprocator model. Each one of those connected control volumes is open to the transfer of mass, enthalpy, and energy in the form of work and heat. The diesel four-stroke cycle is treated as a sequence of continuous processes: intake, compression, combustion (including expansion), and exhaust. Combustion is modeled as a uniformly distributed heat release process that is described by the sum of two algebraic functions, one for the pre-mixed and the other for the diffusion-controlled combustion phase [21]. Heat transfer is included in each process. Convective heat transfer from the gas to each component surface is modeled using available engine correlations based on turbulent flow in pipes. Radiative heat transfer,

based on the predicted flame temperature, is added during combustion. The time-dependent temperature distributions within combustion chamber components are computed using embedded one-dimensional, transient heat transfer models. To validate the diesel system model, simulation predictions have been compared against data obtained from a six-cylinder 14.0-liter, intercooled, turbocompound diesel engine. Good agreement between measured and predicted performance was obtained over the complete load and speed range of this engine [2].

Turbomachinery Modeling. Steady-state performance characteristics for the turbocharger compressor and turbine give the interrelationships among efficiency, pressure ratio, mass flow rate, and rotor speed; the latter two variables are typically corrected for standard inlet conditions. In the standard approach, graphical turbomachinery maps are digitized and entered into the simulation in tabular form, e.g., as a one-dimensional array of rotor speeds ranked in ascending order; and a three-dimensional array of the remaining map variables arranged in ascending order of pressure ratio. At a particular step in the cycle simulation, the tables need to be interpolated in a two-dimensional fashion to calculate two unknown map variables from two known variables. Such interpolation process can be fairly tedious, as described in detail by Assanis [22]. Furthermore, using digitized maps is somewhat limiting when it comes to scaling them for matching a given engine with a family of compressors, i.e., a new map in digitized form needs to be provided for any new compressor configuration. In the proposed alternative approach, map interpolation and map scaling will be replaced with evaluation of the set of Eqs. (2), (3), and (4), representing a neural net. This neural net will be trained using digitized characteristics from standard maps to ensure a high-fidelity representation of compressor performance. The training process need only be conducted once, in a pre-processor, prior to running the diesel simulation. If weights and biases are supplied to the simulation as input, an appropriate neural net routine incorporated into the engine simulation can directly determine turbomachinery performance. Before demonstrating the validity, power, and flexibility of the neural net approach for engine turbocharger-matching, the latter process will be briefly summarized.

Engine-Turbocharger Matching. At a given instant, the values of the variables describing the state of the various system components are known from the integration of the system governing equations over the previous time step. These include the intake and exhaust manifold pressures and the turbocharger rotor speed. Additionally, the compressor inlet pressure and the turbine exhaust pressure are fixed, i.e., atmospheric pressure less intake air filter pressure drop and atmospheric pressure plus the exhaust system pressure drop, respectively. By relating the compressor discharge pressure to the intake manifold pressure and the turbine inlet pressure to the exhaust manifold pressure, the pressure ratio across each turbomachine is determined. Hence, using the calculated pressure ratios and the rotor speed (same for both turbomachines) as inputs, map interpolation routines or neural nets determine the mass flow rate and efficiency for each component for the next time step. From these, the power required to drive the compressor and the power delivered by the turbine are determined. Any excess power will result in a change in the rotor speed according to the turbocharger dynamics.

In order to avoid any oscillations in the matching process, the pressure ratio versus mass flow rate curves are modeled as single-valued, with a small, nonzero slope near the surge and choke lines. Further, if the rotor speed at some instant would become too low for the required boost pressure ratio, the mass flow would have to be to the left of the surge boundary. Under these circumstances, the speed of the rotor is increased until an acceptable mass flow solution at the given input pressure ratio is obtained. Finally, linear extrapolation is performed to extend the range of the map characteristics beyond the normal operating regime in the course of simulation iterations. This extrapolation is subject to

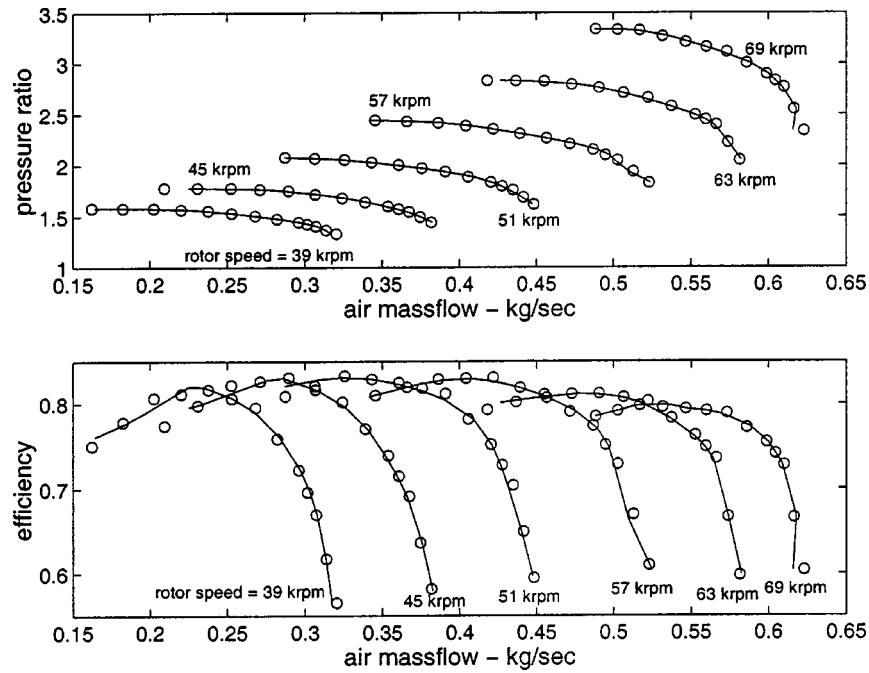


Fig. 3 Compressor pressure ratio and efficiency lines as a function of mass flow and rotational speed calculated using the neural net model

certain checks, so that the operating regimes are not extended beyond the compressor surge line. Furthermore, if the final converged solution for the engine-turbocharger matching is well beyond the normal map regimes, the turbomachinery used is not appropriate for the given engine design and operating conditions. The calculation should be repeated with more suitable turbomachinery components of different size or higher efficiency. More details are given by Assanis [22].

4 Validation of Neural Nets as Compressor Models

In order to validate the use of neural nets for modeling compressors, several neural net models were trained using data from a digitized compressor map. The selected base ANN configuration was a feed-forward net with two hidden layers, the first one having three nodes and the second one having four nodes. Neural nets were trained using the Neural Net Toolbox embedded in MATLAB [23], which employs the Levenberg-Marquardt technique to train a feed-forward network. As mentioned in Section 2, the non-linear nature of neural nets means that for a given set of data the weights and biases are not unique. Hence, in order to assess if the neural net technique can be effectively used to represent a compressor map, it must be shown that the error ϵ in Eq. (5) is sufficiently small for any set of weights and biases. Figure 3 illustrates good agreement between the original data points (O) and the continuous characteristics between the points produced by one of the ten neural nets trained on the same compressor map. When the training process was repeated nine more times to test the fidelity of the representation, different weights and biases were indeed obtained for each neural net, and yet the resulting functions had the same shape as the characteristics plotted in Fig. 3. Overall, individual errors in the efficiency and mass flow values were well below 2% ($\epsilon < 0.02$) and for ω_{max} and ω_{min} they were below 0.2%, proving that only one neural net training run would be sufficient in practice. Next, each one of these neural nets was used in the engine simulation and predictions were compared with the standard, linear interpolation approach to further validate the consistency of the training process.

A 14-liter turbocharged truck diesel engine was used to illustrate matching calculations at several speed and load conditions.

The engine design is in-line, six-cylinder, with bore=0.1397 m, stroke=0.1524 m, connecting rod length=0.3048 mm, and compression ratio=14.5. Figure 4 shows two sets of seven operating points superimposed on the compressor map, with each point corresponding to different engine speeds from 1300 rpm to 1900 rpm in increments of 100 rpm. One set is calculated at full load, for 100% mass of fuel injected in the cylinder, while the other is calculated at part load conditions, for a reduced fueling rate of 50%. Reference points were obtained using the simulation with the standard, linear interpolation subroutine. Those predictions were previously extensively validated through comparisons with experimental measurements [2]. At each operating condition, all ten values calculated by the neural nets are effectively overlapping the reference points. A comparison of integrated engine cycle pa-

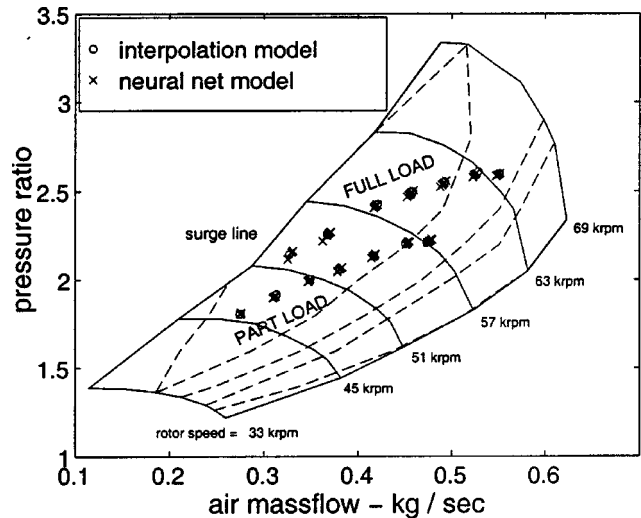


Fig. 4 Predicted steady-state operating points at full load and part load, calculated using the linear interpolation technique (O) and the neural net model (x)

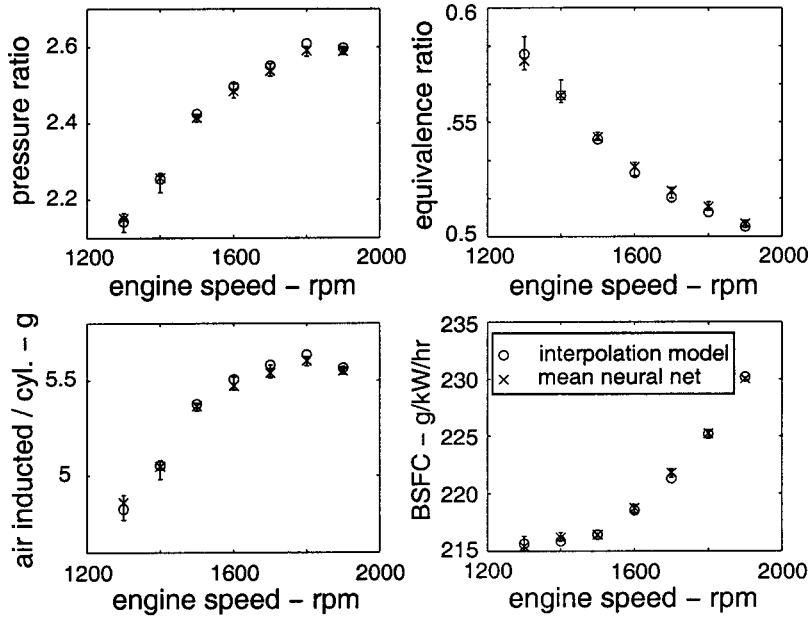


Fig. 5 Predicted boost pressure ratio, equivalence ratio, mass of air induced per cycle and brake specified fuel consumption (BSFC) versus engine speed

rameters computed using both methods is given in Fig. 5. In this figure mean values of ten neural net calculations are shown, together with bars indicating the range of fluctuations between individual runs. The agreement among results from all runs is excellent, indicating that differences in weights and biases for different nets do not affect the overall predictions of the engine system simulation. Simulation runs were also performed for some extreme operating conditions, e.g., under very low load and speed, without any convergence problems. Therefore, we may conclude that the neural net technique is repeatable and robust.

5 Design Parameter as Additional Variable—Simulating the Family of Compressors

Beyond offering a replacement for table interpolation schemes, neural nets can provide a powerful tool that can be used to interpolate between similar compressors. Manufacturers supply compressors in families, each member differing in order to meet a specific mass flow and pressure ratio range. For diesel engine designers, the important questions are *how differences between compressors affect the performance of the turbocharged diesel engine system, and which compressor is the best choice for a desired engine rating.* In the context of variable geometry machines, *the engine system designer needs representation of the variable geometry machine for any setting of the control lever in order to develop and optimize the control strategy.* The next two sections outline a method for answering these questions.

Defining a Family of Compressors. A family of compressors is a set of machines with characteristics that cover a wide flow range. It is assumed that individual compressor trims differ as measured by a few design parameters, designated α_1 through α_N . Physically the quantities α_I ($I=1 \dots N$) represent a compressor design feature, whether it be the number of blades, wheel size, blade angle, scroll geometry, or the position of the VG mechanism control lever. In other words, a family of compressors can be modeled by Eq. (6) through (9), where α_I are just additional inputs, i.e.:

$$\eta = \eta_{net}(\omega, \Pi, \alpha_1, \dots, \alpha_N) \quad (6)$$

$$M = M_{net}(\omega, \Pi, \alpha_1, \dots, \alpha_N) \quad (7)$$

$$\omega_{\max} = \omega_{\max,net}(\Pi, \alpha_1, \dots, \alpha_N) \quad (8)$$

$$\omega_{\min} = \omega_{\min,net}(\Pi, \alpha_1, \dots, \alpha_N). \quad (9)$$

The neural net represented by the above set of four equations must be trained using appropriate data, e.g., a set of only a few of selected compressor maps defining the range of the whole family. The training process provides a set of weights and biases such that the error ϵ calculated using Eq. (10) is minimized.

$$\epsilon = \sum_{k=1}^m (y^k - y_{out}(\omega^k, \Pi^k, \alpha_1^k, \dots, \alpha_N^k))^2. \quad (10)$$

Note that y could be η , M , ω_{\max} , and ω_{\min} . We stress that data points ω^k , Π^k , α_1^k , \dots , α_N^k do not have to be uniformly laid out in the grid, they only need to be reasonably spread out within the range.

However, the modified diesel engine simulation requires weights and biases for neural nets that do not use the design parameter α_I as an input. In order to evaluate the performance of the diesel engine when coupled with a compressor that has a specific value of α_I ($I=1, \dots, N$), a new set of weights and biases must be created based on these models, but the model must be of the form given by Eq. (11) through Eq. (14):

$$\eta = \eta_{net}(\omega, \Pi) \quad (11)$$

$$M = M_{net}(\omega, \Pi) \quad (12)$$

$$\omega_{\max} = \omega_{\max,net}(\Pi) \quad (13)$$

$$\omega_{\min} = \omega_{\min,net}(\Pi). \quad (14)$$

The new weights consist of the old weights corresponding to ω and Π , and the new biases are calculated by augmenting the old biases with the product of the design parameter α_I and the corresponding weight $w_{1,1,\alpha_I}$. This is outlined in Eqs. (15) and (16).

$$\left\{ \begin{array}{ccc} w_{1,1,\omega} & w_{1,1,\Pi} & w_{1,1,\alpha_1} \dots w_{1,1,\alpha_N} \\ \vdots & \vdots & \vdots \\ w_{1,n,\omega} & w_{1,n,\Pi} & w_{1,n,\alpha_1} \dots w_{1,n,\alpha_N} \end{array} \right\} \rightarrow \left\{ \begin{array}{cc} w_{1,1,\omega} & w_{1,1,\Pi} \\ \vdots & \vdots \\ w_{1,n,\omega} & w_{1,n,\Pi} \end{array} \right\} \quad (15)$$

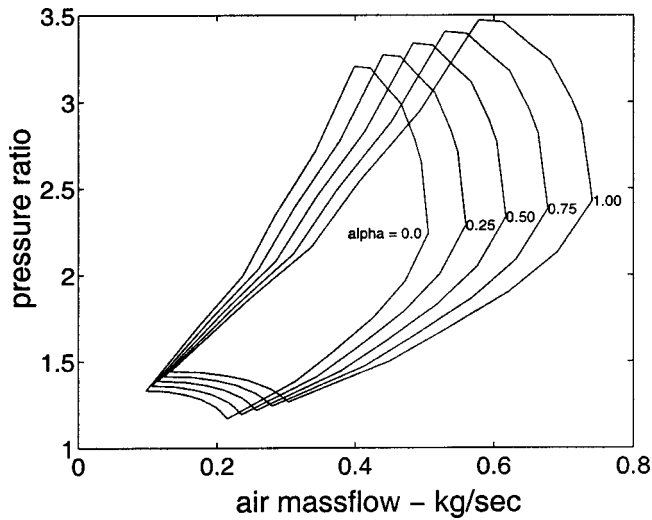


Fig. 6 Five contrived maps for compressors differing only by a fictional design parameter α

$$\begin{Bmatrix} b_{1,1} \\ \vdots \\ b_{1,n} \end{Bmatrix} \rightarrow \begin{Bmatrix} b_{1,1} - (\alpha_1 w_{1,1,\alpha_1} + \dots + \alpha_N w_{1,1,\alpha_N}) \\ \vdots \\ b_{1,n} - (\alpha_1 w_{1,n,\alpha_1} + \dots + \alpha_n w_{1,n,\alpha_n}) \end{Bmatrix} \quad (16)$$

Note that α_I ($I=1 \dots N$) can take on any arbitrary value, not just the values corresponding to the original data points. Effectively, this allows for an interpolation ability within the range covered by the family of compressors.

Simulation Results . As a detailed example, five separate, contrived maps (shown in Fig. 6) were used to train neural net models within a range. Conceptually, these five maps correspond to a family of five similar compressors. These compressors differ

by the value of a single fictional design parameter α which could be the blade angle, number of blades, scroll geometry, angle of swing blades, etc. Using the maps of these compressors, a neural net model can be constructed to simulate the complete range of possible compressors within that family, even giving reasonable interpolative predictions of compressors not represented by the original five.

A neural net model was trained for each performance characteristic. These neural net models are similar to the models used for validation, but as discussed in the previous subsection, the design parameter is introduced as an additional input. Thus, the neural net models are given by Eqs. (6)–(9) with $N=1$.

Although the design parameter α is fictional, it is interesting to illustrate its usefulness in the engine-turbocharger matching process. Figure 7 shows compressor maps for different values of the design parameter α , and their relation to the ones corresponding to the lowest and highest values of the fictional design parameter (shown in dotted lines). Note that the selected values of α are different than those used in the ANN training process. Marked on each map are the engine system operating points calculated for full load (maximum fueling rate) and two different system configurations: “x” marks denote match points for the intercooled engine, while “o” marks denote match points of the nonintercooled engine configuration. Points are obtained for engine speeds varying from 1900 rpm (northeast point) towards 1300 rpm (southwest point) in increments of 100 rpm. Clearly, the “larger” compressor ($\alpha=0.85$) can be barely matched with the nonintercooled engine at the highest speed, while it would surge at all other engine speeds. As α decreases, the nonintercooled engine can operate without surge at speeds lower than 1900 rpm. In fact, with the compressor corresponding to the smallest α (0.1), operation of the nonintercooled turbocharged engine is possible at all speeds, except at 1300 rpm. On the other hand, “smaller” compressors ($\alpha=0.1$ or $\alpha=0.25$) are inadequate for the intercooled engine, which flows more air through it, since operating points at high engine speed are too close to the choke limit on the right-hand side of the map; mass flow is roughly constant there, while

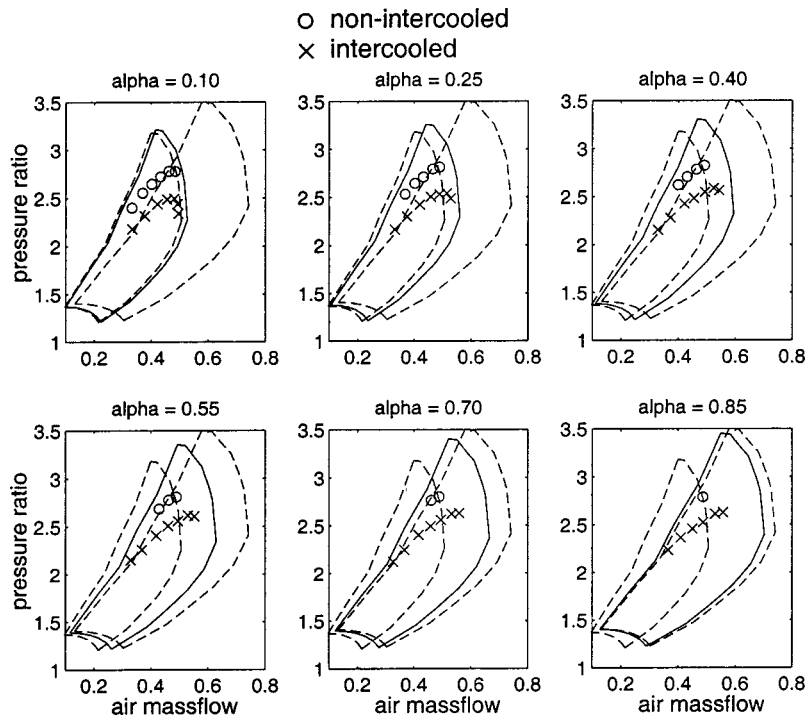


Fig. 7 Predicted steady-state operating points for different speeds and full load of the 14 L diesel engine superimposed on six maps, each one corresponding to a different value of the design parameter α

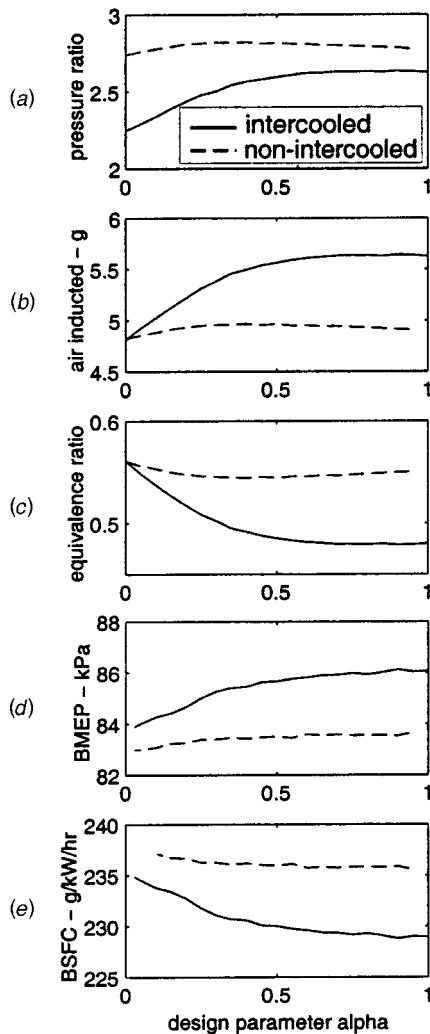


Fig. 8 Predicted steady-state operating parameters of an intercooled and nonintercooled 14 L diesel engine operating at 1900 rpm and full load as a function of the fictional design parameter α

efficiency and pressure ratio drop sharply. This exercise is very useful in selecting the best compressor from a given family for a given engine configuration and a given application. In general, the designer aims towards achieving matching points that lie towards the center of a candidate map's regime, where compressor efficiencies are higher.

The largest weight should be given to the placement of the speed point(s) that are frequently encountered in the engine system's duty cycle. For instance, assume that the turbocharged engine system will be used for electricity generation at a constant speed of 1900 rpm and full load. Detailed performance results from the matching process of intercooled (solid lines) and nonintercooled (dashed lines) engine configurations are plotted in Fig. 8 as a function of the design parameter α . As α increases, compressor mass flow range is larger, peak efficiency is somewhat higher and the operating point is located closer to the region of maximum compressor efficiency in the middle of the map, therefore the system is able to sustain a larger pressure ratio across the compressor (see Fig. 8(a)). As expected, the mass of air inducted into the cylinder also increases (Fig. 8(b)) and the equivalence ratio drops (Fig. 8(c)) since the fuel injected is held constant for all runs. The brake mean effective pressure (BMEP) and brake specific fuel consumption (BSFC) plots (Figs. 8(d) and 8(e)) illustrate how the engine benefits from more favorable process parameters

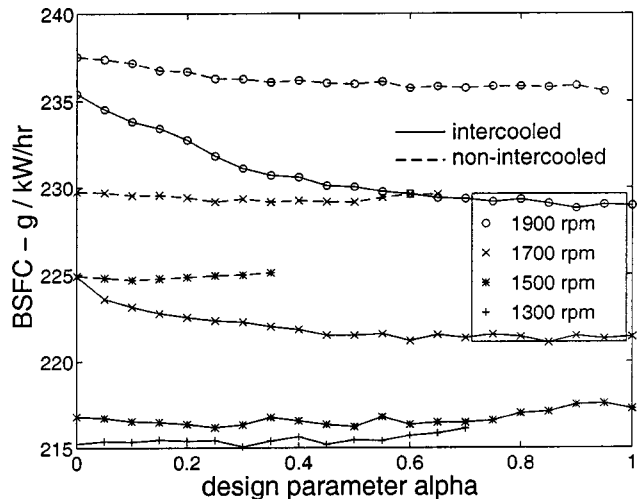


Fig. 9 Predicted steady-state brake specific fuel consumption of an 14 L diesel engine at full load and several operating speeds as a function of the fictional design parameter α

as α becomes larger. Clearly, the gains are dramatic as α increases from 0 to 0.5, and the high speed point is moved away from the choke line; on the other hand, BMEP and BSFC level off around 86 kPa and 228 g/kWh for values of α greater than 0.7, since the corresponding match points fall in generally the same, high efficiency region of the maps (see Fig. 7). Note that the nonintercooled configuration, which flows less air with a higher pressure ratio (i.e., less efficiency, as the air is less dense) benefits much less from increases in the design parameter α beyond 0.4. Clearly, from Fig. 7, placement of match points for the nonintercooled generator engine on maps of larger compressors is quite unfavorable as the operating line approaches the surge line.

The previous example illustrated that if this diesel engine system were to be used continuously at 1900 rpm and full load, then the optimum compressor would correspond to a design parameter of α greater than 0.8. On the other hand, for an automotive diesel engine, speed varies widely during the driving cycle. Therefore, it is necessary to assess engine performance and fuel economy, as well as the possible tendency to surge over a range of speeds. Figure 9 shows how fuel economy varies as a function of α at four engine speeds. As already explained above, the lower mass flow, nonintercooled engine can operate without surge only with the "smaller" compressors at intermediate speeds, and cannot operate at 1300 rpm with any of the given compressors. Fuel consumption is always lower when intercooling is applied. However, at different speeds, the minimum brake specific fuel consumption occurs for different values of the design parameter α , with the optimum point occurring for greater values of α as speed increases. For example, at 1500 rpm, fuel economy would be best for a compressor with α between 0.25 and 0.50, whereas at 1700 rpm the optimum point would shift to $\alpha=0.85$. The effect of compressor design parameter α on fuel economy is much more pronounced with intercooling and at higher speeds. This illustration demonstrates that to achieve optimum fuel consumption during a driving cycle, a compressor with variable geometry to adjust parameter α with speed would be very desirable. Even using compressors of fixed geometry, the neural net approach provides valuable insight and flexibility to arrive at the best possible compromise. In addition, it is invaluable in providing a compressor manufacturer target performance for developing custom trim for a particular engine customer.

6 Concluding Remarks

A neural net-based method for modeling compressors in conjunction with a turbocharged diesel engine simulation has been

developed. The method was validated through the comparison with results based on map interpolation methods. The neural net method was then extended to interpolate effectively between similar compressors utilizing one additional design parameter. This approach enables modeling an entire family of compressors, or a range of compressor trims associated with the application of a variable geometry machine. Based on a fictional family of five compressors, matching studies were performed for intercooled and nonintercooled configurations of a truck type diesel engine. These studies rely on the ability of the proposed technique to simulate any compressor within the family by simply varying the design or control parameter as input.

Results show that the novel technique can be successfully used to continuously vary compressor characteristics and analyze how differences among compressors/compressor trims affect the performance of a given turbocharged diesel engine system. A diesel engine designer can use the proposed technique to optimize the choice of a compressor for a desired engine rating. In the context of variable geometry machines, the technique provides the representation of the variable geometry machine for any setting of the control lever, thus enabling simulation-based development and optimization of the control strategy. The extension of this novel simulation technique to represent turbocharger turbines is apparent.

Acknowledgments

The authors would like to acknowledge the technical and financial support of the Automotive Research Center (ARC) by the National Automotive Center (NAC) located within the U.S. Army Tank-Automotive Research, Development and Engineering Center (TARDEC) in Warren, MI. The ARC is a U.S. Army Center of Excellence for Automotive Research at the University of Michigan, currently in partnership with University of Alaska-Fairbanks, Clemson University, University of Iowa, Oakland University, University of Tennessee, Wayne State University, and University of Wisconsin-Madison. The authors are grateful to the government technical monitor Walt Bryzick for his continuous guidance and support. The authors would also like to thank Andrew J. Vance for his contributions in the early stages of this project.

Nomenclature

ω	= compressor rotational speed
η	= compressor efficiency
Π	= pressure ratio across compressor
M	= mass flow through compressor
w_{ijk}	= weight of the j th neuron in the i th row corresponding to the k th input
b_{ij}	= bias of the j th neuron in the i th row
ϵ	= error of the neural net model
y	= output of a single neuron
y_{out}	= output of a neural net
y_i^k	= desired output of a neural net for input x^k
y_{ij}^k	= output from the j th neuron in the i th row for data point k
x_i^k	= i th input to the neural net for data point k
α	= fictional design parameter

m	= number of data points used to train the net
n	= number of inputs to a neuron
$\partial\epsilon/\partial w_{i,j,k}$	= partial derivative of the error of the neural net model wrt the weights
$\partial\epsilon/\partial b_{i,j}$	= partial derivative of the error of the neural net wrt the biases

References

- [1] Watson, N., and Janota, M. S., 1982, *Turbocharging the Internal Combustion Engine*, John Wiley and Sons, London.
- [2] Assanis, D. N., and Heywood, J. B., 1986, "Development and Use of a Computer Simulation of the Turbocompounded Diesel System for Engine Performance and Component Heat Transfer Studies," SAE Paper No. 860329.
- [3] Harp, J., and Oatway, T. P., 1979, "Centrifugal Compressor Development for Variable Area Turbocharger," SAE Paper No. 790066, special publication *Turbochargers and Turbocharged Engines* SP-442, Warrendale, PA.
- [4] Franklin, P. C., 1989, "Performance Development of the Holset Variable Geometry Turbocharger," SAE Paper No. 890646, SAE special publication *Power Boost—Light, Medium and Heavy Duty Engines* SP-780, Warrendale, PA.
- [5] Hush, D. R., and Horn, B. G., 1993, "Progress in Supervised Neural Networks," *IEEE Signal Process. Mag.*, **10**(1), pp. 8–39.
- [6] Smith, M., 1993, *Neural Nets for Statistical Modeling*, Van Nostrand Reinhold, New York.
- [7] Scaife, M. W., Charlton, S. J., and Mobley, C., 1993, "A Neural Network for Fault Recognition," SAE Paper No. 930861.
- [8] Brace, C. J., Deacon, M., Vaughan, N. D., Charlton, S. J., and Burrows, C. R., 1994, "Prediction of Emissions From a Turbocharged Passenger Car Diesel Engine Using a Neural Network," *Proceedings of the Institute of Mechanical Engineers: Turbochargers and Turbocharging*, Mechanical Engineering Publications Limited, Suffolk UK.
- [9] Shayler, P. J., Goodman, M. S., and Ma, T., 1996, "Transient Air/Fuel Ratio Control of an SI Engine Using Neural Networks," SAE Paper No. 960326.
- [10] Asik, J. R., Peters, J. M., Meyer, G. M., and Tank, D. X., 1997, "Transient A/F Estimation and Control Using Neural Network," SAE Paper No. 970619.
- [11] Lombardo, G., 1996, "Adaptive Control of a Gas Turbine Engine for Axial Compressor Faults," ASME Paper No. 96-GT-445.
- [12] Roemer, M. J., and Pomfret, C., 1996, "Engine Health Monitoring (EHM) System for Advanced Diagnostics Monitoring of Gas Turbine Engines," SAE Paper No. 961305.
- [13] DePold, H. R., and Gass, F. D., 1998, "Application of Expert Systems and Neural Networks to Gas Turbine Prognostics and Diagnostics," ASME Paper No. 98-GT-101.
- [14] Ludwig, C., and Ayobi, M., 1995, "Fault Detection Schemes for a Diesel Engine Turbocharger," *Proceedings of the 1995 American Control Conference*, Part 3, Seattle, WA, pp. 2118–2122.
- [15] Nelson, S., Filipi, Z. S., and Assanis, D. N., 1996, "A Neural Network for Matching the Turbocharger to IC Engine," *Proceedings of the 1996 Spring Technical Conference of the ASME Internal Combustion Engine Division*, Vol. 26-3, ASME, New York, pp. 35–42.
- [16] Kessel, J.-A., Schaffnit, J., and Schmidt, M., 1998, "Modelling and Real Time Simulations of a Turbocharger With Variable Turbine Geometry (VTG)," SAE Paper No. 980770.
- [17] Lippmann, R. P., 1987, "An Introduction to Computing With Neural Nets," *IEEE ASSP Mag.* **4**(2), pp. 4–22.
- [18] Rumelhart, D. E., Hinton, G. E., and Williams, R. J., 1986, "Learning Representations by Back Propagating Errors," *Nature (London)*, **323**, pp. 533–536.
- [19] Rumelhart, D. E., Hinton, G. E., and Williams, R. J., 1986, "Learning Internal Representations by Error Propagation," *Parallel Distributed Processing, Volume 1: Foundations*, M.I.T. Press, Cambridge, MA.
- [20] Jacobs, R. A., 1988, "Increased Rates of Convergence Through Learning Rate Adaptation," *Neural Networks*, **1**(4), pp. 295–308.
- [21] Watson, N., Pilley, A. D., and Marzouk, M., 1980, "A Combustion Correlation for Diesel Engine Simulation," SAE Paper No. 800029.
- [22] Assanis, D. N., 1985, "A Computer Simulation of the Turbocharged Turbocompounded Diesel Engine System for Studies of Low Heat Rejection Engine Performance," Ph.D. thesis, M.I.T., Cambridge, MA.
- [23] Beale, M., and Demuth, H., 1994, *The Neural Net Toolbox User's Guide*, The Math Works Inc., Natick, MA.

Investigation of a Large High-Speed Diesel Engine Transient Behavior Including Compressor Surging and Emergency Shutdown

G. Theotokatos

e-mail: makis@central.ntua.gr

N. P. Kyrtatos

Laboratory of Marine Engineering,
Department of Naval Architecture
and Marine Engineering,
National Technical University of Athens,
P.O. Box 64033,
Zografos 15710, Athens, Greece

The operation of a large high-speed engine under transient loading conditions was investigated, using a detailed simulation code in conjunction with a model capable of predicting compressor surging. Engine loadings were applied, which were considered dangerous for initiating compressor surging and cases where compressor surging could occur were identified. A means of avoiding compressor surging by opening a bypass valve connected between the compressor outlet and turbine inlet was examined. Finally, the case of engine abrupt stopping by rapidly closing the engine emergency shutdown valve, located downstream of the compressor, was also investigated. [DOI: 10.1115/1.1559903]

Introduction

Engine simulation codes are widely used during the design, development and optimization of the reciprocating internal combustion engine, [1–3]. Especially during the recent years, the increasing complexity of engine configurations, [4,5], (using EGR, waste gates or Variable Geometry Turbines) in conjunction with the extensive usage of electronic systems for controlling the various engine parameters, [6], introduced for improving engine performance and reducing exhaust emissions, necessitates the utilization of detailed engine simulation codes in the design process. Using such codes for predicting the steady state as well as the dynamic behavior of the engine and its components, the prototypes manufactured can be designed close to the optimum solution. Detailed engine simulation codes can be used, apart from matching the engine with its turbocharger and testing various engine controllers and engine design options, for investigating the engine and turbocharger transient behavior, [3,7,8], as well as complex phenomena, such as compressor surging, and thus obtaining data which otherwise could only be measured using complicated and costly techniques.

For determining the compressor behavior under surging conditions, a lumped parameter model was introduced in [9]. This model was applied for studying of the dynamics of the surge and rotating stall in an axial flow compression system and was verified experimentally. It was shown in [10], that this model is also applicable to centrifugal compressors. In [11], the compressor shaft speed dynamics were incorporated in the above model, greatly improving the agreement with the surge behavior measured in a turbocharger centrifugal compressor fitted on a single compression system.

In [12], the model presented in [9] was used in conjunction with an engine simulation code for the performance prediction of a sequentially turbocharged marine Diesel engine, including cases where compressor surging occurred. For investigating the turbocharged reciprocating engine behavior under compressor surging conditions, a one-dimensional unsteady flow model was also presented in [13]. This model was capable of predicting the compressor

and engine behavior, but the full geometry of the compressor and its piping system is required and it can be only used in conjunction with one-dimensional codes.

The model presented in [11] was extended by the authors, [14,15], so that the variations of the compressor inlet pressure and temperature during compressor surging cycles were taken into account, and was extensively validated against the experimental results published in [11]. This model was incorporated into a detailed zero-dimensional code, [16,17], as a new compressor model, so that the code can be used for examining special cases of engine running under conditions that may result in compressor surging.

The present paper describes the investigation of the transient behavior of an eight-cylinder, 34.5 L, large high-speed Diesel engine, using the derived engine simulation code. After validating the steady-state simulation results against experimental data, initial transient simulation runs were performed in order to compare the derived results using the existent and the new compressor models. Furthermore, the dynamic behavior of the engine and its turbocharger was investigated, with engine loadings that were considered dangerous for compressor surging. In addition, a way for avoiding compressor surging by opening a bypass valve connected between the compressor outlet and the turbine inlet was examined. Finally, the engine and turbocharger behavior during the engine emergency shutdown procedure was also investigated.

Turbocharged Engine Modeling

For the prediction of the steady-state and transient performance of a turbocharged engine, a detailed zero-dimensional code has been developed and used for a number of years, [16,17]. The code is flexible allowing the simulation of a variety of engine configurations including four-stroke, two-stroke, Diesel, gasoline, natural gas, turbocompound engines, etc.

The code is of “control volume” (filling and emptying) type, and it can also estimate the one-dimensional flow effects inside engine manifolds based on a pseudo-one-dimensional pipe model. A number of basic engineering elements such as flow receivers (cylinders, plenums), flow controllers (valves, compressors, turbines, heat exchangers, pipes), mechanical elements (crankshaft, shafts, gearboxes, clutches, shaft loads), and controller elements (PID speed governor, PID controllers) are available. A turbocharged engine can be modeled as several flow receiver elements

Contributed by the Internal Combustion Engine Division of THE AMERICAN SOCIETY OF MECHANICAL ENGINEERS for publication in the ASME JOURNAL OF ENGINEERING FOR GAS TURBINES AND POWER. Manuscript received by the ICE Division July 2001; final revision received by the ASME Headquarters Mar. 2002. Associate Editor: D. Assanis.

(control volumes) interconnected by flow controller elements. The engine environment is regarded as a fixed fluid element (constant pressure, temperature and composition). Mechanical connections are allowed between cylinders and crankshaft, which in addition can be connected to a shaft load via a gearbox and/or clutch. Although a number of different submodels are available for the simulation of the various components of an engine, only the ones used for the modeling of the engine examined in this paper will be described here.

The flow receivers are treated as open thermodynamic systems where work, heat, and mass transfer take place through their boundaries. The working fluid in each flow receiver is regarded as homogenous mixture of pure air and combustion products, subjected to the perfect gas law. Spatial uniformity of the fluid properties is assumed at any instant. Thus, the instantaneous state of the flow receiver gas is described by its temperature, equivalence ratio and pressure. The first law of thermodynamics, the conservation of mass and the ideal gas law are applied to each flow receiver. The resulting set of coupled differential equations is numerically solved step by step for all volumes in turn.

The rate of change of a flow receiver gas equivalence ratio with respect to time depends on the rate of fuel addition by injection and on the fuel content in the form of combustion products of the gas entering or exiting the flow receiver.

Combustion is modeled as a heat release process. Cumulative fuel burning rate diagrams (S-curve functions, [18]) are used for the simulation of the combustion process.

The heat transfer process between the working gas and its surroundings is considered to consist of two parts: heat transfer from gas to wall and heat transfer from wall to coolant, for both the flow receiver and the flow controller elements. For the first part, in the case of cylinders, the heat transfer coefficient is calculated using the Woschni correlation, [19], whereas Nu-Re-Pr correlations, [20], are used for calculating the heat transfer coefficient in the other flow receivers and flow controllers. For the wall to coolant heat transfer, the surface wall temperature of the various elements are calculated using coefficients that determine how close the wall temperature is to the "adiabatic" temperature of the wall or to the coolant temperature.

In the case of cylinders, the rate of change of a cylinder volume is calculated using the geometry of the piston, crank throw, and connecting rod.

The flow through the inlet and exhaust valves (flow controllers), connected to a flow receiver, is considered to be quasi-steady, [18,21], at each time step and calculated as a function of instantaneous valve effective area and pressure ratio.

The compressor is modeled using a digital representation of its steady-state map. The steady-state compressor map is assumed to apply at all engine operating conditions. The compressor map, which represents the compressor speed and efficiency as functions of corrected flow with respect to pressure ratio, is accessed using the instantaneous values of pressure ratio and turbocharger speed obtained from calculations within the engine simulation program. The compressor corrected flow and efficiency are calculated using interpolation, thus enabling the calculation of the instantaneous compressor mass flow rate. Then, the compressor impeller absorbed torque is calculated by the following equation:

$$\tau_c = \frac{30\gamma R \dot{m}_c T_{o1}}{\pi N (\gamma - 1) \eta_c} (pr_c^{(\gamma-1)/\gamma} - 1). \quad (1)$$

The turbine is modeled using a digital representation of its swallowing capacity and efficiency maps, which usually provide the turbine swallowing capacity (or mass flow rate parameter) and efficiency, as functions of the turbine pressure ratio and the turbocharger speed. The turbine mass flow parameter and efficiency are calculated using the turbine expansion ratio and the turbocharger shaft speed, interpolating between the given points of the turbine maps. Then, the instantaneous turbine torque is calculated by

$$\tau_t = \frac{\dot{m}_t c_p T_{o3} \eta_t (1 - (p_{o4}/p_{o3})^{(\gamma-1)/\gamma}) - \dot{Q}_t}{\pi N / 30}. \quad (2)$$

Turbocharger speed is obtained by integrating the angular momentum conservation equation, governing the turbocharger shaft dynamics:

$$\frac{dN_{TC}}{dt} = \frac{30}{\pi I} (\tau_t - \tau_c). \quad (3)$$

The temperature of air exiting the charge air cooler is calculated using the cooler effectiveness. The air cooler pressure drop is calculated as function of the air cooler mass flow rate.

The gas temperature, mass and equivalence ratio of every flow receiver at each time step are calculated by numerically integrating, through a predictor-corrector scheme, the differential equations giving the time derivatives of gas temperature, mass, and equivalence ratio, respectively. The gas pressure is calculated using the perfect gas law.

For the calculation of the engine crankshaft speed, the engine cylinders are considered to be mechanically connected to the crankshaft, which is in turn connected to the engine load. The cylinders produce torque, whereas the engine load absorbs torque. The engine speed is defined by the angular momentum conservation in the engine crankshaft:

$$\frac{dN_E}{dt} = \frac{30(\sum_{i=1}^{ncyl} \tau_i - \tau_L)}{\pi I_{tot}}. \quad (4)$$

For the calculation of the brake torque developed by the engine cylinders, friction losses, dependent on the mean piston speed and the maximum cylinder pressure, [22], are taken into account.

For the transient engine simulation, an engine speed governor element is used for the control of the fuel rack position, which, in turn, determines the fuel injected into the engine cylinders in order to stabilize the engine speed around a desired point. The output of the engine speed governor is calculated using the PI control law:

$$y = y_{init} + k_p(N_{ord} - N) + k_i \int_{t_0}^t (N_{ord} - N) dt. \quad (5)$$

Compressor Dynamic Response Modeling

In previous studies of the authors, [14,15], a model capable of predicting the compressor dynamic behavior including cases of turbocharger compressor surging was presented. This model was extensively validated using published experimental data for a simple centrifugal compression system.

This model was incorporated into the engine simulation code as an additional compressor model. According to this model, the compressor mass flow rate is calculated using the following equation:

$$\frac{d\dot{m}_c}{dt} = \frac{p_2 - p_p}{L_c/A} \quad (6)$$

where $p_2 = p_1 \cdot pr$.

The above equation was derived considering the compressor as a single pipe and applying the momentum conservation. The cross-sectional area of this pipe is considered to be equal to the compressor impeller eye area and the equivalent length is calculated by

$$\frac{L_c}{A} = \int_{compressor \& \text{ its ducting system}} \frac{d\ell}{A(\ell)}. \quad (7)$$

Using the above equations, the inertia of the air contained inside the compressor and its inlet and outlet ducts is taken into account.

In addition, in order to take into account the departure of the compressor characteristics from their steady-state form when the

compressor operates under dynamic conditions, the following first order differential equation is used for the calculation of the compressor pressure ratio:

$$\frac{dpr}{dt} = \frac{1}{\tau} (pr_{ss} - pr). \quad (8)$$

The time lag, used in the above equation, has the effect of flattening the steady-state compressor characteristics, [11,23], and is considered to be in the order of the compressor throughflow time, [11]:

$$\tau = \frac{L_{mer}}{|c|} \quad (9)$$

where L_{mer} is the meridional length of the compressor impeller and diffuser and c is the meridional average flow velocity.

The additional compressor geometric data, required as input for the new model are, the equivalent length (L_c) for the compressor inlet, impeller, diffuser, volute and outlet ducting system, the impeller eye area (A), the compressor impeller and diffuser meridional length (L_{mer}). In addition, the compressor characteristics in the form of pressure ratio versus flow for various values of rotational speed are required. For the calculation of the compressor torque, the nondimensional torque coefficient as a function of flow coefficient, instead of the efficiency contours, was preferred to be used as input. Plotting the compressor nondimensional torque coefficient versus flow coefficient, the result will be almost a straight line. Thus, only the coefficients of the equation of this line must be given as input. For each point of the compressor map, the compressor nondimensional torque coefficient can be calculated by

$$\Gamma_c = \frac{\tau_c}{\rho A r_2 U^2} \quad (10)$$

where the compressor torque is given by Eq. (1), whereas the compressor flow coefficient can be calculated by

$$\phi_c = \frac{\dot{m}_c}{\rho A U}. \quad (11)$$

Thus, the following equation can be used for the estimation of the compressor nondimensional torque, which is derived by curve fitting using the points of Γ_c and ϕ_c , calculated from the compressor map:

$$\Gamma_c = c_1 \phi_c + c_2. \quad (12)$$

According to the new model, the steady-state compressor map is accessed with the instantaneous values of corrected mass flow rate and corrected speed and the steady-state pressure ratio is calculated using interpolation. The compressor pressure ratio and mass flow rate are calculated at the end of each step by integrating the differential Eqs. (8) and (6), using a predictor corrector scheme. Then, the compressor flow coefficient, the compressor nondimensional torque coefficient and the compressor torque are calculated in turn (Eqs. (11), (12), and (10)). In addition, the compressor efficiency is calculated using Eq. (1). The total temperature at the compressor outlet is calculated by the following equation, which is derived from the energy equation in the compressor, [18]:

$$T_{o2} = T_{o1} + \frac{\tau_c \omega}{\dot{m}_c c_p}. \quad (13)$$

The total enthalpy of the air entering the flow receiver connected downstream of the compressor can then be calculated using the temperature T_{o2} .

The instantaneous turbocharger shaft speed is calculated by integrating the angular momentum conservation equation (Eq. (3)) for the turbocharger shaft.

In case where the calculation of the compressor surging cycle is required, the compressor characteristics as well as the nondimensional torque coefficient for the region to the left of the surge line and for negative flows is needed as input.

In that case, for calculating the complete compressor characteristics and the nondimensional torque coefficient versus flow coefficient for the negative compressor flow region, a meanline analysis method was used in [15], which, however, requires a great amount of compressor geometric input data. Alternatively, a method for the estimation of compressor characteristics and nondimensional torque coefficient, when the compressor map for the normal flow region is available, was presented in [14,15]. According to that, the characteristics of a centrifugal compressor can be estimated using the following second-order polynomial equation for the negative flow region:

$$pr = pr_0 + \frac{pr_{srg} - pr_0}{\dot{m}_{srg}^2} \dot{m}_c^2 \quad (14)$$

whereas, the following third-order polynomial equation, which was proposed in [24], is used for calculating the compressor characteristics for the region between zero flow and surge line:

$$pr = pr_0 + \frac{pr_{srg} - pr_0}{2} \left[1 + 1.5 \left(\frac{2\dot{m}_c}{\dot{m}_{srg}} - 1 \right) - 0.5 \left(\frac{2\dot{m}_c}{\dot{m}_{srg}} - 1 \right)^3 \right] \quad (15)$$

where the compressor pressure ratio at zero flow is calculated by the following equation, [14]:

$$pr_0 = \left[1 + \frac{\gamma - 1}{2\gamma R T_{o1}} \omega^2 (r_2^2 - r_1^2) \right]^{\frac{\gamma}{\gamma - 1}}. \quad (16)$$

For the positive compressor flow region, the nondimensional torque coefficient can be estimated using the equation of the line that fits the points of Γ_c and ϕ_c , calculated from the compressor map (Eq. (12)). For the negative compressor flow region the even extension of this function can be used.

For negative compressor flow, the torque absorbed by the compressor impeller, which is derived using the energy equation in the compressor, is given by

$$\tau_c = \frac{|\dot{m}_c| c_p (T_{o1} - T_{o2})}{\omega}. \quad (17)$$

Thus, the total temperature at the compressor inlet is calculated by

$$T_{o1} = T_{o2} + \frac{\tau_c \omega}{|\dot{m}_c| c_p}. \quad (18)$$

The total enthalpy of the air entering the compressor inlet volume is calculated using the temperature T_{o1} .

Engine Description

The Caterpillar 3508 (CAT 3508) engine is a four-stroke, large high-speed Diesel engine, [25]. It can be used as a propulsion

Table 1 Caterpillar 3508 parameters

Number of cylinders	8
Cylinder arrangement	60° V
Displacement	34.5 L
Bore	170 mm
Stroke	190 mm
Connecting rod length	380 mm
Compression ratio	13
Turbocharger	1 ABB RR-151
Operating speed range	1200–1800 rpm
Power output	785 kW@1800 rpm
BMEP	15.2 bar
Engine total polar moment of inertia	25.9 kg m ²

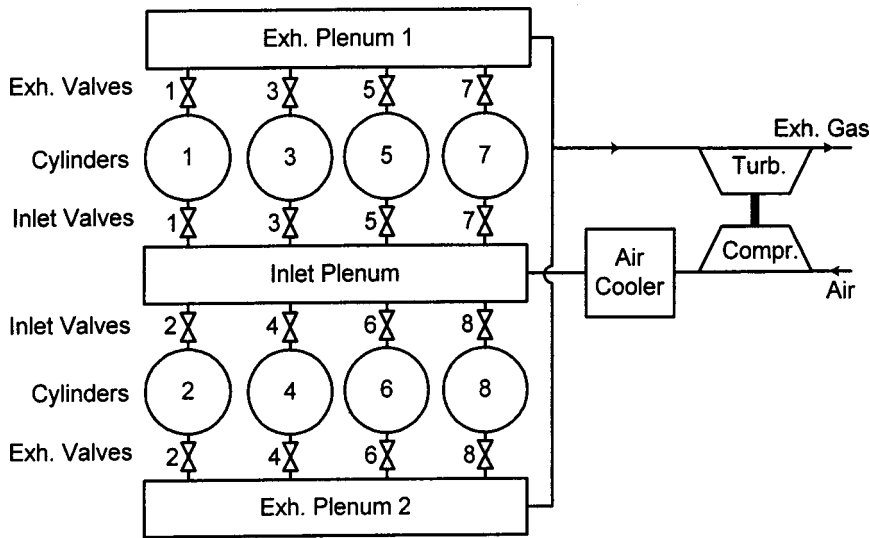


Fig. 1 CAT 3508—engine configuration

plant engine (mainly in tugs, fishing boats, fast ferries, etc.) as well as a generator set engine. A CAT 3508 engine is installed in the testbed of the Laboratory of Marine Engineering (LME) of NTUA, [26], connected to a Zoelner water brake.

The CAT 3508 engine employs the constant pressure turbocharging system. Its intake manifold is located between the two banks of cylinders. The cylinders of each bank discharge their exhaust gas into two different exhaust plenums. The standard production engine has two separate turbochargers, each one connected to the exhaust plenum of one of the two cylinder banks. The CAT 3508 test engine of the LME is equipped with a single ABB RR-151 turbocharger, [27], whose turbine is connected to both exhaust manifolds via a Y-junction. This engine configuration was modeled here.

The basic engine parameters are given in Table 1, whereas the engine configuration is shown in Fig. 1.

Results and Discussion

Initially, steady-state runs for engine operation at 1500 rpm and various loads were performed. The combustion model constants were adjusted so that the measured maximum cylinder pressure as well as the engine torque is adequately predicted. The derived steady-state simulation results are presented in Fig. 2. In the same figure, the respective measured data for the original engine configuration (with two turbochargers) and for the engine configuration with the 1 RR-151 turbocharger, are also given. Good agreement between the measured and the predicted results is observed. However, it must be noted that the turbine of the turbocharger for the simulated configuration was the one that is currently fitted on the engine of the LME testbed, and its nozzle area is smaller than the one of the turbine with which the measurements were performed. Thus, the predicted engine exhaust receiver pressure is

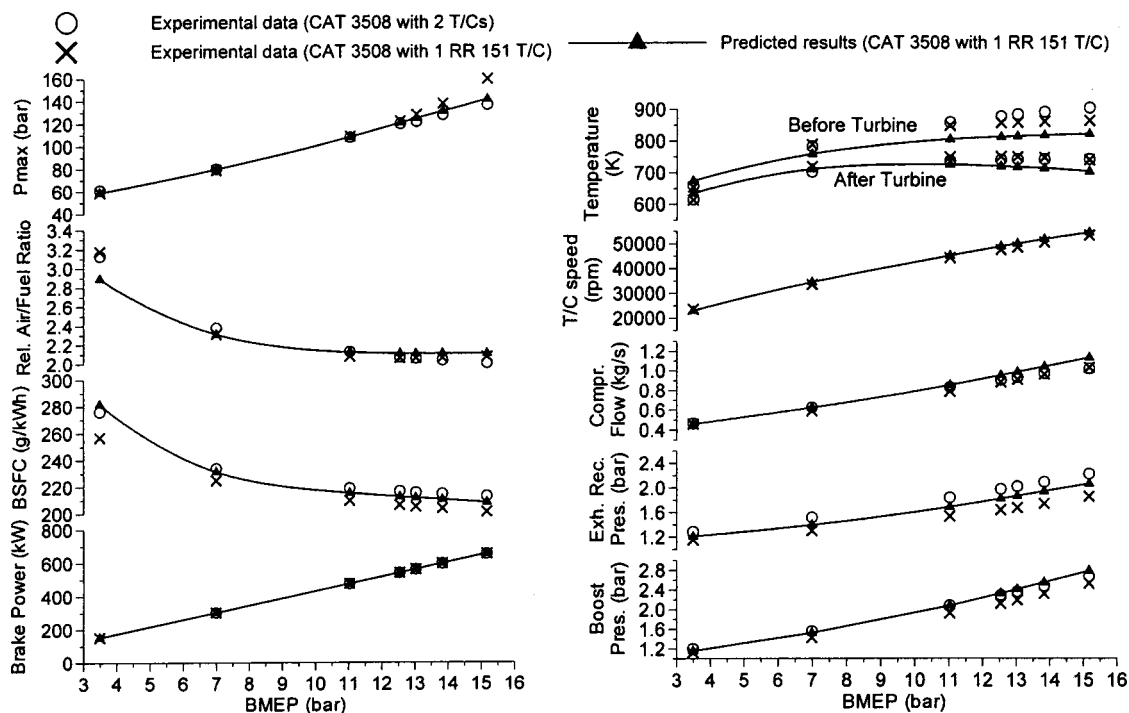


Fig. 2 Steady-state predicted and measured results at 1500 rpm

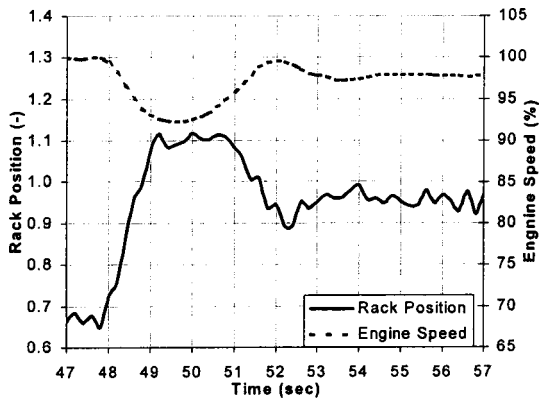


Fig. 3 CAT 3508—measured rack position and engine speed during load increase

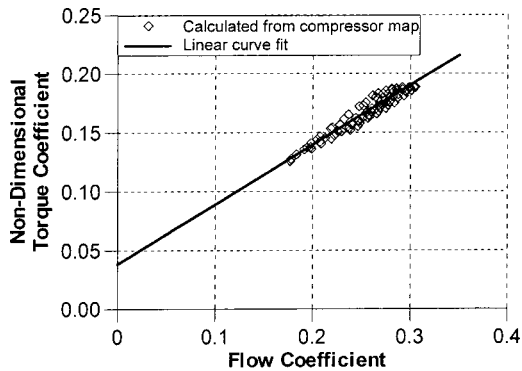


Fig. 4 Compressor nondimensional torque coefficient versus flow coefficient (calculated from compressor map and its linear curve fit)

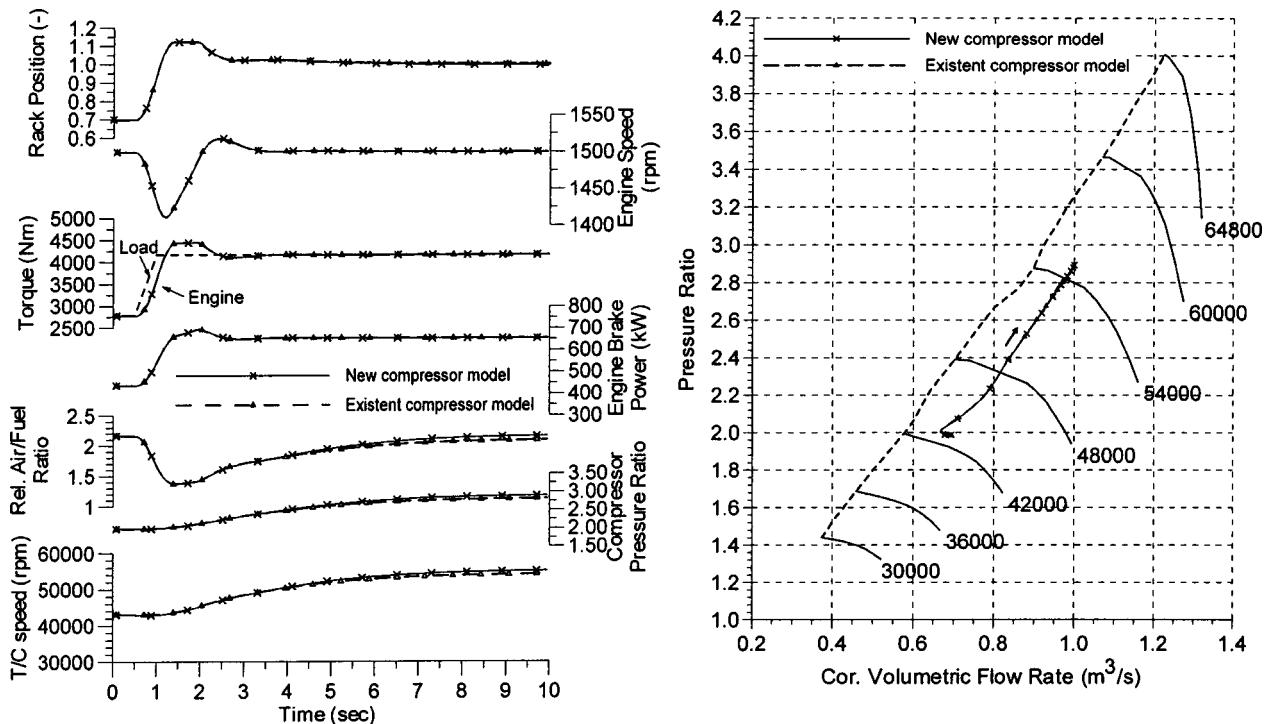


Fig. 5 Simulation results for engine load increase from 70% to 100% at 1500 rpm

slightly greater than the measured one, resulting in slightly higher turbocharger speed, compressor mass flow rate and engine boost pressure. Therefore, more air is available in the engine cylinders for burning almost the same fuel amount, having as a result lower exhaust receiver temperature.

After the steady-state simulation, a case of engine transient simulation with load increase from 70% to 100% was examined. For such a case, measured data for the engine fuel rack position and engine speed were available and shown in Fig. 3. Using these data, the engine PI speed governor constants (see Eq. (5)), were calculated so that the predicted results are in good agreement with the measured ones. These values were found to be: $k_p=0.016$ and $k_i=0.045$. The transient simulation was performed using the existent compressor model as well as the new compressor model. The compressor nondimensional torque coefficient versus flow coefficient points, which were calculated using the compressor map, are shown in Fig. 4. In this figure, the line, which fitted these data and used as input in the calculations, is also presented. For the predictions of the compressor surge cycles presented below in this text, the even extension of this function was used for estimating the nondimensional torque coefficient for the negative compressor flow region. In addition, the third order polynomial Eq. (15) was used for the estimation of the compressor characteristics between zero flow and the surge line, whereas the compressor characteristics for the negative flow region were taken from [15].

A set of the predicted results for the engine transient from 70% to 100% load, including the engine rack position, the engine speed, the engine torque, the engine brake power, the relative air/fuel ratio, the compressor pressure ratio and the turbocharger speed, as well as the trajectory of the compressor operating points superimposed on the compressor map, is given in Fig. 5. In addition, the variation of the compressor parameters within one engine cycle for the cycles after 0.3 sec (corresponding to 70% load) and after 9.5 sec (corresponding to 100% load) is presented in Fig. 6.

As can be seen from these figures, the engine and turbocharger mean cycle parameters derived using the existent and the new compressor models practically coincide. However, the compressor efficiency values for the engine operating region close to 100%

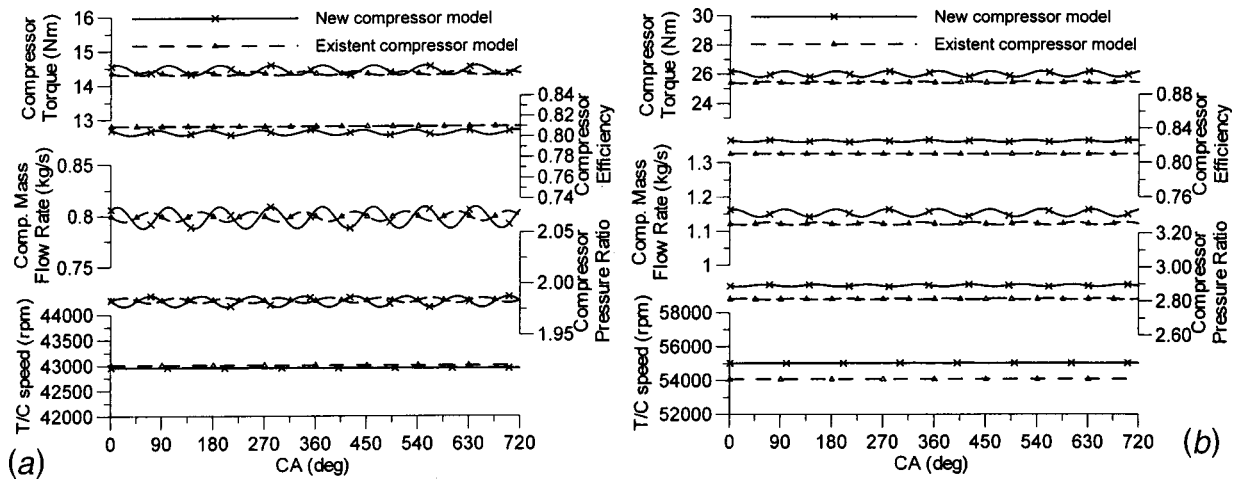


Fig. 6 Compressor parameters versus CA for (a) engine cycle after 0.3 sec (70% load) and (b) engine cycle after 9.5 sec (100% load)

load, predicted with the new model are slightly greater than the ones predicted with the existent model, resulting in slightly higher turbocharger speed, compressor pressure ratio and air/fuel ratio. In addition, the instantaneous values of the compressor parameters calculated using the new model are slightly shifted, compared to the respective ones calculated using the existent model. The former is owing to the fact that the compressor torque was calculated using the linear fit instead of the points derived directly from the compressor map (Fig. 4). The latter is attributed to the way of calculating the compressor mass flow rate and pressure ratio using Eqs. (6) and (8), instead of calculating the mass flow and pressure ratio directly from the steady-state compressor map. However, since the new compressor model gives mean cycle results comparable to the ones derived using the existent compressor model, and additionally, the inertia of the air inside the compression system passages and the departure of the compressor characteristics from their steady-state form are taken into account, it is expected that more realistic predictions can be derived by using the new model.

Next, a transient run was performed, in which engine load changes, “dangerous” for compressor surging, were imposed. The

engine was operating at 1500 rpm with 85% load and the engine load was reduced to 10% at 0.5 sec and then increased again to 100% at 2 sec. The predicted engine rack position, engine speed, engine torque and power, relative air/fuel ratio, compressor pressure ratio and turbocharger speed, as well as the trajectory of the compressor operating points on the compressor map are shown in Fig. 7.

During the load reduction¹ from 85% to 10%, the engine speed increased about 10% (1650 rpm at 1 sec) and as a result, the compressor mass flow also increased.² Thus, the compressor operating point moved towards the choking region on the compressor map. However, due to the engine speed governor response, the engine speed reached the engine setpoint of 1500 rpm at about 2 sec. At that moment, the engine load increased to 100%, causing

¹An engine load reduction may result in engine overspeed when the engine operates close to the upper limit of its speed range. However, no problems are encountered in the running of the turbocharger components.

²For a four-stroke engine, the engine volumetric air flow rate, and as a result the compressor volumetric flow rate, mainly depends on the engine displacement volume and the engine speed.

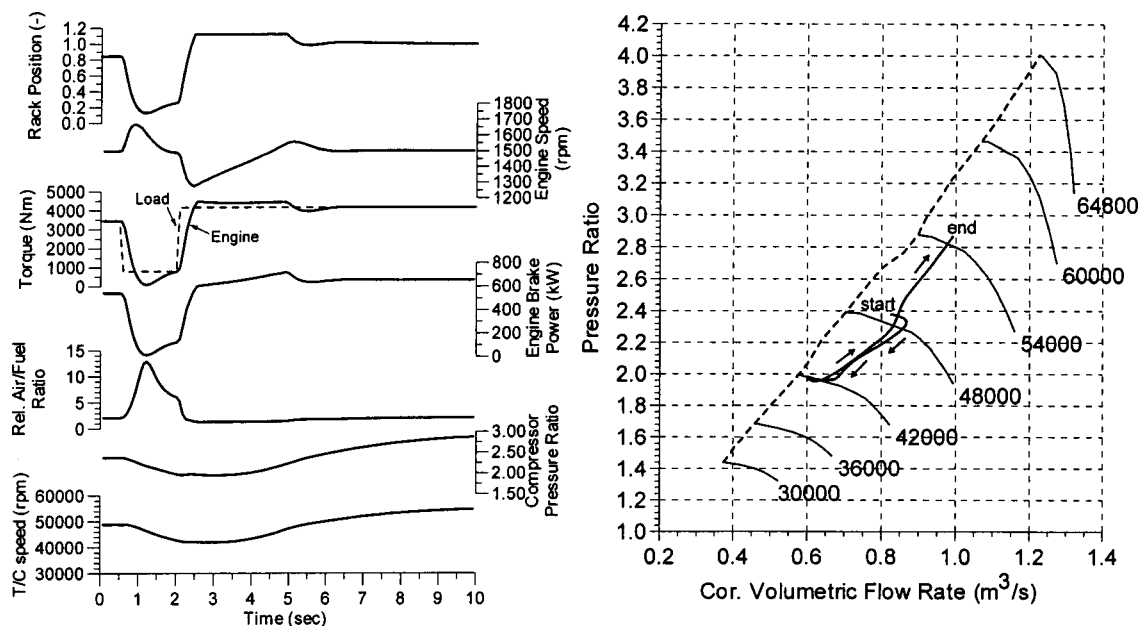


Fig. 7 Simulation results for engine transient operation at 1500 rpm—load changes 85%–10%–100%

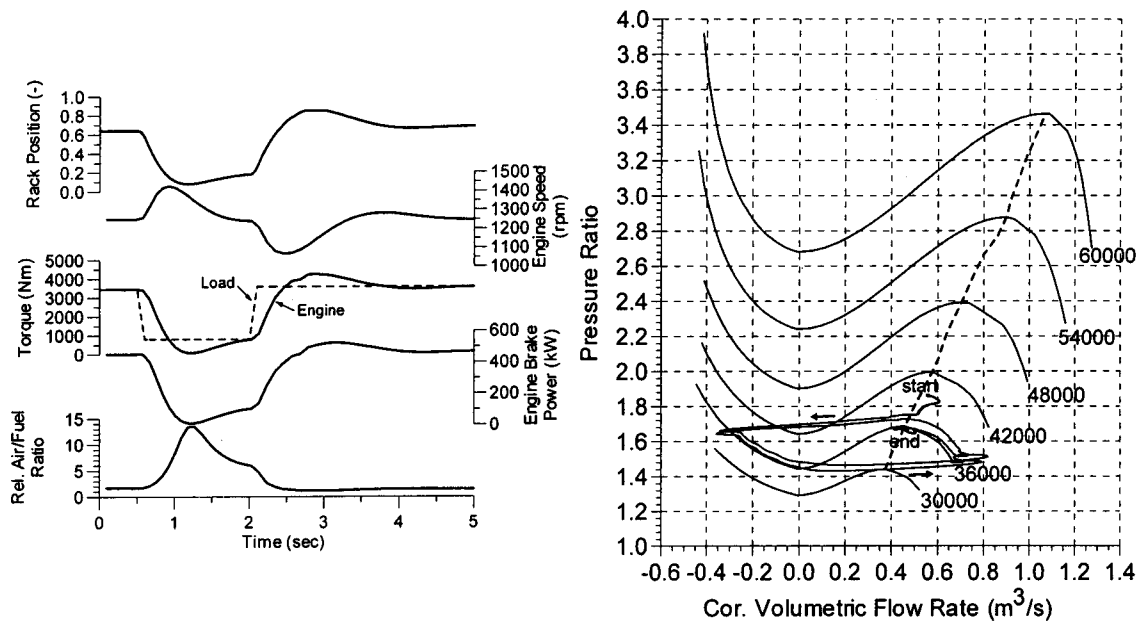


Fig. 8 Simulation results for engine transient operation at 1250 rpm—load changes 85%–10%–90%

an engine speed drop of about 15% (1270 rpm at 2.4 sec). This resulted in the reduction of the compressor mass flow rate, and thus the compressor operating point on the compressor map moved towards the surge line. Subsequently, the engine speed increased due to the action of the engine speed governor, so the compressor mass flow rate increased and as a result the compressor operating point moved away from the compressor surge line.

In the examined case, i.e. with engine running at 1500 rpm, the surge margin was adequate for avoiding compressor surging. However, considering the case where the engine operates at 1250 rpm, the compressor operating point is located closer to the surge line and the surge margin is less than the one for the case of engine running at 1500 rpm. The predicted engine parameters and the trajectory of the compressor operating points, for the case of engine running at 1250 rpm with load changes 85%–10%–90% are given in Fig. 8. The predicted compressor parameters for the same case are shown in Fig. 9. As can be seen from these figures, compressor surging occurred during the engine load increase at about 2.3 sec. At that time, the engine speed had dropped to 1050 rpm, which caused the reduction of the compressor mass flow

rate, and thus the compressor operating point moved inside the compressor unstable area. Subsequently, with the increase of the engine speed due to the response of engine governor, the compressor operating point moved again into the compressor stable operating region. As can be seen from Fig. 9, the compressor surge cycle lasted about 0.2 sec and consists of the period of positive to negative flow reversal (where the compressor flow was almost instantaneously reduced from 0.5 kg/s to -0.4 kg/s), the period of negative flow, the period of the negative to positive flow reversal (where the compressor flow almost instantaneously increased from 0 kg/s to 0.95 kg/s), and the recovery period. During the compressor negative flow period, the pressure downstream of the compressor was reduced from 1.75 bar to 1.45 bar within 0.08 sec, and subsequently, after the negative to positive flow reversal, the pressure downstream of the compressor increased again, reaching 1.7 bar at 2.5 sec, before the next compressor surge cycle. As shown in Fig. 9, during compressor surging the torque absorbed by the compressor impeller rapidly varied (especially during the flow reversals), thus introducing severe torsional loadings to the turbocharger shaft. Due to the changes of compressor

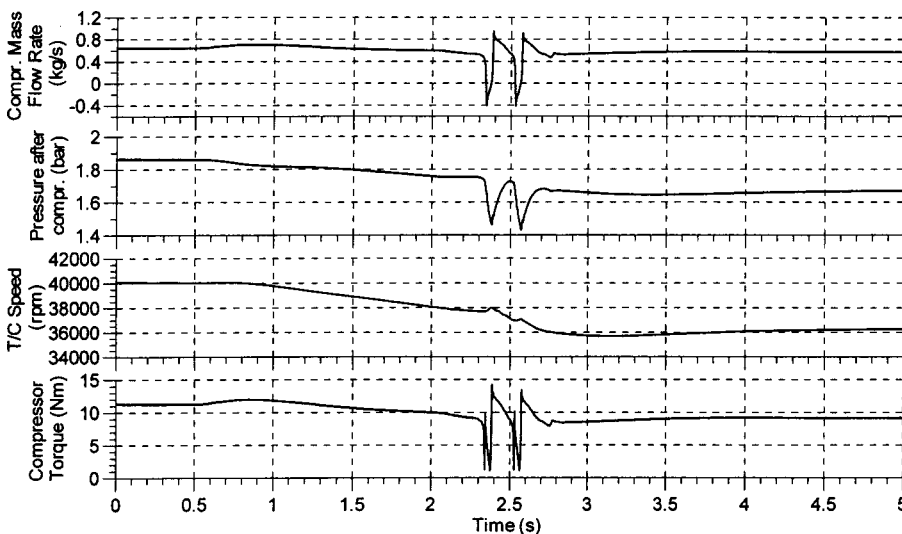


Fig. 9 Predicted compressor parameters for engine transient operation at 1250 rpm—load changes 85%–10%–90%

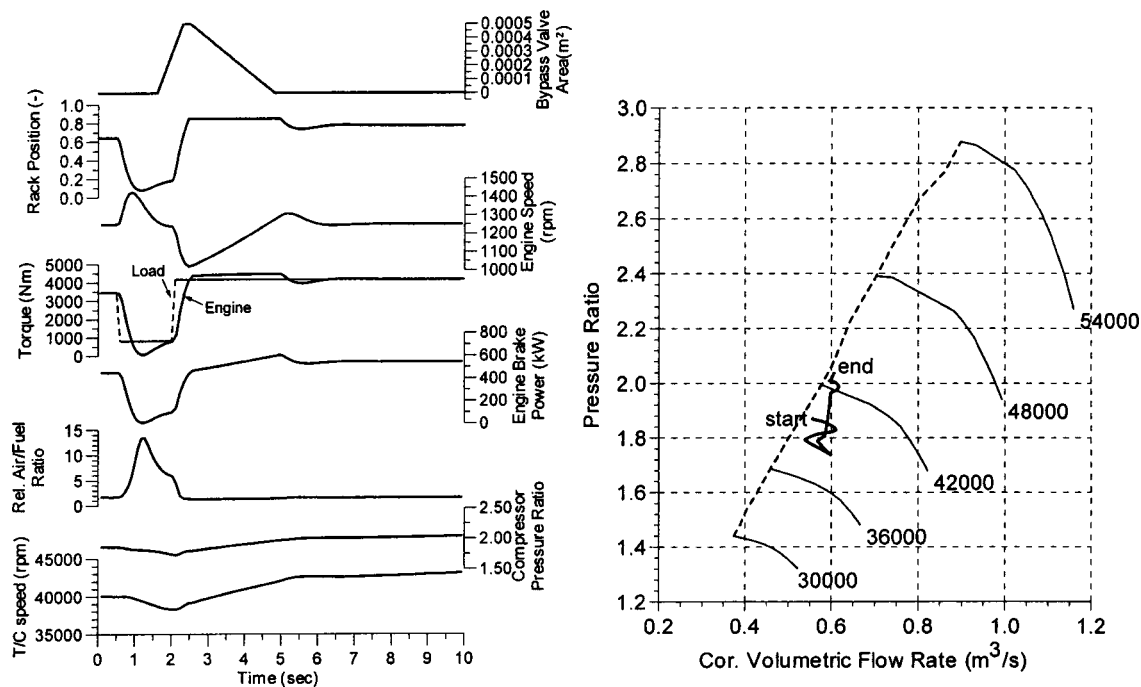


Fig. 10 Simulation results for engine transient operation at 1250 rpm and bypass opening—load changes 85%–10%–100%

torque, the turbocharger speed increased about 200 rpm during the period of negative compressor flow, and was subsequently reduced after the negative to positive flow reversal. It is evident that such flow, pressure, and turbocharger shaft torque oscillations can harmfully influence both the engine and turbocharger operation. In the examined case, the compressor surging lasted less than 0.5 sec, and therefore it cannot critically affect the engine safe running. However, the continuous occurrence of compressor surging can adversely affect the engine running and should be avoided.

A way of avoiding compressor surging, even when the engine operates under dangerous load profiles, is by using a bypass valve, connecting the compressor outlet and the turbine inlet. By opening this valve, some of the compressor air passes into the turbine. In

that way, the turbine and also the compressor mass flow rates are greater than the one required by the engine. In addition, since the energy of the bypass air is used by the turbine (and not wasted, as in the case of a simple pressure relief valve), the turbocharger speed also increases. As a result, the compressor operating point moves further away from the surge line.

The predicted engine and compressor parameters and the trajectory of the compressor operating points, for the case of engine running at 1250 rpm with load changes 85%–10%–100% and bypass valve opening, are shown in Fig. 10. The bypass valve was progressively opened starting from about 1.6 sec, just before the forthcoming engine load increase, till the point of minimum engine speed at about 2.3 sec. Thus, the compressor mass flow was

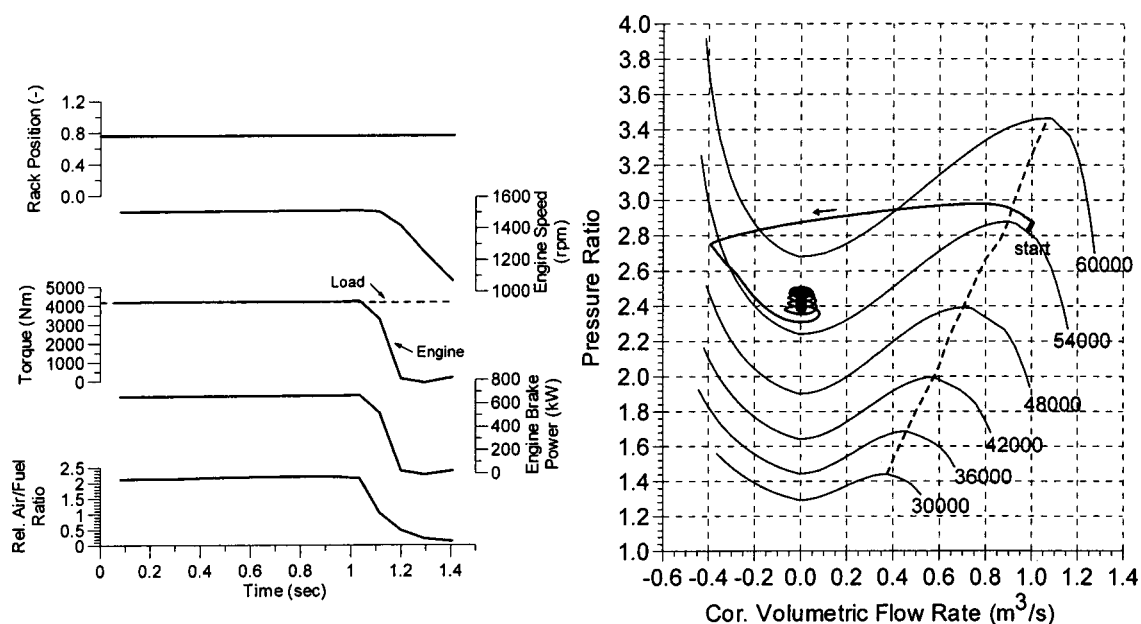


Fig. 11 Simulation results for engine transient operation during emergency shutdown

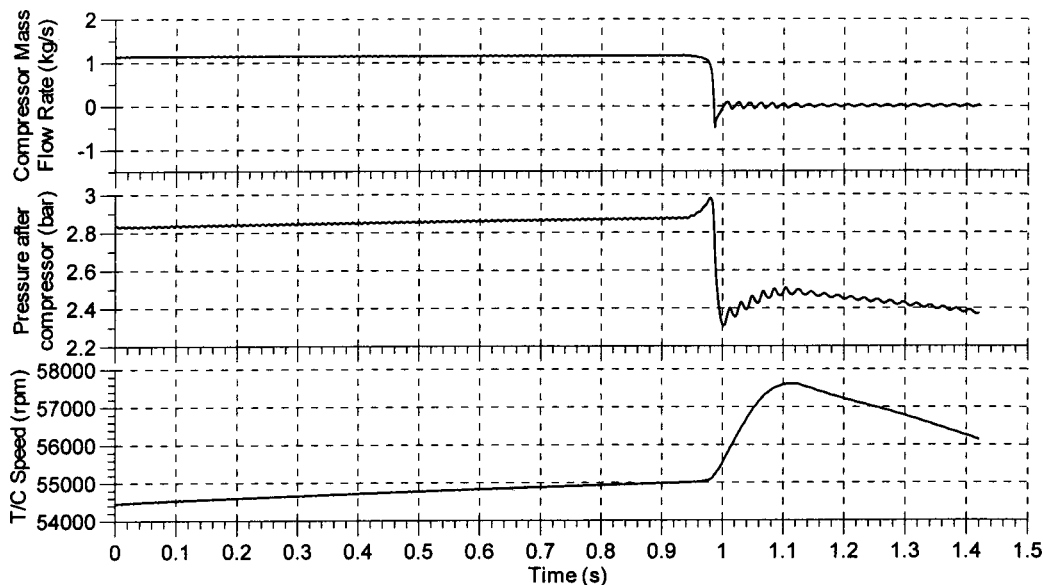


Fig. 12 Predicted compressor parameters for engine transient operation during emergency shutdown

increased and the compressor operating point was moved in an adequate margin away from the surge line at 2 sec. Therefore, the engine speed drop (from 1250 rpm at 2 sec to 1050 rpm at 2.4 sec) did not cause compressor surging. The bypass valve was then progressively closed until its fully closed position at about 4.5 sec, when the engine speed was close to its initial value of 1250 rpm. In addition, as can be seen comparing Figs. 9 and 10, the bypass valve opening also prevented the turbocharger speed reduction for the time period after about 1.8 sec.

Finally, the CAT 3508 engine emergency shutdown was simulated. The engine emergency shutdown valve is located between the compressor outlet and the engine air cooler and it instantaneously closes in any case where an emergency alarm is activated. Thus, the air supply to the engine cylinders is immediately cut and the engine shuts down due to the lack of air to maintain the fuel combustion in the cylinders. The predicted engine parameters and the trajectory of the compressor operating points on the compressor map for such a case are presented in Fig. 11. In addition, the compressor parameters are shown in Fig. 12.

Initially, the engine was operating at 1500 rpm and 100% load. The emergency shutdown procedure was initiated at 0.9 sec. At that instant, the emergency shutdown valve started closing and it fully closed at 1 sec. As Fig. 11 and Fig. 12 show, during the closing of the emergency shutdown valve, the pressure after the compressor was gradually increased, from 2.85 bar at 0.94 sec to almost 3 bar at about 0.98 sec. Therefore, the compressor operating point was driven into the compressor unstable region, and the compressor flow rate became almost instantly negative at about 0.98 sec. However, the surge cycle was not completely followed, since after the negative to positive flow reversal (at about 1 sec), the shutdown valve had been fully closed, so the compressor flow became almost zero. Due to flow reversal, the pressure after compressor was reduced to 2.3 bar at 1 sec, whereas the turbocharger speed increased, from 55,000 rpm at 0.98 sec to 57,600 rpm at about 1.1 sec, because the compressor impeller absorbed torque was reduced due to the reduction of the compressor mass flow. It was only after 1.1 sec that the turbocharger speed was reduced due to the reduction of the exhaust gas energy, which resulted in the reduction of the turbine torque. After the closing of the shutdown valve, and due to the turbocharger rotation, the pressure after compressor followed the changes of the turbocharger shaft speed, i.e., it increased from 2.3 bar at 1 sec to 2.5 bar at 1.1 sec, and then started decreasing since the turbocharger shaft decelerated.

The closing of the emergency shutdown valve resulted in lack of air for combustion (the relative air/fuel ratio dropped below 0.6, which is the limit for combustion). Thus, the engine torque was reduced (almost to 0 within 0.2 sec), and since the load torque was considered to be constant, the engine rapidly decelerated.

Conclusions

The behavior of a four-stroke, large high-speed engine was examined using a detailed engine simulation code in conjunction with a model capable of predicting the compressor dynamic behavior including cases of compressor surging. Initially, the simulation code steady-state results were validated against experimental data. Then, the engine speed governor model was calibrated based on available engine transient measurements. After that, engine transient simulation using the existent as well as the developed compressor models was performed. Subsequently, additional transient runs were performed, in which, "dangerous," for compressor surging, engine load profiles were imposed. Furthermore, a way of avoiding compressor surging by appropriately opening a bypass valve connecting the compressor outlet and the turbine inlet was examined. Finally, the case of the engine emergency shutdown was also investigated.

The main conclusions derived from the present study are as follows:

The engine simulation code combined with the new compressor model can be used for predicting the engine and its turbocharger dynamic behavior providing more realistic compressor transient performance predictions because the inertia of the air inside the compressor passages as well as the departure of the compressor characteristics during transients from their steady-state form are now taken into account. In addition, the engine and turbocharger behavior can be predicted even in cases where the compressor exhibits surging as well as during engine emergency shutdown.

Engine load profiles dangerous for causing compressor surging were identified. The transient simulation results showed that compressor surging can occur under certain loading conditions if there is inadequate compressor surge margin, thus designating the limits for the engine safe operation. In that respect, the results of this study are used from the LME in order to avoid conditions in the CAT 3508 engine testbed that could lead into compressor surging and thus endanger the integrity of the test unit.

During compressor surging, the compressor mass flow rate exhibits large amplitude oscillations, resulting in also severe fluctua-

tion of the pressure downstream of the compressor, which can adversely affect the turbocharger and engine operation. In addition, the almost instant changes of the compressor absorbed torque can introduce severe torsional loading to the turbocharger shaft.

Compressor surging can be avoided by appropriately opening a bypass valve connecting the compressor outlet and the turbine inlet. In such case, the simulation code can provide the required data for designing a controller for the bypass valve.

The simulation of the engine operation with compressor surging as well as the engine emergency shutdown provides results that cannot be easily measured and thus contributes to the better understanding of the dynamic behavior of the engine and its turbocharger in such cases.

Nomenclature

A	= area (m ²)
U	= compressor impeller tip velocity (m/s)
c	= velocity (m/s), constants
c_p	= specific heat at constant pressure (J/kg K)
k	= constants
L	= length (m)
m	= mass (kg)
\dot{m}	= mass flow rate (kg/s)
p	= pressure (N/m ²)
pr	= pressure ratio
\dot{Q}	= heat transfer rate (kW)
R	= gas constant (J/kg K)
r_1	= impeller eye mean geometric radius (m)
r_2	= impeller tip radius (m)
T	= temperature (K)
t	= time (s)
y	= rack position
Γ	= Nondimensional torque coefficient
γ	= ratio of specific heats
η	= efficiency
I	= polar moment of inertia (kg m ²)
N	= rotational speed (rpm)
ϕ	= flow coefficient
ρ	= density (kg/m ³)
τ	= time constant (s), torque (Nm)
ω	= angular speed (rad/s)

Subscripts

o	= total conditions
0	= zero flow
1	= compressor inlet
2	= compressor outlet
3	= turbine inlet
4	= turbine outlet
c	= compressor
E	= engine
I	= I-constant
$init$	= initial
$ncyl$	= number of cylinders
mer	= meridional
L	= load
ord	= ordered
P	= P-constant
p	= plenum
srg	= at surge line
ss	= steady state
TC	= turbocharger
t	= turbine
tot	= total

References

- [1] Watson, N., and Banisoleiman, K., 1987, "Computers in Diesel Engine Turbocharging System Design," *IMEchE*, C05/87.
- [2] Sams, T., Regner, G., and Chmela, F., 2000, "Integration of Simulation Tools to Optimize Engine Concepts," *Motortech. Z.*, (9), pp. 601–608.
- [3] Bartsch, P., Prenninger, P., and Allmer, I., 1998, "Transient Performance Optimization of Turbocharged Engines by Means of Gas Exchange Simulations," *IMEchE International Conference on Turbocharging and Air Management Systems*, C554/016/98, IMechE, London, pp. 237–251.
- [4] Klingmann, R., Fick, W., and Bruggemann, H., 1999, "The new Common Rail Direct Injection Diesel Engines for the updated E-class Part 2: Combustion and Engine Management," *Motortech. Z.*, No. 7/8-1999, pp. 426–437.
- [5] Biaggini, G., Buzio, V., Ellensohn, R., and Knecht, W., 1999, "The New Iveco Cursor 8 Diesel Engine," *Motortech. Z.*, No. 10-1999, pp. 640–649.
- [6] Hild, O., Fieweger, K., Pischinger, S., Rake, H., and Schlosser, A., 1999, "The Controlled System of a Direct-Injection Diesel Engine for Passenger Cars with Regard to the Control of Boost Pressure and Exhaust Gas Recirculation," *Motortech. Z.*, No. 3-1999, pp. 186–192.
- [7] Filipi, Z. S., Wang, Y., and Assanis, D. N., 2001, "Effect of Variable Geometry Turbines on Diesel Engine and Vehicle System Transient Response," SAE Paper No. 2001-01-1247.
- [8] Kyrtatos, N. P., Politis, G., Lambropoulos, V., Theotokatos, G., Xiros, N., Coustas, J. D., 1998, "Optimum Performance of Large Marine Engines Under Extreme Loading Conditions," *22nd CIMAC International Congress*, May 18–21, Copenhagen, CIMAC, Frankfurt, 6, pp. 1539–1553.
- [9] Greitzer, E. M., 1976, "Surge and Rotating Stall in Axial Flow Compressors. Part I: Theoretical Compression System Model," *ASME Journal of Engineering for Power*, 98, pp. 190–198.
- [10] Hansen, K. E., Jørgensen, P., and Larsen, P. S., 1981, "Experimental and Theoretical Study of Surge in a Small Centrifugal Compressor," *ASME Journal of Fluids Engineering*, 103, pp. 391–395.
- [11] Fink, D. A., Cumpsty, N. A., and Greitzer, E. M., 1992, "Surge Dynamics in a Free-Spool Centrifugal Compressor System," *ASME J. Turbomach.* 114, pp. 321–332.
- [12] Chesse, P., Hetet, J. F., Tauzia, X., Roy, P., and Inozu, B., 1998, "Performance Simulation of Sequentially Turbocharged Marine Diesel Engines with Applications to Compressor Surge," *Proceedings of ASME ICE Spring Technical Conference*, ASME, New York, 30-2, pp. 31–40.
- [13] Skopil, M., and Bulaty, T., 1998, "Calculation of Compressor Surge With Unsteady Flow Model," *IMEchE International Conference on Turbocharging and Air Management Systems*, C554/018/98, IMechE, London, pp. 219–225.
- [14] Theotokatos, G., and Kyrtatos, N. P., 2001, "Diesel Engine Transient Operation with Turbocharger Compressor Surging," SAE Paper No. 2001-01-1241.
- [15] Theotokatos, G., 2001, "Analysis of Turbocharger Operation Including Compressor Surging During Transient Loading of Marine Diesel Engines," Dr. Eng. Thesis, Department of Naval Architecture and Marine Engineering/National Technical University of Athens, Athens, Greece.
- [16] Kyrtatos, N. P., and Koumbarelis, I., 1994, "Performance Prediction of Next-Generation Slow Speed Diesel Engines during Ship Manoeuvres," *Trans IMarE*, 106, Part 1, pp. 1–26.
- [17] Kyrtatos, N. P., ed., 1999, *MOTOR THERMODYNAMICS Ver 1.3—USER MANUAL*, PRD Ltd., Athens.
- [18] Watson, N., and Janota, M. S., 1982, *Turbocharging the Internal Combustion Engine*, Macmillan, London.
- [19] Woschni, G., 1967, "Universally Applicable Equation for the Instantaneous Heat Transfer Coefficient in the Internal Combustion Engine," SAE Paper No. 670931.
- [20] Rohsenow, W. M., Hartnett, J. P., and Ganic, E., 1985, *Handbook of Heat Transfer Fundamentals*, 2nd Ed., McGraw-Hill, New York.
- [21] Heywood, J. B., 1988, *Internal Combustion Engines Fundamentals*, McGraw-Hill, New York.
- [22] Ciulli, E., 1992, "A Review of Internal Combustion Engine Losses, Part I: Specific Studies on the Motion of Pistons, Valves and Bearings," *Proc. IMechE*, 206, pp. 223–236.
- [23] Wachter, J., and Lohle, M., 1984, "Experimental Investigation of the Dynamic Behavior of Centrifugal Compressors," Stability, Stall and Surge in Compressors and Pumps, D. Japikse, ed., ASME, New York, ASME FED-Vol. 19, pp. 23–30.
- [24] Moore, F. K., and Greitzer, E. M., 1986, "A Theory of Post-Stall Transients in Axial Compression Systems—Part I: Development of Equations," *ASME J. Eng. Gas Turbines Power*, 108, pp. 68–76.
- [25] Caterpillar Co., 1981, "Technical Information Release—The 3508 Engine", TIR 10-381, 6/81.
- [26] Kyrtatos, N. P., Ioannidis, I. P., Pavlidis, V., Ventouris, K., and Raptis, D., 2001, "The New Laboratory Facility 'MARTHA' for Marine Propulsion Research and Development", 23rd CIMAC World Congress, May 7–10, Hamburg, CIMAC, Frankfurt, pp. 1566–1575.
- [27] Naguib, M., 1986, "Experience With the Modern RR 151 Turbocharger for High-Speed Diesel Engines," *IMEchE Conference on Turbocharging and Turbochargers*, C99/86, IMechE, London, pp. 105–112.

Improvement of the Dynamic Characteristic of an Automotive Engine by a Turbocharger Assisted by an Electric Motor

T. Katrašnik

S. Rodman

F. Trenc

e-mail: ferdinand.trenc@fs.uni-lj.si

Department of Mechanical Engineering,
University of Ljubljana,
Aškerševa 6, SI-1000 Ljubljana, Slovenia

A. Hribernik

Department of Mechanical Engineering,
University of Maribor,
Smetanova 17, SI-2000 Maribor, Slovenia

V. Medica

Faculty of Engineering,
University of Rijeka, Vukovarska 58,
5100 Rijeka, Croatia

Turbocharging and subsequent charge cooling of the working medium usually causes increase of the mean effective pressure in an automotive diesel engine. Poor performance during the engine load increase is attributed to the nature of energy exchange between the engine and the turbocharger. Filling of the intake and exhaust manifolds, as well as consequent increase of the pressure and acceleration of the rotating components of the turbocharger require a certain period of time. Dynamic performance of the turbocharger can be substantially improved by means of an electric motor attached directly to the turbo shaft. A new concept of asynchronous electric motor with a very thin rotor was applied to support the turbocharger during the transient operation of the engine. The experimental work of matching an electrically assisted turbocharger to an engine is rather expensive; it was therefore decided to determine general characteristic of the electric motor separately through experiments, whereas transient response of the turbocharged and inter-cooled diesel engine was simulated by a zero-dimensional filling and emptying computer simulation method. A lot of experimentally obtained data and empirical formulae for the compressor, gas turbine, flow coefficients of the engine valves, intercooler, high-pressure fuel pump with the pneumatic control device (LDA), combustion parameters, etc., were applied to overcome deficiency introduced by the zero-dimensional simulation model. As the result a reliable and accurate program compatible with the experimental results in steady and transient engine operation was developed and is presented in the work. Faster transient response, i.e., better load acceptance of the engine was obtained by applying an adequate electric motor to assist the turbocharger; three versions of electric motors with different torque to mass moment of inertia ratios and different operating regimes were introduced in the simulation program to investigate their influence on the transient behavior of the engine. [DOI: 10.1115/1.1563246]

Introduction

Advanced automotive diesel engines can achieve 2 MPa bmep. A suitable turbocharger consisting of a centrifugal compressor and a radial exhaust gas turbine must ensure high overall efficiency along the operation range of the engine; the principal goals are sufficient air to achieve high bmep and low exhaust emission especially at low engine speed and adequate scavenging of the cylinder with lower pumping losses.

Mass flow of the combustion air through the engine is proportional to the engine speed and to the boost air pressure. Swallowing characteristic of the turbocharger turbine is progressive: when mass flow through the turbine is increased, there is a steep increase of the pressure ratio across the turbine and of the developed torque. Higher turbine torque and higher turbo speed result in higher compressor pressure ratios. The problem of adequate compressor pressure ratios, optimum in-cylinder trapped mass of air at the engine rated conditions, and simultaneous shortage of air at lower engine speed is well known. In addition additional time is required for boost pressure to build up in a turbocharged engine during a sudden load increase; deficiency of combustion air leads—compared to the steady-state values—to insufficient values of the mean effective pressure and, particularly in engines without boost pressure controlled fueling, to higher emission of black

smoke. Air-fuel ratio in the cylinder is lower during the load acceptance period and the combustion temperature is consequently higher; higher turbine torque output is therefore achieved due to higher specific enthalpy of exhaust gasses. This torque is used to accelerate the turbocharger and to raise the compressor boost pressure. The intensity of increase of the boost pressure in the intake manifold influences the trapped mass of the air in the cylinders and strongly depends on the capacity of the intake and exhaust manifolds, turbocharger characteristics, and mass moment of inertia of the turbocharger.

Several methods and systems have been developed to improve the transient response of a turbocharged engine.

- The simplest way to improve the response of the engine to sudden load increase is a small capacity turbine housing: restricted flow area increases pressure drop across the turbine, and simultaneously increases the turbine torque to be used for the acceleration and to increase boost pressure of the turbocharger. If maximum allowable pressure ratios are exceeded, a boost pressure controlled bypass valve is applied as reported by Watson and Zinner [1,2]. Smaller capacity turbine affects and limits the engine power at higher speeds.
- Better dynamic response of the engine can also be achieved by introduction of a gas turbine with variable geometry of the vaned passages from the turbine scroll to the rotor, [1–3]. Adjustment of the flow area is electronically controlled. Consequently a more suitable engine torque curve and better transient response of the engine can be obtained.
- Compensation and increase of the boost pressure in the intake

Contributed by the Internal Combustion Engine Division of THE AMERICAN SOCIETY OF MECHANICAL ENGINEERS for publication in the ASME JOURNAL OF ENGINEERING FOR GAS TURBINES AND POWER. Manuscript received by the ICE Division Oct. 2001; final revision received by the ASME Headquarters Oct. 2002. Associate Editor: D. Assanis.

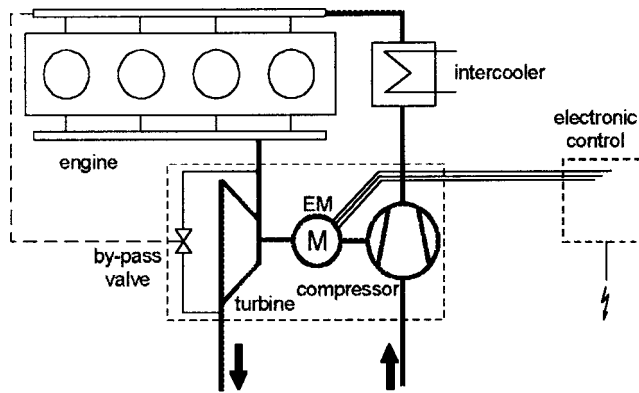


Fig. 1 Scheme of an engine with electrically assisted turbocharger

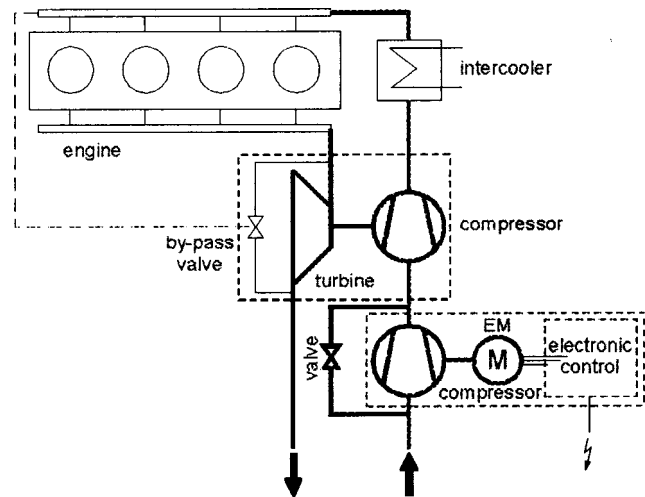


Fig. 2 Scheme of a turbocharged engine with separate electrically driven compressor

manifold during the engine transient can be ensured, according to Watson and Winterbone [1,4], by blowing extra compressed air into intake manifold, exhaust manifold or directly (and most efficiently) into the compressor wheel. Large quantities of extra compressed air with relatively high pressure are required.

- Compressed air can be replaced by a simple Pelton wheel driven by a jet of engine oil as reported by Watson and Winterbone [1,4]. Better acceleration of the engine during the transient can be obtained by means of compressed air, [4].
- According to Zellbeck et al., Shahed et al., and Hoecker et al. [5–7] electrical energy has been more and more applied for acceleration of the turbocharger rotor. An electric motor can be attached to the turbocharger shaft or used for autonomous drive of a separate compressor wheel. Synchronous or asynchronous electric motors are applied during the transient operation of the engine. Certain electric motor assisted systems can be applied also during the steady-state operation of the engine and can substantially increase engine torque and therefore improve performance of the engine, especially at low engine speeds, reported Zellbeck et al. [5]. Supplementary torque and mass moment of inertia of an electric motor, attached to the turbocharger shaft, can significantly affect the dynamic characteristic of the turbocharger and the engine, Fig. 1, [7]. Engine response to the load change can be improved if the following expression is fulfilled.

$$\frac{M_T + M_{EL} - M_c}{J_{TP} + J_{EL}} > \frac{M_T - M_c}{J_{TP}} \quad (1)$$

where M_T , M_{EL} , and M_c denote the torque developed by the turbine and the electric motor, and consumed by the compressor, whereas J_{TP} and J_{EL} denote appropriate mass moments of inertia. An even better control of the turbo speed is achieved by application of a synchronous electric motor proposed by Shahed et al. [6]. At very high rotational speeds electric motor converts to generator and thus helps to reduce rotor speed of the turbocharger.

- Another very interesting approach to improve the dynamic characteristic of the engine was proposed by Hoecker et al. [7], Fig. 2. A separate compressor is driven by an electronically controlled electric motor and is followed by an ordinary turbocharger. A separate electrically driven compressor is applied only during the transient operation of the engine, otherwise air flows through a bypass of the disconnected electrically operated compressor to the intake of the turbocharger compressor. Boost pressure increase is very fast. Air flows through the bypass of the disconnected electrically operated compressor to the intake of the turbocharger compressor. A

very reliable and independent dynamic operation of the turbocharger and the auxiliary compressor is obtained; though the price of the system is high.

The presented paper investigates the influence of an electric motor attached to the turbo shaft on transient response of a turbocharged diesel engine. Comparison based on numerical simulations was made between a conventional turbocharged diesel engine with free floating turbocharger and the same engine with the electrically assisted turbocharger. The paper is organized as follows: A zero-dimensional simulation code was developed and verified by the experiments for stationary and transient operation of a turbocharged diesel engine.

A thin-rotor high-speed asynchronous electric motor was described in the following chapter where its principal characteristics and dimensions were determined. Results of electric tests performed separately on motors with different principal dimensions and performances were applied as boundary conditions for more realistic numerical simulations of the engine transient operation.

Comparison of the conventional turbocharged diesel engine and an electrically assisted turbocharged engine based on numerous numerical simulations during the engine transient operation of the engine were analyzed and are presented in the chapter: "Results of the Simulations With the Electrically Assisted Turbocharged Engine During the Transient Operation."

Setup of the Simulation Program

A zero-dimensional simulation code was applied to investigate steady-state and dynamical behavior of the turbocharged and aftercooled diesel engine. The main scope of the performed simulation is to describe as well as possible mass and energy transfer between the engine and the turbocharger. The simulation of the transient regime of an engine requires processing of many consecutive events, and the application of a zero-dimensional computational code is therefore a good compromise between the expected accuracy of the results and the required computational time. A FORTRAN simulation program was run on a PC with an AMD 1.2 GHz processor. Required time to compute a complete four-stroke six-cylinder turbocharged diesel engine cycle (720° C.A.) amounts to 0.072 s. Numerical simulation of such an engine configuration at 1667 rpm is therefore possible within the real time. For numerical simulation purposes, complete system of a turbocharged diesel engine is described and proposed by Medica [8]. The simulation software can be automatically adapted to the described system consisting of control volumes that are interconnected by appropriate connections for mass and energy transfer.

The observed engine and its components were replaced by control volumes: cylinders, intake manifold, and exhaust manifolds that are interconnected by the compressor, turbine, inlet, and exhaust valves. The exchange of mass and energy was simulated by the filling and emptying method. Perfect mixing of the working medium in control volumes was assumed. Basic equation that describes temperature change within a control volume was derived from the previously mentioned conservation laws and took into account gas properties correlated to the temperature and A/F ratio according to the data published by Jankov [9]. The computer program is described in details by Katrašnik [10].

Accuracy and applicability of the previously mentioned zero-dimensional code strongly depends on the amount of the available experimentally defined input data. Compressor efficiency and its flow characteristic were determined by a two dimensional approximation polynomial. Intercooler characteristic in the simulation program took into account experimental data. Measured swallowing characteristic of the applied twin-entry divided free-floating radial turbine was applied in order to determine nonsteady flow coefficients in particular exhaust manifold branches by the application of a special computer program developed by Hribernik [11]. The same method was also applied to correct measured steady state values of the gas turbine efficiency, [12], for different pressure ratios in particular turbine entries, different mean expansion ratios and different turbo speeds. Flow coefficients of the intake and exhaust valve were determined by experiments and are approximated by a suitable polynomial for the simulation, [13,14]. Fuel delivery rate was determined by experiments as the function of the control rack position. A pneumatically controlled regulator (LDA) operated by the boost pressure is attached to the high pressure pump to limit excess fueling during the acceleration or sudden load increase of the engine, and therefore to avoid excess emission of the black smoke. Its characteristic was measured and expressed as the function of the boost pressure. Injection timing parameters were approximated by a two-dimensional function depending on the engine speed and on the quantity of the injected fuel. Combustion process in the cylinder was approximated by the single Vibe function; its application was justified by relatively late fuel injection that in turn led to a relatively smooth heat release. Vibe parameters were determined by the analysis of the measured p - V diagrams. Mechanical losses were determined by the formula of Thiele [15], which showed good agreement with the data obtained experimentally.

Validation of the Simulated Steady-State and Transient Operation of the Engine. A six-cylinder 6.87-liter turbocharged and aftercooled automotive low emission diesel engine MAN D 0826 LOH 15, with 108/125 mm bore/stroke, compression ratio 18:1, equipped with the HOLSET H1E-8264BF/H16WA8 turbocharger and developing 162 kW/2400 rpm was used in the experiments. Comparisons between measured and computed data were first performed for different steady-state engine running conditions. Individual simulation process was concluded when the difference between the initial and final values of particular simulated parameters in a working cycle didn't differ by more than 0.01%. Agreement between measured and calculated values of the mean boost and exhaust pressure, as well as the turbocharger speed was better than 4%.

Achieved accuracy of transient simulation and good agreement with experimental results (Fig. 3) played a crucial role in later numerical investigations of transient response of the engine with electrically assisted turbocharger. Special care was devoted to the accuracy of the computed boost pressure, as in turn it determines the quantity of the injected fuel. All engine and turbocharger parameters can be continuously followed and inspected throughout the particular working cycles of the performed transient.

A sudden load increase from $bmp=0.4$ to 1.4 MPa at the engine speed of approximately $n=1500$ rpm was performed on the engine dynamometer and simultaneously simulated for the validation of the applied simulation. Control system of the dynamometer

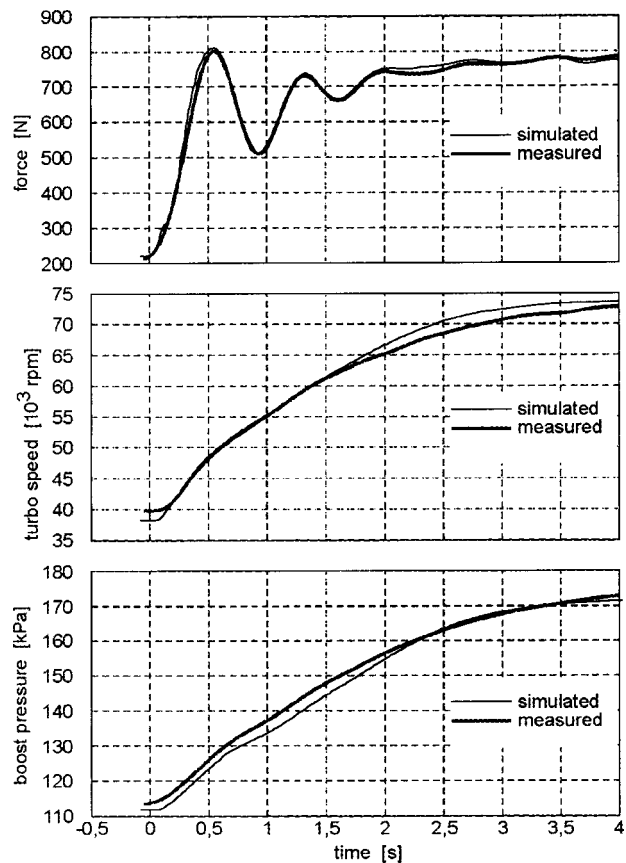


Fig. 3 Results of comparison between measured and simulated transient operation of the engine; B.E.M.P.=0.4→1.4 MPa

has not been designed for transient measurements and can't simultaneously follow the change of the engine torque; oscillations of the engine speed are observed during the initial sequence of the engine transient operation. No data on dynamometer dynamic characteristic were available. Simulated braking force of the dynamometer was calculated from the instantaneous computed engine power and from the corresponding time derivative of the measured instantaneous engine speed. Results of the previously mentioned simulated and measured transient operation of the engine are presented in Fig. 3. When braking force F is considered a very good agreement was achieved. Good agreement can also be observed for the boost pressure and the turbo speed; they are very important for the simulation of the engine torque and power as mentioned earlier.

Application of the Electric Motor to Improve Transient Response of the Engine

A high-speed asynchronous electric motor with a thin rotor was tested separately by the ISKRA Avtoelektrika d.d. from Sempeter pri Gorici, Slovenia, to determine its principal characteristics and dimensions. It was planned for later installation into the turbocharger close to the back plate of the compressor wheel, Fig. 4. Better cooling ability, suitable loading of the existing bearing, and better access for the stator windings can thus be assured. Initial, simple, 10-mm-wide rotor plate was composed of steel plates will cast aluminum core. Maximum voltage of 28 V was applied for the initial measurements. Efficiency of the electric motor was determined as the ratio between the available shaft power and the consumed electric power and amounted to 45%. Outer rotor diameter of 82 mm at EM1 led to an unacceptably high mass moment of inertia and consequently to low torque-mass moment of inertia ratio; Eq. (1) was not fulfilled and therefore further inves-

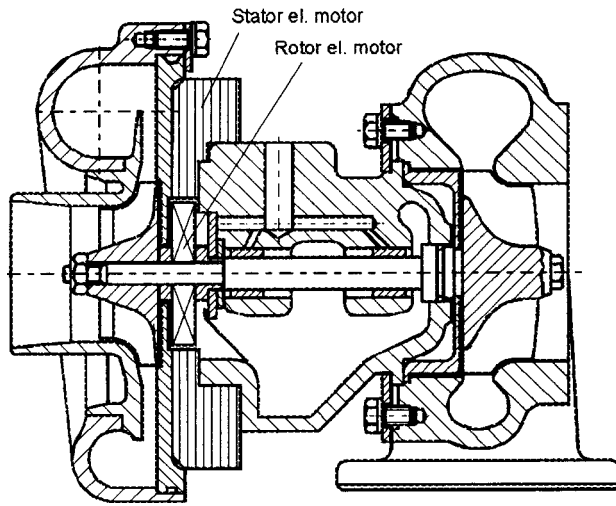


Fig. 4 Layout of the turbocharger with the integrated electric motor

tigations with the EM1 were stopped. The diameter of the rotor was then first reduced to 60 mm (EM2) and the mass moment of inertia was consequently reduced by six times. Better efficiency during the acceleration procedure was obtained by controlling the slip and by applying higher voltage—42 V. Mass moment of inertia was 6.10^{-5} kgm^2 and the maximum developed torque amounted to 0.2 Nm. The obtained ratio between the available torque and the mass moment of inertia was relatively low due to very slim and adapted configuration of the rotor. This ratio was additionally increased by increasing the rotor width to 20 mm and slightly reducing the rotor diameter (motor EM3), see Table 1.

Results of the Simulations With the Electrically Assisted Turbocharged Engine During the Transient Operation. Results of numerical simulations for the transient operation of the engine without and with attached auxiliary electric motors EM2 and EM3 at $n = 1500 \text{ rpm}$, and by sudden change of the fuel rack position to its ultimate value ($b_{mep} = 0.4 \rightarrow 1.5 \text{ MPa}$) are shown in Fig. 5. Acceleration of the turbocharger was performed with both electric motor versions operating up to 70,000 and 80,000 rpm, respectively. These two limiting speeds were selected due to their position just above and below 77,000 rpm at which boost pressure that allows full fueling (LDA controlled) at the engine speed 1500 rpm is achieved. The upper diagram in Fig. 5 represents changes of the turbocharger speed during the transient; both auxiliary electric motors EM2 and EM3 improved the dynamic response of the turbocharger. The best results were obtained by the application of the more powerful EM3 motor; full turbo speed is obtained within 1.8 s. If the turbocharger is supported by the electric motor to only 70,000 rpm, further acceleration is slower due to increased (combined) mass moment of inertia, Eq. (1). Boost pressure is a function of the turbocharger speed; similar trends can therefore be expected. Engine power output is proportional to the quantity of the injected fuel, which is continuously controlled by the boost

Table 1 Characteristic parameters of the observed electric motors

El. Mot. Type	Diameter (mm)	Width (mm)	Mass Moment of Inertia (kgm^2)	Max Torque (Nm)	Torque/Mass Moment of Inertia (Nm/kgm^2)
EM1	83	10	36.10^{-5}	0.3	833
EM2	60	10	6.10^{-5}	0.2	3333
EM3	50	20	6.10^{-5}	0.4	6667

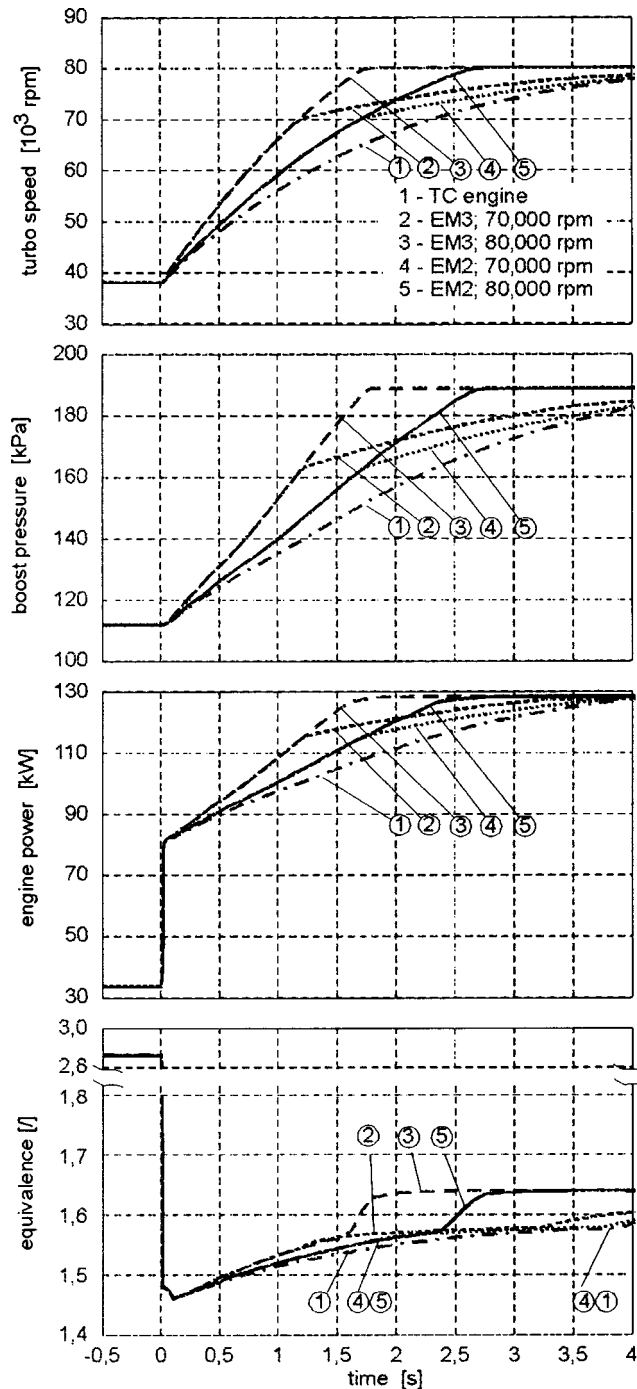


Fig. 5 Simulation of the transient response of the turbocharged engine with different auxiliary driving electric motors

pressure via the LDA pneumatic controller (Fig. 6). Power is therefore directly proportional to the boost pressure dependent cyclic fuel delivery until the boost pressure for full fueling is reached—this phenomenon can be clearly seen in Fig. 5 and Fig. 6. It is therefore not advisable (when developed engine power is considered) to raise the boost pressure by the electric motor assistance above the—by the LDA defined—limiting value at which full fueling is allowed. Value of the equivalence ratio λ is also controlled by setting of the LDA controller; its minimum set value of approximately 1.46 (bottom Fig. 5) during the transient engine operation assures low black smoke emission (black smoke emission is a strong function of the λ). An auxiliary electric motor can

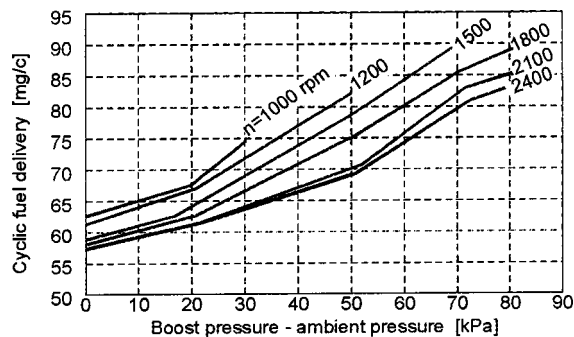


Fig. 6 Boost pressure control of the cyclic fuel delivery for different engine speeds

greatly improve the transient response of a turbocharged engine by a more intensive increase of the boost pressure and consequently by the larger amount of the injected fuel.

Load acceptance of the engine under transient operating conditions at a sudden load increase and different turbocharger configurations is presented in Fig. 7. The simulation introduces a sudden increase of the engine load from 31 to 93 kW at 1500 l/min. Fuel rack was simultaneously pushed into its maximum position. Original turbocharged engine fell out of the operation due to insufficient fueling caused by interaction of the pneumatic controller and the boost pressure. Electric motors EM2 and EM3 ensured faster boost pressure raise and therefore allowed larger quantities of the fuel to be injected in the cylinder. It is evident that the engine equipped with the electrically assisted turbocharger (EM2 and EM3) can accept higher instant increase of load. Lower part of the Fig. 7 shows the time-dependence of the engine speed when a sudden change of the engine load is applied. Maximum decrease of the engine speed obtained by the application of the EM3 under sudden load increase amounts to 7%, whereas with the EM2 auxiliary motor an even larger decrease of 12% is obtained. The first

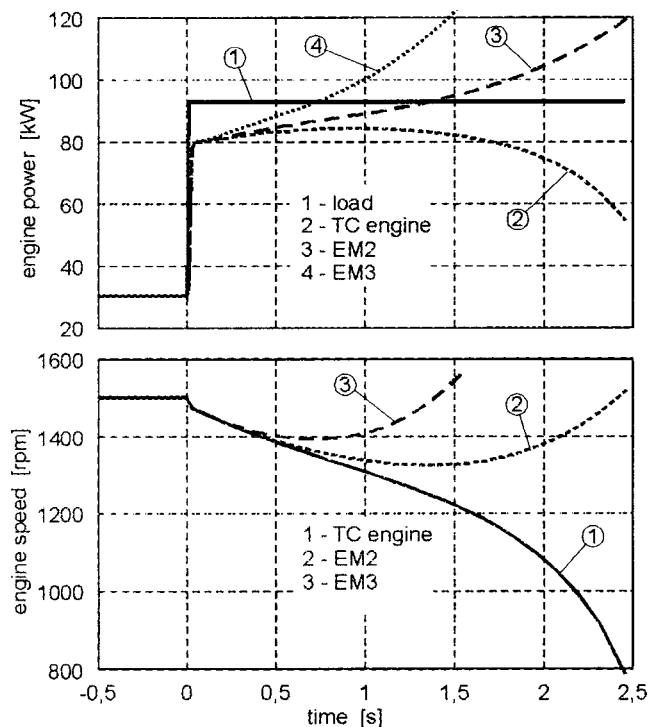


Fig. 7 Simulation of the load acceptance of a turbocharged engine and electrically assisted turbocharged engine

phase (1.5 s) of the described simulation procedure represents realistic conditions of the load acceptance of an engine driving an electric generator.

Conclusion

An accurate and fast zero-dimensional simulation program was developed and is presented in the paper. Accuracy of the simulation was substantially improved by applying experimentally obtained input data. Good agreement of the simulated and measured results was obtained for the steady and transient operation of the turbocharged and aftercooled engine. The simulation can therefore be successfully extended to deal with transient behavior of a turbocharged engine with a supporting electric motor on the turbocharger shaft. An asynchronous electric motor was developed and tested separately to give realistic input data for the numerical simulations. Design variations of the auxiliary electric motor were taken into account for the simulations of the turbocharged diesel engine operating under transient operating conditions. Load acceptance and transient response of the engine were improved by application of the auxiliary electric motor. It was found out that faster transient response of the engine requires as high auxiliary electric motor torque to mass moment of inertia ratio as possible. Such electric motor should have significantly lower mass moment of inertia than that of the turbocharger which provides acceptable dynamic performance of the turbocharger when the electric motor is switched off. Upper electric motor operating speed should be limited by the maximum boost pressure equivalent to the turbocharger speed at which fueling is still restricted by the LDA. Time required to perform transient power increase from 25% to 100% (127 kW) at 1500 rpm amounted to 3.9 s for the original turbocharger, whereas 2.4 s were required with the EM2 electric motor, and 1.7 s when the EM3 motor was applied.

Acknowledgments

The financial support of the Ministry of Science and Technology of the Republic of Slovenia is greatly appreciated. Valuable support of the ISKRA, Autoelektrika d.d.-R&D and MAN GV Slovenia is also gratefully acknowledged.

References

- [1] Watson, N., and Janota, M. S., 1982, *Turbocharging of Internal Combustion Engine*, Camelot Press, Southampton, UK.
- [2] Zinner, K., 1980, *Aufladung von Verbrennungsmotoren*, Springer-Verlag, Berlin.
- [3] Heywood, J. B., 1988, *Internal Combustion Engine Fundamentals*, McGraw-Hill, New York.
- [4] Wintebone, D. E., et al., 1979, "Transient Response of Turbocharged Diesel Engine," *Turbocharging the Internal Combustion Engine*, Short Course, Department of Mechanical Engineering, Imperial College of Science and Technology, London.
- [5] Zellbeck, H., Friedrich, J., and Berger, C., 1999, "Die elektrisch unterstützte Abgasturboladung als neues Aufladekonzept," *Motortech. Z.*, **60**, pp. 386–391.
- [6] Shahed, S. M. et al., 2000, "Turbocharging Systems With Electrical Assistance for Conventional, Hybrid and Fuel Cell Powertrain," *21 Internationales Wiener Motoren-symposium 4-5 Mai*, **1**, pp. 310–324.
- [7] Hoecker, P., et al., 2001, "eBooster Key Component of a New BorgWarner Turbo Systems Charging System for Passenger Cars," *International Wiener Motoren-symposium*, Wien, **2**, pp. 333–352.
- [8] Medica, V., 1989, "Simulation of Turbocharged Diesel Engine driving Electrical Generator Under Dynamic Working Conditions," Dr. Sc. thesis, University of Rijeka, Croatia.
- [9] Jankov, R., 1984, "Matematičko modeliranje strujno-termodinamičkih procesa i pogonskih karakteristika dizel motora," I/II dio, Naučna knjiga, Beograd.
- [10] Katrasnik, T., 2001, "Analysis of Transient Process in a Turbocharged Diesel Engine," Master Sc. thesis No. M/1177, Dep. Mech. Engineering, University of Ljubljana, Slovenia.

- [11] Hribernik, A., 1994, "Modeling of Boundary Conditions for a Twin-Entry Automotive Diesel Engine Turbine," Dr. Sc. thesis, University of Maribor, Slovenia.
- [12] Povhe, T., 2001, "Determination of the Characteristics for a Small Radial Gas Turbine of an Automotive Turbocharger," B. Sc. work No. 5159, Department Mechanical Engineering, University of Ljubljana, Slovenia.
- [13] Prijatelj, S., 2001, "Determination of the Flow Coefficients for the Intake and Exhaust Valves of the Diesel Engine MAN D 0826 LOH 15," B.Sc. work No. d142, Department Mechanical Engineering, University of Ljubljana, Slovenia.
- [14] Adamovič, B., 2001, "Determination of the Valve Timing and Valve Lift of the Turbocharged Diesel Engine MAN 0816 LOH 15, B.Sc. work No. 464, Department Mechanical Engineering, University of Ljubljana, Slovenia.
- [15] Thiele, E., 1982, "Ermittlung der Reibungsverluste in Verbrennungsmotoren," *Motortech. Z.*, **43**, pp. 253–258.

Analysis of Oil Film Thickness on a Piston Ring of Diesel Engine: Effect of Oil Film Temperature

Y. Harigaya

M. Suzuki

Department of Technology Education,
Faculty of Education,
Utsunomiya University,
350 Mine-machi,
Utsunomiya 321-8505 Japan

M. Takiguchi

Department of Mechanical Engineering,
Musashi Institute of Technology,
1-28-1 Tamazutsumi,
Setagaya-ku,
Tokyo 158-8557, Japan

This paper describes an analysis of oil film thickness on a piston ring of a diesel engine. The analysis of the oil film thickness has been performed by using Reynolds equation and unsteady, two-dimensional energy equation with heat generated from viscous dissipation. The mean oil film temperature was determined from the calculation of the temperature distribution in the oil field which was calculated using the energy equation. The oil film viscosity was then estimated using the mean oil film temperature. The effect of oil film temperature on the oil film thickness of a piston ring was examined. This model has been verified with published experimental results. Moreover, the heat flow at ring and liner surfaces was examined. Results show that the oil film thickness could be calculated using the viscosity estimated from the mean oil film temperature. The calculated values generally agree with the measured values. For higher engine speed conditions, the maximum values of the calculated oil film thickness are larger than the measured values.

[DOI: 10.1115/1.1501078]

Introduction

One method utilized to promote energy savings in internal combustion engines is to reduce the power loss caused by mechanical friction on lubricated surfaces of engines. Most of the mechanical friction power loss in the internal combustion engines occur on lubricated surfaces around the piston rings and skirt. Factors that affect these lubrication characteristics in the piston rings are the oil film thickness, the viscosity of oil, the shape of the piston rings, the ring tension, and the operating conditions, etc.

The lubrication between ring and liner is seriously affected by the oil film viscosity that reduces with the increase of temperature in the case of high-temperature lubrication conditions. Therefore, to attain higher efficiency of engines under the conditions of high speed and high power, the temperature dependence of oil viscosity must be taken into consideration in analyzing the lubrication characteristics of piston rings.

In most of the analyses of lubrication characteristics for piston ring, the oil film viscosity was assumed to be a constant during a cycle ([1–3]) or was estimated by using the liner surface temperature ([4–8]). The effect of viscosity on oil film thickness and friction force is very significant. Recently, there is little literature on the analysis of viscosity estimated by using oil film temperature on lubricated surfaces between piston ring and cylinder liner in internal combustion engines. Radakovic et al. [9] presented the appropriate governing equations and numerical solution procedure for treating thermohydrodynamic problems involving thin-film flows in the presence of transverse squeeze and shear-thinning effect, and elucidated the influence of both thermal and shear-thinning effects on the performance of ring. In their study, the steady-state energy equation was used.

On the other hand, Takiguchi et al. [10] measured the variation of oil film thickness of the piston top ring and the second ring of a truck diesel engine during one cycle by capacitance type clearance sensors in the ring sliding surfaces. They analyzed the oil film thickness, taking into account the piston slap motions and ring motions. They also calculated the oil film thickness using viscosity obtained from the cylinder temperature at the center of a

stroke and assumed it to be a constant during a cycle. They presumed that the engine speed has hardly any effect on the oil film thickness, because the oil film temperature between the ring and cylinder liner becomes higher, lowering the oil viscosity.

In our previous papers [11–12], the analysis for the oil film temperature on a piston ring has been carried out by using an unsteady, two-dimensional energy equation. Considering the heat generated from viscous dissipation and the inlet and outlet temperatures of the flow field, this energy equation was applied to the ring sliding face profiles. The variations of temperature, viscosity, and oil film thickness between ring and liner for a cycle were predicted.

In this study, the estimation of the temperature and velocity distributions in the oil film and the effects of oil film temperature variation on the oil film thickness of a piston ring for diesel engine are described.

The oil film thickness was analyzed by using Reynolds equation and an unsteady, two-dimensional energy equation with heat generated from viscous dissipation. Using the energy equation, temperature distributions in the oil film were calculated and the mean oil film temperatures were computed. The viscosity of oil film was estimated by using the mean oil film temperature. This model was verified with published experimental results ([10]). The effect of oil film temperature on the oil film thickness of a piston ring, and the heat flow at ring and liner surfaces were examined.

Analysis of Temperature, Viscosity, and Thickness in Oil Film on a Piston Ring

The lubrication model on a piston ring analyzed in this paper is shown in Fig. 1. In the oil film flow field, the following assumptions are made:

1. The oil is an incompressible liquid and Newtonian fluid with a constant viscosity along the whole ring face.
2. The flow is laminar.
3. The specific heat, heat conductivity, and oil density are constant in a cycle and the oil viscosity is a function of temperature.
4. The lubrication model is considered as pure hydrodynamic lubrication with fully flooded inlet and Reynolds exit conditions.
5. The oil starvation is ignored.

Contributed by the Internal Combustion Engine Division of THE AMERICAN SOCIETY OF MECHANICAL ENGINEERS for publication in the ASME JOURNAL OF ENGINEERING FOR GAS TURBINES AND POWER. Manuscript received by the ICE Division May 2001; final revision received by the ASME Headquarters November 2001. Associate Editor: D. Assanis.

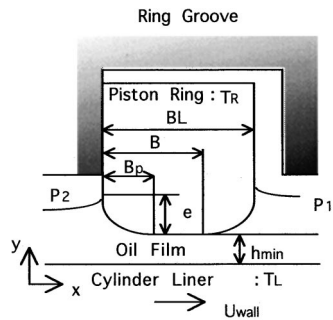


Fig. 1 Lubrication model between ring and liner

6. The ring motions, the cylinder wall deformation, and the relative deformation of ring and cylinder wall are ignored.

Reynolds Eq. (1) was used to analyze the lubrication characteristics

$$\frac{\partial}{\partial x} \left(\frac{h^3}{\mu} \frac{\partial p}{\partial x} \right) = 6U_{\text{wall}} \frac{\partial h}{\partial x} + 12 \frac{dh}{dt} \quad (1)$$

At the oil inlet side, the mean pressure is equal to the ambient pressure, and the oil film breaks down on the downstream side according to the Reynolds boundary condition such as follows:

$$\begin{aligned} p &= p_2 && \text{at inlet side } (x=0) \\ p &= p_1 \text{ and } dp/dx=0 && \text{at the downstream side where} \\ &&& \text{the oil film breaks down } (x=B). \end{aligned}$$

In the present model, the viscosity of oil film was estimated by using the oil film mean temperature. Therefore, the analysis of oil film temperature on the piston ring was performed by unsteady, two-dimensional energy equation. Considering the heat generated from viscous dissipation in the oil film, the energy equation for two-dimensional flow is expressed ([13–15]) as follows:

$$\rho C \left(\frac{\partial T}{\partial t} + u \frac{\partial T}{\partial x} + v \frac{\partial T}{\partial y} \right) = \kappa \left(\frac{\partial^2 T}{\partial x^2} + \frac{\partial^2 T}{\partial y^2} \right) + \phi \quad (2)$$

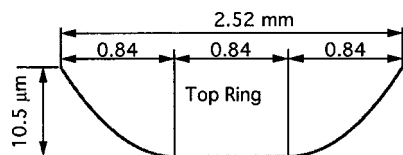


Fig. 2 Geometry of top ring sliding surface

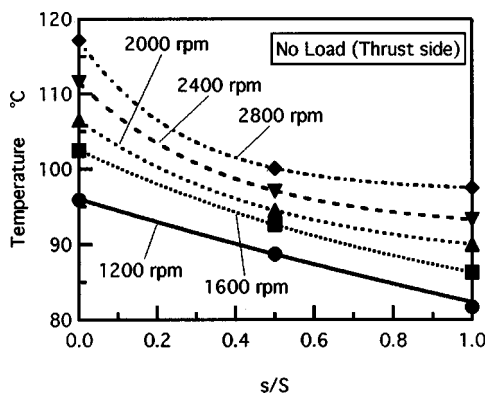


Fig. 3 Cylinder liner surface temperatures (experimental values)

$$\phi = 2\mu \left[\left(\frac{\partial u}{\partial x} \right)^2 + \left(\frac{\partial v}{\partial y} \right)^2 + \frac{1}{2} \left(\frac{\partial u}{\partial y} + \frac{\partial v}{\partial x} \right)^2 \right] \quad (3)$$

Equation (3) represents the viscous dissipation in the oil film. Thermal boundary conditions are as follows:

$$\begin{aligned} T &= T_L && \text{at inflow on inlet side } (x=0) \\ dT/dx &= 0 && \text{at outflow on inlet side } (x=0) \\ dT/dx &= 0 && \text{at the downstream side where the oil film} \\ &&& \text{breaks down } (x=B) \\ T &= T_L && \text{at liner surface } (y=0) \\ T &= T_R && \text{at ring surface } (y=h). \end{aligned}$$

The temperature distribution along the cylinder liner has a higher slope near the top dead center (TDC) and a lower slope near the bottom dead center (BDC) in general. In this work, using the measured temperatures at the TDC, midstroke point and BDC strokes, the following expression is employed to evaluate the liner temperature distribution:

$$T_L(s) = m_0 + m_1 \exp(-m_2 s/S) \quad (4)$$

where s is the displacement from the TDC of the top ring, S is the length of engine stroke, and m_0 , m_1 , and m_2 are correlation parameters.

The ring surface temperature T_R are assumed to be a constant since the cycle to cycle variations of ring surface temperatures are very low.

The oil film mean temperature in effective oil film region T_m is defined as follows:

$$T_m = \frac{1}{hB} \int_0^h \int_0^B T(x,y) dx dy \quad (5)$$

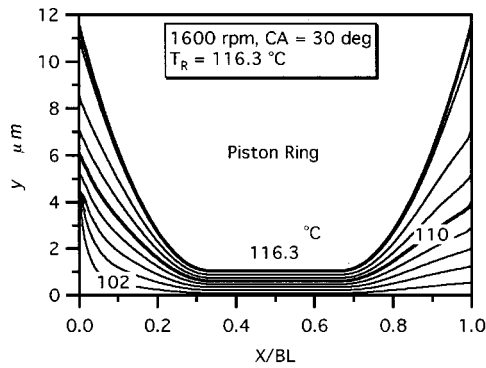
In order to account for the moving ring surface, ring profile, and nonuniformly distributed grid points, the grid in (t,x,y) -coordinates can be mapped onto a stationary and uniformly discretized mesh in (τ,ξ,η) -coordinates.

$$\tau = t, \quad \xi = x/h_{\text{min}}, \quad \eta = y/h_{\text{min}} \quad (6)$$

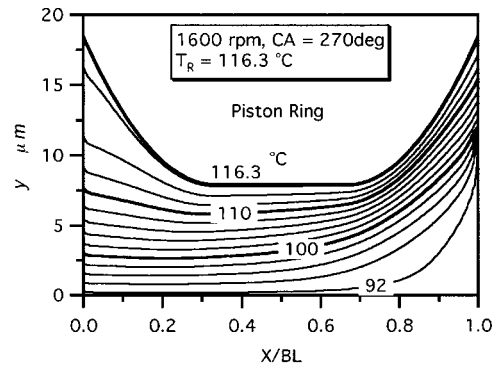
Transferring from (t,x,y) -coordinates to the (τ,ξ,η) -coordinates, the energy equation is expressed ([15]) as follows:

Table 1 Calculation Conditions

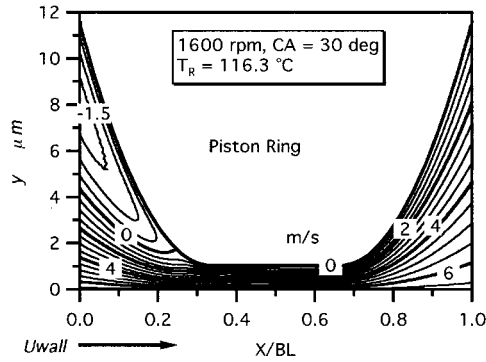
Table 1 Calculation Conditions			
Engine	4-stroke NA DI diesel engine		
	Bore=110 mm		
	stroke=125 mm		
	connecting rod length=198 mm		
Ring	$BL=3$ mm		
	$e=10.5$ μm		
	$P_e=154.4$ kPa		
Oil	$\kappa=0.143$ W/(mK)		
	$C=1.985$ kJ/(kgK)		
	$\rho=872$ kg/m ³		
	SAE 30		
	kinematic viscosity 92.76 mm ² /s (40°C)		
	11.34 mm ² /s (100°C)		
	$a_0=0.0488628$ mPa		
	$\theta_1=1123.35$ °C		
	$\theta_2=111.562$ °C		
Liner temperature correlation parameters			
rpm	m_0 (°C)	m_1 (°C)	m_2
1200	40.726	55.285	0.28406
1600	75.275	27.225	0.90397
2000	87.300	19.200	1.9617
2400	91.950	19.650	2.6783
2800	97.034	20.166	3.7671



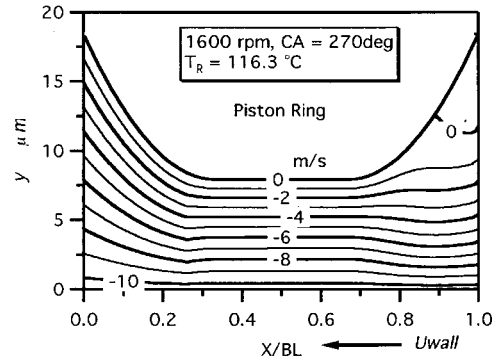
(a) Temperature distribution at CA= 30 deg.



(b) Temperature distribution at CA=270 deg.



(c) Velocity distribution at CA= 30 deg.



(d) Velocity distribution at CA=270 deg.

Fig. 4 Temperature and velocity distributions in oil film between ring and liner (1600 rpm, no load). (a) Temperature distribution at CA=30 deg. (b) Temperature distribution at CA=270 deg. (c) Velocity distribution at CA=30 deg. (d) Velocity distribution at CA=270 deg.

$$\begin{aligned}
 & J \frac{\partial T}{\partial \tau} + (U + J\xi_t) \frac{\partial T}{\partial \xi} + (V + J\eta_t) \frac{\partial T}{\partial \eta} \\
 &= \frac{\partial}{\partial \xi} \{ \Gamma J (q_{11} T_\xi + q_{12} T_\eta) \} \\
 &+ \frac{\partial}{\partial \eta} \{ \Gamma J (q_{21} T_\xi + q_{22} T_\eta) \} + J \cdot S(\xi, \eta) \quad (7)
 \end{aligned}$$

where

$$U = (\xi_x u + \xi_y v) \cdot J \quad V = (\eta_x u + \eta_y v) \cdot J$$

$$\begin{aligned}
 & J = x_\xi y_\eta - x_\eta y_\xi \quad \Gamma = \frac{\kappa}{C_p} \\
 & q_{11} = \xi_x^2 + \xi_y^2 \quad q_{12} = \xi_x \eta_x + \xi_y \eta_y \\
 & q_{21} = q_{12} \quad q_{22} = \eta_x^2 + \eta_y^2 \\
 & S(\xi, \eta) = \frac{2\mu}{C_p} \left[(S_1)^2 + (S_2)^2 + \frac{1}{2} (S_3 + S_4)^2 \right] \\
 & S_1 = \xi_x \frac{\partial u}{\partial \xi} + \eta_x \frac{\partial u}{\partial \eta} \quad S_2 = \xi_y \frac{\partial v}{\partial \xi} + \eta_y \frac{\partial v}{\partial \eta}
 \end{aligned}$$

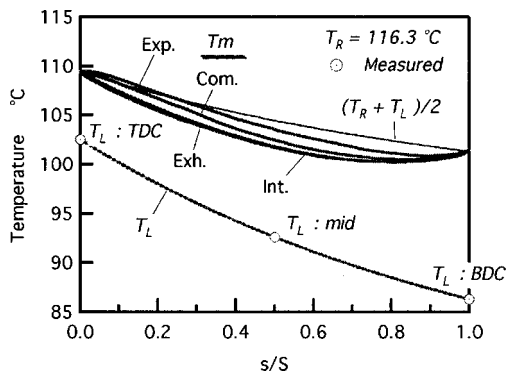


Fig. 5 Mean oil film temperature in a cycle (1600 rpm, no load)

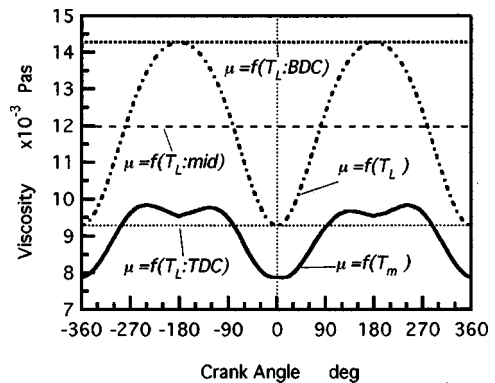


Fig. 6 Oil film viscosity in a cycle (1600 rpm, no load)

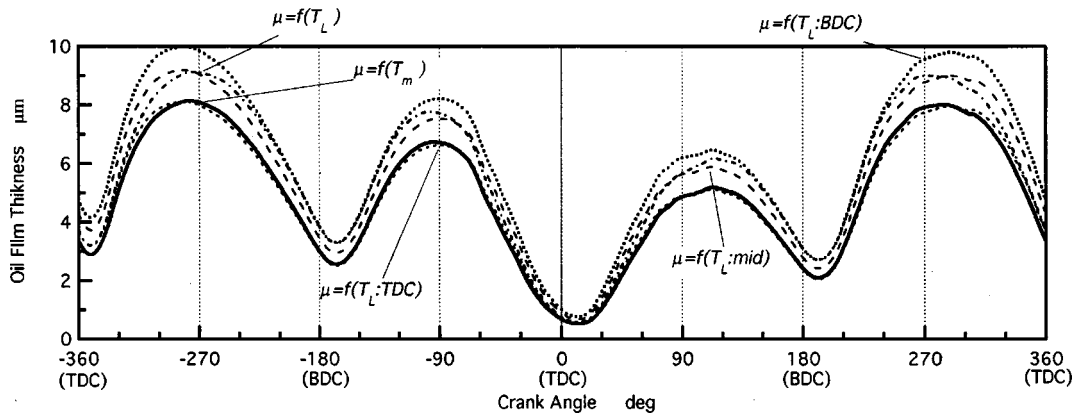


Fig. 7 Oil film thickness (effect of viscosity estimation methods, 1600 rpm, no load)

$$S_3 = \xi_y \frac{\partial u}{\partial \xi} + \eta_y \frac{\partial u}{\partial \eta} \quad S_4 = \xi_x \frac{\partial v}{\partial \xi} + \eta_x \frac{\partial v}{\partial \eta}$$

The temperature dependence of the viscosity is estimated by using the relation between the viscosity and temperature. The Vogel equation ([16]) used in this work is

$$\mu(T) = a_0 \exp[\theta_1 / (\theta_2 + T)] \quad (8)$$

where a_0 , θ_1 , and θ_2 are correlation parameters.

Solution Procedure. The numerical procedure is summarized as follows:

1. The oil film thickness h and the viscosity μ in the oil film at arbitrary crank angle were assumed.
2. The Reynolds equation was solved numerically by the finite difference method, and the pressure, velocity, and temperature distributions were calculated.
3. The viscosity in the oil film was estimated by using the mean oil temperature T_m , and dh/dt was calculated and a prediction of h at a given crank angle was predicted.
4. The calculations (h , T_m , and μ) were repeated until the solution converges to a certain condition.

In the oil film temperature analysis, the energy equation was

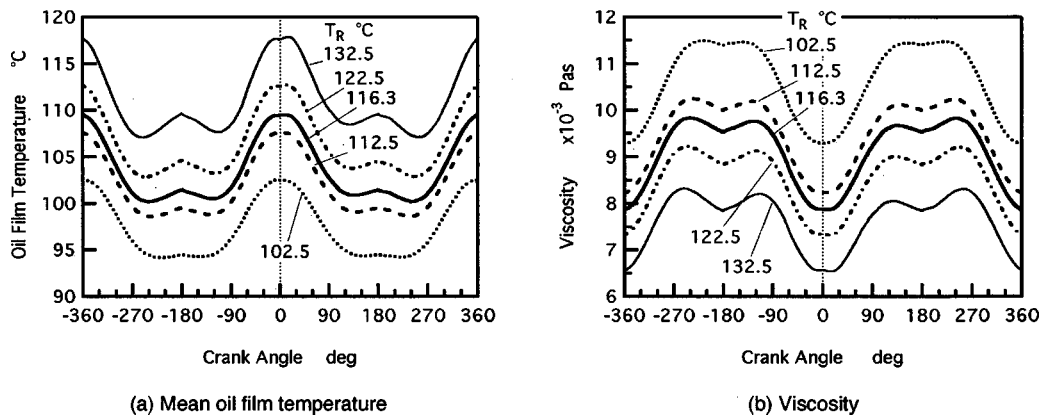


Fig. 8 Mean oil film temperatures and viscosity (effect of ring temperatures, 1600 rpm, no load); (a) mean oil film temperature, (b) viscosity

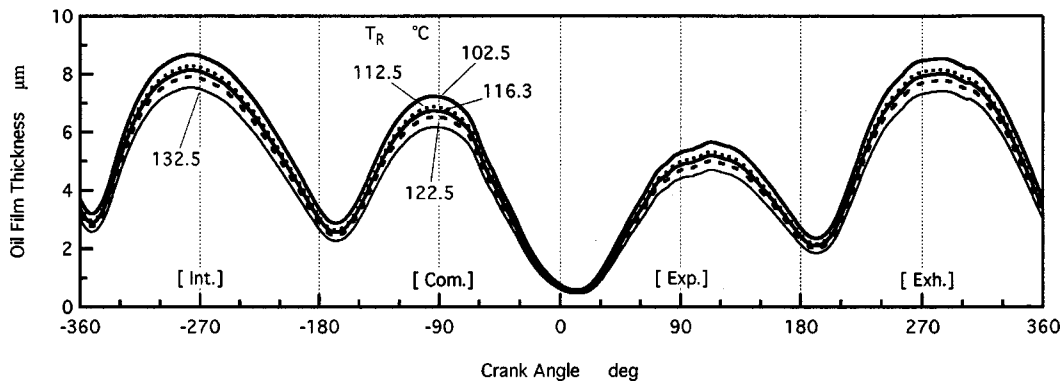


Fig. 9 Oil film thickness (effect of ring temperatures, 1600 rpm, no load)

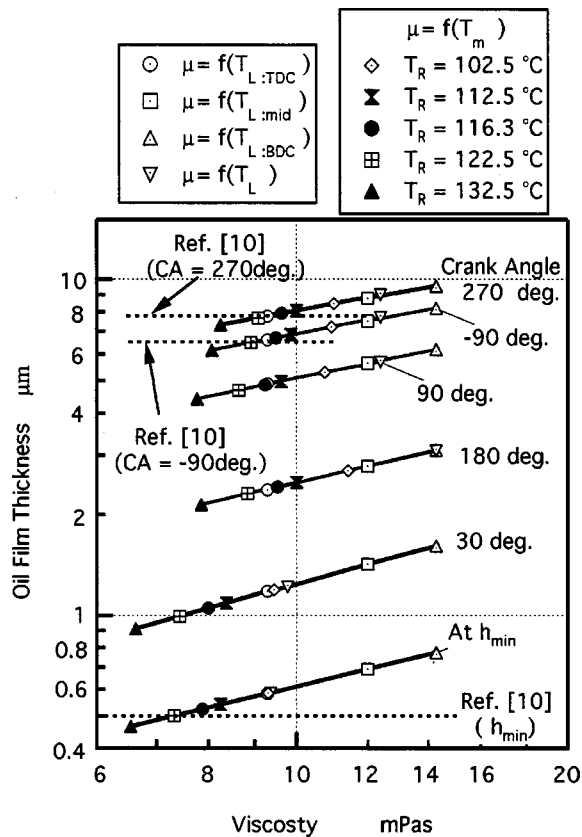


Fig. 10 Relation between oil film thickness and viscosity (1600 rpm, no load)

solved by using the semi-implicit method for pressure-linked equations (SIMPLE) method ([15]). The solution domain representing the oil film on the piston ring was divided into 100 nodes in the direction of ring travel and 40 nodes across the oil film thickness.

Test Engine, Piston Ring, and Liner Temperature. The analysis presented was applied to the piston ring of a direct injection type, natural aspirated four-stroke, six-cylinder diesel engine ([10]). The oil film thickness of the top ring measured by capacitance type clearance sensors in the ring sliding surfaces ([10]) was used to compare with the predicted thickness. The geometry of ring sliding surface is the same as that of the top ring used in the

oil film thickness measurement ([10]) as shown in Fig. 2. The ring profile is flat in the middle part and rounded off at both ends. The measured cylinder liner surface temperatures at each engine speed are shown in Fig. 3. There are three measurement points. These are at the top, middle, and bottom of a stroke. The test lubrication oil used was a CD Class SAE 30 Grade oil. Its specifications and the calculation conditions are shown in Table 1.

Numerical Results and Discussions

Oil Film Temperature. The calculated temperature distributions in the oil film are shown in Figs. 4(a) and (b) at an engine speed of 1600 rpm under no load conditions. These distributions are at a crank angle of 30 deg, that is near the crank angle for the minimum oil film thickness and at a crank angle of 270 deg, that is near the crank angle for the maximum oil film thickness in a cycle. In this calculation, the top ring surface temperature T_R was expressed as $T_R = (T_G + T_{L:TOP})/2$, where T_G , was the measured top ring groove temperature and $T_{L:TOP}$ was the measured liner surface temperature at TDC.

The temperature distribution at a crank angle of 30 deg shows isothermal lines in parallel with the ring surface at the flat part region, and the heat is transferred from the ring to liner by heat conduction. While that at crank angle of 270 deg is influenced by convection flow at the inlet, so that the oil film temperature at near liner surface has low values from inlet side to middle part of ring width and increases along the flow direction.

In the present calculation condition, the reverse flow occurs at ring side of inlet as shown in Figs. 4(c) and (d), so oil film temperature distributions are influenced by the reverse flow. Such the reverse flow had been found at the inlet zone of steeply convergent oil film of journal bearing ([13,17]). The reverse flow in the oil film between the ring and liner is necessary to be confirmed experimentally.

From these temperature distributions, the mean oil film temperatures in the effective oil film region were calculated and that along the cylinder wall is shown in Fig. 5. In this figure, the liner surface temperature T_L and the mean temperature of the ring and the liner $(T_R + T_L)/2$ are also shown. As shown in Fig. 5, the mean temperatures at each stroke show a similar tendency. During the latter half of compression stroke and early expansion stroke, the mean oil film temperatures are higher due to viscous heating, and during the latter half of expansion stroke, these become lower due to convection flow. These temperatures are about 6°C higher near TDC, and about 12° higher than the liner temperature near BDC. Also, the mean oil film temperatures are lower than the mean temperature of the ring and the liner except during early expansion stroke. Thus, the oil viscosity estimated from the mean oil film temperature is lower than that estimated by using the liner

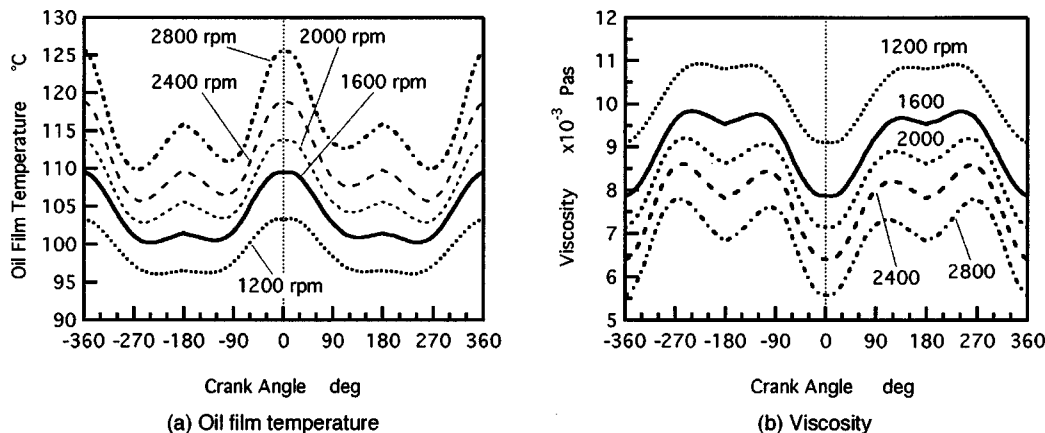


Fig. 11 Oil film temperature and viscosity (effect of engine speeds and no load); (a) oil film temperature, (b) viscosity

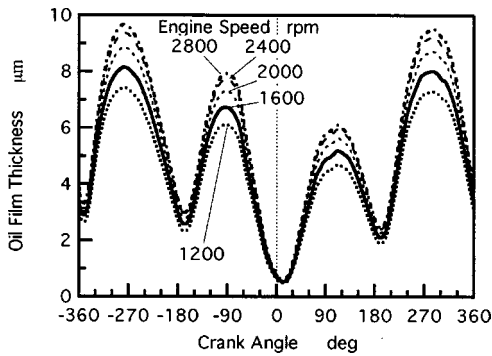


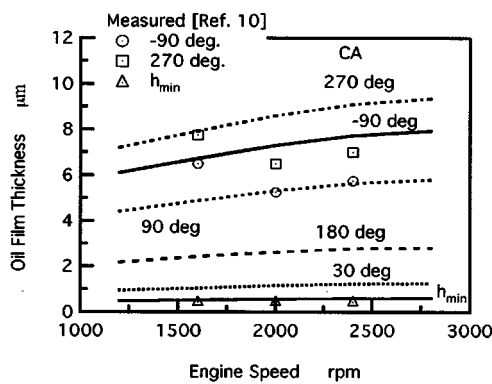
Fig. 12 Oil film thickness (effect of engine speeds, no load)

temperature as shown in Fig. 6. It may be reasonable to presume that the viscosity estimated by the mean oil film temperature is useful for the analysis of lubrication.

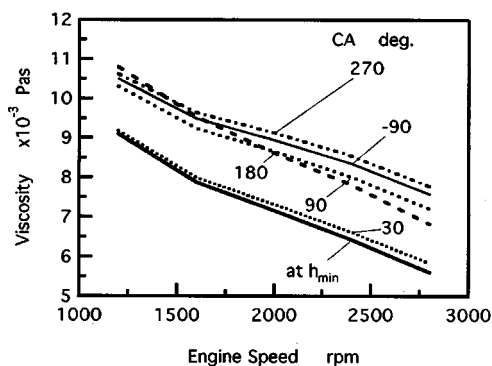
Oil Film Viscosity and Thickness. The effect of estimation methods for viscosity on the oil film thickness was examined. The estimation methods used in this study are listed below.

1. the viscosity estimated by using the liner temperature at each position; $\mu = f(T_{L:TDC})$, $\mu = f(T_{L:mid})$, $\mu = f(T_{L:BCD})$,
2. the viscosity estimated by using the liner surface temperature distribution along the cylinder surface; $\mu = f(T_L)$, and
3. viscosity estimated by using the mean oil film temperature; $\mu = f(T_m)$.

The liner temperatures measured at top dead center, midstroke



(a) Oil film thickness



(b) Viscosity

Fig. 13 Relations between oil film thickness, viscosity and engine speed (no load); (a) oil film thickness, (b) viscosity

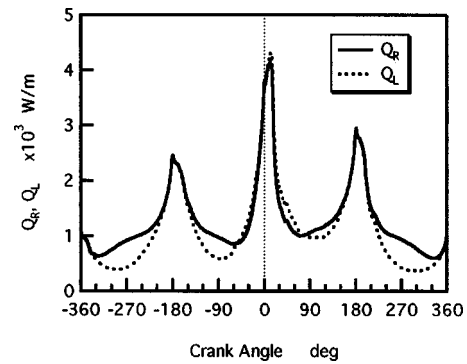


Fig. 14 Heat flow at ring and liner surfaces ($T_R = 116.3^\circ\text{C}$, 1600 rpm, no load)

point and bottom dead center were used. The top ring surface temperature T_R was estimated by using measured top ring groove and liner temperatures. Figure 6 shows the viscosity estimated by each method for the case of an engine speed of 1600 rpm and no load conditions.

Figure 7 shows the effect of estimation methods of viscosity on the oil film thickness. The variations of oil film thickness in one cycle become thinner with the decrease of viscosity due to the elevated temperature. At near the top dead center for combustion, the viscosity [$\mu = f(T_m)$] estimated by using mean oil film temperature is lower about 15% than that of [$\mu = f(T_{L:TDC})$] estimated by using liner temperature at top dead center. Independent of the estimation methods of viscosity, the minimum oil film thickness in one cycle appears to be the same value. The values of the maximum oil film thickness become larger with viscosity increase, particularly at the region of higher ring sliding velocity of the intake and exhaust strokes.

Moreover, the effect of ring temperature on oil film thickness was examined. The mean oil film temperature, viscosity and oil film thickness are shown in Figures 8 and 9. Since the oil viscosity becomes lower with an increase in the ring temperature, the oil film thickness is thinner in one cycle.

The relation between oil film thickness and viscosity at each crank angle is shown in Fig. 10. The results indicate that the oil film thickness at each crank angle increases with the increase of viscosity. At each crank angle, the oil film thickness calculated by viscosity [$\mu = f(T_m)$] estimated using the mean oil film temperature are thinner than that calculated by viscosity [$\mu = f(T_L)$] estimated using the liner temperature. Particularly, at crank angle of minimum oil film thickness near top dead center for combustion, the values of the oil film thickness estimated by using the mean oil film temperature are lesser than those estimated by the liner temperature.

Comparison of the calculated and measured (dotted line as shown Fig. 10) values of oil film thickness in the case of top ring operation condition ([10]) reveal that the calculated oil film thickness for a ring temperature of $T_R = 116.3^\circ\text{C}$ agrees approximately with the measured values at crank angles of 270 and -90 deg. This ring temperature was estimated by the measured ring groove and liner temperatures. Thus, it is considered that the viscosity estimated by using the mean oil film temperature derived from the measured liner temperature and the estimated ring temperature is useful for the evaluation of oil film thickness.

Effect of Engine Speed. The effects of engine speed on the mean oil film temperature, viscosity, and oil film thickness in a cycle are shown in Figs. 11, 12, and 13, respectively. For the oil film thickness calculation, the viscosity estimated by the mean oil film temperature derived from the measured liner temperature shown in Fig. 3, and the estimated ring temperature, were used. Increasing the engine speed raises the mean oil film temperature, and its swing in a cycle is larger due to convection flow effects.

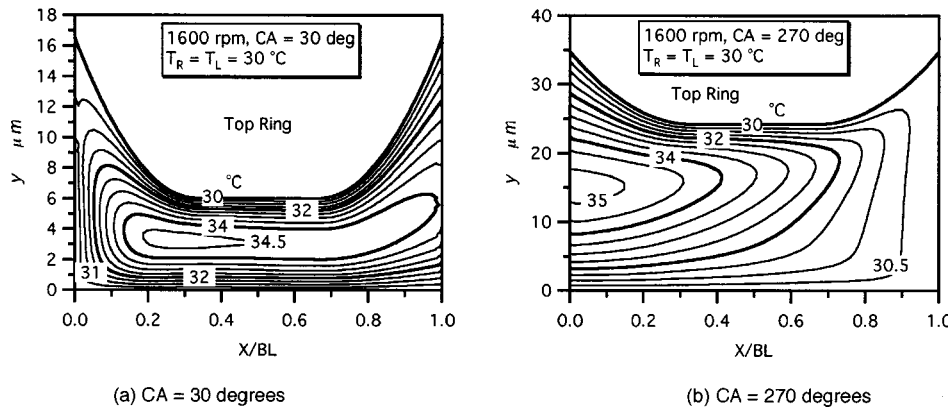


Fig. 15 Temperature distributions in an oil film (condition of low temperature $T_R = T_L = 30^\circ\text{C}$); (a) CA=30 deg, (b) CA=270 deg

With higher engine speeds, the oil film temperature increases thereby reducing oil viscosity. The oil film is thicker for higher engine speeds except near the top dead center for combustion. Wong et al. presented that the oil film thickness increases with the square root of the sliding speed under hydrodynamic lubrication condition ([18]). The present results indicate that the oil film thickness increases with approximately 0.35 power of the engine speed due to decrease of viscosity.

Comparison of calculated and measured values ([10]) show that the maximum thickness of the calculated value is larger than that of measured values in the case of higher engine speed conditions. This is due to the effects of the estimated ring temperature, the inlet oil film temperature, and the oil starvation between ring and liner.

Heat Flow. Heat flows at ring and liner surfaces in a cycle were examined. Heat flows at ring and liner surfaces as shown in Fig. 14 exhibit a peak at top dead center that have essentially constant values. These values become lower at higher ring sliding velocities during half stroke, and heat flow at ring surface Q_R is higher than that at liner surface Q_L . This is considered that the sliding velocity becomes higher, so the oil film thickness increases, the inlet flow is larger and the oil temperature at near the liner surface effected by the inlet flow becomes lower. Therefore the temperature gradient in the vertical direction of oil film at near liner surface is lower than that at near ring surface as shown in Fig. 4(b).

To examine the effect of viscous dissipation, in the case of lower temperature condition such as starting condition, oil film temperature distributions and heat flows were calculated as shown in Figs. 15 and 16. As the oil film thickness increases with in-

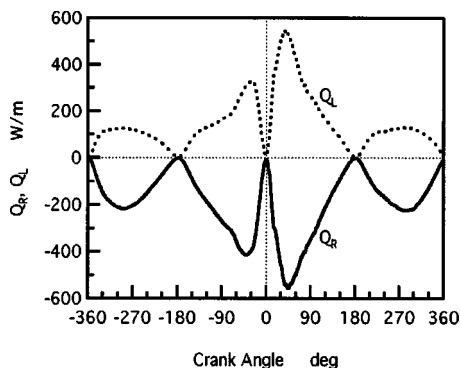


Fig. 16 Heat flow at ring and liner surfaces ($T_R = T_L = 30^\circ\text{C}$, 1600 rpm, no load)

creasing viscosity, viscous dissipation becomes larger. The oil film temperature distribution has a peak at the center in the oil film at a crank angle of 30 deg. At a crank angle of 270 deg, the temperature in the oil film at flow inlet is lower and it increases along the flow direction. The position of maximum temperature in the oil film at outlet side is near the middle between ring and liner. Since the oil film temperature is higher than the ring and liner surface temperatures, heat flows from the oil to the ring and liner surfaces as shown in Fig. 16 due to the increase in viscous dissipation.

Conclusions

In this paper, the analysis of oil film thickness on a piston top ring of a diesel engine has been performed by using Reynolds equation and unsteady, two-dimensional energy equation with the viscous dissipation. The oil film viscosity was estimated by the mean oil film temperature calculated from the temperature distribution in the oil film. The effect of oil film temperature on the oil film thickness of a piston ring and heat flow at ring and liner surfaces were examined. The results are summarized as follows:

1. Oil film thickness could be calculated by using the viscosity estimated by mean oil film temperature. The calculated values agree satisfactorily with the measured values. Oil film thickness estimated from the present method is lesser than that with viscosity estimated by the liner temperature at minimum oil film thickness such as near top dead center. Thus, the lubrication condition for the piston ring becomes more severe.
2. The calculated oil film thickness in a cycle increases with engine speed. The calculated maximum values are larger than the measured values for higher engine speed conditions.
3. Heat flows at ring and liner surfaces in a cycle can be estimated by this model. According to the conditions of ring and liner temperatures, heat flows from the oil film to the ring and liner surfaces or from the ring to the oil film due to viscous dissipation.
4. The oil film temperature between the ring and the liner varies from the liner to the ring as well as from the inlet to outlet. Therefore, it is necessary to be caution about the prediction of oil film thickness using the original Reynolds equation in which a viscosity is assumed to be a constant in the vertical direction of oil film.

Nomenclature

- a_0 = correlation parameter of the Vogel equation
- B = effective ring width
- BL = axial width of ring
- Bp = width of parallel region of ring
- C = specific heat
- e = barrel height of ring

h = oil film thickness
 h_{\min} = minimum film thickness
 m_0, m_1, m_2 = correlation parameter of Eq. (4)
 p = hydrodynamic pressure
 P_e = surface pressure of ring
 p_1 = gas pressure in combustion chamber
 p_2 = inter-ring gas pressure
 Q_R = heat flow at ring surface
 Q_L = heat flow at liner surface
 s = displacement from position at TDC of top ring
 S = length of engine stroke
 T = temperature
 T_m = mean oil film temperature
 T_L = temperature of cylinder liner
 T_R = temperature of ring surface
 t = time
 U_{wall} = sliding velocity of wall
 u = x -direction velocity
 v = y -direction velocity
 κ = oil film thermal conductivity
 ρ = density
 μ = viscosity
 ν = kinematic viscosity
 θ_1, θ_2 = correlation parameter of the Vogel equation

Acknowledgments

This work was supported by the Research Committee 172 of the Japan Society of Mechanical Engineers. Thanks are due to the committee members with whom the authors have discussed this work, in particular Professor Nakahara of Tokyo Institute of Technology, Professor Azetsu of University of Tokyo, and Professor Hamataka of Ohita University.

References

- [1] Furuhashi, S., 1958, "A Dynamic Theory of Piston-Ring Lubrication," *Trans. Jpn. Soc. Mech. Eng.*, **24**(148), p. 1032.
 [2] Wakuri, Y., Soejima, M., and Taniguchi, T., 1977, "Oil Film Behavior of Piston Ring," *Trans. Jpn. Soc. Mech. Eng.*, **43**(370), p. 2319.

- [3] Sanda, S., and Someya, T., 1989, "The Mechanism of Piston Ring Friction and Lubrication (Improvement in Predicting Friction Force by Reconsidering Boundary Conditions)," *Trans. Jpn. Soc. Mech. Eng.*, **55**(516), p. 2175.
 [4] Ting, L. L., and Mayer, J. E., Jr., 1974, "Piston Ring Lubrication and Cylinder Bore Wear Analyses, Part II—Theory Verification," *ASME J. Lubr. Technol.*, **96**, p. 258.
 [5] Wakuri, Y., Hamatake, T., Soejima, M., and Kitahara, T., 1993, "Lubrication of Piston Ring Pack," *Trans. Jpn. Soc. Mech. Eng.*, **59**(561), p. 1504.
 [6] Tian, T., Wong, V. W., and Heywood, J. B., 1996, "A Piston Ring-Pack Film—Thickness and Friction Model for Multigrade Oils and Rough Surfaces," SAE Paper No. 962032.
 [7] Froelunet, K., Schramm, J., Tian, T., Wong, V. W., and Hochgreb, S., 1996, "Analysis of the Piston Ring/Liner Oil Film Development During Warm-Up for an SI-Engine," *ASME ICE-Vol. 27-2 ASME*, New York, p. 25.
 [8] Ma, Ming-Tang, 2000, "Incorporation of Lubricant Shear-Thinning in a Two-Dimensional Lubrication Analysis for Automotive Piston-Ring Packs," *Advances in Powertrain Tribology 2000*, CEC & SAE, p. 69.
 [9] Radakovic, D. J., and Khonsari, M. M., 1997, "Heat Transfer in a Tin-Film Flow in the Presence of Squeeze and Shear Thinning: Application to Piston Rings," *ASME Trans. J. Heat Transfer*, **119**, p. 249.
 [10] Takiguchi, M., Sasaki, R., Takahashi, I., Ishibashi, F., Furuhashi, S., Kai, R., and Sato, M., 2000, "Oil Film Measurement and Analysis of a Three Ring Pack in an Operating Diesel Engine," *Advances in Powertrain Tribology 2000* CEC & SAE, p. 81.
 [11] Harigaya, Y., Tsuji, Y., Kanahashi, H., and Suzuki, M., 1999, "Effect of Oil Film Temperature on Lubrication Characteristics of Piston Ring in Internal Combustion Engines," *Proceedings of the 15th Internal Combustion Engine Symposium (International) in Seoul*, JSAE, p. 179.
 [12] Harigaya, Y., Akagi, J., and Suzuki, M., 2000, "Prediction of Temperature, Viscosity and Thickness in Oil Film Between Ring and Liner of Internal Combustion Engine," *Advances in Powertrain Tribology 2000*, CEC & SAE, p. 109.
 [13] Pinkus, O., 1990, *Thermal Aspects of Fluid Film Tribology*, ASME, New York.
 [14] Namai, T., and Inoue, M., 1992, *Hydrodynamic of Viscous Flow*, Rikogakusha, Tokyo.
 [15] Arakawa, C., 1994, *Computational Fluid Dynamics for Engineering*, University of Tokyo Press, Tokyo.
 [16] Wakuri, Y., Kitahara, T., Hamatake, T., Soejima, M., and Ide, S., 1998, "Friction Characteristics of Piston and Piston Rings," *Trans. Jpn. Soc. Mech. Eng.*, **64**(618), p. 676.
 [17] Hatakenaka, K., Tanaka, M., and Suzuki, K., 2000, "Thermo-Hydrodynamic Performance of Journal Bearings With Partial Reverse Flow and Finger-Type Cavitation Being Considered," *J. Japan Soc. Tribol.*, **45**(8), p. 628.
 [18] Wong, V. V., Casey, S. M., and Tamai, G., 1999, "Lubricant Film Characteristics in the Power Cylinder and Dependence on Location, Oil Properties, and Engine Operating Conditions," *Proceedings of the 15th Internal Combustion Engine Symposium (International) in Seoul*, JSAE, p. 161.

Effect of Biodiesel Utilization of Wear of Vital Parts in Compression Ignition Engine

A. K. Agarwal¹

Department of Mechanical Engineering,
Indian Institute of Technology, Kanpur,
Kanpur 208016, India
e-mail: akag@iitk.ac.in

J. Bijwe

ITTEC,
Indian Institute of Technology, Delhi,
New Delhi 110016, India

L. M. Das

Centre for Energy Studies,
Indian Institute of Technology,
New Delhi 110016, India

The combustion related properties of vegetable oils are somewhat similar to diesel oil. Neat vegetable oils or their blends with diesel, however, pose various long-term problems in compression ignition engines, e.g., poor atomization characteristics, ring-sticking, injector coking, injector deposits, injector pump failure, and lube oil dilution by crank-case polymerization. These undesirable features of vegetable oils are because of their inherent properties like high viscosity, low volatility, and polyunsaturated character. Linseed oil methyl ester (LOME) was prepared using methanol for long-term engine operations. The physical and combustion-related properties of the fuels thus developed were found to be closer to that of the diesel oil. A blend of 20 percent was selected as optimum biodiesel blend. Two similar new engines were completely disassembled and subjected to dimensioning of various vital moving parts and then subjected to long-term endurance tests on 20 percent biodiesel blend and diesel oil, respectively. After completion of the test, both the engines were again disassembled for physical inspection and wear measurement of various vital parts. The physical wear of various vital parts, injector coking, carbon deposits on piston, and ring sticking were found to be substantially lower in case of 20 percent biodiesel-fuelled engine. The lubricating oil samples drawn from both engines were subjected to atomic absorption spectroscopy for measurement of various wear metal traces present. AAS tests confirmed substantially lower wear and thus improved life for biodiesel operated engines. [DOI: 10.1115/1.1454114]

Introduction

The world is presently confronted with the twin crises of fossil fuel depletion and environmental degradation. Indiscriminate extraction and lavish consumption of fossil fuels have led to reduction in underground carbon-based resources. The need to exploit bio-origin-based alternative fuels to quench the world's energy thirst has long been realized. By now, it has been conclusively realized that internal combustion engines form an indispensable part of modern life style. They play a vital role in transportation and modern mechanized agricultural sector. Ever since the advent of the IC engines, vegetable oils have been tried as an alternative to the diesel fuel. The inventor of the diesel engine, Rudolf Diesel, in 1885, used peanut oil as a diesel fuel for demonstration at the 1900 world exhibition in Paris. Speaking to the Engineering Society of St. Louis, Missouri, in 1912, Diesel said, "The use of vegetable oils for engine fuels may seem insignificant today, but such oils may become in course of time as important as petroleum and the coal tar products of the present times." The same petroleum-based fuel used in Diesel's days is still the fuel of choice in modern motorized society ([1]).

It is only in recent years that systematic efforts have been made to utilize vegetable oils as fuels in engines. A review of literature shows that European countries and the U.S.A. have mainly concentrated on saffola, sunflower, peanut oils, etc. as alternative fuels for diesel engines, which are essentially edible in nature. But, in the Indian context, only nonedible vegetable oils can be seriously considered as a fuel for CI engines as the edible oils are in great demand and are far too expensive at present. Moreover, there is a vast forest resource from which oil can be derived and formulated to give combustion-related properties close to that of

diesel oil. Broadly speaking, due to the wide variations in climate, soil conditions, and competing use of land, different nations and researchers look upon different vegetable oils, which are locally available, as potential fuels. For example, Malaysia is pursuing research and development programmes on the use of palm oil and its derivatives as fuels for engines. There is no doubt that the production of oil seeds can be stepped up once they are being adopted for regular use in diesel engines. Considering the huge rates of consumption of petroleum fuels at present, it is clear that vegetable oils can, at best, provide only a partial replacement ([2]).

Kaltschmitt et al. conducted a study, which shows that bioenergy carriers offer some clear ecological advantages over fossil fuels such as conserving fossil energy resources or reducing the green house effect ([3]). Therefore, the process of utilizing biodiesel in the IC engines for transport as well as other applications, is gaining momentum. The international energy agency has recognized biodiesel as an alternative fuel for the transportation sector. The European Commission proposed a 12 percent market share for biofuels by the year 2020 ([4]).

The combustion-related properties of vegetable oils are somewhat similar to diesel oil. Neat vegetable oils or their blends with diesel pose various long-term problems in compression ignition engines, e.g., poor atomization characteristics, ring-sticking, injector-coking, injector deposits, injector pump failure, and lube oil dilution by crank-case polymerization. Such problems are not usually experienced with short-term engine operations. Sometimes the engine fails catastrophically, if run on neat vegetable oils continuously for a longer period. The properties of vegetable oils, responsible for these problems are high viscosity, low volatility, and polyunsaturated character ([5,6]).

In the majority of short-term tests employing vegetable oil as the fuel, peak power outputs ranged from 91 percent to 109 percent of those when equivalent engines were operated with mineral diesel fuel. The thermal efficiencies of the engines were generally

¹To whom all correspondence should be addressed.

Contributed by the Internal Combustion Engine Division of THE AMERICAN SOCIETY OF MECHANICAL ENGINEERS for publication in the JOURNAL OF ENGINEERING FOR GAS TURBINES AND POWER. Manuscript received by the ICE Division, July 1999; final revision received by the ASME Headquarters, August 2001. Editor: D. N. Assanis.

reported to improve with vegetable oils. However, due to its lower energy content, vegetable oil consumption was higher than that of mineral diesel fuel ([7]). Hemmerlein et al. established that all of the engines run on rapeseed oil passed the ECE R49 regulation relating to CO, HC, NO_x, and soot emissions in the 13-mode test. However, some measured emissions increased while others decreased when rapeseed oil was used as a substitute for diesel fuel. Further, higher emissions levels resulted from combustion of rapeseed oil in direct injection (DI) and small-cylinder indirect injection (IDI) engines than combustion in larger-cylinder IDI engines. Emissions of CO and HC increased by up to 100 percent and 290 percent, respectively, compared with those for diesel fuel, but it is likely that these levels could be reduced if the injector timing is advanced. Emissions of NO_x were up to 25 percent lower, due to slower combustion and low maximum combustion temperatures resulting from the use of rapeseed oil. Generally, soot and particulate emissions were also reduced by up to 0.4 Bosch number and 50 percent, respectively, although particulate emissions were up to 140 percent higher, when combustion occurred in DI engines. The emissions of aromatics, aldehydes, ketones, and particulate matter were higher when rapeseed oil was used. PAH emissions were reduced in larger cylinder IDI engines and increased in other engine types ([8]). Freedman et al. experimentally evaluated CNs of vegetable oils and their derivatives by using constant volume combustion bomb ([9]). They also evaluated heat of combustion of various triglycerides, and attempted to find out the relationship between their heats of combustion and molecular properties of vegetable oils ([10]).

The process of transesterification yields vegetable oil esters. Vegetable oil esters have better fuel properties compared to neat vegetable oils. Their viscosity reduces, volatility increases, and they lose their polyunsaturated character after transesterification. The stoichiometry of the overall transesterification reaction requires 1 mole of triglyceride for 3 moles of glycerol. This is a reversible reaction, either acid or alkali catalyzed, and involves stepwise conversions of triglycerides to diglycerides to monoglycerides to glycerol producing 3 moles of ester in the process ([11]). Alkaline catalysts have the advantage of being less corrosive to industrial equipment than acid catalysts. Transesterification process breaks the triglycerides present in vegetable oils into two components, fatty acid esters, and glycerol. Glycerine is a valuable by-product, which is used in pharmaceuticals, cosmetics, toothpaste, and many other commercial products. Biodiesel is often blended with petroleum diesel to offset its high production cost ([12,13]). Pure 100 percent "neat" methyl esters of rapeseed, soybean, sunflower, tallow, and other fats and oils can be used as diesel fuel with little or no modifications of the engine. According to Alan Weber, "Many fleets, however, utilize biodiesel blends called B20, which is a mixture of 20 percent biodiesel and 80 percent petroleum diesel" ([1,14]).

System Selection

As far as the application in rural agricultural sector of a developing country like India is concerned, internal combustion engines should preferably utilize alternative fuels of bio-origin, which are locally available. The present work is carried out using a typical vegetable oil by formulating its properties and bringing them closer to the conventional diesel. System design approach has taken care to see that these modified fuels can be utilized in existing diesel engines without any substantial hardware modifications. India is producing around 6.7 million tons of nonedible oils such as, linseed, castor, karanji (*Pongamia glabra*), neem (*Azadirachta indica*), palash (*Butea monosperma*), and kusum (*Schlelchera trijuga*). Some of these oils produced even now are not being properly utilized, and it has been estimated that some other plant-based forest derived oils have a much higher production potential. From among the large number of vegetable oils produced in the country, linseed oil was chosen for the present investigation because India has the largest acreage under linseed

cultivation, and it is the fourth largest producer of linseed oil in the world ([6,15]). The process of transesterification was selected to prepare suitable fuels for long-term engine operation. The molecular structure of the fatty acid molecules present in the vegetable oil gets modified by way of transesterification. For the present work, linseed oil methyl ester was prepared using methanol in the presence of potassium hydroxide as catalyst, and then separating by-product glycerol formed in the esterification reaction. The use of linseed oil methyl ester (LOME) in compression ignition engines was found to develop a very compatible engine-fuel system with low emission characteristics. The physical and combustion related properties of the fuels thus developed by the process of esterification were determined in the laboratory and most of them were found very close to that of diesel oil. Tests were conducted for determination of properties like density, viscosity, flash point, aniline point /cetane number, calorific value, etc. Some specific tests like infrared spectroscopy, carbon, hydrogen, nitrogen, oxygen analysis, and nuclear magnetic resonance spectroscopy were carried on biodiesel and linseed oil in order to study the effect of transesterification at molecular level.

The constant speed experimental test unit, manufactured by Perry & Co., India, is a compact, portable captive 4 kWh gen-set run by diesel fuel. It is widely used in the country mostly for agricultural purposes and in many small and medium scale commercial purposes. This is a single-cylinder four-stroke vertical water-cooled system that develops 4 kW power output in pure diesel mode. It has a provision of loading electrically, and is flexibly coupled with a single-phase alternator. Detailed specifications of the engines used in present investigations are given in Table 1.

The engine can be started by hand cranking. The engine is provided with a centrifugal speed governor. The inlet valve opens 4.5 deg BTDC and closes 35.5 deg ABDC. The exhaust valve opens 35.5 deg BBDC and closes 4.5 deg ATDC. The test engine is directly coupled to a 220 volts AC generator of sufficient capacity to absorb the maximum power produced by the engine.

Engine Tests

After developing the appropriate fuel, it was tested on the engine, first for its performance and emission characteristics and then through a series of other engine tests. In the long-term endurance test, the effect due to the use of biodiesel on various parts of the engine vis-à-vis diesel fuel was studied. For this purpose, two similar new engines were subjected to similar loading cycles and operating conditions. The assessment of wear of various parts of 20 percent biodiesel and diesel-fueled engines was done after dismantling the various parts of the engine. The various tests on the two-engine systems are conducted as per the procedure specified in IS10000, 1980 ([16]).

Preliminary Runs. The purpose of preliminary run for both the engines is that they should be made trouble free, by operating both the engines for their running-in period. Under the preliminary run, constant speed engines are subjected to a preliminary run of 49 hours at the rated speed under the operating temperature specified by the manufacturer, in nonstop cycles of seven hours each, conforming to the following cycle pattern. The engine loading cycle for the preliminary run is shown in Table 2.

During the preliminary run, attention was paid to engine vibration and quietness. Oil pressure was checked time to time.

Fuel Consumption Test. A fuel consumption test is essential for evaluating the fuel consumption pattern of an engine. This test was used to certify that both the engines are going to perform exactly similar, when subjected to the same fuel. When different fuels are used for running the similar engines under similar operating conditions, any marked difference in their performance is due to the characteristics of the fuel alone. This test was carried out only after the preliminary run, i.e., after stable operating conditions were achieved. The engines were subjected to similar loading conditions, starting from no load, observations were recorded

Table 1 Technical specifications of the test engine

Manufacturers	Perry Engines Ltd, India
Model	Single cylinder CI engine
Bore	87.5 mm
Stroke	110 mm
Displacement	661.7 cm ³
Length	531 mm
Width	356 mm
Height	546 mm
Weight	165 Kg
Rated speed	1500 rpm
Maximum speed	2000 rpm
Minimum speed	1200 rpm
Minimum idling speed	750 rpm
Nozzle pressure	200 bar
Compression ratio	17: 1

at 20 percent, 40 percent, 60 percent, 80 percent, 100 percent, and 110 percent of the rated load. During the fuel consumption test (loop test), observations were recorded after every 30 minutes and a graph was plotted for each engine. Further tests were undertaken, after ensuring that fuel consumption patterns observed were same within measurable accuracy for both the engines.

Performance and Emission Test: Selection of Optimum Blend. This test was carried out on one of the engines, which has already been subjected to preliminary run-in. The period of running in and the test cycles have already been discussed earlier. This test is aimed at optimizing the concentration of ester in the biodiesel blends. To achieve this, several blends of varying concentrations were prepared ranging from 0 percent (neat diesel oil) to 100 percent (neat biodiesel) through 5 percent, 10 percent, 15 percent, 20 percent, 25 percent, 30 percent, 40 percent, 50 percent, and 75 percent. These blends were then subjected to performance and emission tests on the engine. The performance data was then analyzed from the graphs recording power output, torque, specific fuel consumption, and smoke density, etc., for all the blends of biodiesel. The 20 percent biodiesel was found to be the optimum blend from the graphs based on maximum thermal efficiency and smoke opacity considerations ([5]).

Long-Term Endurance Test. After the completion of all these tests, both the engines were dismantled completely and examined physically for the conditions of the various critical parts before endurance test was commenced. After physical examination, the dimensions of various moving, vital parts were recorded, e.g., cylinder head, cylinder bore/cylinder liner, piston, piston rings, gudgeon pin, valves (inlet and exhaust), valve seats (inserts), valve guide, valve springs, connecting rod, big-end bearing, small-end bush, connecting rod bolts and nuts, crankshaft, crankshaft bearings and journals, and camshaft. The engines were re-assembled and mounted on a suitable test beds and again run-in for 12 hours in the manner recommended by the manufacturer. This test was carried out to take care of any misalignments occurring during dismantling and re-assembling of the engine. This test included 11 hours of continuous run, at rated full load at the rated speed followed by one hour run at 10 percent overload. During the running-in period, none of the critical components listed above

Table 2 Loading cycle for preliminary runs of constant speed engine ([16])

Load (% of rated load)	Running time (Hours)
25	1.5
50	2
75	1.5
100	2

Table 3 Test cycle for long-term endurance test ([16])

Load (% of rated load)	Running time (Hours)
100	4
50	4
110	1
No load (Idling)	0.5
100	3
50	3.5

were replaced. The lubricating oil from the oil sump was drained off and the engines were refilled with SAE 30 grade of fresh lubricating oil as specified by the manufacturer and the engines were then ready for long-term endurance test.

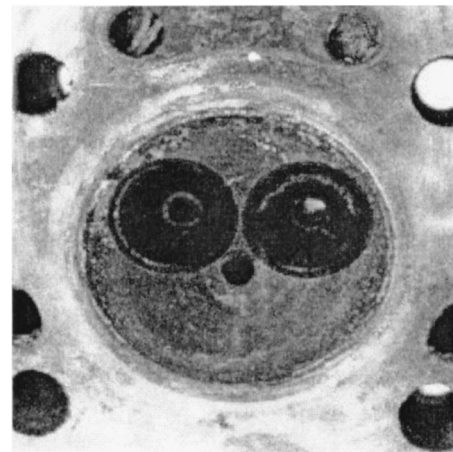
Then both the engines were run for 32 cycles (each of 16 hours continuous running) at rated speed. The test cycle followed is specified in the Table 3.

The first engine was using 20 percent biodiesel blend, and the second engine was using neat diesel oil as fuel. At the end of each 16-hour cycle, both the engines were stopped and necessary servicing, and minor adjustments were carried out in accordance with the manufacturer's schedule, e.g., tappet settings, make up oil addition, etc. Before starting the next cycle, it was ensured that the temperature of the engine sump oil had reached within 5 K of the room temperature. The engines were then topped up with engine oil, if required and the quantity consumed recorded. The lubricating oil samples were collected from the engines after every 128 hours for conducting various tribological studies. In the entire range of engine operation spread over 512 hours, there was no major breakdown.

Comparison of Carbon Deposits. After completion of the long-term endurance test, the engines were completely disassembled and the deposit formations on cylinder head, piston top, and injector tip were investigated. The photographs for all these parts are shown in Figs. 1–6.

Figure 1 shows the carbon deposits on the cylinder head of the diesel-fueled engine and Fig. 2 shows carbon deposits on the cylinder head of the 20 percent biodiesel fueled engine. It can be clearly noticed that the deposits on the cylinder head of 20 percent biodiesel-fueled system are substantially lesser compared to the diesel-fueled system.

Figure 3 shows the carbon deposits on the piston-top of the diesel fueled system and Fig. 4 shows the carbon deposits on the piston top of 20 percent biodiesel-fueled engine. The pistons were weighed and the amount of carbon deposits formed was found

**Fig. 1 Carbon deposits on cylinder head of diesel-fueled engine after 512 hours of engine operation**

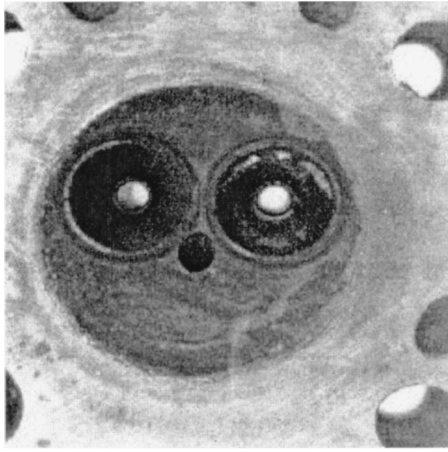


Fig. 2 Carbon deposits on cylinder head of 20 percent biodiesel-fueled engine after 512 hours of engine operation

out. The amount of carbon deposited on biodiesel system was found to be about 40 percent lower compared to the diesel-fueled system. Figure 5 shows the injector tip of the diesel-fueled system after 200 hours of engine operation and Fig. 6 shows the injector tip of 20 percent biodiesel-fueled engine after 512 hours of engine operation. The carbonization of biodiesel injector after 512 hours of operation was far less than the diesel injector after 200 hours of engine operation. There were hardly any carbon deposits noticed on biodiesel fueled injector. This proved that the problem of carbon deposits and coking of injector tip have not only completely disappeared after the esterification of vegetable oils but also these have improved compared to conventional diesel

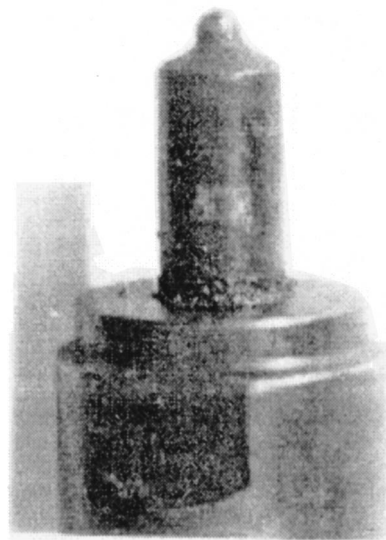


Fig. 5 Carbon deposits on injector tip of diesel-fueled engine after 200 hours of engine operation

fuel. Similar results were also noticed in the figures for deposits on piston ring grooves, intake and exhaust valves.

It is also observed that both diesel and biodiesel followed the same trend of cylinder pressure variation except that the 20 percent biodiesel-fueled engine showed a slightly lower peak cylinder pressure. This may be because of a bit slower rate of combustion of biodiesel fuel compared to diesel fuel. This slow rate of pressure rise leads to relatively smoother engine operation and also affects the wear of engine parts. It is noticed that with the increase in the load of the engine, the peak cylinder pressure increased. Addition of biodiesel decreases the reaction rate and mixture temperature at the end of compression, resulting in a drop in the overall flame temperature with a consequent decrease in flame speed. The addition of biodiesel plays an important role in reducing the maximum rate of pressure rise and peak pressure considerably. Combustion duration is almost similar for both the fuels.

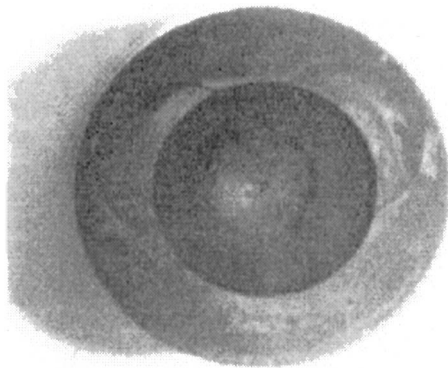


Fig. 3 Carbon deposits on piston top of diesel-fueled engine after 512 hours of engine operation

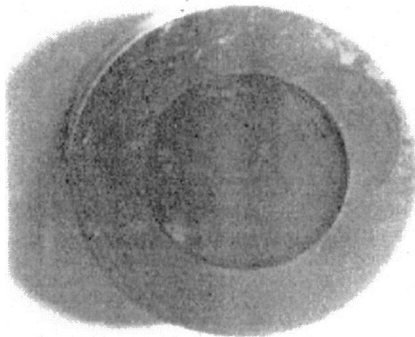


Fig. 4 Carbon deposits on piston top of 20 percent biodiesel-fueled engine after 512 hours of engine operation

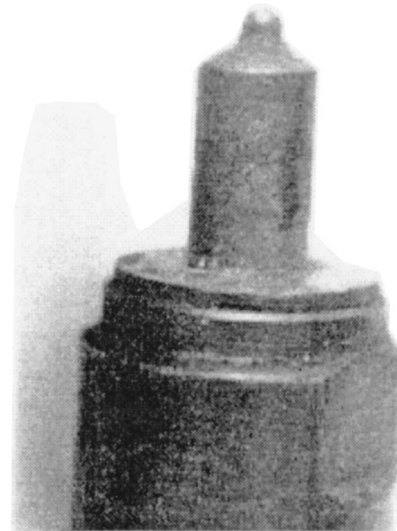
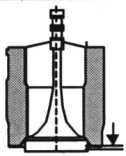

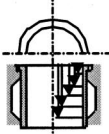


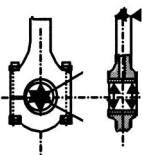
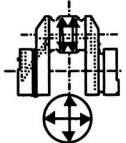
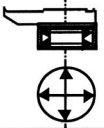
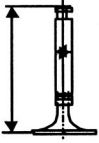
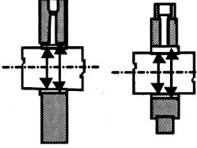


Fig. 6 Carbon deposits on injector tip of 20 percent biodiesel-fueled engine after 512 hours of engine operation

Table 4 Comparative physical wear measurements of vital parts for 20 percent biodiesel-fueled engine vis-à-vis diesel-fueled engine parts

Figure of the moving part	Dimensions	% lower wear for biodiesel
	Distance of valve head from mounting flange face	30
	Diameter of piston at position	33
	Measurements of cylinder bore/ cylinder liner	31
	Measurements for piston rings	34
	Measurements Of gudgeon pin, pin bore, and small end bush of connecting rod	40
	Measurements of connecting rod bearing bore	36
	Measurements of big end bearing (crank pin diameter)	35
	Measurements of end float	25
	Measurements for inlet and exhaust valves	22
	Measurements of cam shaft bearings	28

Wear Measurement

Sliding contact between metallic components of any mechanical system is always accompanied by wear, which results in the generation of minute particles of metal. In diesel engines, the components normally subjected to wear process are the piston, piston rings, cylinder liner, bearings, crankshaft, cam, tappet, and valves. In a lubricated diesel engine system, wear particles are washed away by lubricating oil and remain in suspension in the lubricating oil. By analyzing and examining the variation in the concentration of the metallic particle in the lubricating oil after certain running duration, sufficient information about wear rate, source of wear metals, and engine conditions were predicted.

Physical Wear Measurement of Vital Parts. The wear of various moving parts took place due to prolonged engine operation. Both the engines were operated under identical conditions and the loading cycles of the engines were also similar. The only variation in the operation was that both the engines were operated using two different fuels so that the effect of new fuel on the life of engine hardware could be compared directly. This was thought to be an acid test to analyze the material compatibility of the newly developed fuels vis-à-vis diesel oil. The dimensions of the vital parts and physical condition were noted before the commencement of and after the completion of long-term endurance test. The difference of these two dimensions gave the wear of these parts in the given period of engine operation.

After completion of the long-term endurance test, the engines were again dismantled completely, and the physical condition of various parts inspected carefully. Wear was estimated by accurate measurements of dimensions of various vital parts of the engine, before and after the long-term endurance test. These observations of wear were useful to compare the performance of biodiesel vis-à-vis diesel oil on the wear of the vital engine parts. Observations are summarized in the Table 4.

It is glaringly evident from the table that the wear of vital moving parts of the 20 percent biodiesel operated engine was substantially lower (of the order of about 30 percent lower) compared to the neat diesel operated engine. In small and mid-sized engines, part of the fuel spray jet impinges on combustion chamber walls, thus wetting the cylinder walls. The fuel thus gets mixed with the lubricating oil present on the liner wall. During the piston's reciprocating motion, this biodiesel dilutes lubricating oil and forms a layer between the cylinder liner and piston rings, thus affecting the cylinder lubrication mechanism directly. A series of experiments was planned to investigate this phenomenon through lubricating oils analysis from biodiesel and diesel operated engines.

Wear Debris Transport and Analysis. Oil used for lubrication of the IC engine picks up the wear debris of various metals depending on the origin. The quantitative evaluation of wear particles present in oil gives the magnitude of engine component deterioration and while qualitative analysis indicates its origin, i.e., wearing component. This ultimately provides adequate information about the components that are being deteriorated and the incipient failure of the machine.

A careful look at the literature reveals that the various contaminant metals present in lube oil might have various possible sources in the engines. Table 5 lists the typical sources of metallic elements in wear debris of the lubricating oil.

Ash Content. The lubricating oil samples were kept in the furnace at 450°C for 4 hours and then 600°C for 2 hours to produce ash. The residual ash contains the wear debris of metal primarily. The data on ash content in the lubricating oils for biodiesel and diesel-fueled compression engines have been presented graphically in Fig. 7. It was observed that the ash content for 20 percent biodiesel-operated engine oil was approximately 15 percent lower than that of diesel-operated engine oil.

The 20 percent biodiesel-operated engine has a lower amount

Table 5 Typical sources of metallic elements in wear debris (14)

Element	Typical sources
Aluminum (Al)	Pistons, Bearings, Dirt, Additives, Turbochargers
Antimony (Sb)	Greases, Bearings
Barium (Ba)	Additives, Water, Grease
Boron (B)	Coolant, Oil additives, Anti-freeze agents
Cadmium (Cd)	Bearings, Plating
Calcium (Ca)	Additives, Water, Greases
Chromium (Cr)	Compression rings, Coolant, Crankshaft, Gears, Bearings, Plating of cylinder liner
Cobalt (Co)	Bearings
Copper (Cu)	Bearings, Bronze bushings
Indium (In)	Synthetic oils, Solder
Iron (Fe)	Cylinder liner, Piston, Rings, Valves, Valve guides, Gears, Shafts, Anti-friction bearings, Rust, Crankshaft.
Lead (Pb)	Bearings, Greases, and Paint
Magnesium (Mg)	Bearings, Additives, Supercharger, Gear box
Manganese (Mn)	Steel shafts, Valves
Molybdenum (Mo)	Additives, Piston rings
Nickel (Ni)	Shafts, Gears, Piston rings
Phosphorus (P)	Additives, Gears
Potassium (K)	Coolant, Additives
Silicon (Si)	Defoamants, Dirt, Lubricants
Silver (Ag)	Bearings
Sodium (Na)	Coolant, Additives
Tin (Sn)	Bearings, Solder
Titanium (Ti)	Springs, Valves
Vanadium (V)	Valves
Zinc (Zn)	Additives, Bearings, Plating, Brass components, Neoprene seals

of ash content in its lubricating oil. Hence, it is clear that biodiesel-fueled engine produced a lesser amount of wear debris thus indicating its better performance.

Atomic Absorption Spectroscopy. AAS works on the principle of absorption interaction, where atoms in the vapor-state absorb radiation at a certain wavelength that are well defined and show the characteristics of a particular atomic element. In this process, the source of radiation projects a beam of a specific wavelength through a pure flame (air-acetylene) on to a sensor and the amount of radiation arriving at the photo sensor is recorded. The fluid sample is introduced into the flame and vaporized. The amount of radiation arriving at the photo sensor is reduced in proportion to the quantity of the specific element present in the sample. The schematic diagram of AAS is shown in Fig. 8.

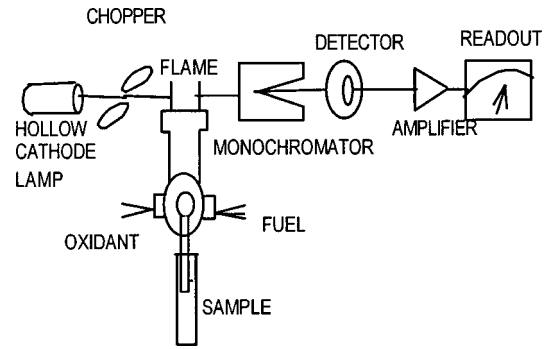


Fig. 8 Schematic diagram for atomic absorption spectroscopy

This technique can be used for quantitative and qualitative analysis of wear debris in lubricating oils. The data can be correlated with the extent in wear and hence, the performance characteristics of either lubricating oils or diagnosis of failure of moving components.

The procedure followed is explained in the following steps:

- Approximately 10 grams of oil sample was weighed in the silica crucible and burnt at 450°C for 4 hours and at 650°C for 2 hours.
- The ash was dissolved in concentrated HCl acid.
- The mixture was diluted with distilled water to make 100 ml solution (Acid: Water: 1:100)
- Standard solutions of various metals (concentrations ranging from 5 PPM to 20 PPM) were prepared.

This test of AAS was done to evaluate the concentration of various metals present in the lubricating oil samples from 20 percent biodiesel and diesel-fueled CI engines. This gave a fair idea about the wear of different parts, material compatibility of the new fuel with the existing engines. In the present study, since many sliding components were involved, it was anticipated that the wear debris originating from different metallic parts appeared in the lubricating oil. Hence, various elements such as Fe, Cu, Zn, Cr, Mg, Co, and Pb were analyzed by AAS and the results are shown in figures given below.

Iron. The iron in wear debris could be because of wear of the cylinder liner, piston, rings, valves, valve guides, gears, shafts, bearing, rust, and crankshaft. The results on concentration of iron as a function of oil usage are shown in Fig. 9. It is clearly seen that for both the systems, iron increased at a higher rate initially up to 128 hours followed by a slower increase. The most important observation was that lubricants from 20 percent biodiesel-fueled system indicated a lower increase in iron content and hence lesser wear, which is because of improved lubricating efficiency of biodiesel fuel.

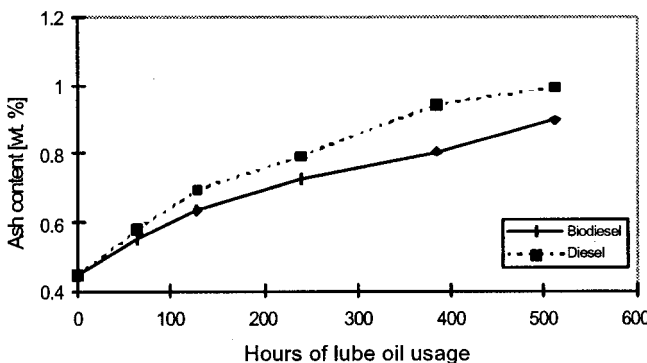


Fig. 7 Ash content versus hours of lube oil usage

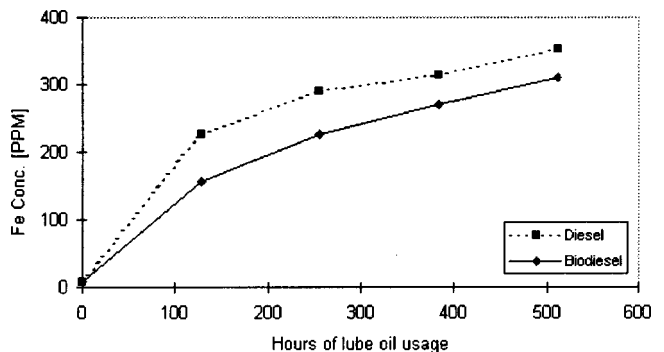


Fig. 9 Iron concentration as a function of lube oil usage

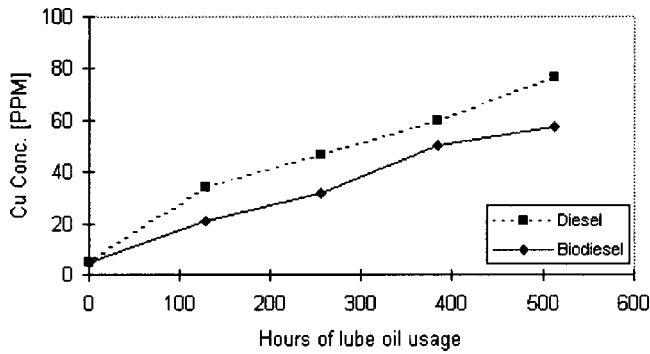


Fig. 10 Copper concentration as a function of lube oil usage

Copper. The copper in wear debris comes from wear of bearings, and bushings. The results on concentration of copper as a function of oil usage are shown in Fig. 10. It is evident that for both the systems, copper increases at a constant rate. An important observation is that lubricant from 20 percent biodiesel-fueled system indicates approximately 25 percent lower copper content and hence lower wear.

Zinc. The zinc in wear debris could be because of additive depletion, extra additives being added due to addition of make-up oil, wear of bearings, brass components, neoprene seals, etc. The results on concentration of zinc as a function of oil usage are shown in Fig. 11. It is observed that for both the systems, zinc increased at a slower rate initially followed by a faster increase in case of diesel-fueled system while the 20 percent biodiesel-fueled system showed steady wear of these components. The main zinc source in the engine is ZDDP, an additive in lubricating oil. An important observation is that lubricant from 20 percent biodiesel-fueled system indicated approximately 65 percent lower zinc content increases, hence lower wear of zinc containing components and lower lubricating oil consumption.

Chromium. The chromium in lubricating oil comes from wear of a cylinder liner, compression rings, gears, crankshaft, and bearings. The results on concentration of chromium as a function of oil usage are shown in Fig. 12. It is glaringly evident that for both the systems, chromium concentration shoots up beyond 128 hours in case of diesel-fueled system, while in the case of a 20 percent biodiesel-fueled system, it happened beyond 256 hours of engine operation. The lubricant from 20 percent biodiesel-fueled system indicated approximately 20 percent lower chromium content increase.

Magnesium. The magnesium in wear debris originates from additive depletion, wear of bearings, and gearbox housing. The results on concentration of magnesium as a function of oil usage are shown in Fig. 13. It can be noticed that for both the systems,

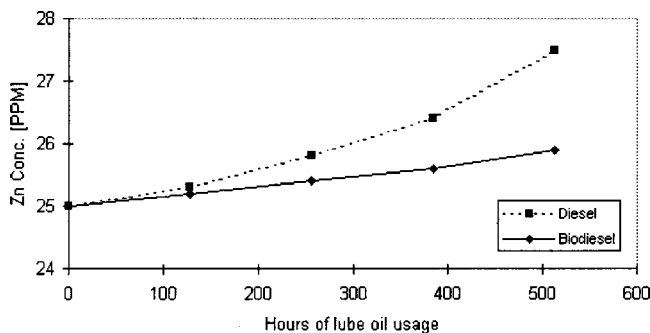


Fig. 11 Zinc concentration as a function of lube oil usage

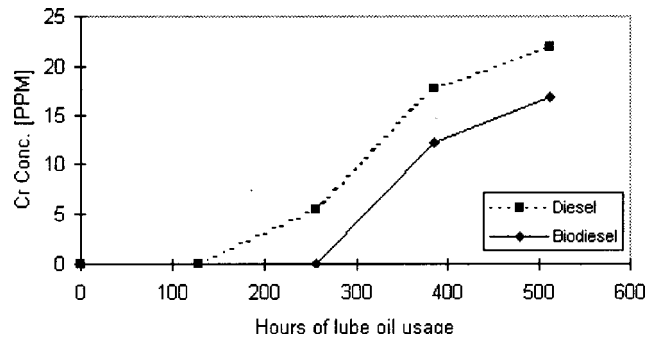


Fig. 12 Chromium concentration as a function of lube oil usage

magnesium concentration increased at a higher rate initially up to 128 hours followed by a slow increase. The lubricant from 20 percent biodiesel-fueled system indicated approximately 10 percent lower magnesium content increase.

Cobalt. The cobalt in wear debris originates from wear of bearings. The results on concentration of cobalt as a function of oil usage are shown in Fig. 14. It is seen that for both the systems, cobalt increased at a steady rate. Lubricant from 20 percent biodiesel-fueled system indicated approximately 40 percent lower increase in cobalt content compared to its diesel engine counterpart.

Lead. The lead in wear debris could be because of wear of bearings, paints, and grease addition. The concentration of lead as a function of oil usage is shown in Fig. 15. For both the systems, lead increased at a steady rate. Lubricant from the 20 percent

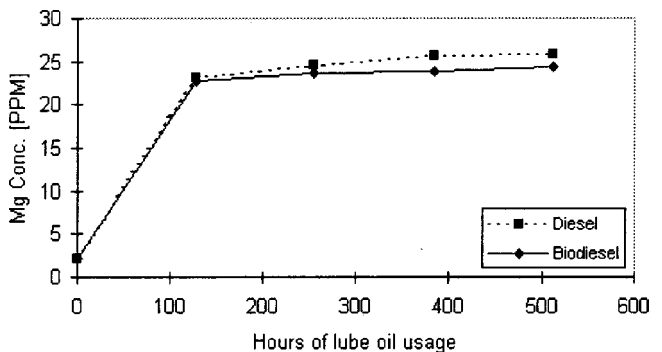


Fig. 13 Magnesium concentration as a function of lube oil usage

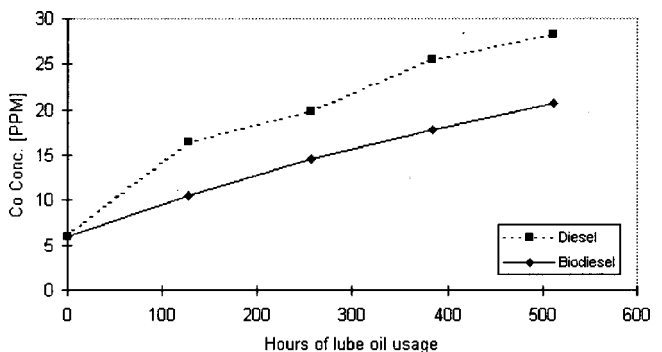


Fig. 14 Cobalt concentration as function of lube oil usage

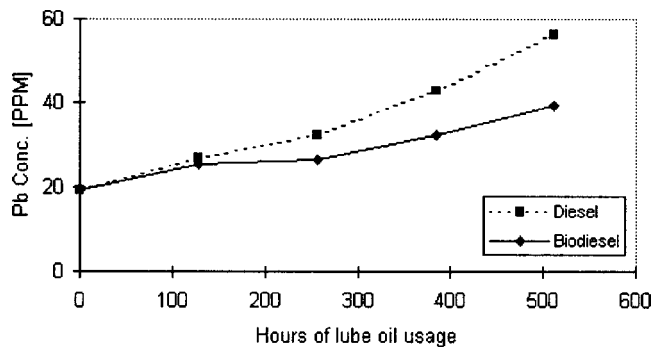


Fig. 15 Lead concentration as a function of lube oil usage

biodiesel-fueled system indicated approximately a 50 percent lower increase in lead content and hence lower wear of lead containing components.

All these observations suggested better additional lubricity properties of biodiesel fuel apart from fuel value, confirming the results of physical wear measurements.

Conclusions

A diesel engine can perform satisfactorily on biodiesel fuel without any engine hardware modifications. Esterification has been found to be an effective technique to prevent all long-term usage problems associated with utilization of vegetable oils such as fuel filter plugging, injector coking, formation of carbon deposits in the combustion chamber, ring sticking, and contamination of lubricating oils. The carbon deposits on piston top and injector coking substantially reduced in 20 percent biodiesel-fueled system.

The wear of various vital parts reduced up to 30 percent because of additional lubricity properties of biodiesel. These results of wear measurements by physical methods were also confirmed by atomic absorption spectroscopy. Oil analysis studies proved to be a powerful tool to estimate not only the condition of the engines, but of other moving parts as well. Moreover, these tests provided valuable and relevant information on the effect of fuel chemistry on the lubricating oil system. Ash content, which mainly represents wear debris, was found to be lesser in the case of a 20 percent biodiesel-fueled system. One of the most interesting studies conducted on the lube oils was for the estimation of individual wear of engine vital parts such as piston, piston rings, cylinder liner, etc. Atomic absorption spectroscopy studies on lube oils indicated that biodiesel fuel led to lesser wear of engine moving parts in terms of lesser amount of metallic debris (such as Fe, Cu, Zn, Mg, Cr, Pb, and Co) present in lube oil samples. Each element, which is present in oil in the form of wear debris, originated from a different moving part. Such an analysis strongly demonstrated that not only the performance characteristics but also wear characteristics of moving parts are better for a 20 percent biodiesel-fueled engine system.

Based on the studies presented, it is concluded that the fuels of bio-origin are superior in wear performance to conventional fuels, environment-friendly, biodegradable, and do not add to global warming problems. Biodiesel can be readily adopted as a substitute fuel to the existing diesel engines, which are widely used in the rural agricultural sector of the country.

Acknowledgments

The authors deeply acknowledge sincere gratitude towards Sh. Attar Singh of Engines and Fuels Laboratory, Center for Energy Studies, IIT, Delhi, for his help and association in conducting the torturous series of experiments. The authors also acknowledge the grant of Senior Research Fellowship by Council for Scientific and Industrial Research, New Delhi, India for conducting research on the above topic.

References

- [1] Krawczyk, T., 1996, "Biodiesel: Alternative Fuel Makes Inroads but Hurdles Remain," *Inform*, 7, No. 8, pp. 801–814.
- [2] Srinivasa, Rao P., and Gopalkrishnan, K. V., 1991, "Vegetable Oils and Their Methyl Esters as Fuels for Diesel Engines," *Indian J. Technol.*, 29, pp. 292–297.
- [3] Kaltschmitt, M., Reinhardt, G. A., and Stelzer, T., 1997, "Life Cycle Analysis of Biofuels Under Different Environmental Aspects," *Biomass Bioenergy*, 12, No. 2, pp. 121–134.
- [4] Korbitz, W., 1999, "Biodiesel Production in Europe and North America, an Encouraging Prospect," *Renewable Energy*, 16, pp. 1078–1083.
- [5] Agarwal, A. K., and Das, L. M., 2000, "Biodiesel Development and Characterization for use as a Fuel in a Compression Ignition Engine," *ASME J. Eng. Gas Turbines Power*, 123, pp. 440–447.
- [6] Agarwal, A. K., 1996, "Performance Evaluation and Emission Characteristics of a Compression Ignition Engine Using Esterified Biodiesel," M.Tech thesis, Center for Energy Studies, Indian Institute of Technology, Delhi (India), p. 82.
- [7] Williamson, A. M., and Badr, O., 1998, "Assessing the Viability of Using Rape Methyl Ester (RME) as an Alternative to Mineral Diesel Fuel for Powering Road Vehicle in the UK," *Appl. Energy*, 59, Nos. 2–3, pp. 187–214.
- [8] Hemmerlein, N., Korte, V., Richter, H., and Schoroder, G., 1991, "Performance, Exhaust Emissions and Durability of Modern Diesel Engines Running on Rapeseed Oil," SAE Technical Paper Series No. 910848, SAE, Warrendale, PA.
- [9] Freedman, B., Bagby, M. O., Callahan, T. J., and Ryan III, T. W. 1990, "Cetane Number of Fatty Esters, Fatty Alcohols and Triglycerides Determined in a Constant Volume Combustion Bomb," SAE Paper 900343.
- [10] Freedman, B., and Bagby, M. O., 1989, "Heats of Combustion of Fatty Esters and Triglycerides," *JAACS*, 66, No. 11, pp. 1601–1605.
- [11] Freedman, B., Butterfield, R. O., and Pryde, E. H., 1986, "Transesterification Kinetics of Soyabean Oil," *JAACS*, 63, No. 10.
- [12] American Biofuel Association, 1994, "Biodiesel: A Technology, Performance and Regulatory Overview," *Information Resources*, Washington, DC.
- [13] Weber, J. A., and Johannes, K., 1996, "Biodiesel Market Opportunity and Potential Barriers," *Liquid Fuels and Industrial Products From Renewable Resources*, J. S. Wnditt et al., eds., Proceedings of the Third Fuel Conference, Sept. 15–17, Nashville, TN, ASAE.
- [14] Agarwal, A. K., 1999, "Performance Evaluation and Tribological Studies on a Biodiesel-Fuelled Compression Ignition Engine," Ph.D. thesis, Center for Energy Studies, Indian Institute of Technology, Delhi (India), p. 344.
- [15] Seventeenth Parliamentary Standing Committee's Report on Vegetable Oils, Government of India, 1995.
- [16] Indian Standard Code IS:10000, Part VIII, 1980, "Methods of Tests for Internal Combustion Engines: Part VIII Performance Tests."

**Errata: “Schlieren Observation of Spark-Ignited Premixed Charge
Combustion Phenomena Using a Transparent Collimating Cylinder Engine”
[ASME J. Eng. Gas Turbines Power, 2003, 125, pp. 336–343]**

K. Kozuka, T. Ozasa, T. Fujikawa, and A. Saito

In the Subscripts section of the Nomenclature (pg. 341), the second item should have appeared as

$c, d = \text{ends of flame}$

Equations (6) through (9), on page 342, should read as follows:

$$Y_{inc} = r_0 \sin \beta_c = Y_{outc} - t_c \sin \gamma_c \quad (6)$$

$$Y_{ind} = r_0 \sin \beta_d = Y_{outd} - t_d \sin \gamma_d \quad (7)$$

$$2r = Y_{inc} - Y_{ind} \quad (8)$$

$$\frac{A_{flame}}{A_{cylinder}} = \frac{2rh}{2r_0h} = \frac{Y_{inc} - Y_{ind}}{2r_0} \quad (9)$$